frontiers | Research Topics

Bioengineering systems for therapeutic and *in vitro* platforms

Edited by
Loredana De Bartolo, Antonella Piscioneri, Dimitrios Stamatialis and Feng-Huei Lin

Published in
Frontiers in Bioengineering and Biotechnology

ISSN 1664-8714
ISBN 978-2-83250-946-3
DOI 10.3389/978-2-83250-946-3

About Frontiers

Frontiers is more than just an open access publisher of scholarly articles: it is a pioneering approach to the world of academia, radically improving the way scholarly research is managed. The grand vision of Frontiers is a world where all people have an equal opportunity to seek, share and generate knowledge. Frontiers provides immediate and permanent online open access to all its publications, but this alone is not enough to realize our grand goals.

Frontiers journal series

The Frontiers journal series is a multi-tier and interdisciplinary set of open-access, online journals, promising a paradigm shift from the current review, selection and dissemination processes in academic publishing. All Frontiers journals are driven by researchers for researchers; therefore, they constitute a service to the scholarly community. At the same time, the *Frontiers journal series* operates on a revolutionary invention, the tiered publishing system, initially addressing specific communities of scholars, and gradually climbing up to broader public understanding, thus serving the interests of the lay society, too.

Dedication to quality

Each Frontiers article is a landmark of the highest quality, thanks to genuinely collaborative interactions between authors and review editors, who include some of the world's best academicians. Research must be certified by peers before entering a stream of knowledge that may eventually reach the public - and shape society; therefore, Frontiers only applies the most rigorous and unbiased reviews. Frontiers revolutionizes research publishing by freely delivering the most outstanding research, evaluated with no bias from both the academic and social point of view. By applying the most advanced information technologies, Frontiers is catapulting scholarly publishing into a new generation.

What are Frontiers Research Topics?

Frontiers Research Topics are very popular trademarks of the *Frontiers journals series*: they are collections of at least ten articles, all centered on a particular subject. With their unique mix of varied contributions from Original Research to Review Articles, Frontiers Research Topics unify the most influential researchers, the latest key findings and historical advances in a hot research area.

Find out more on how to host your own Frontiers Research Topic or contribute to one as an author by contacting the Frontiers editorial office: frontiersin.org/about/contact

Bioengineering systems for therapeutic and *in vitro* platforms

Topic editors

Loredana De Bartolo — National Research Council (CNR), Italy

Antonella Piscioneri — Institute for Membrane Technology, Department of Chemical Sciences and Materials Technologies, National Research Council (CNR), Italy

Dimitrios Stamatialis — University of Twente, Netherlands

Feng-Huei Lin — National Taiwan University, Taiwan

Citation

De Bartolo, L., Piscioneri, A., Stamatialis, D., Lin, F.-H., eds. (2022). *Bioengineering systems for therapeutic and* in vitro *platforms*. Lausanne: Frontiers Media SA.

doi: 10.3389/978-2-83250-946-3

Table of contents

frontiers | Frontiers in Bioengineering and Biotechnology

TYPE Editorial
PUBLISHED 22 November 2022
DOI 10.3389/fbioe.2022.1090317

OPEN ACCESS

EDITED AND REVIEWED BY
Ranieri Cancedda,
Independent Researcher, Genova, Italy

*CORRESPONDENCE
Loredana De Bartolo,
l.debartolo@itm.cnr.it

SPECIALTY SECTION
This article was submitted to Tissue Engineering and Regenerative Medicine, a section of the journal Frontiers in Bioengineering and Biotechnology

RECEIVED 05 November 2022
ACCEPTED 11 November 2022
PUBLISHED 22 November 2022

CITATION
De Bartolo L, Piscioneri A, Stamatialis D and Lin F-H (2022), Editorial: Bioengineering systems for therapeutic and *in vitro* platforms.
Front. Bioeng. Biotechnol. 10:1090317.
doi: 10.3389/fbioe.2022.1090317

Editorial: Bioengineering systems for therapeutic and *in vitro* platforms

Loredana De Bartolo[1]*, Antonella Piscioneri[1], Dimitrios Stamatialis[2,3] and Feng-Huei Lin[4]

[1]National Research Council of Italy, Institute on Membrane Technology, CNR-ITM, Rende, Italy, [2]Advanced Organ Bioengineering and Therapeutics-Technical Medical Center, University of Twente, Enschede, Netherlands, [3]Department of Nephrology- Radboud University Medical Center, Radboud Institute for Molecular Life Sciences, Nijmegen, Netherlands, [4]National Health Research Institute of Biomedical Engineering and Nanomedicine, Zhunan, Taiwan

KEYWORDS

biomimetic interfaces, functional biomaterials, tissue repair, *in vitro* tools, microfluidic devices, disease modelling, drug testing, bioreactor

Editorial on the Research Topic
Bioengineering systems for therapeutic and *in vitro* platforms

The works presented in this editorial provide a wide and multidisciplinary overview of the latest strategies for the realization of bioengineered systems for therapeutic and *in vitro* platforms. These platforms must ensure that the tissue complexity is recapitulated and maintained to provide reliable novel scientific outcomes. The Research Topic covers various strategies for creating permissive environments, where cells can organize according to a proper architecture (Baptista et al., 2021). The use and the realization of alternative cell culture strategies also allows the fine tuning of operational parameters which offers the possibility to mimic tissue physiology and the appropriate cell niche. To accomplish this fundamental task different approaches are applied. The employment of bioactive material promotes cell material interaction at the interface thus boosting the cellular response in terms of adhesion, proliferation and differentiation. Surface functionalization enhances the performance of the tissue engineered construct by tailoring the biomaterial surface with key functional groups and moieties whose presence recapitulate the physiological surrounding. Other approaches involve the development of dynamic systems as bioreactor or chip devices (Piscioneri et al., 2018). The dynamic cell culture microenvironments realized there enhance nutrients transport and waste removal ensuring at the same time a proper supply of gases. The precise set up of these parameters ensure that cells are grown in a very controlled and optimized microenvironment (Morelli et al., 2019). Moreover, dynamic *in vitro* platform devices are quite versatile systems; indeed, their flexible control of different operational setting pave their use for the replication of cellular and extracellular features of different organs and tissue. The versatility of these multifunctional devices allows the expansion of cell types and therefore the investigation of a wide range of tissue districts, disclosing new

insight related to physiological and/or pathological conditions (Morelli et al., 2021). On the basis of these main features these tools can be broadly used for several applications which include the promotion of tissue repair, *in vitro* diseases modelling and preclinical drug screening of potential therapeutic compounds.

The Research Topic summarizes the latest advances in the field of biomimetic therapeutic material and *in vitro* multifunctional platforms that offer an optimal surrounding for cell growth and tissue reconstruction as investigational tools. Original Research articles and case reports from leading experts in their fields highlight the latest exciting achievements referring to the development and application of multifunctional biomaterials and devices in tissue engineering and regenerative medicine.

Recent advances in 3D printing technology have allowed to develop biocompatible materials to be used for repair of tissues and organs as well as for the creation of *in vitro* cellular platforms to establish disease pathogenesis and drug screening model. In this context, Cui et al. developed 3D-printed polylactide cold jackets for laparoscopic complete intracorporeal renal auto transplantation to preserve the renal function of severe renal artery stenosis patients. They presented the first successful application of this concept in the treatment of renal artery stenosis.

A 3D co-culture environment to mimic pathological characteristics of rheumatoid arthritis pannus tissue has been created by Lin et al. This system, based on 3D scaffold constructed by bioprinting technology with synovial fibroblasts, vascular endothelial cells and gelatin/alginate hydrogels, could be suitable for high-throughput drug screening *in vitro* model to evaluate drug efficacy and safety.

The clinical translation of several therapeutic approaches that are at the forefront of scientific and technological innovation, is hindered by the poor predictive capacity of the currently available *in vitro* pathophysiological models. Coentro et al., established an *in vitro* model of skin fibrosis for testing the capacity to decrease collagen synthesis and/or deposition of anti-fibrotic molecules with different mechanisms of action. This study advocated the use of macromolecular crowding and TGFβ 1 in the development of skin fibrosis specific *in vitro* models.

Dynamic devices such as bioreactors show promise in tissue engineering, since they are able to recapitulate the *in vivo* physiological cell environment thanks to a continuous perfusion of gases and nutrients while removing waste products, ensuring the homeostasis of tissue. The study of Yamada et al., emphasized the necessity of optimization of a custom-designed perfusion bioreactor for bone tissue engineering taking into account the key experimental variables to address issues common to perfusion bioreactors for bone tissue engineering.

Within this framework, Ene-Iordache et al. developed a 3D nichoid microenvironment within a miniaturized optically accessible bioreactor housing. There, the combination of the nichoids with the millifluidic bioreactor allows to culture 3D organoids of few millimeters in size under continuous perfusion of the culture medium.

Kumar et al., developed a microfluidic alveolus model to study lung biomechanics. This system consisted of pneumatic and fluidic chambers separated by a thin membrane that supports alveolar epithelial cell culture. The device mimicked strain heterogeneity experienced during alveolar expansion due to breathing and it could serve as a tool to delineate the role of alveolar micromechanics in physiological and pathological outcomes in the lung.

Microfluidic devices are suitable to investigate complex constructs with accurate and controllable environment by high resolution spectroscopies and real-time imaging. A microfluidic platform compatible with advanced widefield- and confocal microscopy was developed to recapitulate an *in vitro* intestinal epithelial barrier for investigating the cellular uptake and cross-barrier transport of biologics (Weller et al.). The microfluidic platform was validated as a suitable model for intestinal drug transport studies by correlating the transport of small molecule drugs to the corresponding human absorption data.

In the context of *in vitro* models, a bioengineered 3D platform based on human intrahepatic cholangiocyte organoids cultured onto polyethersulfone hollow fiber membrane replicated the biological structure and function of native bile ducts (Wang et al.). This platform may be suitable for studying cholangiopathies and therapeutic strategies.

Marzagalli et al. presented an organ-on-chip (OOC)-based approach for recapitulating the immune cell migration under physiological fluid flow. This model was used to study the infiltration within a 3D tumour matrix, and activation against neuroblastoma cancer cells in a fully-humanized, fluid-dynamic, and clinically relevant-sized environment.

In the last years, organoid models using pluripotent stem cells have been implemented for diagnostic and therapeutic utilities. Kakni et al., developed organoids consisting of a simple columnar epithelium patterned into crypt-like and villus-like structures. These organoids reflecting the structural and functional characteristics of the *in vivo* counterparts, could represent a powerful new tool for studies related to diseases, microbiota nutrient absorption and drugs.

In tissue engineering, the impact of the cell type on the degradation of biomaterials has been studied by Boucard et al. They investigated the capacity of primary and immortalized fibroblasts of distinct origins to degrade a fibrin-based biomaterial establishing that fibrin degradation through the secretion of serine protease.

Multifunctional platforms that perform diagnostic functions and serve as responsive biomaterials to tumour microenvironment are encouraging. Sivasubramanian et al., developed a hybrid nanoplatform that harnesses the tumour

microenvironment factors for dual targeted magnetic resonance imaging and assessment of tumour oxygen status by photoacoustic imaging. They reported the fabrication of a novel enzyme responsive T1 magnetic resonance imaging contrast agent that can modulate oxygen in the tumour microenvironment *via* the catalytic conversion of H_2O_2 to O_2.

Peripheral nerve transection is one of the most common peripheral nerve injuries. Although neurons have a limited ability to regenerate, axons have a great potential for regeneration. To find an effective treatment strategy for sciatic nerve injury, Lin et al., explored the protective effect of GDF11 on neurons *in vitro*, and a lentiviral vector to induce GDF11 overexpression with the aim to create and maintain a local microenvironment conducive to nerve regeneration.

In the tissue engineering scenario decellularized matrices are used as natural scaffolds to promote the differentiation of implant cells and tissue remodelling. Owing to the removal of immunogenic components, the decellularized matrix has good biocompatibility and safety, which can be used in autologous, allogeneic, and xenogeneic tissue engineering. Tang et al., investigated the effects of tissue origins on the adipogenic capacity of the decellularized matrix exploring the mechanisms that decellularized adipose-derived matrix promotes adipose tissue formation and provides further insight into tissue specificity, which could be applied in different tissue repair and regeneration.

Finally, Kuan et al., synthesized a sonosensitizer of Eu-doped $CaCO_3$ to combine with low-intensity ultrasound as a non-invasive treatment for the body sculpture for body sculpture. The $CaCO_3$: Eu had good biocompatibility and could produce ROS in adipocytes for lipolysis. The results showed that developed sonosensitizer could effectively inhibit the adipogenesis, after treated with low-intensity ultrasound, without skin burning and charred sounding tissue.

Author contributions

All authors listed have made a substantial, direct, and intellectual contribution to the work and approved it for publication.

Conflict of interest

The authors declare that the research was conducted in the absence of any commercial or financial relationships that could be construed as a potential conflict of interest.

Publisher's note

All claims expressed in this article are solely those of the authors and do not necessarily represent those of their affiliated organizations, or those of the publisher, the editors and the reviewers. Any product that may be evaluated in this article, or claim that may be made by its manufacturer, is not guaranteed or endorsed by the publisher.

References

Baptista, D., Teixeira, L. M., Birgani, Z. T., van Riet, S., Pasman, T., Poot, A., et al. (2021). 3D alveolar *in vitro* model based on epithelialized biomimetically curved culture membranes. *Biomaterials* 266, 120436. doi:10.1016/j.biomaterials.2020.120436

Morelli, S., Piscioneri, A., Curcio, E., Salerno, S., Chen, C.-C., and De Bartolo, L. (2019). Membrane bioreactor for investigation of neurodegeneration. *Mater. Sci. Eng. C* 103, 109793. doi:10.1016/j.msec.2019.109793

Morelli, S., Piscioneri, A., Guarnieri, G., Morelli, A., Drioli, E., and De Bartolo, L. (2021). Anti-neuroinflammatory effect of daidzein in human hypothalamic GnRH neurons in an *in vitro* membrane-based model. *Biofactors* 47, 93–111. doi:10.1002/biof.1701

Piscioneri, A., Ahmed, H. M. M., Morelli, S., Khakpour, S., Giorno, L., Drioli, E., et al. (2018). Membrane bioreactor to guide hepatic differentiation of human mesenchymal stem cells. *J. Memb. Sci.* 564, 832–841. doi:10.1016/j.memsci.2018.07.083

frontiers in Bioengineering and Biotechnology

ORIGINAL RESEARCH
published: 26 October 2021
doi: 10.3389/fbioe.2021.756399

Adapting the Scar-in-a-Jar to Skin Fibrosis and Screening Traditional and Contemporary Anti-Fibrotic Therapies

*João Q. Coentro[1], Ulrike May[2], Stuart Prince[2], John Zwaagstra[3], Olli Ritvos[4], Tero A.H. Järvinen[2,5] and Dimitrios I. Zeugolis[1,6]**

[1]Regenerative, Modular and Developmental Engineering Laboratory (REMODEL) and Science Foundation Ireland (SFI) Centre for Research in Medical Devices (CÚRAM), National University of Ireland Galway (NUI Galway), Galway, Ireland, [2]Faculty of Medicine and Health Technology, Tampere University, Tampere, Finland, [3]Human Health Therapeutics Research Centre, National Research Council Canada, Montreal, QC, Canada, [4]University of Helsinki, Helsinki, Finland, [5]Tampere University Hospital, Tampere, Finland, [6]Regenerative, Modular and Developmental Engineering Laboratory (REMODEL), Charles Institute of Dermatology, Conway Institute of Biomolecular and Biomedical Research and School of Mechanical and Materials Engineering, University College Dublin (UCD), Dublin, Ireland

Skin fibrosis still constitutes an unmet clinical need. Although pharmacological strategies are at the forefront of scientific and technological research and innovation, their clinical translation is hindered by the poor predictive capacity of the currently available *in vitro* fibrosis models. Indeed, customarily utilised *in vitro* scarring models are conducted in a low extracellular matrix milieu, which constitutes an oxymoron for the in-hand pathophysiology. Herein, we coupled macromolecular crowding (enhances and accelerates extracellular matrix deposition) with transforming growth factor β1 (TGFβ1; induces trans-differentiation of fibroblasts to myofibroblasts) in human dermal fibroblast cultures to develop a skin fibrosis *in vitro* model and to screen a range of anti-fibrotic families (corticosteroids, inhibitors of histone deacetylases, inhibitors of collagen crosslinking, inhibitors of TGFβ1 and pleiotropic inhibitors of fibrotic activation). Data obtained demonstrated that macromolecular crowding combined with TGFβ1 significantly enhanced collagen deposition and myofibroblast transformation. Among the anti-fibrotic compounds assessed, trichostatin A (inhibitors of histone deacetylases); serelaxin and pirfenidone (pleiotropic inhibitors of fibrotic activation); and soluble TGFβ receptor trap (inhibitor of TGFβ signalling) resulted in the highest decrease of collagen type I deposition (even higher than triamcinolone acetonide, the gold standard in clinical practice). This study further advocates the potential of macromolecular crowding in the development of *in vitro* pathophysiology models.

Keywords: *In vitro* tools, drug testing, disease modelling, macromolecular crowding, fibrosis, anti-fibrotic molecules

OPEN ACCESS

Edited by:
Loredana De Bartolo, National Research Council (CNR), Italy

Reviewed by:
Sourabh Ghosh, Indian Institute of Technology Delhi, India
Abhigyan Satyam, Harvard Medical School, United States

****Correspondence:***
Dimitrios I. Zeugolis
dimitrios.zevgolis@ucd.ie

Specialty section:
This article was submitted to Tissue Engineering and Regenerative Medicine, a section of the journal Frontiers in Bioengineering and Biotechnology

Received: *10 August 2021*
Accepted: *11 October 2021*
Published: *26 October 2021*

Citation:
Coentro JQ, May U, Prince S, Zwaagstra J, Ritvos O, Järvinen TAH and Zeugolis DI (2021) Adapting the Scar-in-a-Jar to Skin Fibrosis and Screening Traditional and Contemporary Anti-Fibrotic Therapies. Front. Bioeng. Biotechnol. 9:756399. doi: 10.3389/fbioe.2021.756399

Abbreviations: αSMA, α smooth muscle actin; ACVR2B, Activin IIB receptor inhibitor; ANOVA, Analysis of variance; BAPN, β-aminopropionitrile; DF, Dermal fibroblasts; DAPI, 4,6-diamidino-2-phenylindole; DMEM, Dulbecco's Modified Eagle's Medium; DSC, Differential scanning calorimetry; DxS, Dextran sulphate; ECM, Extracellular matrix; EDTA, Ethylenediaminetetraacetic acid; EMT, Epithelial–mesenchymal transition; FBS, Foetal bovine serum; GDF-8/11, Growth differentiation factor-8/11; HDACs, class I and II mammalian histone deacetylases; LOX, Lysyl oxidase; MMC, Macromolecular crowding; MSTN/GDF-8, Myostatin; PBS, Phosphate buffered saline; Pirf, Pirfenidone; RLX-2, Recombinant human relaxin-2 (Serelaxin); SDS-PAGE, Sodium dodecyl sulphate-polyacrylamide gel electrophoresis; Smad 2/3, Small mothers against decapentaplegic protein 2/3; T22d35, T122bt, TGFβ type II receptor-based trap; TAC, Triamcinolone acetonide; TBS, Tris-buffered saline; TGFβ1, Transforming growth factor β1; TSA, Trichostatin A.

INTRODUCTION

Skin fibrosis is characterised by the formation of excessive fibrous connective tissue, which leads to alteration of the architecture of the dermis and compromises skin's function and mechanical properties (Coentro et al., 2018). Skin fibrosis manifests either locally (after skin wounding) or systemically (as a result of autoimmune skin disease), with clinical outcomes ranging from small cosmetic imperfections to functional impairment. Skin fibrosis affects over 100 million patients every year (Sund and Arrow, 2000) and is associated with annual healthcare expenditure in excess of US$ 12 billion in the US alone (Griffin et al., 2020).

Fibrosis and skin wound-related scarring are complex, multi-stage (inflammatory, proliferative and remodelling) processes, involving numerous cells, molecules and signalling pathways (Zeng et al., 2011). The key feature in fibrosis formation is the transformation of normal fibroblasts to myofibroblasts, which are contraction capable cells and responsible for scar and fibrosis formation in different diseases (Schulz et al., 2018; Pakshir et al., 2020). *De novo* expression of α smooth muscle actin (αSMA), a marker of late stage myofibroblast transformation (Pakshir et al., 2020), is ultimately associated with fibrosis. Biological (e.g., transforming growth factor β1, TGFβ1) and biophysical (e.g., mechanical stress (Seo et al., 2020)) stimuli trigger fibroblast transition into myofibroblast lineage (Hinz et al., 2012), which is associated with the establishment of several characteristic hallmarks of fibrosis, such as atypical collagen synthesis and deposition, alterations in collagen type I/III ratio and distorted extracellular matrix (ECM) architecture (Jarvinen and Ruoslahti, 2010; Henderson et al., 2020; Pakshir et al., 2020).

Anti-fibrotic therapeutics are the first line of defence in scar-wars (Jarvinen and Ruoslahti, 2010; Desallais et al., 2014). Different classes of molecules have been assessed over the years, largely classified as: corticosteroids; inhibitors of histone deacetylases, collagen crosslinking and deposition, TGFβ signalling or pleiotropic fibrotic activation (**Supplementary Table S1**). Unfortunately, the development of anti-fibrotic approaches has been hindered by side effects encountered. For example, TGFβ inhibitors may compromise immunity and induce autoimmune diseases (Henderson et al., 2020). Other potential factors that have further limited the development of anti-fibrotic therapies include the use of time consuming and low throughput and specificity (due to genetic, epigenetic, immune status and physiological differences between humans and animals) *in vivo* models that fail to recapitulate human disease states and effectively screen potential drugs (Padmanabhan et al., 2019). *In vitro* models have their share of shortcomings (**Supplementary Table S2**). For example, the low ECM levels present in many traditional *in vitro* models (an oxymoron for a fibroplasia model) is liable for cell genetic and epigenetic drift and restrains/inhibits cell-ECM interactions and paracrine signalling cascades, resulting in failure of the models to predict *in vitro* relevant *in vivo* toxicity of the under investigation molecules (Chen et al., 2009).

Macromolecular crowding (MMC), a biophysical technique based on volume exclusion effect, accelerates the enzymatic conversion of water-soluble procollagen to insoluble collagen resulting in enhanced and accelerated collagen type I and associated ECM deposition (Raghunath and Zeugolis, 2021; Tsiapalis and Zeugolis, 2021; Zeugolis, 2021). In 2009, the first pathophysiologically relevant *in vitro* fibrosis model (termed *Scar-in-the-Jar*) was published that utilised the principles of MMC (to enhance and accelerate ECM deposition) and TGFβ1 (to induce myofibroblast transformation of WI-38 lung fibroblasts) (Chen et al., 2009). Since then, several fibrotic models based on MMC have been developed for screening anti-fibrotics in different fibrotic diseases (e.g., dermal (Fan et al., 2019; Fan et al., 2020), lung (Good et al., 2019; Rønnow et al., 2020), vocal fold (Graupp et al., 2015; Graupp et al., 2018) scarring). Unfortunately, these dermal scar models might be incomplete as the optimal crowding molecule was not used (Chen et al., 2009). Although MMC agents, such as Ficoll® (Fan et al., 2019) and polyvinylpyrrolidone (Rashid et al., 2014), have been used as crowding agents, dextran sulphate has demonstrated pro-fibrotic potency by transforming corneal fibroblasts to myofibroblasts (Kumar et al., 2015), possibly due to its binding and releasing capacity of growth factors, such as TGFβ1 (Walton, 1952; Logeart-Avramoglou et al., 2002; Maire et al., 2005).

Considering the above, herein, we first modified and adopted the *Scar-in-the-Jar* model (Chen et al., 2009; Stebler and Raghunath, 2021) for skin fibrosis by using dextran sulphate as MMC agent, primary dermal fibroblasts as tissue-specific cell population and TGFβ1 to induce their myofibroblast trans-differentiation (**Supplementary Figure S1**). We then assessed the model's anti-fibrotic screening potential (through collagen deposition and cell metabolic activity, DNA concentration and viability) by using different anti-fibrotic compounds (corticosteroids: Triamcinolone acetonide, TAC; inhibitors of histone deacetylases: Trichostatin A, TSA; inhibitors of collagen crosslinking: β-aminopropionitrile, BAPN; inhibitors of TGFβ signalling: soluble TGFβ type II receptor-based 2 traps, recombinant proteins T22d35 and T122bt and an activin IIB receptor inhibitor, ACVR2B; and pleiotropic inhibitors of fibrotic activation: Serelaxin, RLX-2 and Pirfenidone, Pirf).

MATERIALS AND METHODS

Materials

All labware were obtained from Sarstedt (Ireland) and Thermo Fisher Scientific (Ireland) and all chemicals and reagents were purchased from Sigma-Aldrich (Ireland), unless stated otherwise.

Recombinant Protein Production, Purification and Analysis

A TGFβ type II receptor-based (TβRII)2, single-chain trap was designed, termed T22d35, where two TβRII ligand binding domains are separated by a 35 amino acid long native linker (Zwaagstra et al., 2012). In addition, we also created a heterovalent trap, termed T122bt, where the TβRI domain was added to two TβRII ligand binding domains separated by a 60

amino acid long native linker (O'Connor-Mccourt et al., 2013) (**Supplementary Figure S2**). Both TGFβ traps were expressed in a mammalian expression system, purified by chromatography and characterized in detail. TGFβ neutralisation curves were plotted, and the determined IC_{50}-values were tabulated (**Supplementary Table S3**).

Cell Culture and Fibrotic Model Induction

Normal adult dermal fibroblasts (DF, PCS-201-012, ATCC, United States) were routinely sub-cultured and used between passages 3 and 6, with DMEM supplemented with 10% FBS and 1% penicillin/streptomycin; media were changed every 2–3 days. For the various experiments, cells were cultured at 25,000 cells/cm^2 and allowed to attach for 24 h, after which the culture media were changed to media containing 100 μM L-ascorbic acid 2-phosphate sesquimagnesium salt hydrate, 100 μg/ml 500 kDa Dextran Sulphate (DxS), 5 ng/ml TGFβ1 and in combination with or without the following anti-fibrotic substances: BAPN (Acros Organics, Belgium, 0.1, 0.25, 0.5 and 1 mM) and TAC (0.025, 0.050, 0.1 and 0.2 mM) were dissolved in sterile 20% dimethyl sulfoxide solution and then were added into the media; TSA (0.5, 1, 2 and 5 μM), RLX-2 (5, 10, 25 and 50 nM), Pirf (0.25, 0.5, 1 and 1.5 mM) ACVR2B (5, 10, 25 and 50 nM), T22d25 (25, 50, 100 and 200 nM) and T122bt (25, 50, 100 and 200 nM) were dissolved in supplemented media. Tested drug concentrations for different anti-fibrotic molecules were based on previously published data. From the review of the literature we chose reported concentration ranges that proved to have a therapeutic effect *in vitro* (1–20 μM for TAC (Cancela and Rebut-Bonneton, 1987; Carroll et al., 2002; Yang et al., 2018); 0.1–1 μM for TSA (Rombouts et al., 2002; Ghosh et al., 2007; Chen et al., 2009); 5–17 nM for RLX-2 (Unemori and Amento, 1990; Unemori et al., 1992; Samuel et al., 2003); 0.5–5.4 mM for Pirf (Saito et al., 2012; Hall et al., 2018; Wells and Leung, 2020); ~IC50 TGFβ neutralising values of 2.5–8.2 nM for T22d35 and T122bt (Zwaagstra et al., 2012; O'Connor-Mccourt et al., 2013), which were also used for ACVR2B; and 0.1–1 mM for BAPN (Redden and Doolin, 2003; Péterszegi et al., 2008; Chen et al., 2009)). The anti-fibrotic substances were added to the culture media only once. Supplemented media were changed every 3 days and cells were analysed at the appropriate time points.

SDS-PAGE Analysis

Cell layers were analysed by SDS-PAGE as described elsewhere (Capella-Monsonís et al., 2018). Briefly, culture media were aspirated, cell layers were washed with PBS and digested with 0.1 mg/ml pepsin solution (porcine gastric mucosa, 3,500–4,200 U/mg) in 0.5 M acetic acid. The cell layers were then scraped, neutralised with 1 M NaOH, denatured at 95°C and resolved under non-reducing conditions using in-house resolving and stacking polyacrylamide gels (5 and 3% respectively) on a Mini-Protean 3 (Bio-Rad Laboratories, United Kingdom) system. Purified collagen type I (Symatese, France) was used as standard. Samples were stained using a SilverQuest™ Silver Staining Kit (Invitrogen, Ireland) according to the manufacturer's instructions. Densitometric analysis was performed on α1(I), α2(I), β11(I), β12(I) or γ(I) bands, as appropriate, using ImageJ software (NIH, United States).

Immunocytochemistry Analysis

Cells layers were washed with PBS, fixed with 4% paraformaldehyde and permeabilised with 0.25% Triton X-100. Cells layers were then blocked with 5% donkey serum in PBS for 1 h at room temperature and incubated with primary antibodies [rabbit α-human collagen type I 1:300: PA2140-2 (Boosterbio, United States); mouse α-human αSMA 1:300: ab7817 (Abcam, United Kingdom)] for a minimum of 90 min at room temperature. Cell layers were then washed 3 times with PBS and incubated with appropriate secondary antibodies (Alexa Fluor™ 594 donkey anti-rabbit 1:500: R37119 or Alexa Fluor™ 488 donkey anti-mouse 1:400: R37114; both from Thermo Fisher Scientific, United States) for 60 min. Cell nuclei were counterstained with 4,6-diamidino-2-phenylindole (DAPI) for 5 min and washed 3 times with PBS. Cells layers were then imaged with an inverted fluorescence microscope (Olympus IX-81, Olympus Corporation, Japan) and further processed with ImageJ software (NIH, United States).

DNA Concentration Analysis

Cell proliferation was assessed using the Quant-iT™ PicoGreen™ dsDNA Assay Kit for quantifying DNA concentration (Invitrogen, United States) as per the manufacturer's instructions. Briefly, cells were washed with PBS, ultrapure water was added and three cycles of freezing and thawing to promote cell lysis were followed. DNA standards of known concentrations were prepared, both samples and standards were mixed with Tris-HCl-Ethylenediaminetetraacetic acid (EDTA) buffer and PicoGreen™ reagent and incubated in dark. Fluorescence was measured at 480 nm excitation and 520 nm emission with a Varioskan Flash Spectral scanning multimode reader (Thermo Fisher Scientific, United States).

Metabolic Activity Analysis

Cell metabolic activity was assessed using the alamarBlue® assay (ThermoFisher Scientific, United States) as per the manufacturer's instructions. Briefly, cells were washed with PBS and incubated with a 10% alamarBlue® solution in PBS for 3 h at 37°C in a humidified atmosphere of 5% CO_2. Absorbance was then measured at 550 and 595 nm with a Varioskan Flash Spectral scanning multimode reader (Thermo Fisher Scientific, United States). Cell metabolic activity was expressed as percentage reduction of the alamarBlue® dye and normalised by the respective quantity of DNA and to the non-treated control.

Viability Analysis

Calcein AM (live cell marker) and ethidium homodimer I (dead cell marker) stainings were used to assess the influence of MMC, TGFβ1 and anti-fibrotic molecule supplementation on cell viability. Briefly, at each time point, cells were carefully washed with PBS and incubated with a solution of calcein AM (4 μM) and ethidium homodimer I (2 μM) in PBS for 30 min at 37°C in a humidified atmosphere of 5% CO_2. Afterwards, cells

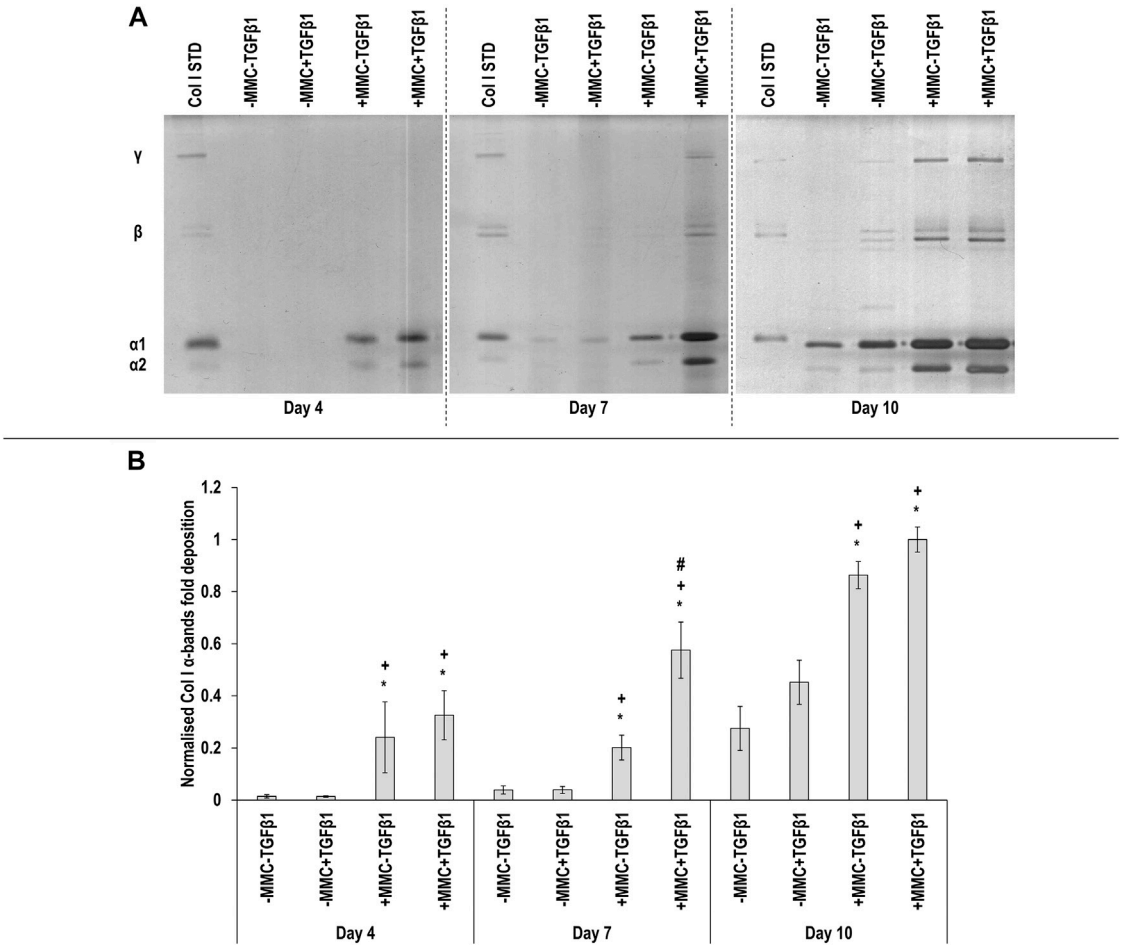

FIGURE 1 | Macromolecular crowding and TGFβ1 increase collagen deposition. Adult dermal fibroblasts were cultured in the presence of dextran sulphate and TGFβ1 for up to 10 days. SDS-PAGE **(A)** and densitometry of α(I)1 and α(I)2 bands **(B)** analyses revealed that MMC increased collagen type I deposition and MMC coupled with TGFβ1 increased further collagen type I deposition. Col I STD: 0.1 mg/ml. One-way ANOVA and Tukey's post-hoc analysis for pairwise comparisons were conducted. *: $p < 0.05$ indicates a statistically significant difference when compared to the negative control (-MMC-TGFβ1) of the respective time point. +: $p < 0.05$ indicates a statistically significant difference when compared to the -MMC+TGFβ1 group of the respective time point. #: $p < 0.05$ indicates a statistically significant difference when compared to the +MMC-TGFβ1 group of the respective time point. $n = 3$.

were imaged with an inverted fluorescence microscope Olympus IX-81 (Olympus Corporation, Japan), using the FITC filter for calcein AM and the Texas Red filter for ethidium homodimer.

Statistical Analysis

Statistical evaluation of the data was performed using the statistical program MiniTab® version 17 (Minitab Inc., United States). All data are expressed as mean values ± standard deviations. Datasets were assessed for normal distribution (Anderson-Darling) and equal variance (Levene's test for homogeneity of variances). When the assumptions of parametric analysis were confirmed, one-way analysis of variance (ANOVA) was used for multiple comparisons and Tukey's post hoc test was used for pairwise comparisons. When either or both assumptions were violated, non-parametric analysis was conducted using Kruskall-Wallis test for multiple comparisons and Mann-Whitney U test for pairwise comparisons. Statistical significance was accepted at $p < 0.05$.

RESULTS

Fibrotic Model Establishment

SDS-PAGE (**Figure 1A**) and complementary densitometry analysis of collagen type I α(I)1 and α(I)2 bands (**Figure 1B**) made apparent that at day 4 and day 7 almost no collagen was deposited in the control and the TGFβ1 groups, whilst MMC groups significantly ($p < 0.05$) increased collagen deposition at all time points, which was further increased ($p < 0.05$) with +MMC+TGFβ1 at day 7. Densitometry analysis also showed a significant increase ($p < 0.05$) of β11(I), β12(I) dimers for the +MMC+TGFβ1 group at day 4 and day 7 (**Supplementary**

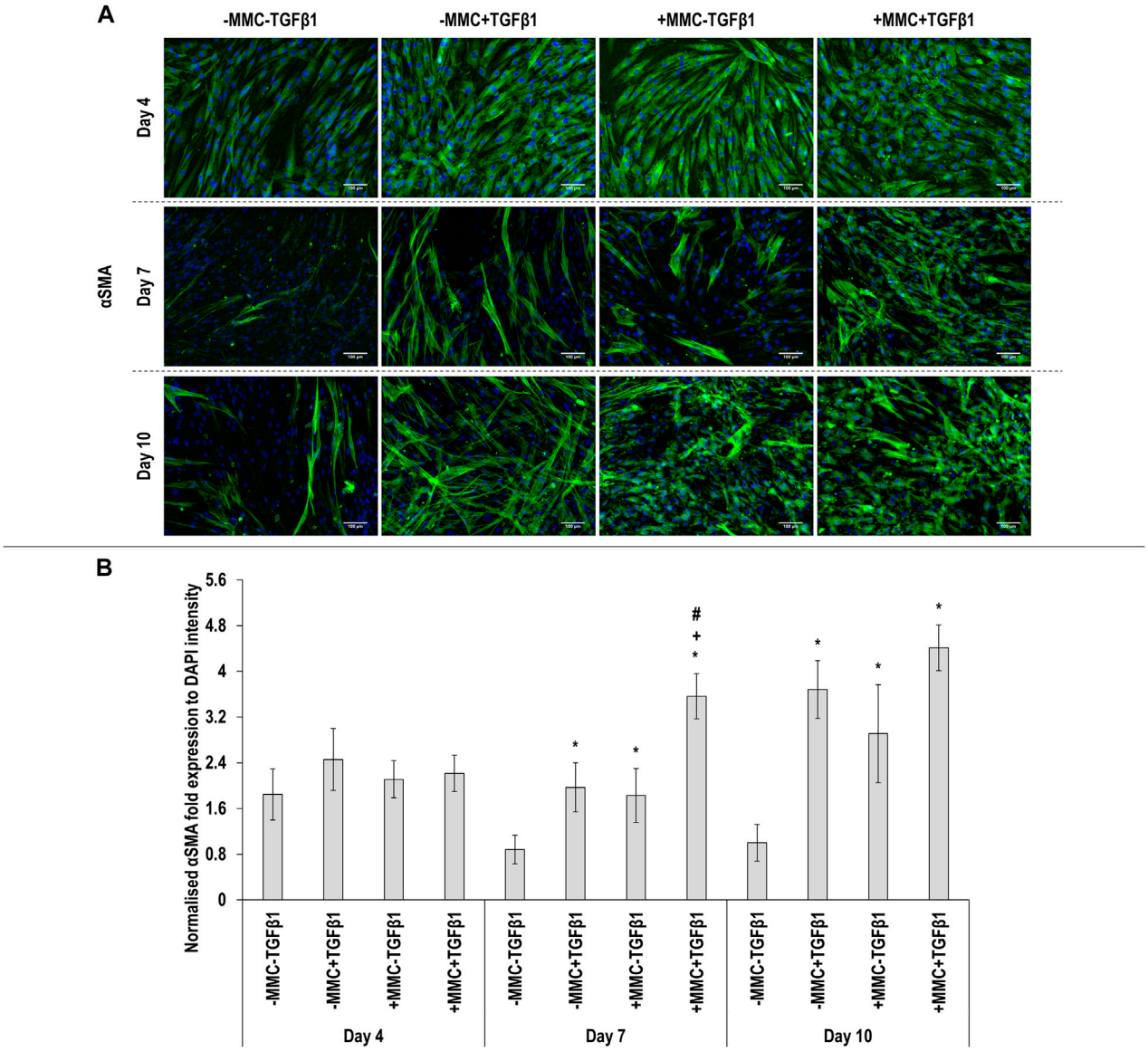

FIGURE 2 | Macromolecular crowding and TGFβ1 increase αSMA expression. Immunocytochemistry **(A)** and image intensity analysis for αSMA **(B)** revealed no differences in αSMA expression between the groups at day 4; the +MMC+TGFβ1 group induced the highest αSMA expression at day 7; the -MMC-TGFβ1 group induced the lowest αSMA expression at day 10. One-way ANOVA and Tukey's post-hoc comparison test or Kruskal Wallis and Mann Whitney post-hoc analyses were conducted. *: $p < 0.05$ indicates a statistically significant difference when compared to the negative control (-MMC-TGFβ1) of the respective time point. +: $p < 0.05$ indicates a statistically significant difference when compared to the -MMC+TGFβ1 group of the respective time point. #: $p < 0.05$ indicates a statistically significant difference when compared to the +MMC-TGFβ1 group of the respective time point. $n = 3$.

Figure S3A) and of γ(I) trimers for the +MMC+TGFβ1 group at day 4 and day 10 (**Supplementary Figure S3B**).

Immunocytochemistry (**Figure 2A** for αSMA and **Figure 3A** for collagen type I) analysis made apparent that when the cells were cultured with +MMC+TGFβ1, clear stress fibres were observed and the collagen fibres were aligned parallel to the stress fibres, albeit collagen type I deposition showed a granular pattern when MMC was used, whilst in its absence, a meshwork architecture was evidenced. Complementary image intensity (**Figure 2B** for αSMA and **Figure 3B** for collagen type I) analyses revealed that, in comparison to the control, the addition of TGFβ1 resulted in a significant ($p < 0.05$) increase in αSMA expression at day 7 and day 10 and collagen type I deposition at day 4. MMC resulted in a significant ($p < 0.05$) increase compared to the control for both molecules in almost all time points. This was also observed for +MMC+TGFβ1, which led to an even greater ($p < 0.05$) increase in αSMA at day 7 and collagen I at day 4.

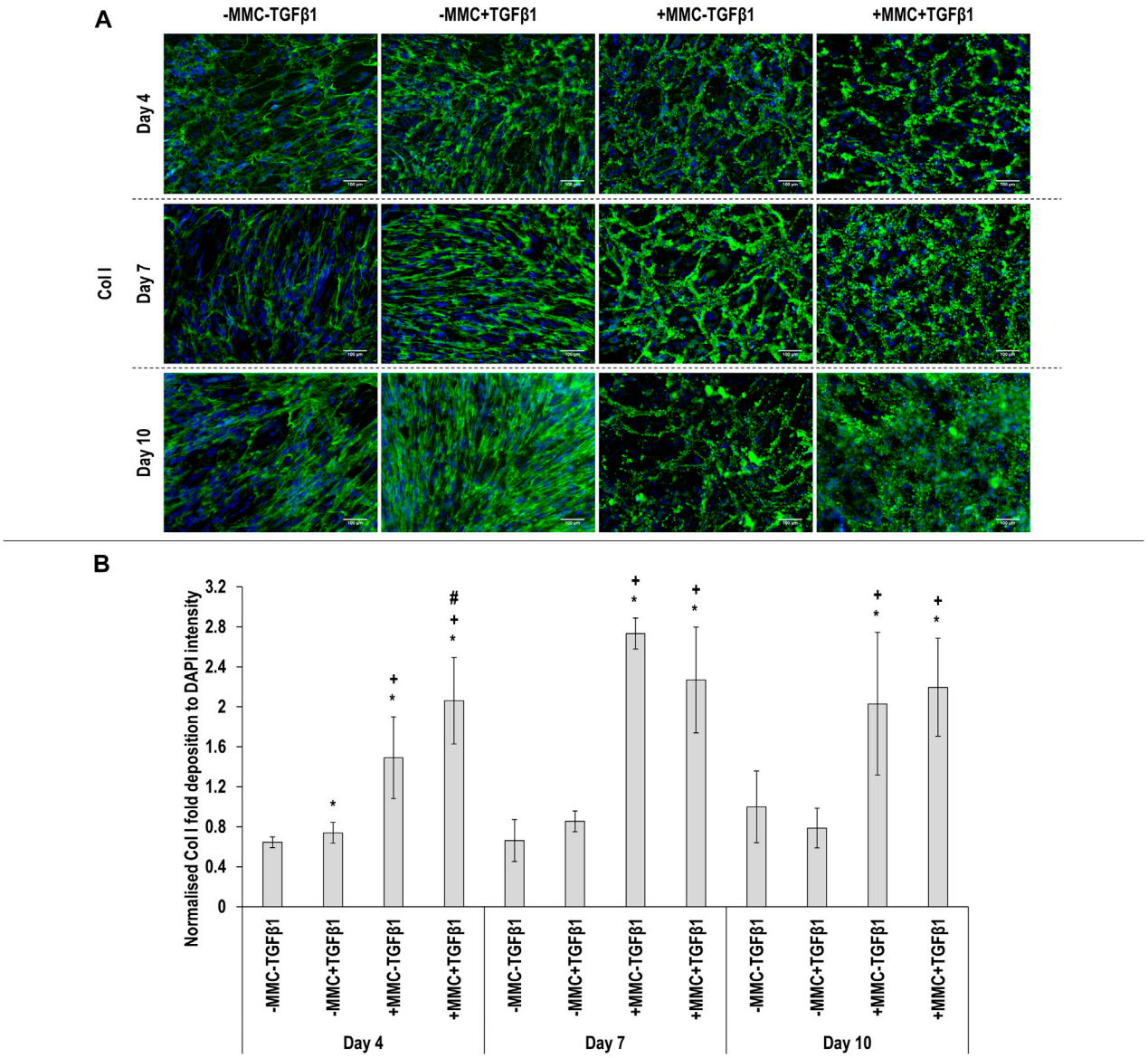

FIGURE 3 | Macromolecular crowding and TGFβ1 increase collagen deposition. Immunocytochemistry **(A)** and image intensity analysis for collagen type I **(B)** revealed that the +MMC-TGFβ1 and +MMC+TGFβ1 groups induced the highest collagen deposition at all time points. One-way ANOVA and Tukey's post-hoc comparison test or Kruskal Wallis and Mann Whitney post-hoc analyses were conducted. *: $p < 0.05$ indicates a statistically significant difference when compared to the negative control (-MMC-TGFβ1) of the respective time point. +: $p < 0.05$ indicates a statistically significant difference when compared to the -MMC+TGFβ1 group of the respective time point. #: $p < 0.05$ indicates a statistically significant difference when compared to the +MMC-TGFβ1 group of the respective time point. $n = 3$.

Screening of Anti-Fibrotic Molecules in the *in vitro* Fibrotic Model

SDS-PAGE (**Figure 4A**) and densitometry analysis of α(I)1 and α(I)2 bands (**Figure 4B**) revealed that all TAC concentrations resulted in significant ($p < 0.05$) decrease of α(I)1 and α(I)2 chains deposition at day 7 and day 10, when compared to the +MMC+TGFβ1 group at the respective time point. No significant ($p < 0.05$) differences in the deposition of β11(I), β12(I) dimers (**Supplementary Figure S4A**) and γ(I) trimers (**Supplementary Figure S4B**) were observed. At day 7 the +MMC+TGFβ1+TAC groups exhibited significantly ($p < 0.05$) higher and at day 10 significantly ($p < 0.05$) lower DNA concentration than the +MMC+TGFβ1 group (**Supplementary Figure S5A**). At day 4 and 7 almost all the +MMC+TGFβ1+TAC groups exhibited significantly ($p < 0.05$) lower and at day 10 significantly ($p < 0.05$) higher metabolic activity than the +MMC+TGFβ1 group (**Supplementary Figure S5B**).

SDS-PAGE (**Figure 5A**) and densitometry of α(I)1 and α(I)2 bands (**Figure 5B**) analyses revealed that all TSA concentrations in +MMC+TGFβ1 at day 7 and the 1, 2.5 and 5 μM TSA

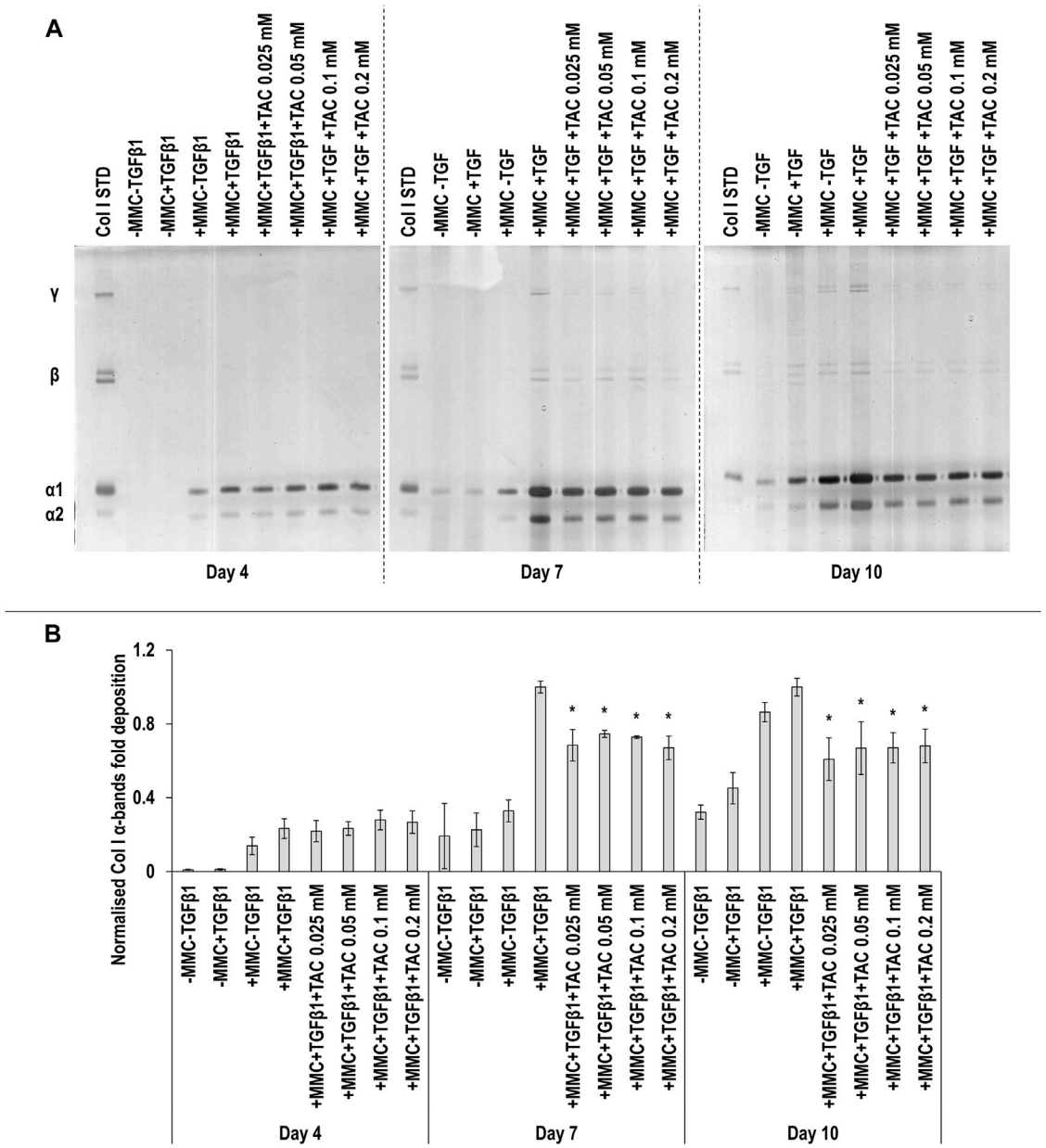

FIGURE 4 | TAC moderately reduces collagen deposition. All TAC concentrations resulted in reduced collagen deposition at day 7 and day 10, in comparison to +MMC+TGFβ1 group, as judged by SDS-PAGE **(A)** and densitometry of α(I)1 and α(I)2 bands analyses **(B)**. Col I STD: 0.1 mg/ml. One-way ANOVA and Tukey's post-hoc comparison tests were conducted. *: $p < 0.05$ denotes a significant difference when compared to the +MMC+TGFβ1 group of the respective time point. $n = 3$.

concentrations in +MMC+TGFβ1 at day 10 resulted in significant ($p < 0.05$) decrease of α(I)1 and α(I)2 chains deposition, when compared to the +MMC+TGFβ1 group at the respective time point. The 2.5 and 5 μM TSA concentrations in +MMC+TGFβ1 at day 7 and all concentrations of TSA in +MMC+TGFβ1 at day 10 resulted in significant ($p < 0.05$) decrease of β11(I), β12(I) dimers (**Supplementary Figure S6A**) and γ(I) trimers deposition (**Supplementary Figure S6B**). The 1, 2.5 and 5 μM TSA concentrations in +MMC+TGFβ1 resulted in significant ($p < 0.05$) reduction of DNA concentration at day 4 and the 2.5 and 5 μM TSA concentrations in +MMC+TGFβ1 resulted in significant ($p < 0.05$) reduction of DNA concentration at day 7 and day 10, all in comparison to the +MMC+TGFβ1 group (**Supplementary Figure S7A**). The 0.5 and 2.5 μM TSA concentrations in +MMC+TGFβ1 resulted in significant ($p < 0.05$) reduction of metabolic activity at day 7 in comparison to the +MMC+TGFβ1 group (**Supplementary Figure S7B**).

SDS-PAGE (**Figure 6A**) and densitometry analysis of α(I)1 and α(I)2 (**Figure 6B**), β11(I), β12(I) (**Supplementary Figure S8A**) and γ(I) bands (**Supplementary Figure S8B**) revealed that

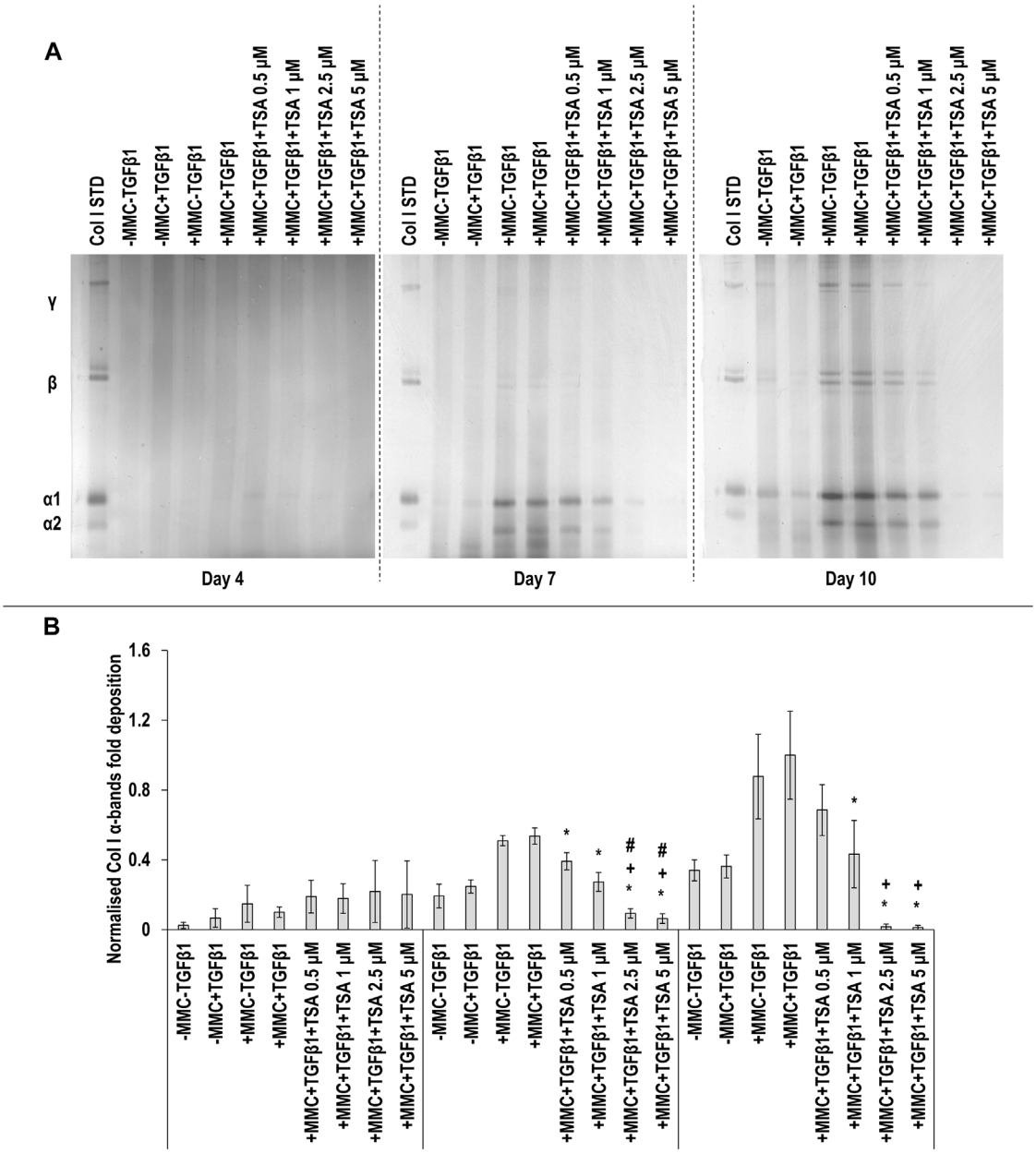

FIGURE 5 | High concentrations of TSA reduce collagen deposition. The 2.5 and 5 µM TSA concentrations in +MMC+TGFβ1 at day 7 and day 10 induced the lowest collagen deposition in comparison to +MMC+TGFβ1 group, as revealed by SDS-PAGE **(A)** and densitometry of α(I)1 and α(I)2 bands **(B)**. Col I STD: 0.1 mg/ml. One-way ANOVA and Tukey's post-hoc comparison tests were conducted. *: $p < 0.05$ indicates a statistically significant difference when compared to the +MMC+TGFβ1 group of the respective time point. +: $p < 0.05$ indicates a statistically significant difference when compared to the +MMC+TGFβ1+TSA 0.5 µM group of the respective time point. #: $p < 0.05$ indicates a statistically significant difference when compared to the +MMC+TGFβ1+TSA 1 µM group of the respective time point. n = 3.

all RLX-2 concentrations in +MMC+TGFβ1 at all time points resulted in a significant ($p < 0.05$) decrease of the deposition of α(I)1 and α(I)2, β11(I), β12(I) and γ(I) components, when compared to the +MMC+TGFβ1 group at the respective time point. At day 7, all concentrations of RLX-2 in +MMC+TGFβ1 resulted in significant ($p < 0.05$) increase of DNA concentration in comparison to the +MMC+TGFβ1 group (**Supplementary Figure S9A**). At day 7, all concentrations of RLX-2 in +MMC+TGFβ1 resulted in significant ($p < 0.05$) decrease of metabolic activity in comparison to the +MMC+TGFβ1 group (**Supplementary Figure S9B**).

SDS-PAGE (**Figure 7A**) and densitometry analysis of α(I)1 and α(I)2 bands (**Figure 7B**) revealed that all Pirf concentrations at day 4, the 1 and 1.5 mM Pirf concentrations at day 7 and all Pirf concentrations at day 10, all in +MMC+TGFβ1, resulted in significant ($p < 0.05$)

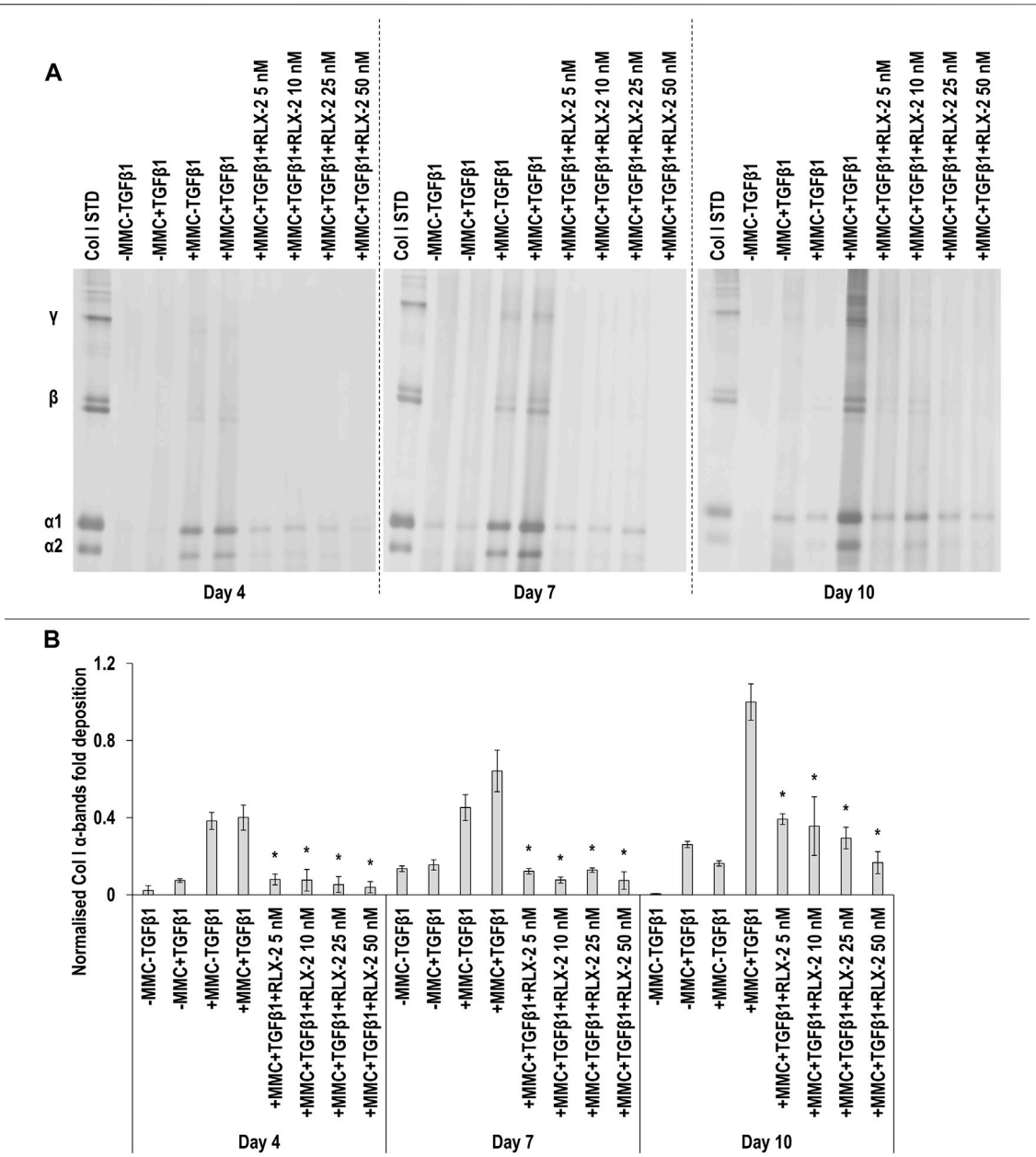

FIGURE 6 | RLX-2 reduces collagen deposition at all time points. All RLX-2 concentrations in +MMC+TGFβ1 at all time points resulted in significant ($p < 0.05$) decrease of collagen deposition, as judged by SDS-PAGE **(A)** and densitometry analysis of α(I)1 and α(I)2 bands **(B)**. Col I STD: 0.1 mg/ml. One-way ANOVA and Tukey's post-hoc comparison tests were conducted. *: $p < 0.05$ indicates a statistically significant difference when compared to the +MMC+TGFβ1 group of the respective time point. $n = 3$.

decrease of α(I)1 and α(I)2 chains deposition, all when compared to the +MMC+TGFβ1 group. The 1 mM and the 1.5 mM Pirf concentrations at day 7 and all Pirf concentrations at day 10, all in +MMC+TGFβ1, resulted in a significant ($p < 0.05$) decrease of β11(I), β12(I) dimer deposition, all when compared to the +MMC+TGFβ1 group (**Supplementary Figure S10A**). All Pirf concentrations at day 4 and 10, all in +MMC+TGFβ1, resulted in a significant ($p < 0.05$) decrease of γ(I) trimer deposition, all when compared to the +MMC+TGFβ1 group (**Supplementary Figure S10B**). The 1.5 mM Pirf concentration in +MMC+TGFβ1 resulted in a significant ($p < 0.05$) decrease of DNA concentration at day 4 and day 7, when compared to +MMC+TGFβ1 group (**Supplementary Figure S11A**). The 1.5 mM Pirf concentration in +MMC+TGFβ1 resulted in significant ($p < 0.05$) increase of metabolic activity at day 4 and day 7, when compared to +MMC+TGFβ1 group (**Supplementary Figure S11B**).

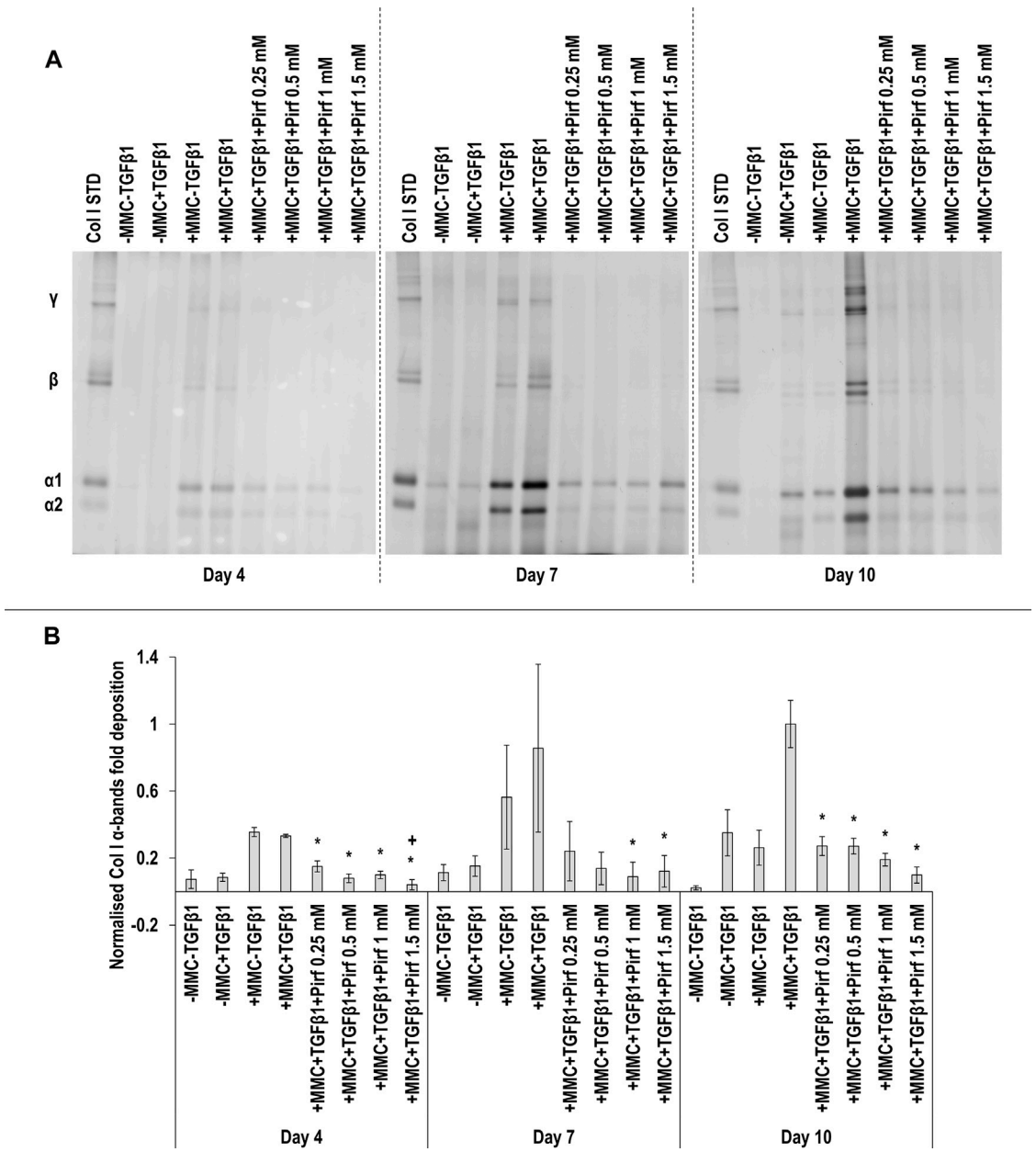

FIGURE 7 | Pirf reduces collagen deposition. The 1 and 1.5 mM Pirf concentrations in +MMC+TGFβ1 resulted in significant decrease of collagen deposition, as judged by SDS-PAGE **(A)** and densitometry analysis of α(I)1 and α(I)2 bands. Col I STD: 0.1 mg/ml. One-way ANOVA and Tukey's post-hoc comparison tests were conducted. *: $p < 0.05$ indicates a statistically significant difference when compared to the +MMC+TGFβ1 group of the respective time point. +: $p < 0.05$ indicates a statistically significant difference when compared to the +MMC+TGFβ1+Pirf 0.25 mM group of the respective time point. $n = 3$.

SDS-PAGE (**Figure 8A**) and densitometry analysis of α(I)1 and α(I)2 bands (**Figure 8B**) revealed that all T122bt concentrations in +MMC+TGFβ1 at day 4 and day 7 and the 250 nM T122bt concentration in +MMC+TGFβ1 at day 10 significantly ($p < 0.05$) reduced α(I)1 and α(I)2 chains deposition. Further densitometry analysis of β11(I), β12(I) bands (**Supplementary Figure S12A**) revealed that all T122bt concentrations in +MMC+TGFβ1 at day 4 and day 7 and the 100 and 250 nM T122bt concentrations in +MMC+TGFβ1 at day 10 significantly ($p < 0.05$) reduced β11(I), β12(I) dimer deposition. Additional densitometry analysis of γ(I) bands (**Supplementary Figure S12B**) revealed that all T122bt concentrations in +MMC+TGFβ1 at all time points significantly ($p < 0.05$) reduced γ(I) trimer deposition.

No T122bt concentrations in +MMC+TGFβ1 induced any significant ($p < 0.05$) differences in DNA concentration at any time point, in comparison to the +MMC+TGFβ1 group (**Supplementary Figure S13A**). Only the 250 nM T122bt

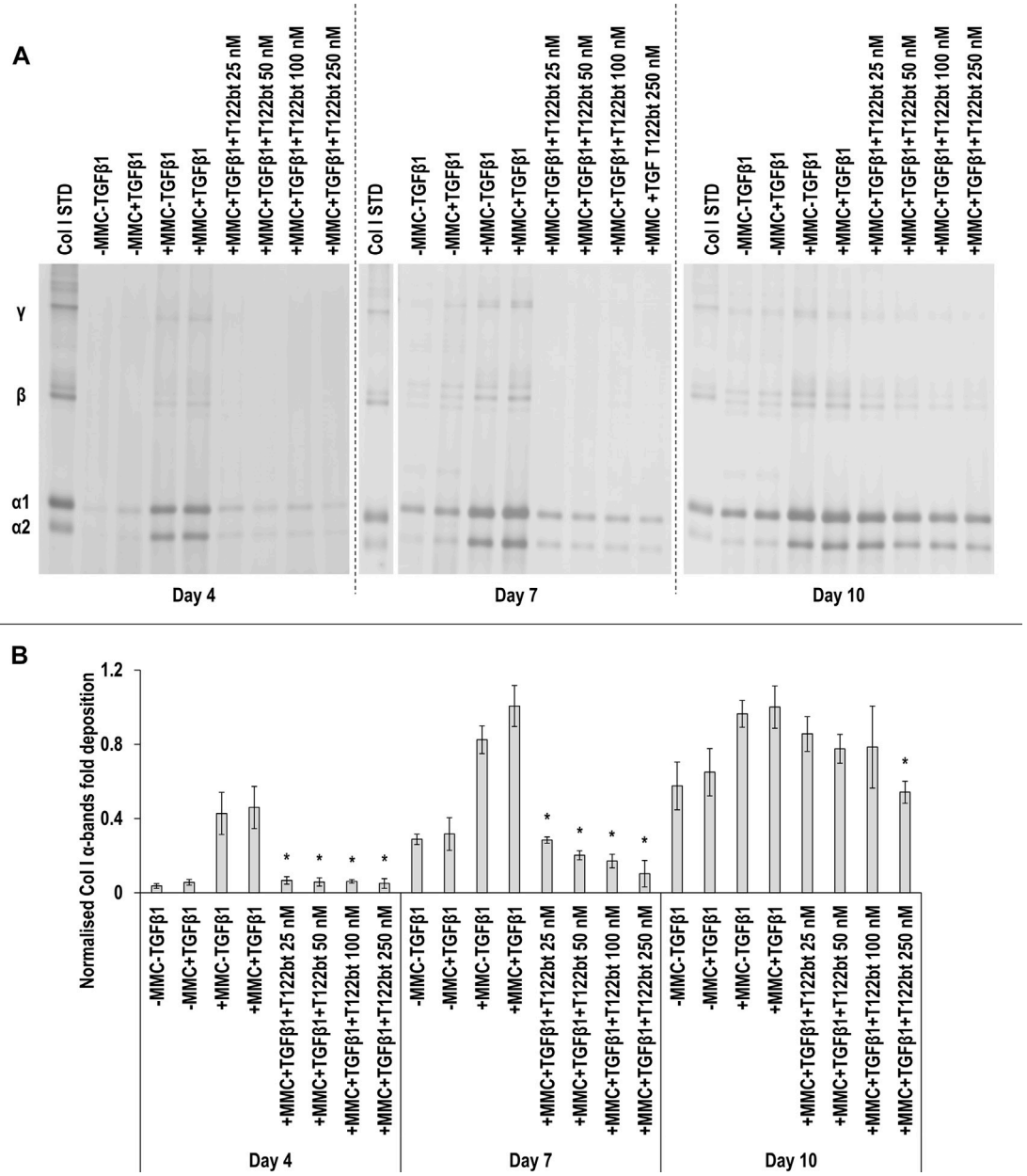

FIGURE 8 | The highest concentrations of TGFβ1 type II receptor-based trap (T122bt) reduce collagen deposition. The 100 and 250 nM T122bt concentrations in +MMC+TGFβ1 significantly reduced collagen deposition at all time points, in comparison to +MMC+TGFβ1 group, as judged by SDS-PAGE **(A)** and densitometry of α(I)1 and α(I)2 bands **(B)**. Col I STD: 0.1 mg/ml. One-way ANOVA and Tukey's post-hoc comparison test or Kruskal Wallis and Mann Whitney post-hoc analyses were conducted, as appropriate. *: $p < 0.05$ indicates a statistically significant difference when compared to the +MMC+TGFβ1 group of the respective time point. $n = 3$.

concentrations in +MMC+TGFβ1 significantly ($p < 0.05$) increased metabolic activity, in comparison to the +MMC+TGFβ1 group, at day 4 (**Supplementary Figure S13B**).

SDS-PAGE (**Supplementary Figure S14A**) and densitometry analysis of α (**Supplementary Figure S14B**), β11(I), β12(I) (**Supplementary Figure S15A**) and γ(I) bands (**Supplementary Figure S15B**) revealed that no T22d35 concentration significantly ($p < 0.05$) reduced collagen deposition in comparison to the +MMC+TGFβ1 group. Only the 50 nM T22d35 in +MMC+TGFβ1 significantly ($p < 0.05$) increased DNA concentration, in comparison to +MMC+TGFβ1 group, at day 10 (**Supplementary Figure S16A**). Only the 25 nM T22d35 in +MMC+TGFβ1 significantly ($p < 0.05$) increased metabolic activity, in comparison to +MMC+TGFβ1 group, at day 4 (**Supplementary Figure S16B**).

SDS-PAGE (**Figure 9A**) and densitometry analysis of α(I)1 and α(I)2 (**Figure 9B**), β11(I), β12(I) (**Supplementary Figure S17A**) and γ(I) (**Supplementary Figure S17B**) bands revealed

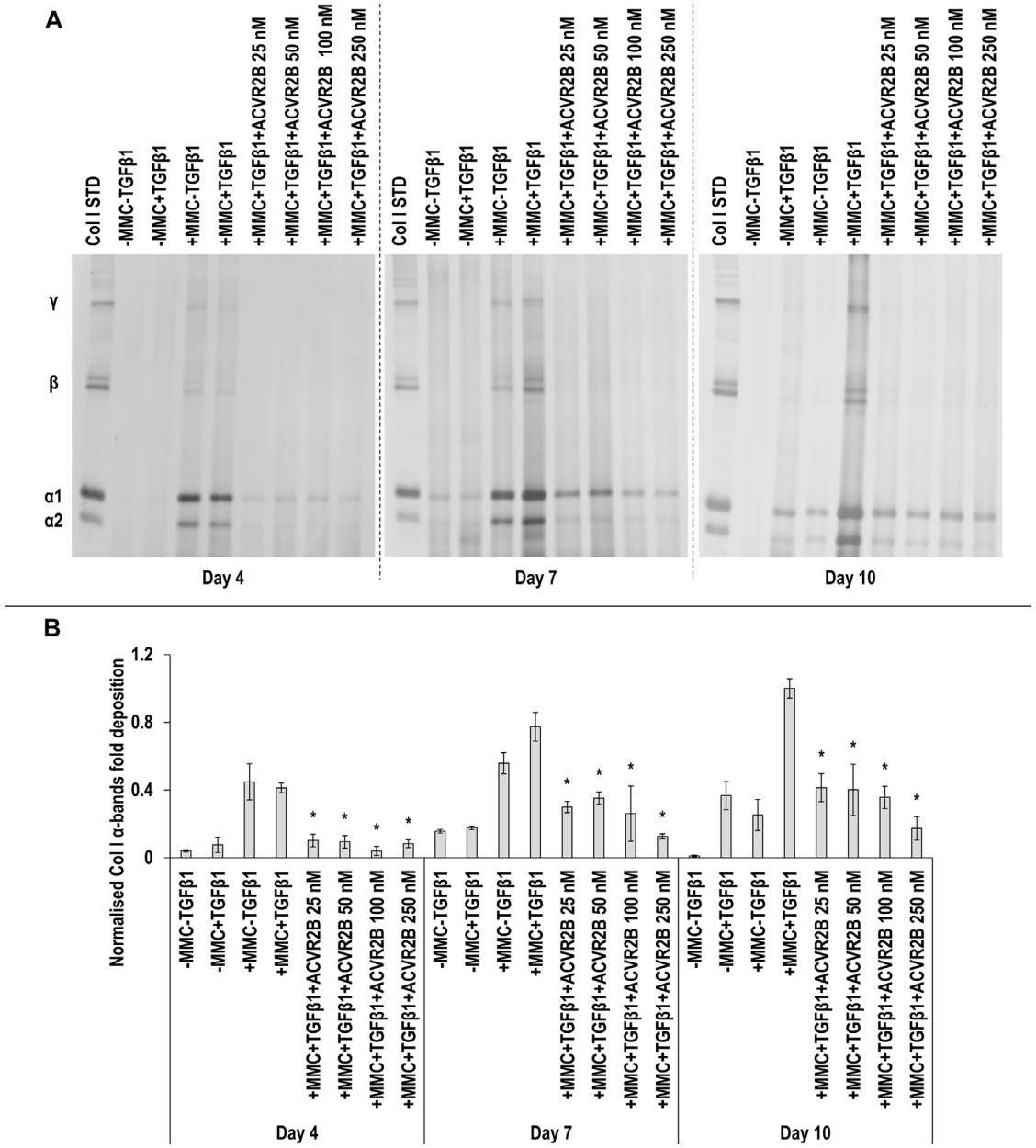

FIGURE 9 | ACVR2B reduces collagen deposition. All ACVR2B concentrations in +MMC+TGFβ1 at all time points significantly reduced collagen deposition, in comparison to +MMC+TGFβ1 group, as judged by SDS-PAGE **(A)** and densitometry analysis of α(I)1 and α(I)2 bands **(B)**. Col I STD: 0.1 mg/ml. One-way ANOVA and Tukey's post-hoc comparison tests or Kruskal Wallis and Mann Whitney post-hoc analyses were conducted, as appropriate. *: $p < 0.05$ indicates a statistically significant difference when compared to the +MMC+TGFβ1 group of the respective time point. $n = 3$.

that all ACVR2B concentrations in +MMC+TGFβ1 at all time points significantly ($p < 0.05$) reduced the deposition of α(I)1 and α(I)2, β11(I), β12(I) and γ(I) components, in comparison to the +MMC+TGFβ1 group. Only the 25 and 50 nM ACVR2B concentrations in +MMC+TGFβ1 significantly ($p < 0.05$) increased DNA concentration, in comparison to +MMC+TGFβ1 group, at day 7 (**Supplementary Figure S18A**). The 25, 50 and 100 nM ACVR2B concentrations in +MMC+TGFβ1 significantly ($p < 0.05$) decreased metabolic activity, in comparison to +MMC+TGFβ1 group, at day 7 and the 250 nM concentration at day 10 (**Supplementary Figure S18B**).

SDS-PAGE (**Supplementary Figure S19A**) and densitometry of α(I)1 and α(I)2 bands (**Supplementary Figure S19B**) revealed that all concentrations of BAPN in +MMC+TGFβ1 at day 4 and the 0.1, 0.25 and the 0.5 mM concentrations of BAPN in +MMC+TGFβ1 at day 10 significantly ($p < 0.05$) increased α(I)1 and α(I)2 deposition in comparison to the

+MMC+TGFβ1 group at the respective time points. No significant ($p < 0.05$) differences in the deposition of β11(I), β12(I) (**Supplementary Figure S20A**) and γ(I) components (**Supplementary Figure S20B**) were observed. The 1 mM concentration of the BAPN in +MMC+TGFβ1 significantly reduced DNA concentration at day 7 and day 10 in comparison to the +MMC+TGFβ1 group (**Supplementary Figure S21A**). The 0.5 mM and the 1 mM BAPN concentration in +MMC+TGFβ1 resulted in significantly increased metabolic activity at day 10 in comparison to the +MMC+TGFβ1 group (**Supplementary Figure S21B**).

Qualitative cell viability assessment revealed that TAC did not have a negative affect; TSA, BAPN and T122bt had a negative effect at high concentrations (the latter, only at the latest time point); and RLX-2, Pirf, T22d35 and ACV2R had a negative effect mostly at later time points, regardless of concentration (**Supplementary Figures S22–S29**).

DISCUSSION

Fibrosis is not just the outcome of devastating skin diseases, but it can also be the result of abnormal skin wound healing and scarring. One of the fundamental roadblocks in the use of traditional *in vitro* models for screening anti-fibrotic molecules is that they do not recapitulate the excessive and altered ECM characteristic of human fibrotic diseases (Chen et al., 2009). To address this deficiency, we ventured to assess whether MMC (that dramatically enhances and accelerates ECM deposition) coupled with TGFβ1 (that induces myofibroblast trans-differentiation) can generate an efficient skin fibrosis model.

Starting with the establishment of the fibrotic model, TGFβ1 is a key player in many fibrotic conditions (Lodyga and Hinz, 2020), with its signalling pathway involved in transformation of fibroblasts into myofibroblasts (Sarrazy et al., 2011; Lichtman et al., 2016). MMC significantly increased collagen deposition and *a*SMA expression in TGFβ1 supplemented cultures and resulted in the formation of an ECM-rich substrate, magnifying the profibrotic effect of TGFβ1, a prerequisite for the development of a scarring model.

Although a quantitative analysis of cell and ECM orientation was not performed in this study, it was still possible to observe that treatment with macromolecular crowding and TGFβ1 resulted in an alteration of the deposited ECM. Deposition of densely packed granular collagen type I (resembling the formation of scar tissue (Pakshir and Hinz, 2018)) was observable. On the other hand, in the absence of macromolecular crowding treatment, it was observed the normal meshwork architecture of healthy skin ECM (Goto et al., 2020). The formation of αSMA stress fibres alongside the deposition axis of collagen type I also seems to confirm this.

In accordance with previous publications, several other organ-specific fibrotic models induced by MMC supplementation have been developed (Chen et al., 2009; Graupp et al., 2015; Graupp et al., 2018; Fan et al., 2019; Good et al., 2019; Fan et al., 2020; Rønnow et al., 2020; De Pieri et al., 2021). It is worth noting that cocktails of pro-inflammatory cytokines have been used for more accurate recapitulation of fibrosis *in vitro* (Chawla and Ghosh, 2018) and such approach should be studied further in the future in combination with MMC.

After establishment of the *in vitro* model of skin fibrosis, several anti-fibrotic molecules with different mechanisms of action were tested to assess their capacity to decrease collagen synthesis and/or deposition. We also assessed their effect on basic cellular functions (cell metabolic activity, viability, DNA concentration) to assess how selective their mode of action is. Tested drug concentrations were based on previously published data that had been shown to have a therapeutic effect *in vitro*. This explains the different orders of magnitude in concentrations used for different anti-fibrotic molecules, which allowed us to validate the model and select the best, as judged by maximum collagen reduction and adequate profile regarding basic cellular functions, anti-fibrotic molecules.

The first molecule tested was TAC, and in this study, only a very moderate effect in the reduction of the deposition of collagen type I was observed. This synthetic corticosteroid, used to reduce inflammation, is currently one of the most used molecules for the treatment of hypertrophic scars and keloids in humans and arguably the "gold standard" treatment (Ogawa, 2010; Berman et al., 2017; Hietanen et al., 2019). Despite its wide usage, TAC presents only moderate response rates, while presenting relatively high recurrence rates (Ogawa, 2010; Hietanen et al., 2019) and considerable side effects on skin (Sadeghinia and Sadeghinia, 2012). We have recently demonstrated in a randomised controlled trial that keloids that respond to either TAC or 5-FU show a reduction in myofibroblasts (Hietanen et al., 2020). This is a secondary effect as neither TAC nor 5-FU have a direct influence on myofibroblast transformation. Our results support clinical data and illustrate that more effective and safer therapies than TAC should be developed for keloids and hypertrophic scars.

Another molecule tested was TSA and we observed an overall reduction in collagen type I deposition and cell proliferation. This is not surprising considering that it is an inhibitor of class I and II mammalian histone deacetylases (HDACs), which alter gene expression by altering the access of transcription factors to DNA. TSA has been shown to reduce αSMA expression and collagen type I deposition; inhibit cellular proliferation in fibroblasts; and promote apoptosis in certain experimental skin fibrosis models (Rombouts et al., 2002; Huber et al., 2007; Diao et al., 2011). HDACs, in general, have been implicated in TGFβ1-induced epithelial-mesenchymal transition (EMT) (Jones et al., 2019; Qiao et al., 2020). HDAC suppress epithelial-specific genes and mediate TGFβ1-induced mesenchymal enhancer reprogramming, which results in EMT of the cells (Qiao et al., 2020). As myofibroblast transformation is a central feature in fibrosis and our results demonstrate that TSA can inhibit it, this makes it a viable therapeutic candidate.

After treatment with RLX-2, a decrease in collagen type I deposition was observed, with no significant negative effects on basic cellular functions. To substantiate this, one should consider that recombinant human relaxin-2 (RLX-2), a naturally occurring peptide, binds to its receptor, RLX family peptide receptor 1. This has been shown to suppress not only Smad 2/3 and consequently,

TGFβ1 signalling pathways in cardiac fibroblasts, but also angiotensin II type 2 receptors and interleukin-1β and the potential interaction of these signalling pathways with the TGFβ axis (Yuan et al., 2017; Wu et al., 2018), as well as with the inflammasome (Pinar et al., 2020). In addition to those, RLX-2 can increase the expression and activity of matrix metalloproteinases that facilitate ECM degradation (Li et al., 2021). Its application in other diseases, mainly fibrotic, has been postulated, although the clinical trials have been inconclusive on its therapeutic efficacy (Samuel et al., 2017; Yuan et al., 2017; Blessing et al., 2019; Hinz and Lagares, 2020).

When testing Pirf, our study showed decreased collagen deposition and an absence of significant adverse effects on basic cellular functions at the lowest drug concentrations tested. However, when compared to the other molecules tested, very high relative concentrations of the molecule were required to obtain anti-fibrotic activity. This follows the reported literature, as Pirf is a small molecule inhibitor and a Food and Drug Administration approved drug for idiopathic lung fibrosis, but large doses are required (Noble et al., 2011; Lancaster et al., 2017). It has been investigated as a treatment for several other fibrotic diseases, such as liver (Seniutkin et al., 2018), kidney (Salah et al., 2019), intestinal (Sun et al., 2018) and skin (Hall et al., 2018). It functions by inhibiting TGFβ1 (and its production) and platelet-derived growth factor-activated signalling pathways (Lv et al., 2020) in conjunction with anti-inflammatory activity (Mora et al., 2015; Hall et al., 2018). Due to the high doses required, Pirf is associated with side-effects and organ toxicity (Anderson et al., 2016; Lancaster et al., 2017), which require rigorous supervision and limit its therapeutic potential. One option could be to combine a low dose of pirfenidone with another anti-fibrotic molecule. By that approach, side-effects could hopefully be avoided, and the therapeutic effect enhanced.

Following treatment with both TGFβ traps, no significant effects on collagen deposition were observed for T22d35, while T122bt resulted in a significant decrease of collagen deposition, at a concentration several orders of magnitude lower than for some of the other molecules. Neither of the TGFβ trap molecules elicited a negative response regarding basic cellular functions. This is expected, as given the importance of the TGFβ signalling pathway in the transition to a fibrotic phenotype, recombinant TGFβ traps, i.e., soluble ligand binding parts of the TGFβ receptors can act as inhibitors of this pathway. They can bind different isoforms of TGFβ, namely -β1 and -β3 for T22d35 and all three isoforms for T122bt. Both molecules can inhibit different isoforms of TGFβ at almost picomolar concentration, which is to our knowledge, the lowest concentration that has been attained against TGFβ (Zwaagstra et al., 2012; O'Connor-Mccourt et al., 2013). Concerning the difference between the two traps and TGFβ isoforms, TGFβ2 augments the profibrotic functions of TGFβ1 (Jagadeesan and Bayat, 2007), whereas TGFβ3 has been hypothesised to possess anti-fibrotic functions (Occleston et al., 2008; Lichtman et al., 2016). Thus, the T122b trap has a preferential TGFβ inhibitory profile than T22d35. Furthermore, both tested molecules have demonstrated substantial anti-tumour effect in TGFβ-driven cancer models *in vivo* (Zwaagstra et al., 2012; O'Connor-Mccourt et al., 2013). As TGFβ1 was the only growth factor supplied in the media, our results indicate that these traps are very potent and specific in their inhibitory activity.

We also tested an activin IIB receptor antagonist, a soluble ligand binding domain part of the receptor. Despite a substantial decrease in collagen type I deposition, a decrease in basic cellular functions was observed for ACVR2B. This can be explained as this antagonist blocks signalling of activins A and B, myostatin (MSTN/GDF-8), its close homolog, growth differentiation factor-11 (GDF-11) and bone morphogenetic protein-10 (Lautaoja et al., 2019; Magga et al., 2019; Szabó et al., 2020). Both activins are involved in Smad 2/3 signalling and consequently play a role in fibrosis (Werner and Alzheimer, 2006; Canady et al., 2013; Walton et al., 2017; Itoh et al., 2018). The expression of activins is induced during wound repair and activin A leads to accelerated wound healing (Cangkrama et al., 2020). However, its most striking effect is on the granulation tissue formation as it induces excessive scar formation (Cangkrama et al., 2020; Wietecha et al., 2020). This is attributed to the expression of its target genes in fibroblasts, which include both ACTA2 and COL1A1 (αSMA and collagen type I) (Cangkrama et al., 2020). Both MMC and TGFβ1, in turn, induce the expression of activins and myostatin in fibrotic disorders (Erämaa and Ritvos, 1996; Cianciolo et al., 2020; Winter et al., 2020). As activins are produced in mature, active form, they can induce cell signalling immediately (Cangkrama et al., 2020). Furthermore, whereas TGFβ1 signalling becomes refractory for extended periods of time due to receptor internalisation and degradation, the activin signalling remains active all the time due to constant receptor renewal at cell surface (Miller et al., 2019). Thus, our model could involve activin activity although activins were not supplemented to the culture media.

Treatment with BAPN resulted in decreased cell proliferation, although no significant decrease in collagen type I deposition was observed, which is in accordance with what was reported in previous studies. Given its action as a lysyl oxidase (LOX) inhibitor, which inhibits collagen crosslinking (Redden and Doolin, 2003), its use has been previously suggested as an anti-fibrotic (Trackman, 2016). However, several safety concerns related to osteolathyrism, a collagen cross-linking deficiency (Wilmarth and Froines, 1992; Rosenthal, 2003) have been reported following its use. The target enzyme, LOX, has a wide variety of biological effects beyond collagen cross-linking, which also influences matrix stiffness and cell proliferation and migration (Saatci et al., 2020; Freeberg et al., 2021; Kozma et al., 2021; Sflomos et al., 2021). This is an indicator of its unsuitability as an anti-fibrotic molecule and potentially the reason for the molecule's failures in clinical trials.

CONCLUSION

The low extracellular matrix content in the traditional *in vitro* fibrosis models results in poor imitation of the tissue pathology and to scattered predictive capacity. This study advocates the use of macromolecular crowding (to enhance and accelerate

extracellular matrix deposition) and TGFβ 1 (to induce dermal fibroblast trans-differentiation to myofibroblast) in the development of skin fibrosis specific *in vitro* models. We further identified trichostatin A, serelaxin, pirfenidone and soluble TGFβ trap as potent anti-fibrotic therapies.

DATA AVAILABILITY STATEMENT

The raw data supporting the conclusions of this article will be made available by the authors, without undue reservation.

AUTHOR CONTRIBUTIONS

Funding: JC, TJ, and DZ. Methodology: JC, UM, SP, JZ, and OR. Data analysis: JC. Manuscript writing and editing: JC, TJ, and DZ. Final manuscript approval: All authors.

FUNDING

This work has received funding from the European Research Council (ERC) under the European Union's Horizon 2020 research and innovation programme, grant agreement No. 866126. This publication has emanated from research supported in part by grants from Science Foundation Ireland (SFI) under grant numbers 15/CDA/3629 and 19/FFP/6982 and Science Foundation Ireland (SFI) and European Regional Development Fund (ERDF) under grant number 13/RC/2073_2. This research was also funded by the Finnish National Agency for Education (EDUFI), Academy of Finland, Päivikki and Sakari Sohlberg Foundation, Tampere Tuberculosis Foundation, Tampere University Hospital Research Fund and Pirkanmaa Hospital District Research Foundation. The funders had no role in the design of the study; in the collection, analyses, or interpretation of data; in the writing of the manuscript, or in the decision to publish the results.

ACKNOWLEDGMENTS

The authors want to thank Marianne Karlsberg for the recombinant protein expression and purification work. The authors acknowledge the Biocenter Finland (BF) and Tampere Imaging Facility (TIF) for their services. The graphical abstract (**Supplementary Figure S1**) was created with BioRender.com.

SUPPLEMENTARY MATERIAL

The Supplementary Material for this article can be found online at: https://www.frontiersin.org/articles/10.3389/fbioe.2021.756399/full#supplementary-material

REFERENCES

Anderson, A., Shifren, A., and Nathan, S. D. (2016). A Safety Evaluation of Pirfenidone for the Treatment of Idiopathic Pulmonary Fibrosis. *Expert Opin. Drug Saf.* 15, 975–982. doi:10.1080/14740338.2016.1187129

Berman, B., Maderal, A., and Raphael, B. (2017). Keloids and Hypertrophic Scars: Pathophysiology, Classification, and Treatment. *Dermatol. Surg.* 43 Suppl 1 (Suppl. 1), S3–S18. doi:10.1097/DSS.0000000000000819

Blessing, W. A., Okajima, S. M., Cubria, M. B., Villa-Camacho, J. C., Perez-Viloria, M., Williamson, P. M., et al. (2019). Intraarticular Injection of Relaxin-2 Alleviates Shoulder Arthrofibrosis. *Proc. Natl. Acad. Sci. USA* 116, 12183–12192. doi:10.1073/pnas.1900355116

Canady, J., Karrer, S., Fleck, M., and Bosserhoff, A. K. (2013). Fibrosing Connective Tissue Disorders of the Skin: Molecular Similarities and Distinctions. *J. Dermatol. Sci.* 70, 151–158. doi:10.1016/j.jdermsci.2013.03.005

Cancela, L., and Rebut-Bonneton, C. (1987). Regulation of 24-hydroxylase Activity in Mouse Skin Fibroblasts by Cholecalciferol Derivatives, Triamcinolone Acetonide and a Calcium Modulating Agent, Nicardipine. *J. Steroid Biochem.* 28, 479–484. doi:10.1016/0022-4731(87)90505-x

Cangkrama, M., Wietecha, M., and Werner, S. (2020). Wound Repair, Scar Formation, and Cancer: Converging on Activin. *Trends Mol. Med.* 26, 1107–1117. doi:10.1016/j.molmed.2020.07.009

Capella-Monsonís, H., Coentro, J. Q., Graceffa, V., Wu, Z., and Zeugolis, D. I. (2018). An Experimental Toolbox for Characterization of Mammalian Collagen Type I in Biological Specimens. *Nat. Protoc.* 13, 507–529. doi:10.1038/nprot.2017.117

Carroll, L. A., Hanasono, M. M., Mikulec, A. A., Kita, M., and Koch, R. J. (2002). Triamcinolone Stimulates bFGF Production and Inhibits TGF-β1 Production by Human Dermal Fibroblasts. *Dermatol. Surg.* 28, 704–709. doi:10.1046/j.1524-4725.2002.02012.x

Chawla, S., and Ghosh, S. (2018). Regulation of Fibrotic Changes by the Synergistic Effects of Cytokines, Dimensionality and Matrix: Towards the Development of an *In Vitro* Human Dermal Hypertrophic Scar Model. *Acta Biomater.* 69, 131–145. doi:10.1016/j.actbio.2018.01.002

Chen, C., Peng, Y., Wang, Z., Fish, P., Kaar, J., Koepsel, R., et al. (2009). The Scar-In-A-Jar: Studying Potential Antifibrotic Compounds from the Epigenetic to Extracellular Level in a Single Well. *Br. J. Pharmacol.* 158, 1196–1209. doi:10.1111/j.1476-5381.2009.00387.x

Cianciolo, G., La Manna, G., Capelli, I., Gasperoni, L., Galassi, A., Ciceri, P., et al. (2020). The Role of Activin: the Other Side of Chronic Kidney Disease-mineral Bone Disorder? *Nephrol. Dial. Transpl.* 36, 966–974. doi:10.1093/ndt/gfaa203

Coentro, J. Q., Pugliese, E., Hanley, G., Raghunath, M., and Zeugolis, D. I. (2018). Current and Upcoming Therapies to Modulate Skin Scarring and Fibrosis. *Adv. Drug Deliv. Rev.* 146, 37–59. doi:10.1016/j.addr.2018.08.009

De Pieri, A., Korman, B. D., Jüngel, A., and Wuertz-Kozak, K. (2021). Engineering Advanced *In Vitro* Models of Systemic Sclerosis for Drug Discovery and Development. *Adv. Biol.* 5, e2000168. doi:10.1002/adbi.202000168

Desallais, L., Avouac, J., Fréchet, M., Elhai, M., Ratsimandresey, R., Montes, M., et al. (2014). Targeting IL-6 by Both Passive or Active Immunization Strategies Prevents Bleomycin-Induced Skin Fibrosis. *Arthritis Res. Ther.* 16, R157. doi:10.1186/ar4672

Diao, J.-S., Xia, W.-S., Yi, C.-G., Wang, Y.-M., Li, B., Xia, W., et al. (2011). Trichostatin A Inhibits Collagen Synthesis and Induces Apoptosis in Keloid Fibroblasts. *Arch. Dermatol. Res.* 303, 573–580. doi:10.1007/s00403-011-1140-1

Erämaa, M., and Ritvos, O. (1996). Endocrinology and Paracrinology. *Mol. Hum. Reprod.* 2, 815–822. doi:10.1093/molehr/2.11.815

Fan, C., Lim, L. K. P., Loh, S. Q., Ying Lim, K. Y., Upton, Z., and Leavesley, D. (2019). Application of "Macromolecular Crowding" *In Vitro* to Investigate the Naphthoquinones Shikonin, Naphthazarin and Related Analogues for the Treatment of Dermal Scars. *Chem. Biol. Interact.* 310, 108747. doi:10.1016/j.cbi.2019.108747

Fan, C., Lim, L. K. P., Wu, Z., Sharma, B., Gan, S. Q., Liang, K., et al. (2020). *In Vitro* Model of Human Cutaneous Hypertrophic Scarring Using Macromolecular Crowding. *J. Vis. Exp.* (159), e61037. doi:10.3791/61037

Freeberg, M. A. T., Perelas, A., Rebman, J. K., Phipps, R. P., Thatcher, T. H., and Sime, P. J. (2021). Mechanical Feed-Forward Loops Contribute to Idiopathic Pulmonary Fibrosis. *Am. J. Pathol.* 191, 18–25. doi:10.1016/j.ajpath.2020.09.008

Ghosh, A. K., Mori, Y., Dowling, E., and Varga, J. (2007). Trichostatin A Blocks TGF-β-Induced Collagen Gene Expression in Skin Fibroblasts: Involvement of Sp1. *Biochem. Biophys. Res. Commun.* 354, 420–426. doi:10.1016/j.bbrc.2006.12.204

Good, R. B., Eley, J. D., Gower, E., Butt, G., Blanchard, A. D., Fisher, A. J., et al. (2019). A High Content, Phenotypic 'scar-In-A-Jar' Assay for Rapid Quantification of Collagen Fibrillogenesis Using Disease-Derived Pulmonary Fibroblasts. *BMC Biomed. Eng.* 1, 14. doi:10.1186/s42490-019-0014-z

Goto, H., Tada, A., Ibe, A., and Kitajima, Y. (2020). Basket-weave Structure in the Stratum Corneum Is an Important Factor for Maintaining the Physiological Properties of Human Skin as Studied Using Reconstructed Human Epidermis and Tape Stripping of Human Cheek Skin. *Br. J. Dermatol.* 182, 364–372. doi:10.1111/bjd.18123

Graupp, M., Gruber, H.-J., Weiss, G., Kiesler, K., Bachna-Rotter, S., Friedrich, G., et al. (2015). Establishing Principles of Macromolecular Crowding for *In Vitro* Fibrosis Research of the Vocal Fold Lamina Propria. *Laryngoscope* 125, E203–E209. doi:10.1002/lary.25103

Graupp, M., Rinner, B., Frisch, M. T., Weiss, G., Fuchs, J., Sundl, M., et al. (2018). Towards an *In Vitro* Fibrogenesis Model of Human Vocal Fold Scarring. *Eur. Arch. Otorhinolaryngol.* 275, 1211–1218. doi:10.1007/s00405-018-4922-7

Griffin, M. F., desJardins-Park, H. E., Mascharak, S., Borrelli, M. R., and Longaker, M. T. (2020). Understanding the Impact of Fibroblast Heterogeneity on Skin Fibrosis. *Dis. Model. Mech.* 13, dmm044164. doi:10.1242/dmm.044164

Hall, C. L., Wells, A. R., and Leung, K. P. (2018). Pirfenidone Reduces Profibrotic Responses in Human Dermal Myofibroblasts, *In Vitro*. *Lab. Invest.* 98, 640–655. doi:10.1038/s41374-017-0014-3

Henderson, N. C., Rieder, F., and Wynn, T. A. (2020). Fibrosis: From Mechanisms to Medicines. *Nature* 587, 555–566. doi:10.1038/s41586-020-2938-9

Hietanen, K., Järvinen, T., Huhtala, H., Tolonen, T., Kuokkanen, H., and Kaartinen, I. (2019). Treatment of Keloid Scars with Intralesional Triamcinolone and 5-fluorouracil Injections - a Randomized Controlled Trial. *J. Plast. Reconstr. Aesthet. Surg.* 72, 4–11. doi:10.1016/j.bjps.2018.05.052

Hietanen, K. E., Järvinen, T. A. H., Huhtala, H., Tolonen, T. T., and Kaartinen, I. S. (2020). Histopathology and Immunohistochemical Analysis of 5-fluorouracil and Triamcinolone Treated Keloids in Double-blinded Randomized Controlled Trial. *Wound Rep. Reg.* 28, 385–399. doi:10.1111/wrr.12803

Hinz, B., and Lagares, D. (2020). Evasion of Apoptosis by Myofibroblasts: A Hallmark of Fibrotic Diseases. *Nat. Rev. Rheumatol.* 16, 11–31. doi:10.1038/s41584-019-0324-5

Hinz, B., Phan, S. H., Thannickal, V. J., Prunotto, M., Desmoulière, A., Varga, J., et al. (2012). Recent Developments in Myofibroblast Biology. *Am. J. Pathol.* 180, 1340–1355. doi:10.1016/j.ajpath.2012.02.004

Huber, L. C., Distler, J. H. W., Moritz, F., Hemmatazad, H., Hauser, T., Michel, B. A., et al. (2007). Trichostatin A Prevents the Accumulation of Extracellular Matrix in a Mouse Model of Bleomycin-Induced Skin Fibrosis. *Arthritis Rheum.* 56, 2755–2764. doi:10.1002/art.22759

Itoh, Y., Saitoh, M., and Miyazawa, K. (2018). Smad3-STAT3 Crosstalk in Pathophysiological Contexts. *Acta Biochim. Biophys. Sin.* 50, 82–90. doi:10.1093/abbs/gmx118

Jagadeesan, J., and Bayat, A. (2007). Transforming Growth Factor Beta (TGFβ) and Keloid Disease. *Int. J. Surg.* 5, 278–285. doi:10.1016/j.ijsu.2006.04.007

Jarvinen, T. A. H., and Ruoslahti, E. (2010). Target-seeking Antifibrotic Compound Enhances Wound Healing and Suppresses Scar Formation in Mice. *Proc. Natl. Acad. Sci.* 107, 21671–21676. doi:10.1073/pnas.1016233107

Jones, D. L., Haak, A. J., Caporarello, N., Choi, K. M., Ye, Z., Yan, H., et al. (2019). Tgfβ-induced Fibroblast Activation Requires Persistent and Targeted HDAC-Mediated Gene Repression. *J. Cel Sci.* 132, jcs233486. doi:10.1242/jcs.233486

Kozma, K. J., Done, S. J., and Egan, S. E. (2021). The Tumor Cell-Derived Matrix of Lobular Breast Cancer: A New Vulnerability. *EMBO Mol. Med.* 13, e13807. doi:10.15252/emmm.202013807

Kumar, P., Satyam, A., Fan, X., Rochev, Y., Rodriguez, B. J., Gorelov, A., et al. (2015). Accelerated Development of Supramolecular Corneal Stromal-like Assemblies from Corneal Fibroblasts in the Presence of Macromolecular Crowders. *Tissue Eng. C: Methods* 21, 660–670. doi:10.1089/ten.tec.2014.0387

Lancaster, L. H., de Andrade, J. A., Zibrak, J. D., Padilla, M. L., Albera, C., Nathan, S. D., et al. (2017). Pirfenidone Safety and Adverse Event Management in Idiopathic Pulmonary Fibrosis. *Eur. Respir. Rev.* 26, 170057. doi:10.1183/16000617.0057-2017

Lautaoja, J. H., Lalowski, M., Nissinen, T. A., Hentilä, J., Shi, Y., Ritvos, O., et al. (2019). Muscle and Serum Metabolomes Are Dysregulated in colon-26 Tumor-Bearing Mice Despite Amelioration of Cachexia with Activin Receptor Type 2B Ligand Blockade. *Am. J. Physiol. Endocrinol. Metab.* 316, E852–E865. doi:10.1152/ajpendo.00526.2018

Li, Y., Shen, M., Ferens, D., Broughton, B. R. S., Murthi, P., Saini, S., et al. (2021). Combining Mesenchymal Stem Cells with Serelaxin Provides Enhanced Renoprotection against 1K/DOCA/salt-induced Hypertension. *Br. J. Pharmacol.* 178, 1164–1181. doi:10.1111/bph.15361

Lichtman, M. K., Otero-Vinas, M., and Falanga, V. (2016). Transforming Growth Factor Beta (TGF-β) Isoforms in Wound Healing and Fibrosis. *Wound Rep. Reg.* 24, 215–222. doi:10.1111/wrr.12398

Lodyga, M., and Hinz, B. (2020). TGF-β1 - A Truly Transforming Growth Factor in Fibrosis and Immunity. *Semin. Cel Dev. Biol.* 101, 123–139. doi:10.1016/j.semcdb.2019.12.010

Logeart-Avramoglou, D., Huynh, R., Chaubet, F., Sedel, L., and Meunier, A. (2002). Interaction of Specifically Chemically Modified Dextrans with Transforming Growth Factor β1: Potentiation of its Biological Activity. *Biochem. Pharmacol.* 63, 129–137. doi:10.1016/s0006-2952(01)00834-6

Lv, Q., Wang, J., Xu, C., Huang, X., Ruan, Z., and Dai, Y. (2020). Pirfenidone Alleviates Pulmonary Fibrosis *In Vitro* and *In Vivo* through Regulating Wnt/GSK-3β/β-Catenin and TGF-β1/Smad2/3 Signaling Pathways. *Mol. Med.* 26, 49. doi:10.1186/s10020-020-00173-3

Magga, J., Vainio, L., Kilpiö, T., Hulmi, J. J., Taponen, S., Lin, R., et al. (2019). Systemic Blockade of ACVR2B Ligands Protects Myocardium from Acute Ischemia-Reperfusion Injury. *Mol. Ther.* 27, 600–610. doi:10.1016/j.ymthe.2019.01.013

Maire, M., Logeart-Avramoglou, D., Degat, M.-C., and Chaubet, F. (2005). Retention of Transforming Growth Factor β1 Using Functionalized Dextran-Based Hydrogels. *Biomaterials* 26, 1771–1780. doi:10.1016/j.biomaterials.2004.06.003

Miller, D. S. J., Schmierer, B., and Hill, C. S. (2019). TGF-β Family Ligands Exhibit Distinct Signalling Dynamics that Are Driven by Receptor Localisation. *J. Cel Sci.* 132, jcs234039. doi:10.1242/jcs.234039

Mora, D. A. L.-d. l., Sanchez-Roque, C., Montoya-Buelna, M., Sanchez-Enriquez, S., Lucano-Landeros, S., Macias-Barragan, J., et al. (2015). Role and New Insights of Pirfenidone in Fibrotic Diseases. *Int. J. Med. Sci.* 12, 840–847. doi:10.7150/ijms.11579

Noble, P. W., Albera, C., Bradford, W. Z., Costabel, U., Glassberg, M. K., Kardatzke, D., et al. (2011). Pirfenidone in Patients with Idiopathic Pulmonary Fibrosis (CAPACITY): Two Randomised Trials. *Lancet* 377, 1760–1769. doi:10.1016/s0140-6736(11)60405-4

Occleston, N. L., Laverty, H. G., O'Kane, S., and Ferguson, M. W. J. (2008). Prevention and Reduction of Scarring in the Skin by Transforming Growth Factor Beta 3 (TGFβ3): from Laboratory Discovery to Clinical Pharmaceutical. *J. Biomater. Sci. Polym. Ed.* 19, 1047–1063. doi:10.1163/156856208784909345

O'Connor-Mccourt, M., Sulea, T., Zwaagstra, J., and Baardsnes, J. (2013). Antagonists of Ligands and Uses Thereof. US8574548B2. Available at: https://patentscope.wipo.int/search/en/detail.jsf?docId=WO2008113185.

Ogawa, R. (2010). The Most Current Algorithms for the Treatment and Prevention of Hypertrophic Scars and Keloids. *Plast. Reconstr. Surg.* 125, 557–568. doi:10.1097/prs.0b013e3181c82dd5

Padmanabhan, J., Maan, Z. N., Kwon, S. H., Kosaraju, R., Bonham, C. A., and Gurtner, G. C. (2019). *In Vivo* models for the Study of Fibrosis. *Adv. Wound Care* 8, 645–654. doi:10.1089/wound.2018.0909

Pakshir, P., and Hinz, B. (2018). The Big Five in Fibrosis: Macrophages, Myofibroblasts, Matrix, Mechanics, and Miscommunication. *Matrix Biol.* 68-69, 81–93. doi:10.1016/j.matbio.2018.01.019

Pakshir, P., Noskovicova, N., Lodyga, M., Son, D. O., Schuster, R., Goodwin, A., et al. (2020). The Myofibroblast at a Glance. *J. Cel Sci.* 133, jcs227900. doi:10.1242/jcs.227900

Péterszegi, G., Andrès, E., Molinari, J., Ravelojaona, V., and Robert, L. (2008). Effect of Cellular Aging on Collagen Biosynthesis. *Arch. Gerontol. Geriatr.* 47, 356–367. doi:10.1016/j.archger.2007.08.019

Pinar, A. A., Yuferov, A., Gaspari, T. A., and Samuel, C. S. (2020). Relaxin Can Mediate its Anti-fibrotic Effects by Targeting the Myofibroblast NLRP3 Inflammasome at the Level of Caspase-1. *Front. Pharmacol.* 11, 1201. doi:10.3389/fphar.2020.01201

Qiao, Y., Wang, Z., Tan, F., Chen, J., Lin, J., Yang, J., et al. (2020). Enhancer Reprogramming within Pre-existing Topologically Associated Domains Promotes TGF-β-Induced EMT and Cancer Metastasis. *Mol. Ther.* 28, 2083–2095. doi:10.1016/j.ymthe.2020.05.026

Raghunath, M., and Zeugolis, D. I. (2021). Transforming Eukaryotic Cell Culture with Macromolecular Crowding. *Trends Biochem. Sci.* 46, 805–811. doi:10.1016/j.tibs.2021.04.006

Rashid, R., Lim, N. S. J., Chee, S. M. L., Png, S. N., Wohland, T., and Raghunath, M. (2014). Novel Use for Polyvinylpyrrolidone as a Macromolecular crowder for Enhanced Extracellular Matrix Deposition and Cell Proliferation. *Tissue Eng. Part C: Methods* 20, 994–1002. doi:10.1089/ten.tec.2013.0733

Redden, R. A., and Doolin, E. J. (2003). Collagen Crosslinking and Cell Density Have Distinct Effects on Fibroblast-Mediated Contraction of Collagen Gels. *Skin Res. Technol.* 9, 290–293. doi:10.1034/j.1600-0846.2003.00023.x

Rombouts, K., Niki, T., Greenwel, P., Vandermonde, A., Wielant, A., Hellemans, K., et al. (2002). Trichostatin A, a Histone Deacetylase Inhibitor, Suppresses Collagen Synthesis and Prevents TGF-β1-Induced Fibrogenesis in Skin Fibroblasts. *Exp. Cel Res.* 278, 184–197. doi:10.1006/excr.2002.5577

Rønnow, S. R., Dabbagh, R. Q., Genovese, F., Nanthakumar, C. B., Barrett, V. J., Good, R. B., et al. (2020). Prolonged Scar-In-A-Jar: An *In Vitro* Screening Tool for Anti-Fibrotic Therapies Using Biomarkers of Extracellular Matrix Synthesis. *Respir. Res.* 21, 108. doi:10.1186/s12931-020-01369-1

Rosenthal, G. (2003). *Toxic Constituents and Their Related Metabolites, Plant Nonprotein Amino and Imino Acids: Biological, Biochemical, and Toxicological Properties*. New York: Academic Press, 57–157.

Saatci, O., Kaymak, A., Raza, U., Ersan, P. G., Akbulut, O., Banister, C. E., et al. (2020). Targeting Lysyl Oxidase (LOX) Overcomes Chemotherapy Resistance in Triple Negative Breast Cancer. *Nat. Commun.* 11, 2416. doi:10.1038/s41467-020-16199-4

Sadeghinia, A., and Sadeghinia, S. (2012). Comparison of the Efficacy of Intralesional Triamcinolone Acetonide and 5-fluorouracil Tattooing for the Treatment of Keloids. *Dermatol. Surg.* 38, 104–109. doi:10.1111/j.1524-4725.2011.02137.x

Saito, M., Yamazaki, M., Maeda, T., Matsumura, H., Setoguchi, Y., and Tsuboi, R. (2012). Pirfenidone Suppresses Keloid Fibroblast-Embedded Collagen Gel Contraction. *Arch. Dermatol. Res.* 304, 217–222. doi:10.1007/s00403-011-1184-2

Salah, M. M., Ashour, A. A., Abdelghany, T. M., Abdel-Aziz, A.-A. H., and Salama, S. A. (2019). Pirfenidone Alleviates Concanavalin A-Induced Liver Fibrosis in Mice. *Life Sci.* 239, 116982. doi:10.1016/j.lfs.2019.116982

Samuel, C. S., Sakai, L. Y., and Amento, E. P. (2003). Relaxin Regulates Fibrillin 2, but Not Fibrillin 1, mRNA and Protein Expression by Human Dermal Fibroblasts and Murine Fetal Skin. *Arch. Biochem. Biophys.* 411, 47–55. doi:10.1016/s0003-9861(02)00710-5

Samuel, C. S., Royce, S. G., Hewitson, T. D., Denton, K. M., Cooney, T. E., and Bennett, R. G. (2017). Anti-fibrotic Actions of Relaxin. *Br. J. Pharmacol.* 174, 962–976. doi:10.1111/bph.13529

Sarrazy, V., Billet, F., Micallef, L., Coulomb, B., and Desmoulière, A. (2011). Mechanisms of Pathological Scarring: Role of Myofibroblasts and Current Developments. *Wound Repair Regen.* 19 (Suppl. 1), s10–s15. doi:10.1111/j.1524-475x.2011.00708.x

Schulz, J.-N., Plomann, M., Sengle, G., Gullberg, D., Krieg, T., and Eckes, B. (2018). New Developments on Skin Fibrosis - Essential Signals Emanating from the Extracellular Matrix for the Control of Myofibroblasts. *Matrix Biol.* 68-69, 522–532. doi:10.1016/j.matbio.2018.01.025

Seniutkin, O., Furuya, S., Luo, Y.-S., Cichocki, J. A., Fukushima, H., Kato, Y., et al. (2018). Effects of Pirfenidone in Acute and Sub-chronic Liver Fibrosis, and an Initiation-Promotion Cancer Model in the Mouse. *Toxicol. Appl. Pharmacol.* 339, 1–9. doi:10.1016/j.taap.2017.11.024

Seo, B. R., Chen, X., Ling, L., Song, Y. H., Shimpi, A. A., Choi, S., et al. (2020). Collagen Microarchitecture Mechanically Controls Myofibroblast Differentiation. *Proc. Natl. Acad. Sci. USA* 117, 11387–11398. doi:10.1073/pnas.1919394117

Sflomos, G., Battista, L., Aouad, P., De Martino, F., Scabia, V., Stravodimou, A., et al. (2021). Intraductal Xenografts Show Lobular Carcinoma Cells Rely on Their Own Extracellular Matrix and LOXL1. *EMBO Mol. Med.* 13, e13180. doi:10.15252/emmm.202013180

Stebler, S., and Raghunath, M. (2021). The : *In Vitro* Fibrosis Model for Anti-fibrotic Drug Testing. *Methods Mol. Biol.* 2299, 147–156. doi:10.1007/978-1-0716-1382-5_11

Sun, Y.-W., Zhang, Y.-Y., Ke, X.-J., Wu, X.-j., Chen, Z.-F., and Chi, P. (2018). Pirfenidone Prevents Radiation-Induced Intestinal Fibrosis in Rats by Inhibiting Fibroblast Proliferation and Differentiation and Suppressing the TGF-β1/Smad/CTGF Signaling Pathway. *Eur. J. Pharmacol.* 822, 199–206. doi:10.1016/j.ejphar.2018.01.027

Sund, B., and Arrow, A. K. (2000). New Developments in Wound Care. *Clin. Rep.* 45, 379.

Szabó, Z., Vainio, L., Lin, R., Swan, J., Hulmi, J. J., Rahtu-Korpela, L., et al. (2020). Systemic Blockade of ACVR2B Ligands Attenuates Muscle Wasting in Ischemic Heart Failure without Compromising Cardiac Function. *FASEB j.* 34, 9911–9924. doi:10.1096/fj.201903074rr

Trackman, P. C. (2016). Lysyl Oxidase Isoforms and Potential Therapeutic Opportunities for Fibrosis and Cancer. *Expert Opin. Ther. Targets* 20, 935–945. doi:10.1517/14728222.2016.1151003

Tsiapalis, D., and Zeugolis, D. I. (2021). It Is Time to Crowd Your Cell Culture media - Physicochemical Considerations with Biological Consequences. *Biomaterials* 275, 120943. doi:10.1016/j.biomaterials.2021.120943

Unemori, E. N., and Amento, E. P. (1990). Relaxin Modulates Synthesis and Secretion of Procollagenase and Collagen by Human Dermal Fibroblasts. *J. Biol. Chem.* 265, 10681–10685. doi:10.1016/s0021-9258(18)87000-4

Unemori, E. N., Bauer, E. A., and Amento, E. P. (1992). Relaxin Alone and in Conjunction with Interferon-γ Decreases Collagen Synthesis by Cultured Human Scleroderma Fibroblasts. *J. Invest. Dermatol.* 99, 337–342. doi:10.1111/1523-1747.ep12616665

Walton, K. L., Johnson, K. E., and Harrison, C. A. (2017). Targeting TGF-β Mediated SMAD Signaling for the Prevention of Fibrosis. *Front. Pharmacol.* 8, 461. doi:10.3389/fphar.2017.00461

Walton, K. W. (1952). The Biological Behaviour of a New Synthetic Anticoagulant (Dextran Sulphate) Possessing Heparin-like Properties. *Br. J. Pharmacol.* 7, 370–391. doi:10.1111/j.1476-5381.1952.tb00705.x

Wells, A. R., and Leung, K. P. (2020). Pirfenidone Attenuates the Profibrotic Contractile Phenotype of Differentiated Human Dermal Myofibroblasts. *Biochem. Biophys. Res. Commun.* 521, 646–651. doi:10.1016/j.bbrc.2019.10.177

Werner, S., and Alzheimer, C. (2006). Roles of Activin in Tissue Repair, Fibrosis, and Inflammatory Disease. *Cytokine Growth Factor. Rev.* 17, 157–171. doi:10.1016/j.cytogfr.2006.01.001

Wietecha, M. S., Pensalfini, M., Cangkrama, M., Müller, B., Jin, J., Brinckmann, J., et al. (2020). Activin-mediated Alterations of the Fibroblast Transcriptome and Matrisome Control the Biomechanical Properties of Skin Wounds. *Nat. Commun.* 11, 2604. doi:10.1038/s41467-020-16409-z

Wilmarth, K. R., and Froines, J. R. (1992). *In Vitro* and *In Vivo* Inhibition of Lysyl Oxidase Byaminopropionitriles. *J. Toxicol. Environ. Health* 37, 411–423. doi:10.1080/15287399209531680

Winter, A., Salamonsen, L. A., and Evans, J. (2020). Modelling Fibroid Pathology: Development and Manipulation of a Myometrial Smooth Muscle Cell Macromolecular Crowding Model to Alter Extracellular Matrix Deposition. *Mol. Hum. Reprod.* 26, 498–509. doi:10.1093/molehr/gaaa036

Wu, X.-p., Wang, H.-j., Wang, Y.-l., Shen, H.-r., and Tan, Y.-z. (2018). Serelaxin Inhibits Differentiation and Fibrotic Behaviors of Cardiac Fibroblasts by Suppressing ALK-5/Smad2/3 Signaling Pathway. *Exp. Cel Res.* 362, 17–27. doi:10.1016/j.yexcr.2017.10.004

Yang, T.-H., Gingery, A., Thoreson, A. R., Larson, D. R., Zhao, C., and Amadio, P. C. (2018). Triamcinolone Acetonide Affects TGF-β Signaling Regulation of Fibrosis in Idiopathic Carpal Tunnel Syndrome. *BMC Musculoskelet. Disord.* 19, 342. doi:10.1186/s12891-018-2260-y

Yuan, Y., Zhang, Y., Han, X., Li, Y., Zhao, X., Sheng, L., et al. (2017). Relaxin Alleviates TGFβ1-Induced Cardiac Fibrosis via Inhibition of Stat3-dependent Autophagy. *Biochem. Biophysical Res. Commun.* 493, 1601–1607. doi:10.1016/j.bbrc.2017.09.110

Zeng, Q., Macri, L. K., Prasad, A., Clark, R. A. F., Zeugolis, D. I., Hanley, C., et al. (2011). "Skin Tissue Engineering," in *Comprehensive Biomaterials*. Editor P. Ducheyne (Oxford: Elsevier), 467–499. doi:10.1016/b978-0-08-055294-1.00186-0

Zeugolis, D. I. (2021). Bioinspired *In Vitro* Microenvironments to Control Cell Fate: Focus on Macromolecular Crowding. *Am. J. Physiology-Cell Physiol.* 320, C842–C849. doi:10.1152/ajpcell.00380.2020

Zwaagstra, J. C., Sulea, T., Baardsnes, J., Lenferink, A. E. G., Collins, C., Cantin, C., et al. (2012). Engineering and Therapeutic Application of Single-Chain Bivalent TGF-β Family Traps. *Mol. Cancer Ther.* 11, 1477–1487. doi:10.1158/1535-7163.mct-12-0060

Conflict of Interest: JZ and OR are the owners of the TGFβ traps and ACVR2B, respectively.

The remaining authors declare that the research was conducted in the absence of any commercial or financial relationships that could be construed as a potential conflict of interest.

Publisher's Note: All claims expressed in this article are solely those of the authors and do not necessarily represent those of their affiliated organizations, or those of the publisher, the editors and the reviewers. Any product that may be evaluated in this article, or claim that may be made by its manufacturer, is not guaranteed or endorsed by the publisher.

frontiers in Bioengineering and Biotechnology

ORIGINAL RESEARCH
published: 12 November 2021
doi: 10.3389/fbioe.2021.764212

A Three-Dimensional Co-Culture Model for Rheumatoid Arthritis Pannus Tissue

*Jietao Lin[1,2,3], Antonia RuJia Sun[1,2,3], Jian Li[1,2,3], Tianying Yuan[4], Wenxiang Cheng[1,2,3], Liqing Ke[1,2,3], Jianhai Chen[1,2,3], Wei Sun[4], Shengli Mi[4] and Peng Zhang[1,2,3]**

[1]Center for Translational Medicine Research and Development, Shenzhen Institute of Advanced Technology, Chinese Academy of Science, Shenzhen, China, [2]University of Chinese Academy of Sciences, Beijing, China, [3]Shenzhen Engineering Research Center for Medical Bioactive Materials, Shenzhen, China, [4]Biomanufacturing Center, Department of Mechanical Engineering, Tsinghua University, Beijing, China

Three-dimensional (3D) co-culture models have closer physiological cell composition and behavior than traditional 2D culture. They exhibit pharmacological effects like *in vivo* responses, and therefore serve as a high-throughput drug screening model to evaluate drug efficacy and safety *in vitro*. In this study, we created a 3D co-culture environment to mimic pathological characteristics of rheumatoid arthritis (RA) pannus tissue. 3D scaffold was constructed by bioprinting technology with synovial fibroblasts (MH7A), vascular endothelial cells (EA.hy 926) and gelatin/alginate hydrogels. Cell viability was observed during 7-day culture and the proliferation rate of co-culture cells showed a stable increase stage. Cell-cell interactions were evaluated in the 3D printed scaffold and we found that spheroid size increased with time. TNF-α stimulated MH7A and EA.hy 926 in 3D pannus model showed higher vascular endothelial growth factor (VEGF) and angiopoietin (ANG) protein expression over time. For drug validation, methotrexate (MTX) was used to examine inhibition effects of angiogenesis in 3D pannus co-culture model. In conclusion, this 3D co-culture pannus model with biological characteristics may help the development of anti-RA drug research.

Keywords: rheumatoid arthritis, 3D bioprinting, tissue engineering, pannus tissue model, drug screening

OPEN ACCESS

Edited by:
Feng-Huei Lin,
National Taiwan University, Taiwan

Reviewed by:
Xin Zhao,
Hong Kong Polytechnic University, Hong Kong SAR, China
Menekse Ermis Sen,
Terasaki Institute for Biomedical Innovation, United States

****Correspondence:***
Peng Zhang
peng.zhang@siat.ac.cn

Specialty section:
This article was submitted to Tissue Engineering and Regenerative Medicine, a section of the journal Frontiers in Bioengineering and Biotechnology

Received: *25 August 2021*
Accepted: *27 October 2021*
Published: *12 November 2021*

Citation:
Lin J, Sun AR, Li J, Yuan T, Cheng W, Ke L, Chen J, Sun W, Mi S and Zhang P (2021) A Three-Dimensional Co-Culture Model for Rheumatoid Arthritis Pannus Tissue. Front. Bioeng. Biotechnol. 9:764212. doi: 10.3389/fbioe.2021.764212

INTRODUCTION

Joint is a dynamic tissue that supports us to move, but it may suffer destruction of bone and cartilage because of arthritis like RA. Due to the genetic factor or immune system disorder, synovial membrane in RA patients presents abnormal proliferation of synovial cells and migration of inflammatory cells (Deane et al., 2017). Synovial joint is usually rich in blood vessels, which is a unique manifestation of RA. New vessels and hyperplastic fibrous tissue contribute to angiogenic disorders and form a complex vascular tissue called pannus (Veale et al., 2017). Angiogenesis not only provides more means for the spread of inflammatory cytokines and the infiltration of leukocyte but aggravate the formation of pannus (Maruotti et al., 2006; Elshabrawy et al., 2015). RA pannus is an aggressive and invasive tissue with massive leukocyte infiltration, proliferative synovial membranes and neovascularization, which is directly responsible for cartilage destruction and bone erosion (Lee and Weinblatt, 2001). The development of pannus is highly relevant to the growth factors, pro-inflammatory cytokines and chemokines. Growth factors, such as vascular endothelial growth factor (VEGF) and basic fibroblast growth factor (bFGF) are described as the key regulators

in proliferation, migration and vascular formation. Pro-inflammatory cytokines like tumor necrosis factor (TNF)-α, interleukin (IL)-6, which provide inflammatory conditions in RA synovium, have direct and indirect effects on other cell types to produce pro-angiogenic factors (Semerano et al., 2011).

In recent years, RA have become the most common form of inflammatory arthritis. Patients need to rely on drugs for control as it is an incurable disease (Doan and Massarotti, 2005; Yu et al., 2018). Inhibition of angiogenesis can be a helpful strategy for early prevention and treatment of RA (Veale and Fearon, 2006; MacDonald et al., 2018; Balogh et al., 2019). However, RA drug testing has low accuracy and drug development cycle is long. Although animal model is the most effective way to study RA drugs before clinical trials, ethics and experimental accuracy limits rapid and efficient evaluation of drug safety and efficacy (Li and Izpisua Belmonte, 2019). To overcome these difficulties, co-culture models are often used to mimic physiological environment of pannus for RA study and anti-RA drug screening (D'andrea et al., 1998; Kasama et al., 2001; Nozaki et al., 2007; Chu et al., 2018; Gou et al., 2018). IBOLD et al. developed a 3D pannus model *in vitro* as a high-throughput screening assay. Chondrocytes from porcine donors were isolated and seeded them into wells to form extracellular matrix (ECM). After 14 days, it would be coated with human synovial fibroblasts. They found that intercellular communication between these 2 cell types occurs both through gap junctions and ATP-mediated paracrine stimulation. (D'andrea et al., 1998). In the co-culture model of chondrocytes and synovial cells, D'ANDREA et al. found that the Ca + signal between these 2 cell types can be affected by 18α-glycyrrhetinic acid, suggesting they have communication in pannus tissue (Nozaki et al., 2007). Monocytes or polymorphonuclear neutrophils (PMNs) were seeded onto fibroblasts and Kasama et al. found that the expression of VEGF in co-culture groups are higher than synovial fibroblasts, monocytes or PMNs alone groups, which means VEGF expression in pannus can be also regulated by the interaction of synovial fibroblasts and activated leukocytes (Chu et al., 2018). Nozaki et al. isolated pannus tissue from RA patients and the inflammatory cells including macrophages, T cells and fibroblasts. They collected these cell types without enzyme digestion and found that inflammatory cells could develop into pannus-like tissue spontaneously *in vitro*. This pannus model continuously secreted MMP-9 and TNF-α, IL-8 and M-CSF, which related with osteoclastogenesis (Gou et al., 2018). Although these studies revealed useful characteristics of 3D pannus models *in vitro*, it is still difficult to construct a long lasting and strong repeatability pannus model to test anti-RA drugs due to the limitations of fabrication techniques.

Recent advances in 3D fabrication technology have allowed direct assembly of cells and biocompatible materials to form *in vitro* cellular models for artificial organ regenerations, the study of disease mechanisms and drug screening. This promising technique has the advantages of accurate control of cell distribution, high simulation of physiological microenvironments and cost-effectiveness, which is suitable for constructing complex 3D *in vitro* models (Mandrycky et al., 2016; Ma et al., 2018; Ong et al., 2018; Zhu et al., 2020). Therefore, 3D printing has been applied in the establishments of disease pathogenesis and drug screening model in hepatocellular carcinoma (Sun et al., 2020; Xie et al., 2021), breast cancer (Swaminathan et al., 2019; Lv et al., 2021), cervical tumor (Zhao et al., 2014; Pang et al., 2018), bladder cancer (Kim et al., 2019), and neurodegenerative diseases (Thomas and Willerth, 2017). To apply the potential value of 3D printing on anti-RA drug research, in this paper we constructed the *in vitro* pannus model by 3D printing of endothelial cells (EA.hy 926)/Synovial fibroblasts (MH7A) and gelatin/alginate and characterized its biological function. To our knowledge, RA synovial tissue fibroblasts produce pro-angiogenic growth factors, cytokines under the induction of inflammatory mediators or hypoxia. Under the condition of pro-angiogenic and inflammatory factors, endothelial cells therefore promote cell proliferation, migration and tube formation (Szekanecz et al., 2005; Elshabrawy et al., 2015; Alam et al., 2017; Croft et al., 2019). Both MH7A cell line (synovial fibroblasts) and EA.hy 926 cell line (endothelial cells) are widely used to be the cell model in RA research as they are considered valuable in preclinical trials (Komorowski et al., 2006; Cheng et al., 2019; Qu et al., 2019; Kong et al., 2020). In addition, we used gelatin/alginate as they can mimics ECM to provide the cells a better natural microenvironment. They show good biocompatibility and good molding effect when building 3D biological scaffolds, and these structures could have long retention time (Sun et al., 2020; Lv et al., 2021). The schematic of 3D pannus scaffold printing process has been showed in **Figure 1**. Biological characterization of 3D printed pannus models on calcium cross-linking toxicity, cell proliferation, cell survival, cell morphology and VEGF and Angiopoietin (ANG) protein expression will be evaluated. Our findings may offer a basic view of 3D printed pannus model in drug screening application.

MATERIALS AND METHODS

Cell Culture

Human endothelial cells (EA.hy 926) were generously given by professor Qin's Laboratory and the cells were cultured in Dulbecco Modified Eagle Medium (DMEM) with 4.5 g/L glucose, supplemented with 10% fetal bovine serum (Gibco, Thermo Fisher Scientific) and 1% penicillin/streptomycin (Sigma-Aldrich, MO, United States). Human synovial fibroblasts (MH7A) were purchased from the Riken Cell Bank (Tsukuba, Japan). The cells were maintained in Roswell Park Memorial Institute (RPMI) cultivation medium (Hyclone, Thermo Fisher Scientific, Wilmington, DE, United States) plus 10% fetal bovine serum (Gibco, Thermo Fisher Scientific) and 1% penicillin/streptomycin (Sigma-Aldrich). For TNF-α co-culture model, EA.hy 926 and MH7A were pretreated with 20 ng/ml TNF-α for 6 h before printing. All culture experiments are under the condition of humidified air with 5% CO_2 in 37°C.

Bioink Preparation

Gelatin/alginate was purchased from Sunp Biotech (Beijing, China). The lyophilized powder was dissolved in DMEM

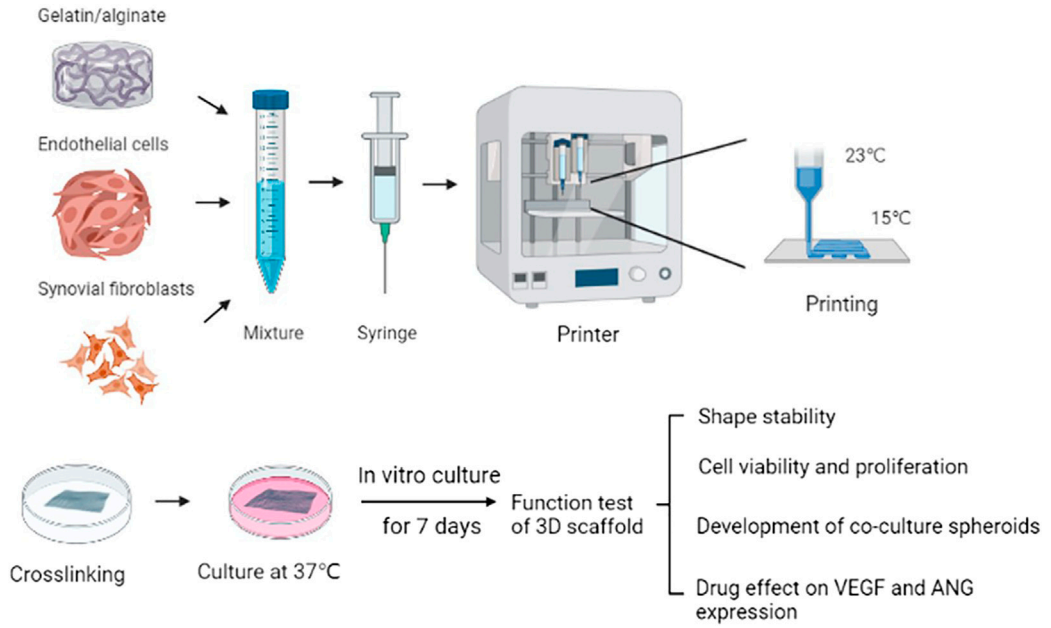

FIGURE 1 | Schematic of the 3D scaffold printing process. Fabrication of pannus mimic with gelatin /alginate and EA.hy 926/MH7A cells.

medium at 56°C. The mixed ink should be pasteurized by 70°C for 30 min and 4°C for 10 min three times at constant temperature water bath and stored at 4°C until use. Before the experiment, the ink was kept at 37°C for 2 h. For co-culture bioink, 2.5×10^6 cells of each EA.hy 926 and MH7A were resuspended in DMEM medium and homogeneously mixed with gelatin/alginate ink at a volume ratio at 1:4, resulting in a final cells density of 10^6 cells/ml.

3D Scaffold Formation and Culture

3D Cell Printer (SPP1603, SUNP, China) were used to fabricate all the 3D scaffold models. The temperature of the nozzle and printing bed were 23 and 15°C, respectively. 25G needle was chosen and the scanning speed was controlled at 3 mm/s. The models were printed in an eight-layered square grid pattern with the size of 10 × 10 mm cross sectional area and 2.4 mm thickness. The inks were loaded into 3 ml printing syringe and precooled at the printing chamber for 10 min. Preprinted on the 35 mm petri dishes and ensured that the bioink was smoothly extruded. After printing, hydrogel scaffolds were immersed in $CaCl_2$ solution for 5 min for crosslinking with alginate, providing better strength to the scaffolds. All scaffolds were gently blown with a pipette to remove bubbles. Then the scaffolds were washed with sterile physiologic saline once and finally cultured in DMEM medium. The scaffolds were crosslinked and the medium was changed every 3 days.

Calcium Cross-Linking Toxicity

EA.hy 926, MH7A and co-culture mixed cells were seeded into 96-well culture plates (3,000 cells/well) for 24 h. The cells were stimulated by 3% $CaCl_2$ solution for 5 min and washed by physiologic saline, and then they were cultured in DMEM medium for another 24 or 48 h. To evaluate cellular metabolic activity, Cell counting kit-8 (CCK-8, Dojindo, Japan) were added into each well at the volume of 10% of the total, protected against exposure to light. After 3 h incubation at 37°C, fluorescence of the culture medium was detected by microplate reader (PerkinElmer, Waltham, MA) at 450 nm. The data was then normalized to the standard and calculated cell viability.

Cell Proliferation Analysis

Cell proliferation in printed scaffolds was studied using CCK-8 on cultured days 1, 3, 5 and 7. Cells were incubated in a mixture of culture medium and CCK-8 for 2 h. The values of fluorescence at 450 nm were compared among different printed groups.

Cell Survival

Cell survival test in 3D scaffolds was carried out on day 1, 3, 5, 7 after printing. Fluorescent Live/Dead assay (C2015M, Beyotime, China) was used according to the instruction manual. Briefly, medium was removed and the scaffolds were then washed twice with phosphate buffer solution (PBS). Subsequently, Calcein-AM and propidium iodide (PI) was mixed with detection buffer at the dilution ratio of 1:1,000 and 1.5:1,000, respectively. The cell laden scaffolds were incubated at 37°C for 30 min in dark, then washed three times with PBS. Calcein-AM marks viable cells green and propidium iodide (PI) shows dead cells red. Images were obtained from fluorescence microscopy (Leica, Germany).

Cell Morphology Imaging and Analysis

The scaffold shapes were taken with camera (**Supplementary Figure S1**). Two dimensional cell morphology of EA.hy 926 and MH7A was captured using inverted optical microscope (Carl Zeiss, Germany) at cell density of 80%. Three-dimensional scaffold was examined by using fluorescence microscope (Leica, Germany) on cultured days 1, 3, 5 and 7. The images were taken in three random fields at 100× magnification. Cell diameters were measured by Image J (NIH, United States) software and analyzed by Origin (Originlab, United States).

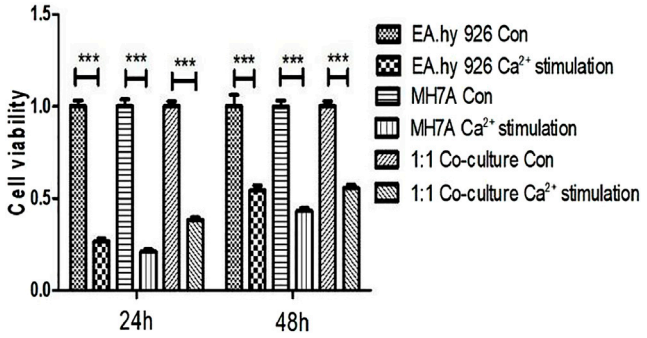

FIGURE 2 | Cytotoxicity of calcium on EA.hy 926 and MH7A and 1:1 co-culture mixture in 2D planar. Cells were treated with CaCl2 solution for 5 min and washed with physiologic saline once. After 24 and 48 h, their viability was determined using CCK-8 assay (mean ± SD, $*p < 0.05$; $**p < 0.01$; $***p < 0.001$, t-test). Con = no calcium stimulation; SD = standard deviation.

Enzyme-Linked Immunosorbent Assay

The experiment was divided into four groups: blank (no cell) group, co-culture group, TNF-α pannus model group and TNF-α pannus treated by 100 nM MTX for 24 h group. The concentrations of VEGF and ANG protein in the culture medium of 3D scaffold were detected on day 1, 3, 5, 7. Secretory cytokines were examined using corresponding commercial ELISA kits (R&D Systems, United States). A standard curve was constructed for each assay according to the manufacturer's instructions. The cytokine concentrations of each sample were calculated on the basis of the standard curve.

Statistical Analysis

All the data were presented as mean ± SD. Statistical significance was evaluated by Students T Test. Differences were considered to be significant for $p < 0.05$. $*p < 0.05$; $**p < 0.01$; $***p < 0.001$. Each experiment was performed in triplicate ($n = 3$) on at least independent three samples ($N \geq 3$).

RESULTS

Calcium Toxicity on Cells in 2D Planar Culture

To test the cytotoxic effect of calcium on EA.hy 926 and MH7A and 1:1 co-culture mixture, CCK-8 was used to determine the cell viability. As is shown in **Figure 2**, after stimulating by calcium for 5 min and cultured in DMEM for 24 h, The percentage of EA.hy 926 cell viability decreased to 26.53 ± 4.34, but it rose to 54.49 ± 6.17 at 48 h MH7A cells also had the same trend, 21.05 ± 3.30 percent at 24 h and 43.01 ± 4.24 percent at 48 h, respectively. In terms of 1:1 co-culture mixture, they performed 38.29 ± 3.71 at 24 h and 55.62 ± 4.17 at 48 h.

Cell Distribution and Viability in 3D Scaffolds

To determine cell distribution and survival in 3D gelatin/alginate/EA.hy 926/MH7A model, we used calcein-AM/PI staining assay to analyze live/dead cells on day 1, 3, 5 and 7. As we can see, the cells were evenly distributed in gelatin/alginate scaffold. Cell viability was stable about 80% during the *in vitro* culture of EA.hy 926/MH7A in 3D scaffold (**Figure 3A**). The cellular proliferation in 3D scaffolds was detected using CCK-8 kit on the same time. **Figure 3B** demonstrates that compared with day 1, cells had 1.36-fold proliferation on day 3, 1.75-fold proliferation on day 5, and 2.03-fold proliferation on day 7. There were significant differences between day 1 (0.39 ± 0.12) and day 5 (0.68 ± 0.05) and 7 (0.79 ± 0.05). Overall, the proliferation rate of co-culture cells had a stable increase stage from day 1 to day 7.

Development of Co-Culture Spheroids Within Cell Laden Scaffold

Inverted optical microscope was used to observe the cell morphology in 2D planar culture. EA.hy 926 shows epithelioid morphology and MH7A shows epithelioid and polygonal morphology (**Figure 4A**). The cells and cellular distribution pattern in printed scaffolds were characterized using fluorescence microscope on day 1, 3, 5, 7. Compared with 2D planar culture, cells turned to be spheroids within 3D scaffolds, and they were observed to form larger spheroids after 3 days of bioprinting. The spheroid size increased over time. **Figure 4B** shows spheroid distribution in the 3D co-culture cell laden scaffold. At day 1, 7.09% of the spheroids were at the diameter range of 20–30 μm. At day 3, the size between 20–30 μm was up to 28%. The percentages of over 30 μm at day 5 and day 7 were 10.65 and 14.73%, respectively (**Figure 4C**).

Effect of 3D Engineered Scaffold on VEGF and ANG Expression

The experiment was divided into four groups: blank (no cell) group, co-culture group, TNF-α pannus model group and TNF-α pannus treated by MTX group. The culture medium of the three-dimensional scaffold was collected on day 1, 3, 5, 7. **Figure 5A** shows that the cell co-culture scaffold and pannus scaffold secreted more VEGF protein on day 5 and 7 compared with that on the first day, but there was no significant difference compared with the no cell group on the same day ($p > 0.05$). **Figure 5B** illustrates the content of ANG secreted protein in the co-culture scaffold on day 1 was different from that of the no cell group ($p < 0.05$), and there was a significant difference from day 3 to day 7 ($p < 0.001$). On the day 7, the ANG protein concentration of the TNF-α pannus model group was different from that of the blank group ($p < 0.05$). Although the ANG concentration decreased in the pannus MTX group, there was no significant difference when compared with that in TNF-α pannus group.

DISCUSSION

RA is a chronic and systemic autoimmune disease, and immune dysregulation occurs earlier than joint inflammation. Current medications for RA are glucocorticoids (GCs), nonsteroidal anti-inflammatory drugs (NSAIDs), disease-modifying antirheumatic drugs (DMARDs) and biological therapies, which provide clinically meaningful pain relief and control inflammation in

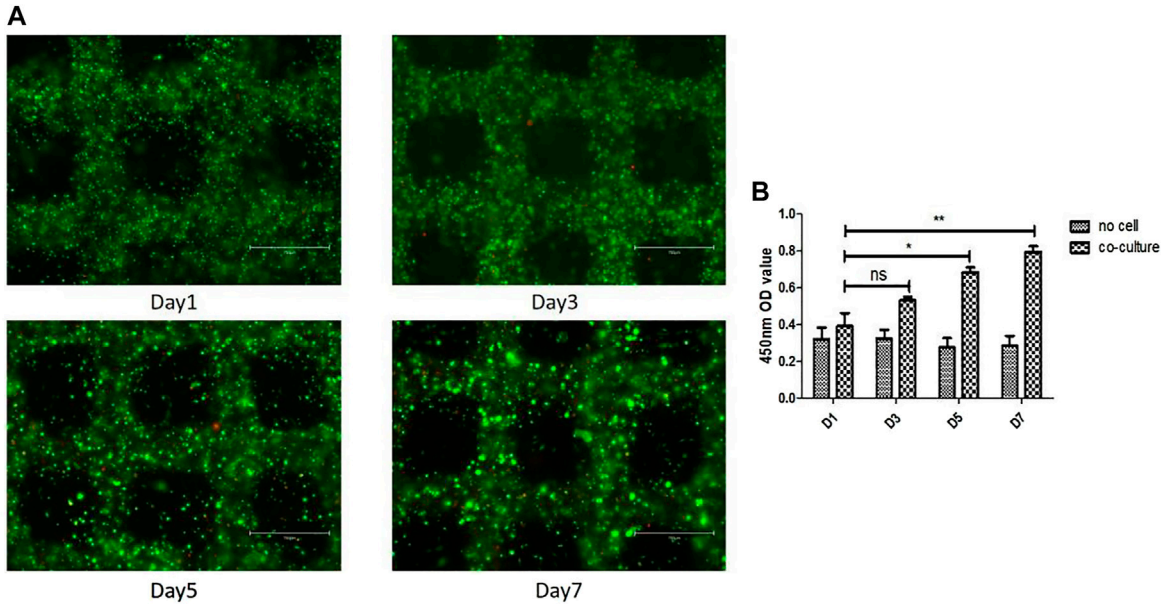

FIGURE 3 | Cell survival and proliferation in the 3D cell laden pannus tissue model. **(A)** Cell survival at different time points after printing. Live and dead cells were labelled with calcein-AM (green) and PI (red), respectively. Scale bar, 750 μm. **(B)** Proliferation rates of cells in 3D co-culture cell laden scaffolds at day 1, 3, 5, and 7.

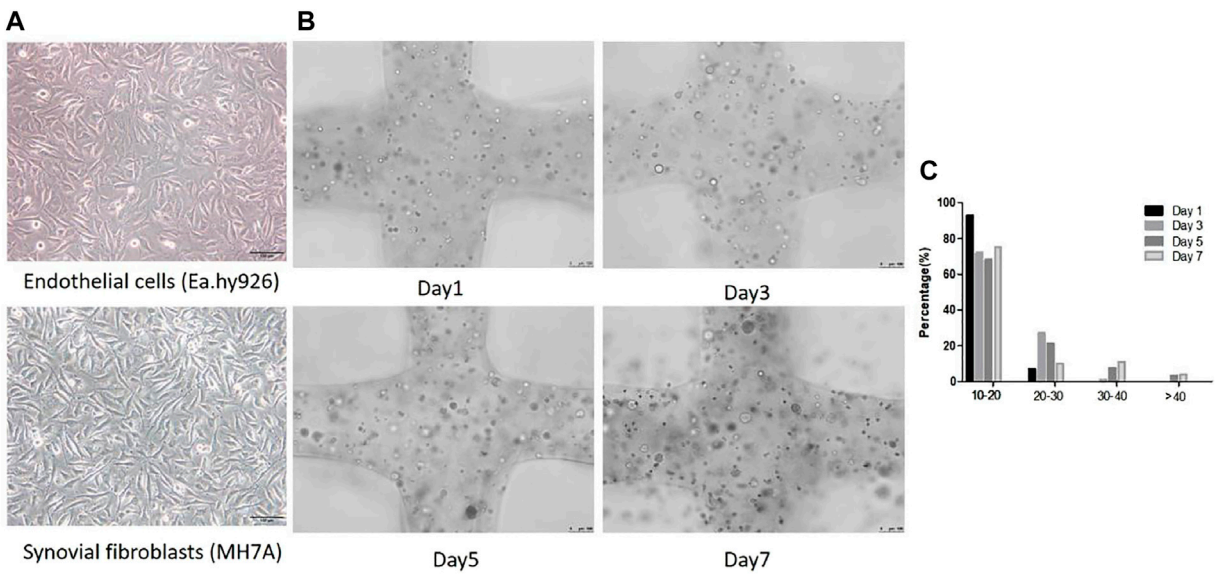

FIGURE 4 | Cellular morphological differences between 2D planar culture and 3D scaffolds. **(A)** EA.hy 926 and MH7A cells morphology in 2D planar culture. EA.hy 926 cells look epithelioid and MH7A cells are epithelioid and polygonal. Scale bar, 100 μm. **(B)** 3D Gelatin /alginate/EA.hy 926/MH7A scaffolds observed by a fluorescence microscope on culture days 1, 3, 5, and 7. Scale bar, 100 μm. Black arrows indicate cells and cellular spheroids in 3D scaffolds. **(C)** Distribution of spheroid diameter in 3D cell laden scaffolds on day 1, 3, 5, and 7.

patients. However, several side effects, including cytopenia, psoriasis, lung disease and liver damage, have been proved in treatments with these drugs (Burmester and Pope, 2017; Abbasi et al., 2019). Thus, the discovery of a safe and effective drug for RA treatment remains a crucial challenge.

Over the last 2 decades, angiogenesis has been reported to play an important role in the deterioration of RA. RA pannus is an aggressive and invasive tissue with rich proinflammatory cytokines like TNF-α, IL-1β and IL-6, which is directly responsible for cartilage destruction and bone erosion (Lee and Weinblatt,

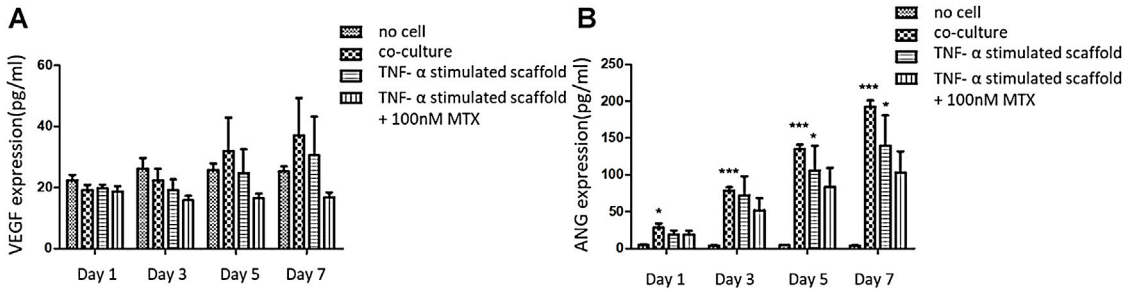

FIGURE 5 | Concentration of VEGF and ANG secreted protein in the supernatant of the three-dimensional scaffold on Day 1, 3, 5, and 7. **(A)** A. VEGF secreted protein concentration (pg/ml); **(B)** ANG secreted protein concentration (pg/ml).

2001; MacDonald et al., 2018). Numerous researchers have studied on inhibition of angiogenesis in RA (Zhang et al., 2017; Yang et al., 2018; Li et al., 2019; Zhai et al., 2019). In order to screen anti-RA drugs in a more accurate and efficient way, here we developed a 3D printed model to mimic the microenvironment of RA pannus. In terms of cell composition, we chose vascular endothelial cells and synovial fibroblast. Since EA.hy 926 and MH7A cells are widely used in drug discovery in RA and they are cell lines, we chose them to ensure the effectiveness and repeatability of our model. However, single cell model failed to offer a complex microenvironment to evaluate cellular response to drugs accurately (Sun et al., 2019). In the microenvironment, we added inflammatory factors (TNF-α) to simulate the inflammatory microenvironment. Compared to monolayer cell culture, 3D printing model is close to the space environment of the actual RA pannus tissue, enhancing the communication between cells and thereby improving the accuracy and efficiency of drug detection. For example, Kim et al. showed that cells grown in 2D culture conditions exhibit different gene and protein expression from those observed *in vivo*. And it was confirmed that cell proliferation rates in 3D culture was higher than that in the 2D cell culture because they mimic cell-to-cell interaction. They also found that there was a different anticancer effect between these two models. The drug effect in the 2D cell culture model is exaggerated, which explains why immunotherapies have shown excellent efficacy in research studies but not in clinical studies and patients (Kim et al., 2019). Thus, in this study we constructed the 3D pannus model based on the co-culture system of MH7A and EA.hy 926 cells. Alginate and gelatin are natural biomaterials. Both of them have high printability and good biocompatibility with cells. In addition, micro-extrusion printing has been shown that they can print cell laden scaffold in a controllable way with high cell viability. Despite cells experience stress condition during printing, they still have good cell viability with hydrogel (Mandrycky et al., 2016; Panwar and Tan, 2016). To maintain sufficient mechanical strength, printed scaffold needs to crosslink with $CaCl_2$ solution every 3 days. Our result showed that $CaCl_2$ solution had a cytotoxic effect among EA.hy 926 cells, MH7A cells, and 1:1 co-culture mixture groups in 2D planar. Cell viability decreased to around 30% after calcium stimulation for 5 min at 24 h, but cell viability regulated to around half at 48 h. According to the manufacturer's instruction, the recommendation time for crosslinking is 4–8 min, and we chose 5 min in order to hold the shape of the scaffold. As the concentration and ratio of gelatin and sodium alginate are confidential and there would be difference between 2D culture and 3D hydrogel scaffold, we further tested cell survival using calcein-AM/PI staining assay and measured cell proliferation using CCK-8 assay in 3D cell laden scaffold. The survival result showed that the viability of the co-culture mixture was around 80%. The proliferation rate of co-culture cells increased steadily from day 1 to day 7, which illustrates the gelatin/alginate bioink is biocompatible with cell growth. Earlier studies have demonstrated that cell viability and behavior in the scaffold is influenced by biomaterial type, material viscosity, printing speed, printing temperature and extrusion pressure (Zhao et al., 2015; Li et al., 2018). During our exploration on printing process, we noticed that too low temperature would lead to over coagulation of bioink. The bioink was so difficult to extrude that shear forces increased, resulting in cellular injury and death.

Compared with the morphology of MH7A cells and EA.hy 926 in 2D planar culture and 3D printed scaffold, we found that MH7A showed epithelioid and polygonal morphology and EA.hy 926 presented epithelioid morphology while they looked spheroids from day 1 to day 7. What's more, after we measured the diameter of cellular spheroids on day 1, 3, 5 and 7, we observed that cells were assembled to be larger spheroid with time.

VEGF and ANG are considered fundamental in the formation of pannus. VEGF is one of the key regulators of angiogenesis as they are related to proliferation, migration and vascular tube formation (Marrelli et al., 2011). ANG acts later in the pathogenesis of pannus compared to VEGF. ANG is increased to form and increase blood vessel stability (Clavel et al., 2003). In order to verify the biological function of our 3D printed scaffold, we conducted ELISA assay to detect concentrations of VEGF and ANG protein. The results showed that the expression of VEGF and ANG in the co-culture and pannus group increased with days, but the co-culture group showed a more obvious effect. This may be because the cells in pannus group was induced by TNF-α before the model was constructed, but we did not provide an external inflammatory environment afterwards, resulting in the incomplete performance of the pannus characteristics. MTX has been showed that it could reduce VEGF content in CIA rat model to relieve angiogenesis (Chen et al., 2021). Hirata S also illustrated that MTX inhibited both basal and vascular endothelial cell growth

factor-stimulated tritiated deoxyuridine (3H-UdR) incorporation into vascular endothelial cell in a dose-dependent manner (Hirata et al., 1989). So MTX was added after the model was printed, and the concentration of pro-angiogenic factors decreased compared with the pannus group for 7 days.

However, there are some differences between our 3D pannus scaffold and the actual pannus tissue. Here we only chose vascular endothelial cells and synovial fibroblast to mimic the cell composition of RA pathological pannus tissue instead of using all cell types. The pro-angiogenic factors *in vivo*, such as growth factors, hypoxia inducible factors, cytokines, chemokines, matrix metalloproteinase and adhesion molecules are also complex in deterioration of pannus. In this study, we constructed a 3D co-culture model for RA pannus tissue and provided a basic view of its biological characteristics. Further work on the comparison of pathological characteristics between pannus model of RA *in vitro* and clinical pannus specimens is needed, and improvements of this scaffold should be processed in the future.

CONCLUSION

We report the construction of *in vitro* RA pannus co-culture model by applying 3D printing technique with EA.hy 926/MH7A and gelatin/alginate. The 3D pannus model showed a good cell viability and interaction to mimic the microenvironment of pannus *in vivo*. The concentration of VEGF and ANG protein in the supernatant of the 3D pannus model increased over time. In addition, adding MTX to the 3D pannus model can down-regulate the expression of pro-angiogenic factors. Further studies are required to develop more details to construct the platform for drug screening, but this study may offer a basic view of 3D printed pannus model in drug screening application.

DATA AVAILABILITY STATEMENT

The raw data supporting the conclusion of this article will be made available by the authors, without undue reservation.

AUTHOR CONTRIBUTIONS

JtL, AS, JnL, WC, and PZ contributed to the conception of the study. JnL, TY, LK, and JC conducted the experiment. SM and WS provided the 3D printing machine. JtL, JnL, and JC performed the data analyses and wrote the manuscript. PZ supervised and trained JtL and he has been the corresponding author for the manuscript.

FUNDING

This research was supported by the National Key R&D Program of China, China: 2018YFC1705205; Foreign cooperation project of Chinese Academy of Sciences, China: 172644KYSB20190032; National Natural Science Foundation of China, China: 92068117 and 81871809; Guangdong Basic and Applied Basic Research Fund, China: 2020B1515120052; Sanming Project of Medicine in Shenzhen, China: SZSM201808072; Development and Reform Commission of Shenzhen Municipality, China: XMHT20190106001. Shenzhen Double Chain Project for Innovation and Development Industry supported by Bureau of Industry and Information Technology of Shenzhen, China: 201908141541. The flow chart of 3D scaffold printing process was made on Biorender.com.

ACKNOWLEDGMENTS

Authors also wish to acknowledge the great help from Prof. Mi and Prof. Sun of Tsinghua University.

SUPPLEMENTARY MATERIAL

The Supplementary Material for this article can be found online at: https://www.frontiersin.org/articles/10.3389/fbioe.2021.764212/full#supplementary-material

REFERENCES

Abbasi, M., Mousavi, M. J., Jamalzehi, S., Alimohammadi, R., Bezvan, M. H., Mohammadi, H., et al. (2019). Strategies toward Rheumatoid Arthritis Therapy; the Old and the New. *J. Cell. Physiol.* 234 (7), 10018–10031. doi:10.1002/jcp.27860

Alam, J., Jantan, I., and Bukhari, S. (2017). Rheumatoid Arthritis: Recent Advances on its Etiology, Role of Cytokines and Pharmacotherapy. *Biomed. Pharmacother.* 92, 615–633. doi:10.1016/j.biopha.2017.05.055

Balogh, E., Biniecka, M., Fearon, U., Veale, D. J., and Szekanecz, Z. (2019). Angiogenesis in Inflammatory Arthritis. *The Isr. Med. Assoc. J.* 21 (5), 345–352.

Burmester, G. R., and Pope, J. E. (2017). Novel Treatment Strategies in Rheumatoid Arthritis. *Lancet (London, England)* 389 (10086), 2338–2348. doi:10.1016/S0140-6736(17)31491-5

Chen, J., Cheng, W., Li, J., Wang, Y., Chen, J., Shen, X., et al. (2021). Notch-1 and Notch-3 Mediate Hypoxia-Induced Activation of Synovial Fibroblasts in Rheumatoid Arthritis. *Arthritis Rheumatol.* 73 (10), 1810–1819. doi:10.1002/art.41748

Cheng, W. X., Huang, H., Chen, J. H., Zhang, T. T., Zhu, G. Y., Zheng, Z. T., et al. (2019). Genistein Inhibits Angiogenesis Developed during Rheumatoid Arthritis through the IL-6/JAK2/STAT3/VEGF Signalling Pathway. *J. orthopaedic translation* 22, 92–100. doi:10.1016/j.jot.2019.07.007

Chu, J., Wang, X., Bi, H., Li, L., Ren, M., and Wang, J. (2018). Dihydromyricetin Relieves Rheumatoid Arthritis Symptoms and Suppresses Expression of Pro-inflammatory Cytokines via the Activation of Nrf2 Pathway in Rheumatoid Arthritis Model. *Int. immunopharmacol* 59, 174–180. doi:10.1016/j.intimp.2018.04.001

Clavel, G., Bessis, N., and Boissier, M. C. (2003). Recent Data on the Role for Angiogenesis in Rheumatoid Arthritis. *Jt. bone Spine.* 70 (5), 321–326. doi:10.1016/s1297-319x(03)00088-5

Croft, A. P., Campos, J., Jansen, K., Turner, J. D., Marshall, J., Attar, M., et al. (2019). Distinct Fibroblast Subsets Drive Inflammation and Damage in Arthritis. *Nature* 570 (7760), 246–251. doi:10.1038/s41586-019-1263-7

D'andrea, P., Calabrese, A., and Grandolfo, M. (1998). Intercellular Calcium Signalling between Chondrocytes and Synovial Cells in Co-culture. *Biochem. J.* 329 (Pt 3), 681–687. doi:10.1042/bj3290681

Deane, K. D., Demoruelle, M. K., Kelmenson, L. B., Kuhn, K. A., Norris, J. M., and Holers, V. M. (2017). Genetic and Environmental Risk Factors for Rheumatoid Arthritis. Best Practice & Research. *Clin. Rheumatol.* 31 (1), 3–18. doi:10.1016/j.berh.2017.08.003

Doan, T., and Massarotti, E. (2005). Rheumatoid Arthritis: an Overview of New and Emerging Therapies. *J. Clin. Pharmacol.* 45 (7), 751–762. doi:10.1177/0091270005277938

Elshabrawy, H. A., Chen, Z., Volin, M. V., Ravella, S., Virupannavar, S., and Shahrara, S. (2015). The Pathogenic Role of Angiogenesis in Rheumatoid Arthritis. *Angiogenesis* 18 (4), 433–448. doi:10.1007/s10456-015-9477-2

Gou, K. J., Zeng, R., Ren, X. D., Dou, Q. L., Yang, Q. B., Dong, Y., et al. (2018). Anti-rheumatoid Arthritis Effects in Adjuvant-Induced Arthritis in Rats and Molecular Docking Studies of Polygonum Orientale L. Extracts. *Immunol. Lett.* 201, 59–69. doi:10.1016/j.imlet.2018.11.009

Hirata, S., Matsubara, T., Saura, R., Tateishi, H., and Hirohata, K. (1989). Inhibition of *In Vitro* Vascular Endothelial Cell Proliferation and *In Vivo* Neovascularization by Low-Dose Methotrexate. *Arthritis Rheum.* 32 (9), 1065–1073. doi:10.1002/anr.1780320903

Kasama, T., Shiozawa, F., Kobayashi, K., Yajima, N., Hanyuda, M., Takeuchi, H. T., et al. (2001). Vascular Endothelial Growth Factor Expression by Activated Synovial Leukocytes in Rheumatoid Arthritis: Critical Involvement of the Interaction with Synovial Fibroblasts. *Arthritis Rheum.* 44 (11), 2512–2524. doi:10.1002/1529-0131(200111)44:11<2512:aid-art431>3.0.co;2-o

Kim, M. J., Chi, B. H., Yoo, J. J., Ju, Y. M., Whang, Y. M., and Chang, I. H. (2019). Structure Establishment of Three-Dimensional (3D) Cell Culture Printing Model for Bladder Cancer. *PloS one* 14 (10), e0223689. doi:10.1371/journal.pone.0223689

Komorowski, J., Jerczyńska, H., Siejka, A., Barańska, P., Ławnicka, H., Pawłowska, Z., et al. (2006). Effect of Thalidomide Affecting VEGF Secretion, Cell Migration, Adhesion and Capillary Tube Formation of Human Endothelial EA.Hy 926 Cells. *Life Sci.* 78 (22), 2558–2563. doi:10.1016/j.lfs.2005.10.016

Kong, L., Wang, L., Zhao, Q., Di, G., and Wu, H. (2020). Rhodojaponin II Inhibits TNF-α-Induced Inflammatory Cytokine Secretion in MH7A Human Rheumatoid Arthritis Fibroblast-like Synoviocytes. *J. Biochem. Mol. Toxicol.* 34 (10), e22551. doi:10.1002/jbt.22551

Lee, D. M., and Weinblatt, M. E. (2001). Rheumatoid Arthritis. *Lancet (London, England)* 358 (9285), 903–911. doi:10.1016/S0140-6736(01)06075-5

Li, M., and Izpisua Belmonte, J. C. (2019). Organoids - Preclinical Models of Human Disease. *New Engl. J. Med.* 380 (6), 569–579. doi:10.1056/NEJMra1806175

Li, Y., Yang, B., Bai, J. Y., Xia, S., Mao, M., Li, X., et al. (2019). The Roles of Synovial Hyperplasia, Angiogenesis and Osteoclastogenesis in the Protective Effect of Apigenin on Collagen-Induced Arthritis. *Int. immunopharmacol.* 73, 362–369. doi:10.1016/j.intimp.2019.05.024

Li, Z., Huang, S., Liu, Y., Yao, B., Hu, T., Shi, H., et al. (2018). Tuning Alginate-Gelatin Bioink Properties by Varying Solvent and Their Impact on Stem Cell Behavior. *Scientific Rep.* 8 (1), 8020. doi:10.1038/s41598-018-26407-3

Lv, K., Zhu, J., Zheng, S., Jiao, Z., Nie, Y., Song, F., et al. (2021). Evaluation of Inhibitory Effects of Geniposide on a Tumor Model of Human Breast Cancer Based on 3D Printed Cs/Gel Hybrid Scaffold. *Mater. Sci. Eng. C, Mater. Biol. Appl.* 119, 111509. doi:10.1016/j.msec.2020.111509

Ma, X., Liu, J., Zhu, W., Tang, M., Lawrence, N., Yu, C., et al. (2018). 3D Bioprinting of Functional Tissue Models for Personalized Drug Screening and *In Vitro* Disease Modeling. *Adv. Drug Deliv. Rev.* 132, 235–251. doi:10.1016/j.addr.2018.06.011

MacDonald, I. J., Liu, S. C., Su, C. M., Wang, Y. H., Tsai, C. H., and Tang, C. H. (2018). Implications of Angiogenesis Involvement in Arthritis. *Int. J. Mol. Sci.* 19 (7), 2012. doi:10.3390/ijms19072012

Mandrycky, C., Wang, Z., Kim, K., and Kim, D. H. (2016). 3D Bioprinting for Engineering Complex Tissues. *Biotechnol. Adv.* 34 (4), 422–434. doi:10.1016/j.biotechadv.2015.12.011

Marrelli, A., Cipriani, P., Liakouli, V., Carubbi, F., Perricone, C., Perricone, R., et al. (2011). Angiogenesis in Rheumatoid Arthritis: a Disease Specific Process or a Common Response to Chronic Inflammation? *Autoimmun. Rev.* 10 (10), 595–598. doi:10.1016/j.autrev.2011.04.020

Maruotti, N., Cantatore, F. P., Crivellato, E., Vacca, A., and Ribatti, D. (2006). Angiogenesis in Rheumatoid Arthritis. *Histology and histopathol* 21 (5), 557–566. doi:10.14670/HH-21.557

Nozaki, T., Takahashi, K., Ishii, O., Endo, S., Hioki, K., Mori, T., et al. (2007). Development of an *Ex Vivo* Cellular Model of Rheumatoid Arthritis: Critical Role of CD14-Positive Monocyte/macrophages in the Development of Pannus Tissue. *Arthritis Rheum.* 56 (9), 2875–2885. doi:10.1002/art.22849

Ong, C. S., Yesantharao, P., Huang, C. Y., Mattson, G., Boktor, J., Fukunishi, T., et al. (2018). 3D Bioprinting Using Stem Cells. *Pediatr. Res.* 83 (1-2), 223–231. doi:10.1038/pr.2017.252

Pang, Y., Mao, S. S., Yao, R., He, J. Y., Zhou, Z. Z., Feng, L., et al. (2018). TGF-β Induced Epithelial-Mesenchymal Transition in an Advanced Cervical Tumor Model by 3D Printing. *Biofabrication* 10 (4), 044102. doi:10.1088/1758-5090/aadbde

Panwar, A., and Tan, L. P. (2016). Current Status of Bioinks for Micro-extrusion-based 3D Bioprinting. *Molecules (Basel, Switzerland)* 21 (6), 685. doi:10.3390/molecules21060685

Qu, S. P., Li, G. W., Ma, H., and Xing, Q. (2019). MicroRNA-193a-3p Participates in the Progression of Rheumatoid Arthritis by Regulating Proliferation and Apoptosis of MH7A Cells through Targeting IGFBP5. *Eur. Rev. Med. Pharmacol. Sci.* 23 (11), 4850–4857. doi:10.26355/eurrev_201906_18072

Semerano, L., Clavel, G., Assier, E., Denys, A., and Boissier, M. C. (2011). Blood Vessels, a Potential Therapeutic Target in Rheumatoid Arthritis? *Jt. bone Spine* 78 (2), 118–123. doi:10.1016/j.jbspin.2010.06.004

Sun, L., Yang, H., Wang, Y., Zhang, X., Jin, B., Xie, F., et al. (2020). Application of a 3D Bioprinted Hepatocellular Carcinoma Cell Model in Antitumor Drug Research. *Front. Oncol.* 10, 878. doi:10.3389/fonc.2020.00878

Sun, W., Luo, Z., Lee, J., Kim, H. J., Lee, K., Tebon, P., et al. (2019). Organ-on-a-Chip for Cancer and Immune Organs Modeling. *Adv. Healthc. Mater.* 8 (15), e1900754. doi:10.1002/adhm.201900754

Swaminathan, S., Hamid, Q., Sun, W., and Clyne, A. M. (2019). Bioprinting of 3D Breast Epithelial Spheroids for Human Cancer Models. *Biofabrication* 11 (2), 025003. doi:10.1088/1758-5090/aafc49

Szekanecz, Z., Gáspár, L., and Koch, A. E. (2005). Angiogenesis in Rheumatoid Arthritis. *Front. Biosci.* 10, 1739–1753. doi:10.2741/1657

Thomas, M., and Willerth, S. M. (2017). 3-D Bioprinting of Neural Tissue for Applications in Cell Therapy and Drug Screening. *Front. Bioeng. Biotechnol.* 5, 69. doi:10.3389/fbioe.2017.00069

Veale, D. J., and Fearon, U. (2006). Inhibition of Angiogenic Pathways in Rheumatoid Arthritis: Potential for Therapeutic Targeting. Best Practice & Research. *Clin. Rheumatol.* 20 (5), 941–947. doi:10.1016/j.berh.2006.05.004

Veale, D. J., Orr, C., and Fearon, U. (2017). Cellular and Molecular Perspectives in Rheumatoid Arthritis. *Semin. immunopathol* 39 (4), 343–354. doi:10.1007/s00281-017-0633-1

Xie, F., Sun, L., Pang, Y., Xu, G., Jin, B., Xu, H., et al. (2021). Three-dimensional Bio-Printing of Primary Human Hepatocellular Carcinoma for Personalized Medicine. *Biomaterials* 265, 120416. doi:10.1016/j.biomaterials.2020.120416

Yang, G., Chang, C. C., Yang, Y., Yuan, L., Xu, L., Ho, C. T., et al. (2018). Resveratrol Alleviates Rheumatoid Arthritis via Reducing ROS and Inflammation, Inhibiting MAPK Signaling Pathways, and Suppressing Angiogenesis. *J. Agric. Food Chem.* 66 (49), 12953–12960. doi:10.1021/acs.jafc.8b05047

Yu, M. B., Firek, A., and Langridge, W. (2018). Predicting Methotrexate Resistance in Rheumatoid Arthritis Patients. *Inflammopharmacol* 26 (3), 699–708. doi:10.1007/s10787-018-0459-z

Zhai, K. F., Duan, H., Cui, C. Y., Cao, Y. Y., Si, J. L., Yang, H. J., et al. (2019). Liquiritin from Glycyrrhiza Uralensis Attenuating Rheumatoid Arthritis via Reducing Inflammation, Suppressing Angiogenesis, and Inhibiting MAPK Signaling Pathway. *J. Agric. Food Chem.* 67 (10), 2856–2864. doi:10.1021/acs.jafc.9b00185

Zhang, W., Li, F., and Gao, W. (2017). Tripterygium Wilfordii Inhibiting Angiogenesis for Rheumatoid Arthritis Treatment. *J. Natl. Med. Assoc.* 109 (2), 142–148. doi:10.1016/j.jnma.2017.02.007

Zhao, Y., Li, Y., Mao, S., Sun, W., and Yao, R. (2015). The Influence of Printing Parameters on Cell Survival Rate and Printability in Microextrusion-Based 3D Cell Printing Technology. *Biofabrication* 7 (4), 045002. doi:10.1088/1758-5090/7/4/045002

Zhao, Y., Yao, R., Ouyang, L., Ding, H., Zhang, T., Zhang, K., et al. (2014). Three-dimensional Printing of Hela Cells for Cervical Tumor Model *In Vitro*. *Biofabrication* 6 (3), 035001. doi:10.1088/1758-5082/6/3/035001

Zhu, X., Li, H., Huang, L., Zhang, M., Fan, W., and Cui, L. (2020). 3D Printing Promotes the Development of Drugs. *Biomed. Pharmacother.* 131, 110644. doi:10.1016/j.biopha.2020.110644

Conflict of Interest: The authors declare that the research was conducted in the absence of any commercial or financial relationships that could be construed as a potential conflict of interest.

Publisher's Note: All claims expressed in this article are solely those of the authors and do not necessarily represent those of their affiliated organizations, or those of the publisher, the editors and the reviewers. Any product that may be evaluated in this article, or claim that may be made by its manufacturer, is not guaranteed or endorsed by the publisher.

frontiers in Bioengineering and Biotechnology

ORIGINAL RESEARCH
published: 19 November 2021
doi: 10.3389/fbioe.2021.765630

The Synthesis of Europium-Doped Calcium Carbonate by an Eco-Method as Free Radical Generator Under Low-Intensity Ultrasonic Irradiation for Body Sculpture

Che-Yung Kuan[1,2], Yu-Ying Lin[2,3], I-Hsuan Yang[1,2], Ching-Yun Chen[4], Chih-Ying Chi[2,3,5], Chi-Han Li[2,3], Zhi-Yu Chen[1,2], Li-Ze Lin[6], Chun-Chen Yang[7]† and Feng-Huei Lin[1,2]*†*

[1]Institute of Biomedical Engineering, College of Medicine and College of Engineering, National Taiwan University, Taipei, Taiwan, [2]Institute of Biomedical Engineering and Nanomedicine, National Health Research Institutes, Miaoli County, Taiwan, [3]Ph.D. Program in Tissue Engineering and Regenerative Medicine, National Chung Hsing University, Taichung, Taiwan, [4]Department of Biomedical Sciences and Engineering, National Central University, Taoyuan, Taiwan, [5]Biomaterials Translational Research Center, China Medical University Hospital, Taichung, Taiwan, [6]Department of Materials Science and Engineering, National United University, Miaoli County, Taiwan, [7]Department of Materials Science and Engineering, National Taiwan University, Taipei, Taiwan

Body sculpture is a common method to remove excessive fat. The diet and exercise are the first suggestion to keep body shape; however, those are difficult to keep adherence. Ultrasound has been developed for fat ablation; however, it could only serve as the side treatment along with liposuction. In the study, a sonosensitizer of europium-doped calcium carbonate ($CaCO_3$: Eu) would be synthesized by an eco-method and combined with low-intensity ultrasound for lipolysis. The crystal structure of $CaCO_3$: Eu was identified by x-ray diffractometer (XRD). The morphology of $CaCO_3$: Eu was analyzed by scanning electron microscope (SEM). The chemical composition of $CaCO_3$: Eu was evaluated by energy-dispersed spectrophotometer (EDS) and inductively coupled plasma mass spectrometer (ICP-MS). The electronic diffraction pattern was to further check crystal structure of the synthesized individual grain by transmission electron microscope (TEM). The particle size was determined by Zeta-sizer. Water-soluble tetrazolium salt (WST-1) were used to evaluate the cell viability. Chloromethyl-2′,7′-dichlorofluorescein diacetate (CM-H_2DCFDA) and live/dead stain were used to evaluate feasibility *in vitro*. SD-rat was used to evaluate the safety and efficacy *in vivo*. The results showed that $CaCO_3$: Eu had good biocompatibility and could produce reactive oxygen species (ROS) after treated with low-intensity ultrasound. After 4-weeks, the $CaCO_3$: Eu exposed to ultrasound irradiation on SD rats could significantly decrease body weight, waistline, and subcutaneous adipose tissue. We believe that ROS from sonoluminescence, CO_2-bomb and locally increasing Ca^{2+} level would be three major mechanisms to remove away adipo-tissue and inhibit adipogenesis. We could say that the combination of the $CaCO_3$: Eu and low-intensity ultrasound would be a non-invasive treatment for the body sculpture.

Keywords: calcium carbonate, europium, reactive oxygen species, body sculpture, ultrasound

OPEN ACCESS

Edited by:
Bin Li,
Soochow University, China

Reviewed by:
Huan Zhou,
Hebei University of Technology, China
Xing Zhang,
Institute of Metals Research (CAS), China

***Correspondence:**
Chun-Chen Yang
kh61604@hotmail.com
Feng-Huei Lin
double@ntu.edu.tw

†These authors have contributed equally to this work

Specialty section:
This article was submitted to Tissue Engineering and Regenerative Medicine, a section of the journal Frontiers in Bioengineering and Biotechnology

Received: *27 August 2021*
Accepted: *20 October 2021*
Published: *19 November 2021*

Citation:
Kuan C-Y, Lin Y-Y, Yang I-H, Chen C-Y, Chi C-Y, Li C-H, Chen Z-Y, Lin L-Z, Yang C-C and Lin F-H (2021) The Synthesis of Europium-Doped Calcium Carbonate by an Eco-Method as Free Radical Generator Under Low-Intensity Ultrasonic Irradiation for Body Sculpture. Front. Bioeng. Biotechnol. 9:765630. doi: 10.3389/fbioe.2021.765630

INTRODUCTION

The excessive localized fat is a matter of great concern among subjects from current society. It affects image and body shape negatively; and results in dissatisfaction on individual (de Gusmao et al., 2020). Body sculpture refers to the use of either surgical or non-invasive techniques to modify the body for those who desire to fat reduction for specific problem areas, such as, abdomen, hips, thighs (Jewell et al., 2012). In 2018, the global market to body sculpture reached to US$ 6.1 billion; that might increase to $16.5 billion by 2025 (Michon, 2021).

Generally, the diet and exercise are the first suggestion to keep body shape in normal or as so-called attraction (Kordi et al., 2015). However, strict diets and intense daily exercise are difficult to maintain routinely for much longer time; that may result to fail (Mason et al., 2018). Liposuction is a surgical technique used to remove fat tissue to make people have a desired contour, which is among the top five cosmetic surgical procedures performed in United States (Jalian and Avram, 2012). Unfortunately, the side effects of liposuction include lidocaine toxicity, infections, numbness, fat embolism, or even death. Furthermore, the skin may locally appear contour irregularities, for instance, bumpy, wavy or withered due to uneven fat removal, poor skin elasticity and unusual healing (Mrad et al., 2019; Witte et al., 2020; O'Neill et al., 2021). Along with safety concerns, several noninvasive nonsurgical approaches have been developed for body sculpting, which have drawn more attentions in recent years (Jalian and Avram, 2012; Shek et al., 2014).

Ultrasound is one of powerful tools in medical image for diagnosis and very popular in rehabilitation as a therapeutic modality (Moreno-Moraga et al., 2007). Over the last decade, ultrasound has been developed to a commercial set in plastic surgery as physical lipolysis for body sculpture by specific ultrasonic parameters to break down fat tissue around the patients' waist.

As known, low-intensity ultrasound (0.5–17.5 W/cm^2) would increase the inertial cavitation and then go through the bubble growth, finally to bubble implosion to generate the heat and stress to destroy the fat tissue for lipolysis (Zhou et al., 2017); however, the result of breaking down the fat tissue is not so promising, and it could only serve as the side treatment along with the liposuction (Tonucci et al., 2014). Alternatively, high-intensity focused ultrasound (HIFU) was developed to burn-down subcutaneous adipose tissue by high intensity (1,000 W/cm^2) with a special focusing plate to converge the ultrasonic waves to the intended ablation area. HIFU has been reported to induce rapid cell necrosis by the high energy and temperature generated from cavitation explosion; that might effectively dissipate adipose tissue. However, HIFU has been reported to burn the surface skin and charred surrounding tissues, causing a serious inflammatory response.

In summary, lipolysis by low-intensity ultrasonic provides a good method for non-invasive and low-risk body sculpturing, without requiring a recovery period. However, non-invasive ultrasonic lipolysis still has some potential shortcomings that need to be improved and to skip the shortages from HIFU. In the study, a sonodynamic microparticles of europium-doped calcium carbonate would be synthesized to combine with low-intensity ultrasound for lipolysis on body sculpture by a mild and non-invasive way.

Calcium carbonate ($CaCO_3$) is the candidate material selected for the study due to its excellent biocompatibility and stability (Xiao et al., 2021). $CaCO_3$ is a biodegradable material that can decompose into carbon dioxide (CO_2) and calcium ions (Ca^{2+}) in the acidic environment of endosome-lysosome complex. It is also one of materials with the property of sonoluminescence; where the particle could absorb the energy from the explosion of ultrasonic cavitation to generate heat to react with oxygen or biomolecules to induce reactive oxygen species (ROS) generation, and then convert into different free radicals to de-nature the proteins for cell necrosis (Jonnalagadda et al., 2021). In addition, CO_2 decomposed from $CaCO_3$ may serve as bomb to make cell damage under explosive stress, that could further kill the adipocyte (Yang et al., 2019). Ca^{2+} released from the breaking down of $CaCO_3$ at the acidic endosome-lysosome complex would increase the local calcium level around the adipose tissue; that might inhibit the differentiation of mesenchymal stem cells toward adipogenesis (Li et al., 2018). We believe that ROS from sonoluminescence, CO_2-bomb and locally increasing Ca^{2+} level would be three major mechanisms to effectively remove away adipo-tissue for body sculpture.

In order to increase the sonoluminescent effect, a rare element Eu, would be doped into the crystal lattice to partially replace the Ca^{2+} in the lattice site of $CaCO_3$. A green method was developed to synthesize the particle of Eu-doped $CaCO_3$ ($CaCO_3$: Eu) at relative-lower temperature without organic solvent involved in.

In this study, x-ray diffractometer (XRD) was used for the crystal structure identification of the synthesized $CaCO_3$: Eu. The morphology of the developed particle was observed by scanning electron microscope (SEM). The semi-quantitative chemical composition of the developed particle was examined and evaluated by energy-dispersed spectrophotometer (EDS) and inductively coupled plasma mass spectrometer (ICP-MS). The electronic diffraction pattern was to further check the crystal structure of the synthesized individual grain by transmission electron microscope (TEM). The particle size was determined using a Zeta-sizer. The water-soluble tetrazolium salt (WST-1) on L-929 cells were used to evaluate the cell viability of the developed material; that would be in terms of *in vitro* cytotoxicity. Chloromethyl-2′,7′-dichlorofluorescein diacetate (CM-H_2DCFDA) and live/dead stain were used to evaluate how the combination of $CaCO_3$: Eu and low-intensity ultrasound works on 3T3-L1; the results would serve as first screening *in vitro*. Finally, SD-rat was used as the target animal to evaluate the safety and efficacy *in vivo*; where the body weight, body temperature, waist line, the weight of subcutaneous adipose tissue on ultrasonic area, histological sectioning, blood element analysis, and serological analysis would be measured and checked to prove the concept.

The scenario of the study was firstly to synthesize a high-sonoluminescent $CaCO_3$: Eu particles by a new developed method. Secondly, the synthesized particles would be injected to abdomen area and then locally applied with low-intensity ultrasound to prevent from the skin burning and charred

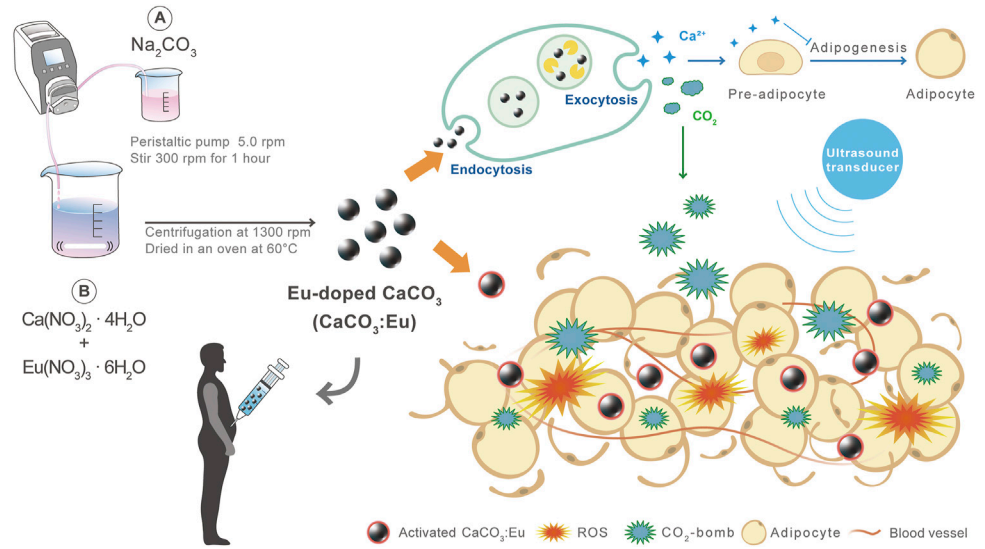

FIGURE 1 | The major mechanisms of $CaCO_3$: Eu with low-intensity ultrasound treatment to effectively remove away adipo-tissue and inhibit adipogenesis for body sculpture.

surrounding tissue. The combination of sonoluminescent $CaCO_3$: Eu and low-power ultrasound would generate ROS to damage the adipo-tissue under the stress of free radicals. The CO_2 and Ca^{2+} decomposed from $CaCO_3$: Eu would serve as CO_2-bomb and increase local Ca^{2+} level to further break-down the adipo-tissue and to inhibit local adipogenesis. The overall process would be schemed in **Figure 1**.

MATERIALS AND METHODS

Europium-Doped Calcium Carbonate Preparation

$CaCO_3$: Eu was synthesized by an innovative method at room temperature without organic solvent addition for environment friendly. The process was briefly described as follows. Firstly, 1.18 g of calcium nitrate and 0.223 g of europium nitrate was dissolved in 50 ml of ddH_2O. Then, 50 ml of 0.1 M sodium carbonate was added drop-by-drop into the previously prepared calcium/europium nitrate solution by peristaltic pump at 5.0 rpm and stirred by magnetic stirrer at room temperature for 3 h, and the solution was centrifugated at 1,300 rpm for 20 min (5500, Kubota, Japan). The precipitate was washed by ddH_2O for three times, and dried overnight in a freeze dryer (FDU-1100, EYELA, Japan) to obtain $CaCO_3$: Eu. The synthesized particles were stored in desiccator for later use.

The Crystal Structure Identification

The crystal structure of the synthesized particles was identified by XRD (MiniFlex II, Rigaku, Japan) with Copper Kα-II radiation at 30 kV and 15 mA at a scan rate of 4°/min from 20 to 60°. The sample was passed 230 mesh and pressed onto a sample holder with an area of 2 cm × 2 cm.

The Morphological Examination and Grain Size Evaluation Under SEM

The morphology and grain size of the synthesized particles were examined and observed by a SEM (Hitachi TM-1000, Japan). The sample were mounted on an aluminum-made SEM sample stage and then coated with a platinum film by a sputtering PVD. The sample edge was spotted with silver gel to prevent from undesired discharge to result in a blurry image.

The Analysis of Morphology and Electronic Diffraction Pattern by TEM

The morphology and electronic diffraction pattern of the developed particles were observed and analyzed by TEM (Tecnai G2 F20, FEI, United States). 5 mg of the particles were dispersed in 10 ml ddH_2O and homogenized by ultrasonic vibration for 15 min 20 μl of the dispersed and homogenized particles were dropped on the carbon-coated copper mesh, and dried at room temperature in a petri-dish with lid covered to prevent from pollution from air. The accelerated voltage was 200 kV. The electronic diffraction pattern was obtained by selected area diffraction mode (SAD-mode).

Chemical Composition Analysis

The chemical composition of the material was analyzed by an EDS (JSM-5600, JEOL, Japan). The sample preparation was similar to process of the sample for SEM, but coated with a pyrolytic carbon rather than platinum film. The energy of the accelerated x-ray beam was 20 kV. The chemical composition of sample was further confirmed by an inductively coupled plasma mass spectrometer (ICP-MS, NexION 2000, PerkinElmer, United States). In brief, 20 mg of sample was dissolved in 200 μl of pure nitric acid (438073, Sigma, United States), and

added with ddH_2O to 10 ml. The simple was diluted (1:10,000) with ddH_2O and performed by ICP-MS with kinetic energy discrimination (KED) mode.

The Analysis of Particle Size Distribution

The particle size distribution of the synthesized particles was analyzed by using a Zeta-sizer (Nano ZS, Malvern, United Kingdom). The sample was firstly suspended in ddH_2O and homogenized by an ultrasonic vibration. The homogenized suspension was placed in a Zeta-sizer cell and then measured using Dynamic Light Scattering (DLS) at room temperature.

In Vitro Study

Evaluation of Cell Viability

The cell viability was evaluated by WST-1 on L-929 cell (RM60091, Bioresource Collection and Research Center, Taiwan); that would be in terms of *in-vitro* cytotoxicity based on the guideline of ISO 10993-5.

Briefly, L-929 cells were cultured in α-MEM (11900-024, Gibco, United States) supplemented with 10% fetal bovine serum (FBS, A31606-02, Hyclone, United States) and 1% of 100X antibiotic-antimycotic (Anti-anti, 15240-062, Gibco, United States); and then seeded to a 96-well culture plate with a cell density of 1×10^4 per well and cultured at 37°C under 5% CO_2 for 24 h.

The culture medium would be used as the extraction vehicle to prepare sample extracted solution. 0.2 g of developed particles, aluminum oxide (11028, Sigma, United States) and polyurethane film containing 0.1% zinc diethyldithiocarbamate (ZDEC, RM-A, Hatano Research Institute, Food and Drug Safety Center, Japan) were immersed in 1 ml of culture medium, individually, at 37°C under 5% CO_2 for 24 h. The extracted solutions would be separately cultured with previous seeded cells and daily refreshed to evaluate cell viability; those would be named and abbreviated as experimental group ($CaCO_3$: Eu), negative control (N-control) and positive control (P-control), respectively. The result of L-929 cells cultured with medium were the control group abbreviated as Control.

After 1-day incubation, the medium was removed and then added in 90 μl culture medium and 10 μl WST-1 reagent (11644807001, Roche, United States); that was reacted at 37°C under 5% CO_2 for 1 h in dark. The culture plate was mounted on ELISA reader (VersaMax™, Molecular Devices, Canada); where the absorbance at the wavelength of 450 nm was recorded to evaluate the cell viability (Hsiao et al., 2019).

3T3-L1 Culture and Differentiation

Briefly, 3T3-L1 pre-adipocytes cell line (60159, Bioresource Collection and Research Center, Taiwan) was seeded to a 12-well culture plate with a cell density of 1×10^4 per well and cultured at 37°C under 5% CO_2 in Dulbecco Modified Eagle Medium (DMEM, high glucose, 12800-017, Gibco, United States) supplemented with 10% calf bovine serum (16170-078, Gibco, United States) and 1% of 100X Anti-anti. After confluence, it were further cultured in starvation condition for 2 days to keep cells in the status of G_0/G_1 phase at least 85% in all population (Cao et al., 2012). The confluent 3T3-L1 cells were cultured in an adipo-differentiated medium to convert cells into adipocytes; where the adipo-differentiated medium was DMEM supplemented with 10% FBS, 1% of 100X Anti-anti, 1 mM dexamethasone (D4902, Sigma, United States), 0.2 M indomethacin (I7378, Sigma, United States), 0.1% insulin and 0.25 M 3-Isobutyl-1-methylxanthine (IBMX, I5879, Sigma, United States). The adipocytes were cultured in DMEM supplemented 10% FBS and 1% of 100X Anti-anti; and medium was refreshed every 3 days, until the oil droplets were observed by a fluorescence microscope (TS-100, Nikon, Japan) stained with Nile red (N1142, Invitrogen, United States) (Park et al., 2017).

ROS Generation

The ROS generation of adipocytes, induced by synthesized $CaCO_3$: Eu and exposed to low-intensity ultrasound, was measured by CM-H_2DCFDA (C6827, Invitrogen, United States).

In brief, 3T3-L1 cells were seeded into 96-well culture plate with a density of 1×10^4 cells per well and differentiated to adipocyte as described in *3T3-L1 Culture and Differentiation*. 100 μl of 0.75 mg/ml $CaCO_3$: Eu in culture medium was added into each well and further cultured for 4 h, and then exposed to low-intensity ultrasound from the bottom of the culture plate in degassed water by an ultrasound transducer with a diameter of 2.0 cm. The distance between ultrasound transducer and the bottom of the cell culture plate was around 5 mm. The ultrasound irradiation was conducted with a function generator (33521A, Agilent, United States) at a resonant frequency of 1.0 MHz and a duty cycle of 50%. A power amplify was used to generate a square wave with a negative pressure of 0.33 MPa and intensity of 1.8 W/cm^2 for 90 s (Yang et al., 2020). It was further cultured for 1 h in the incubator. The medium was removed and the cells were stained with 25 μM CM-H_2DCFDA at room temperature for 45 min. The fluorescence was excited at the wavelength of 493 nm; and the intensity of emission light was measured by a multi-label plate reader (EnSpire, PerkinElmer, United States) at the wavelength of 523 nm that was the ROS concentration.

The experiment was divided into four groups and abbreviated in brace as follows: the cells were cultured in medium, 1) without $CaCO_3$: Eu addition and no ultrasound applied on (Control); 2) applied with low-intensity ultrasound without $CaCO_3$: Eu addition (US); 3) with $CaCO_3$: Eu addition but no expose to low-intensity ultrasound ($CaCO_3$: Eu); 4) with $CaCO_3$: Eu addition and expose to low-intensity ultrasound (US-$CaCO_3$: Eu).

The *In Vitro* Screening of Adipocyte Treated With Synthesized $CaCO_3$: Eu and Low-Intensity Ultrasound by WST-1 Assay and Live/Dead Stain

The cell viability and cytotoxicity of adipocyte, treated with synthesized $CaCO_3$: Eu and exposed to low-intensity ultrasound, were evaluated by WST-1 assay and live/dead stain, respectively. The experiments were used as first screening *in-vitro,* trying to know the possibility of body sculpture *in vivo* once adipo-tissue treated with developed particles and followed by low-intensity ultrasound irradiation.

In brief, 3T3-L1 cells were seeded on 12-well culture plate with a density of 6×10^4 cells per well and then differentiated into

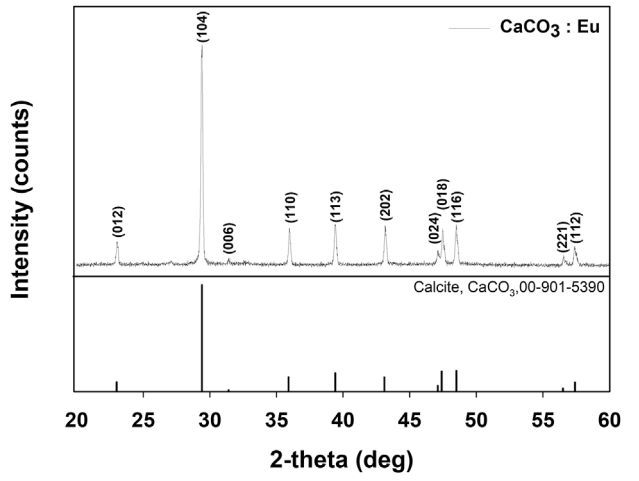

FIGURE 2 | XRD pattern of $CaCO_3$: Eu.

adipocyte. 0.75 mg/ml $CaCO_3$: Eu was added into each well and further cultured for 4 h, and then exposed to low-intensity ultrasound. It was further cultured for 1 h in the incubator. The medium was removed and then added in 900 μl culture medium and 100 μl WST-1 reagent; that was reacted at 37°C under 5% CO_2 for 1 h in dark. The culture plate was mounted on ELISA reader (EnSpire, PerkinElmer, United States); where the absorbance at the wavelength of 450 nm was recorded to evaluate the cell viability.

In the live/dead staining, the staining solution was prepared as follows; in which 50 μl of calcein AM (Ex/Em: 494/517 nm, C1430, Invitrogen, United States) and 16.5 μl of propidium iodide (PI, Ex/Em: 536/617 nm, P1304MP, Invitrogen, United States) reagents were well-mixed in phosphate buffered saline (PBS) and then added PBS to 5 ml, at pH 7.4. As previous description, the adipocytes were treated by developed $CaCO_3$: Eu and low-intensity ultrasound. After further cultured for 1 h, the medium was removed and added in 400 μl of staining solution, reacted for 15 min at room temperature in dark. The culture plate was mounted on fluorescence microscope (TS100, Nikon, Japan), with which the living cells and dead cells would be labelled by calcein AM in green color and propidium iodide in red, respectively, under the proper excitation light.

In Vivo Study

Experimental Animals and Surgical Procedure

Sprague Dawley rat age 10-weeks old, 325 g body weight in average and male in gender was used in the study. The rats were purchased from BioLASCO, Taiwan, and delivered to Laboratory Animal Center, National Health Research Institutes, Taiwan, 7 days before the experiment started to accommodate the environment. One cage for one rat was conducted to all the experimental period with controlled temperature and humidity of 22°C and 55%, respectively, by light turn-off and turn-on alternatively every 12 h. The study protocol was approved by the Institutional Animal Care and Use Committee of the National Health Research Institutes (NHRI-IACUC-108012).

3.75 g of $CaCO_3$: Eu was mixed within 1 ml of normal saline. The 100 μl of mixture was injected into the fat tissue of abdomen area on the SD rats once a week for 4 weeks. The low-intensity ultrasound was applied on the area where $CaCO_3$: Eu was injected; and treated consecutively 3 days every week for 4 weeks, each day 90 s. The low-intensity ultrasound was generated by a function generator at a resonant frequency of 1.0 MHz, a duty cycle of 50%, a square wave with a negative pressure of 0.33 MPa and intensity of 1.8 W/cm^2.

The study was divided into three groups that was described and abbreviated as follows: 1) the rats without any treatment were categorized to Control Group (Control); 2) the rat received injection on abdomen fat tissue once a week by 100 μl normal saline was Sham Control; 3) the rat injected with $CaCO_3$: Eu once a week and received ultrasound treatment consecutively 3 days every week was the major experimental group, abbreviated as US-$CaCO_3$: Eu.

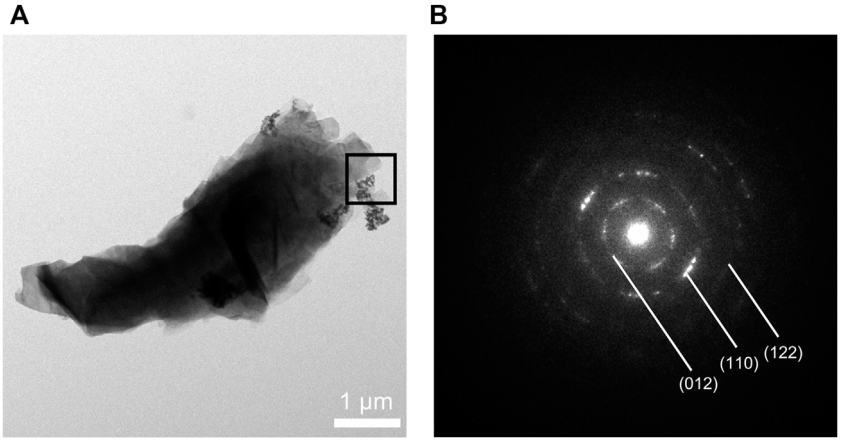

FIGURE 3 | (A) TEM photo of $CaCO_3$: Eu, **(B)** selected area electronic diffraction pattern of $CaCO_3$: Eu.

The body weight, body temperature, weight and waistline of the experimental rats were measured and recorded every week. At the end of the experiment, the rats were sacrificed and the blood was collected directly from the heart. The subcutaneous fat and organs were harvested for further analysis.

Serological and Blood Elements Analysis

In the serum analysis, the blood was collected in a blood collection tube (450533, Greiner bio-one, Austria), and centrifuged at 3,500 rpm for 10 min in a centrifuge (5500, Kubota, Japan). The supernatant was collected and analyzed. Blood lipid (TC, TG), liver function (AST, ALT), renal function (BUN, Creatinine, UA), and calcium (Ca) were analyzed by serology analyzer (DRI/CHEN NX-500 I, Fuji, Japan).

In the blood elements, the blood was collected in a purple collection tube containing an EDTA anticoagulant, and mixed homogeneously for analysis. The number of white blood cells (WBC), red blood cells (RBC), hemoglobin (HGB), hematocrit ratio (HCT), platelets (PLT), neutrophil (NE), eosinophilic multinuclear (EO), basophil (BA), lymphocytes (LY), and mononuclear spheres (MO) were analyzed by hematology analyzer (BC-5000 VET, Mindray, China).

The two analysis were to check the safety of the new developed lipolysis method on the experimental animal. The results were recorded and summarized in the **Supplementary Data Sheet S1**.

Histological Sectioning With Hematoxylin and Eosin Stain

The tissue sample of heart, liver, spleen, lungs, and kidneys were harvested by a sterilized surgical instrument. The tissues were carefully trimmed the surroundings and cleaned by PBS; and then placed in a 10% formalin solution (HT501128, Sigma, United States) for fixation. It was then immersed in acetone to de-oil and dehydrated by series of alcohol from 70 to 100%. The tissue was paraffin embedding in a tissue embedder (TEC-6, Tissue-Tek, United States). The paraffin blocks were sectioned (5 mm thick sections) on a rotary microtome (RM 215, Leica, Germany), and then the sections were fixed in 4% paraformaldehyde for 20 min, and washed 2 times by ddH_2O for 30 s. Dipped the slides into a Coplin jar containing hematoxylin solution for 30 s. Rinsed slides by ddH_2O for 1 min, and then stained with 1% eosin Y solution for 20 s. Dehydrated the sections with 2 times by 95% alcohol and two changed of 100% alcohol. The sections were cleaned by xylene for 5 min and put on cover slide by mounting media (Zihayat et al., 2018). The images were observation by an optical microscope (Eclipse 80i, Nikon, Japan). The results were summarized in the **Supplementary Data Sheet S1**.

Statistic Method

All the experiments were conducted at least in triplicate, and the data was presented with means ± SD. Statistical analyses were performed by one-way ANOVA. The results were considered significant difference when the p-value < 0.05.

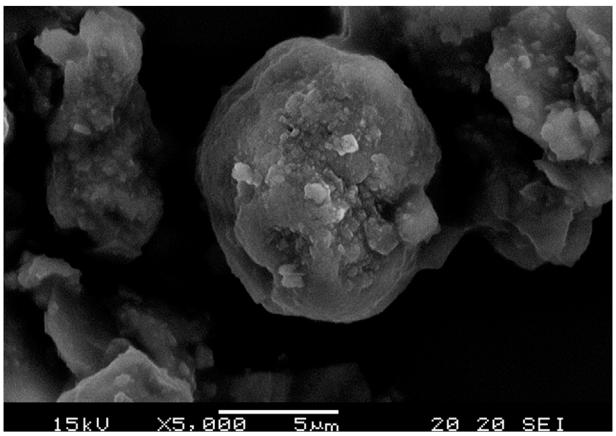

FIGURE 4 | SEM image of $CaCO_3$: Eu.

RESULTS

Material Characterization

The Crystal Structure Identification

Figure 2 showed XRD patterns of the synthesized $CaCO_3$: Eu. The characteristic peaks appeared at 2θ of 23.0°, 29.4°, 31.4°, 35.9°, 39.4°, 43.1°, 47.1°, 47.4°, 48.5°,56.5°, and 57.4 were corresponding to the plane of (012), (104), (006), (110), (113), (202), (024), (018), (116), (221), and (112), respectively. The peaks and relative intensities of the synthesized $CaCO_3$: Eu were fully matched to the calcite $CaCO_3$ as Crystallography Open Database (COD) No. 00-901-5390.

The synthesized $CaCO_3$: Eu further examined under the TEM; that showed a "nailhead" or "dogtooth" spar of calcite crystals that grew and aggregated with different habits, as shown in the edge in upper right of the **Figure 3A**. The selected electronic diffraction pattern (**Figure 3B**) was a classic ring pattern; with which the d-spacings calculated from the ring pattern were in agreement with the plane of (012), (110), and (122) in calcite crystal structure coded with COD No. 00-901-5390.

The Morphological Examination and Grain Size Evaluation Under SEM

The surface morphologies of the developed $CaCO_3$: Eu were examined under SEM as shown in **Figure 4**. It was aggregated into a particle approximately 4 μm in average; that was composed by many small rhombohedral grains stacking into a particle. The particle was shaped as scalenohedron or prism by the nano-sized grains; that could be seen from the edge of TEM photo as **Figure 3A**.

Chemical Composition Analysis

The overall elements composed in the synthesized $CaCO_3$: Eu was detected by energy dispersed spectrophotometry to analyze the energy status of the electrons in different orbits as shown in **Figure 5A**; where the major elements were carbon, oxygen, calcium and europium. The average weight percentage (weight %) and average atomic percentage (atomic%) of each element were shown in **Figure 5B**. An ICP-MS was used to further confirm the concentration of Eu in synthesized particle. The

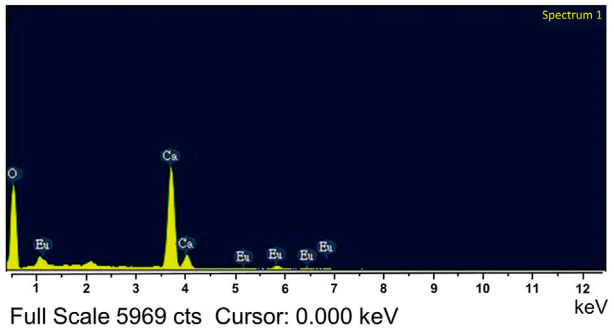

B

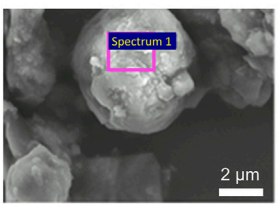

	Weight (%)	Atomic (%)
C K	8.66	13.59
O K	63.79	75.15
Ca K	22.65	10.65
Eu L	4.90	0.61
Totals	100	100

FIGURE 5 | (A) The chemical composition of the synthesized $CaCO_3$: Eu by EDS, and **(B)** the weight percentage and atomic percentage in average of each element.

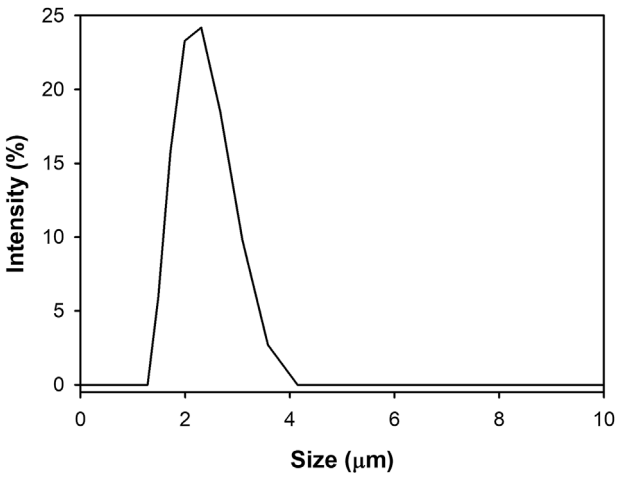

FIGURE 6 | Size distribution of $CaCO_3$: Eu.

concentration of Eu in $CaCO_3$: Eu was 112.5 mg/g (**Supplementary Table S1**). In this study, the molar ratio of europium to calcium in the $CaCO_3$: Eu was 0.084; that was high substitution rate of Eu to Ca in the calcite lattice site as 8.4% due to similar atomic radius and valence.

The Analysis of Particle Size Distribution

A Zeta-sizer was used to analyze the particle size and distribution of the synthesized $CaCO_3$: Eu. As shown in **Figure 6**, the particle size of $CaCO_3$: Eu was approximately 2.1 μm in average, and the

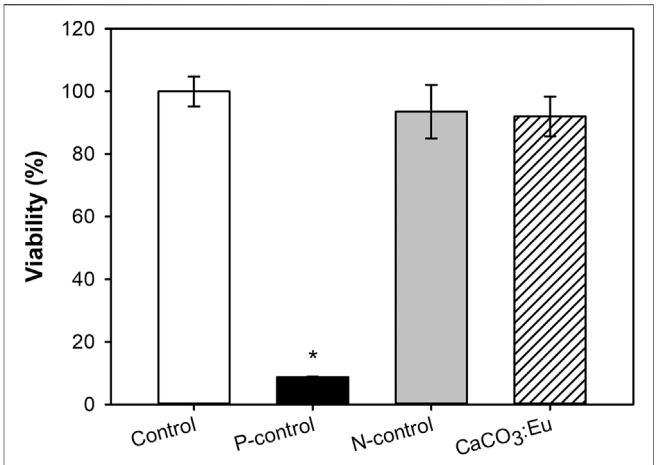

FIGURE 7 | The evaluation of cell viability of synthesized $CaCO_3$: Eu. *$p < 0.05$.

size distribution of $CaCO_3$: Eu is from 1.48 to 3.58 μm; that was very close to the 4 μm in average observed under SEM. In the SEM picture (**Figure 4**), the particle might more aggregate into a bigger one during drying process in the sample preparation. We believe that the developed $CaCO_3$: Eu with adequate particle size could be uptake by the defense cells, such as phagocyte, macrophage etc., for the later-on controlled release by endosome-lysosome complex breaking down and pumping out to extra-cellular matrix, finally delivered to whole body by the surrounding capillary system. We would prove it in the later experiments.

Evaluation of Cytotoxicity *In Vitro*

Figure 7 showed the cell viability of the developed $CaCO_3$: Eu followed the guideline of ISO 10993-5. The cell viability of the control group, P-control, N-control and experimental group of $CaCO_3$: Eu were 100 ± 4.82, 8.70 ± 0.19, 93.57 ± 8.54, and 92.05 ± 6.293, respectively. The difference of OD value between control group and $CaCO_3$: Eu was less than 25%. We could tell that the synthesized $CaCO_3$: Eu would not induce cytotoxicity to L-929 cells; and would keep cellular metabolism and mitochondrial functions in normal.

ROS Generation of $CaCO_3$: Eu Expose to Ultrasonic Irradiation

Intracellular ROS production was measured by a staining kit of CM-H_2DCFDA. The average fluorescence intensity of the control group was normalized as 1; the value of the other groups was normalized based on the intensity of control group as the relative value. The relative value would be in terms of the relative ROS production. After 3T3-L1 cells uptake the developed $CaCO_3$: Eu and then exposed to ultrasonic irradiation, the relative ROS production of Control, US, $CaCO_3$: Eu and US-$CaCO_3$: Eu were 1.00 ± 0.02, 1.12 ± 0.67, 1.07 ± 0.01, and 1.61 ± 0.01, respectively, as shown in **Figure 8**. We could see that the 3T3-L1 treated separately only

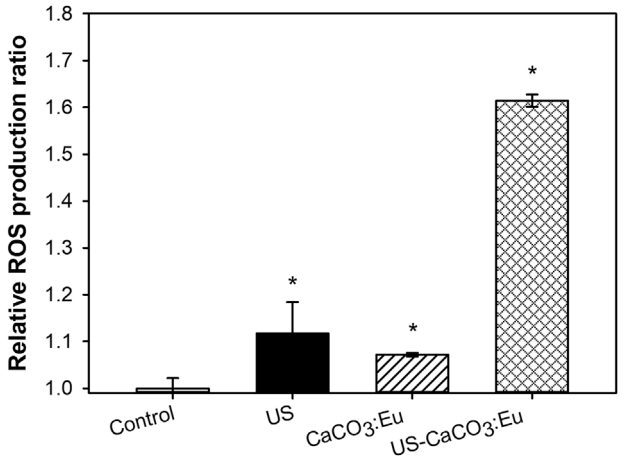

FIGURE 8 | ROS production of 3T3-L1 cells treated with $CaCO_3$: Eu under ultrasound irradiation, $^*p < 0.05$.

by ultrasound irradiation (US) and the $CaCO_3$: Eu particles ($CaCO_3$: Eu) would induce only small amount of ROS production; whereas the cells treated the combination of ultrasonic irradiation and the synthesized $CaCO_3$: Eu (US-$CaCO_3$: Eu) would induce great amount ROS generation.

From the results, we could tell that the developed $CaCO_3$: Eu would be a good sonosensitizer to generate energy under the excitation of ultrasound irradiation to produce ROS for lipolysis application.

The Efficacy of $CaCO_3$: Eu Exposed to Ultrasound Stimulation to Induce Adipocyte Necrosis Under ROS Stress

The efficacy of $CaCO_3$: Eu exposed to ultrasound stimulation to induce adipocyte necrosis under ROS stress was evaluated by WST-1 assay and live/dead stain to check the mitochondria activity and cell death rate, respectively.

The cell viability is the same as the previous description to normalize the OD value to the control group as 1; and then the value in the other groups was normalized referred to the control group to obtain a relative value. In **Figure 9A**, the adipocyte treated separately only by ultrasonic irradiation (US) and the developed $CaCO_3$: Eu ($CaCO_3$: Eu) would keep the mitochondria in normal function as control group (Control). In the contrary, the mitochondria function or cell viability was far less than that of the control group for the cells treated the combination of ultrasound irradiation and the developed $CaCO_3$: Eu (US-$CaCO_3$: Eu).

In the **Figure 9B**, the death rate of the adipocyte evaluated by live/dead stain had the same results as the previous WST-1 test; where the cell in green and in red were representative to living and dead cells, respectively. The results showed that the cells treated with the combination of ultrasound and developed particles had the highest death rate of 75%, compared with the control group.

From the results of WST-1 and live/dead stain, we believe that the cells treated with the combination of ultrasound and developed particles could effectively generate ROS to make the adipocyte toward necrosis under the stress.

The Body Weight Growing Rate of the Rat Treated With $CaCO_3$: Eu and Exposed to Ultrasonic Irradiation

The **Figure 10** was the body weight growing rate of the rats injected with $CaCO_3$: Eu to abdomen area and then applied with low-intensity ultrasound. The body weight growing rate of the rats without any treatment (Control) was much higher than the rats treated with the combination of $CaCO_3$: Eu injection and low-intensity ultrasonic irradiation (US-$CaCO_3$: Eu). The growth rate of control group was 7.57, 11.99, and 18.01 at week 2, 3, and 4, respectively. The growth rate of the group US- $CaCO_3$: Eu was 4.16, 7.83, and 10.67, respectively, at week 2, 3, and 4.

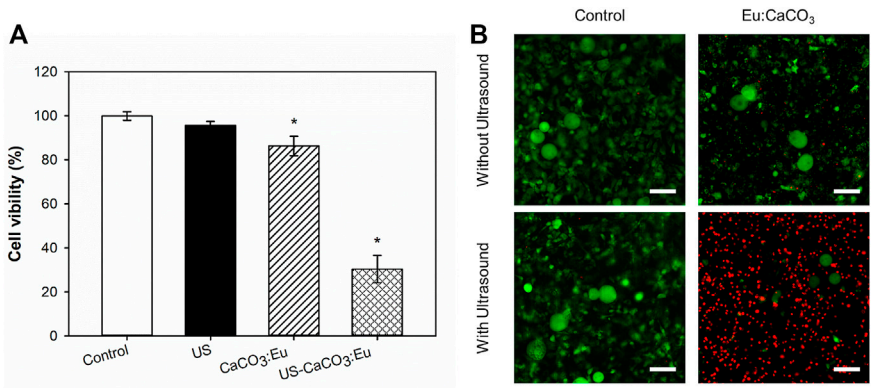

FIGURE 9 | The cell viability of $CaCO_3$: Eu exposed to ultrasound stimulation, evaluated by **(A)** WST-1 assay, $^*p < 0.05$, and **(B)** Live/dead staining (scale bar: 100 μm).

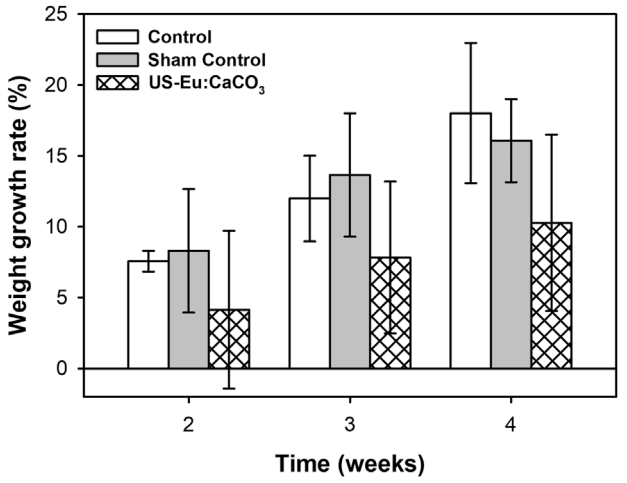

FIGURE 10 | The weight growth rate of SD rats treated with $CaCO_3$: Eu and exposed to ultrasonic irradiation.

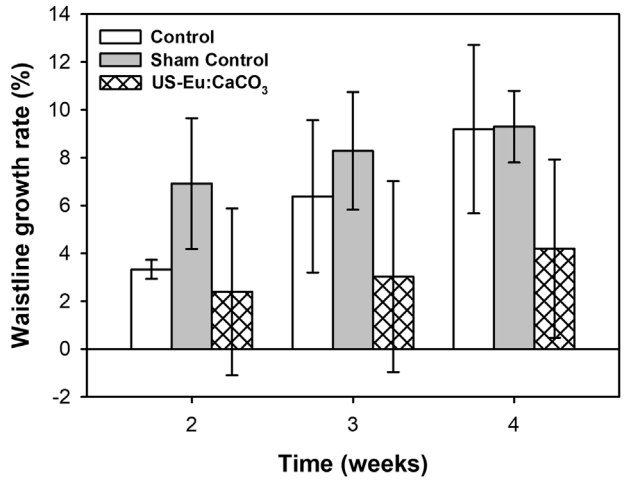

FIGURE 11 | The growth rate of waistline in SD rats after treated with $CaCO_3$: Eu injection and ultrasound irradiation.

Waistline Measurement

Figure 11 was the waistline measurement of the experiment rats. The waistline of the rats treated with the combination of developed particle and low-power ultrasound was much lower than the control group and sham group. The waistline for the combination treatment was about 2.39, 3.02, and 4.19 at week 2, 3, and 4, respectively. The tendency was quite similar to the that of the body weight growth.

The Growth Rate of Subcutaneous Fat

The growth rate of the subcutaneous fat was as shown in **Supplementary Figure S1**. The growth rate of the subcutaneous fat for the rats treated with the combination of the $CaCO_3$: Eu injection and ultrasound stimulation at week 4 was 78.28%, compared with control group as 100%.

From the results of the experiment, the combination treatment could effectively inhibit growth rate on body weight, waistline, and subcutaneous fat.

DISCUSSION

$CaCO_3$, comprises more than 4% of the mineral on earth's crust and is found throughout the world. Its most common natural forms are chalk, limestone, and marble, produced by the sedimentation of the shells of small fossilized snails, shellfish, and coral over millions of years (Mar and Phyo, 2013; Castro-Alonso et al., 2019). $CaCO_3$ has been widely used in medical applications, such as bone graft for tissue repair, biodegradable vehicle for drug and gene delivery etc. (Maleki et al., 2015; Song et al., 2018). In this study, we used Eu-doped calcium carbonate as sonodynamic reagent to combine with ultrasonic irradiation for body sculpture. Eu is a non-toxic rare earth element with an atomic number of 63, which belongs to the trivalent ion (Li et al., 2020). Eu could replace the calcium ion position of calcium carbonate to promote defects in calcium carbonate and increase the number of electron-hole pairs. Compared to divalent Ca ions, the doped Eu ions can obtain additional electrons, which creates a new energy level near the conduction band to reduce the energy gap effectively (Han et al., 2014; Wang et al., 2014). This makes the sonosensitizer more susceptible to ultrasonic irradiation and stimulates the generation of singlet oxygen and ROS in adipocytes for increasing the effective on lipolysis.

The $CaCO_3$: Eu was successfully synthesized using the eco-friendly method. The crystal structure was identified by XRD, which was matched with the standard pattern of calcite $CaCO_3$ (**Figure 2**). Zeta-sizer was used to analyze the particle size and distribution of the synthesized particles. The average particle size of $CaCO_3$: Eu was 2.1 μm, which fall in the range of optimum particle size for cellular endocytosis (0.5–10 μm) (Hirota and Ter, 2012; Foroozandeh and Aziz, 2018). The particle size was further evaluated by TEM and SEM, those supposedly larger than that of Zeta-sizer due to the aggregation during the sample preparation before examined under electronic microscope. The real grain size was around 100–300 nm as shown in the electron-penetrated edge of the TEM picture (**Figure 3A**).

Sonosensitizers can be divided into organic-based compounds and inorganic-based particles (Rosenthal et al., 2004; Chen et al., 2014). The organic-based materials, such as porphyrin-based structures, were reported to have short life span under ultrasound irradiation and showed great cytotoxicity. The inorganic-based particles, such as Ag, Au, Pt, TiO_2, and quantum dots, etc., have been used as sonosensitizer on sonodynamic therapy (SDT) for tumor/cancer treatment with better biostability and much longer life span (Xu et al., 2016). However, this kinds of material produce too much of ROS after exposed to ultrasonic stimulation, that is too strong and may result to the higher cytotoxicity (Serpe et al., 2012). In addition, the inorganic-based materials are not biodegradable in the

human body. In the study, we develop a mild sonosensitizer $CaCO_3$: Eu for body sculpture after exposed to ultrasound. It is a biodegradable particle that can be decomposed in endosome-lysosome complex, and then turn into carbon dioxide (CO_2) and calcium ions (Ca^{2+}), as described in the following series of reactions (Yang et al., 2019).

$$CaCO_{3(s)} \rightarrow Ca^{2+} + CO_3^{2-} \quad (1)$$

$$CO_3^{2-} + H^+ \rightarrow HCO^{3-} \quad (2)$$

$$HCO^{3-} + H^+ \rightarrow H_2CO_3 \quad (3)$$

$$H_2CO_3 \rightarrow H_2O + CO_2 \quad (4)$$

where the CO_2 could serve as bomb to break down the endosome-lysosome complex and as one of mechanisms to kill the adipocytes in the fat tissue. The high concentration of Ca^{2+} ions, decomposed from the $CaCO_3$: Eu, could create a osmotic pressure to quickly escape from the complex environment. The adipose tissue with locally high level of Ca^{2+} ions would have the effect to the inhibition on the conversion of pre-adipocyte to adipocyte as following discussions.

Ca^{2+} ion has been investigated that was in association with adipocyte lipid metabolism, such as lipid synthesis and catabolism (Shapses et al., 2004; Duncan et al., 2007). Extracellular Ca^{2+} is also involved in the modulation of adipogenesis. It has been reported that high extracellular Ca^{2+} inhibits adipogenesis in 3T3-L1 pre-adipocytes (Jensen et al., 2004; Zhai et al., 2020). The process of pre-adipocyte differentiation of mature adipocytes is regulated by complex transcription factors, which can regulate the expression of hundreds of proteins responsible for establishing mature adipocyte phenotypes (Lowe et al., 2011). The two major adipogenic factors are peroxisome proliferator-activated receptor (PPARγ) and cytosine-cytosine-adenosine-adenosine-thymidine/enhancer-binding protein (C/EBP) (Farmer, 2006; Payne et al., 2009). Once the $CaCO_3$: Eu is decomposed by cells, calcium ions diffuse into the interstitial space, turning the entire local environment into a high-calcium environment. A high-calcium concentration in the microenvironment activates the preadipocyte factor 1 (PREF1) expression, which causes the up-regulation of the transcription factor SOX9 (Wang and Sul, 2009), that could inhibit the formation of sterol regulatory element-binding protein (SREBP), C/EBP, and PPARγ for pre-adipogenic cell maturation (Jensen et al., 2004; Vergara et al., 2016; Das and Choudhuri, 2017; Pramme-Steinwachs et al., 2017). In this study, we cultured the cells with different concentration of calcium ions in the cell culture medium, this result was verified that, 3T3-L1 cells under high-calcium ion environment were inhibited the differentiation of fat precursor cells into adipocytes (**Supplementary Figure S2**).

Sonoluminescence is a sonosensitizer absorb energy from inertial cavitation followed bubble rapture after ultrasound applied to the local tissue to produce ROS. The ROS include superoxide ions (O_2^-), peroxide ions (O_2^{2-}), hydroxyl radicals (OH), and singlet oxygen ($^1O_2$), which can cause to cell death in fat tissue (Kuroki et al., 2007; Trendowski, 2014, 2015; Pang et al., 2016). The CMH_2-DCFDA fluorescent dye was used to detect hydroxyl, peroxyl, and other ROS-active oxides in the cells. In this study, ROS production in the US group was 1.12 times higher than that in the control group. It is speculated that under the action of ultrasound, the generation of inertial cavitation finally causes the bubble to rupture, it could release strong energy that causes pyrolysis of surrounding water molecules, and producing hydroxyl groups in adipocytes. The production of ROS in the $CaCO_3$: Eu group was not observed. In addition, compare with US-$CaCO_3$: Eu and bare $CaCO_3$ under ultrasound irradiation (US-$CaCO_3$) group, ROS production of US-$CaCO_3$: Eu was 1.24 times high than US-$CaCO_3$ (**Supplementary Figure S3**). Meanwhile, in the US-$CaCO_3$: Eu group, the ROS production is 1.61 times higher than control, which is presumed to be inertial cavitation and the generation of sonoluminescence, causing the acoustic-sensitive materials to be excited and produce singlet oxygen and superoxide. The results show that the combination of $CaCO_3$: Eu and ultrasound treatment could produce more ROS free radicals on adipocytes. In addition, we also used the WST-1 and live/dead assays to verify the *in vitro* carving effect of $CaCO_3$: Eu under ultrasound irradiation. The US group showed that only inertial cavitation acts on the pyrolysis of water molecules to produce hydroxyl, which has limited oxidative damage capacity in adipocyte. When ultrasound is applied to activate $CaCO_3$: Eu, inertial cavitation pyrolysis produces hydroxyl and sonoluminescence excitation material, causing sonosensitizers to be excited to produce singlet oxygen and ROS. These results indicated that combination of $CaCO_3$: Eu and ultrasound treatment could cause significant damage to the adipocyte.

The results of animal study did not remarkably change between the groups at the beginning. Nevertheless, at a specific time, the US-$CaCO_3$: Eu sonodynamic treatment groups had a change in waistline within 4 weeks, and a statistical difference was reached in the fourth week. As the animal model used in this study was Sprague Dawley rats, the abdominal viscera and muscle tissue were removed, and the subcutaneous fat was measured based on the actual waist circumference. The results indicated the US-$CaCO_3$: Eu on SD rats could significantly decrease the growth rate of body weight and waistline and reduce the storage of adipose tissue by the weight of subcutaneous fats. In addition, the reduction in subcutaneous fat cell volume was observed from fat tissue section between Control and US-$CaCO_3$: Eu group (**Supplementary Figure S4**). Body temperature changes (**Supplementary Figure S5**), tissue sections (**Supplementary Figure S6**), and blood analysis (**Supplementary Table S2**) of the above animal experiments showed that the injection of acoustically sensitive materials in animals and the effects of ultrasound of the rats are safe, and does not affect the physiological condition and organs of the rats by the ultrasound effect. the CaCO3: Eu exposed to ultrasound irradiation on SD rats could significantly decrease body weight, waistline, and subcutaneous adipose tissue. In summary, the US-$CaCO_3$: Eu sonodynamic treatment is demonstrated that has a great potential in the application of body sculpture.

CONCLUSION

In the study, a sonosensitizer of Eu-doped $CaCO_3$ was successfully synthesized to combine with low-intensity ultrasound for body sculpture. The results showed that the $CaCO_3$: Eu had good biocompatibility and could produce ROS in adipocytes for lipolysis. In addition, the results showed that developed sonosensitizer could effectively inhibit the adipogenesis after treated with low-intensity ultrasound. After 4-weeks animal study, the developed $CaCO_3$: Eu exposed to ultrasound irradiation on SD rats could significantly decrease the growth rate of body weight and waistline; and could reduce the storage of adipose tissue by the weight of subcutaneous fats. We could say that the combination of the developed Eu-doped $CaCO_3$ and low-intensity ultrasound could effectively inhibit the adipogenesis without skin burning and charred sounding tissue; that would be a mild and non-invasive treatment for the body sculpture.

DATA AVAILABILITY STATEMENT

The original contributions presented in the study are included in the article/**Supplementary Material**, further inquiries can be directed to the corresponding authors.

ETHICS STATEMENT

The animal study was reviewed and approved by the study protocol was approved by the Institutional Animal Care and Use Committee of the National Health Research Institutes (NHRI-IACUC-108012).

AUTHOR CONTRIBUTIONS

C-YK: Methodology, Validation, Formal analysis, Writing - original draft. Y-YL: Methodology, Writing - review and editing. I-HY: Methodology, Writing - review and editing. C-YC: Methodology, Validation. C-YC: Methodology. C-HL: Methodology. Z-YC: Methodology. L-ZL: Methodology. C-CY: Supervision, Writing - review and editing. F-HL: Conceptualization, Methodology, Formal analysis, Writing - review and editing, Supervision.

FUNDING

This work was financially supported by the National Health Research Institutes (BN-110-PP-01 and BN-110-GP-07).

ACKNOWLEDGMENTS

We would like to gratitude to Institute of Biomedical Engineering, National Taiwan University for the equipment and administration help to the research.

SUPPLEMENTARY MATERIAL

The Supplementary Material for this article can be found online at: https://www.frontiersin.org/articles/10.3389/fbioe.2021.765630/full#supplementary-material

REFERENCES

Cao, Z., Yang, H., Kong, L., Gu, D., He, Z., Xu, Z., et al. (2012). Growth Arrest Induction of 3T3-L1 Preadipocytes by Serum Starvation and Their Differentiation by the Hormonal Adipogenic Cocktail. *J. Cel Anim. Biol.* 6 (5), 57–65. doi:10.5897/jcab11.074

Castro-Alonso, M. J., Montañez-Hernandez, L. E., Sanchez-Muñoz, M. A., Macias Franco, M. R., Narayanasamy, R., and Balagurusamy, N. (2019). Microbially Induced Calcium Carbonate Precipitation (MICP) and its Potential in Bioconcrete: Microbiological and Molecular Concepts. *Front. Mater.* 6, 126. doi:10.3389/fmats.2019.00126

Chen, H., Zhou, X., Gao, Y., Zheng, B., Tang, F., and Huang, J. (2014). Recent Progress in Development of New Sonosensitizers for Sonodynamic Cancer Therapy. *Drug Discov. Today* 19, 502–509. doi:10.1016/j.drudis.2014.01.010

Das, S., and Choudhuri, D. (2017). Role of Low Calcium and High Calcium Diet on Adipocyte Metabolism with Respect to Serum Parathyroid Hormone (PTH) Levels in Male Wistar Rats. *Indian J. Physiol. Pharmacol.* 61, 430–439.

Duncan, R. E., Ahmadian, M., Jaworski, K., Sarkadi-Nagy, E., and Sul, H. S. (2007). Regulation of Lipolysis in Adipocytes. *Annu. Rev. Nutr.* 27, 79–101. doi:10.1146/annurev.nutr.27.061406.093734

Farmer, S. R. (2006). Transcriptional Control of Adipocyte Formation. *Cel Metab.* 4, 263–273. doi:10.1016/j.cmet.2006.07.001

Foroozandeh, P., and Aziz, A. A. (2018). Insight into Cellular Uptake and Intracellular Trafficking of Nanoparticles. *Nanoscale Res. Lett.* 13 (1), 339. doi:10.1186/s11671-018-2728-6

Gusmão, P. R., Canella, C., Gusmão, B. R., Filippo, A. d. A., and Filippo, G. R. (2020). Cryolipolysis for Local Fat Reduction in Adults from Brazil: A Single-arm Intervention Study. *J. Cosmet. Dermatol.* 19 (11), 2898–2905. doi:10.1111/jocd.13389

Han, Y.-X., Yang, C.-L., Wang, M.-S., and Ma, X.-G. (2014). Tuning the Band gap and Optical Properties of γ-Si3N4 with Rare Earth Element Ce. *RSC Adv.* 4, 55452–55458. doi:10.1039/c4ra10519b

Hirota, K., and Ter, H. (2012). Endocytosis of Particle Formulations by Macrophages and its Application to Clinical Treatment. *Molecular Regulation of Endocytosis*. IntechOpen. doi:10.5772/45820

Hsiao, M.-Y., Lin, P. C., Lin, A.-C., Wu, Y.-W., Chen, W.-S., and Lin, F.-H. (2019). Oxidized Hyaluronic Acid/adipic Acid Dihydrazide Hydrogel as Drug-Carrier for Cytoprotective Medications - Preliminary Results. *Biomed. Eng. Appl. Basis Commun.* 31 (05), 1950036. doi:10.4015/s1016237219500364

Jalian, H. R., and Avram, M. M. (2012). Body Contouring: the Skinny on Noninvasive Fat Removal. *Semin. Cutan. Med. Surg.* 31 (2), 121–125. doi:10.1016/j.sder.2012.02.004

Jensen, B., Farach-Carson, M. C., Kenaley, E., and Akanbi, K. A. (2004). High Extracellular Calcium Attenuates Adipogenesis in 3T3-L1 Preadipocytes. *Exp. Cel Res.* 301, 280–292. doi:10.1016/j.yexcr.2004.08.030

Jewell, M. L., Weiss, R. A., Baxter, R. A., Cox, S. E., Dover, J. S., Donofrio, L. M., et al. (2012). Safety and Tolerability of High-Intensity Focused Ultrasonography for Noninvasive Body Sculpting: 24-week Data from a Randomized, Sham-Controlled Study. *Aesthet. Surg. J.* 32 (7), 868–876. doi:10.1177/1090820X12455190

Jonnalagadda, U. S., Su, X., and Kwan, J. J. (2021). Nanostructured TiO2 Cavitation Agents for Dual-Modal Sonophotocatalysis with Pulsed Ultrasound. *Ultrason. Sonochem.* 73, 105530. doi:10.1016/j.ultsonch.2021.105530

Kordi, R., Dehghani, S., Noormohammadpour, P., Rostami, M., and Mansournia, M. A. (2015). Effect of Abdominal Resistance Exercise on Abdominal

Subcutaneous Fat of Obese Women: a Randomized Controlled Trial Using Ultrasound Imaging Assessments. *J. Manipulative Physiol. Ther.* 38 (3), 203–209. doi:10.1016/j.jmpt.2014.12.004

Kuroki, M., Hachimine, K., Abe, H., Shibaguchi, H., Kuroki, M., Maekawa, S., et al. (2007). Sonodynamic Therapy of Cancer Using Novel Sonosensitizers. *Anticancer Res.* 27, 3673–3677.

Li, S., Lu, X., Shi, S., Chen, L., Wang, Z., and Zhao, Y. (2020). Europium-Doped Ceria Nanowires as Anode for Solid Oxide Fuel Cells. *Front. Chem.* 8, 348. doi:10.3389/fchem.2020.00348

Li, X., Yang, X., Liu, X., He, W., Huang, Q., Li, S., et al. (2018). Calcium Carbonate Nanoparticles Promote Osteogenesis Compared to Adipogenesis in Human Bone-Marrow Mesenchymal Stem Cells. *Prog. Nat. Sci. Mater. Int.* 28 (5), 598–608. doi:10.1016/j.pnsc.2018.09.004

Lowe, C. E., O'Rahilly, S., and Rochford, J. J. (2011). Adipogenesis at a Glance. *J. Cel Sci* 124, 2681–2686. doi:10.1242/jcs.079699

Maleki, S., Barzegar-Jalali, M., Zarrintan, M. H., Adibkia, K., and Lotfipour, F. (2015). Calcium Carbonate Nanoparticles; Potential Applications in Bone and Tooth Disorders. *Pharm. Sci.* 20 (4), 175–182.

Mar, A. A., and Phyo, H. M. (2013). Utilization of Calcium Carbonate (Clam Shell). *Universities Research Journal* 6

Mason, A. E., Jhaveri, K., Cohn, M., and Brewer, J. A. (2018). Testing a mobile Mindful Eating Intervention Targeting Craving-Related Eating: Feasibility and Proof of Concept. *J. Behav. Med.* 41 (2), 160–173. doi:10.1007/s10865-017-9884-5

Michon, A. (2021). A Prospective Study Determining Patient Satisfaction with Combined Cryolipolysis and Shockwave Therapy Treatment for Noninvasive Body Contouring. *Aesth Plast. Surg.* 45, 2317–2325. doi:10.1007/s00266-021-02139-0

Moreno-Moraga, J., Valero-Altés, T., Riquelme, A. M., Isarria-Marcosy, M. I., and de la Torre, J. R. (2007). Body Contouring by Non-invasive Transdermal Focused Ultrasound. *Lasers Surg. Med.* 39 (4), 315–323. doi:10.1002/lsm.20478

Mrad, S., El Tawil, C., Sukaiti, W. A., Chebl, R. B., Dagher, G. A., and Kazzi, Z. (2019). Cardiac Arrest Following Liposuction: A Case Report of Lidocaine Toxicity. *Omna Med. J.* 34 (4), 341–345. doi:10.5001/omj.2019.66

O'Neill, R. C., Hanson, S. E., Reece, E., and Winocour, S. (2021). Safety Considerations of Fat Grafting in Buttock Augmentation. *Aesthet. Surg. J.* 41 (Suppl. ment_1), S25–S30. doi:10.1093/asj/sjab092

Pang, X., Xu, C., Jiang, Y., Xiao, Q., and Leung, A. W. (2016). Natural Products in the Discovery of Novel Sonosensitizers. *Pharmacol. Ther.* 162, 144–151. doi:10.1016/j.pharmthera.2015.12.004

Park, Y.-K., Obiang-Obounou, B., Lee, J., Lee, T.-Y., Bae, M.-A., Hwang, K.-S., et al. (2017). Anti-Adipogenic Effects on 3T3-L1 Cells and Zebrafish by Tanshinone IIA. *Int. J. Mol. Sci.* 18 (10), 2065. doi:10.3390/ijms18102065

Payne, V. A., Au, W.-S., Lowe, C. E., Rahman, S. M., Friedman, J. E., O'Rahilly, S., et al. (2009). C/EBP Transcription Factors Regulate SREBP1c Gene Expression during Adipogenesis. *Biochem. J.* 425, 215–224. doi:10.1042/BJ20091112

Pramme-Steinwachs, I., Jastroch, M., and Ussar, S. (2017). Extracellular Calcium Modulates Brown Adipocyte Differentiation and Identity. *Sci. Rep.* 7, 8888. doi:10.1038/s41598-017-09025-3

Rosenthal, I., Sostaric, J. Z., and Riesz, P. (2004). Sonodynamic Therapy-Aa Review of the Synergistic Effects of Drugs and Ultrasound. *Ultrason. Sonochem.* 11, 349–363. doi:10.1016/j.ultsonch.2004.03.004

Serpe, L., Foglietta, F., and Canaparo, R. (2012). Nanosonotechnology: the Next challenge in Cancer Sonodynamic Therapy. *Nanotechnology Rev.* 1, 173–182. doi:10.1515/ntrev-2011-0009

Shapses, S. A., Heshka, S., and Heymsfield, S. B. (2004). Effect of Calcium Supplementation on Weight and Fat Loss in Women. *J. Clin. Endocrinol. Metab.* 89 (2), 632–637. doi:10.1210/jc.2002-021136

Shek, S. Y. N., Yeung, C. K., Chan, J. C. Y., and Chan, H. H. L. (2014). Efficacy of High-Intensity Focused Ultrasonography for Noninvasive Body Sculpting in Chinese Patients. *Lasers Surg. Med.* 46 (4), 263–269. doi:10.1002/lsm.22232

Song, J., Wang, R., Liu, Z., and Zhang, H. (2018). Preparation and Characterization of Calcium Carbonate Microspheres and Their Potential Application as Drug Carriers. *Mol. Med. Rep.* 17 (6), 8403–8408. doi:10.3892/mmr.2018.8879

Tonucci, L. B., Mourão, D. M., Ribeiro, A. Q., and Bressan, J. (2014). Noninvasive Body Contouring: Biological and Aesthetic Effects of Low-Frequency, Low-Intensity Ultrasound Device. *Aesth Plast. Surg.* 38, 959–967. doi:10.1007/s00266-014-0391-6

Trendowski, M. (2014). The Promise of Sonodynamic Therapy. *Cancer Metastasis Rev.* 33, 143–160. doi:10.1007/s10555-013-9461-5

Trendowski, M. (2015). Using the Promise of Sonodynamic Therapy in the Clinical Setting against Disseminated Cancers. *Chemother. Res. Pract.* 2015, 1–16. doi:10.1155/2015/316015

Vergara, E. J. S., Dela Cruz, J., Kim, C. M., and Hwang, S. G. (2016). Increased Adipocyte Differentiation May Be Mediated by Extracellular Calcium Levels through Effects on Calreticulin and Peroxisome Proliferator Activated Receptor Gamma Expression in Intramuscular Stromal Vascular Cells Isolated from Hanwoo Beef Cattle. *Ital. J. Anim. Sci.* 15, 256–263. doi:10.1080/1828051x.2016.1186503

Wang, H. Y., Gong, F. Z., Zhou, L. Y., and Sun, L. (2014). Facile Synthesis of CaCo3 and CaCo3: Eu3+ Phosphors by Solid State Reaction at Room Temperature and the Luminescence Properties. *Mater. Sci. Forum* 809-810, 711–718. doi:10.4028/www.scientific.net/MSF.809-810.711

Wang, Y., and Sul, H. S. (2009). Pref-1 Regulates Mesenchymal Cell Commitment and Differentiation through Sox9. *Cel Metab.* 9, 287–302. doi:10.1016/j.cmet.2009.01.013

Witte, T., Dadras, M., Heck, F.-C., Heck, M., Habermalz, B., Welss, S., et al. (2020). Water-jet-assisted Liposuction for the Treatment of Lipedema: Standardized Treatment Protocol and Results of 63 Patients. *J. Plast. Reconstr. Aesthet. Surg.* 73 (9), 1637–1644. doi:10.1016/j.bjps.2020.03.002

Xiao, D., Cheng, J., Liang, W., Sun, L., and Zhao, J. (2021). Metal-phenolic Coated and Prochloraz-Loaded Calcium Carbonate Carriers with pH Responsiveness for Environmentally-Safe Fungicide Delivery. *Chem. Eng. J.* 418, 129274. doi:10.1016/j.cej.2021.129274

Xu, H., Zhang, X., Han, R., Yang, P., Ma, H., Song, Y., et al. (2016). Nanoparticles in Sonodynamic Therapy: State of the Art Review. *RSC Adv.* 6 (56), 50697–50705. doi:10.1039/C6RA06862F

Yang, C.-C., Wang, C.-X., Kuan, C.-Y., Chi, C.-Y., Chen, C.-Y., Lin, Y.-Y., et al. (2020). Using C-Doped TiO2 Nanoparticles as a Novel Sonosensitizer for Cancer Treatment. *Antioxidants* 9 (9), 880. doi:10.3390/antiox9090880

Yang, C.-C., Wang, W.-Y., Lin, F.-H., and Hou, C.-H. (2019). Rare-Earth-Doped Calcium Carbonate Exposed to X-ray Irradiation to Induce Reactive Oxygen Species for Tumor Treatment. *Int. J. Mol. Sci.* 20 (5), 1148. doi:10.3390/ijms20051148

Zhai, M., Yang, D., Yi, W., and Sun, W. (2020). Involvement of Calcium Channels in the Regulation of Adipogenesis. *Adipocyte* 9 (1), 132–141. doi:10.1080/21623945.2020.1738792

Zhou, B., Leung, B. Y. K., and Sun, L. (2017). The Effects of Low-Intensity Ultrasound on Fat Reduction of Rat Model. *Biomed. Res. Int.* 2017, 1–8. doi:10.1155/2017/4701481

Zihayat, B., Khodadadi, A., Torabi, M., Mehdipour, M., Basiri, M., and Asadi-Shekarri, M. (2018). Wound Healing Activity of Sheep's Bladder Extracellular Matrix in Diabetic Rats. *Biomed. Eng. Appl. Basis Commun.* 30 (02), 1850015. doi:10.4015/S1016237218500151

Conflict of Interest: The authors declare that the research was conducted in the absence of any commercial or financial relationships that could be construed as a potential conflict of interest.

Publisher's Note: All claims expressed in this article are solely those of the authors and do not necessarily represent those of their affiliated organizations, or those of the publisher, the editors and the reviewers. Any product that may be evaluated in this article, or claim that may be made by its manufacturer, is not guaranteed or endorsed by the publisher.

frontiers in Bioengineering and Biotechnology

ORIGINAL RESEARCH
published: 17 December 2021
doi: 10.3389/fbioe.2021.799594

Characterization of the Microflow Through 3D Synthetic Niche Microenvironments Hosted in a Millifluidic Bioreactor

Bogdan Ene-Iordache[1]*, *Chiara Emma Campiglio*[2], *Manuela Teresa Raimondi*[3]*† and *Andrea Remuzzi*[2†]

[1]Department of Biomedical Engineering, Istituto di Ricerche Farmacologiche Mario Negri IRCCS, Ranica, Italy, [2]Department of Management, Information and Production Engineering, University of Bergamo, Dalmine, Italy, [3]Department of Chemistry, Materials and Chemical Engineering "Giulio Natta", Politecnico di Milano, Milan, Italy

OPEN ACCESS

Edited by:
Loredana De Bartolo,
National Research Council (CNR), Italy

Reviewed by:
Nazely Diban,
University of Cantabria, Spain
Elisa Cimetta,
University of Padua, Italy

***Correspondence:**
Bogdan Ene-Iordache
bogdan.ene-iordache@marionegri.it
Manuela Teresa Raimondi
manuela.raimondi@polimi.it

†These authors have contributed equally to this work

Specialty section:
This article was submitted to Tissue Engineering and Regenerative Medicine, a section of the journal Frontiers in Bioengineering and Biotechnology

Received: 21 October 2021
Accepted: 23 November 2021
Published: 17 December 2021

Citation:
Ene-Iordache B, Campiglio CE, Raimondi MT and Remuzzi A (2021) Characterization of the Microflow Through 3D Synthetic Niche Microenvironments Hosted in a Millifluidic Bioreactor. Front. Bioeng. Biotechnol. 9:799594. doi: 10.3389/fbioe.2021.799594

Background: Development of new medicines is a lengthy process with high risk of failure since drug efficacy measured *in vitro* is difficult to confirm *in vivo*. Intended to add a new tool aiding drug discovery, the MOAB-NICHOID device was developed: a miniaturized optically accessible bioreactor (MOAB) housing the 3D engineered scaffold NICHOID. The aim of our study was to characterize the microflow through the 3D nichoid microenvironment hosted in the MOAB-NICHOID device.

Methods: We used computational fluid dynamics (CFD) simulations to compute the flow field inside a very fine grid resembling the scaffold microenvironment.

Results: The microflow inside the multi-array of nichoid blocks is fed and locally influenced by the mainstream flow developed in the perfusion chamber of the device. Here we have revealed a low velocity, complex flow field with secondary, backward, or local recirculation micro-flows induced by the intricate architecture of the nichoid scaffold.

Conclusion: Knowledge of the microenvironment inside the 3D nichoids allows planning of cell experiments, to regulate the transport of cells towards the scaffold substrate during seeding or the spatial delivery of nutrients and oxygen which affects cell growth and viability.

Keywords: miniaturized optically accessible bioreactor, NICHOID, stem cells, computational fluid dynamics, microflow

INTRODUCTION

The development of a new drug is subjected to regulatory approvals following three stages: laboratory discovery *in vitro*, animal testing *in vivo* and clinical trials on patients. This process may last longer than 10 years but, among thousands of new molecules, only one arrives to the market. Thus, drug development is a process with very high failure rate in the pre-clinical testing phase since drug efficacy measured *in vitro* is almost never confirmed in animals (Scannell et al., 2012). In fact, many pharmaceutical companies do not develop new drugs because costs exceed 1 billion euros (Ashburn and Thor, 2004), (Pammolli et al., 2011).

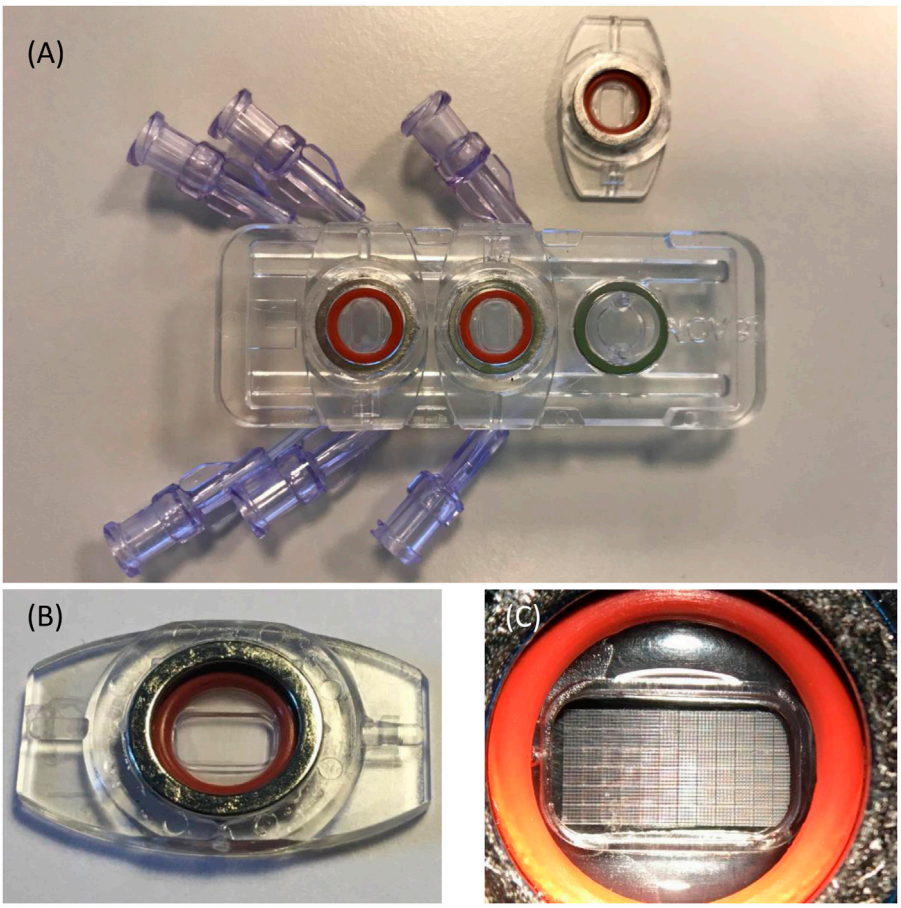

FIGURE 1 | The MOAB-NICHOID bioreactor. **(A)** The device is composed of three perfusion chambers, one is open; **(B)** The removable part containing the perfusion chamber; **(C)** Zoom on **(B)** showing the nichoid blocks on the bottom of perfusion chamber.

With the aim to add new device in drug discovery for testing the effects of drugs on 3D tissue-equivalents and organoids, a miniaturized optically accessible bioreactor (MOAB) was developed (Raimondi et al., 2020). Thanks to the optical transparency and low thickness of the components, it is optically accessible and may be exploited as a 4D bioreactor for prolonged culture. The MOAB may be used to assess the effect of several parameters on engineered tissue growth with time by viable staining and standard fluorescence microscopy. Moreover, the MOAB can be used as stand-alone or can be combined with several types of cell culture substrates, like for example bone matrices (Marturano-Kruik et al., 2018), hydrogel substrates (Tunesi et al., 2016), or the microscopic NICHOID scaffold.

The "nichoid" is a novel cell substrate inspired by the natural stem cells' niche. This polymer-engineered scaffold is composed of three-dimensional (3D) grids composed of horizontal and vertical rods that perfectly recreate the natural stem cell niche, ensuring at the same time good optical accessibility. Early studies on nichoids as cell scaffold have obtained promising results. When cells were grown inside the nichoid they had a round nucleus, similarly to stem cells' physiological morphology (Boeri et al., 2019). The nichoids promoted pluripotency of embryonic stem cells during expansion, counteracting cell migration between adjacent niche by means of its microarchitecture (Nava et al., 2016). Rat mesenchymal stem cells seeded and grown in the nichoids fabricated directly onto circular glass cover slips, had reduced cell motility and nuclear pore dimensions and increased expression of the mechano-transducer transcription factor YAP (Remuzzi et al., 2020). These mechanobiology effects may be useful for preserving cell stemness and function during *in vitro* culture to potentially obtain more favorable effects in cell therapy.

Combining the nichoids into the MOAB allows to culture 3D organoids of few millimeters in size under continuous perfusion of the culture medium, infusion of drugs to be tested and diagnose of the cell response either in real time or post-cultivation. The flow microenvironment inside the 3D nichoids modulates the transport of cells towards the scaffold substrate during cell seeding or the spatial distribution of nutrients and oxygen which is related to cell growth and viability (Olivares and Lacroix, 2012; Nava et al., 2013; Hossain et al., 2015). Moreover, the fluid shear stress exerted on cells affects cell response (Sikavitsas et al., 2003; Becquart et al., 2016). Therefore, acquisition of the spatial fluid flow conditions inside the 3D scaffold is essential to understand the fluid-induced cell behavior, the convective transport of solute and to control tissue development. The aim of our

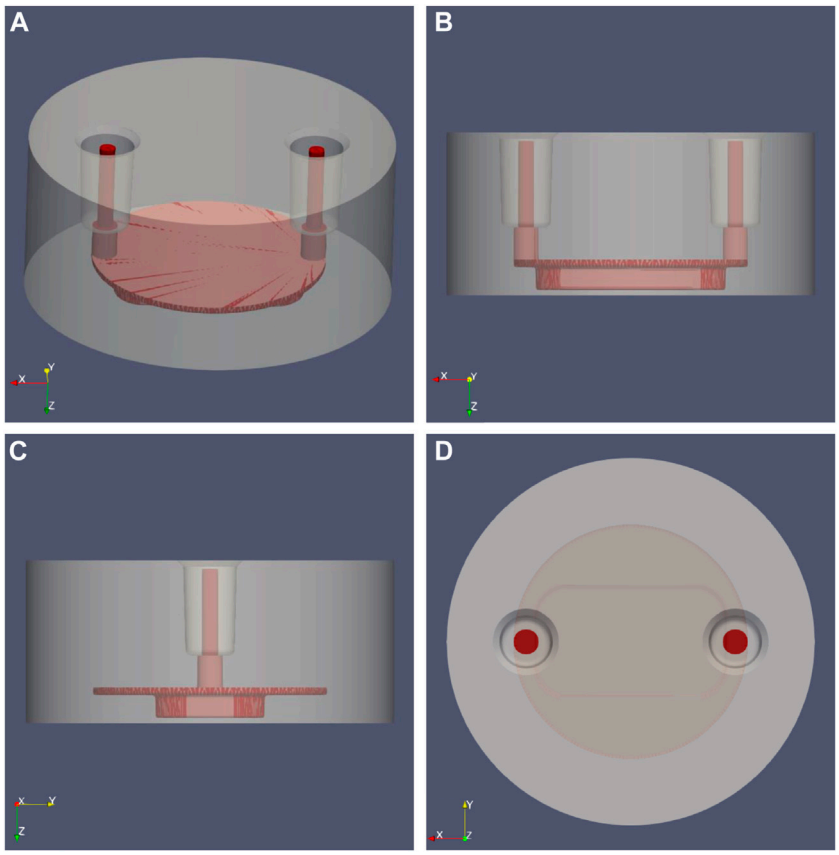

FIGURE 2 | MOAB-NICHOID perfusion chamber: the main body (grey) was set transparent to reveal the shape of the internal fluidic path (red). **(A)** Isometric view; **(B)** Side view from Y axis; **(C)** Side view from X axis; **(D)** Top view, Z axis.

study was thus to characterize the microflow through the 3D nichoid microenvironment hosted in the MOAB-NICHOID device.

MATERIALS AND METHODS

The MOAB-NICHOID Device

The MOAB-NICHOID is basically the integration of the nano-engineered 3D substrate for stem cell culture nichoid into the MOAB, as shown in **Figure 1**. The MOAB-NICHOID device has three separate perfusion lines with optically accessible micro-chambers (**Figure 1A**) which allow to simultaneously cultivate three independent scaffolds in the same experiment. Each micro-chamber is composed of two parts, one fixed and one removable that can be easily sealed through a magnet with O-ring system (**Figures 1A,B**). The removable part contains the perfusion chamber itself with blocks of nichoids on its bottom (**Figure 1C**) where the cells are cultured. Since the removable part can be inspected by common microscopes, the MOAB-NICHOID device allows culturing in triplicate 3D tissue equivalents of few million cells, that can be further harvested and analyzed during and at the end of experiments.

The Perfusion Chamber of MOAB-NICHOID Device

The perfusion chamber of the MOAB device is formed by a body and a lid as shown in **Figure 2**. The cylindrical body (diameter 11.6 mm x height 5.15 mm) is made of plexiglass in which the fluidic path is excavated. The fluidic path is made of two vertical cylinders for flow inlet and outlet, made by microbore tubes of internal diameter 0.5 mm, which are connected to the scaffold chamber as shown in **Figure 2**. On the bottom of the scaffold chamber there is a lid made of round cover glass for microscopy, 0.16 mm in thickness, on which nichoids can be seeded in multiple blocks.

The 3D NICHOID Scaffold

The structure of the 3D cell culture support is composed by a matrix of 12 × 6 basic blocks (**Figure 1C**) manufactured on the bottom of the perfusion chamber. The spacing between adjacent basic blocks is 30 μm. As shown in **Figure 3A**, one basic block is made of interconnected horizontal and vertical rods of 2 μm in size, the whole block being 33 μm high and 450 μm wide. The basic block itself is composed of 5 × 5 elementary niches that are 90 μm wide (**Figure 3B**). Of note, the external walls of an elementary niche are formed by 7 horizontal rods, while the intermediate walls are formed by 3 horizontal rods only. Nichoid

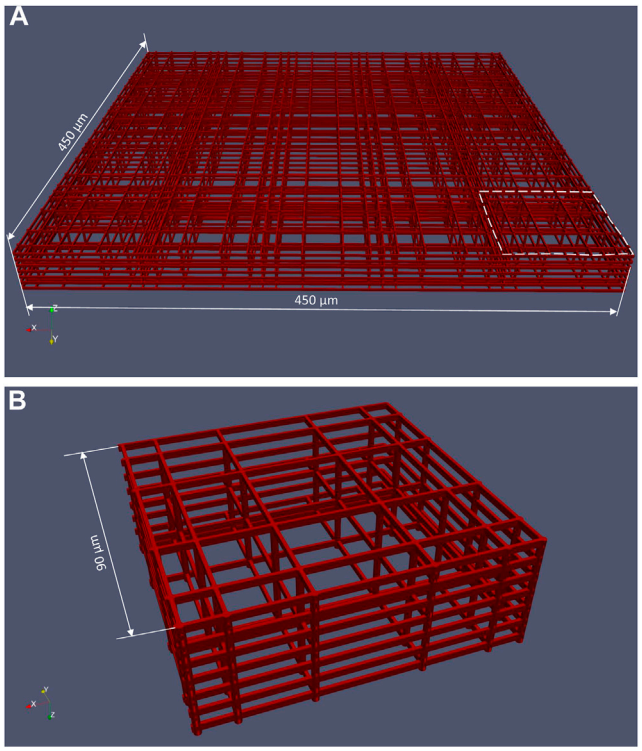

FIGURE 3 | CAD file of a basic nichoid block. **(A)** A nichoid block is formed by 5 × 5 elementary niche; **(B)** Elementary niche (shown in the dashed area in **(A)**).

blocks are polymerized with a laser in biocompatible resin (SZ2080 photoresist) using "two-photon laser polymerization" as described in detail previously (Ricci et al., 2017).

Dimensional Assessment of the Nichoids Seeded on the MOAB-NICHOID Device

To obtain the real dimensions of the nichoid blocks inside the MOAB perfusion chamber we analyzed the nichoids on images acquired at scanning electron microscopy (SEM). Five measurements of basic nichoid blocks and of the distance between them were acquired and averaged as shown in **Table 1**. According to these data, the side length of a basic block that should be theoretically 450 µm is in reality about 434 µm, while the distance between two blocks that should be theoretically 30 µm, is in reality around 20 µm in average. Thus, we have found that there is a physical contraction of individual blocks in the process of fabrication of the nichoid substrate of the bioreactor.

Validation of Pressure Losses in the MOAB Flow System

Experimental Measurements of Pressure Inside the MOAB Circuit

We measured experimentally the pressure drop over the MOAB flow system. The experimental flow system is shown in **Figure 4A**. A syringe pump (Pump 11, Harvard Apparatus, Holliston, MA) circulates water at 24°C in a silicone rubber tubing circuit in which a pressure transducer (MP150 Biopac Systems, Goleta, CA) and the MOAB device are included. Using a flow rate of 2.295 ml/min, the experimentally measured pressure drop was 11.86 mmHg.

CFD Simulation of the MOAB Flow Circuit

Full details of the numerical simulation of the MOAB full circuit are provided in the **Supplementary Material**. Briefly, a detailed model of the MOAB flow circuit was generated using a CAD program (FreeCAD, https://www.freecadweb.org/). The entire fluid path surface was exported in stereolithography (STL) file format and then was subdivided into separate parts representing the patches used in CFD simulations like inlet, outlet, and walls. The computational grid of the MOAB flow circuit was generated with the *snappyHexMesh* pre-processor of the OpenFOAM CFD toolbox (OpenCFDLtd, 2020). A fine mesh composed of more than 5.7 million cells was generated. Steady simulations were run using the solver *simpleFoam* of OpenFOAM suite. The fluid considered was the same used in experimental measurements of pressure, i.e., water at 24°C, for which we assumed density (ρ) equal to 0.9973 g cm^{-3} and dynamic viscosity (μ) equal to 0.0091 g $cm^{-1}{\cdot}s^{-1}$. Newtonian rheology model was assumed. As boundary conditions, we set a constant volumetric flow rate at the inlet equal to that used in the experimental setting, which was 2.295 ml/min. On the outlet, a zero-pressure condition was set, and no-slip condition was set on all system walls.

To derive the characteristic flow-pressure curve of the whole circuit, as well as of the scaffold chamber alone, we have run steady simulations with a set of volumetric flow rates and medium commonly used *in vitro* experiments on cells using the MOAB device. For the medium for cells at 37°C we assumed a density of 0.99 g cm^{-3} and a dynamic viscosity of 0.0076 g $cm^{-1}{\cdot}s^{-1}$ (Franzoni et al., 2016).

Generation of the Computational Grid of the Flow Chamber Including the Scaffold

Since we are mainly interested in the flow field inside the 3D scaffold, a fine computational mesh must be generated in the region of perfusion chamber with nichoids seeded on its bottom. Of note, the geometric scale has different orders of

TABLE 1 | Measurements of basic (5 × 5 niche) nichoid blocks and of the distance between blocks.

#	5 × 5 block side (µm)	Distance between blocks (µm)
1	434.786	19.135
2	428.873	19.462
3	433.642	20.229
4	436.529	18.895
5	436.529	18.911
average	433.677	19.326
SD	2.88	0.55

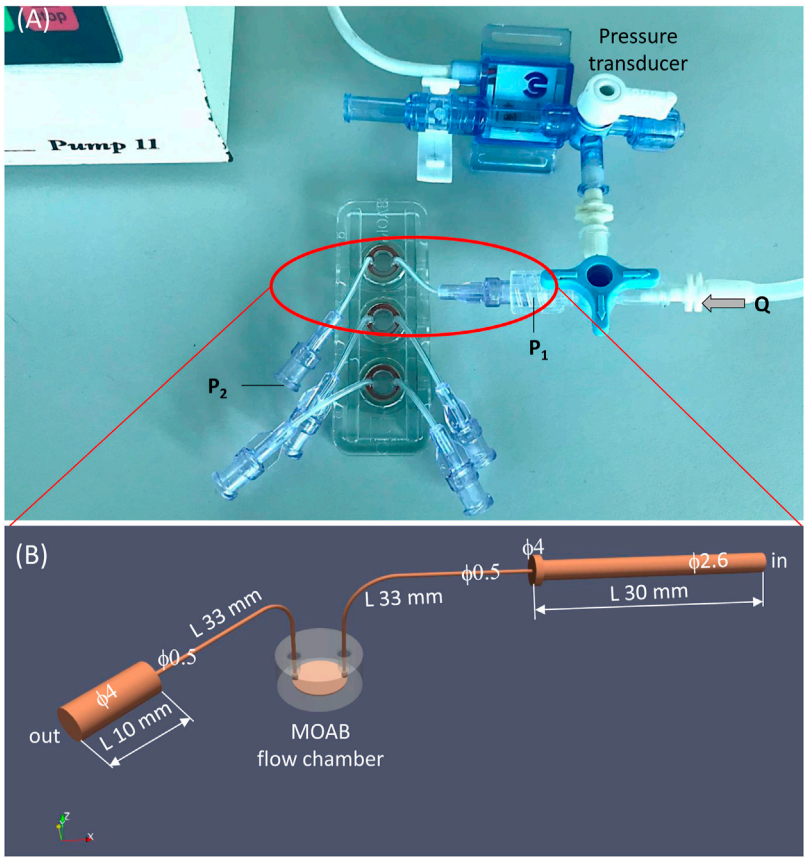

FIGURE 4 | The experimental setting for measurement and validation of pressure drop in the MOAB flow system. **(A)** Experimental setting composed of syringe pump, silicone rubber tubing circuit, pressure transducer and the MOAB flow system; **(B)** CAD model of the MOAB circuit shown in **(A)**: inlet luer and tube, scaffold chamber and outlet tube with luer.

magnitude e.g., the fluidic path of the chamber is in mm (order 10^{-3} m), whereas the nichoid structures are composed of multiple rods having thickness of 2 μm (order 10^{-6} m). Therefore, we have performed a preliminary meshing study of a basic nichoid block and of the fluidic path chamber (see **Supplementary Material**). Regarding the grid of a nichoid block, we have found that it must be refined at the μm level, otherwise its rods, especially the horizontal ones, will not be created and distorted cells will be generated nearby. According to this analysis, a nichoid block should have more than 5.4 million cells to achieve a well refined mesh for accurate numerical solution. Since the real substrate of nichoids is composed of a matrix of 12 × 6 blocks, for which the total mesh would result in more than 380 million cells, we decided to consider the symmetry of the chamber to reduce the computational grid.

The computational mesh was created starting from CAD files in stereolithography (.stl) format of both perfusion chamber and nichoid block. Three preparation steps were needed to setup the geometry for meshing. Firstly, the. stl file of a basic block (**Figure 3**) was re-scaled such as to match 434 μm width as found in the dimensional analysis described earlier. The second step was generation of a matrix of 12 × 3 nichoid blocks with a distance between blocks of 20 μm. Finally, as shown in **Figures 5A,B**, this matrix of blocks was rotated and translated such as to be aligned on the bottom of the fluidic-path chamber, as the real nichoid blocks in the MOAB-NICHOID bioreactor.

The computational grid was created using *cfMesh* generator of OpenFOAM CFD toolbox (OpenCFDLtd, 2020) by setting a very fine refinement level in the region of nichoid scaffold. The final mesh has more than 188 million of cells, the majority of which are hexahedral (**Table 2**). The mesh is shown in **Figure 5**. Obviously, the highest number of cells (>180 millions) are concentrated in the region of nichoid 3D scaffold where the refinement level reaches the μm resolution (see **Figure 5D**). Examples of nichoid rods refinement are shown in **Figure 5E**; **Figure 5F**. The numerical grid was carefully inspected visually and compared with the original surface (**Figure 5G**) to be sure that the entire shape of nichoid blocks is well preserved.

Moreover, the quality of the mesh was assessed with the *checkMesh* utility of OpenFOAM, as reported in **Table 3**. Regarding the quality checks, the computational grid is composed predominantly (88%) of hexahedral cells, and it has

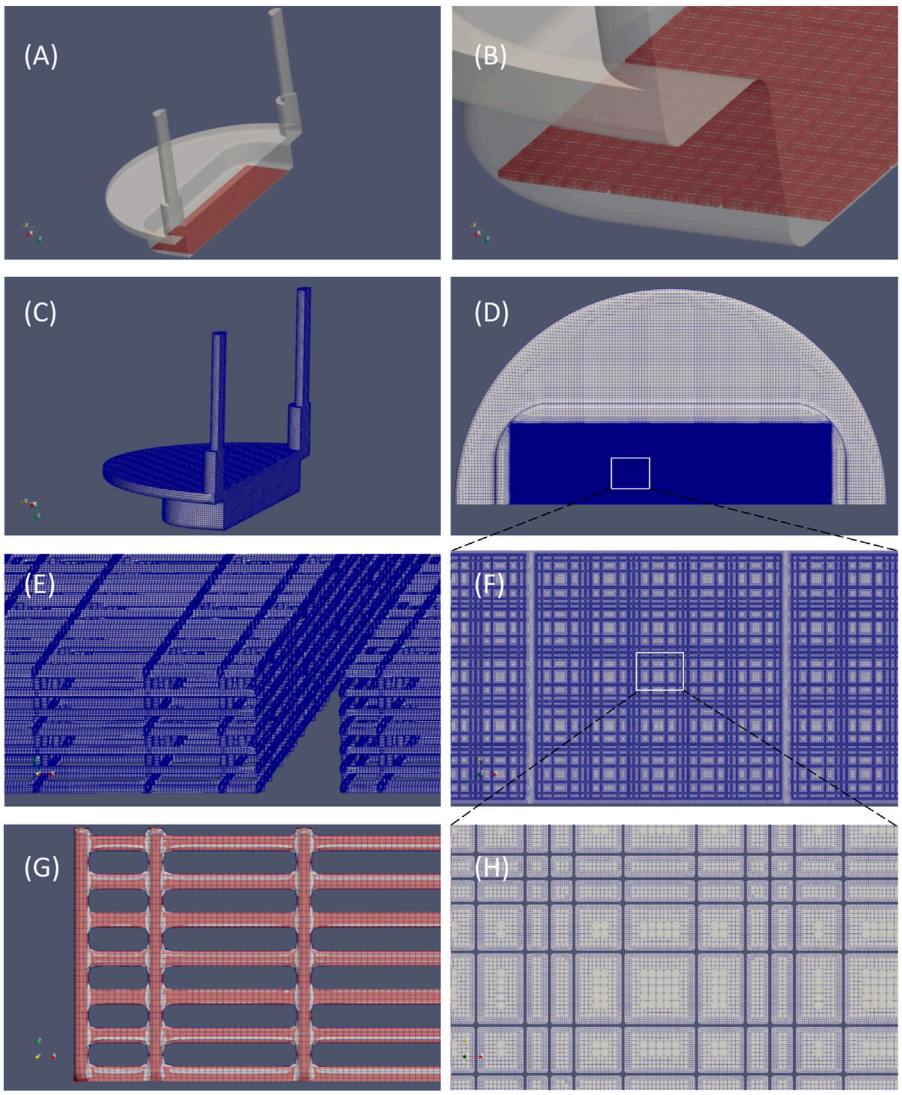

FIGURE 5 | Original CAD files and the computational grid. **(A)** Isometric view of the fluidic path chamber (in transparent grey) and nichoid blocks arranged in a 12 × 3 matrix (in red); **(B)** Detail of **(A)** showing the three rows of nichoid blocks; **(C)** The computational mesh; **(D)** View of **(C)** seen from bottom, showing the nichoid scaffold zone; **(E)** Detail of the grid of nichoid rods; **(F)** Detail of the area in **(D)** showing the fine grid in the nichoid zone; **(G)** Comparison of the mesh (gray) with the original. stl file (in red); **(H)** Detail of the area in **(F)** showing the level of refinement in the nichoid zone.

TABLE 2 | Characteristics of the computational grid with 12 × 3 matrix of nichoid blocks.

Total N of cells	N of hexahedra	Faces/cell	N of non-orthogonal faces	N of skew faces
188,653,366	165,139,943 (88%)	6.3384	178	5

only 178 non-orthogonal and 5 skew faces, which is very low for such a huge mesh.

CFD Simulation of the Perfusion Chamber of MOAB-NICHOID Bioreactor

Steady flow simulations were run using the solver *simpleFoam* (OpenCFDLtd, 2020). A second order-accurate scheme was used for the discretization of convective terms. The residual control for the SIMPLE algorithm was set to 10^{-4} for both pressure and velocity. The fluid considered was medium for cells at 37°C for which Newtonian rheology was assumed. The physical characteristics of the medium were density (ρ) of 0.99 g cm^{-3} and dynamic viscosity (μ) of 0.0076 g $cm^{-1}{\cdot}s^{-1}$ (Franzoni et al., 2016). As boundary conditions, we set a constant volumetric flow rate at the inlet equal to the flow rate of the infusion pump, which

TABLE 3 | Input volumetric flow rates and corresponding pressure drops.

Q inlet (*ml/min*)	Water at 24°C		Medium for cells at 37°C	
	$\Delta P_{circuit}$ (*mmHg*)	$\Delta P_{flow\ chamber}$ (*mmHg*)	$\Delta P_{circuit}$	$\Delta P_{flow\ chamber}$ (*mmHg*)
0.3	1.38	0.15	1.15	0.12
0.45	2.08	0.22	1.74	0.18
0.6	2.79	0.30	2.34	0.25
1.2	5.76	0.64	4.86	0.53
2.295	**11.67**	1.34	9.97	1.17
2.4	12.27	1.42	10.49	1.24

***Note**: in bold type values used in the experimental validation of numerical procedure.*

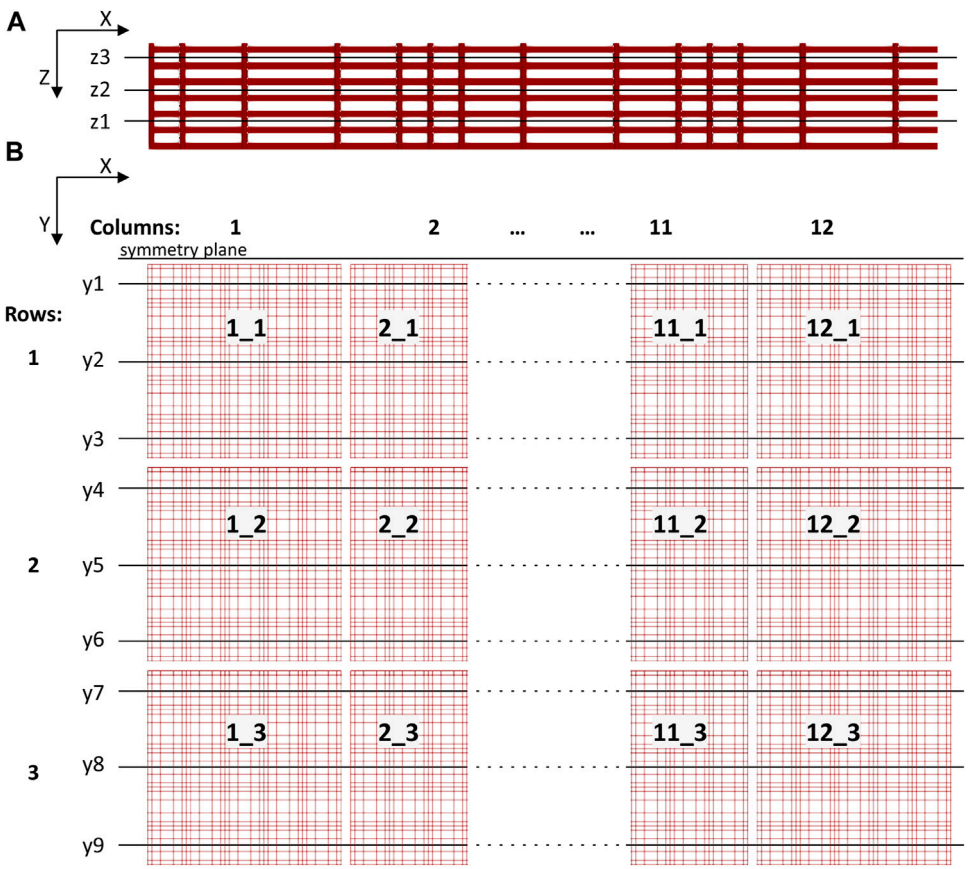

FIGURE 6 | Sketch showing cutting planes for postprocessing through the 3D scaffold structure. **(A)** Three horizontal planes (z1 to z3, normal to Z axis) defined through a basic nichoid block (not in scale with **(B)**; **(B)** The 12 × 3 matrix of nichoid blocks seen from top and the vertical planes (y1 to y9, normal to Y axis).

is 0.45 ml/min. Because we deal with symmetry which affect the flow entrance and exit as well (see **Figure 5**), the imposed flow rate was halved at the inlet i.e., 0.225 ml/min. On the vertical cutting wall, a boundary condition of symmetry was set. On the outlet, a zero-pressure condition was set, and no-slip boundary condition was set on all perfusion chamber and nichoids walls.

Due to the huge number of cells of the 3D domain in the scaffold zone, both grid generation as well as the numerical simulation were carried out on a High-Performance Computing (HPC) cloud infrastructure (https://cloudhpc.cloud/).

Data Post-processing

Pressure and velocity fields from the 3D nichoid substrate were probed in vertical and horizontal planes cutting the 3D geometry. We identified three horizontal planes, normal to Z axis, as shown in **Figure 6A**. Precisely, plane z1 was defined at a height of 8.6 μm from the bottom of the perfusion chamber, plane z2 at a height of 18.6 μm, and z3 at a height of 28.6 μm. We also defined nine vertical planes (y1 to y9) normal to Y axis, traversing the nichoid blocks in the middle and more laterally, as shown in **Figure 6B**.

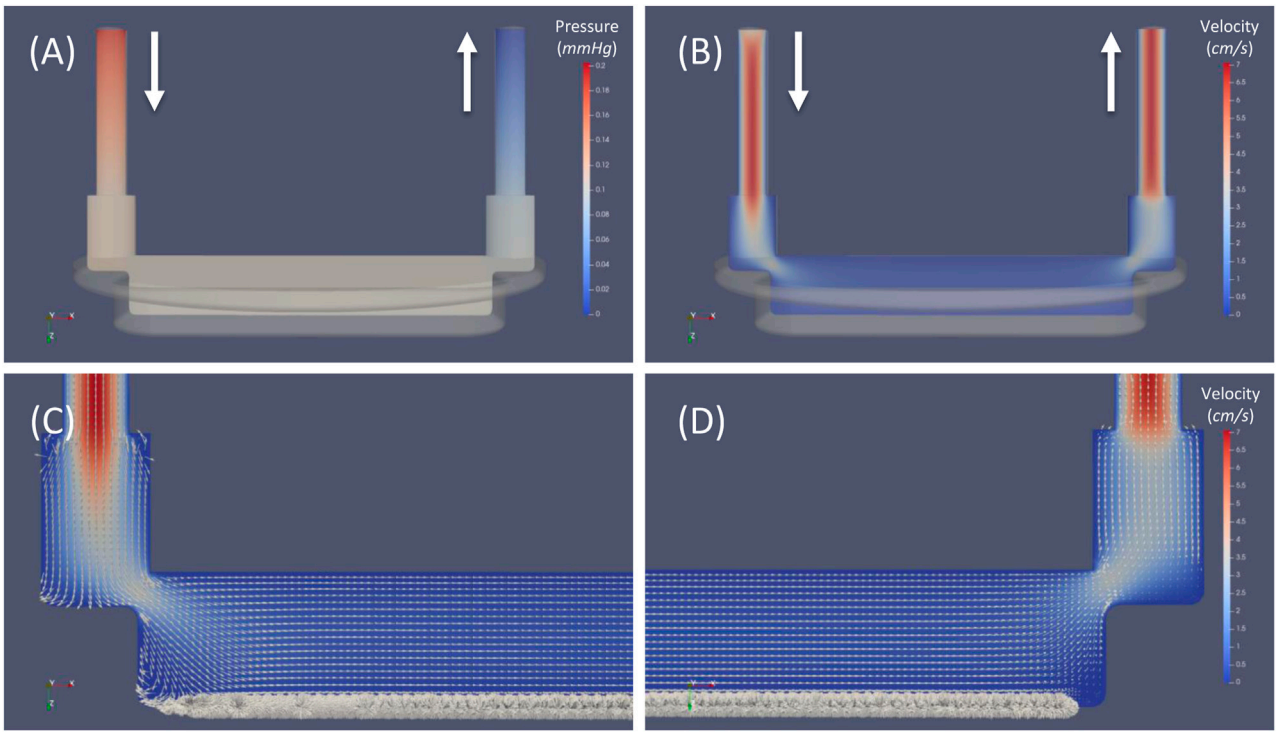

FIGURE 7 | General flow field of the perfusion chamber of MOAB-NICHOID bioreactor. **(A)** Pressure contours; **(B)** Velocity magnitude contours; **(C)** Zoom view near the inlet zone; **(D)** Zoom view near the outlet zone. Note: superimposed vectors in **(C)** and **(D)** were normalized (set magnitude = 1); bold arrows indicate the inlet and outlet of the flow circuit.

Moreover, we considered the 12 × 3 matrix organization of the cellular scaffold such as to name each block with an objective rule, considering the main direction of flow in the perfusion chamber, which is from left to right along the X axis. There are 12 basic nichoid blocks along the X axis and 3 blocks along the Y axis. A basic block is labelled with the X_Y rule i.e., first its position along the X axis and then its position along the Y axis.

Results of the numerical simulations such as general flow field, velocity and wall shear stress (WSS) patterns were post-processed with the open-source, data analysis and visualization program *ParaView* (Paraview, 2020).

RESULTS

Pressure Losses in the MOAB Flow Circuit and in the Scaffold Flow Chamber

For the flow rate and type of fluid used in the experimental setting (e.g., 2.295 ml/min and water at 24°C), the numerical calculated pressure drop over the MOAB circuit resulted 11.67 mmHg. Since the experimentally measured pressure drop was 11.86 mmHg, we concluded that the numerical simulations may well predict the pressure losses over the MOAB flow system.

We therefore report in **Table 3** the characteristic pressures vs. flow rate values of the entire MOAB flow system as well as of the scaffold chamber alone.

General Flow Field of the Perfusion Chamber of MOAB-NICHOID Bioreactor

The general flow field of the perfusion chamber of the MOAB-NICHOID bioreactor is shown in **Figure 7**. Pressure contours are shown in a plane very near the symmetry plane of the perfusion chamber (**Figure 7A**). The maximum pressure occurs at the chamber inlet, while zero pressure was set at the outlet. For this case we calculated a pressure drop of 0.19 mmHg over the entire flow chamber.

Velocity magnitude contours in the same plane are shown in **Figure 7B**. The maximum velocity around 7 cm/s is reached in both inlet and outlet vertical cylinders. As the fluid moves further from the inlet channel, the volume of perfusion chamber increases, and the velocity decreases proportionally.

To allow visualization of the flow features we first normalized all velocity vectors and then superimposed the normalized vectors over the velocity contours in **Figures 7C,D**. Such visualization allows to distinct well between the general flow of the chamber and the microflow inside the nichoid 3D substrate: while the flow in the chamber is smooth and laminar in the top layers, it becomes very complex and heterogeneous through the scaffold, owing to its complex 3D architecture. Although probed in a plane, most velocity vectors in the nichoid substrate region are oriented out of plane or even in opposite direction respect to the main direction of flow.

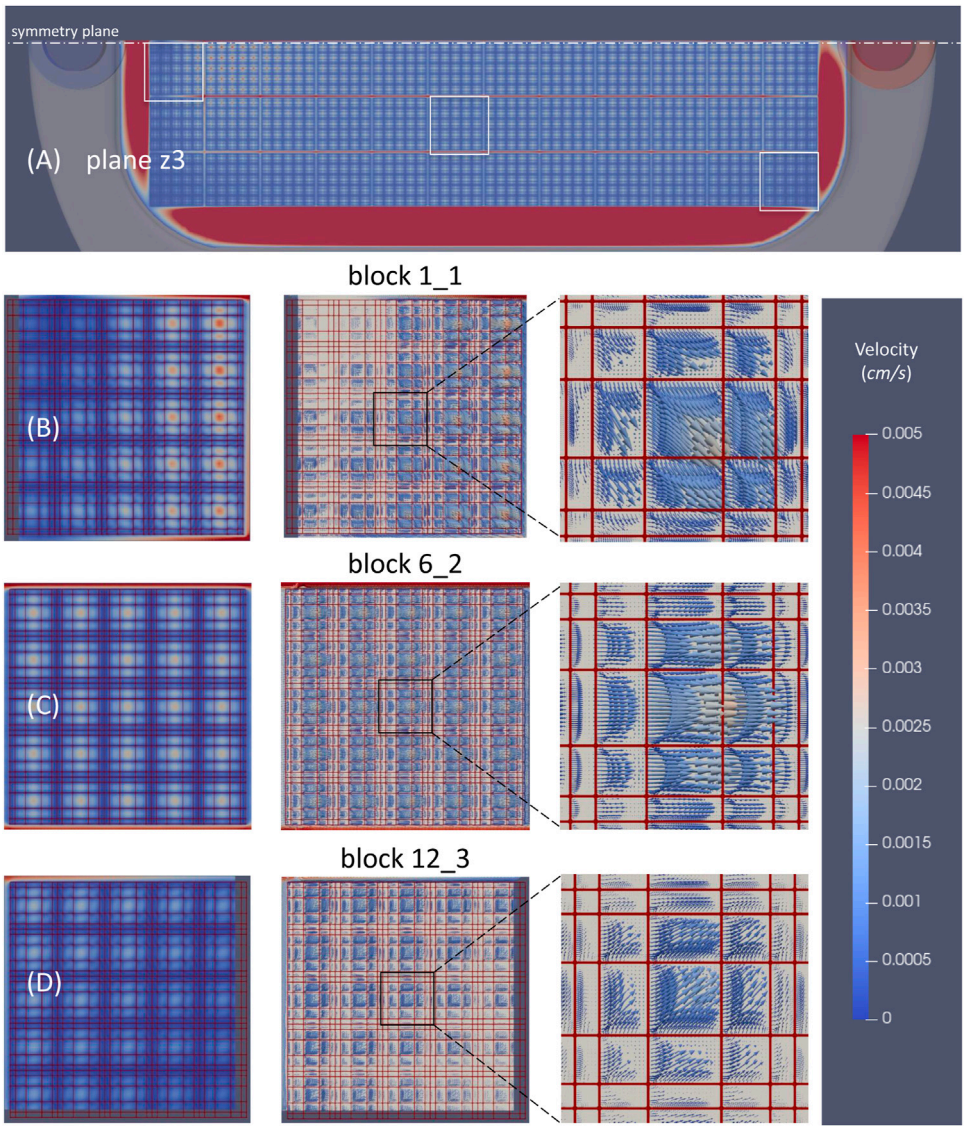

FIGURE 8 | Velocity distribution through the 3D scaffold in the horizontal plane z3. **(A)** Velocity magnitude contours through all nichoid bocks; **(B)** Velocity magnitude contours and vectors in a block that is at the beginning of the matrix (1_1); **(C)** Velocity magnitude contours and vectors in a block in the middle (6_2); **(D)** Velocity magnitude contours and velocity vectors in the block at the end of the matrix (12_3). Note: the position of plane z3 is as shown in **Figure 6A**; velocity scale cutoff is 0.005 cm/s; the main direction of flow in the perfusion chamber is from left to right.

Velocity Distribution Through the 3D Scaffold

The flow velocities inside nichoid blocks resulted much lower than the corresponding velocities of upper free layers and turned out to be lower and lower towards the bottom of scaffold. We have calculated an average value of 5.6, 1.3, and 0.5, and a maximum value of 76, 8.8 and 2.1 μm/s for the three planes z3, z2 and z1, respectively. An example of the velocity field in the horizontal plane z3 is shown in **Figure 8**. It is worth mentioning that the maximum velocities are achieved in the longitudinal channels between adjacent nichoid blocks where the fluid is accelerated.

Velocity magnitude contours in all nichoid blocks revealed a rather non-uniform distribution in those blocks in vicinity of the entrance and exit of flow, and a uniform distribution in the central blocks, especially from the 4th up to the 9th columns (**Figure 8A**). The non-uniform distribution of velocity is better observed as vectors in the detailed view for the block 1_1, near the symmetry plane and near entrance, and for block 12_3, near the exit of the flow (**Figures 8B, D**). At the contrary, the velocity vectors inside the block 6_2 are all oriented in the same direction of the main flow (**Figure 8C**).

The velocity vectors probed in the vertical planes crossing the above three nichoid blocks are presented in **Figure 9**.

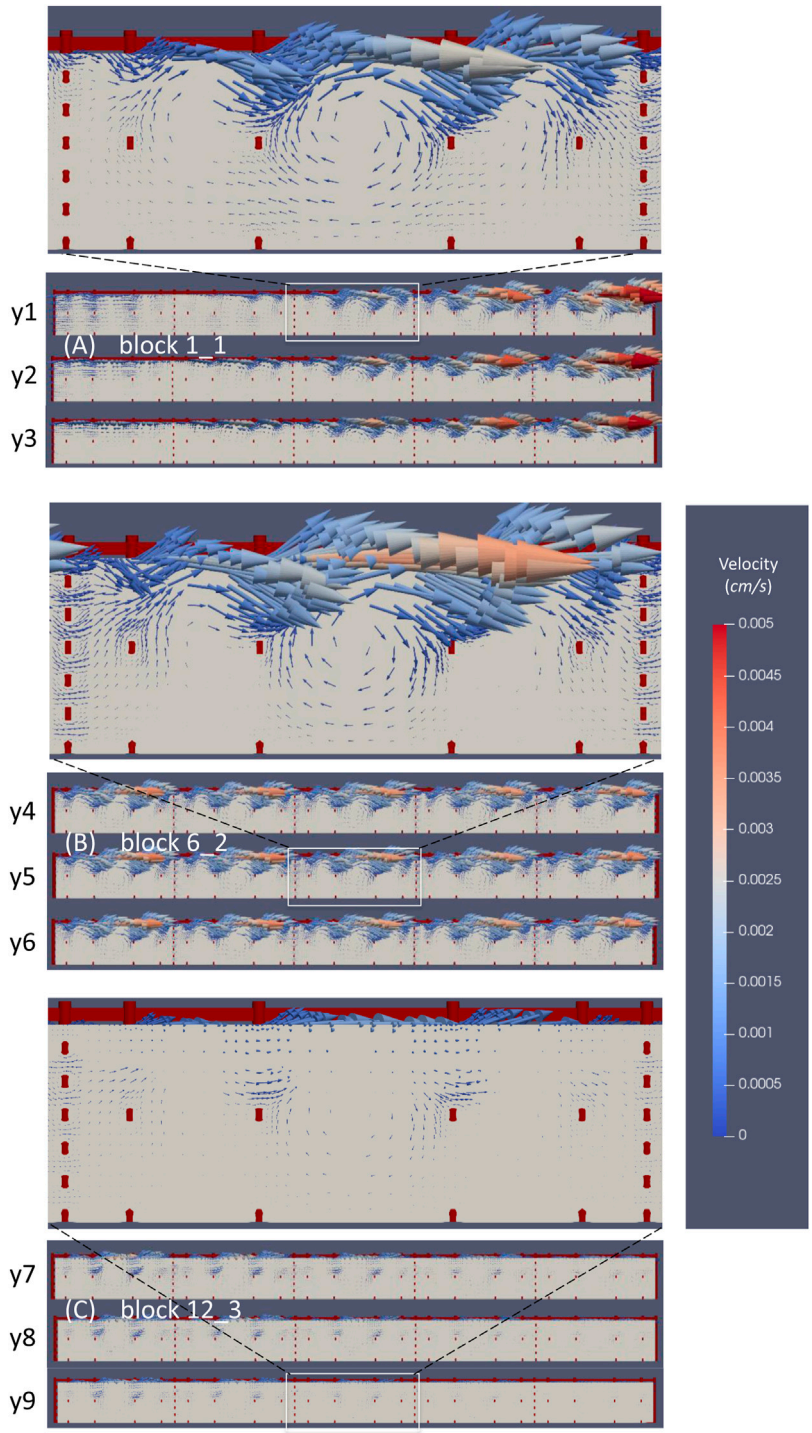

FIGURE 9 | The microflow inside three nichoid blocks. **(A)** Velocity vectors probed in three vertical planes inside the nichoid block 1_1; **(B)** Velocity vectors probed in three vertical planes inside the nichoid block 6_2; **(C)** Velocity vectors probed in three vertical planes inside the nichoid block 12_3.

The flow inside the 3D scaffold is very complex, featuring recirculation zones and important secondary motions. Moreover, the flow inside the nichoid blocks is influenced locally by the main flow. For example, the big recirculation flow near the entrance affects the inner microflow that develops inside block 1_1. **Figure 9A** illustrates well how the velocity vectors in the left zone of the block are oriented opposite, whereas the vectors in the right region are oriented as the main flow. The detailed

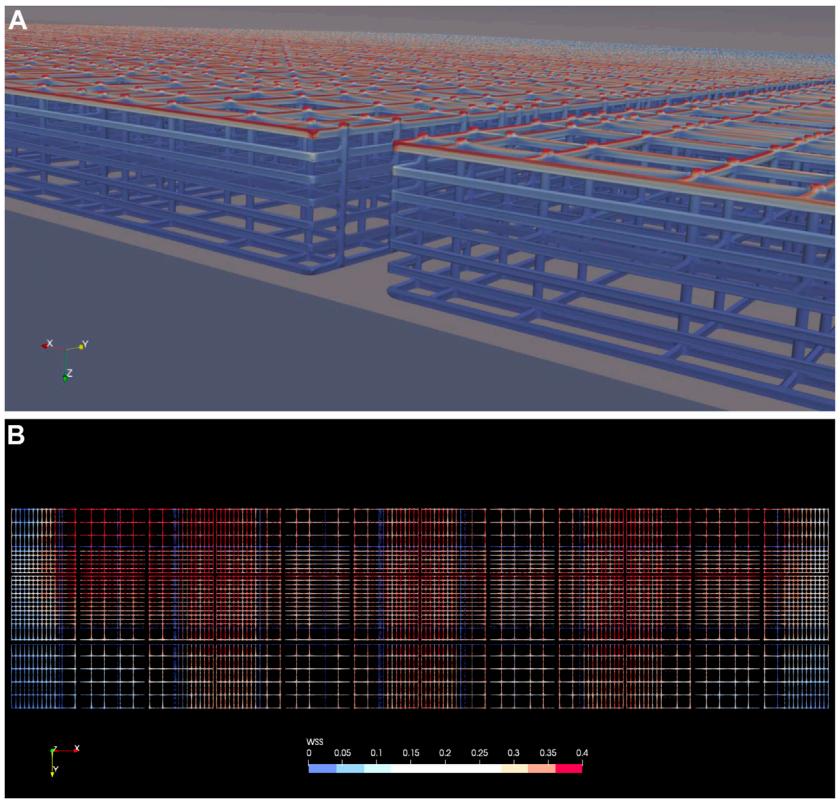

FIGURE 10 | Wall shear stress on the nichoid rods. **(A)** WSS on the nichoid blocks, isometric view from the symmetry plane showing the space between the second and third columns of blocks; **(B)** WSS on all nichoid blocks seen from top. Note: a cutoff value of 0.4 dyne/cm^2 was intentionally set as maximum.

inset image reveals the microflows between the horizontal rods and recirculation flows developing in each single niche.

The velocity vectors at the upper part of block 6_2 are oriented in the same direction with the main flow of the perfusion chamber (**Figure 9B**). Also in this case, the inset image reveals microflows between the horizontal rods and recirculation flows.

The microcirculation inside block 12_3 is influenced by the main flow that here is oriented towards the outlet of the perfusion chamber (**Figure 9C**). In this case, the vectors are oriented diagonally out of plane and are better spotted in the inset image. Recirculation microflows are observed here, too.

WSS Distribution on Scaffold Rods

Wall shear stress distribution on the nichoid blocks is presented in **Figure 10**. Due to the low velocities inside the scaffold blocks, the WSS is low on all rods except those on top that are hit directly by the mainstream fluid flow, as depicted in **Figure 10A**.

Patterns of WSS on the top of all nichoid blocks are shown in **Figure 10B**, where 0.4 dyne/cm^2 was intentionally set as maximum scale. For all blocks we have calculated a maximum value slightly lower than 1 dyne/cm^2 (0.947).

WSS Distribution on the Bottom of Perfusion Chamber

The microflow environment inside each 3D niche give rise of micro-shear stresses on the bottom side of the perfusion chamber. These are presented in **Figure 11**. The WSS distribution under all nichoid blocks is very similar with the velocity magnitude pattern (**Figure 11A**). Note however, the maximum scale which was set to 0.005 dyne/cm^2.

In the same manner, patterns and WSS vectors were depicted in **Figures 11B–D** in zones under the nichoid blocks 1_1, 6_2, and 12_3. Interesting enough, in the smaller niches the WSS vectors are oriented as the mainstream flow, whereas in the bigger niches, the WSS vectors are oriented in opposite direction due to the micro-recirculation flows.

DISCUSSION

In this study we characterized the microflow inside an array of 3D nichoid blocks manufactured on the bottom of the perfusion chamber of the millifluidic bioreactor commonly known as MOAB-NICHOID. To perform this, we used computational fluid dynamics simulations to compute the flow fields inside a very fine grid resembling the scaffold microenvironment. In

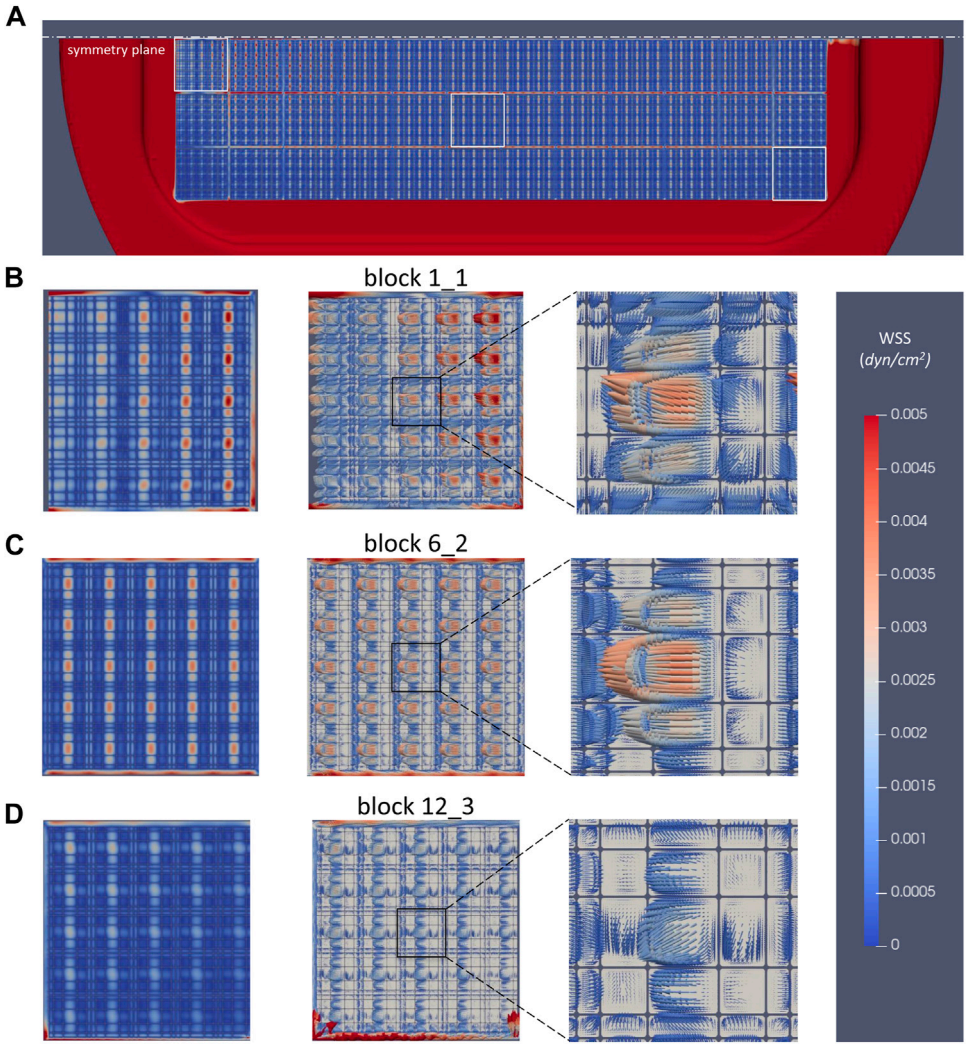

FIGURE 11 | Wall shear stress distribution on the bottom of perfusion chamber. **(A)** WSS under all nichoid blocks, view from top; **(B)** WSS pattern and vectors under the nichoid block 1_1; **(C)** WSS pattern and vectors under the nichoid block 6_2; **(D)** WSS pattern and vectors under the nichoid block 12_3.

particular, the model geometry and boundary conditions corresponded to the macro-environment formed by the perfusion chamber together with the microenvironment created by the 3D scaffold multi-array architecture. We have unveiled a very complex fluid field with myriads of secondary, backward, and local recirculation microflows induced by the intricate architecture of the nichoid scaffold. At the same time, the microflow inside the array of nichoid blocks is fed and influenced by the mainstream flow developed in the perfusion chamber of MOAB-NICHOID device.

In post-processing the results, we have established an objective method to analyze each nichoid block by its position in the matrix array. For the sake of clarity and space here we only presented flow analysis images for three representative blocks i.e., one near the flow entrance, the second in the middle and the third near the flow exit of the perfusion chamber.

The biggest challenge in our study was to generate the computational grid for all nichoid blocks. On the one hand the bigger the number of refined cells, the better will be characterized the flow inside the 3D nichoid scaffold. On the other hand, such a big mesh requires proportionally high computational resources for the numerical solving of the solution, as well as similar resources for post-processing. We therefore resolved this issue by relying on a cloud HPC service that allows scaling of the computational power on-demand. Although we meshed only half of the geometry by taking advantage of the symmetry of the system, the final mesh had more than 188 million cells. It is worth noting that such a huge number of cells is not common in the biomedical literature, where computational grids up to 10 million cells are considered big and are usually used in patient-specific transitional or turbulent flow studies (Hose et al., 2019).

The velocity map of the mainstream flow reveals the highest velocity (~ 7 cm/s) in the two vertical cylinders for inlet and outlet and much lower velocities (<0.5 cm/s) in the main body of the perfusion chamber. There is a slight acceleration of the fluid in both zones of conjunction between the two vertical cylinders and the main body and a recirculation zone, involving also the nichoids, forms under the flow entrance but not under the exit flow area (**Figure 7**). For the perfusion chamber hosting the array of 3D nichoids we have calculated a pressure drop of 0.19 mmHg corresponding to the inflow volumetric flow rate of 0.45 ml/min. This is in line with the pressure drop over the flow chamber calculated by considering the whole device flow circuit (**Table 3**). Thus, we were able to draw the characteristic flow-pressure curves for the MOAB-NICHOID bioreactor for either water or medium for cells. Considering that these flow-pressure relationships are mostly linear (**Supplementary Figure S4**), our results may help researchers in setting future experiments with this device under flow conditions.

The flow inside the 3D scaffold for cell culture is extremely complex but is at very low velocities. For instance, we have calculated an in-plane maximum velocity of 76 μm/s at 28.6 μm, decreasing up to 2.1 μm/s at 8.6 μm from the bottom of perfusion chamber.

The WSS was relatively high (approx. 1 dyne/cm^2) on the top rods of nichoids which are hit directly by the mainstream flow, whereas it was three orders of magnitude lower on the bottom of perfusion chamber under the nichoid blocks. Interestingly, the flow inside every single niche resembles the flow in the classical lid-driven cavity problem where the fluid in a cubic or rectangular cavity is moved by the tangential in-plane motion of the top bounding wall (Shankar and Deshpande, 2000). In fact, as seen in **Figure 9B** a primary vortex develops in the center of the niche. Development of such recirculation zones has direct implication in the development of WSS on the bottom of niche, that will be directed opposite the main flow at the top of niche. However, it is worth noting that such microenvironment may only exist *in vitro* experiments when the scaffold is free of cells, or for some limited time at the beginning of cell seeding process. At this stage of the research, we know that cell seeded for 2 weeks in 3D non-perfused nichoids grow and proliferate, modifying profoundly the geometry of scaffold void, with a consequent reduction in the free volume (Remuzzi et al., 2020). Here we can only speculate that the cultured cells positioned on top of the scaffold will sense a similar shear stress found here (i.e., in the order of 1 dyne/cm^2, **Figure 10A**). The hydrodynamic stress exerted by the flow on cultured cells inside the 3D nichoids may still be estimated by fine reconstruction of the porous-like mesh by micro-CT (Cioffi et al., 2006; Raimondi et al., 2006) or nano-CT (Vojtova et al., 2019) images.

Regarding the adequacy of our device for stem cell cultures, we predicted fluid velocities varying between 2 μm/s near the bottom of the nichoid, up to 80 μm/s near the top surface of the nichoid, lapped by the culture medium flow. These velocity gradients generated fluid shear stresses varying between 0.001 dyne/cm^2 at the bottom of the nichoid, up to 1 dyne/cm^2 near the top of the nichoid grid. The lower values predicted near the bottom of the nichoid correspond well with physiologically-relevant levels of interstitial fluid velocity (of average 0.6 μm/s, up to 2 μm/s) measured *in situ* in tissue (Chary and Jain, 1989). This implies that the MOAB-NICHOID allows to reproduce *in vitro* a realistic hydrodynamic 3D microenvironment surrounding adherent cells, for example mimicking the interstitial flows sensed by mesenchymal or hematopoietic progenitors resident in the perivascular interstitium. A correct reproduction of interstitial flow is in fact crucial to engineering *in vitro* aspects of tissue morphogenesis and vascular sprouting, which are known to depend on flow velocity and niche topology (Rutkowski and Swartz, 2007; Song and Munn, 2011). In this regard, the presence of cells proliferating in the nichoid grid and the consequent reduction in free volume should slightly decrease the fluid velocity to values below 2 μm/s, which would still fall well within physiologically-relevant levels of interstitial fluid velocity.

Our present study approaches future developments like analysis of microflow when cells are cultured in the MOAB-NICHOID bioreactor, where the fluid shear stress exerted on cells affects cell response, or even simulation of macromolecules and/or nanoparticles transport inside the device to help new drug discovery processes.

CONCLUSION

In conclusion, in the present study we have characterized the microenvironment of 3D scaffold for stem cells that was manufactured on the bottom of the perfusion chamber of the MOAB-NICHOID bioreactor. The flow microenvironment inside the 3D nichoids is very complex, with myriads of secondary, backward, and local recirculation microflows induced by the intricate architecture of the nichoid scaffold. Characterization of the spatial fluid flow conditions inside the 3D scaffold is essential to understand the convective transport of solute, the fluid-induced cells behavior, and to control tissue development.

DATA AVAILABILITY STATEMENT

The original contributions presented in the study are included in the article/**Supplementary Material**, further inquiries can be directed to the corresponding authors.

AUTHOR CONTRIBUTIONS

Conceptualization: AR and MR. Performed pressure loss experiments: CC and AR. Performed CFD simulations: BE-I. Analysed/interpreted the data: BE-I, AR and MR. Project supervision: AR. Writing original draft: BE-I, CC, and AR. Project administration and funding acquisition: MR. All authors have read and agreed to the published version of the manuscript.

FUNDING

The research was funded by the European Research Council (ERC) under the European Union's Horizon 2020 research and innovation program (G.A. No. 825159 – MOAB).

SUPPLEMENTARY MATERIAL

The Supplementary Material for this article can be found online at: https://www.frontiersin.org/articles/10.3389/fbioe.2021.799594/full#supplementary-material

REFERENCES

Ashburn, T. T., and Thor, K. B. (2004). Drug Repositioning: Identifying and Developing New Uses for Existing Drugs. *Nat. Rev. Drug Discov.* 3, 673–683. doi:10.1038/nrd1468

Becquart, P., Cruel, M., Cruel, M., Hoc, T., Sudre, L., Pernelle, K., et al. (2016). Human Mesenchymal Stem Cell Responses to Hydrostatic Pressure and Shear Stress. *eCM* 31, 160–173. doi:10.22203/ecm.v031a11

Boeri, L., Albani, D., Raimondi, M. T., and Jacchetti, E. (2019). Mechanical Regulation of Nucleocytoplasmic Translocation in Mesenchymal Stem Cells: Characterization and Methods for Investigation. *Biophys. Rev.* 11, 817–831. doi:10.1007/s12551-019-00594-3

Chary, S. R., and Jain, R. K. (1989). Direct Measurement of Interstitial Convection and Diffusion of Albumin in normal and Neoplastic Tissues by Fluorescence Photobleaching. *Proc. Natl. Acad. Sci.* 86, 5385–5389. doi:10.1073/pnas.86.14.5385

Cioffi, M., Boschetti, F., Raimondi, M. T., and Dubini, G. (2006). Modeling Evaluation of the Fluid-Dynamic Microenvironment in Tissue-Engineered Constructs: a Micro-CT Based Model. *Biotechnol. Bioeng.* 93, 500–510. doi:10.1002/bit.20740

Franzoni, M., Cattaneo, I., Longaretti, L., Figliuzzi, M., Ene-Iordache, B., and Remuzzi, A. (2016). Endothelial Cell Activation by Hemodynamic Shear Stress Derived from Arteriovenous Fistula for Hemodialysis Access. *Am. J. Physiol.-Heart Circ. Physiol.* 310, H49–H59. doi:10.1152/ajpheart.00098.2015

Hose, D. R., Lawford, P. V., Huberts, W., Hellevik, L. R., Omholt, S. W., and Van De Vosse, F. N. (2019). Cardiovascular Models for Personalised Medicine: Where Now and where Next? *Med. Eng. Phys.* 72, 38–48. doi:10.1016/j.medengphy.2019.08.007

Hossain, M. S., Bergstrom, D. J., and Chen, X. B. (2015). Computational Modelling of the Scaffold-free Chondrocyte Regeneration: a Two-Way Coupling between the Cell Growth and Local Fluid Flow and Nutrient Concentration. *Biomech. Model. Mechanobiol.* 14, 1217–1225. doi:10.1007/s10237-015-0666-0

Marturano-Kruik, A., Nava, M. M., Yeager, K., Chramiec, A., Hao, L., Robinson, S., et al. (2018). Human Bone Perivascular Niche-On-A-Chip for Studying Metastatic Colonization. *Proc. Natl. Acad. Sci. USA* 115, 1256–1261. doi:10.1073/pnas.1714282115

Nava, M. M., Raimondi, M. T., and Pietrabissa, R. (2013). A Multiphysics 3D Model of Tissue Growth under Interstitial Perfusion in a Tissue-Engineering Bioreactor. *Biomech. Model. Mechanobiol.* 12, 1169–1179. doi:10.1007/s10237-013-0473-4

Nava, M. M., Piuma, A., Figliuzzi, M., Cattaneo, I., Bonandrini, B., Zandrini, T., et al. (2016). Two-photon Polymerized "Nichoid" Substrates Maintain Function of Pluripotent Stem Cells when Expanded under Feeder-Free Conditions. *Stem Cel. Res. Ther.* 7, 132. doi:10.1186/s13287-016-0387-z

Olivares, A. L., and Lacroix, D. (2012). Simulation of Cell Seeding within a Three-Dimensional Porous Scaffold: a Fluid-Particle Analysis. *Tissue Eng. C: Methods* 18, 624–631. doi:10.1089/ten.tec.2011.0660

OpenCFD Ltd (2020). About OpenFOAM® [Online]. Available: https://www.openfoam.com/ (Accessed November, 2020).

Pammolli, F., Magazzini, L., and Riccaboni, M. (2011). The Productivity Crisis in Pharmaceutical R&D. *Nat. Rev. Drug Discov.* 10, 428–438. doi:10.1038/nrd3405

Paraview (2020). Welcome to Paraview [Online]. Available: http://www.paraview.org/ (Accessed February, 2020).

Raimondi, M. T., Moretti, M., Cioffi, M., Giordano, C., Boschetti, F., Laganà, K., et al. (2006). The Effect of Hydrodynamic Shear on 3D Engineered Chondrocyte Systems Subject to Direct Perfusion. *Biorheology* 43, 215–222.

Raimondi, M. T., Donnaloja, F., Barzaghini, B., Bocconi, A., Conci, C., Parodi, V., et al. (2020). Bioengineering Tools to Speed up the Discovery and Preclinical Testing of Vaccines for SARS-CoV-2 and Therapeutic Agents for COVID-19. *Theranostics* 10, 7034–7052. doi:10.7150/thno.47406

Remuzzi, A., Bonandrini, B., Tironi, M., Longaretti, L., Figliuzzi, M., Conti, S., et al. (2020). Effect of the 3D Artificial Nichoid on the Morphology and Mechanobiological Response of Mesenchymal Stem Cells Cultured *In Vitro*. *Cells* 9, 1873. doi:10.3390/cells9081873

Ricci, D., Nava, M. M., Zandrini, T., Cerullo, G., Raimondi, M. T., and Osellame, R. (2017). Scaling-Up Techniques for the Nanofabrication of Cell Culture Substrates via Two-Photon Polymerization for Industrial-Scale Expansion of Stem Cells. *Materials (Basel)* 10, 66. doi:10.3390/ma10010066

Rutkowski, J. M., and Swartz, M. A. (2007). A Driving Force for Change: Interstitial Flow as a Morphoregulator. *Trends Cel Biol.* 17, 44–50. doi:10.1016/j.tcb.2006.11.007

Scannell, J. W., Blanckley, A., Boldon, H., and Warrington, B. (2012). Diagnosing the Decline in Pharmaceutical R&D Efficiency. *Nat. Rev. Drug Discov.* 11, 191–200. doi:10.1038/nrd3681

Shankar, P. N., and Deshpande, M. D. (2000). Fluid Mechanics in the Driven Cavity. *Annu. Rev. Fluid Mech.* 32, 93–136. doi:10.1146/annurev.fluid.32.1.93

Sikavitsas, V. I., Bancroft, G. N., Holtorf, H. L., Jansen, J. A., and Mikos, A. G. (2003). Mineralized Matrix Deposition by Marrow Stromal Osteoblasts in 3D Perfusion Culture Increases with Increasing Fluid Shear Forces. *Proc. Natl. Acad. Sci.* 100, 14683–14688. doi:10.1073/pnas.2434367100

Song, J. W., and Munn, L. L. (2011). Fluid Forces Control Endothelial Sprouting. *Proc. Natl. Acad. Sci.* 108, 15342–15347. doi:10.1073/pnas.1105316108

Tunesi, M., Fusco, F., Fiordaliso, F., Corbelli, A., Biella, G., and Raimondi, M. T. (2016). Optimization of a 3D Dynamic Culturing System for *In Vitro* Modeling of Frontotemporal Neurodegeneration-Relevant Pathologic Features. *Front. Aging Neurosci.* 8, 146. doi:10.3389/fnagi.2016.00146

Vojtová, L., Zikmund, T., Pavliňáková, V., Šalplachta, J., Kalasová, D., Prosecká, E., et al. (2019). The 3D Imaging of Mesenchymal Stem Cells on Porous Scaffolds Using High-Contrasted X-ray Computed Nanotomography. *J. Microsc.* 273, 169–177. doi:10.1111/jmi.12771

Conflict of Interest: MR is co-founder of a university spin-off company, MOAB S.r.l., and holds shares.

The remaining authors declare that the research was conducted in the absence of any commercial or financial relationships that could be construed as a potential conflict of interest.

Publisher's Note: All claims expressed in this article are solely those of the authors and do not necessarily represent those of their affiliated organizations, or those of the publisher, the editors and the reviewers. Any product that may be evaluated in this article, or claim that may be made by its manufacturer, is not guaranteed or endorsed by the publisher.

frontiers in Bioengineering and Biotechnology

CASE REPORT
published: 03 January 2022
doi: 10.3389/fbioe.2021.738434

3D-Printed Cold Preservation Device in Renal Autotransplantation for the Treatment of a Patient With Renal Artery Stenosis

Dong Cui[1], Bin Wu[1], Dali He[1], Yanen Wang[2], Yong Jiao[1] and Bo Zhang[1]**

[1]Department of Urology, Tangdu Hospital, The Air Force Medical University, Xi'an, China, [2]Industry Engineering Department, School of Mechanical Engineering, Northwestern Polytechnical University, Xi'an, China

Percutaneous transluminal angioplasty (PTRA) is a common treatment method for renal vascular disease (RVD). However, PTRA may not be effective in patients with abnormal vascular disease. Renal autotransplantation (RAT) has been used as an alternative therapy for these diseases. Restrictions due to intracorporeal kidney cold preservation and the renal function of intracorporeal RAT were not as well protected compared with open operation. We developed this technique of 3D-printed polylactide (PLA) cold jackets for laparoscopic complete intracorporeal RAT for the purpose of better protecting the renal function and determining the feasibility of this novel procedure. The procedure was successfully applied to a 51-year-old woman with bilateral renal artery stenosis. The operation time was 5 hours, and blood loss was 200 ml. The patient's blood pressure remained constant throughout the operation, and the pressure was maintained at 120-140/70–90 mmHg without antihypertensive drugs 1 week after the operation. B-ultrasound showed that the blood flow signal of the transplanted kidney was normal and the boundary between the skin and medulla was clear. The patient was discharged 2 weeks after surgery. One year postoperatively, Doppler ultrasound of the autotransplant showed that the transplanted kidney was normal in size and shape. Radionuclide renal dynamic imaging revealed that the glomerular filtration rate (GFR) of the transplanted kidney was 36.9 ml/min. 3D-printed polylactide (PLA) cold jackets for laparoscopic complete intracorporeal RAT are a safe and effective method for the treatment of renal artery stenosis and represent a feasible method for preserving the renal function of severe renal artery stenosis patients; however, the technology is still at the exploratory stage and has room for further improvements.

Keywords: 3D print, polylactide, kidney diseases, kidney transplantation, laparoscopic surgery, rat

OPEN ACCESS

Edited by:
Feng-Huei Lin,
National Taiwan University, Taiwan

Reviewed by:
Feza Korkusuz,
Hacettepe University, Turkey
Guo-Chung Dong,
National Health Research Institutes, Taiwan

****Correspondence:***
Yong Jiao
cuidong8@foxmail.com
Bo Zhang
zhangbo@fmmu.edu.cn

Specialty section:
This article was submitted to Tissue Engineering and Regenerative Medicine, a section of the journal Frontiers in Bioengineering and Biotechnology

Received: *08 July 2021*
Accepted: *29 November 2021*
Published: *03 January 2022*

Citation:
Cui D, Wu B, He D, Wang Y, Jiao Y and Zhang B (2022) 3D-Printed Cold Preservation Device in Renal Autotransplantation for the Treatment of a Patient With Renal Artery Stenosis. Front. Bioeng. Biotechnol. 9:738434. doi: 10.3389/fbioe.2021.738434

INTRODUCTION

3D printing technology is a new manufacturing process that gradually developed after the 1980s. 3D printing (rapid prototyping or additive manufacturing) is the process of creating solid 3D objects from a collection of images in the form of a digital file. The printer deposits layers of materials (such as plastic, resin, or metal) in a volumetric manner such that a replica of the object is obtained. This innovative technology will likely revolutionize our knowledge and understanding of the structure of

human tissues and organs, and it also has therapeutic applications. In recent years, as biomedical polymer materials have been widely used in the field of medicine, the use of 3D printing technology to prepare biomedical polymer materials has attracted the attention of many researchers and achieved important results, such as bone repair projects in orthopedics and neurology, nerve tissue engineering scaffold material projects, and surgical planning projects. These projects have produced ideal repair effects and greatly reduced medical costs.

Renal vascular disease (RVD) is a rare but important cause of hypertension. Because essential hypertension is increasingly common and blood pressure is not commonly measured, RVD is not usually diagnosed at an early stage. Percutaneous transluminal angioplasty (PTRA) is a common treatment method for RVD (Buck et al., 2016), and this technology has improved over time and is now increasingly used, such as for placing vascular stents at the level of artery stenosis after forced dilation in a balloon (Kari et al., 2015; Chavent et al., 2017; Agrawal et al., 2018; Bacic et al., 2020; Raborn et al., 2020). This method may provide a minimally invasive alternative for certain patients who appear to be resistant to PTRA (Kim et al., 2017; Safdar et al., 2020).

However, PTRA may not be effective and could even be dangerous in patients with dysplasia or atherosclerotic lesions involving infrahilar branches or inflammatory lesions, such as those associated with Takayasu disease (TD). Therefore, the role of PTRA in the treatment of renovascular hypertension (RVH) is still controversial, especially in patients who present complicated renal vascular lesions or patients for whom antihypertensive drugs either are ineffective or carry a potential risk of acute renal failure.

At present, renal autotransplantation (RAT) has been used as an alternative therapy for renovascular hypertension. Traditional renal autotransplantation using an open technique with one or two incisions is required for nephrectomy or anastomosis of renal vessels. Currently, the benefits of laparoscopic surgery are well established and have led to its widespread adoption, including in the field of transplantation (Giacomoni et al., 2016; Cantrell and Oberholzer, 2018; Choi et al., 2018; Perkins et al., 2018; Spinoit et al., 2019). Some studies reported the use of laparoscopic and robot renal autotransplantation (RAT). In most studies, the use of laparoscopy is limited and mostly applied for nephrectomy (Hiess and Seitz, 2016; Siena et al., 2019; Kishore et al., 2020). After nephrectomy, renal vessels are extracted from the abdominal cavity and transferred to the bench table, and a separate incision is required to anastomose the renal vessels with the iliac vessels (Kubota et al., 2020; Pomy et al., 2020; Smith et al., 2020). Although some studies have reported intracorporeal robot-assisted renal autotransplantation and restrictions due to kidney cold preservation *in vivo*, the kidney is not cold preserved continuously during the operation after vessel dissociation (Breda et al., 2021). The results of these studies suggest that compared with intracorporeal renal autotransplantation, faster renal function recovery and shorter cold ischemia time occur with extracorporeal robot-assisted renal autotransplantation, suggesting that in intracorporeal renal autotransplantation, renal function was not best protected. At present, the use of continuous cold preservation in laparoscopic complete intracorporeal of human renal autotransplantation has not been reported.

Hypothermic perfusion and preservation technology are necessary conditions for renal autotransplantation. Cold perfusion can provide sufficient time and an appropriate operating environment for autologous kidney transplantation. Hypothermic perfusion fluid can protect renal function during renal ischemia (Lin et al., 2020), but one disadvantage of this method of continuous perfusion is that the effect is not accurate, and cell necrosis, apoptosis, and acute tubular necrosis are caused by blood supply recovery, especially when blood vessel anastomosis cannot be carried out (Urbanellis et al., 2020). The common method is adding ice water during suture, but continuous insertion of ice slush in the abdominal cavity not only distracts the surgeon and increases operative time but also is a rudimental method that does not guarantee a homogeneous parenchymal cooling effect with the possibility of compromising graft function. Cold ischemia preservation is the best preservation method (Kaths et al., 2017). A device covering the whole renal surface isolates the kidneys from surrounding tissue and maintains a constant low temperature, potentially preserving the renal function for a longer time, and by an insulation layer, it avoids cooling-related complications to the surrounding abdominal organs; this may be a perfect way to preserve the kidney. 3D solid models according to the shape of the kidney, and the greatest advantage of 3D printing is that artificial implants can be customized accurately and effectively. So we use 3D printing technology to develop a cooling jacket that consists of two sealed films that completely cover the kidney to form a channel for the cooling solution from one end to the other, and apply cold ischemia preservation continuously for the kidney.

This 3D-printed cold jacket can completely cover the graft, avoid the gradual melting of ice in the abdominal cavity, control the kidney temperature, and reduce the potential graft impairment, and it can be continued during the process of suturing. Its effect may be equivalent to that of cold preservation *in vitro*. Currently, some studies reported the use of cold preservation devices for pig intraperitoneal kidney transplantation (Menon et al., 2014; Meier et al., 2018; Samuels et al., 2019). However, they are all in the exploratory stage. There were no reports on the use of this 3D printing device in completely minimally invasive human kidney transplantation.

Polylactide (PLA), a kind of linear thermoplastic aliphatic polyester, is mainly prepared from starch raw materials through saccharification, fermentation, and certain chemical reactions. PLA has good biocompatibility and biodegradability and can be completely degraded under specific conditions, and the final products are carbon dioxide and water (Madhavan Nampoothiri et al., 2010; Tyler et al., 2016). In addition, PLA also has good thermal stability, solvent resistance, excellent gloss, transparency, resistance to certain bacteria, and flame retardancy (Farah et al., 2016). Based on the advantage of its unique plasticity and transparency, 3D-printed polylactide (PLA) cold jackets can be used completely intracorporeally. We can clearly observe the kidney condition and the color of the kidney during the whole process of vascular anastomosis, and it is convenient for

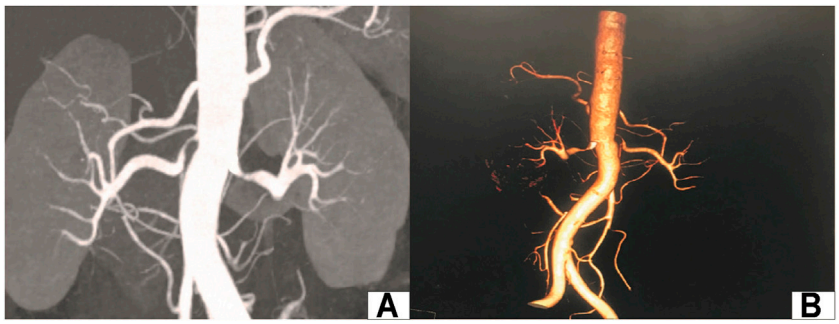

FIGURE 1 | Preoperative images of the renal artery. **(A)**: CT renal angiography; **(B)**: CT 3D reconstruction of renal vessels.

operation and can apply cold ischemia preservation continuously during the operation after vessel dissociation; thus, the kidney function can be protected to the maximum extent. This technology may make complete intracorporeal renal autotransplantation convenient, effective, and safe. Such surgery may be unique with no incision to extract or introduce kidneys, and cold ischemia preservation can be applied as same as the *in vitro* approach. Currently, there have been no reports on the use of this continuous cold ischemia preservation technology in laparoscopic complete intracorporeal of human renal autotransplantation. We developed this 3D-printed polylactide (PLA) cold jacket technique for completely intracorporeal laparoscopic RAT for the purpose to investigate the feasibility of this novel procedure and describe the first successful application of this concept in the treatment of renal artery stenosis.

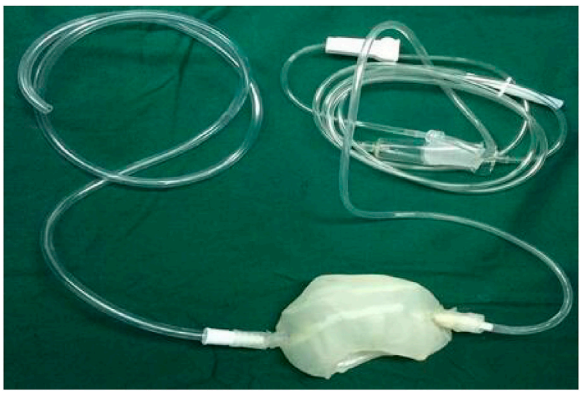

FIGURE 2 | 3D printing cold jacket of the kidney.

MATERIALS AND METHODS

Patient

The patient is a 51-year-old woman who was admitted to the urology department of our hospital on February 21, 2017. The blood pressure of the patient was elevated and fluctuated in the range of 160-200/90–100 mmHg. Nifedipine and indapamide were used, which provided poor blood pressure control. Thyroid functions and blood biochemical examination showed no extensive abnormalities. The plasma renin activity, angiotensin, and aldosterone were normal. Ultrasonic examination showed that the inner diameter at the beginning of the left and right renal arteries was 2.2 and 1.5 mm, respectively. Renal artery CTA showed 80% stenosis in the proximal segment of the left renal artery and 90% stenosis in the initial segment of the right renal artery **(Figures 1A,B)**. The CT examination of the adrenal glands showed no significant abnormalities in either adrenal glands. Bilateral radionuclide renal dynamic imaging showed that the glomerular filtration rate (GFR) of the left and right kidneys was 56.0 ml/min and 21.5 ml/min, respectively. Complete intracorporeal laparoscopic right kidney renal autotransplantation was proposed. After the operation, the operation time, bleeding loss, hot ischemia time (from ligation of the right renal artery to initiation of renal cold perfusion), cold ischemia time (from initiation of renal cold perfusion and preservation to completion of venous anastomosis), time of venous and arterial anastomosis, postoperative blood pressures, and GFR were recorded.

3D Printing

Thin-layer CT scan images of the patients' kidneys were extracted, DICOM format files were extracted from the CT scans, and images were processed with Mimics 17.0 software (Materialise Inc., Leuven, Belgium). After using threshold selection, region growth, multilayer editing, and modification techniques, three-dimensional reconstruction images of different parts of the kidney were obtained and then combined into a complete kidney. Using Mimics 17.0 software (Materialise Inc., Leuven, Belgium) cold jackets were designed.

The cool jacket is 2 mm larger than the real kidney, which is convenient for operation. The cooling jacket consists of two sealed films that completely cover the kidney to form a channel for the cooling solution from one end to the other. The equipment connects inflow and outflow to form a circuit, and the cooling solution operates at a constant volume and temperature, isolating the kidneys from surrounding tissue, which avoids the injury of adjacent abdominal organs and the heat and excessive cold injury of the kidney. The transparent and elastic PLA material is used for 3D rinting, suitably maintains the

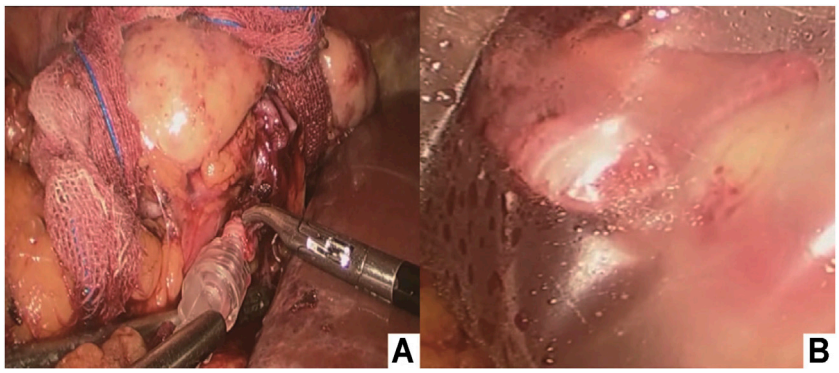

FIGURE 3 | (A) Intracorporeal cold perfusion of the kidney using a cannula and tubing passed through the assistant port to allow renal artery perfusion until clear effluent was seen from the renal vein and the color of the right kidney was pale; **(B)** 3D-printed cold jacket was completely covered on the surface of the free kidney.

temperature of the kidney, and allows easy extraction of the device. A window was designed to access the renal hilum for vascular anastomosis, while the kidney is still in the cold jacket. Finally, a standardized STL file of the cool jacket for 3D printing was output.

The STL files were formatted to meet printing parameters of the 3D printer (Shanghai liantai Technology Co., Ltd. rs4500 China). A PLA filament (Nature Work Inc., USA) is extruded from a 0.3-mm nozzle at the optimum temperature of 210°C. The external thickness of the cool jacket was 1.5 mm, the internal thickness was 1 mm, the distance between the two layers is 2 mm, and the diameter of inflow and outflow pipes is 3 mm. The printing time is 8 hours; after the printing, the cold jacket is rinsed in 70% ethanol overnight and sterilized for 90 min using the low-temperature plasma hydrogen peroxide sterilizer (Shandong Xinhua Medical Instrument Co., LTD., SQ-D, China) (**Figure 2**).

Surgical Technique

Complete intracorporeal laparoscopic right renal autotransplantation was performed. General anesthesia and indwelling catheter: a 10-mm trocar was inserted at the outer edge of the rectus abdominis parallel to the umbilicus as the laparoscopic lens hole. Approximately 6 cm from the laparoscopic lens hole, two 10-mm trocars were inserted at the hypogastrium and medial side of the anterior superior iliac spine (as an isosceles triangle). The right external iliac artery and vein, proximal to the bifurcation of the iliac vessels, distal to the abdominal wall, were carefully dissociated. Approximately 4 cm from the umbilicus at the edge of the rectus abdominis, a 10-mm trocar was inserted as the laparoscopic lens hole, and approximately 3 cm from the costal margin, a 10-mm trocar was inserted in the midclavicular line.

After the colon was dissociated, the renal vessels were completely dissociated to the maximum extent and completely dissociated from the right kidney. The excess perirenal fat was removed, and the fat that maintained the blood supply of the ureter between the lower pole of the kidney and the ureter was retained, and the adipose tissue around the ureter was properly retained. The ureter was distally dissociated as far as possible, and the upper and lower poles of the right kidney were bound with yarn strips as the extraction points of the kidney. From the root of the renal arteriovenous artery, the renal artery was ligated using laparoscopic clips close to the aorta, and the renal vein was then ligated in a similar manner. The renal artery and vein were then transected above the clips, and arteriovenous dissociation was carefully performed.

Immediately after dividing the vessels, the perfusion cannula was inserted in the transected artery lumen, which was continuously flushed with ice-cold perfusion liquid (hypertonic purine citrate fluid) solution under gravity until the clear effluent was seen from the renal vein and the color of the right kidney was pale (**Figure 3A**). The 3D-printed cold jacket completely covered the surface of the free kidney, and ice-cold saline water was continuously infused through the infusion pipeline. The kidney was carefully placed in the pelvis, and the opening of the renal artery and vein were placed close to the external iliac vessels (**Figure 3B**; **Figure 4**).

The external iliac vein was clamped with laparoscopic bulldog clamps, and a venotomy incision was made. A running end-to-side anastomosis was created between the renal vein and the external iliac vein using a 5-0 Prolene line. Before the last suture was placed, the lumen was irrigated with heparinized saline through a 5-Fr ureteral catheter to remove intraluminal air. After completing the venous anastomosis, a bulldog clamp was placed on the renal vein, and the clamps were released from the external iliac vein. End-to-side arterial anastomosis was performed, similar to that for the vein. The 3D-printed cold jacket was then removed from the surface of the kidney. Upon completion, the clamps were removed, beginning with the distal external iliac artery, followed by the renal vein and then the proximal external iliac artery.

RESULTS

The operation time was 5 hours, and the hot ischemia time (from ligation of the right renal artery to initiation of renal cold perfusion) was 2 min. The cold ischemia time (from initiation of renal cold perfusion and preservation to the completion of venous anastomosis) was 76 min. The time for venous and arterial anastomosis was 23 and 27 min, respectively. In addition, the estimated blood loss was 200 ml (**Table 1**). The blood pressure

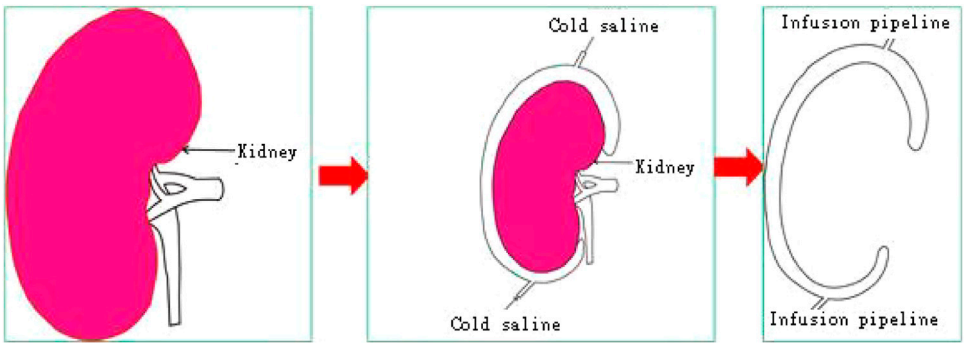

FIGURE 4 | 3D-printed model of the cold jacket covered on the surface of free kidney.

TABLE 1 | Outcomes of operation.

Item	Outcomes
Operation time	301 min
Blood loss	200 ml
Hot ischemia time	2 min
Cold ischemia time	76 min
Venous anastomosis	23 min
Arterial anastomosis	27 min

remained constant throughout the operation. Postoperative rehydration and infection prevention were administered. Blood pressure monitoring was maintained at 120-140/70–90 mmHg without antihypertensive drugs. The patient was discharged 2 weeks after surgery. One 1 year postoperatively, Doppler ultrasound of the autotransplant showed that the transplanted kidney was normal in size and shape, and the boundary between the skin and medulla was clear (**Figure 5A**). The blood flow signal of the transplanted kidney was not abnormal, the transplanted kidney was supplied by the right external iliac artery, and the vein returned to the right external iliac vein (**Figure 5B**). The arteriovenous phase and excretory phase were well developed. Radionuclide renal dynamic imaging revealed that the GFR of the transplanted kidney was 36.9 ml/min.

DISCUSSION

Currently, renal autotransplantation (RAT) has been reported as an effective treatment model for managing complex renal/ureteral lesions. The first RAT in humans was performed by Hardy in 1963 to address an extensive ureteral lesion. Over the past 30 years, RAT has been used in the surgical management of complex ureteral lesions, renal artery aneurysms, RVH, renal tumors, low back pain syndrome, and hematuria (Gwon et al., 2017; Ruiz et al., 2017; Doumerc et al., 2018; Haberal et al., 2018; Chen et al., 2020). RVH caused by renal artery stenosis presents as refractory hypertension and with poor drug treatment effect. It generally consists of percutaneous transluminal renal angioplasty (PTRA), *in situ* vascular reconstruction, or renal autotransplantation (RAT). These procedures aim to normalize the blood flow to the affected kidney with the fewest possible surgical complications. However, PTRA may be unsuccessful and even hazardous in patients with dysplastic or atherosclerotic lesions involving infrahilar branches or with inflammatory lesions, such as those associated with TD. RAT has been used as an alternative treatment for the aneurysmal or complex occlusive disease of the renal artery. In the studied case of bilateral renal artery severe stenosis, stenosis of the right renal artery was more severe than that on the left, with the right renal artery accounting for approximately 90% of the stenosis. Narrowing was observed in the proximal renal artery, and because of the poor right kidney function, interventional therapy was difficult. Therefore, we selected RAT as an alternative treatment for this patient to obtain the best long-term results, improve the right kidney blood supply, and obtain compensatory right-side functions. If poor postoperative blood pressure control is achieved, then further treatment of left renal artery stenosis can be administered.

Laparoscopy and robot surgery have been used for donor nephrectomy and renal autotransplantation. Restrictions due to kidney cold preservation *in vivo*, most studies take the kidney extracted from the abdominal cavity and transfer to the bench table, and a separate incision is required to anastomose the renal vessels with the iliac vessels; the kidney is not cold preserved continuously during the operation (Ju et al., 2016; Kumar et al., 2018; Tiong et al., 2018; Ölçücüoğlu, 2020).Currently, some studies reported the use of cold preservation devices for pig intraperitoneal kidney transplantation (Menon et al., 2014; Meier et al., 2018; Samuels et al., 2019). However, they are all in the exploratory stage. In addition, some researchers reported using cold preserve in living donor's kidney transplants (Territo et al., 2021), but this method requires an additional incision to insert the cold preserve device and donor's kidney. There were no reports on the use of this device to human completely minimally invasive renal autotransplantation.

In this study, the patient underwent laparoscopic complete intracorporeal renal autotransplantation, the blood pressure was maintained at a normal level, the blood supply of the transplanted kidney recovered to normal levels, and the GFR was significantly recovered. Therefore, we believe that laparoscopic complete intracorporeal renal autotransplantation may be the preferred

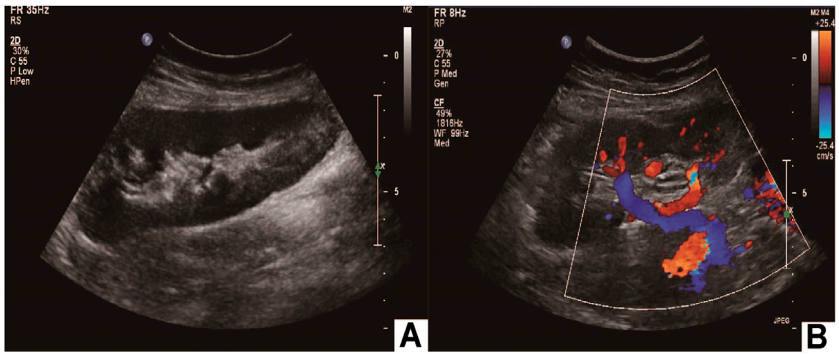

FIGURE 5 | Postoperative imaging confirmed autotransplantation success. **(A)** Doppler ultrasound of autotransplant showing that the transplanted kidney was of normal size and shape; **(B)** the transplanted kidney was supplied by the right external iliac artery, and the vein returned to the right external iliac vein.

treatment for severe renal artery stenosis for which interventional therapy is not appropriate.

3D printing technology converts two-dimensional images into specified materials for printing through computer design software (Atalay et al., 2017; Ghazi et al., 2017; Bai et al., 2020). With the concept of biological manufacturing, the application of 3D printing technology in medicine has received increasing attention from researchers worldwide. At present, great progress has been made in reflecting the anatomical details of human organs by 3D printing, which was first used in preoperative planning and surgical simulation of complex operations (Ali et al., 2020; Xu et al., 2020). It has been more commonly used in orthopedics, stomatology, and cranial maxillofacial surgery. Giovinco (Giovinco et al., 2012) applied 3D printing technology in preoperative training for Charcot's foot orthopedic surgery and achieved good results. In the operation to repair an acetabular fracture, a simulated pelvis model of the patient was printed with 3D technology, and plate pre-bending, screw length measurement, and screw entry direction design were carried out on the model, which greatly reduced the operation time and surgical complications; moreover, the fracture model can be used to train new doctors. 3D printing technology has been applied in urology to print individual 3D solid models according to the shape of the kidney, and the greatest advantage of 3D printing is that artificial implants can be customized accurately and effectively. In this study, we used 3D printing technology to produce a temporary "cold jacket" for the kidney, and its effect was the same as that of *in vitro* cold preservation. This new method of 3D printing technology combined with cold preservation was first successfully applied in the treatment of renal artery stenosis, and this technology has not been previously reported.

PLA, a kind of linear thermoplastic aliphatic polyester, is mainly prepared from starch raw materials through saccharification, fermentation, and certain chemical reactions (Madhavan Nampoothiri et al., 2010; Tyler et al., 2016). It has good thermal stability, solvent resistance, excellent gloss, transparency, resistance to certain bacteria, and flame retardancy (Farah et al., 2016). Because of its unique performance, PLA is widely used in medical tissue engineering research, and it is feasible to make a cold storage device with this material. In this study, our novel cold storage devices overcome the restriction of kidney preservation in the process of complete intracorporeal renal autotransplantation. The kidney was preserved continuously, and the kidney function was protected to the maximum extent; this technology is safe and feasible for use in the process of human autologous kidney transplantation.

However, there are some limitations. First, this study applied 3D printing cold jackets for renal autotransplantation, and the proposed method was only applied to one patient. Additionally, although this new method is very promising, random comparisons with traditional renal autotransplantation were not performed, and the long-term effects and large sample outcomes have not been determined. Finally, whether the technique is suitable for different types of renal transplantation patients requires further clarification; thus, this cold jacket should be optimized in future research.

CONCLUSION

A 3D-printed polylactide (PLA) cold jacket for laparoscopic completely intracorporeal renal autotransplantation is a safe, effective, and less complicated method for the treatment of renal artery stenosis; however, the technology is at the exploratory stage and, thus, still has room for improvement. Every step still needs further research and elaboration, the cases need to be carefully selected, and the surgeon must be skilled in laparoscopic techniques, especially laparoscopy vascular sutures.

DATA AVAILABILITY STATEMENT

The original contributions presented in the study are included in the article/Supplementary Material, further inquiries can be directed to the corresponding authors.

ETHICS STATEMENT

The studies involving human participants were reviewed and approved by the Local Ethics Committee of Tangdu Hospital. The

patients/participants provided their written informed consent to participate in this study. Written informed consent was obtained from the individual(s) for the publication of any potentially identifiable images or data included in this article.

AUTHOR CONTRIBUTIONS

DC and BZ contributed to the conception and design of the study, discussion of the results, and drafting of the manuscript. HDL, BW, and BZ were responsible for the diagnosis and treatment of the disease. YEW, YJ, and DC organized the follow-up research. YEW, YJ, and YCZ performed the imaging examinations and data collection. DC, BZ, and YEW carried out the 3D modeling, data post-processing, and stent manufacturing. All authors contributed to the article and approved the submitted version.

ACKNOWLEDGMENTS

We are grateful for the teams of the Department of Radiology and Department of Ultrasound Diagnostics (Tangdu Hospital) for identifying potential research participants and providing facilities. We would also like to thank Prof. He Wang for providing helpful advice and suggestions.

REFERENCES

Ali, S., Sirota, E., Ali, H., Bezrukov, E., Okhunov, Z., Bukatov, M., et al. (2020). Three-Dimensionally Printed Non-Biological Simulator for Percutaneous Nephrolithotomy Training. *Scand J. Urol.* 54, 349–354. doi:10.1080/21681805.2020.1773529

Agrawal, H., Moodie, D., Qureshi, A. M., Acosta, A. A., Hernandez, J. A., Braun, M. C., et al. (2018). Interventions in Children with Renovascular Hypertension: A 27-year Retrospective Single-center Experience. *Congenit. Heart Dis.* 13, 349–356. doi:10.1111/chd.12608

Atalay, H. A., Canat, H. L., Ülker, V., Alkan, İ., Özkuvanci, Ü., and Altunrende, F. (2017). Impact of Personalized Three-Dimensional (3D) Printed Pelvicalyceal System Models on Patient Information in Percutaneous Nephrolithotripsy Surgery: a Pilot Study. *Int. Braz. J. Urol.* 43, 470–475. doi:10.1590/s1677-5538.ibju.2016.0441

Bacic, J., Liu, T., Thompson, R. H., Boorjian, S. A., Leibovich, B. C., Golijanin, D., et al. (2020). Emulating Target Clinical Trials of Radical Nephrectomy with or without Lymph Node Dissection for Renal Cell Carcinoma. *Urology* 140, 98–106. doi:10.1016/j.urology.2020.01.039

Bai, F., Wu, H., Zhang, N., Chen, J., and Wen, J. (2020). The Feasibility, Safety, and Efficacy of the Preemptive Indwelling of Double-J Stents in Percutaneous Nephrolithotomy Surgery: A Randomized Controlled Trial. *Urol. J.* 17, 232–236. doi:10.22037/uj.v0i0.4957

Breda, A., Diana, P., Territo, A., Gallioli, A., Piana, A., Gaya, J. M., et al. (2021). Intracorporeal versus Extracorporeal Robot-Assisted Kidney Autotransplantation: Experience of the ERUS RAKT Working Group. *Eur. Urol.* 12, S0302–S2838. doi:10.1016/j.eururo.2021.07.023

Buck, D. B., Curran, T., McCallum, J. C., Darling, J., Mamtani, R., van Herwaarden, J. A., et al. (2016). Management and Outcomes of Isolated Renal Artery Aneurysms in the Endovascular Era. *J. Vasc. Surg.* 63, 77–81. doi:10.1016/j.jvs.2015.07.094

Cantrell, L. A., and Oberholzer, J. (2018). Robotic Pancreas Transplantation: the State of the Art. *Curr. Opin. Organ. Transpl.* 23, 423–427. doi:10.1097/MOT.0000000000000555

Chavent, B., Duprey, A., Lavocat, M.-P., Fichtner, C., Beraud, A.-M., Albertini, J.-N., et al. (2017). Renovascular Hypertension: Results in Adulthood of Renal Autotransplantation Performed in Children. *Pediatr. Nephrol.* 32, 1935–1940. doi:10.1007/s00467-017-3664-x

Chen, X., Zhao, J., Yuan, D., Yang, Y., and Huang, B. (2020). Restenosis of Bilateral Aorta-Renal Saphenous Vein Grafts after the Surgical Repair of Takayasu Arteritis-Induced Bilateral Renal Arteries Stenosis: Case Report. *Ann. Vasc. Surg.* 62, e1–498. doi:10.1016/j.avsg.2019.06.021

Choi, C. I., Kim, D. I., Baek, S. H., Chung, Y. S., Kim, D. H., Jeon, T. Y., et al. (2018). Initial Experience with Hand-Assisted Laparoscopic Living Donor Nephrectomy: Training and Clinical Practice as a General Surgeon. *Transplant. Proc.* 50, 3113–3120. doi:10.1016/j.transproceed.2018.08.052

Doumerc, N., Beauval, J.-B., Roumiguié, M., Roulette, P., Laclergerie, F., Sallusto, F., et al. (2018). Total Intracorporeal Robotic Renal Auto-Transplantation: A New Minimally Invasive Approach to Preserve the Kidney after Major Ureteral Injuries. *Int. J. Surg. Case Rep.* 49, 176–179. doi:10.1016/j.ijscr.2018.06.017

Farah, S., Anderson, D. G., and Langer, R. (2016). Physical and Mechanical Properties of PLA, and Their Functions in Widespread Applications - A Comprehensive Review. *Adv. Drug Deliv. Rev.* 107, 367–392. doi:10.1016/j.addr.2016.06.012

Ghazi, A., Campbell, T., Melnyk, R., Feng, C., Andrusco, A., Stone, J., et al. (2017). Validation of a Full-Immersion Simulation Platform for Percutaneous Nephrolithotomy Using Three-Dimensional Printing Technology. *J. Endourol.* 31, 1314–1320. doi:10.1089/end.2017.0366

Giacomoni, A., Di Sandro, S., Lauterio, A., Concone, G., Buscemi, V., Rossetti, O., et al. (2016). Robotic Nephrectomy for Living Donation: Surgical Technique and Literature Systematic Review. *Am. J. Surg.* 211, 1135–1142. doi:10.1016/j.amjsurg.2015.08.019

Giovinco, N. A., Dunn, S. P., Dowling, L., Smith, C., Trowell, L., Ruch, J. A., et al. (2012). A Novel Combination of Printed 3-dimensional Anatomic Templates and Computer-Assisted Surgical Simulation for Virtual Preoperative Planning in Charcot Foot Reconstruction. *J. Foot Ankle Surg.* 51, 387–393. doi:10.1053/j.jfas.2012.01.014

Gwon, J. G., Kim, Y. H., and Han, D. J. (2017). Real Renal Function after Renal Autotransplantation through the Analysis of Solitary Kidney Autotransplantation Cases. *Transplant. Proc.* 49, 2055–2059. doi:10.1016/j.transproceed.2017.09.030

Haberal, H. B., Tonyali, S., Peynircioğlu, B., Arici, M., Demircin, M., and Aki, F. T. (2018). Renal Autotransplantation with Autologous Saphenous Vein Graft in a Patient with Takayasu Arteritis and Existing Renal Artery Stent in Her Solitary Kidney. *Urol. Int.* 100, 181–184. doi:10.1159/000475509

Ju, X., Li, P., Shao, P., Lv, Q., Wang, Z., Qin, C., et al. (2016). Retroperitoneal Laparoscopic Nephrectomy Combined with Bench Surgery and Autotransplantation for Renal Cell Carcinoma in the Solitary Kidney or Tumor Involving Bilateral Kidneys: Experience at a Single Center and Technical Considerations. *Urol. Int.* 97, 473–479. doi:10.1159/000448594

Kari, J. A., Roebuck, D. J., McLaren, C. A., Davis, M., Dillon, M. J., Hamilton, G., et al. (2015). Angioplasty for Renovascular Hypertension in 78 Children. *Arch. Dis. Child.* 100, 474–478. doi:10.1136/archdischild-2013-305886

Kaths, J. M., Echeverri, J., Linares, I., Cen, J. Y., Ganesh, S., Hamar, M., et al. (2017). Normothermic *Ex Vivo* Kidney Perfusion Following Static Cold Storage-Brief, Intermediate, or Prolonged Perfusion for Optimal Renal Graft Reconditioning? *Am. J. Transpl.* 17, 2580–2590. doi:10.1111/ajt.14294

Kim, M. J., Lee, K. W., Park, J. B., and Kim, S. J. (2017). Hand-Assisted Laparoscopic Nephrectomy and Auto-Transplantation for a Hilar Renal Artery Aneurysm: A Case Report. *VSI* 33, 84–87. doi:10.5758/vsi.2017.33.2.84

Kishore, T. A., Kuriakose, M. J., Pathrose, G., Raveendran, V., Kumar, K. V., and Unni, V. N. (2020). Robotic Assisted Kidney Transplantation in Grafts with Multiple Vessels: Single center Experience. *Int. Urol. Nephrol.* 52, 247–252. doi:10.1007/s11255-019-02305-z

Kubota, R., Araki, M., Wada, K., Kawamura, K., Maruyama, Y., Mitsui, Y., et al. (2020). Robotic Renal Autotransplantation: A Feasibility Study in a Porcine Model. *Acta Med. Okayama* 74, 53–58. doi:10.18926/AMO/57953

Kumar, A., Chaturvedi, S., Gulia, A., Maheshwari, R., Dassi, V., and Desai, P. (2018). Laparoscopic Live Donor Nephrectomy: Comparison of Outcomes Right versus Left. *Transplant. Proc.* 50, 2327–2332. doi:10.1016/j.transproceed.2018.03.034

Lin, D., Xiang, T., Qiu, Q., Leung, J., Xu, J., Zhou, W., et al. (2020). Aldehyde Dehydrogenase 2 Regulates Autophagy via the Akt-mTOR Pathway to Mitigate Renal Ischemia-Reperfusion Injury in Hypothermic Machine Perfusion. *Life Sci.* 253, 117705. doi:10.1016/j.lfs.2020.117705

Madhavan Nampoothiri, K., Nair, N. R., and John, R. P. (2010). An Overview of the Recent Developments in Polylactide (PLA) Research. *Bioresour. Techn.* 101, 8493–8501. doi:10.1016/j.biortech.2010.05.092

Meier, R. P. H., Piller, V., Hagen, M. E., Joliat, C., Buchs, J.-B., Nastasi, A., et al. (2018). Intra-Abdominal Cooling System Limits Ischemia-Reperfusion Injury during Robot-Assisted Renal Transplantation. *Am. J. Transpl.* 18, 53–62. doi:10.1111/ajt.14399

Menon, M., Sood, A., Bhandari, M., Kher, V., Ghosh, P., Abaza, R., et al. (2014). Robotic Kidney Transplantation with Regional Hypothermia: A Step-by-step Description of the Vattikuti Urology Institute-Medanta Technique (IDEAL Phase 2a). *Eur. Urol.* 65, 991–1000. doi:10.1016/j.eururo.2013.12.006

Ölçücüoğlu, E. (2020). Comparing the Complications of Laparoscopically Performed Simple, Radical and Donor Nephrectomy. *Turk J. Med. Sci.* 50, 922–929. doi:10.3906/sag-1910-120

Perkins, S. Q., Giffen, Z. C., Buck, B. J., Ortiz, J., Sindhwani, P., and Ekwenna, O. (2018). Initial Experience with the Use of a Robotic Stapler for Robot-Assisted Donor Nephrectomy. *J. Endourol.* 32, 1054–1057. doi:10.1089/end.2018.0461

Pomy, B., Glousman, B., and Macsata, R. (2020). Management of Bilateral Renal Artery Aneurysms with Laparoscopic Nephrectomy, *Ex Vivo* Reconstruction, and Autotransplantation in a Woman Planning Pregnancy. *J. Vasc. Surg. Cases, Innov. Tech.* 6, 126–128. doi:10.1016/j.jvscit.2020.01.006

Raborn, J., McCafferty, B. J., Gunn, A. J., Moawad, S., Mahmoud, K., Aal, A. K. A., et al. (2020). Endovascular Management of Neurofibromatosis Type I-Associated Vasculopathy: A Case Series and Brief Review of the Literature. *Vasc. Endovascular Surg.* 54, 182–190. doi:10.1177/1538574419885257

Ruiz, M., Hevia, V., Fabuel, J.-J., Fernández, A.-A., Gómez, V., and Burgos, F.-J. (2017). Kidney Autotransplantation: Long-Term Outcomes and Complications. Experience in a Tertiary Hospital and Literature Review. *Int. Urol. Nephrol.* 49, 1929–1935. doi:10.1007/s11255-017-1680-1

Safdar, O., Alaifan, F., Alshammakh, S., Hakami, M., and Alghaithi, D. F. (2020). Diagnostically Challenging Case of Renal Artery Stenosis in a Pediatric Patient. *Cureus* 12, e6538. doi:10.7759/cureus.6538

Samuels, J. A., Zavala, A. S., Kinney, J. M., and Bell, C. S. (2019). Hypertension in Children and Adolescents. *Adv. Chronic Kidney Dis.* 26, 146–150. doi:10.1053/j.ackd.2019.02.003

Seitz, C., and Hiess, M. (2016). Robot-assisted Renal Surgery: Current Status and Future Directions. *Robot Surg.* 3, 1–12. doi:10.2147/RSRR.S71328

Siena, G., Vignolini, G., Mari, A., Li Marzi, V., Caroassai, S., Giancane, S., et al. (2019). Full Robot-Assisted Living Donor Nephrectomy and Kidney Transplantation in a Twin Dedicated Operating Room: Initial Experience from a High-Volume Robotic Center. *Surg. Innov.* 26, 449–455. doi:10.1177/1553350619835429

Smith, M., Lazar, A., Morrissey, N., and Ratner, L. (2020). Laparoscopic Nephrectomy with *Ex Vivo* Repair of Aneurysm and Autotransplantation. *J. Vasc. Surg. Cases, Innov. Tech.* 6, 24–26. doi:10.1016/j.jvscit.2019.11.009

Spinoit, A.-F., Moreels, N., Raes, A., Prytula, A., De Groote, R., Ploumidis, A., et al. (2019). Single-setting Robot-Assisted Kidney Transplantation Consecutive to Single-Port Laparoscopic Nephrectomy in a Child and Robot-Assisted Living-Related Donor Nephrectomy: Initial Ghent Experience. *J. Pediatr. Urol.* 15, 578–579. doi:10.1016/j.jpurol.2019.08.005

Territo, A., Piana, A., Fontana, M., Diana, P., Gallioli, A., Gaya, J. M., et al. (2021). Step-by-step Development of a Cold Ischemia Device for Open and Robotic-Assisted Renal Transplantation. *Eur. Urol.* 21, 01795–1804. doi:10.1016/j.eururo.2021.05.026

Tiong, H. Y., Goh, B. Y. S., Chiong, E., Tan, L. G. L., and Vathsala, A. (2018). Robotic Kidney Autotransplantation in a Porcine Model: a Procedure-specific Training Platform for the Simulation of Robotic Intracorporeal Vascular Anastomosis. *J. Robotic Surg.* 12, 693–698. doi:10.1007/s11701-018-0806-5

Tyler, B., Gullotti, D., Mangraviti, A., Utsuki, T., and Brem, H. (2016). Polylactic Acid (PLA) Controlled Delivery Carriers for Biomedical Applications. *Adv. Drug Deliv. Rev.* 107, 163–175. doi:10.1016/j.addr.2016.06.018

Urbanellis, P., Hamar, M., Kaths, J. M., Kollmann, D., Linares, I., Mazilescu, L., et al. (2020). Normothermic *Ex Vivo* Kidney Perfusion Improves Early DCD Graft Function Compared with Hypothermic Machine Perfusion and Static Cold Storage. *Transplantation* 104, 947–955. doi:10.1097/TP.0000000000003066

Xu, Y., Yuan, Y., Cai, Y., Li, X., Wan, S., and Xu, G. (2020). Use 3D Printing Technology to Enhance Stone Free Rate in Single Tract Percutaneous Nephrolithotomy for the Treatment of Staghorn Stones. *Urolithiasis* 48, 509–516. doi:10.1007/s00240-019-01164-8

Conflict of Interest: The authors declare that the research was conducted in the absence of any commercial or financial relationships that could be construed as a potential conflict of interest.

Publisher's Note: All claims expressed in this article are solely those of the authors and do not necessarily represent those of their affiliated organizations, or those of the publisher, the editors, and the reviewers. Any product that may be evaluated in this article, or claim that may be made by its manufacturer, is not guaranteed or endorsed by the publisher.

frontiers in Bioengineering and Biotechnology

ORIGINAL RESEARCH
published: 04 January 2022
doi: 10.3389/fbioe.2021.803052

The GDF11 Promotes Nerve Regeneration After Sciatic Nerve Injury in Adult Rats by Promoting Axon Growth and Inhibiting Neuronal Apoptosis

Junhao Lin[1†], Jie Shi[1,2,3†], Xiang Min[4], Si Chen[5], Yunpeng Zhao[1], Yuanqiang Zhang[1] and Lei Cheng[1*]*

[1]Department of Orthopaedic, Qilu Hospital, Cheeloo College of Medicine, Shandong University, Jinan, China, [2]Cheeloo College of Medicine, Shandong University, Jinan, China, [3]NHC Key Laboratory of Otorhinolaryngology, Qilu Hospital, Cheeloo College of Medicine, Shandong University, Jinan, China, [4]Department of Health Management Center, Qilu Hospital, Cheeloo College of Medicine, Shandong University, Jinan, China, [5]Department of Neurosurgery, Qilu Hospital, Shandong University, Jinan, China

OPEN ACCESS

Edited by:
Feng-Huei Lin,
National Taiwan University, Taiwan

Reviewed by:
Renjie Chai,
Southeast University, China
Srinivas Madduri,
University Hospital of Basel, Switzerland

***Correspondence:**
Yuanqiang Zhang
gkzyq09098@qiluhospital.com
Lei Cheng
chenglei@email.sdu.edu.cn

[†]These authors have contributed equally to this work and share first authorship

Specialty section:
This article was submitted to Tissue Engineering and Regenerative Medicine, a section of the journal Frontiers in Bioengineering and Biotechnology

Received: 12 November 2021
Accepted: 15 December 2021
Published: 04 January 2022

Citation:
Lin J, Shi J, Min X, Chen S, Zhao Y, Zhang Y and Cheng L (2022) The GDF11 Promotes Nerve Regeneration After Sciatic Nerve Injury in Adult Rats by Promoting Axon Growth and Inhibiting Neuronal Apoptosis. Front. Bioeng. Biotechnol. 9:803052. doi: 10.3389/fbioe.2021.803052

Introduction: Sciatic nerve injury is a common injury of the nervous system. Stem cell-based therapies, drug-based therapies and rehabilitation physiotherapy therapies are currently available, but their limited therapeutic efficacy limits their use. Here, we aimed to explore a novel lentiviral-based gene therapeutic strategy and to elaborate its mechanism.

Materials and Methods: Recombinant GDF11 protein was used for the *in vitro* treatment of dorsal root ganglion (DRG) cells. Lentivirus was used to construct a vector system for the *in vivo* expression of GDF11. The nerve conduction function was detected using action-evoked potentials at different time periods, and the regulatory effect of nerves on target organs was detected by weighing the gastrocnemius muscle. Immunofluorescence of NF200 and S100 was used to show the regeneration of the sciatic nerve, and myelin and Nissl staining were performed to observe the pathological features of the tissue. Western was used to validate signaling pathways. The expression of related genes was observed by qPCR and Western blotting, and cell apoptosis was detected by flow cytometry.

Result: GDF11 promotes the axonal growth of DRG cells and inhibits DGR cell apoptosis *in vitro*. GDF11 acts by activating the Smad pathway. GDF11 promotes the recovery of damaged sciatic nerve function in rats, the regeneration of damaged sciatic nerves in rats, and myelin regeneration of damaged sciatic nerves in rats. GDF11 also exerts a protective effect on neuronal cells in rats.

Conclusion: Based on the present study, we conclude that GDF11 promotes axonal growth and inhibits DRG cell apoptosis *in vitro* through the Smad pathway, and lentivirus-mediated GDF11 overexpression *in vivo* can promote the recovery of sciatic nerves after transection by promoting axonal growth and inhibiting neuronal apoptosis in the spinal cord.

Keywords: sciatic nerve injury, nerve regeneration, lentiviral vector, growth differentiation factor 11, smad pathway

INTRODUCTION

Peripheral nerve injury is more common than central nervous system injury but has not received sufficient attention. Peripheral nerve injury often leads to heavy psychological stress and a decline in quality of life and thus results in a heavy social and economic burden (Geuna, 2015; Liu et al., 2018). Peripheral nerve transection is one of the most common peripheral nerve injuries, but its current treatment does not yield satisfactory effects. Transection injuries are caused by a cutting object (for example, knife wounds, broken glass, metal shards, chainsaw blades, wood splinters, and animal bites) (Wang C.-X. et al., 2018). Although neurons have a limited ability to regenerate, axons have a great potential for regeneration (Guo et al., 2016; He et al., 2016; Fang et al., 2019; Yang et al., 2020), and peripheral nerve damage is thus more likely to heal than central nervous system damage (Gu et al., 2014; Geissler and Stevanovic, 2019). The sciatic nerve is accompanied by nerve degeneration and nerve regeneration after injury. Although the specific molecular mechanism of sciatic nerve degeneration and regeneration is not very clear, it is generally believed that this is a complex series of events, which includes local macrophage activation after injury, the attraction of circulating immune cells participating in necrosis (Shi et al., 2018; Fan et al., 2019; Kalinski et al., 2020) and neural axon degeneration and atrophy (Yu et al., 2018) due to an abnormal neuronal cell body leads to increased Schwann cell apoptosis increased (Jia et al., 2020; Yardim et al., 2021), the demyelination of nerve fibers and the local proliferation of fibroblasts to induce scar formation (Que et al., 2013). During this process, the body will gradually adjust to these adverse factors such that the injured nerve slowly undergoes incomplete repair.

Neurotrophic factors are cytokines that regulate the growth and development of the nervous system. Endogenous neurotrophic factors can inhibit neuronal apoptosis (Xue et al., 2021), promote neuronal axon growth and regulate neuronal differentiation (de León et al., 2021). Different neurotrophic factors play different roles, and these roles can be synergistic or even opposite. At present, the treatment of peripheral nerve injury mainly includes stem cell therapy (Zhao et al., 2019; Xia et al., 2020; Zhou et al., 2020; Guo et al., 2021a; Guo et al., 2021b; Yuan et al., 2021), biomaterial research (Shang et al., 2018; Li G. et al., 2019; Tang et al., 2019; Guo J. et al., 2020; Han et al., 2020; Lin et al., 2020), and injection of bioactive drugs (Li et al., 2018; Li D. et al., 2019; Pukos et al., 2019; Cai et al., 2021; Yang et al., 2021), among others. Many studies have shown that the injection of neurotrophic factors can promote the recovery of nerve function after peripheral nerve transection, promote the growth of nerve axons, inhibit neuronal apoptosis and promote nerve regeneration (Gris et al., 2004; Gong et al., 2017; Waqas et al., 2017). However, these methods themselves may cause secondary iatrogenic injuries, which limits their application in the treatment of peripheral nerve injuries. Therefore, the identification of an effective cytokine for promoting nerve regeneration is very important.

Growth differentiation factor 11 (GDF11) is a transforming growth factor β (TGFβ) protein. Some studies have suggested that GDF11 plays a negative role in the regulation of the normally developing nervous system (Kim et al., 2005; Kong et al., 2020), but other studies have shown that GDF11 can inhibit cell apoptosis (Mei et al., 2016), promote axon and synaptic development (Hocking et al., 2008; Augustin et al., 2017), induce neurovascular regeneration and improve nervous system function in elderly individuals (Katsimpardi et al., 2014). However, due to the half-life of the injected cytokines and neurotrophic factors, their effects in the body are relatively short, multiple injections are needed, or their high cost limits their development.

To find a more effective treatment strategy for sciatic nerve injury, our study confirmed the protective effect of GDF11 on neurons *in vitro*, and in a further study, we used a lentiviral vector to induce GDF11 overexpression and thus create and maintain a local microenvironment conducive to nerve regeneration. Lentivirus is a safe *in vivo* expression vector that is currently widely used (Anger-Gora et al., 2021; Reyne et al., 2021). Specifically, we found that lentivirus can transfer the GDF11 gene into the peripheral nervous system and overexpress GDF11 to continuously produce a large amount of GDF11 locally and thus promote the recovery of nerve function after peripheral nerve transection. The *in vivo* transfection of lentiviral GDF11 can effectively avoid secondary iatrogenic injury, has the advantage of reducing the treatment costs, and provides a new treatment strategy for peripheral nerve injury. Based on these findings, we hope to find a strategy for regulating the microenvironment at the site of injury, promote the repair of an injured sciatic nerve, and explore its mechanism to provide a new vision for exploring the mechanism of sciatic nerve injury and developing treatment strategies.

MATERIALS AND METHODS

Animals

Wistar rats were obtained from the Laboratory Animal Centre of Shandong University. A total of 40 male Wistar rats were randomly divided into two groups (each with 20 rats): a control group (rats were injected with lentiviral virus after sciatic nerve transection) and a GDF11 group (rats were injected with lentiviral GDF11 virus after sciatic nerve transection). All animals were maintained under controlled light/dark (12/12 h), temperature (22°C), and humidity (60%) conditions. Food and water were available ad libitum. The pain and numbers of the experimental rats were reduced as much as possible while still meeting the experimental objectives.

Ethics Statement

The protocol was approved and monitored by the International Guiding Principles for Animal Research, as stipulated by the World Health Organization and as adopted by the Laboratory Animal Centre of Shandong University.

Surgical Procedures

To simulate sciatic nerve injury in rats, a rat sciatic nerve transection model was used in this study. The operation was performed under deep anesthesia through the intravenous

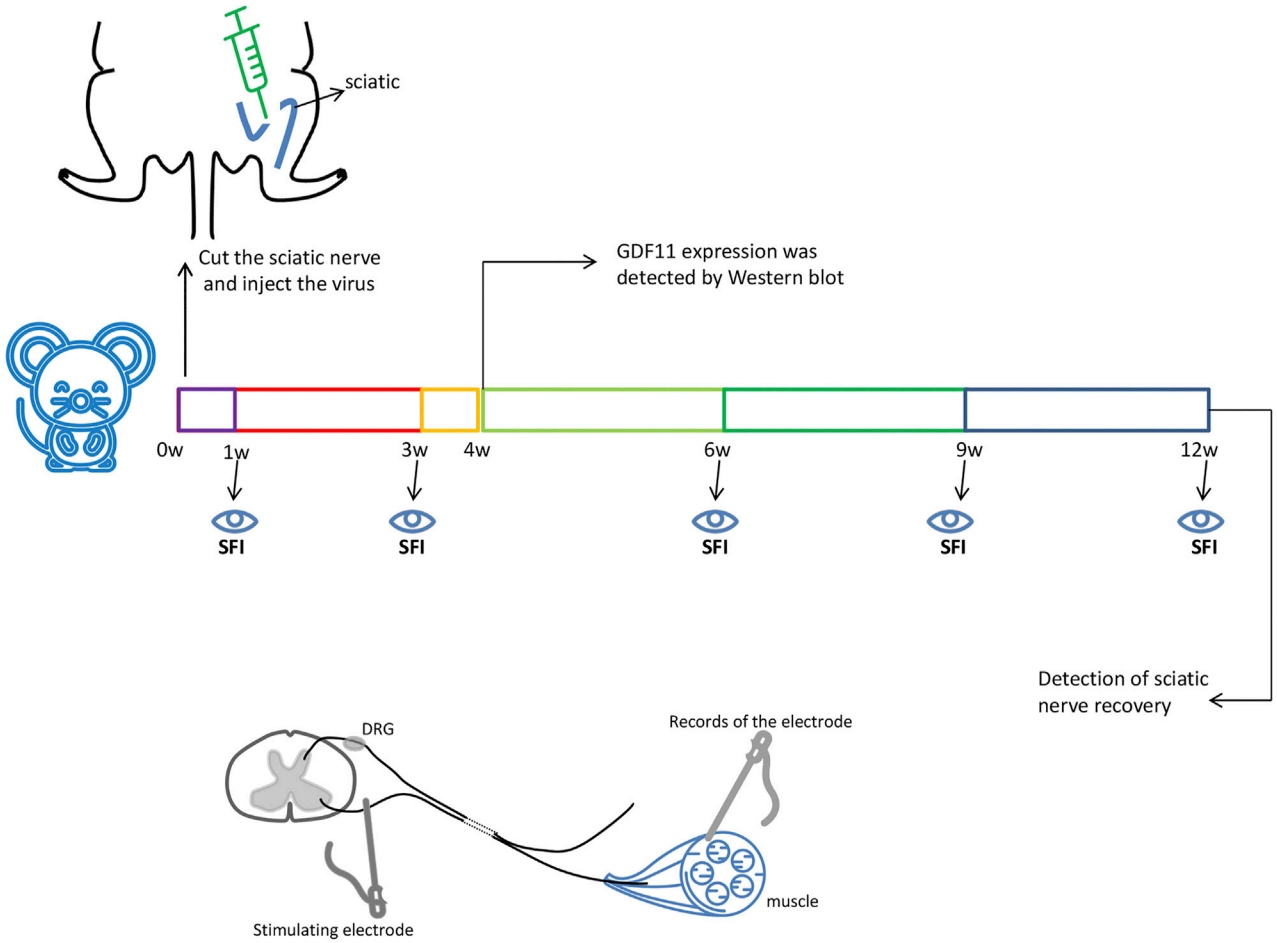

FIGURE 1 | The sciatic nerve of rats was surgically cut off 8mm, and then injected with GDF11 lentivirus or control virus immediately. The sciatic nerve of rats was taken 4 weeks after surgery to detect the expression of GDF11, and SFI values were measured at 1, 3, 6, 9, and 12 weeks, respectively. The sciatic nerve recovery was measured at 12 weeks. Stimulating electrodes were used at the proximal end of the injury, and evoked potentials were detected at the distal muscle.

injection of pentobarbital sodium (20 mg/ kg). The surgical site was first shaved and prepared with 75% surgical alcohol. The operation was performed under aseptic conditions as much as possible, and the left sciatic nerve was then exposed through a gluteus cleavage incision and severed with microsurgical scissors. All animals were immediately subjected to a tension-free suture of the transected sciatic nerve with a nerve pontine (silicone tube, Shandong Institute of Medical Instruments, Shandong, China) to obtain an 8-mm gap between the proximal and distal stump. Subsequently, 20 μL of control lentiviral or lentiviral GDF11 virus (5.5×10^8 TU/ ml) was injected into the injured area, the muscle tissue was replaced, the skin was sutured, and the animals were returned to their cages (**Figure 1**), Nerves within 1 cm of injury were used to detect subsequent experimental indicators.

Culture of Dorsal Root Ganglion (DRG) Cells

Two-to three-day-old newborn Wistar rats (provided by the Animal Experimental Center of Shandong University) were used for extraction of the DRG, and the rats were removed and killed. The rats were then impregnated in 75% ethanol and disinfected for 5 min. The DRG was carefully removed, and the residual nerve roots were resected with a stereoscopic microscope. DRG cells were then plated on PDL-coated slides and placed in 6- or 24-well plate with neurobasal medium containing 2% B27, 0.3% L-glutamine and 1% penicillin-streptomycin in an incubator at 37°C with 5% CO_2 and 95% humidity. The medium was changed every 3 days, and recombinant GDF11 (10 ng/ ml) was added on the first day of culture.

Western Blot Analysis

Cell or tissue lysates were prepared in RIPA buffer (Beyotime Biotechnology, Shanghai, China). After the total protein concentrations were detected using a bicinchoninic acid (BCA) protein assay (Beyotime, China), an equal amount of protein from each sample was resolved by SDS-PAGE on 10% SDS-polyacrylamide gels and transferred to a polyvinylidene difluoride (PVDF) membrane for immunoblot analyses. The membranes were incubated with the following primary antibodies overnight at 4°C: rabbit anti-GDF11 (1:1000; Abcam, ab124721,

United States), rabbit anti-Bax (1:1000; affinity Biosciences, AF0120, United States), rabbit anti-caspase3 (1:1000; affinity Biosciences, DF6879, United States), rabbit anti-Bcl2 (1:500, Proteintech, 12789-1-AP, United States), rabbit anti-smad2/3 (1:1000, CST, 8685S,United States), rabbit anti-p-smad2/3 (1: 1000, CST, 8828S, United States), rabbit anti-smad1/5/8 (1:1000, abcam, ab66737, United States), rabbit anti-p-smad1/5/8 (1:1000, CST, 13820S, United States), and mouse anti-β-actin (1:10000; CST, 8H10D10, United States). The unbound antibodies on the PVDF membranes were washed, the secondary antibody (1: 10000, CST, 5470P, United States), and (1:10000, CST, 5366P, United States) was added, and the bands were visualized with an infrared laser imaging system (Li-COR, United States). ImageJ software (National Institutes of Health, United States) was used for densitometry analysis.

RT-PCR

Total RNA was extracted from the tissue or cells using the TRIzol (Invitrogen) reagent according to the manufacturer's instructions. The RNA samples were reverse-transcribed after the genomic DNAs were removed using a reverse transcription kit (Takara, Tokyo, Japan). The cDNA product was stored at –20°C. For real-time PCR, a 10-μL reaction mixture containing 50 ng of cDNA was used. The reactions were performed with a PCR instrument (ABI-7900, United States). The primer sequences were as follows: β-actin forward, 5′-CTCTGTGTG GATTGGTGGCT-3′, and reverse: 5′-CGCAGCTCAGTAACA GTCCG -3′; Bcl2 forward, 5′-CTGAGTACCTGAACCGGCAT-3′, and reverse, 5′-ATATAGTTCCACAAAGGCATCCCAG-3′; Bax forward, 5′-TTTGCTACAGGGTTTCATCCAGG-3′, and reverse: 5′-CGCTCAGCTTCTTGGTGGAT-3′; and caspase3 forward, 5′-CGGACCTGTGGACCTGAAAA-3′, and reverse, 5′-CGGCCTCCACTGGTATCTTC-3′.

HE Staining

Twelve weeks after injury, sciatic nerve specimens from the injured area were stained with hematoxylin-eosin (HE). The slices were then dehydrated with 70 and 100% gradient ethanol and sealed with polyxylene transparent adhesive for 10 min. The stained sections were examined under a microscope (BX-51, Olympus).

Nissl Staining

After dewaxing and hydration, Nissl staining was performed with 0.5% cresyl violet solution for 1 min. The stained sections were examined under a microscope (BX-51, Olympus). The number of normal neurons in the spinal cord area was counted by two pathologists.

IF Analysis

IF staining of sciatic nerve tissue was performed with antibodies against various markers to evaluate the recovery of the sciatic nerve after transection. The tissue was incubated with the anti-Schwann cell marker antibodies S100 (1:100, Abcam, ab52642, United States) and neurofilament 200 (1:400; CST, 2836, United States) for 2 h at 37°C. The samples were then washed 3 times with phosphate-buffered saline and treated with anti-rabbit DyLight-488 (1:200; Abbkine, A23220, United States) and anti-mouse DyLight-594 antibodies (1:200; Abbkine, A23410, United States) for 1 h at 37°C. Subsequently, 40,6-diamidino-2-phenylindole (DAPI) counterstaining was performed for the visualization of cell nuclei. S100 is a Schwann cell marker, NF-200 is a marker for large myelinated A-fiber neurons, and DAPI serves as a marker for the number of nuclei in the captured images. For cellular immunofluorescence, cultured cells were fixed with 4% paraformaldehyde and stained with Neurofilament 200 (1:400; CST, 2836, United States) at 37°C for 2 h. The samples were then washed 3 times with phosphate-buffered saline and treated with anti-mouse Dylihgt-488 (1:200; Abbkine, A23210, United States) for 1 h at 37°C, and 40,6-diamidino-2-phenylindole (DAPI) counterstaining was performed for the visualization of cell nuclei. Images were acquired with a fluorescence microscope (Leica DM5500B) and a digital camera (Leica DFC345 FX, Leica Application Suite X software) and then analyzed using ImageJ software (version 1.45s, National Institute of Health, United States).

Flow Cytometric Analysis

Cells in a 6-well plate were washed three times with cooled PBS and then collected in a centrifuge tube for further operation. An Annexin V-FITC/PI kit (E-CK-A211, Wuhan, China) was used to determine whether the cells were apoptotic. The cells were resuspended in 1 × binding buffer at a concentration of 1×10^6 cells/mL. Subsequently, 100 μL of this solution was transferred into a 5-ml culture tube, and 5 μL of FITC Annexin V (or PE Annexin V) and 5 μL of PI were added. The cells were gently vortexed and incubated for 15 min at room temperature in the dark, and 400 μL of 1 × binding buffer was then added to the tube. Flow cytometry was conducted within 1 h with a BD Accuri C6 Plus flow cytometer (San Diego, CA, United States), and the data were analyzed using FlowJo V10 software (BD, San Diego, CA, United States).

Target Muscle Weight

Twelve weeks after surgery, the animals were euthanized, and the gastrocnemius muscle from the operated limbs of three rats in each group was exposed, dissected, removed and weighed immediately as a simple and direct measure of the effect of GDF11 on the target muscle and nerve function.

Functional Analysis

For the assessment of sciatic nerve recovery, the degree of recovery was monitored by evaluating the walking patterns of the hind limbs to obtain the sciatic function index (SFI), as described by Bain et al. At weeks 1, 3, 6, 9, and 12 after surgery, three random rats of each group were subjected to a walking track assay, and the SFI was measured based on a previously described protocol. The paw length and toe spreads were measured and used to calculate the SFI using the following formula: SFI = 109.5 (ETSNTS)/NTS38.3 (EPLNPL)/NPL +13.3 (EITNIT)/NIT8.8. In this equation, EPL indicates the operated experimental paw length, NPL is the normal paw length, ETS refers to the operated experimental toe spread, which represents the

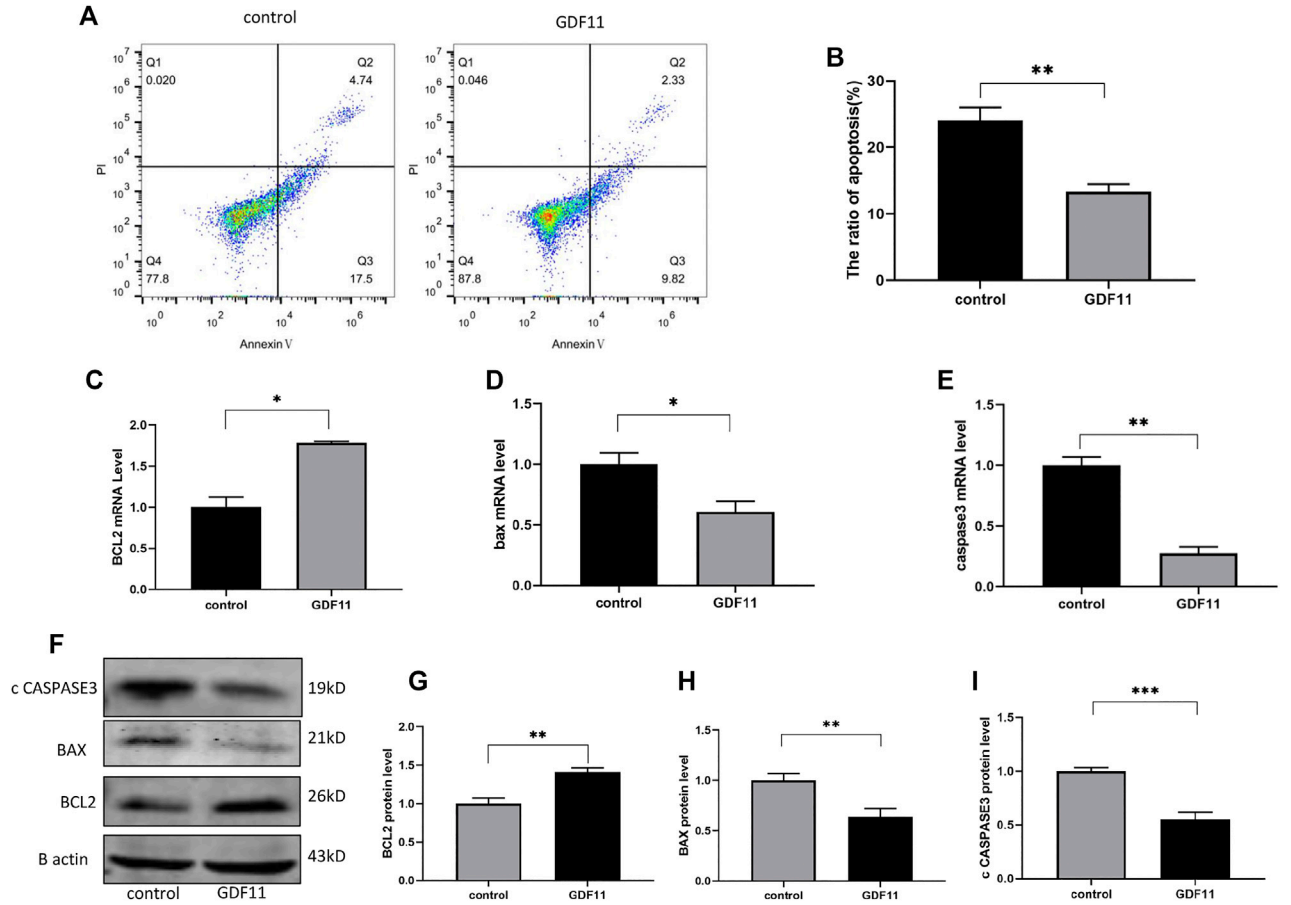

FIGURE 2 | GDF11 inhibited apoptosis of DGR *in vitro*. **(A and B).** Flow cytometry was used to detect the degree of apoptosis of DRG after cultured with recombinant GDF11 for 3 days. **(C, D and E).** DRG were cultured with recombinant GDF11 for 3 days, and mRNA expression of apoptosis-related genes Bcl2, Bax and caspase3 were detected by RT-PCR. **(F, G, H and I).** After DRG were cultured with recombinant GDF11 for 3 days, the protein expressions of apoptosis-related genes Bcl2, Bax and caspase3 were detected by Western blot. Statistical analysis was based on at least three different biological samples and three technical replicates, $p < 0.05$ was considered to be statistically significant.

distance between the first and fifth toes, NTS is the normal toe spread, EIT represents the operated experimental intermediary toe spread, which represents the distance between the second and fourth toes, and NIT is the normal intermediary toe spread. A value of 100 indicates total impairment, and a value of 0 indicates normal or complete recovery.

Motion-Evoked Potential

Under aseptic conditions, the skin of the injured thigh of the rats was cut open to expose the sciatic nerve, and the sciatic nerve was stimulated with a stimulation electrode at an intensity of 0.65 mA. At the same time, the recording electrode was inserted into the gastrocnemius muscle, and the reference electrode was inserted into the healthy gastrocnemius muscle. An intraoperative neuromonitor (Endeavor CR, United States) was used to record the evoked potential.

Transmission Electron Microscopy

The nerve tissue was fixed with 2% glutaraldehyde in sodium dimethyl arsenate buffer (0.1 M, pH 7.2) overnight at 4°C and then fixed with 1% osmium tetroxide solution for 1 h. Digital images were acquired with a JEM-1230 high-contrast TEM and soft scan imaging system (JEOL, Tokyo, Japan).

Statistical Analysis

All the data are presented as the means ± SDs. The statistical significance of the differences was analyzed by *t*-test or one-way ANOVA. $p < 0.05$ was considered to indicate statistical significance. GraphPad Prism eight software (GraphPad Software, La Jolla, CA, United States) was used for all statistical analyses.

RESULTS

GDF11 Inhibits the Apoptosis of DGR Cells *in vitro*

To investigate the influence of GDF11 on neuronal cells, DRG cells were isolated from rats and cultured with neuronal selective medium to simulate the effect of GDF11 on neuronal cells *in vitro*. One day after the isolation and culture of DRG cells, we added or did not add

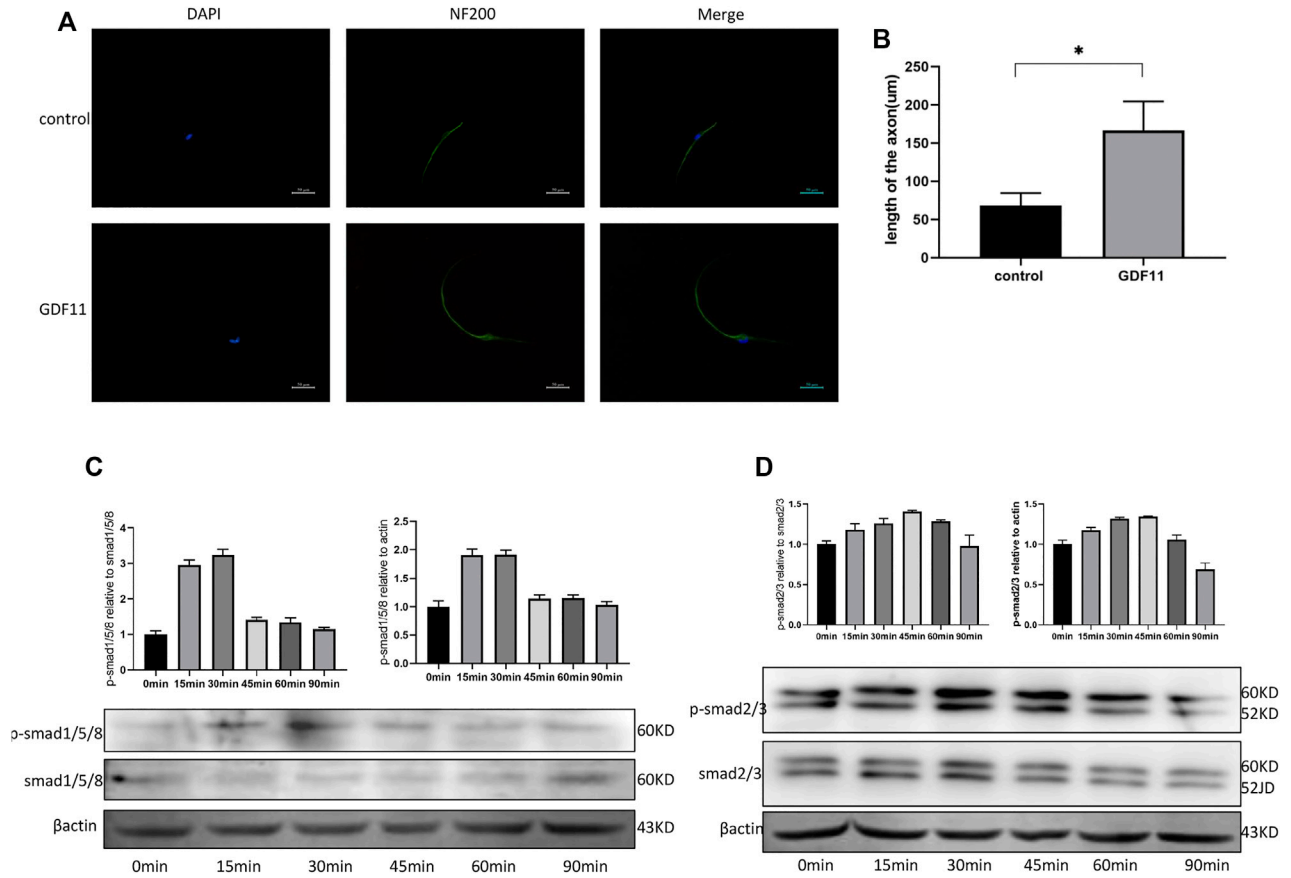

FIGURE 3 | GDF11 promotes axonal growth of DRG cells *in vitro*. **(A and B).** After DRG cells were cultured with recombinant GDF11 for 7 days, axon length was measured by NF200 immunofluorescence. **(C).** Western analysis showed increased phosphorylation of Smad1/5/8 when DRG cells were treated with GDF11. **(D).** Western analysis showed increased phosphorylation of Smad2/3 when DRG cells were treated with GDF11. Statistical analysis was based on at least three different biological samples and three technical replicates, $p < 0.05$ was considered to be statistically significant. Representative images are shown.

10 ng/ ml recombinant GDF11 to the medium, continued to culture the cells for 3 days, and then harvested the cells. Flow cytometry was used for the detection of cell apoptosis. Basic cell apoptosis occurred under normal culture conditions, whereas the apoptotic rate of the cells cultured with GDF11 was significantly decreased (**Figures 2A,B**). To further confirm the inhibitory effect of GDF11 on cell apoptosis, we detected the expression of genes and proteins in the GDF11 and control groups by Western blotting and qPCR, and the results showed that Bcl2 expression was significantly higher in the GDF11 group than in the control group (**Figures 2C,F,G**), whereas Bax and caspase3 expression was significantly decreased (**Figures 2D–F,H,I**); in addition, the results obtained for mRNA and protein expression showed the same trend. These results indicate that GDF11 can regulate the expression of DRG cell apoptosis-related genes and then inhibits DRG cell apoptosis.

GDF11 Promotes Axonal Growth of DRG Cells *in vitro*

To explore the influence of GDF11 on the growth of neuronal axons, DRG cells were isolated and cultured with neuronal selective medium, recombinant GDF11 (10 ng/ ml) protein was added or not added to the medium, and neuronal axons were labeled with NF200. The immunofluorescence results showed that the neuronal axons in the GDF11 group were significantly longer than those in the control group (**Figures 3A,B**). This result suggests that GDF11 can promote neuronal axon growth. To explore the pathway by which GDF11 acts, phosphorylation of Smad was detected at different time points. The results showed that the phosphorylation of Smad2/3 and Smad1/5/8 was significantly activated after treatment with recombinant GDF11, suggesting that GDF11 may play a role through Smad signaling pathway (**Figures 3C,D**).

GDF11 Promotes the Recovery of Damaged Sciatic Nerve Function in Rats

Based on previous functional studies of GDF11 and our above-described findings, we explored whether continuous delivery of GDF11 *in vivo* could promote restoration of the normal function of the damaged peripheral nervous system, and we constructed a lentiviral vector expressing GDF11. Twenty microliters of control

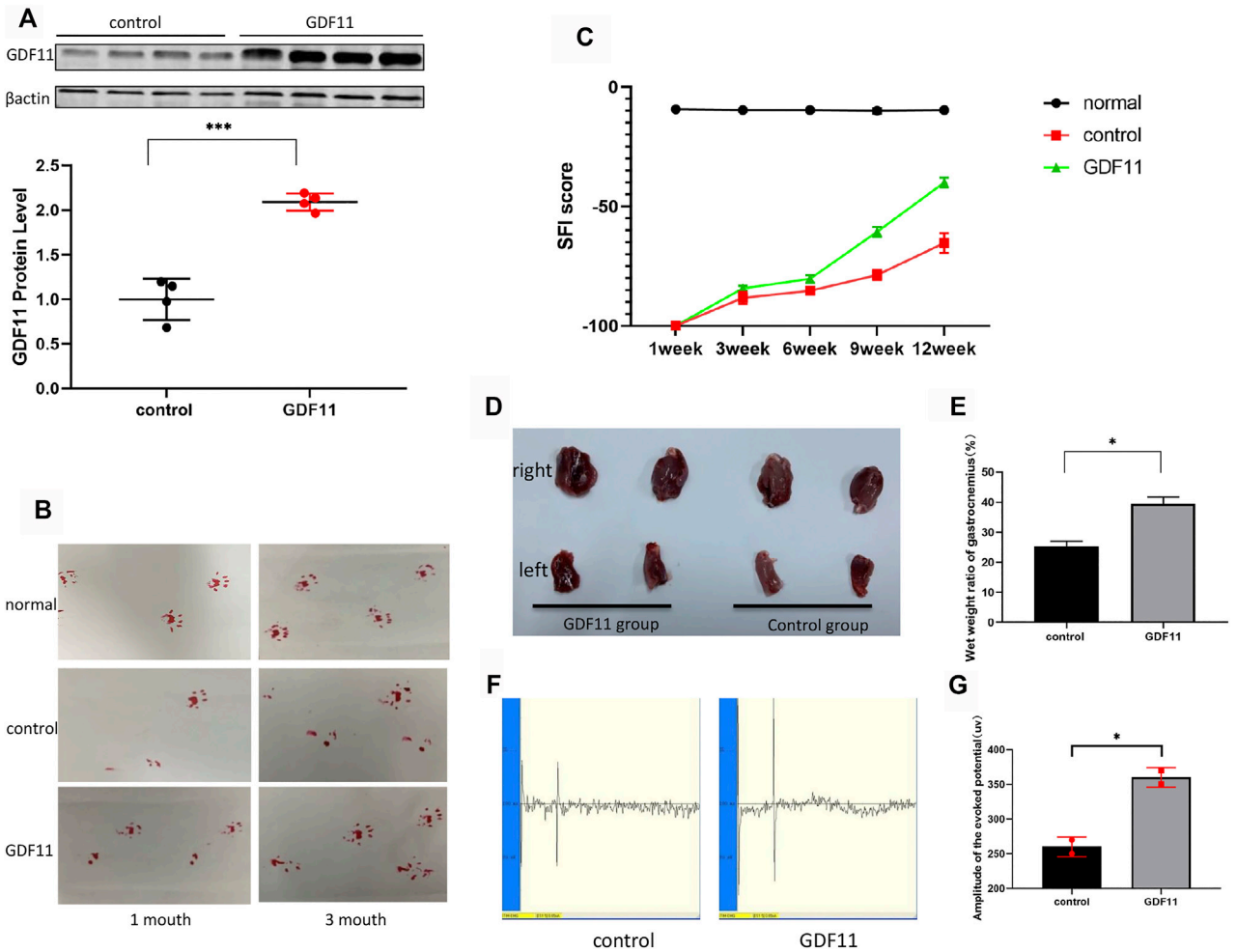

FIGURE 4 | GDF11 promotes the recovery of damaged sciatic nerve function in rats. **(A).** One month after surgery, the sciatic nerves of four rats in each group were randomly selected, and the expression of GDF11 was detected by Western blot. **(B).** The recovery of sciatic nerve function was observed by foot print test at 1 and 3 months after operation. **(C).** SFI value was used to evaluate the recovery of sciatic nerve function in rats at different time points (n = 3). **(D and E).** Gastrocnemius atrophy of rats 3 months after operation (n = 3). **(F and G).** The nerve conduction function of rat sciatic nerve was measured by action evoked potential (MEP) at 3 months after operation (n = 3). Statistical analysis was based on at least three different biological samples and three technical replicates, $p < 0.05$ was considered to be statistically signiandfilig;cant. Representative images are shown.

lentivirus and 20 μL of lentivirus-GDF11 were injected at the nerve transection sites in the rats belonging to the control and experimental groups, respectively, immediately after surgery. One month later, four random sciatic nerves from each group were collected for the extraction of proteins from the site of injury in the rats, and the expression of GDF11 was then detected. The results showed that the expression of GDF11 in the lentiviral GDF11 group was significantly higher than that in the control group (**Figure 4A**). One month after surgery, the affected lateral footprints in the control and GDF11 groups were significantly less likely to land than those in the normal and normal groups (a slight improvement was observed in the GDF11 group). Three months after surgery, we detected the footprints again and found that the abduction and status of the affected lateral footprints in the GDF11 group were better than those in the control group (**Figure 4B**). For detection of the nerve conduction function of the rats, we assessed the motion-evoked potential of the rats 3 months after the operation, and the results showed that the detection potential of the GDF11 group exhibited a larger amplitude and a shorter latency than that of the control group (**Figures 4F,G**). We executed the rats immediately after this assessment and carefully stripped the fresh gastrocnemius muscle. The weighing of the gastrocnemius muscle revealed that the ratio of the affected to the healthy side of the gastrocnemius muscle in the GDF11 group was significantly higher than that in the control group (**Figures 4D,E**), which further confirmed restoration of sciatic nerve impulse conduction and muscle dominance. In addition, we recorded the recovery of the sciatic nerve function in the rats based on the SFI score on a weekly basis for a period of 3 months after surgery. The experimental results showed that the SFI score of the rats with GDF11 overexpression was higher than that of the control group at the same time point, which indicated that the rats belonging to the former group exhibited better recovery of sciatic nerve function (**Figure 4C**).

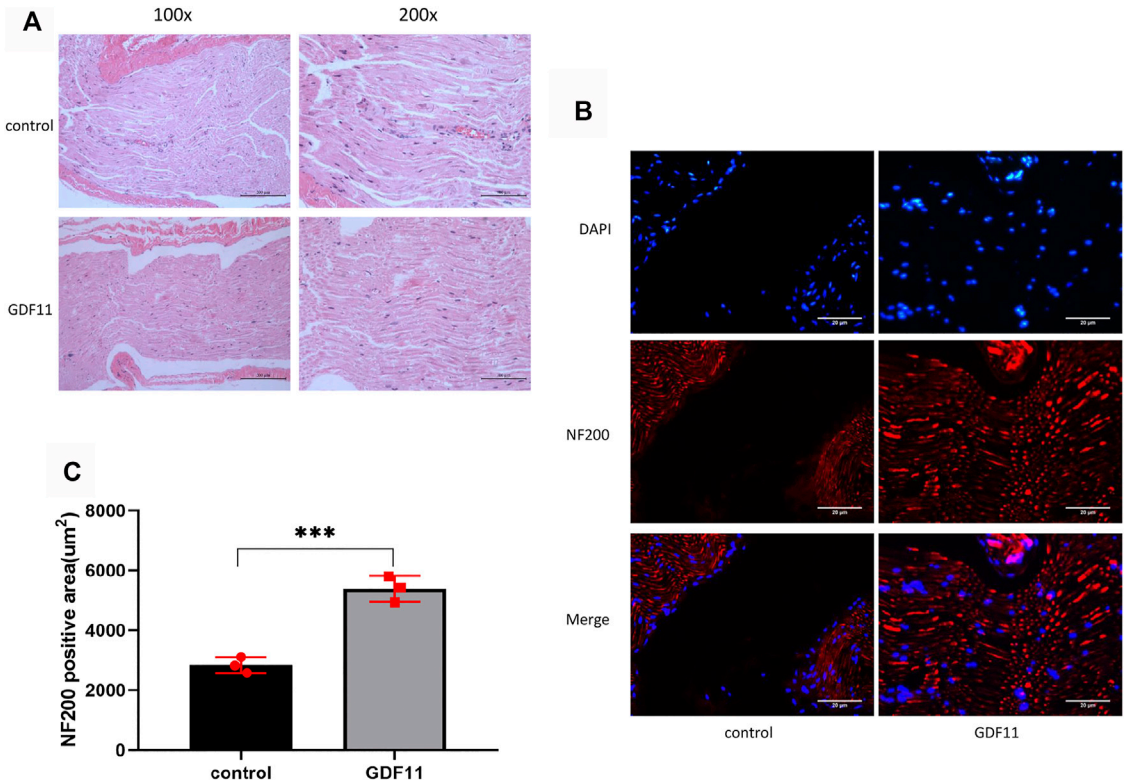

FIGURE 5 | GDF11 promotes regeneration of damaged sciatic nerve in rats. **(A).** HE staining was used to observe the recovery of rat sciatic nerve 3 months after operation ($n = 3$). **(B and C).** The nerve fibers were labeled with NF200 and the nerve growth was detected by immunofluorescence ($n = 3$). Statistical analysis was based on at least three different biological samples and three technical replicates, $p < 0.05$ was considered to be statistically signiandfilig;cant. Representative images are shown.

These experiments suggest that GDF11 overexpression can promote the functional recovery of the transverse sciatic nerve.

GDF11 Promotes Regeneration of Damaged Sciatic Nerves in Rats

In the following experiment, we performed HE staining to observe the morphological characteristics of the sciatic nerve. The results showed that the nerve fibers in the control group were disorganized and had little nerve growth, whereas the nerve fibers in the GDF11 group had more nerve growth, were closely arranged and showed a compact structure and regular shape in the lesion area (**Figure 5A**). We then stained the tissue with NF200, and the results showed that the nerve fibers in the control group were sparse and that almost no nerve growth in the transverse region. The nerve fibers in the GDF11 group were closely arranged, grew at the cross-section (**Figures 5B,C**), which was consistent with the HE staining results. These findings indicate that GDF11 promotes the growth of nerve fibers.

GDF11 Promotes Myelin Regeneration of Damaged Sciatic Nerves in Rats

Neural function cannot be separated from the normal myelin structure. To clarify the influence of GDF11 on the myelin sheath of nerve fibers, the myelin sheath of the sciatic nerve was subjected to myelin staining, and the results showed the appearance of a large number of areas with myelin staining in the new junction area in the GDF11 group, whereas the control group showed fewer myelin sheath-stained areas in the cross section (**Figures 6A,B**), which indicated that GDF11 exerted an obvious promoting effect on myelin regeneration. We then labelled Schwann cells with S100 and found that the stained areas of Schwann cells in the GDF11 group were more abundant and formed links (**Figures 6C,D**), which indicated that GDF11 promotes the proliferation of Schwann cells. In further experiments, we performed electron microscopy to observe the ultramicroscopic structure of the sciatic nerve. The results showed that the myelin sheath in the GDF11 group was more regular and thicker than that in the control group (**Figures 6E,F**). These studies suggest that GDF11 could promote myelination of the transverse sciatic nerve.

GDF11 Exerts a Protective Effect on Neuronal Cells in Rats

The sciatic nerve and spinal cord segments have many contacts. To further investigate whether local injection of lentiviral GDF11 into the sciatic nerve can protect the

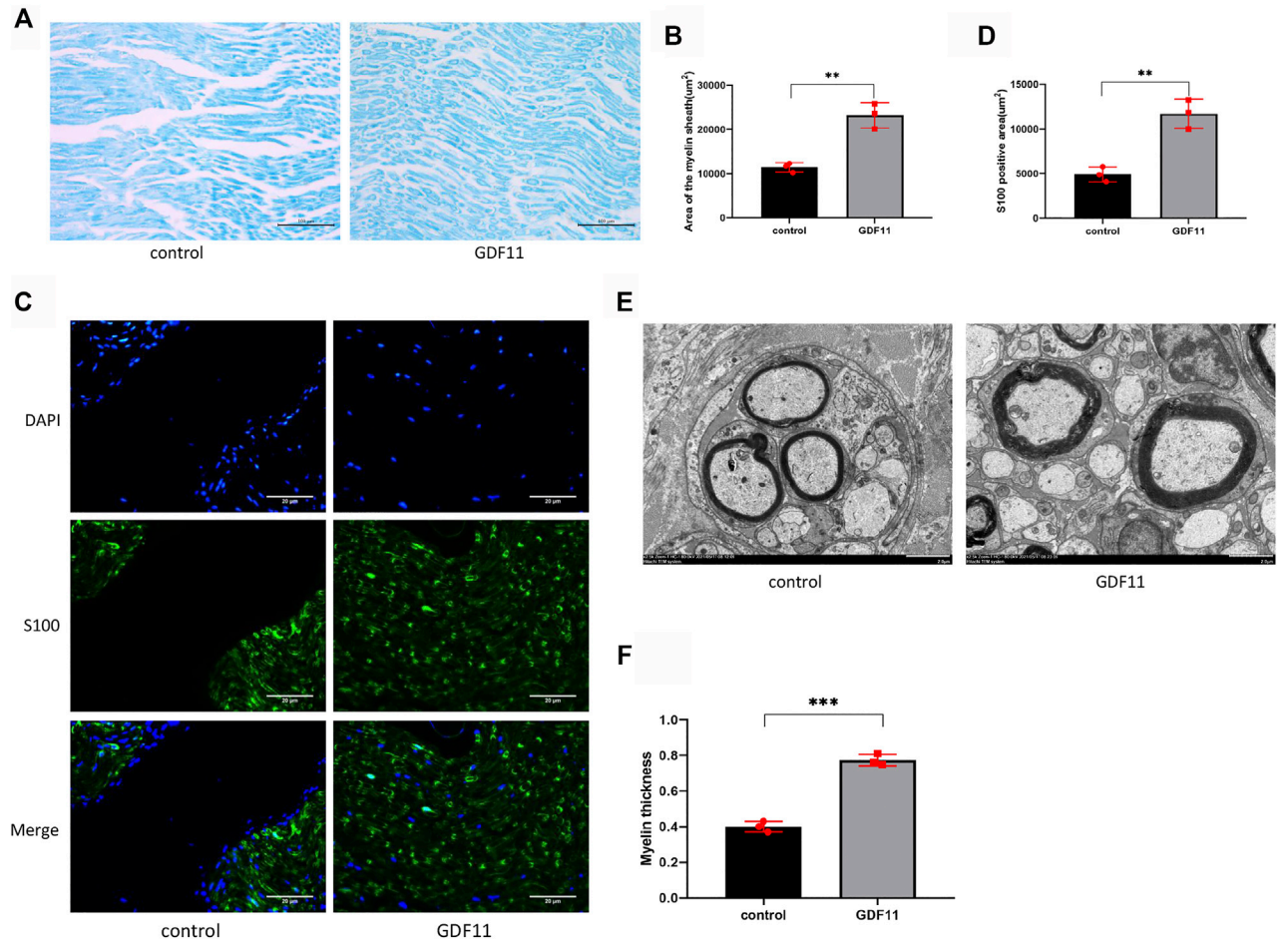

FIGURE 6 | GDF11 promotes myelin regeneration of damaged sciatic nerve in rats. **(A and B).** At 3 months postoperatively, myelin staining was used to assess the extent of myelination in the injured sciatic nerve area in rats (n = 3). **(C and D).** Three months after surgery, S100 was labeled with Schwann cells to detect Schwann cells in the damaged area (n = 3). **(E and F).** Three months after surgery, a transmission electron microscope was performed on the sciatic nerve in the injured area of rats, and myelin sheath thickness and neovascularization were assessed (n = 3). Statistical analysis was based on at least three different biological samples and three technical replicates, $p < 0.05$ was considered to be statistically signiandfilig;cant. Representative images are shown.

spinal neurons of corresponding segments, we obtained slices of the spinal cord of rats 3 months after surgery and then detected the neuronal state by Nissl staining. The results showed that the number of neurons in the GDF11 group was higher than that in the control group (**Figures 7A,B**). These results suggest that transection of the sciatic nerve induces death of the corresponding spinal neurons due to loss of neurotrophic effects, and the overexpression of GDF11 can promote survival of the corresponding neurons. Because *in vitro* cell experiments showed that GDF11 inhibits apoptosis, we explored whether the overexpression of GDF11 could also play the same role *in vivo*. The results showed that the expression of apoptosis-related genes was decreased in the GDF11 group (**Figures 7D–F,H,I**), but the expression of the apoptosis-related gene Bcl2 was increased (**Figures 7C,F,G**). The above-mentioned experimental results suggest that GDF11 overexpression *in vivo* could inhibit apoptosis and thus protect sciatic nerve function.

DISCUSSION

Our study demonstrated that GDF11 can inhibit DRG cell apoptosis and promote axon growth *in vitro*. In addition, the *in vivo* continuous delivery of GDF11 via lentivirus promoted functional recovery of the transected sciatic nerve.

Transection of the peripheral nerve changed the microenvironment of the lesion, and this effect was followed by degeneration of the nerve cells (Sun et al., 2016; Yan et al., 2018; Liu et al., 2019; Liu et al., 2021), deformation and apoptosis of Schwann cells, degradation of the myelin sheath into debris, and inflammatory activation (Caillaud et al., 2019). Modulation of the damaged microenvironment is an effective treatment, and the use of cytokines has been shown to promote axonal regeneration (Jubran and Widenfalk, 2003). However, there is no cure so far, so it is important to explore new therapeutic strategies and their potential mechanisms. Many previous studies suggested promoting the outgrowth of the neuronal axons is important for the maturation

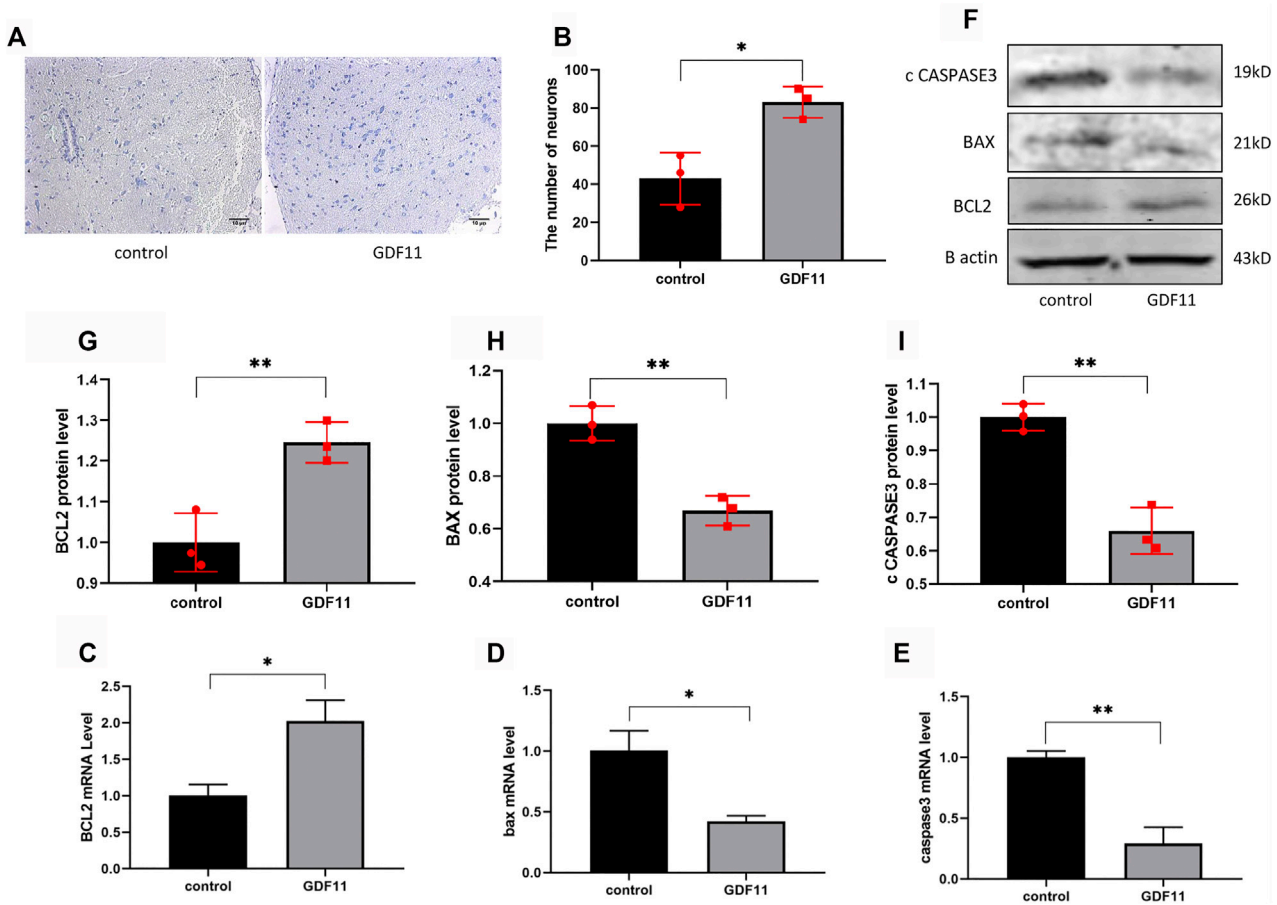

FIGURE 7 | GDF11 has a protective effect on neuronal cells in rats. **(A and B).** Three months after surgery, spinal cords of the rats were sected for Nissl staining to assess the number of neurons alive (n = 3). **(C, D and E).** Three months after surgery, the spinal cord of the rats was extracted for RNA, and the mRNA levels of apoptosis-related genes were detected by RT-PCR(n = 3). **(F, G, H and I).** Three months after surgery, the spinal cord of the rats was extracted for proteins, and then Western blot was used to measure the protein levels of apoptosis-related genes (n = 3). Statistical analysis was based on at least three different biological samples and three technical replicates, $p < 0.05$ was considered to be statistically signiandfilig;cant. Representative images are shown.

and function of the neuron (Guo et al., 2019; Guo R. et al., 2020; Hu et al., 2021; Wei et al., 2021). Our *in vitro* experiments showed that recombinant GDF11 can promote growth of the neuronal axons of DRG cells. Studies have also shown that GDF11 can promote neural stem cell axon growth and even retinal ganglion cell dendrites. Wang et al. showed that GDF11 can induce apoptosis and suppress migration in a dose-dependent manner (Wang Z. et al., 2018), but some studies suggest that GDF11 can inhibit apoptosis (Song et al., 2019; Xiao et al., 2021). In our current study, we treated DRG cells with recombinant GDF11 and found that GDF11 could inhibit DRG cell apoptosis. Previous studies have shown that the TGF family, including GDF11, plays a role through the Smad signaling pathway (Hofer and Schwab, 2019; Luo et al., 2019). Although, the receptor and specific mechanism of GDF11 on neurons should be further explored in future studies, in our study, we demonstrated that GDF11 activates Smad2/3 and Smad1/5/8. Therefore, we hypothesized that GDF11 promotes axon growth and inhibits apoptosis through the Smad signaling pathway, thereby promoting the recovery of damaged sciatic nerve function. Although GDF11 has recently been reported to play an anti-inflammatory role in RA by antagonizing NFκB pathway (Li W. et al., 2019), the role of NFκB in the nervous system remains to be further studied. In addition, some studies have shown that the lentiviral vector overexpression system can continuously express target genes *in vivo* and promote the recovery of neurological function (Hu et al., 2005). The *in vivo* overexpression of GDF11 by viral vectors has been proven to be very helpful for the treatment of many diseases (Dai et al., 2020; Ren et al., 2021). Considering the beneficial effects of lentivirus, a lentiviral vector was used in this study for the *in vivo* overexpression of GDF11 and found that the rats with GDF11 overexpression had higher SFI scores than the control group, which indicated that the sciatic nerve function of the GDF11 group exhibited improved recovery. The detection of action-evoked potentials revealed that the nerve conduction function of the rats in the GDF11 group was better. Action-evoked potentials are an important method for the detection of nerve conduction function, and some previous studies have also indicated that a higher amplitude of action-evoked potentials indicates better nerve conduction function (Zhao et al., 2014). In addition, the wet weight of the gastrocnemius muscle was measured at 3 months, which was consistent with previous studies (Salehi et al., 2019). The degree of

atrophy on the diseased side of the gastrocnemius muscle in the GDF11 group, which exhibited better functional recovery, was less severe than that in the control group. This finding also confirms that GDF11 treatment significantly improves recovery of the neurotrophic effects of the sciatic nerve on the muscle that it innervates to a certain extent. However, the environment inside the lesion is complex, thus, the restoration of sciatic nerve function is not simply due to a single cell type (do Carmo Oliveira et al., 2021).

Previous studies have also shown that GDF11 is widely expressed in both neurons and glial cells (Liang et al., 2014), and some studies have shown that GDF11 affects neurogenesis and modulates neurons morphology (Gokoffski et al., 2011; Augustin et al., 2017). After *in vivo* delivery of GDF11 using lentiviral vectors, our results indicate that regardless of the cell in which GDF11 is expressed, the focal area will be a high GDF11 environment, a microenvironment conducive to neural recovery. the HE staining and NF200 labeling of nerve fibers revealed that the overexpression of GDF11 was beneficial to the regeneration of nerve fibers. The recovery of nerve function depends on the myelin sheath structure outside the nerve axon. Thus, we used myelin staining and S100-labeled Schwann cells to confirm that GDF11 overexpression can indeed promote the formation of extra-axonal myelin structures. Previous studies have shown that the growth of neuronal axons promotes myelination, and the existence and migration of Schwann cells guide neuronal axons (Chen et al., 2019). Therefore, we hypothesize that GDF11 promotes the growth of nerve fibers, which in turn leads to Schwann cell proliferation and myelin formation. Further analysis of the submicroscopic structure of most tissues by electron microscopy revealed that GDF11 overexpression resulted in a thicker myelin sheath. Interestingly, we also found that the GDF11 group showed more new blood vessels, whereas previous studies have shown that GDF11 can promote neurovascular regeneration. Neurovascular regeneration can provide a good blood supply for nerve regeneration (Merolli et al., 2009; Goedee et al., 2013). However, whether there is a receptor for GDF11 on Schwann cells, whether GDF11 delivered *in vivo* can directly act on Schwann cells and its potential mechanism will be further explained in the future.

Our results showed that GDF11 inhibits apoptosis both *in vivo* and *in vitro*, and the corresponding number of neurons in the spinal cord segment was higher, which might have been observed because stimulation of the nerve in the injured sciatic nerve focal area leads to apoptosis of the corresponding neurons. In fact, the injured sciatic nerve terminal is very sensitive to the injured environment and synthesizes some special signaling molecules to reverse transport to the neuronal cell body. When the neuronal cell body receives signal stimulation, it initiates the transcription of apoptotic genes (Yudin et al., 2008), and delivery of GDF11 improves the microenvironment at the site of damage. GDF11 can protect neurons from apoptosis Correspondingly, good spinal cord function is more positively important for the nutrition and innervation of nerve fibers, and a variety of complex factors promote improved recovery of sciatic nerve function.

In general, based on the present study, we conclude that GDF11 promotes axonal growth and inhibits DRG cell apoptosis *in vitro*. In addition, the *in vivo* overexpression of GDF11 by lentivirus can promote the recovery of sciatic nerves after transection by promoting axonal growth and inhibiting neuronal apoptosis in the spinal cord.

DATA AVAILABILITY STATEMENT

The original contributions presented in the study are included in the article/supplementary material, further inquiries can be directed to the corresponding authors.

ETHICS STATEMENT

The animal study was reviewed and approved by Laboratory Animal Centre of Shandong University.

AUTHOR CONTRIBUTIONS

Study concept and design: LC, YAZ, JS, JL. Acquisition of data: LC, JS, JL. Analysis and interpretation of data: XM, SC. Statistical analysis: YNZ. Drafting of the manuscript: LC, YAZ. All authors read and approved the final manuscript.

FUNDING

The study was supported by the Shandong University Qilu Hospital Clinical Practical New Technology Fund (2019-8), and National key research and development program (2020YFC2009004) in the role of design of the study, collection, analysis data and writing manuscript.

REFERENCES

Anger-Góra, N., Węgierek-Ciura, K., Szczygieł, A., Mierzejewska, J., Pajtasz-Piasecka, E., and Rossowska, J. (2021). Treatment with Lentiviral Vectors Encoding shRNA against Interleukin 10 Modulates the Immunosuppressive Activity of Murine colon Carcinoma-associated M-yeloid-derived S-uppressor C-ells. *Oncol. Lett.* 22 (2), 582. doi:10.3892/ol.2021.12843

Augustin, H., McGourty, K., Steinert, J. R., Cochemé, H. M., Adcott, J., Cabecinha, M., et al. (2017). Myostatin-like Proteins Regulate Synaptic Function and Neuronal Morphology. *Development* 144 (13), 2445–2455. doi:10.1242/dev.152975

Billet, F., Caillaud, M., Richard, L., Vallat, J.-M., and Desmoulière, A. (2019). Peripheral Nerve Regeneration and Intraneural Revascularization. *Neural Regen. Res.* 14 (1), 24–33. doi:10.4103/1673-5374.243699

Cai, L., Zhao, C., Chen, H., Fan, L., Zhao, Y., Qian, X., et al. (2021). Suction-Cup-Inspired Adhesive Micromotors for Drug Delivery. *Adv. Sci.*, 2103384. doi:10.1002/advs.202103384

Chen, S., Du, Z., Zou, J., Qiu, S., Rao, Z., Liu, S., et al. (2019). Promoting Neurite Growth and Schwann Cell Migration by the Harnessing Decellularized Nerve Matrix onto Nanofibrous Guidance. *ACS Appl. Mater. Inter.* 11 (19), 17167–17176. doi:10.1021/acsami.9b01066

Dai, Z., Song, G., Balakrishnan, A., Yang, T., Yuan, Q., Möbus, S., et al. (2020). Growth Differentiation Factor 11 Attenuates Liver Fibrosis via Expansion

of Liver Progenitor Cells. *Gut* 69 (6), 1104–1115. doi:10.1136/gutjnl-2019-318812

de León, A., Gibon, J., and Barker, P. A. (2021). NGF-dependent and BDNF-dependent DRG Sensory Neurons Deploy Distinct Degenerative Signaling Mechanisms. *eNeuro* 8 (1), 0277. doi:10.1523/ENEURO.0277-20.2020

do Carmo Oliveira, T. G., Dos Santos, A. C. M., Assis, A. D., Borges, R. T., da Costa Silva, J. R., Ueira-Vieira, C., et al. (2021). TNF-mimetic Peptide Mixed with Fibrin Glue Improves Peripheral Nerve Regeneration. *Brain Res. Bull.* 174, 53–62. doi:10.1016/j.brainresbull.2021.06.001

Fan, K.-q., Li, Y.-y., Wang, H.-l., Mao, X.-t., Guo, J.-x., Wang, F., et al. (2019). Stress-Induced Metabolic Disorder in Peripheral CD4+ T Cells Leads to Anxiety-like Behavior. *Cell* 179 (4), 864–879. doi:10.1016/j.cell.2019.10.001

Fang, Q., Zhang, Y., Chen, X., Li, H., Cheng, L., Zhu, W., et al. (2019). Three-Dimensional Graphene Enhances Neural Stem Cell Proliferation through Metabolic Regulation. *Front. Bioeng. Biotechnol.* 7, 436. doi:10.3389/fbioe.2019.00436

Geissler, J., and Stevanovic, M. (2019). Management of Large Peripheral Nerve Defects with Autografting. *Injury* 50, S64–S67. doi:10.1016/j.injury.2019.10.051

Geuna, S. (2015). The Sciatic Nerve Injury Model in Pre-clinical Research. *J. Neurosci. Methods* 243, 39–46. doi:10.1016/j.jneumeth.2015.01.021

Goedee, H. S., Brekelmans, G. J. F., van Asseldonk, J. T. H., Beekman, R., Mess, W. H., and Visser, L. H. (2013). High Resolution Sonography in the Evaluation of the Peripheral Nervous System in Polyneuropathy - a Review of the Literature. *Eur. J. Neurol.* 20 (10), 1342–1351. doi:10.1111/ene.12182

Gokoffski, K. K., Wu, H.-H., Beites, C. L., Kim, J., Kim, E. J., Matzuk, M. M., et al. (2011). Activin and GDF11 Collaborate in Feedback Control of Neuroepithelial Stem Cell Proliferation and Fate. *Development* 138 (19), 4131–4142. doi:10.1242/dev.065870

Gong, J., Wang, X., Zhu, C., Dong, X., Zhang, Q., Wang, X., et al. (2017). Insm1a Regulates Motor Neuron Development in Zebrafish. *Front. Mol. Neurosci.* 10, 274. doi:10.3389/fnmol.2017.00274

Gris, D., Marsh, D. R., Oatway, M. A., Chen, Y., Hamilton, E. F., Dekaban, G. A., et al. (2004). Transient Blockade of the CD11d/CD18 Integrin Reduces Secondary Damage after Spinal Cord Injury, Improving Sensory, Autonomic, and Motor Function. *J. Neurosci.* 24 (16), 4043–4051. doi:10.1523/JNEUROSCI.5343-03.2004

Gu, X., Ding, F., and Williams, D. F. (2014). Neural Tissue Engineering Options for Peripheral Nerve Regeneration. *Biomaterials* 35 (24), 6143–6156. doi:10.1016/j.biomaterials.2014.04.064

Guo, J., Yu, Y., Sun, L., Zhang, Z., Zhao, Y., Chai, R., et al. (2020a). Bio-inspired Multicomponent Carbon Nanotube Microfibers from Microfluidics for Supercapacitor. *Chem. Eng. J.* 397, 125517. doi:10.1016/j.cej.2020.125517

Guo, R., Li, J., Chen, C., Xiao, M., Liao, M., Hu, Y., et al. (2021a). Biomimetic 3D Bacterial Cellulose-Graphene Foam Hybrid Scaffold Regulates Neural Stem Cell Proliferation and Differentiation. *Colloids Surf. B: Biointerfaces* 200, 111590. doi:10.1016/j.colsurfb.2021.111590

Guo, R., Liao, M., Ma, X., Hu, Y., Qian, X., Xiao, M., et al. (2021b). Cochlear Implant-Based Electric-Acoustic Stimulation Modulates Neural Stem Cell-Derived Neural Regeneration. *J. Mater. Chem. B* 9 (37), 7793–7804. doi:10.1039/d1tb01029h

Guo, R., Ma, X., Liao, M., Liu, Y., Hu, Y., Qian, X., et al. (2019). Development and Application of Cochlear Implant-Based Electric-Acoustic Stimulation of Spiral Ganglion Neurons. *ACS Biomater. Sci. Eng.* 5 (12), 6735–6741. doi:10.1021/acsbiomaterials.9b01265

Guo, R., Xiao, M., Zhao, W., Zhou, S., Hu, Y., Liao, M., et al. (2020b). 2D Ti3C2TxMXene Couples Electrical Stimulation to Promote Proliferation and Neural Differentiation of Neural Stem Cells. *Acta Biomater.* S1742-7061, 30749–30752. doi:10.1016/j.actbio.2020.12.035

Guo, R., Zhang, S., Xiao, M., Qian, F., He, Z., Li, D., et al. (2016). Accelerating Bioelectric Functional Development of Neural Stem Cells by Graphene Coupling: Implications for Neural Interfacing with Conductive Materials. *Biomaterials* 106, 193–204. doi:10.1016/j.biomaterials.2016.08.019

Han, S., Xu, Y., Sun, J., Liu, Y., Zhao, Y., Tao, W., et al. (2020). Isolation and Analysis of Extracellular Vesicles in a Morpho Butterfly wing-integrated Microvortex Biochip. *Biosens. Bioelectron.* 154, 112073. doi:10.1016/j.bios.2020.112073

He, Z., Zhang, S., Song, Q., Li, W., Liu, D., Li, H., et al. (2016). The Structural Development of Primary Cultured Hippocampal Neurons on a Graphene Substrate. *Colloids Surf. B: Biointerfaces* 146, 442–451. doi:10.1016/j.colsurfb.2016.06.045

Hocking, J. C., Hehr, C. L., Chang, R.-Y., Johnston, J., and McFarlane, S. (2008). TGFβ Ligands Promote the Initiation of Retinal Ganglion Cell Dendrites *In Vitro* and *In Vivo*. *Mol. Cell Neurosci.* 37 (2), 247–260. doi:10.1016/j.mcn.2007.09.011

Hofer, A.-S., and Schwab, M. E. (2019). Enhancing Rehabilitation and Functional Recovery after Brain and Spinal Cord Trauma with Electrical Neuromodulation. *Curr. Opin. Neurol.* 32 (6), 828–835. doi:10.1097/WCO.0000000000000750

Hu, Y., Leaver, S. G., Plant, G. W., Hendriks, W. T. J., Niclou, S. P., Verhaagen, J., et al. (2005). Lentiviral-mediated Transfer of CNTF to Schwann Cells within Reconstructed Peripheral Nerve Grafts Enhances Adult Retinal Ganglion Cell Survival and Axonal Regeneration. *Mol. Ther.* 11 (6), 906–915. doi:10.1016/j.ymthe.2005.01.016

Hu, Y., Li, D., Wei, H., Zhou, S., Chen, W., Yan, X., et al. (2021). Neurite Extension and Orientation of Spiral Ganglion Neurons Can Be Directed by Superparamagnetic Iron Oxide Nanoparticles in a Magnetic Field. *Ijn* 16, 4515–4526. doi:10.2147/IJN.S313673

Jia, B., Huang, W., Wang, Y., Zhang, P., Wang, Z., Zheng, M., et al. (2020). Nogo-C Inhibits Peripheral Nerve Regeneration by Regulating Schwann Cell Apoptosis and Dedifferentiation. *Front. Neurosci.* 14, 616258. doi:10.3389/fnins.2020.616258

Jubran, M., and Widenfalk, J. (2003). Repair of Peripheral Nerve Transections with Fibrin Sealant Containing Neurotrophic Factors. *Exp. Neurol.* 181 (2), 204–212. doi:10.1016/s0014-4886(03)00041-4

Kalinski, A. L., Yoon, C., Huffman, L. D., Duncker, P. C., Kohen, R., Passino, R., et al. (2020). Analysis of the Immune Response to Sciatic Nerve Injury Identifies Efferocytosis as a Key Mechanism of Nerve Debridement. *Elife 9* 9, e60223. doi:10.7554/eLife.60223

Katsimpardi, L., Litterman, N. K., Schein, P. A., Miller, C. M., Loffredo, F. S., Wojtkiewicz, G. R., et al. (2014). Vascular and Neurogenic Rejuvenation of the Aging Mouse Brain by Young Systemic Factors. *Science* 344 (6184), 630–634. doi:10.1126/science.1251141

Kim, J., Wu, H.-H., Lander, A. D., Lyons, K. M., Matzuk, M. M., and Calof, A. L. (2005). GDF11 Controls the Timing of Progenitor Cell Competence in Developing Retina. *Science* 308 (5730), 1927–1930. doi:10.1126/science.1110175

Kong, F.-Q., Zhao, S.-J., Sun, P., Liu, H., Jie, J., Xu, T., et al. (2020). Macrophage MSR1 Promotes the Formation of Foamy Macrophage and Neuronal Apoptosis after Spinal Cord Injury. *J. Neuroinflammation* 17 (1), 62. doi:10.1186/s12974-020-01735-2

Li, A., You, D., Li, W., Cui, Y., He, Y., Li, W., et al. (2018). Novel Compounds Protect Auditory Hair Cells against Gentamycin-Induced Apoptosis by Maintaining the Expression Level of H3K4me2. *Drug Deliv.* 25 (1), 1033–1043. doi:10.1080/10717544.2018.1461277

Li, D., Yan, X., Hu, Y., Liu, Y., Guo, R., Liao, M., et al. (2019a). Two-Photon Image Tracking of Neural Stem Cells via Iridium Complexes Encapsulated in Polymeric Nanospheres. *ACS Biomater. Sci. Eng.* 5 (3), 1561–1568. doi:10.1021/acsbiomaterials.8b01231

Li, G., Chen, K., You, D., Xia, M., Li, W., Fan, S., et al. (2019b). Laminin-Coated Electrospun Regenerated Silk Fibroin Mats Promote Neural Progenitor Cell Proliferation, Differentiation, and Survival *In Vitro*. *Front. Bioeng. Biotechnol.* 7, 190. doi:10.3389/fbioe.2019.00190

Li, W., Wang, W., Liu, L., Qu, R., Chen, X., Qiu, C., et al. (2019c). GDF11 Antagonizes TNF-α-induced Inflammation and Protects against the Development of Inflammatory Arthritis in Mice. *FASEB j.* 33 (3), 3317–3329. doi:10.1096/fj.201801375RR

Liang, X., Hu, Q., Li, B., McBride, D., Bian, H., Spagnoli, P., et al. (2014). Follistatin-like 1 Attenuates Apoptosis via Disco-Interacting Protein 2 Homolog A/Akt Pathway after Middle Cerebral Artery Occlusion in Rats. *Stroke* 45 (10), 3048–3054. doi:10.1161/STROKEAHA.114.006092

Lin, Y.-J., Lee, Y.-W., Chang, C.-W., and Huang, C.-C. (2020). 3D Spheroids of Umbilical Cord Blood MSC-Derived Schwann Cells Promote Peripheral Nerve Regeneration. *Front. Cell Dev. Biol.* 8, 604946. doi:10.3389/fcell.2020.604946

Liu, W., Xu, L., Wang, X., Zhang, D., Sun, G., Wang, M., et al. (2021). PRDX1 Activates Autophagy via the PTEN-AKT Signaling Pathway to Protect against Cisplatin-Induced Spiral Ganglion Neuron Damage. *Autophagy*, 1–23. doi:10.1080/15548627.2021.1905466

Liu, W., Xu, X., Fan, Z., Sun, G., Han, Y., Zhang, D., et al. (2019). Wnt Signaling Activates TP53-Induced Glycolysis and Apoptosis Regulator and Protects against Cisplatin-Induced Spiral Ganglion Neuron Damage in the Mouse Cochlea. *Antioxid. Redox Signaling* 30 (11), 1389–1410. doi:10.1089/ars.2017.7288

Liu, Z., Tang, M., Zhao, J., Chai, R., and Kang, J. (2018). Looking into the Future: Toward Advanced 3D Biomaterials for Stem-Cell-Based Regenerative Medicine. *Adv. Mater.* 30 (17), 1705388. doi:10.1002/adma.201705388

Luo, H., Guo, Y., Liu, Y., Wang, Y., Zheng, R., Ban, Y., et al. (2019). Growth Differentiation Factor 11 Inhibits Adipogenic Differentiation by Activating TGF-beta/Smad Signalling Pathway. *Cell Prolif* 52 (4), e12631. doi:10.1111/cpr.12631

Mei, W., Xiang, G., Li, Y., Li, H., Xiang, L., Lu, J., et al. (2016). GDF11 Protects against Endothelial Injury and Reduces Atherosclerotic Lesion Formation in Apolipoprotein E-Null Mice. *Mol. Ther.* 24 (11), 1926–1938. doi:10.1038/mt.2016.160

Merolli, A., Rocchi, L., Catalano, F., Planell, J., Engel, E., Martinez, E., et al. (2009). *In Vivo* regeneration of Rat Sciatic Nerve in a Double-Halved Stitch-Less Guide: a Pilot-Study. *Microsurgery* 29 (4), 310–318. doi:10.1002/micr.20622

Pukos, N., Goodus, M. T., Sahinkaya, F. R., and McTigue, D. M. (2019). Myelin Status and Oligodendrocyte Lineage Cells over Time after Spinal Cord Injury: What Do We Know and what Still Needs to Be Unwrapped? *Glia* 67 (11), 2178–2202. doi:10.1002/glia.23702

Que, J., Cao, Q., Sui, T., Du, S., Kong, D., and Cao, X. (2013). Effect of FK506 in Reducing Scar Formation by Inducing Fibroblast Apoptosis after Sciatic Nerve Injury in Rats. *Cell Death Dis* 4, e526. doi:10.1038/cddis.2013.56

Ren, K., Li, B., Liu, Z., Xia, L., Zhai, M., Wei, X., et al. (2021). GDF11 Prevents the Formation of Thoracic Aortic Dissection in Mice: Promotion of Contractile Transition of Aortic SMCs. *J. Cell Mol Med* 25 (10), 4623–4636. doi:10.1111/jcmm.16312

Reyne, N., Cmielewski, P., McCarron, A., Delhove, J., Parsons, D., and Donnelley, M. (2021). Single-Dose Lentiviral Mediated Gene Therapy Recovers CFTR Function in Cystic Fibrosis Knockout Rats. *Front. Pharmacol.* 12, 682299. doi:10.3389/fphar.2021.682299

Shang, L., Yu, Y., Gao, W., Wang, Y., Qu, L., Zhao, Z., et al. (2018). Bio-Inspired Anisotropic Wettability Surfaces from Dynamic Ferrofluid Assembled Templates. *Adv. Funct. Mater.* 28, 1705802. doi:10.1002/adfm.201705802

Shi, H., Zhang, X., Weng, Y.-L., Lu, Z., Liu, Y., Lu, Z., et al. (2018). m6A Facilitates Hippocampus-dependent Learning and Memory through YTHDF1. *Nature* 563 (7730), 249–253. doi:10.1038/s41586-018-0666-1

Song, H., Feng, X., Zhang, H., Luo, Y., Huang, J., Lin, M., et al. (2019). METTL3 and ALKBH5 Oppositely Regulate m6A Modification of TFEB mRNA, Which Dictates the Fate of Hypoxia/reoxygenation-Treated Cardiomyocytes. *Autophagy* 15 (8), 1419–1437. doi:10.1080/15548627.2019.1586246

Sun, G., Liu, W., Fan, Z., Zhang, D., Han, Y., Xu, L., et al. (2016). The Three-Dimensional Culture System with Matrigel and Neurotrophic Factors Preserves the Structure and Function of Spiral Ganglion NeuronIn Vitro. *Neural Plasticity* 2016, 1–15. doi:10.1155/2016/4280407

Tang, M., Li, J., He, L., Guo, R., Yan, X., Li, D., et al. (2019). Transcriptomic Profiling of Neural Stem Cell Differentiation on Graphene Substrates. *Colloids Surf. B: Biointerfaces* 182, 110324. doi:10.1016/j.colsurfb.2019.06.054

Wang, C.-X., Cui, G.-S., Liu, X., Xu, K., Wang, M., Zhang, X.-X., et al. (2018a). METTL3-mediated m6A Modification Is Required for Cerebellar Development. *Plos Biol.* 16 (6), e2004880. doi:10.1371/journal.pbio.2004880

Wang, Z., Dou, M., Liu, F., Jiang, P., Ye, S., Ma, L., et al. (2018b). GDF11 Induces Differentiation and Apoptosis and Inhibits Migration of C17.2 Neural Stem Cells via Modulating MAPK Signaling Pathway. *PeerJ* 6, e5524. doi:10.7717/peerj.5524

Waqas, M., Sun, S., Xuan, C., Fang, Q., Zhang, X., Islam, I.-u., et al. (2017). Bone Morphogenetic Protein 4 Promotes the Survival and Preserves the Structure of Flow-Sorted Bhlhb5+ Cochlear Spiral Ganglion Neurons *In Vitro*. *Sci. Rep.* 7 (1), 3506. doi:10.1038/s41598-017-03810-w

Wei, H., Chen, Z., Hu, Y., Cao, W., Ma, X., Zhang, C., et al. (2021). Topographically Conductive Butterfly Wing Substrates for Directed Spiral Ganglion Neuron Growth. *Small* 17 (38), 2102062. doi:10.1002/smll.202102062

Xia, L., Shang, Y., Chen, X., Li, H., Xu, X., Liu, W., et al. (2020). Oriented Neural Spheroid Formation and Differentiation of Neural Stem Cells Guided by Anisotropic Inverse Opals. *Front. Bioeng. Biotechnol.* 8, 848. doi:10.3389/fbioe.2020.00848

Xiao, A., Zhang, Y., Ren, Y., Chen, R., Li, T., You, C., et al. (2021). GDF11 Alleviates Secondary Brain Injury after Intracerebral Hemorrhage via Attenuating Mitochondrial Dynamic Abnormality and Dysfunction. *Sci. Rep.* 11 (1), 3974. doi:10.1038/s41598-021-83545-x

Xue, J., Liu, Y., Zhang, S., Ding, L., Shen, B., Shao, Y., et al. (2021). Caffeine Improves Bladder Function in Diabetic Rats via a Neuroprotective Effect. *Exp. Ther. Med.* 21 (5), 501. doi:10.3892/etm.2021.9932

Yan, W., Liu, W., Qi, J., Fang, Q., Fan, Z., Sun, G., et al. (2018). A Three-Dimensional Culture System with Matrigel Promotes Purified Spiral Ganglion Neuron Survival and Function *In Vitro*. *Mol. Neurobiol.* 55 (3), 2070–2084. doi:10.1007/s12035-017-0471-0

Yang, Y., Gao, B., Hu, Y., Wei, H., Zhang, C., Chai, R., et al. (2021). Ordered Inverse-Opal Scaffold Based on Bionic Transpiration to Create a Biomimetic Spine. *Nanoscale* 13 (18), 8614–8622. doi:10.1039/d1nr00731a

Yang, Y., Zhang, Y., Chai, R., and Gu, Z. (2020). A Polydopamine-Functionalized Carbon Microfibrous Scaffold Accelerates the Development of Neural Stem Cells. *Front. Bioeng. Biotechnol.* 8, 616. doi:10.3389/fbioe.2020.00616

Yardım, A., Kandemir, F. M., Çomaklı, S., Özdemir, S., Caglayan, C., Kucukler, S., et al. (2021). Protective Effects of Curcumin against Paclitaxel-Induced Spinal Cord and Sciatic Nerve Injuries in Rats. *Neurochem. Res.* 46 (2), 379–395. doi:10.1007/s11064-020-03174-0

Yu, J., Chen, M., Huang, H., Zhu, J., Song, H., Zhu, J., et al. (2018). Dynamic m6A Modification Regulates Local Translation of mRNA in Axons. *Nucleic Acids Res.* 46 (3), 1412–1423. doi:10.1093/nar/gkx1182

Yuan, T.-F., Dong, Y., Zhang, L., Qi, J., Yao, C., Wang, Y., et al. (2021). Neuromodulation-Based Stem Cell Therapy in Brain Repair: Recent Advances and Future Perspectives. *Neurosci. Bull.* 37 (5), 735–745. doi:10.1007/s12264-021-00667-y

Yudin, D., Hanz, S., Yoo, S., Iavnilovitch, E., Willis, D., Gradus, T., et al. (2008). Localized Regulation of Axonal RanGTPase Controls Retrograde Injury Signaling in Peripheral Nerve. *Neuron* 59 (2), 241–252. doi:10.1016/j.neuron.2008.05.029

Zhao, J., Tang, M., Cao, J., Ye, D., Guo, X., Xi, J., et al. (2019). Structurally Tunable Reduced Graphene Oxide Substrate Maintains Mouse Embryonic Stem Cell Pluripotency. *Adv. Sci.* 6 (12), 1802136. doi:10.1002/advs.201802136

Zhao, J., Zheng, X., Fu, C., Qu, W., Wei, G., and Zhang, W. (2014). FK506-loaded Chitosan Conduit Promotes the Regeneration of Injured Sciatic Nerves in the Rat through the Upregulation of Brain-Derived Neurotrophic Factor and TrkB. *J. Neurol. Sci.* 344 (1-2), 20–26. doi:10.1016/j.jns.2014.06.005

Zhou, L. N., Wang, J. C., Zilundu, P. L. M., Wang, Y. Q., Guo, W. P., Zhang, S. X., et al. (2020). A Comparison of the Use of Adipose-Derived and Bone Marrow-Derived Stem Cells for Peripheral Nerve Regeneration *In Vitro* and *In Vivo*. *Stem Cell Res Ther* 11 (1), 153. doi:10.1186/s13287-020-01661-3

Salehi, M., Bagher, Z., Kamrava, S. K., Ehterami, A., Alizadeh, R., Farhadi, M., et al. (2019). Alginate/chitosan Hydrogel Containing Olfactory Ectomesenchymal Stem Cells for Sciatic Nerve Tissue Engineering. *J. Cell Physiol* 234, 15357–15368. doi:10.1002/jcp.28183

Conflict of Interest: The authors declare that the research was conducted in the absence of any commercial or financial relationships that could be construed as a potential conflict of interest.

Publisher's Note: All claims expressed in this article are solely those of the authors and do not necessarily represent those of their affiliated organizations, or those of the publisher, the editors and the reviewers. Any product that may be evaluated in this article, or claim that may be made by its manufacturer, is not guaranteed or endorsed by the publisher.

frontiers in Bioengineering and Biotechnology

ORIGINAL RESEARCH
published: 18 February 2022
doi: 10.3389/fbioe.2022.848699

An *In Vitro* Microfluidic Alveolus Model to Study Lung Biomechanics

Vardhman Kumar[1], *Sajeesh Kumar Madhurakkat Perikamana*[2], *Aleksandra Tata*[3], *Jiaul Hoque*[2], *Anna Gilpin*[1], *Purushothama Rao Tata*[3,4] *and Shyni Varghese*[1,2,5]*

[1]Department of Biomedical Engineering, Duke University, Durham, NC, United States, [2]Department of Orthopaedic Surgery, Duke University School of Medicine, Durham, NC, United States, [3]Department of Cell Biology, Duke University School of Medicine, Durham, NC, United States, [4]Regeneration Next, Duke University, Durham, NC, United States, [5]Department of Mechanical Engineering and Material Science, Duke University, Durham, NC, United States

The gas exchange units of the lung, the alveoli, are mechanically active and undergo cyclic deformation during breathing. The epithelial cells that line the alveoli contribute to lung function by reducing surface tension *via* surfactant secretion, which is highly influenced by the breathing-associated mechanical cues. These spatially heterogeneous mechanical cues have been linked to several physiological and pathophysiological states. Here, we describe the development of a microfluidically assisted lung cell culture model that incorporates heterogeneous cyclic stretching to mimic alveolar respiratory motions. Employing this device, we have examined the effects of respiratory biomechanics (associated with breathing-like movements) and strain heterogeneity on alveolar epithelial cell functions. Furthermore, we have assessed the potential application of this platform to model altered matrix compliance associated with lung pathogenesis and ventilator-induced lung injury. Lung microphysiological platforms incorporating human cells and dynamic biomechanics could serve as an important tool to delineate the role of alveolar micromechanics in physiological and pathological outcomes in the lung.

Keywords: microfluidics, organ-on-a-chip, lung, microphysiological system, *in vitro* system

OPEN ACCESS

Edited by:
Loredana De Bartolo, National Research Council (CNR), Italy

Reviewed by:
Josue Sznitman, Technion Israel Institute of Technology, Israel
Ludovica Cacopardo, University of Pisa, Italy

***Correspondence:**
Shyni Varghese
shyni.varghese@duke.edu

Specialty section:
This article was submitted to Tissue Engineering and Regenerative Medicine, a section of the journal Frontiers in Bioengineering and Biotechnology

Received: *05 January 2022*
Accepted: *25 January 2022*
Published: *18 February 2022*

Citation:
Kumar V, Madhurakkat Perikamana SK, Tata A, Hoque J, Gilpin A, Tata PR and Varghese S (2022) An In Vitro Microfluidic Alveolus Model to Study Lung Biomechanics. Front. Bioeng. Biotechnol. 10:848699. doi: 10.3389/fbioe.2022.848699

INTRODUCTION

The lung is a key organ that ensures blood oxygenation by means of respiration. Mechanical cues arising from cyclic expansion and contraction of alveoli during breathing have an important role in maintaining tissue homeostasis (Ingenito et al., 2005; Faffe and Zin, 2009; Perlman et al., 2011; Chen et al., 2014; Hsia et al., 2016; Knudsen and Ochs, 2018; Plantier et al., 2018). Conventional *in vitro* models of lung tissues frequently neglect the dynamic tissue biomechanics associated with respiration. Development of microfluidic organ-on-a-chip technology enables recapitulation of mechanical and structural aspects of the organ microenvironment, thus potentially narrowing the gap between *in vitro* and *in vivo* models (Bhatia and Ingber, 2014; Aung et al., 2016, 2020; Agrawal et al., 2017; Kumar and Varghese, 2019; Low et al., 2021). Toward this, various microphysiological platforms such as lung-on-a-chip, airway-on-a-chip, and alveolus-on-chip have been developed to model lung functions such as barrier properties, immune responses to infections, and lung pathologies such as asthma, edema, thrombosis, and lung cancer progression (Huh et al., 2010, 2012; Stucki et al., 2015, 2018; Benam et al., 2016a, 2016b, 2017; Jain et al., 2018; Park et al., 2018; Felder et al., 2019; Elias-Kirma et al., 2020; Ishahak et al., 2020; Jimenez-Valdes et al., 2020; Khalid et al.,

2020; Mejías et al., 2020; Nawroth et al., 2020; Shrestha et al., 2020, 2021; Zamprogno et al., 2021).

Lung distention occurs in three dimensions (3D) as a result of not only the alveolar air pressure but also the difference between the alveolar air pressure and the pleural fluid pressure, the transpulmonary pressure. Model systems incorporate such dynamic mechanical movements associated with breathing using deformable membranes subjected to dynamic pressure (Guenat and Berthiaume, 2018). While most *in vitro* studies and microphysiological systems incorporating dynamic stretch have been limited to generating in-plane strain or uniaxial strain in the 5–12% range reported *in vivo* (Birukov et al., 2003; Guenat and Berthiaume, 2018; Nossa et al., 2021; Sznitman, 2021), recent studies have delved into incorporating out-of-plane stretching to mimic the 3D movements of the alveoli during respiration (Stucki et al., 2018; Doryab et al., 2021a; Huang et al., 2021; Zamprogno et al., 2021). These advances offer unique *in vitro* tools to study the micromechanical changes such as the strain heterogeneity that develops as a result of the out-of-plane stretch and its subsequent role in lung physiology and pathology. Although the precise strain profile that develops in the lung during respiration is yet to be accurately mapped, it is well established that not just different regions of the lung but even a single alveolus experiences varying strains during respiration (Roan and Waters, 2011). These spatially varying mechanical cues have been shown to be associated with several lung conditions and vulnerabilities. For example, regions with intrinsically high strains—such as in aerated alveoli next to fluid-filled alveoli—are prone to experiencing increased strains during mechanical ventilation, thus predisposing them to ventilator-induced lung injury (VILI) (Perlman et al., 2011; Smith, 2016). Apart from such spatial variations in strain during breathing, progressive changes in local tissue mechanics (e.g., changes in compliance) are key characteristics of various respiratory disorders such as pulmonary fibrosis and emphysema (Ingenito et al., 2005; Faffe and Zin, 2009; Plantier et al., 2018; Hurtado et al., 2020).

In this study, we report a microfluidic alveolar tissue model that mimics dynamic out-of-plane stretching akin to alveolar inflation and deflation associated with breathing. The device consists of a fluidic and pneumatic layer separated by a thin polydimethylsiloxane (PDMS) membrane, which was functionalized by covalent conjugation of collagen-I to enable cell culture. We characterized the heterogeneous strain experienced by the membrane as a result of breathing-like movements by using computational analyses and examined the effect of spatial heterogeneity on cell alignment. Employing this platform, we also examined the effect of biomechanics on the function of alveolar epithelial cells. Specifically, we studied the effect of breathing-like movements on surfactant production by alveolar epithelial cells and how it is affected by heterogeneous strain and altered matrix compliance. Furthermore, we incorporated transpulmonary pressure into the device to have the membrane deform in response to a combination of pneumatic and hydrostatic pressure. Using this approach, we determined the applicability of this platform to model ventilator-induced lung injury (VILI). Finally, we also examined the potential of the platform to support the culture of human primary alveolar epithelial type 2 (AT2) cells and AT2 cells derived from human induced pluripotent stem cells (hiPSC).

METHODS

Photolithography of the Master Mold

Silicon wafers (UniversityWafers) were used for patterning arrays of 200-μm-wide and 100-μm-high channels by using SU-8 photolithography. Briefly, 4 ml of SU-8 100 photoresist was spin-coated on a cleaned wafer at 3,000 rpm/s for 30 s. The wafer was baked at 65°C for 10 min, followed by 95°C for 30 min. The wafer was then exposed to 365 nm wavelength light through a custom photomask designed in AutoCAD and baked at 65°C for 1 min and 95°C for 10 min. The wafer was then rinsed with SU-8 developer to remove the undeveloped photoresist. The resulting master mold was cleaned with isopropanol followed by water and stored until use.

Device Fabrication, Assembly, and Operation

To fabricate the device, a 10:1 (base:crosslinker) polydimethylsiloxane (PDMS) (Sylgard 184, Dow Inc.) precursor solution containing the crosslinker was poured onto the master mold and allowed to cure for 2 h at 60°C. Post curing, PDMS was cut around the channels and 8 mm diameter holes were punched in the top fluidic layer and bottom pneumatic layer to create cell culture chambers and pneumatic chambers, respectively (**Figure 1A**). The same channel dimensions were used for both fluidic and pneumatic channels. One-mm-diameter inlet and outlet were punched in the fluidic layer, and a 1-mm-diameter inlet was punched in the pneumatic layer of the device (**Figure 1A**). PDMS membranes were prepared by curing the precursor solution between two glass slides separated using stainless steel spacers with a thickness of 250 μm. The cell culture chamber was capped on the top by a glass coverslip using either double-sided tape (for reversible adhesion) or plasma bonding (for irreversible adhesion). The fluidic microchannels were capped at the base by plasma bonding the PDMS membrane to the fluidic layer. Separately, the pneumatic chamber and the pneumatic channels were capped at the bottom by plasma bonding a rectangular coverslip to the pneumatic layer (**Figure 1B**). The fluidic and pneumatic layers were assembled using double-sided tape to get a reversible adhesion between the two layers. This enabled easy disassembly of the device for imaging. The PTFE tubing from the programmable air pump (Elveflow) was connected to the inlet of the pneumatic layer, while the inlets of the fluidic layer were fed through syringes loaded onto a syringe pump (Harvard Apparatus) at a rate of 50 μl/h unless stated otherwise. For all experiments involving breathing-like motions, sinusoidal pressure waveforms with a minimum and maximum at 0 and 50 mbar, respectively, at a frequency of 0.5 Hz were used unless stated otherwise.

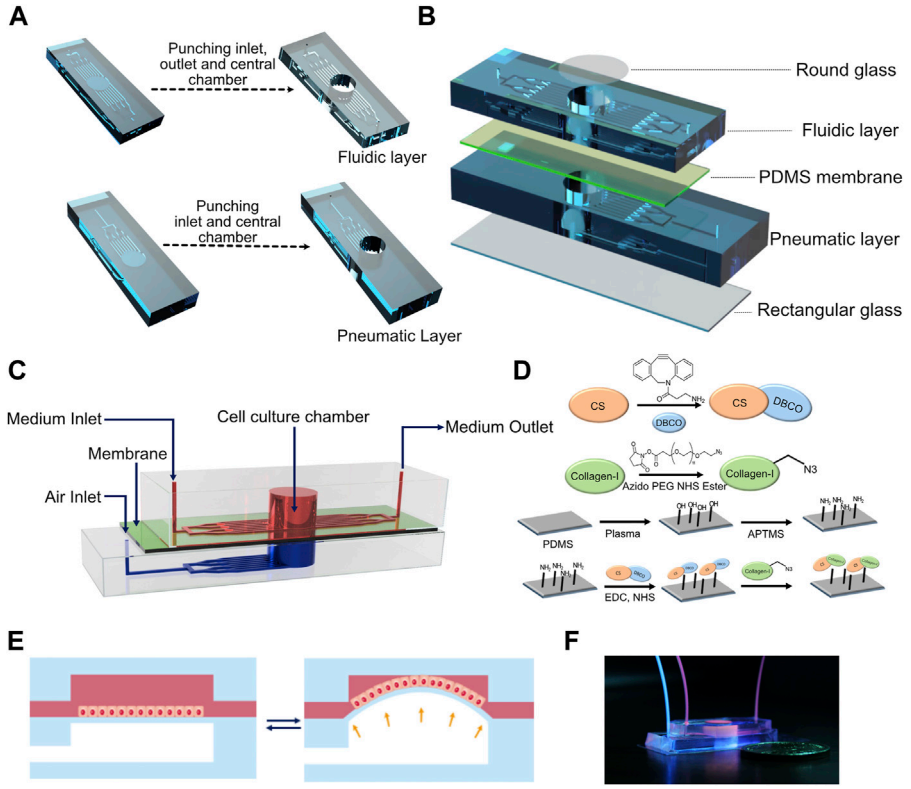

FIGURE 1 | (A) Computer-aided design (CAD) of the fabrication process of fluidic and pneumatic layers with microchannels. **(B)** Schematic of device assembly showing the different layers of the device in an exploded view. **(C)** Schematic depicting the assembled device. **(D)** Reaction scheme used for collagen functionalization of the PDMS membrane. **(E)** Schematic of breathing-like movements within the device. **(F)** Digital photograph of the device showing the media/cell chamber (red) and air chamber (blue).

Computational Modeling to Determine Strain Fields

The breathing movements of the membrane were modeled in COMSOL. The membrane was modeled as a cylindrical disc made from PDMS. A Mooney–Rivlin hyperelastic model (Rivlin, 1948) was used to describe the membrane:

$$W_s = \sum_{i,j=0}^{n} C_{i,j} (I_1 - 3)^i (I_2 - 3)^j + \frac{1}{2} K (J_{el} - 1)^2, \quad (1)$$

where I_1 and I_2 are the first and second invariant of the left isochoric Cauchy-Green deformation tensor, K is the bulk modulus, J_{el} is the elastic Jacobian, and $C_{i,j}$ are material parameters.

Two-parameter Mooney–Rivlin material parameters for the PDMS membrane of 10:1 base to crosslinker were approximated from Yoon et al. (2010). The values used are listed in **Supplementary Table S1**. Zero displacement boundary condition was applied at the curved surface of the cylindrical membrane, while load (resulting from air pressure) was applied at the base of the membrane. Displacement field was used to calculate the resulting radial and circumferential strain as a function of radial distance from the center of the membrane (Winkler et al., 2014).

$$Radial\ Strain = \frac{\left|(x_2^s - x_1^s) + (y_2^s - y_1^s) + (z_2^s - z_1^s)\right| - \left|(x_2 - x_1) + (y_2 - y_1) + (z_2 - z_1)\right|}{\left|(x_2 - x_1) + (y_2 - y_1) + (z_2 - z_1)\right|} \quad (2)$$

$$Circumferential\ Strain = \frac{2\pi r^s - 2\pi r}{2\pi r}, \quad (3)$$

where (x_1, y_1, z_1) and (x_2, y_2, z_2) are coordinates of two arbitrary points on the membrane before stretching and (x_1^s, y_1^s, z_1^s) and (x_2^s, y_2^s, z_2^s) are the coordinates of the points after stretching. Similarly, r and r^s are the radial distance of a point from the center of the membrane before and after stretching, respectively.

Synthesis of Chondroitin Sulfate–Dibenzocyclooctyne and Collagen Azide

Five hundred milligrams of chondroitin sulfate (CS) (Alfa Aesar, J60341) was dissolved into 60 ml DI water. To this, 35 ml of dimethyl

sulfoxide (DMSO) was added, followed by 287.5 mg of 1-ethyl-3-(3-dimethylaminopropyl) carbodiimide hydrochloride (EDC.HCl) (TCI Chemical, D1601). Then 172.6 mg of *N*-hydroxy succinimide (NHS) (Sigma, 130672) and 138.15 mg of dibenzocyclooctyne–amine (DBCO-amine) (Click Chemistry Tools, A103) were dissolved in 5 ml of DMSO and were added to the reaction mixture at 15-min intervals. The reaction was continued for 24 h under constant stirring. The reaction mixture was then dialyzed against water for 4 days and freeze-dried to obtain DBCO-conjugated chondroitin sulfate (CS-DBCO). The product was stored at −20°C until use. The product was characterized by a combination of Fourier transform infrared spectroscopy (FTIR) and proton nuclear magnetic resonance (^{1}HNMR) spectroscopy. The peaks in attenuated total reflection (ATR) FTIR spectra at 1,612 cm^{-1} due to C=O stretching and 1,559 cm^{-1} due to N–H deformation in the CS spectrum were shown to be shifted to 1,648 and 1,569 cm^{-1} in the CS-DBCO spectrum, respectively, indicating the presence of new amide bonds formed via the reaction between the carboxylic acid group of CS and the amine group of DBCO. In addition, peaks were observed at 1,480 and 1,441 cm^{-1}, which represented the aromatic C=C stretching in the rings of DBCO (**Supplementary Figure S1**). The successful conjugation of DBCO to CS was further confirmed by ^{1}HNMR where the spectrum showed the appearance of aromatic protons from DBCO at 7.34–7.44 ppm. The degree of DBCO conjugation was calculated by taking the ratio of area under the curve for the aromatic protons of DBCO at 7.34–7.44 ppm to the $-CH_3$ protons of the $-NHCOCH_3$ groups of CS at 1.9 ppm and found to be 39 ± 2% with respect to the dimeric sugar unit of CS (**Supplementary Figure S2**).

For collagen azide, 1 mg of collagen type I (Corning, 354236) and 500 µl of azide-polyethylene glycol-NHS) (Click Chemistry Tools, AZ103) were dissolved in 10 ml PBS each. The reaction was performed by mixing the solutions under constant stirring for 3 h at 0–4°C. The reaction mixture was then dialyzed against water at 4°C for 3 days. The product was freeze-dried and stored at -20°C until use. The product was characterized via FTIR spectroscopy where the spectra revealed a sharp peak at 2,141 cm^{-1} characteristic to the N≡N stretching frequency of the azide functional group (**Supplementary Figure S3**).

Collagen Functionalization of the Membrane

The PDMS membrane in the bonded devices was treated with corona treater (ETP, BD-20AC) for 1 min to plasma-activate the surface. Approximately 100 µl of 2% (v/v) (3-aminopropyl)-trimethoxysilane (APTMS) (Sigma, 281778) in 100% ethanol was introduced into the cell culture chamber, and the devices were incubated for 60 min at room temp and washed with distilled water. Meanwhile, 5 mg of CS-DBCO was dissolved in 1 ml of PBS and reacted with 5 mg of EDC for 15 min, followed by 2.1 mg of NHS to convert CS-DBCO into CS-DBCO-NHS ester. The devices were incubated with this activated CS-DBCO-NHS ester at 37°C for overnight to covalently immobilize CS-DBCO on the PDMS surface. The next day, the devices were washed 2–3 times with distilled water, and 10 µg/ml of collagen-azide solution in PBS was introduced into the devices. The devices were incubated overnight to immobilize collagen onto the PDMS surface via a strain-promoted azide–alkyne cycloaddition (SPAAC) reaction between the azide group of collagen zide and the DBCO group of surface-bound CS-DBCO. The devices were washed with PBS before culturing cells.

Isolation and Culture of Human Primary AT2 Cells

Healthy human lungs were procured through the BioRepository and Precision Pathology Center at Duke University in accordance with institutional procedures (Duke University Pro00082379—"Human Lung Stem Cells"; exempt research as described in 45 CFR 46.102(f), 21 CFR 56.102(e) and 21 CFR 812.3(p) which satisfies the Privacy Rule as described in 45CFR164.514). Human lung dissociation was performed as described previously (Zacharias et al., 2018). Briefly, approximately 2 g human lung tissue was cut into small pieces and incubated with 30 ml of enzyme mixture (collagenase type I (Gibco, 17100–017): 1.68 mg/ml, dispase (Corning, 354235): 5 U/ml, DNase (Thermo Fisher Scientific, 10104159001): 10 U/ml) at 37°C for 1 h with continuous rotation. The cells were filtered through a 100-µm cell strainer and rinsed with DMEM/F12 containing 10% FBS and anti-anti through the strainer. The sample was centrifuged at 450 g for 10 min, and the cell pellet was resuspended in red blood cell lysis buffer for 10 min, washed with DMEM/F12 containing 10% FBS, and filtered through a 40-µm strainer. Total cells were centrifuged at 450 g for 5 min at 4°C and the cell pellet was processed for alveolar type 2 cell (AT2s) purification. AT2s were isolated by magnetic-activated cell sorting (MACS) or fluorescence-activated cell sorting (FACS)-based protocols as described previously (Katsura et al., 2020). Approximately 2–10 million total human lung cells were resuspended in MACS buffer and incubated with Human TruStain FcX (Biolegend, 422032) for 15 min at 4°C, followed by incubation with HTII-280 (Terrace Biotech, TB-27AHT2-280) (1:60 dilution) antibody for 1 h at 4°C. The cells were washed twice with MACS buffer and incubated with anti-mouse IgM microbeads for 15 min at 4°C. The sample was loaded into the LS column (Miltenyi Biotec), and cells were collected magnetically. For FACS based purification of human AT2s, the total lung cell pellets were resuspended in MACS buffer and the EpCAM-positive population was purified using microbeads according to the manufacturer's instructions (Miltenyi Biotec, 130-061-101). CD326-positive cells were stained with HTII-280 and LysoTracker (Thermo Fisher Scientific, L7526) at 37°C for 25 min, followed by incubation with secondary antibody Alexa anti-mouse IgM-488 (Thermo Fisher Scientific, 10680) for 10 min at 37°C, washed twice and sorted using a FACS Vantage SE and SONY SH800 S. The cells were expanded as alveolospheres in growth factor reduced Matrigel (Corning, 354230) as described previously (Katsura et al., 2020), using Advanced DMEM/F12 medium containing 10 µM SB431542 (Abcam, 120163), 3 µM CHIR99021 (Tocris, 4423), 1 µM BIRB796 (Tocris, 5989), 10 µM Y27632 (Selleckchem, S1049) (for first 4 days of culture), 50 ng/ml Human EGF (Gibco, PHG0313), 10 ng/ml Human FGF10 (Biolegend, 559304),

5 μg/ml Heparin (Sigma, H3149), 1X B27 supplement (Thermo Fisher Scientific, 17504044), 1X Antibiotic-Antimycotic (Thermo Fisher Scientific, A5955), 15 mM HEPES, 1X Glutamax (Thermo Fisher Scientific, 35050061), and 1.25 mM N-Acetyl-L-Cysteine (Sigma, A9165).

Culture of Human Induced Pluripotent Stem Cell (hiPSC)-Derived AT2 Cells (iAT2 Cells)

IPSCs-derived human alveolar type 2 cells (iAT2s) (differentiated from the SPC2-ST-B2 iPSC line) were expanded as alveolospheres in growth factor reduced Matrigel (Corning, 354230) as described elsewhere (Jacob et al., 2019). The iAT2s were maintained in IMDM medium containing 25% Ham's F12 (Cellgro, 10–080-CV), 1% B27 supplement, 0.5% N2 supplement, 0.05% BSA (Invitrogen, 15260037), 200 ng/ml Primocin (Invivogen, NC9141851), 1X GlutaMAX, 50 μg/ml ascorbic acid (Sigma, A4544), 0.45 mM monothioglycerol (Sigma, M6145), 3 μM CHIR99021, 10 ng/ml rhKGF (R&D, 251-KG-010), 50 nM Dexamethasone (Sigma, D4902), 10 μM Y27632 (for first 3 days of culture), 0.1 mM 8-bromoadenosine 3′,5′-cyclic monophosphate sodium salt (Sigma, B7880), and 0.1 mM 3-isobutyl-1-methylxanthine (Sigma, I5879).

Culture of MLE-12 and H441 Cell Lines

MLE-12 cells were maintained in HITES medium consisting of DMEM/F12 (ATCC, 30-2006), 2% fetal bovine serum (FBS), 0.005 mg/ml insulin, 0.01 mg/ml transferrin (Fitzgerald, 31C-CH1026), 30 nM sodium selenite (Santa Cruz, 253595), 10 nM hydrocortisone (Sigma, H0888), 10 nM β-estradiol, 10 mM HEPES (Gibco, 15630106), 2 mM L-glutamine (Gibco, 25030081), and 1% Pen-Step (Gibco, 15140122). H441 cells were maintained in RPMI-1640 (ATCC, 30-2001) medium supplemented with 10% FBS and 1% Pen-Strep.

Cell Seeding Within the Device

For seeding hAT2s and iAT2s into the devices, alveolosphere dissociation was carried out by incubating the cultures in 2 mg/ml dispase for 30 min to release the alveolospheres from the Matrigel matrix. This was followed by centrifugation at 200 g for 4 min and resuspension of the alveolospheres in 0.05% Trypsin-EDTA for 5 min. The cell suspension was centrifuged at 300 g for 5 min and the cells were resuspended in their medium before counting. For cell lines, the cells were detached from the culture plate using 0.25% trypsin–EDTA, centrifuged, and resuspended in medium before counting.

Single cells were suspended in their corresponding medium at a concentration of 2×10^5 cells/ml; 100 μl of the cell suspension was perfused into the fluidic chamber of the device. The cell-loaded devices were left undisturbed (2 h for cell lines and 6 h for hAT2s and iAT2 cells) to allow the cells to adhere to the membrane before they were connected to the syringe pump to start the perfusion. The cells were cultured in a submerged condition within the device. A tubing was connected from the fluidic outlet into an Eppendorf tube to collect the perfusate. Twenty-four hours after cell seeding, the air pump was connected to the pneumatic inlet of the devices to induce breathing-like motion.

Immunofluorescence Staining and Quantification

The fluidic layer was separated from the pneumatic layer, and the cover slip was removed from the top. The cells were washed three times with PBS and fixed with 4% PFA for 15 min. The cells were washed again with PBS and treated with a permeabilization solution for 15–20 min (PBS/0.1% Triton-X). After permeabilization, the cells were blocked using 5% normal donkey serum in 1% BSA. Cells were then treated with anti-prosurfactant protein C primary antibody (Sigma, AB3786) for overnight at 4°C (1:150). The next day, the cells were washed 3 times with PBS and incubated with the secondary antibody (anti-rabbit Alexa Flour 647, 1:200) for 1 h. The staining solution was then removed, Hochest (1:1,000) was added, and the mixture was incubated for 4 min. Finally, cells were washed and imaged using a Keyence BZ microscope. Mean fluorescence intensity was quantified using ImageJ. Another set of cultures were stained with phalloidin (1:200) for 1 h and with Hochest (1:1,000) for 4 min. The cells were washed, and images of various locations within the membrane were acquired. OrientationJ plugin (Püspöki et al., 2016) within ImageJ was used to analyze the images.

Surfactant Protein-A ELISA

For Surfactant Protein-A (SP-A) ELISA experiments, devices were seeded with H441 cells, which were allowed to grow to confluence for 3 days before exposing them to breathing-like motions. Just before the start of the experiments, the outlet reservoir was emptied, and the flow rate was reduced to 5 μl/h to concentrate the secreted surfactant. After 24 h of breathing, it was visually confirmed under a microscope that the cell layer had not detached during the experiment. Perfusate collected in the outlet reservoir was used for surfactant protein-A ELISA using the SP-A kit (Biovender, RD191139200R) according to the manufacturer's instructions.

Determining Concave Volume and Compliance Curves

The concave volume of the membrane in response to applied air pressure (0–50 mbar) was calculated using COMSOL. The side view of the computational model of the membrane in stretched position was projected onto a 2D plane. The boundary of the membrane was traced to obtain the spatial points. A 6-order polynomial curve was fitted onto the points to obtain the equation for the curve. The volume encompassed was calculated by integrating the equation in three dimensions using Wolfram Alpha. This was done for membranes of different thicknesses 250 μm and 1,000 μm subjected to different pressures. The obtained volumes were plotted against the corresponding applied pressure to obtain the compliance plot.

Transpulmonary Pressure Setup

To introduce hydrostatic pressure, the outlet of the fluidic microchannels was blocked using knotted PTFE tubing. A 10-ml syringe was filled with cell culture medium and its plunger was removed to expose the media to the atmosphere. A lid was placed at the end of the syringe to reduce the chances of contamination.

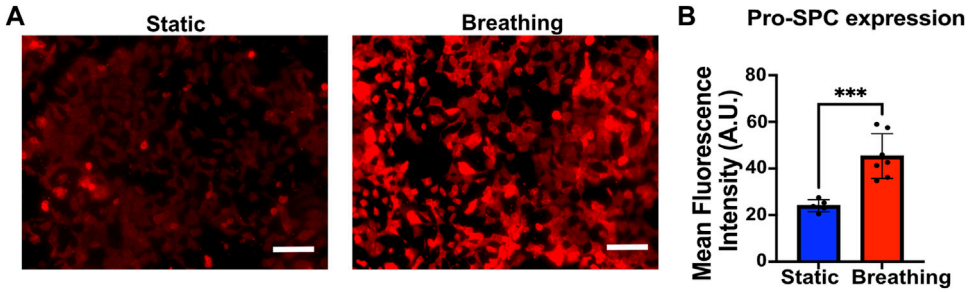

FIGURE 2 | (A) Immunofluorescent staining of Pro-SPC (red) of MLE-12 cells cultured under static and breathing conditions. **(B)** Quantification of the fluorescent intensity reveals that cells exposed to breathing-like motions express significantly higher pro-SPC. Each data point is an average of fluorescence intensity measurement from 6 to 11 images per independent device (N = 5 for static and N = 7 for breathing). Scale: 100 μm.

Tubing was connected from the syringe to the inlet of the fluid microchannels of the device. To generate positive hydrostatic pressure of 50 mbar, the syringe was placed 50 cm above the height of the device throughout the experiment.

Live-Dead Analysis

A viability/cytotoxicity kit (Thermo Fisher Scientific, L3224) was used to determine cell viability. Briefly, media was aspirated from the fluidic layer of the device, and the cells were washed with PBS. Then 100 μl of solution containing 0.05% calcein AM and 0.2% ethidium homodimer-1 was introduced into the device. The cells were incubated in the solution for 30 min before washing them with PBS and imaging them.

Statistics

Statistical analysis was performed on GraphPad Prism 9. An unpaired *t*-test was used to compare the mean fluorescent intensity in **Figure 2** and **Figure 6**; the cell shape in **Figure 6** and the SP-A levels in **Supplementary Figure S5**. For comparison of mean fluorescence intensity of cells cultured on 250- and 1,000-μm-thick membranes across center and edge, respectively, 2-way repeated measures ANOVA followed by multiple comparisons was used, with "center" and "edge" values being the repeated measures for each device. $N \geq 3$ independent devices per experimental group were used across all experiments. p-values < 0.05 were considered statistically significant.

RESULTS AND DISCUSSION

Device Fabrication and Cell Culture

The device consists of a bottom pneumatic layer and a top fluidic layer separated by a thin PDMS membrane (**Figure 1C**). The top layer consists of an inlet that diverges into an array of microchannels leading to a cylindrical cell culture chamber. This chamber is lined with a thin membrane at the base. Another array of microchannels connects the cell culture chamber to the device outlet. These channels are used for cell seeding and medium perfusion. In the bottom layer, the inlet diverges into an array of microchannels that lead to a cylindrical chamber whose ceiling is formed by the thin membrane and whose base is capped by a cover glass. The bottom layer is devoid of any outlets so that the device can be subjected to a pressure waveform to induce breathing-like movements. The PDMS membrane facing the fluid side was functionalized with collagen type I to promote cell attachment (**Figure 1D**). When subjected to a positive pressure in the bottom layer, the membrane concaves downward, which induces stretching of the membrane (**Figure 1E**). Applying a pressure waveform *via* the air pump facilitates cyclic stretching of the membrane, thus mimicking the breathing movements of alveoli (**Supplementary Movie S1**). Digital images of the device and of the setup are shown in **Figure 1F** and **Supplementary Figure S4**, respectively. Cells were perfused into the device *via* the inlet channel and allowed to adhere before introducing continuous perfusion of medium. The cells were cultured for 24 h before subjecting them to breathing-like movements. The device supported culture of alveolar epithelial cell lines, human primary alveolar epithelial cells (hAT2s) and human induced pluripotent (hiPSC)-derived alveolar epithelial cells (iAT2s).

Effect of Breathing-Like Motion on Surfactant Production

To study the effect of breathing-like motion-mediated active mechanical cues on alveolar cell functions, the epithelial cells within the device were subjected to cyclic stretching. The MLE-12 cells were subjected to breathing-like motions for 24 h, following which they were fixed and stained for surfactant protein-C (pro-SPC). Cells that were exposed to breathing-like motion expressed significantly higher levels of pro-SPC than cells cultured in static conditions (**Figures 2A, B**). Higher surfactant production in breathing cultures was further confirmed by H441 cells. As shown in **Supplementary Figure S5**, the cells subjected to dynamic breathing showed more secreted surfactant protein-A (SP-A). These results are in line with previous reports which showed increased surfactant production in response to cells subjected to stretching (Sanchez-Esteban et al., 1998; Torday and Rehan, 2002). The effect of mechanical cues on surfactant production has also been established in *in vivo* studies where mechanical ventilation-induced stretch has been reported to increase surfactant production in rat lungs (Martinez et al., 2004).

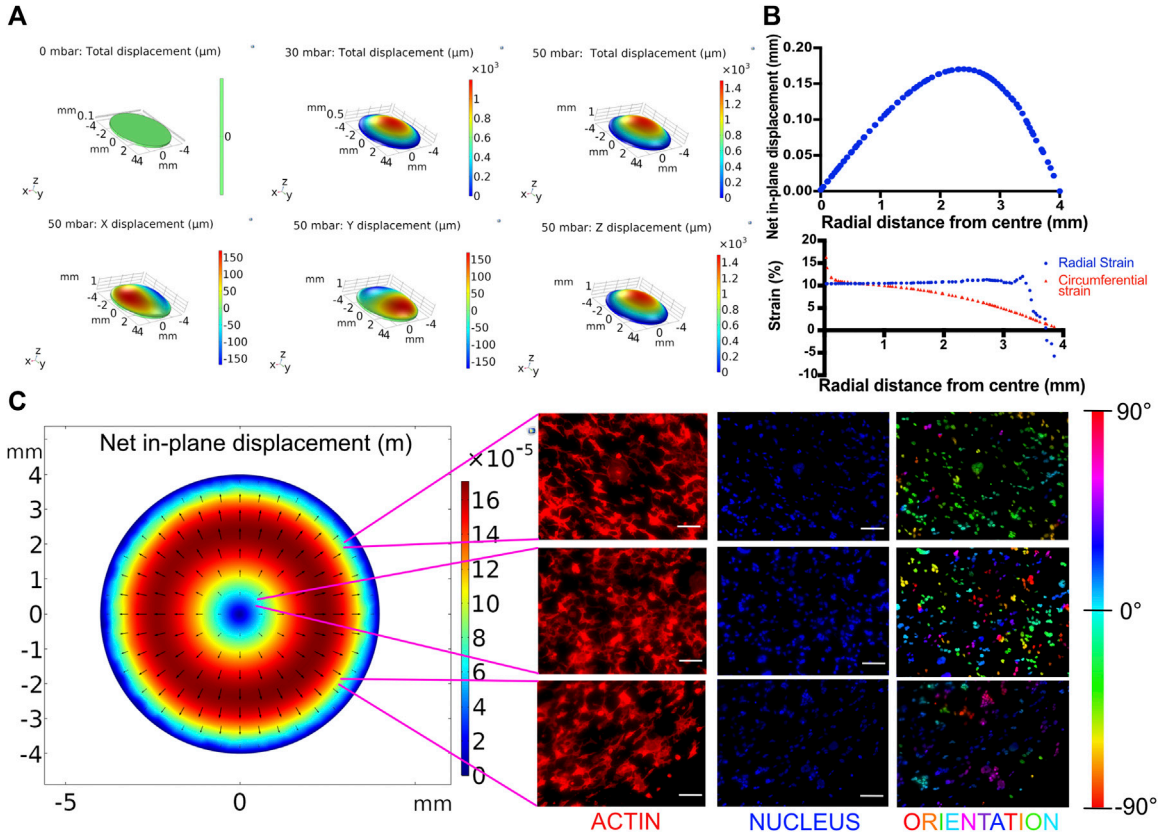

FIGURE 3 | (A) Displacement profiles of the breathing membrane subjected to various peak pressures. **(B)** In-plane displacement, radial strain and circumferential strain profile of the cell culture membrane at 50 mbar. **(C)** Effect of spatial strain heterogeneity of the cell culture substrate on cell alignment. Left: COMSOL computed in-plane displacement of the cell culture membrane. Right: Cellular alignment of MLE-12 cells was visualized by phalloidin (first column), and nucleus (second column) staining and cellular alignment at different locations in breathing devices was quantified using nuclear orientation (third column) where color of the nuclei in the third column represents their angle of alignment. Cells at the center of the membrane align randomly while those away from center align perpendicular to the radius. Scale: 100 μm.

Breathing-Induced Heterogeneous Strain Profile and Its Effect on Cell Shape

While dynamic stretching was found to promote surfactant production overall, we next analyzed the out-of-plane stretching-induced heterogeneous strain profile and its effect on the cells. Toward this, the membrane deformation during cyclic stretch was modeled in COMSOL as detailed in the experimental section. The effect of applied pressure on the membrane displacement field was determined by mapping the strain profile (**Figure 3A**). Using the displacement field, radial and circumferential strains were calculated at a peak pressure of 50 mbar. This pressure was chosen as it falls within the range of air pressure in the human lung during breathing and also results in physiological levels of strain (Roan and Waters, 2011). At this pressure, the in-plane displacement increases with increasing radial distance from the center (r) and gradually decreases, peaking at around r = 2.5 mm (**Figure 3B**). The circumferential strain was found to gradually decrease from 17 to 0% with increasing radial distance from the center. The radial strain largely remains constant at around 10% until a sharp decline after r > 3 mm due to the membrane being constricted at the edges (**Figure 3B**). MLE-12 cells on the membrane responded to the radial strain heterogeneity and exhibited a differential alignment. Specifically, at the center of the membrane, the cells were aligned randomly, while away from the center, they were aligned perpendicular to the direction of the major strain (i.e., the direction of radial displacement) (**Figure 3C**). In addition to epithelial cells, we have also examined the effect of strain heterogeneity on NIH 3T3 cells as fibroblasts are known to be highly sensitive to mechanical cues, including cyclic strain (Neidlinger-Wilke et al., 2002). Akin to epithelial cells, the fibroblasts displayed strain profile-dependent cell alignment, where cells away from the center aligned perpendicular to the direction of major strain, while those at the center were randomly aligned (**Supplementary Figure S6**). The strain-dependent alignment was more pronounced in the case of fibroblasts than in the epithelial cells, which is most likely attributed to the propensity of fibroblasts to polarize in cultures and acquire elongated morphology.

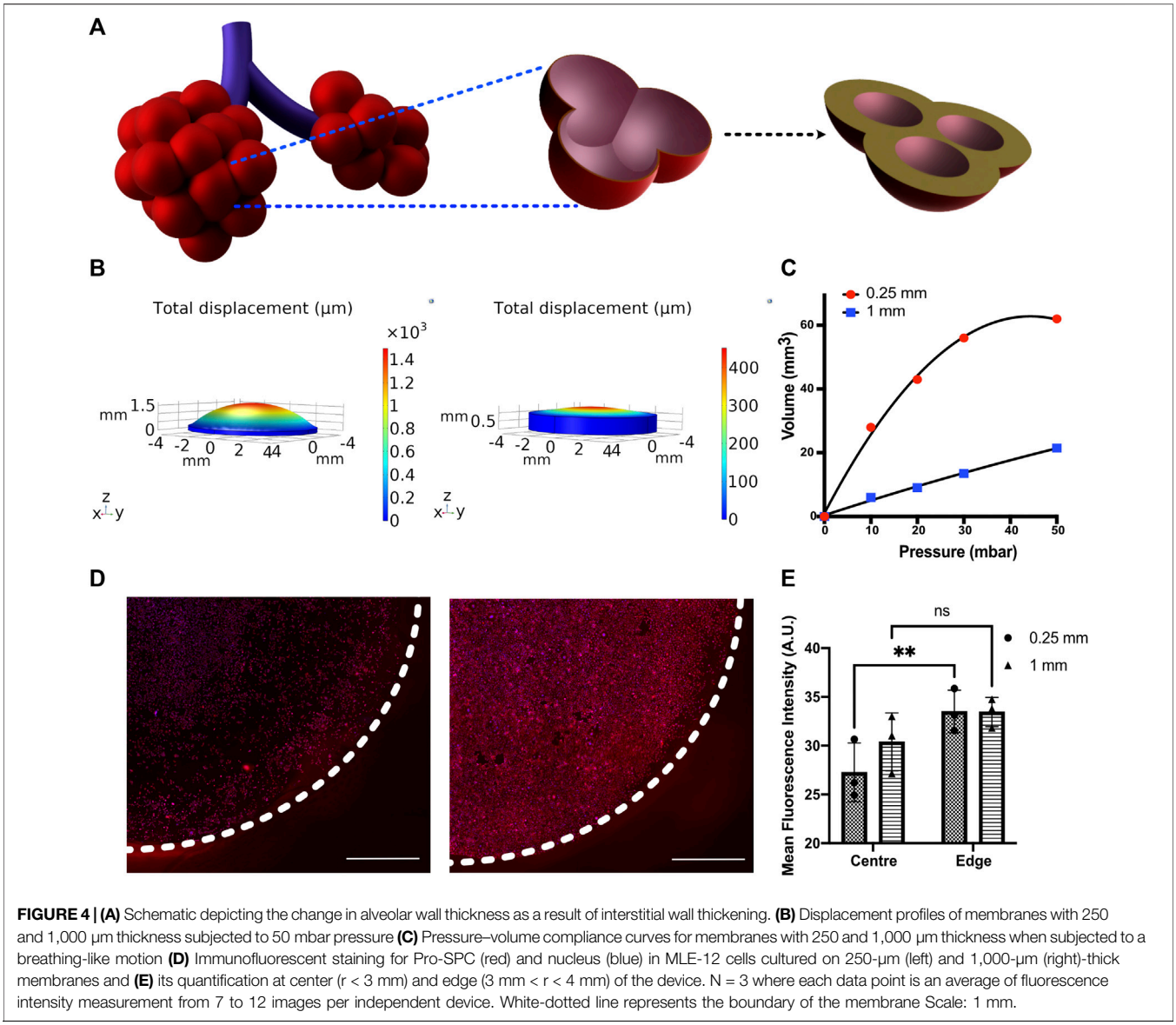

FIGURE 4 | (A) Schematic depicting the change in alveolar wall thickness as a result of interstitial wall thickening. **(B)** Displacement profiles of membranes with 250 and 1,000 μm thickness subjected to 50 mbar pressure **(C)** Pressure–volume compliance curves for membranes with 250 and 1,000 μm thickness when subjected to a breathing-like motion **(D)** Immunofluorescent staining for Pro-SPC (red) and nucleus (blue) in MLE-12 cells cultured on 250-μm (left) and 1,000-μm (right)-thick membranes and **(E)** its quantification at center ($r < 3$ mm) and edge (3 mm $< r < 4$ mm) of the device. N = 3 where each data point is an average of fluorescence intensity measurement from 7 to 12 images per independent device. White-dotted line represents the boundary of the membrane Scale: 1 mm.

Modeling Matrix Compliance

Changes in tissue compliance are a key characteristic of various lung diseases. For example, diseases like pulmonary fibrosis are characterized by alveolar wall thickening due to excessive accumulation of extracellular matrix and an increase in tissue stiffness, resulting in lowered compliance (**Figure 4A**). We have modeled the lowered tissue compliance by increasing the thickness of the membrane from 250 to 1,000 μm. With increasing thickness, the membrane will offer higher resistance to the same pressure profile than a 250-μm membrane, which results in less expansion/contraction and thereby a different breathing pattern (**Supplementary Movie S2**). The pulmonary compliance, which is expressed as the change in lung volume in response to a change in pressure ($\frac{\Delta V}{\Delta P}$), was calculated by computationally measuring the changes in the concave volume of the membrane as a function of pressure during breathing-like movements (**Figures 4B,C**). We chose a membrane thickness of 250 and 1,000 μm as they offer ~2.8 fold difference in volume at peak pressure, which is in the range of volume differences observed between healthy and fibrotic human lungs (Harris, 2005).

We examined the membrane compliance-mediated strain profile for an applied peak pressure of 50 mbar. As expected, the high compliance membrane (i.e., 250-μm membrane) encountered a significantly higher strain heterogeneity than the low compliance membrane (1,000 μm membrane). This is attributed to the lower resistance imposed by the 250 μm membrane, permitting higher deformation (**Figure 4B**). To examine the effect of cell response to the altered matrix compliance, MLE-12 cells were cultured in the device with membranes of thickness 250 μm and 1,000 μm and analyzed after subjecting them to 24 h of breathing-like motion. A significant difference in cell number was observed between the two, with the 1,000-μm membrane that experiences lower strains

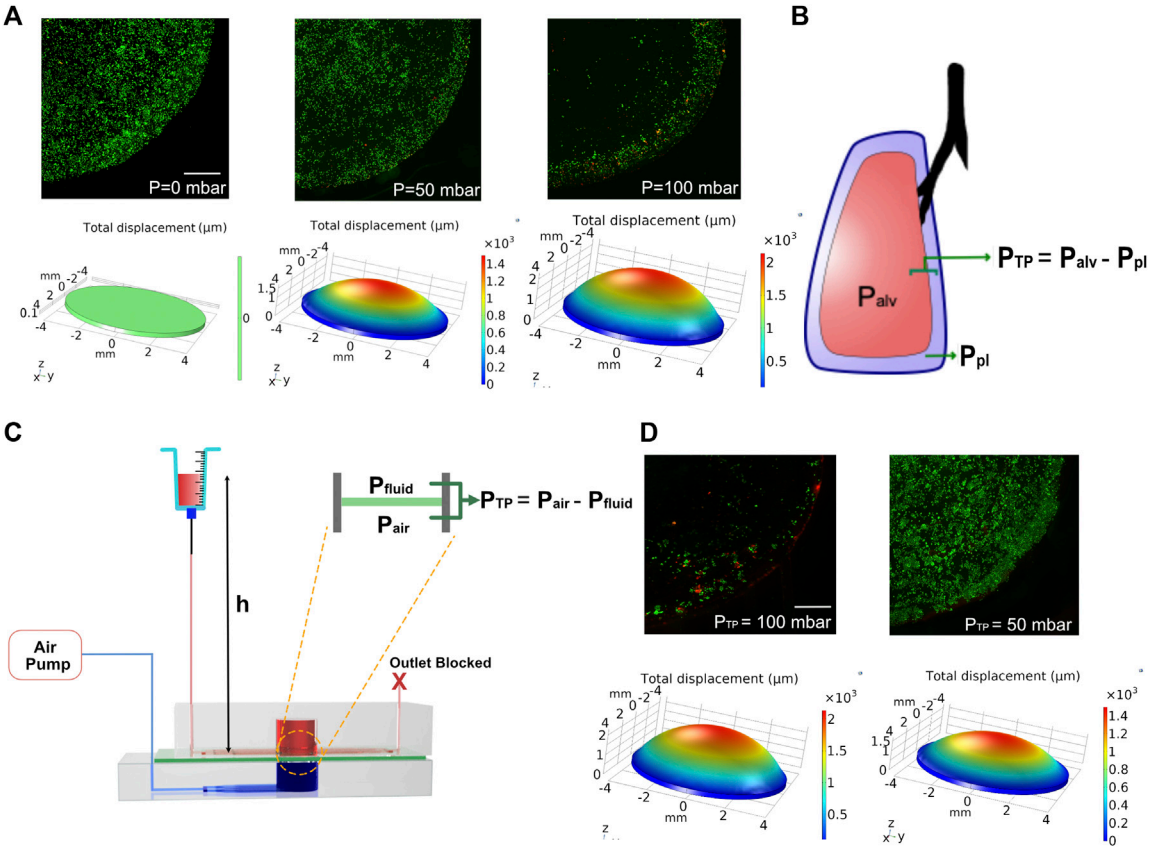

FIGURE 5 | (A) COMSOL modeling and corresponding cell experiments for studying the effect of volutrauma as a result of applied air pressure of 0 mbar, 50, and 100 mbar. Higher air pressure leads to higher concave volume. Viability of MLE-12 cells was determined using live-dead assay. Live cells are stained green while the dead cells are stained red. **(B)** Schematic depicting transpulmonary pressure in a lung. P_{TP}, P_{alv}, and P_{pl} are transpulmonary pressure, air pressure in the alveoli and pleural pressure, respectively. **(C)** Schematic showing the modeling of transpulmonary pressure in the device. P_{air} and P_{fluid} represent the air pressure and hydrostatic pressure in the device. **(D)** COMSOL modeling and corresponding cell experiment for studying barotrauma as a result of applied transpulmonary pressure of 50 and 100 mbar. Scale: 1 mm.

showing the presence of more cells (**Figure 4D**). Furthermore, the strain-dependent spatial variation in cell number was prominently observed on the 250-μm membrane, where the strain varies spatially over a wider range. Specifically, areas with high displacement exhibited lower cell numbers. On the contrary, such regional differences in cell number were not observed in the 1,000-μm membrane. Concomitant with these findings, spatial differences in surfactant production were also observed between the two conditions, as evident from the quantification of pro-SPC immunofluorescence intensity (**Figure 4D**).

Modeling Transpulmonary Pressure and Ventilator-Induced Lung Injury

Ventilator-induced lung injury (VILI) is thought to be closely related to strain heterogeneity in the lung, such that the injury occurs at high-strain regions (Beitler et al., 2016). The described fluidic-pneumatic platform is thus an ideal platform to model VILI. The two most commonly observed ventilator-induced lung injuries are volutrauma and barotrauma, which are closely related and result from alveolar overdistension caused by high tidal volumes and high transpulmonary pressure, respectively. To model volutrauma, the peak pressure of the air pressure waveform was increased from 50 to 100 mbar to generate increased concave volume and overdistension of the membrane. The concave volume for 50 and 100 mbar was 62.46 and 101.926 mm^3, respectively. As evident from the live/dead assay for MLE-12 cell cultures under these conditions, the increased pressure and the associated overdistention caused cell death and/or detachment of the cells (**Figure 5A**). At higher pressures/volumes, the effect of spatial strain heterogeneity on cell number was amplified, as seen in the case of 100 mbar, where more cells were found to be at the edges (3 mm < r < 4 mm) than in the center (r < 3 mm). Among the two pressures imposed, the devices exposed to 50 mbar air pressure had higher cell numbers at the edges than those exposed to 100 mbar. Comparing the experimental observations with the corresponding strain derived from COMSOL simulation suggests that strains above ~18% could be detrimental to the cells.

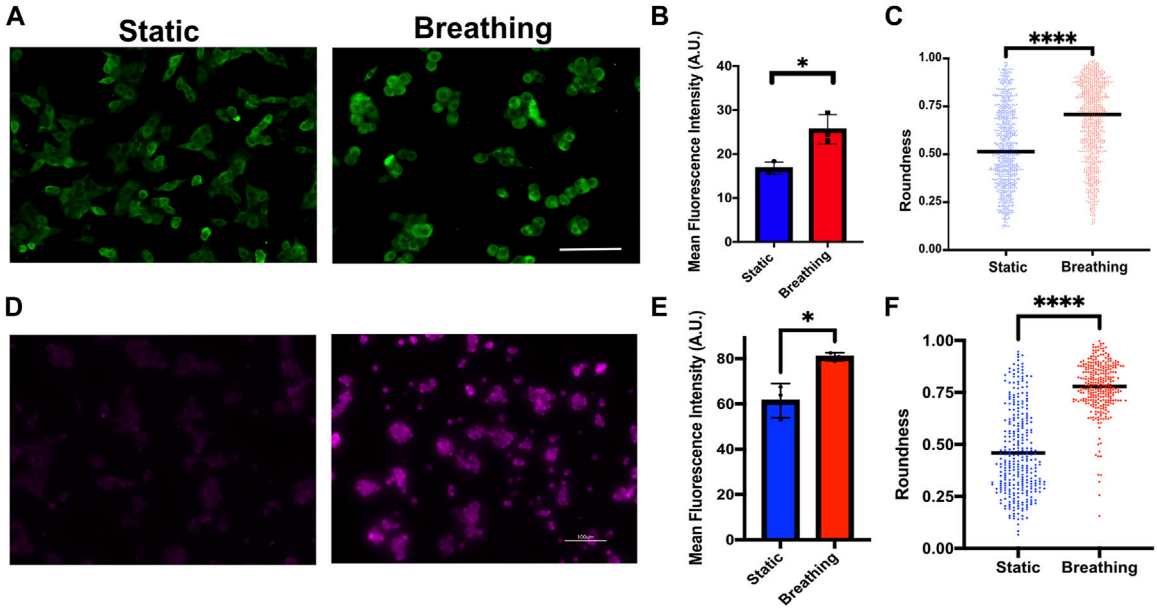

FIGURE 6 | (A) Immunofluorescence staining of Pro-SPC (green) in primary human AT2 cells cultured under static and breathing conditions and **(B)** its quantification. N = 3 where each data point is an average of fluorescence intensity measurement from 8 to 15 images per independent device. **(C)** Quantification of cell morphology in static and breathing conditions. **(D)** Immunofluorescent staining of Pro-SPC (magenta) in iAT2 cells cultured under static and breathing conditions and **(E)** its quantification. N = 3 where each data point is an average of fluorescence intensity measurement from 9 to 13 images per independent device. **(F)** Quantification of cell morphology in static and breathing conditions. Scale: 100 μm.

To model the lung transpulmonary pressure (alveolar air pressure—pleural fluid pressure) (**Figure 5B**), we have made a slight modification to the device to incorporate pleural fluid pressure. This was achieved by blocking the outlet of the media channels and replacing the syringe pump at the inlet with an open-ended syringe whose height can be easily varied (**Figure 5C**). The hydrostatic pressure developed in the chip by increasing the height of the syringe was used to mimic the pleural pressure, which applies a force on the membrane opposite to that of the air pressure, thus allowing us to define the transpulmonary pressure of the device as follows:

$$P_{TP} = P_{air} - P_{fluid} = P_{air} - \rho g h\,, \tag{4}$$

where P_{TP} is the transpulmonary pressure of the device, P_{air} is the applied peak pressure through the air pump, P_{fluid} is the hydrostatic pressure on the fluid side of the device, ρ is the density of the medium, g is the gravitational constant, and h is the height of the syringe above the device.

Leveraging this approach, we tested two conditions of varying transpulmonary pressure (50 and 100 mbar). To generate transpulmonary pressures of 50 mbar and 100 mbar, the syringe height was raised to 50 cm above the device height or kept at device height, respectively, while maintaining the applied air pressure at 100 mbar in both conditions. After 24 h of breathing, devices that were subjected to a transpulmonary pressure of 50 mbar showed minimal cell loss, despite the high air pressure encountered (**Figure 5D**). This is due to the hydrostatic pressure from the medium in the syringe opposing the high air pressure supplied from the air pump, which is akin to pleural fluid pressure opposing the high air pressure in the lung. Together these data highlight the ability of this biomechanically active platform to model VILI and its associated components and how such systems can be used as a predictive tool for determining regions that are predisposed to injury when subjected to mechanical ventilation.

Device Supports Human Alveolar Cell Cultures

Finally, we examined the potential of the platform to support human primary alveolar epithelial type 2 (hAT2) cells and human iPSC-derived alveolar type 2 (iAT2) cells. These cells were grown as alveolospheres in 3D cultures before dissociating them and seeding them onto the devices. Although the device can support long-term cultures of the cells (**Supplementary Figure S7**), hAT2 cells readily differentiate into alveolar type 1 (AT1) cells in 2D cultures and cease surfactant production. Therefore, the studies reported here were performed within 48 h of seeding the cells. The primary hAT2 cells were seeded at a density of 60,000 cells/cm^2 and cultured on collagen type 1-coated membranes. The cells were exposed to breathing-like motion for 24 h and compared against the corresponding static cultures. We observed significantly higher levels of pro SP-C in cells that encountered breathing-like motions (**Figures 6A, B**). Additionally, we also observed distinct differences in cell morphology between the two conditions, wherein the cells that were exposed to breathing-like motions were significantly more rounded than cells in static conditions (**Figure 6C**). The

roundness of the cell, which is defined as $\frac{4*area}{\pi*major\ axis^2}$, was uniform across the device cultured in the static condition and no difference was observed between the center and edge of the membrane. On the contrary, the cells that were exposed to breathing-like motions displayed a significant difference between the edge and the center of the membrane. The cells at the center of the membrane were significantly more rounded than those at the edges, likely due to the spatially heterogeneous strain profile in the two regions (**Supplementary Figure S8**). We observed similar results with iAT2 cells, where cells cultured under breathing-like movements displayed significantly higher expression of pro-SPC as than static cultures (**Figures 6D, E**). As observed with primary hAT2 cells, iAT2 displayed more rounded morphologies in breathing-like conditions as than cells in static conditions (**Figure 6F**), although spatial differences in morphology were not observed in these cells. These results highlight the ability of culturing human alveolar epithelial cells within the device, a more clinically relevant cell source to model tissue-specific functions.

CONCLUSION

This study describes the development of a microfluidic–pneumatic platform consisting of pneumatic and fluidic chambers separated by a thin membrane that supports alveolar epithelial cell culture. The device utilizes out-of-plane stretching of the membrane *via* cyclic air pressurization to mimic strain heterogeneity experienced during alveolar expansion due to breathing, thus allowing us to study the effect of strain heterogeneity within a single device.

Our results show that breathing-like motions and micromechanics in the local environment had a significant effect on cell morphology and critical functions of alveolar epithelial cells, such as surfactant production. We also utilized this platform to model VILI by incorporating transpulmonary pressure. One of the limitations of the current study is that the dimensions of the membrane used are much greater than alveolar size, which can prevent the cells from feeling curvature at a cellular level during stretch (Nossa et al., 2021). The length scale of the alveolar architecture will have a significant effect on the strain heterogeneity generated from breathing-like motions. Recent studies have recapitulated alveolar size and curvature within lung-on-chip systems (Huang et al., 2021; Zamprogno et al., 2021), although further studies are needed to characterize heterogeneous strain and its effect on cells within such systems mimicking the alveolar architecture. While our device incorporates only the epithelial cells in its current configuration, our approach provides a framework for developing more complex systems that capture alveolar micromechanics and spatial strain heterogeneity. The incorporation of other distal lung cells such as fibroblasts within these devices will facilitate the study of progressive changes in lung biomechanics in diseases involving heterotypic cell–cell interactions such as pulmonary fibrosis. Replacing the non-porous PDMS membrane used in this study with porous membranes would allow cell–cell interactions, while also enabling air–liquid interface culture (Huh et al., 2010; Stucki et al., 2018; Doryab et al., 2021a, Doryab et al., 2021b; Huang et al., 2021; Zamprogno et al., 2021). Finally, although we have only modeled positive pleural pressure by raising the height of the syringe, negative pleural pressure can be similarly modeled by lowering the syringe height below the device height and dynamic pleural pressure changes by using an automated system that adjusts the height of the syringe in concert with the air pressure. Apart from providing insights into the role of biomechanics on lung function, these platforms can also potentially serve as important predictive tools to prevent lung injuries or for drug screening (Artzy-Schnirman et al., 2021).

DATA AVAILABILITY STATEMENT

The raw data supporting the conclusions of this article will be made available by the authors, without undue reservation.

AUTHOR CONTRIBUTIONS

SV and VK conceived the idea. VK, SP, and AG performed the experiments and collected the data. JH helped with the synthesis of chemicals. AT helped with human lung cell isolation. All authors wrote and edited the manuscript.

FUNDING

The authors would like to acknowledge support from the Kaganov Research Initiative grant from Duke. The authors would also like to acknowledge support from NIH grant 3UH3TR002142-04S1. Part of this study was performed at the Duke University Shared Materials Instrumentation Facility (SMIF), a member of the North Carolina Research Triangle Nanotechnology Network (RTNN), which is supported by the National Science Foundation (award number ECCS-2025064) as part of the National Nanotechnology Coordinated Infrastructure (NNCI).

ACKNOWLEDGMENTS

We acknowledge the BioRepository and Precision Pathology Center (BRPC), a shared resource of the Duke University School of Medicine and Duke Cancer Institute, for supporting this project under Institutional Review Board oversight. The infrastructure receives support from P30 CA014236 and UM1 CA239755. We would also like to thank Dr. Darrell N. Kotton at Boston University and his laboratory members for providing the iAT2 cells.

SUPPLEMENTARY MATERIAL

The Supplementary Material for this article can be found online at: https://www.frontiersin.org/articles/10.3389/fbioe.2022.848699/full#supplementary-material

REFERENCES

Agrawal, G., Aung, A., and Varghese, S. (2017). Skeletal Muscle-On-A-Chip: an *In Vitro* Model to Evaluate Tissue Formation and Injury. *Lab. Chip* 17, 3447–3461. doi:10.1039/C7LC00512A

Artzy-Schnirman, A., Arber Raviv, S., Doppelt Flikshtain, O., Shklover, J., Korin, N., Gross, A., et al. (2021). Advanced Human-Relevant *In Vitro* Pulmonary Platforms for Respiratory Therapeutics. *Adv. Drug Deliv. Rev.* 176, 113901. doi:10.1016/j.addr.2021.113901

Aung, A., Bhullar, I. S., Theprungsirikul, J., Davey, S. K., Lim, H. L., Chiu, Y.-J., et al. (2016). 3D Cardiac μtissues within a Microfluidic Device with Real-Time Contractile Stress Readout. *Lab. Chip* 16, 153–162. doi:10.1039/C5LC00820D

Aung, A., Kumar, V., Theprungsirikul, J., Davey, S. K., and Varghese, S. (2020). An Engineered Tumor-On-A-Chip Device with Breast Cancer-Immune Cell Interactions for Assessing T-Cell Recruitment. *Cancer Res.* 80, 263–275. doi:10.1158/0008-5472.CAN-19-0342

Beitler, J. R., Malhotra, A., and Thompson, B. T. (2016). Ventilator-induced Lung Injury. *Clin. Chest Med.* 37, 633–646. doi:10.1016/j.ccm.2016.07.004

Benam, K. H., Mazur, M., Choe, Y., Ferrante, T. C., Novak, R., and Ingber, D. E. (2017). Human Lung Small Airway-On-A-Chip Protocol. *Methods Mol. Biol.* 1612, 345–365. doi:10.1007/978-1-4939-7021-6_25

Benam, K. H., Novak, R., Nawroth, J., Hirano-Kobayashi, M., Ferrante, T. C., Choe, Y., et al. (2016a). Matched-Comparative Modeling of Normal and Diseased Human Airway Responses Using a Microengineered Breathing Lung Chip. *Cel Syst.* 3, 456–466. e4. doi:10.1016/j.cels.2016.10.003

Benam, K. H., Villenave, R., Lucchesi, C., Varone, A., Hubeau, C., Lee, H.-H., et al. (2016b). Small Airway-On-A-Chip Enables Analysis of Human Lung Inflammation and Drug Responses *In Vitro*. *Nat. Methods* 13, 151–157. doi:10.1038/nmeth.3697

Bhatia, S. N., and Ingber, D. E. (2014). Microfluidic Organs-On-Chips. *Nat. Biotechnol.* 32, 760–772. doi:10.1038/nbt.2989

Birukov, K. G., Jacobson, J. R., Flores, A. A., Ye, S. Q., Birukova, A. A., Verin, A. D., et al. (2003). Magnitude-dependent Regulation of Pulmonary Endothelial Cell Barrier Function by Cyclic Stretch. *Am. J. Physiology-Lung Cell Mol. Physiol.* 285, L785–L797. doi:10.1152/ajplung.00336.2002

Chen, Z.-l., Chen, Y.-z., and Hu, Z.-y. (2014). A Micromechanical Model for Estimating Alveolar wall Strain in Mechanically Ventilated Edematous Lungs. *J. Appl. Physiol.* 117, 586–592. doi:10.1152/japplphysiol.00072.2014

Doryab, A., Taskin, M. B., Stahlhut, P., Schröppel, A., Orak, S., Voss, C., et al. (2021a). A Bioinspired *In Vitro* Lung Model to Study Particokinetics of Nano-/Microparticles under Cyclic Stretch and Air-Liquid Interface Conditions. *Front. Bioeng. Biotechnol.* 9, 616830. doi:10.3389/fbioe.2021.616830

Doryab, A., Taskin, M. B., Stahlhut, P., Schröppel, A., Wagner, D. E., Groll, J., et al. (2021b). A Biomimetic, Copolymeric Membrane for Cell-Stretch Experiments with Pulmonary Epithelial Cells at the Air-Liquid Interface. *Adv. Funct. Mater.* 31, 2004707. doi:10.1002/adfm.202004707

Elias-Kirma, S., Artzy-Schnirman, A., Das, P., Heller-Algazi, M., Korin, N., and Sznitman, J. (2020). In Situ-Like Aerosol Inhalation Exposure for Cytotoxicity Assessment Using Airway-On-Chips Platforms. *Front. Bioeng. Biotechnol.* 8, 91. doi:10.3389/fbioe.2020.00091

Faffe, D. S., and Zin, W. A. (2009). Lung Parenchymal Mechanics in Health and Disease. *Physiol. Rev.* 89, 759–775. doi:10.1152/physrev.00019.2007

Felder, M., Trueeb, B., Stucki, A. O., Borcard, S., Stucki, J. D., Schnyder, B., et al. (2019). Impaired Wound Healing of Alveolar Lung Epithelial Cells in a Breathing Lung-On-A-Chip. *Front. Bioeng. Biotechnol.* 7, 3. doi:10.3389/fbioe.2019.00003

Guenat, O. T., and Berthiaume, F. (2018). Incorporating Mechanical Strain in Organs-On-A-Chip: Lung and Skin. *Biomicrofluidics* 12, 042207. doi:10.1063/1.5024895

Harris, R. S. (2005). Pressure-volume Curves of the Respiratory System. *Respir. Care* 50 (1), 78–79.

Hsia, C. C. W., Hyde, D. M., and Weibel, E. R. (2016). Lung Structure and the Intrinsic Challenges of Gas Exchange. *Compr. Physiol.* 6, 827–895. doi:10.1002/cphy.c150028

Huang, D., Liu, T., Liao, J., Maharjan, S., Xie, X., Pérez, M., et al. (2021). Reversed-engineered Human Alveolar Lung-On-A-Chip Model. *Proc. Natl. Acad. Sci. USA* 118, e2016146118. doi:10.1073/pnas.2016146118

Huh, D., Leslie, D. C., Matthews, B. D., Fraser, J. P., Jurek, S., Hamilton, G. A., et al. (2012). A Human Disease Model of Drug Toxicity-Induced Pulmonary Edema in a Lung-On-A-Chip Microdevice. *Sci. Transl. Med.* 4, 159ra147 LP. doi:10.1126/scitranslmed.3004249

Huh, D., Matthews, B. D., Mammoto, A., Montoya-Zavala, M., Hsin, H. Y., and Ingber, D. E. (2010). Reconstituting Organ-Level Lung Functions on a Chip. *Science* 328, 1662 LP–1668. doi:10.1126/science.1188302

Hurtado, D. E., Erranz, B., Lillo, F., Sarabia-Vallejos, M., Iturrieta, P., Morales, F., et al. (2020). Progression of Regional Lung Strain and Heterogeneity in Lung Injury: Assessing the Evolution under Spontaneous Breathing and Mechanical Ventilation. *Ann. Intensive Care* 10, 107. doi:10.1186/s13613-020-00725-0

Ingenito, E. P., Tsai, L. W., Majumdar, A., and Suki, B. (2005). On the Role of Surface Tension in the Pathophysiology of Emphysema. *Am. J. Respir. Crit. Care Med.* 171, 300–304. doi:10.1164/rccm.200406-770PP

Ishahak, M., Hill, J., Amin, Q., Wubker, L., Hernandez, A., Mitrofanova, A., et al. (2020). Modular Microphysiological System for Modeling of Biologic Barrier Function. *Front. Bioeng. Biotechnol.* 8, 581163. doi:10.3389/fbioe.2020.581163

Jacob, A., Vedaie, M., Roberts, D. A., Thomas, D. C., Villacorta-Martin, C., Alysandratos, K.-D., et al. (2019). Derivation of Self-Renewing Lung Alveolar Epithelial Type II Cells from Human Pluripotent Stem Cells. *Nat. Protoc.* 14, 3303–3332. doi:10.1038/s41596-019-0220-0

Jain, A., Barrile, R., van der Meer, A., Mammoto, A., Mammoto, T., De Ceunynck, K., et al. (2018). Primary Human Lung Alveolus-On-A-Chip Model of Intravascular Thrombosis for Assessment of Therapeutics. *Clin. Pharmacol. Ther.* 103, 332–340. doi:10.1002/cpt.742

Jimenez-Valdes, R. J., Can, U. I., Niemeyer, B. F., and Benam, K. H. (2020). Where We Stand: Lung Organotypic Living Systems that Emulate Human-Relevant Host-Environment/Pathogen Interactions. *Front. Bioeng. Biotechnol.* 8, 989. doi:10.3389/fbioe.2020.00989

Katsura, H., Sontake, V., Tata, A., Kobayashi, Y., Edwards, C. E., Heaton, B. E., et al. (2020). Human Lung Stem Cell-Based Alveolospheres Provide Insights into SARS-CoV-2-Mediated Interferon Responses and Pneumocyte Dysfunction. *Cell Stem Cell* 27, 890–904. e8. doi:10.1016/j.stem.2020.10.005

Khalid, M. A. U., Kim, Y. S., Ali, M., Lee, B. G., Cho, Y.-J., and Choi, K. H. (2020). A Lung Cancer-On-Chip Platform with Integrated Biosensors for Physiological Monitoring and Toxicity Assessment. *Biochem. Eng. J.* 155, 107469. doi:10.1016/j.bej.2019.107469

Knudsen, L., and Ochs, M. (2018). The Micromechanics of Lung Alveoli: Structure and Function of Surfactant and Tissue Components. *Histochem. Cel Biol.* 150, 661–676. doi:10.1007/s00418-018-1747-9

Kumar, V., and Varghese, S. (2019). *Ex Vivo* Tumor-on-a-Chip Platforms to Study Intercellular Interactions within the Tumor Microenvironment. *Adv. Healthc. Mater.* 8, 1801198. doi:10.1002/adhm.201801198

Low, L. A., Mummery, C., Berridge, B. R., Austin, C. P., and Tagle, D. A. (2021). Organs-on-chips: into the Next Decade. *Nat. Rev. Drug Discov.* 20, 345–361. doi:10.1038/s41573-020-0079-3

Martinez, F., Lewis, J., Copland, I., Engelberts, D., Kavanagh, B. P., Post, M., et al. (2004). Mechanical Ventilation Effect on Surfactant Content, Function, and Lung Compliance in the Newborn Rat. *Pediatr. Res.* 56, 19–25. doi:10.1203/01.PDR.0000128980.82797.29

Mejías, J. C., Nelson, M. R., Liseth, O., and Roy, K. (2020). A 96-well Format Microvascularized Human Lung-On-A-Chip Platform for Microphysiological Modeling of Fibrotic Diseases. *Lab. Chip* 20, 3601–3611. doi:10.1039/D0LC00644K

Nawroth, J. C., Lucchesi, C., Cheng, D., Shukla, A., Ngyuen, J., Shroff, T., et al. (2020). A Microengineered Airway Lung Chip Models Key Features of Viral-Induced Exacerbation of Asthma. *Am. J. Respir. Cel Mol. Biol.* 63, 591–600. doi:10.1165/rcmb.2020-0010MA

Neidlinger-Wilke, C., Grood, E., Claes, L., and Brand, R. (2002). Fibroblast Orientation to Stretch Begins within Three Hours. *J. Orthop. Res.* 20, 953–956. doi:10.1016/S0736-0266(02)00024-4

Nossa, R., Costa, J., Cacopardo, L., and Ahluwalia, A. (2021). Breathing *In Vitro*: Designs and Applications of Engineered Lung Models. *J. Tissue Eng.* 12, 204173142110086. doi:10.1177/20417314211008696

Park, J. Y., Ryu, H., Lee, B., Ha, D.-H., Ahn, M., Kim, S., et al. (2018). Development of a Functional Airway-On-A-Chip by 3D Cell Printing. *Biofabrication* 11, 015002. doi:10.1088/1758-5090/aae545

Perlman, C. E., Lederer, D. J., and Bhattacharya, J. (2011). Micromechanics of Alveolar Edema. *Am. J. Respir. Cel Mol. Biol.* 44, 34–39. doi:10.1165/rcmb.2009-0005OC

Plantier, L., Cazes, A., Dinh-Xuan, A.-T., Bancal, C., Marchand-Adam, S., and Crestani, B. (2018). Physiology of the Lung in Idiopathic Pulmonary Fibrosis. *Eur. Respir. Rev.* 27, 170062. doi:10.1183/16000617.0062-2017

Püspöki, Z., Storath, M., Sage, D., and Unser, M. (2016). Transforms and Operators for Directional Bioimage Analysis: A Survey. *Adv. Anat. Embryol. Cel Biol.* 219, 69–93. doi:10.1007/978-3-319-28549-8_3

Rivlin, R. S. (1948). Large Elastic Deformations of Isotropic Materials IV. Further Developments of the General Theory. *Phil. Trans. R. Soc. Lond. A.* 241, 379–397. doi:10.1098/rsta.1948.0024

Roan, E., and Waters, C. M. (2011). What Do We Know about Mechanical Strain in Lung Alveoli? *Am. J. Physiology-Lung Cell Mol. Physiol.* 301, L625–L635. doi:10.1152/ajplung.00105.2011

Sanchez-Esteban, J., Tsai, S.-W., Sang, J., Qin, J., Torday, J. S., and Rubin, L. P. (1998). Effects of Mechanical Forces on Lung-specific Gene Expression. *Am. J. Med. Sci.* 316, 200–204. doi:10.1097/00000441-199809000-00009

Shrestha, J., Razavi Bazaz, S., Aboulkheyr Es, H., Yaghobian Azari, D., Thierry, B., Ebrahimi Warkiani, M., et al. (2020). Lung-on-a-chip: the Future of Respiratory Disease Models and Pharmacological Studies. *Crit. Rev. Biotechnol.* 40, 213–230. doi:10.1080/07388551.2019.1710458

Shrestha, J., Ryan, S. T., Mills, O., Zhand, S., Razavi Bazaz, S., Hansbro, P. M., et al. (2021). A 3D-Printed Microfluidic Platform for Simulating the Effects of CPAP on the Nasal Epithelium. *Biofabrication* 13, 035028. doi:10.1088/1758-5090/abe4c1

Smith, B. J. (2016). Strain Heterogeneity in the Injured Lung: Cause or Consequence? *J. Appl. Physiol.* 121, 1363–1364. doi:10.1152/japplphysiol.00818.2016

Stucki, A. O., Stucki, J. D., Hall, S. R. R., Felder, M., Mermoud, Y., Schmid, R. A., et al. (2015). A Lung-On-A-Chip Array with an Integrated Bio-Inspired Respiration Mechanism. *Lab. Chip* 15, 1302–1310. doi:10.1039/C4LC01252F

Stucki, J. D., Hobi, N., Galimov, A., Stucki, A. O., Schneider-Daum, N., Lehr, C.-M., et al. (2018). Medium Throughput Breathing Human Primary Cell Alveolus-On-Chip Model. *Sci. Rep.* 8, 14359. doi:10.1038/s41598-018-32523-x

Sznitman, J. (2021). Revisiting Airflow and Aerosol Transport Phenomena in the Deep Lungs with Microfluidics. *Chem. Rev.* doi:10.1021/acs.chemrev.1c00621

Torday, J. S., and Rehan, V. K. (2002). Stretch-stimulated Surfactant Synthesis Is Coordinated by the Paracrine Actions of PTHrP and Leptin. *Am. J. Physiology-Lung Cell Mol. Physiol.* 283, L130–L135. doi:10.1152/ajplung.00380.2001

Winkler, M., Simon, M. G., Vu, T., Gartner, T. L., Jester, J. V., Lee, A. P., et al. (2014). A Microfabricated, Optically Accessible Device to Study the Effects of Mechanical Cues on Collagen Fiber Organization. *Biomed. Microdevices* 16, 255–267. doi:10.1007/s10544-013-9829-x

Yoon, S.-H., Reyes-Ortiz, V., Kim, K.-H., Seo, Y. H., and Mofrad, M. R. K. (2010). Analysis of Circular PDMS Microballoons with Ultralarge Deflection for MEMS Design. *J. Microelectromech. Syst.* 19, 854–864. doi:10.1109/JMEMS.2010.2049984

Zacharias, W. J., Frank, D. B., Zepp, J. A., Morley, M. P., Alkhaleel, F. A., Kong, J., et al. (2018). Regeneration of the Lung Alveolus by an Evolutionarily Conserved Epithelial Progenitor. *Nature* 555, 251–255. doi:10.1038/nature25786

Zamprogno, P., Wüthrich, S., Achenbach, S., Thoma, G., Stucki, J. D., Hobi, N., et al. (2021). Second-generation Lung-On-A-Chip with an Array of Stretchable Alveoli Made with a Biological Membrane. *Commun. Biol.* 4, 168. doi:10.1038/s42003-021-01695-0

Conflict of Interest: The authors declare that the research was conducted in the absence of any commercial or financial relationships that could be construed as a potential conflict of interest.

Publisher's Note: All claims expressed in this article are solely those of the authors and do not necessarily represent those of their affiliated organizations, or those of the publisher, the editors, and the reviewers. Any product that may be evaluated in this article, or claim that may be made by its manufacturer, is not guaranteed or endorsed by the publisher.

frontiers in Bioengineering and Biotechnology

ORIGINAL RESEARCH
published: 25 March 2022
doi: 10.3389/fbioe.2022.811942

Optimization and Validation of a Custom-Designed Perfusion Bioreactor for Bone Tissue Engineering: Flow Assessment and Optimal Culture Environmental Conditions

Shuntaro Yamada[1]*, *Mohammed A. Yassin*[1], *Thomas Schwarz*[2], *Kamal Mustafa*[1] and *Jan Hansmann*[2,3,4]*

[1]Centre of Translational Oral Research, Tissue Engineering Group, Department of Clinical Dentistry, University of Bergen, Bergen, Norway, [2]Translational Centre Regenerative Therapies, Fraunhofer Institute for Silicate Research ISC, Würzburg, Germany, [3]Chair of Tissue Engineering and Regenerative Medicine, University Hospital Würzburg, Würzburg, Germany, [4]Department Electrical Engineering, University of Applied Sciences Würzburg-Schweinfurt, Würzburg, Germany

OPEN ACCESS

Edited by:
Dimitrios Stamatialis,
University of Twente, Netherlands

Reviewed by:
Sinan Guven,
Dokuz Eylul University, Turkey
Feihu Zhao,
Swansea University, United Kingdom

***Correspondence:**
Shuntaro Yamada
shuntaro.yamada@uib.no
Jan Hansmann
jan.hansmann@fhws.de

Specialty section:
This article was submitted to Tissue Engineering and Regenerative Medicine, a section of the journal Frontiers in Bioengineering and Biotechnology

Received: 09 November 2021
Accepted: 07 March 2022
Published: 25 March 2022

Citation:
Yamada S, Yassin MA, Schwarz T, Mustafa K and Hansmann J (2022) Optimization and Validation of a Custom-Designed Perfusion Bioreactor for Bone Tissue Engineering: Flow Assessment and Optimal Culture Environmental Conditions. Front. Bioeng. Biotechnol. 10:811942. doi: 10.3389/fbioe.2022.811942

Various perfusion bioreactor systems have been designed to improve cell culture with three-dimensional porous scaffolds, and there is some evidence that fluid force improves the osteogenic commitment of the progenitors. However, because of the unique design concept and operational configuration of each study, the experimental setups of perfusion bioreactor systems are not always compatible with other systems. To reconcile results from different systems, the thorough optimization and validation of experimental configuration are required in each system. In this study, optimal experimental conditions for a perfusion bioreactor were explored in three steps. First, an *in silico* modeling was performed using a scaffold geometry obtained by microCT and an expedient geometry parameterized with porosity and permeability to assess the accuracy of calculated fluid shear stress and computational time. Then, environmental factors for cell culture were optimized, including the volume of the medium, bubble suppression, and medium evaporation. Further, by combining the findings, it was possible to determine the optimal flow rate at which cell growth was supported while osteogenic differentiation was triggered. Here, we demonstrated that fluid shear stress up to 15 mPa was sufficient to induce osteogenesis, but cell growth was severely impacted by the volume of perfused medium, the presence of air bubbles, and medium evaporation, all of which are common concerns in perfusion bioreactor systems. This study emphasizes the necessity of optimization of experimental variables, which may often be underreported or overlooked, and indicates steps which can be taken to address issues common to perfusion bioreactors for bone tissue engineering.

Keywords: perfusion, bioreactor, dynamic cell culture, bone tissue engineering, regenerative medicine, mesenchymal stem cell, shear stress

INTRODUCTION

Critical sized bony defects have only a limited capacity for spontaneous healing. Repair requires extensive surgical intervention using autografts, allografts, xenografts or alloplastic materials (Roddy et al., 2018). However, none of the conventional clinical approaches has achieved the complete repair of native anatomy and function. Tissue engineering approaches, where multipotent cells are combined with scaffold biomaterials to regenerate bone, first emerged in the mid-1980s. Since then, there have been numerous *in vitro* and *in vivo* studies and by 2020, around 150 clinical trials of cell-based bone regenerative therapies had been registered by the U.S. National Library of Medicine (Amini et al., 2012). Mesenchymal stem/stromal cells (MCS) are among the most widely used sources for bone regeneration. MSC are abundantly available from various mesenchymal tissues such as bone marrow, adipose tissue, umbilical cord, and dental tissues (Marquez-Curtis et al., 2015). For scaffolding, three-dimensional (3D) porous scaffolds are preferred, as they mimic the structure of cancellous bone, stimulating MSC towards the osteogenic lineage (Zhang et al., 2018).

A major disadvantage of 3D scaffolds is the low passive diffusion-based mass transport of nutrients and gases, which leads to uneven cell growth within the scaffolds (Rouwkema et al., 2009). To overcome this disparity, various perfusion bioreactor systems have been developed specifically for bone regeneration (Rauh et al., 2011; Yeatts et al., 2013). Perfusion bioreactors provide uniform nutrient supply within the scaffolds while removing waste products, improving cell wellbeing (Rauh et al., 2011). Furthermore, attempts have been made to induce/promote osteogenesis by controlling the mechanical stimulus exerted by fluid flow (Gaspar et al., 2012). In fact, in recent years an increasing number of studies have reported the positive effect of fluid flow on MSC growth and osteogenesis. However, inconsistent results owing to system variation impede a clear understanding of biological responses to the stimuli. This is not only because experimental configuration such as bioreactor design and flow characteristics varies significantly among systems, but also because 3D dynamic cell culture involves various technical challenges which are not encountered in conventional cell culture protocols (Mandenius and Mandenius, 2016). Consequently, each system is to be operated under specific conditions. This is determined by a series of optimization steps: estimation of the magnitude of mechanical stimuli, conditioning of the culture environment and determination of the optimal flow rate for osteogenic differentiation. Nevertheless, environmental conditions applied in dynamic systems seem to be underreported. Indeed, a general caution has recently been issued, noting that a majority of cell culture studies omitted to monitor, control, or report environmental factors such as temperature, gas concentration and medium conditions (Klein et al., 2021).

The first step would be to estimate a promising flow rate by evaluating mechanical stimuli exerted by fluid flow. In the case where a porous geometry is assumed to be isotropic throughout the scaffold, shear stress can be corelated by the Kozeny-Carman equation (Arramon and Nauman, 2001; Daish et al., 2017). However, the equation requires an empirical constant which depends on the geometry of pores, and it may not be suitable for anisotropic and multiphasic porous scaffolds (Truscello et al., 2012). The estimation of fluidics can be alternatively performed by *in silico* modeling, where the flow of culture medium is computationally reproduced in accordance with imported geometry and assigned parameters. In bone tissue engineering, using a scaffold with highly irregular pore geometry and distribution, the high computational cost is a barrier to precise simulation (Zhao et al., 2019). Ideally, a full scaffold geometry acquired by microcomputed tomography (microCT) should be used, but it may not always be feasible because of high computational demand (Jungreuthmayer et al., 2009; Acosta Santamaría et al., 2013). Alternatively, simplified geometry with porous parameters may be employed as a porous medium domain, despite lack of consensus as to its accuracy and predictive power (Campos Marin and Lacroix, 2015). The next step would be to optimize the culture environment. Optimization and validation of each environmental factor are required for successful operation. In conventional culture this may not be given close attention. For example, a perfusion bioreactor often requires a large volume of culture medium to establish continuous flow. The optimal amount depends on the number of vital cells on the scaffolds, and deficiency or excess may cause inhibition of cell growth and paracrine signaling (Schreivogel et al., 2019). Other environmental factors such as temperature, humidity, and static pressure alter MSC behavior, and this needs to be considered in designing systems. A stand-alone bioreactor, namely a bioreactor designed not to be used in a conventional incubator, often consists of complex electric appliances such as various sensors, heating system, gas ejectors, electric outlets and conductors in addition to pump systems (Schuerlein et al., 2017). The installation of these appliances is essential to condition the atmosphere, but highly humid environment is likely to be incompatible with such electrical systems (Rauh et al., 2011; Lane et al., 2014). A major technical challenge is the suppression of air bubble formation, which disturbs fluid flow and damages cells (Sobolewski et al., 2012; Walls et al., 2017; Walsh et al., 2017). Fluidic systems for bone tissue engineering tend to fulfil conditions for bubble formation: highly porous geometry, hydrophobic biomaterials, surfactant in the culture medium, and medium agitation (Sung and Shuler, 2009; Piola et al., 2013; Yu et al., 2017a; Yamada et al., 2021a). All these factors influence cell behavior, and therefore represent uncertainties if not addressed and correctly controlled. Once optimization is completed, the effect of fluid flow on cell behavior may be tested.

The successful operation of perfusion bioreactors for tissue engineering depends largely on the identification and validation of proper culture conditions. Unfortunately, despite an increasing number of studies on 3D dynamic cell culture in bone tissue engineering, comparison of study results is difficult, because each bioreactor system is operated with a unique experimental configuration. Nevertheless, most experimental issues which arise are common to all perfusion bioreactors.

To date, the literature in this field reveals the need for thorough optimization of experimental variables in a perfusion bioreactor. There is also a need to identify and address specific challenges which may arise in using a perfusion bioreactor for 3D dynamic culture. It is important that methods developed to address these issues are readily transferable for application in different bioreactors and can thus serve as general guidelines for designing and setting up flow bioreactor systems. The aim of this study was therefore to identify and optimize experimental variables in a laminar flow bioreactor with an integrated incubation system, by exploring basic cell culture conditions which can be adjusted towards stable dynamic cell culture. The study covers validation of the method applied to estimate fluid effects, the optimization of environmental factors such as medium volume, humidity control, air bubble suppression, and the identification of optimal flow rate. The study was based on rat bone marrow-derived mesenchymal stem/stromal cells (rBMSC), seeded onto 3D polymeric scaffolds for osteogenic differentiation.

MATERIALS AND METHODS

rBMSC Isolation and Expansion

The study was approved by the Norwegian Animal Research Authority (local approval number 20146866) and conducted in compliance with the European Convention for the Protection of Vertebrates used for Scientific Purposes.

rBMSC were isolated as previously described (Yassin et al., 2015). rBMSC from the femurs of Lewis rats were maintained in growth medium consisting of alpha minimum essential medium (α-MEM: 22571-020, Gibco™, United States) supplemented with 1% penicillin and streptomycin (SV30010, HyClone, United States) and 10% fetal bovine serum (FBS: 10270-106, Gibco™, United States) at 37°C in 5% CO_2 humidified atmosphere. The characterization of rBMSC including the expression of putative MSC markers and the ability of multi-lineage differentiation was previously described (Yamada et al., 2021a). rBMSC from the third to fifth passages were used in the study.

3D Porous Scaffold Preparation and Cell Seeding

3D microporous scaffolds (diameter 12 mm, thickness 1.2 mm) were produced by a solvent casting technique as previously described (Odelius et al., 2005; Yamada et al., 2021b). Briefly, a solution of Poly (L-lactide-co-trimethylene carbonate) (LTMC) (RESOMER. LT706 S, Evonik) in chloroform was mixed with sodium chloride (NaCl) particles with a diameter of 90–600 μM in Petri dishes and left with the lids on to allow gradual evaporation of the chloroform. After complete evaporation, the dried constructs were punched into 12 mm pieces and washed thoroughly in distilled water to remove the remaining NaCl particles. The scaffolds were then placed in 48-well plates and exposed to ultraviolet radiation for 2 h, following to washing with 70% ethanol for sterilization. Prior to cell seeding, the scaffolds were pre-wetted in the growth medium for 24 h. 250,000 rBMSC were seeded per scaffold and incubated for 72 h before being transferred into the culture chamber of the bioreactor.

MicroCT Scanning and Structural Analysis of the Porous Scaffolds

The microstructure of the scaffolds was scanned by microcomputed tomography (microCT) using a voltage of 40 kV and a current of 250 mA at 10 μm spatial resolution (SkyScan 1172: Bruker-MicroCT, Kontich, Belgium). The acquired geometry was exported in *.stl* file for further *in silico* modeling.

Configuration of the Laminar Flow Bioreactor

The laminar flow bioreactor was developed in the Fraunhofer Institute for Silicate Research. It comprises peristaltic pumps and an integrated incubator system, including a heating pad, electric fans, hydropressure sensors, a CO_2 sensor, and a temperature sensor (**Figure 1A**). The standard components for dynamic cell culture under perfusion are demonstrated in **Figure 1B**. The culture chamber, made of stainless steel, was designed to accommodate 3D scaffolds with a maximum diameter of 12 mm. The following sections present the experimental design in detail, including descriptions of specific settings (i.e., tubing, position of medium reservoir, scaffold placement). The perfusion experiment was conducted at 37°C in 5% CO_2 atmosphere.

In silico Modeling for Fluid Dynamics Simulation

In order to make the microCT data applicable in the simulation, a reference geometry was segmented from the *.stl* file, and a hypothetical whole-scaffold geometry was then reconstructed computationally, by assuming that the segmented geometry represented the microstructure of the scaffold. Precisely, the one fourth of the scanned geometry was repaired and then mirrored to reconstruct a disk-shaped geometry due to a substantial computational burden. Scanning defects such as self-intersections, paper-thin regions, too-narrow edges (i.e., edges smaller than defined minimum element size as mentioned below), and holes were repaired using computer-aided design (CAD) software, MeshLab ver. 2021.05 (Cignoni et al., 2008), Blender ver. 2.92 (Blender, 2021), and Rhino 7 (Robert McNeel & Associates, United States). *In silico* modeling was undertaken in the COMSOL Multiphysics version 5.6 (COMSOL AB, Sweden). Briefly, a simplified geometry was designed with a cylindrical disc with a diameter of 12 mm, which was defined as a porous domain. For the porous domain, porosity was measured by microCT analysis, and permeability was obtained as described previously by measuring pressure drop over cylindrical scaffolds and applying the Darcy's law (Ramani-Mohan et al., 2018). The microCT geometry was imported as a solid object. A domain comprising a stack of six scaffolds was then placed in a cylindrical

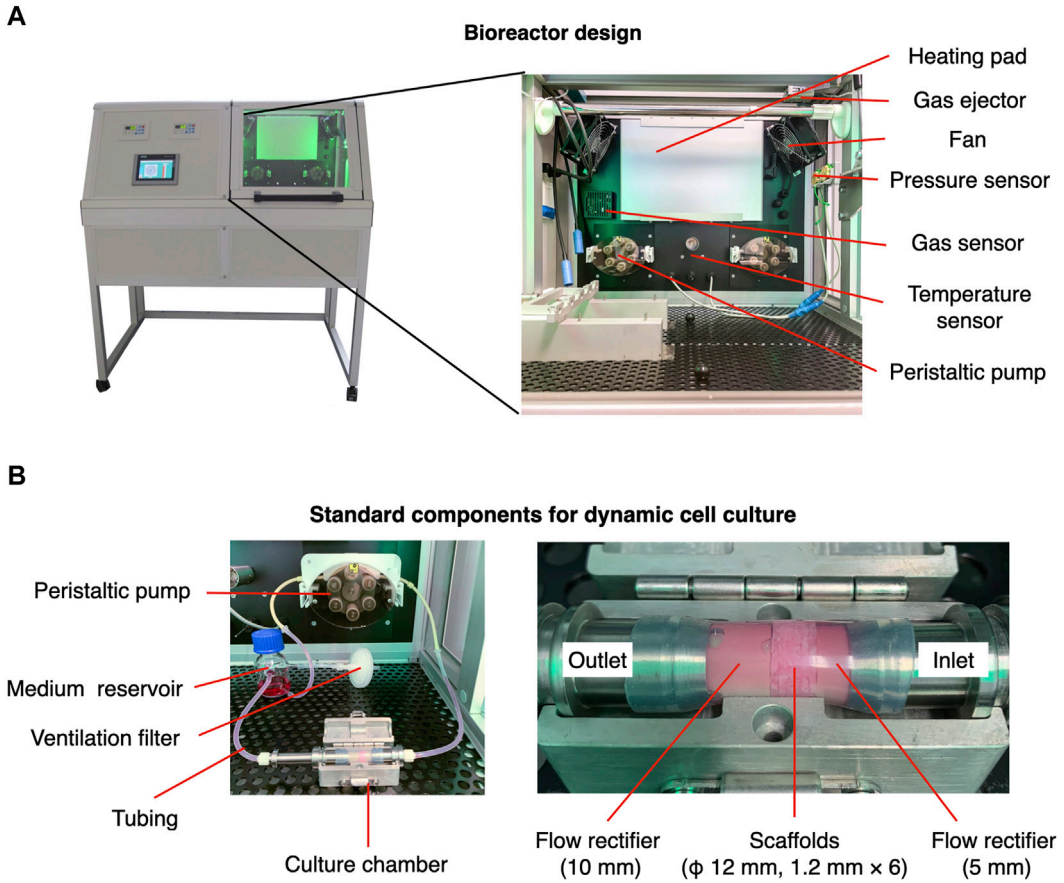

FIGURE 1 | Configuration of perfusion bioreactor used in the present study. **(A)** The bioreactor comprises a controlling/monitoring part (left) and an integrated incubator part (right). The integrated part is designed to maintain the desired temperature and gas concentration for cell culture. **(B)** A medium reservoir and culture chamber where scaffolds are placed are connected by silicon tubes. The flow velocity is controlled by a peristaltic pump.

fluid path with a diameter of 12.5 mm, where fully developed flow at either 0.8, 1.6, or 3.2 ml/min was prescribed. It was assumed that fluid flow within scaffolds could be laminar flow because of extremely low flow velocity. Assigned fluid was defined as incompressible Newtonian fluid with the viscosity of water at 37°C (i.e., 0.6913 mPa·s) and density 997 kg/m^3. Non-slip boundary conditions were enforced at the solid walls. For computation, the geometries were then meshed into linier tetrahedron elements using a physics-controlled mesh module with prescribed mesh resolution "Finer" where the maximum element size, minimum element size, maximum element growth rate, curvature factor, and resolution of narrow regions were defined as 0.429 mm, 0.0464 mm, 1.1, 0.4, 0.9, respectively. Finally, computation was performed by the stationary solver.

A laminar flow was defined by the Navier-Stokes equation as follows:

$$\rho(u.\nabla)u = \nabla.[-pI + K] + F$$
$$\rho\nabla.u = 0$$
$$K = \mu\left(\nabla u + (\nabla u)^T\right)$$

where ρ, u, I, p, μ, and F, denote fluid density, fluid velocity, identity vector, pressure, dynamic viscosity, and volume force. For the porous domain used in the simplified geometry, the Darcy flow model was used with Darcy-Brinkman equation as follows:

$$\frac{1}{\varepsilon_p}\rho(u2.\nabla)u\frac{1}{\varepsilon_p} = \nabla.[-pI + K] - \left(\mu\kappa^{-1} + \frac{Q_m}{\varepsilon_p^2}\right)u + F$$
$$\rho\nabla.u = Qm$$
$$K = \mu\frac{1}{\varepsilon_p}\left(\nabla u + (\nabla u)^T\right) - \frac{2}{3}\mu\frac{1}{\varepsilon_p}(\nabla.u)\mathrm{I}$$
$$F = 0,\ Qm = 0$$

where ε_p, κ, and Qm denote porosity, permeability, and mass souse. The effect of gravity was not included for simplification. It was modeled by assuming zero mass source and zero volume force due to low fluid viscosity and Reynolds number below 1 (data not shown). Shear stress τ was then computed as previously described using the equation (Egger et al., 2017):

$$\tau = \mu\frac{\partial\mu}{\partial n}$$

where n indicates the x-, y-, and *z*-direction. Shear stress was presented using volume and surface area in the simplified and in the microCT approach, respectively.

Quantification of Double Strand DNA

Samples were collected in 0.1% Triton X-100, and the cell lysate was obtained by three freeze-thaw cycles. Double strand DNA (dsDNA) was quantified using Quant-iT™ PicoGreen™ dsDNA Assay Kit (P7589, Thermo Fisher Scientific, United States) in accordance with the manufacturer's protocol. The fluorescence intensity was measured at Ex/Em = 480/520 nm using a microplate reader (VLBL00D0, ThermoFisher Scientific, Finland).

Quantification of Alkaline Phosphatase Activity

The cell lysate, which was obtained by freeze-thaw cycles, was incubated with P-nitrophenyl phosphate (20-106, Sigma-Aldrich, Germany) for 15 min at room temperature. Absorbance was measured at 405 nm using the microplate reader. ALP activity was normalized by the amount of dsDNA in the samples.

Immunofluorescent Staining and Confocal Microscopy

Samples were fixed in 4% paraformaldehyde (PFA) for 15 min at room temperature and permeabilized in 0.1% Triton X-100 in PBS (PBSTx) for 15 min at room temperature. Nonspecific binding was blocked with 20% goat serum (G6767, Sigma, United States) in 0.1% Tween-20 in PBS (PBSTw) for 60 min at room temperature. The samples were then incubated with anti-Ki67 monoclonal antibody conjugated with eFluor 660 (50-5698-82, Thermo Fisher Scientific, United States) overnight at 4°C. Filamentous actin (F-actin) and nuclei were counterstained with Phalloidin Alexa Fluor 488 (1:250; A12379, Thermo Fisher Scientific, United States) and 4′,6-diamidino-2-phenylindole (DAPI, 1:5000; 62247, Thermo Fisher Scientific, United States) for 60 min at room temperature, followed by washing five times, for 5 min each, with PBSTw. The samples were mounted in ProLong™ Gold antifade reagent (P36939; Thermo Fisher Scientific, United States). Z-Stack images were acquired by confocal microscopy (TCS SP8; Leica, Germany) and the multichannel images were processed with Fiji/ImageJ (Schindelin et al., 2012). All images in the study were presented as maximum projection z-stack images of 100 µm thickness.

Live/Dead Staining

For Live/Dead staining, a Live/Dead Cell Viability Kit was used in accordance with the manufacturer's protocol. Briefly, the samples were washed with Dulbecco's phosphate-buffered saline (DPBS; 14190-144, Gibco™, United States) 3 times and incubated with 2 µM calcein AM and 4 µM Ethidium homodimer-1 for 30 min at room temperature. The samples were then visualized by confocal microscopy.

Reverse Transcription Quantitative Polymerase Chain Reaction

Samples for gene expression assay were snap-frozen in liquid nitrogen and stored at −80°C. Total RNA was extracted using a Maxwell® 16 Cell LEV Total RNA Purification Kit (AS1280; Promega, United States) in accordance with the manufacturer's protocol. Reverse transcription was then undertaken using a High-Capacity cDNA reverse Transcription Kit (4368814; Applied Biosystems, United States). RT-qPCR was performed with the StepOne™ real-time PCR system (4376357, Applied Biosystems, United States) with TaqMan™ Gene Expression Assay (4331182, Thermo Fisher Scientific, United States). The primers used were Runt-related transcription factor 2 (RUNX2, Rn01512298_m1, Thermo Fisher Scientific, United States), Osterix (Rn01761789 m1, Thermo Fisher Scientific, United States), and Glyceraldehyde-3-phosphate dehydrogenase (GAPDH, Rn01749022 g, Thermo Fisher Scientific, United States). The amplification was performed as follows: initial denaturation at 95°C for 20 s followed by 40 cycles at 95°C for 1 s and 60°C for 20 s. Relative gene expression was calculated by the ΔΔCt method, normalized by the endogenous control, GAPDH (Livak and Schmittgen, 2001). The data are presented as a mean value ± standard error (s.e.m) of three replicates.

Alizarin Red S Staining and Quantification

Samples were fixed in 4% PFA for 40 min and washed three times in Milli-Q® water. The samples were then incubated with 0.1% Alizarin Red S staining (A5533; Sigma-Aldrich, United States) for 20 min at room temperature, followed by thorough washing with Milli-Q® water. For quantification, the dye was extracted in 100 mM cetylpyridium chloride overnight at room temperature. Absorbance was measured at 540 nm using the microplate reader.

Evaluation of the Effect of Growth Medium Volume on Cell Growth

To evaluate the effect of medium volume on cell growth on a 2D mono-surface and the 3D porous scaffolds, cell growth was evaluated in different volumes of growth medium. For 2D experiments, rBMSC were seeded into wells of 12-well plates at the standard initial seeding density of 5,000 cells/cm^2. For testing, the cells were separated into three different groups, according to the volume of growth medium: 0.76 ml, the lowest limit of the manufacturer's recommendation, 1.52 ml, and 3.04 ml, which corresponded to 0.04 µl/cell, 0.08 µl/cells, and 0.16 µl/cells, respectively, at the time of seeding. After 3 and 7 days of incubation at 37°C in 5% CO_2 humidified atmosphere, the cells were trypsinised, stained with 0.4% Trypan Blue (T10282, Thermo Fisher Scientific, United States), and analyzed by the Countess 2 Automated Cell Counter (Thermo Fisher Scientifics, United States). Likewise, the optimal ratio of cell-to-medium volumes was evaluated on the 3D scaffolds where 250,000 cells were seeded.

According to a previous report, the seeding efficiency was estimated to be 50% (Yamada et al., 2021b), and therefore, 125,000 cells were considered to have attached to the scaffold initially. Five scaffolds, corresponding to 625,000 cells, were then incubated with the growth medium at medium-to-cell ratios of either 0.04 µl/cell (i.e., 25 ml), 0.08 µl/cell (i.e., 50 ml), or 0.16 µl/cell (i.e., 100 ml) at 37°C in 5% CO_2 humidified atmosphere. The medium was refreshed every 72 h. Cell growth was analyzed on days 3 and 7 by quantification of dsDNA.

Evaluation of the Effect of Humidification on Cell Growth and Viability

To measure medium evaporation during perfusion in the bioreactor, 25 ml of the growth medium was perfused at 0.8 ml/min, 5 ml/min and 10 ml/min at 37°C in 5% CO_2 environment. During perfusion, the ventilation filter was subjected to either environmental humidity, or humidity enhanced by a water bath (open humidification), or an additional water flask connected to the medium reservoir through a ventilation filter (closed humidification). Gas exchange took place through a ventilation filter attached on the medium reservoir and on the water flask for humidification in the open and closed configuration, respectively. As a control, 25 ml medium was placed statically. Glucose concentration was calculated based on the original concentration and the volume loss of the growth medium. Using growth medium perfused at 10 ml/min for 72 h with and without humidification, rBMSC were incubated at 37°C in 5% CO_2 humidified atmosphere for a further 72 h in 12-well plates at an initial seeding density of 5,000 cells/cm^2, or on the scaffolds. Cell growth and viability on the mono-surface were assessed by the Countess 2 Automated Cell Counter (Thermo Fisher Scientifics, United States) and on the scaffolds by Live/Dead staining.

Evaluation of the Effect of Air Bubbles on Cell Growth and Osteogenic Properties

A dynamic culture system was established by connecting silicon tubes through the medium reservoir, the peristaltic pump, and the culture chamber where six scaffolds with rBMSC were placed. 25 ml of the growth medium was perfused at 0.8 ml/min (i.e., 3 rpm in the system) at 37°C in 5% CO_2 environment. The medium was refreshed every 72 h. The medium reservoir was either placed at the same level as the culture chamber or approximately 30 cm higher than the chamber, to apply an additional 20 mmHg hydrostatic pressure. After 3 days of perfusion culture, cell growth was evaluated by immunofluorescence with a proliferation marker, Ki67, and quantification of dsDNA.

Evaluation of Differential Flow Rate and Osteogenic Differentiation

To determine the optimal flow rate for cell growth and osteogenic induction, multiple flow rates were compared. Using the previously determined optimal conditions, the bioreactor was humidified by a water bath and 20 mmHg hydrostatic pressure was applied to the culture chamber. Six scaffolds with rBMSC were placed in the culture chamber, and 25 ml of the growth medium was perfused at 0.8 ml/min (i.e., 3 rpm), 1.6 ml/min (i.e., 6 rpm), or 3.2 ml/min (12 rpm) for 8 h or 24 h per day at 37°C, 5% CO_2 in a humidified environment. After 7 days of perfusion culture, cell morphology was assessed by immunofluorescence staining. Further analysis was performed on 0.8 ml/min perfusion for 8 h a day. Cell distribution in the first, third, and sixth scaffolds from the inlet was visualized by 0.5% Crystal Violet on day 7. Osteogenic differentiation was assessed by RT-qPCR, Alizarin Red S staining and ALP activity compared to the static culture conditions.

Statistics

All data are represented as mean ± standard error of mean (SEM) unless stated otherwise (sample size: $n = 5$, except for RT-qPCR $n = 3$). Statistical analysis was performed using SPSS Statistics version 25 (IBM, United States). For pairwise comparison of 2 groups, data were evaluated by Student's t-test. For multiple comparison, data were evaluated by one-way ANOVA followed by Bonferroni's multiple comparison test. A p value <0.05 was considered statistically significant.

RESULTS

Simplified yet Parameterized Geometry as a Substitute for High-Resolution Geometry Obtained From microCT

Usually, the magnitude of flow effect on cells is expressed as fluid shear stress. Fluid dynamics simulation was therefore undertaken to estimate shear stress exerted on the scaffold surfaces (i.e., the cells on the scaffold). Conventionally, a simplified geometry parameterized with porosity and permeability is adopted to reduce the computational burden. Therefore, the present study compared such a methodology and whole scaffold geometry, obtained by microCT, to validate predictive power and computational cost (**Figure 2A**). Despite the same predefined mesh resolution, minimum element size in microCT geometry was notably smaller, and the number of elements comprising the geometry reached nearly one hundred million, while the simplified geometry comprised fewer than 600,000 elements (**Figure 2B**; **Table 1**). This resulted in significantly longer free meshing time in the microCT geometry. Likewise, the enormous number of degrees of freedom solved for accounted for substantially longer computation time in the microCT geometry. Both models confirmed that fluid permeated the scaffold domains and showed comparable velocity fields (mean velocity: simplified, 0.15 mm/s; microCT, 0.12 mm/s). Highest flow velocity was estimated along with the wall of fluid column in the microCT model (**Figure 2C**). This tendency was correlated with the higher shear stress at the peripheral than at the core

parts (**Figure 2D**). In the simplified model, the magnitude of shear stress was more averaged within the scaffold domain. However, the microCT geometry tended to fluctuate more and this was assumed to be due to its geometrical specificity. The estimated values of shear stress varied between the models: the mean and maximum value of shear stress were 0.70 and 3.00 mPa in the simplified geometry and 0.87 and 10.28 mPa in the microCT geometry, respectively (**Figure 2E**). Despite the difference between the approaches, the frequent distribution of the magnitude of shear stress showed similar trend, converging into the range below 5 mPa (**Figure 2F**). This suggests that appropriately parameterized geometry may be used to calculate shear stress in an averaged manner but not be suitable for the evaluation of spatial characteristics.

Optimization of Medium Volume Required for Optimal Cell Growth in 2D and 3D Culture

The necessary and sufficient volume of culture medium allows cells to elicit their active kinetics from a paracrine effect while diluting waste products. In most studies, a medium-to-cell ratio is not well described and not standardized. To determine the optimal volume of culture medium for the bioreactor system, rBMSC were cultured for 7 days in different volumes of culture medium, on 2D mono-surfaces and on 3D porous scaffolds (**Figure 3A**). On the 2D surface, rBMSC maintained high viability of approximately 98% on days 3 and 7, regardless of medium volume (**Figure 3B**). Cell density on day 3 was slightly lower in the 0.16 µl/cell group, but there was no statistical significance (**Figure 3C**). On day 7, cell density increased as

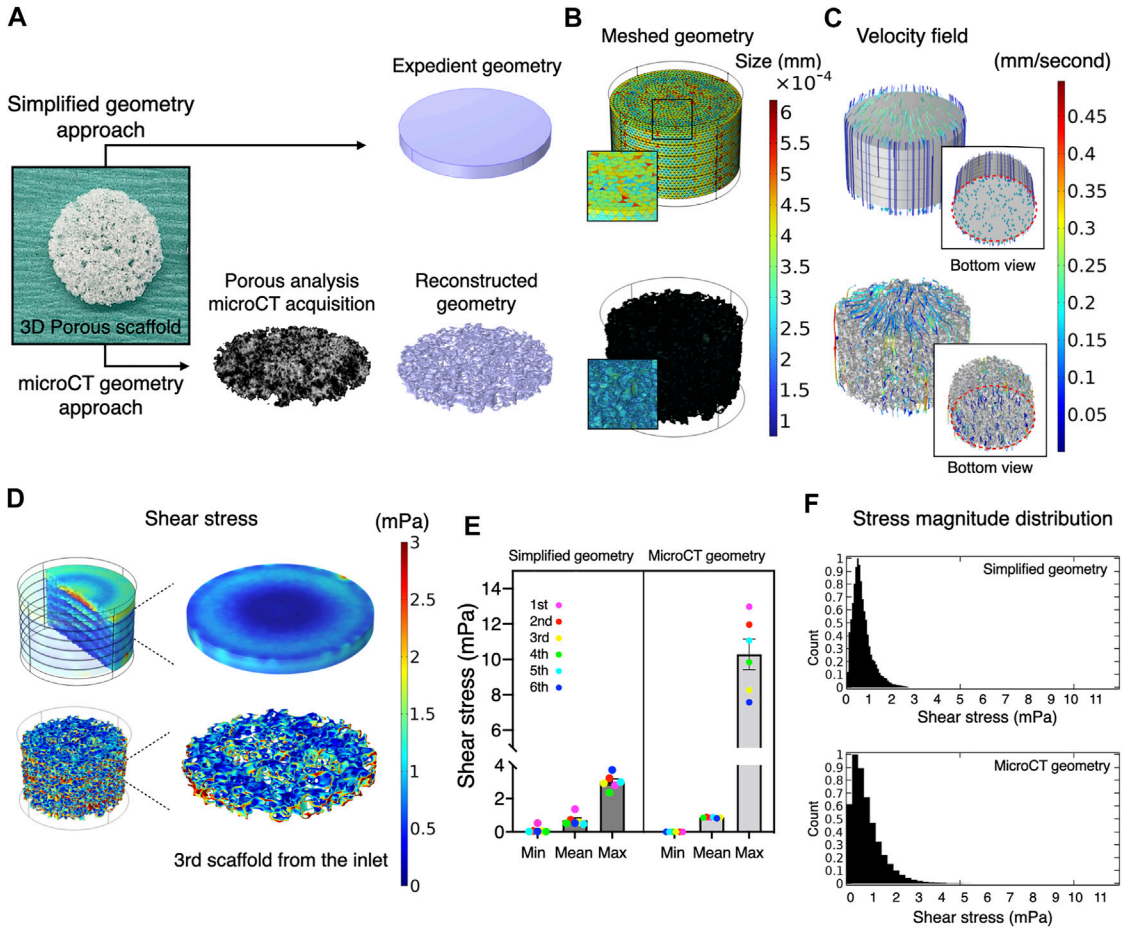

FIGURE 2 | Comparative validation of different modeling methods in fluid dynamics simulation. **(A)** A three-dimensional porous scaffold was modeled by different methods. For the simplified geometry approach, the scaffold was assigned as a porous domain parameterized with porosity and permeability. For the microCT geometry approach, an acellular scaffold was scanned by microCT, and the geometry was imported as a .stl file in CAD software. **(B)** The reconstructed geometry was then meshed for computation. The element size of simplified geometry was significantly smaller than that of the microCT geometry. **(C)** At a flow rate of 0.8 ml/minutes, medium permeated uniformly inside the scaffolds at flow velocities ranging from nearly 0 to 0.5 mm/second in both models. **(D)** Estimated magnitude of shear stress was more patterned in the expedient geometry than in the microCT geometry. The microCT geometry offered more locally specific variation. **(E)** Estimated mean and minimum but not maximum shear stress in the simplified approach was compatible with the microCT approach. **(F)** The distribution of shear stress magnitude shows monophasic peak around 0.5–1 mPa both in the simplified and microCT approaches.

TABLE 1 | Parameters for meshing and computation in the *in silico* modeling.

		Simplified geometry	microCT geometry
Meshing			
	Predefined mesh resolution	Finer	
	Minimum element size (mm)	0.0464	
	Maximum element size (mm)	0.429	
	Maximum element growth rate	1.1	
	Curvature factor	0.4	
	Resolution of narrow regions	0.9	
	Actual mesh resolution		
	Minimum element size (mm)	0.072428	0.013097
	Maximum element size (mm)	0.4242	0.2669
	Number of element	569570	83848571
	Free meshing time	31 s	1 h 30 min 1 s
Computation			
	Degrees of freedom solved for	203209	45218141
	Computation time	1 min 52 s	28 h 15 min 54 s
	RAM/Processor used	32 GB RAM 2.9 GHz 6 core Intel Core i9	

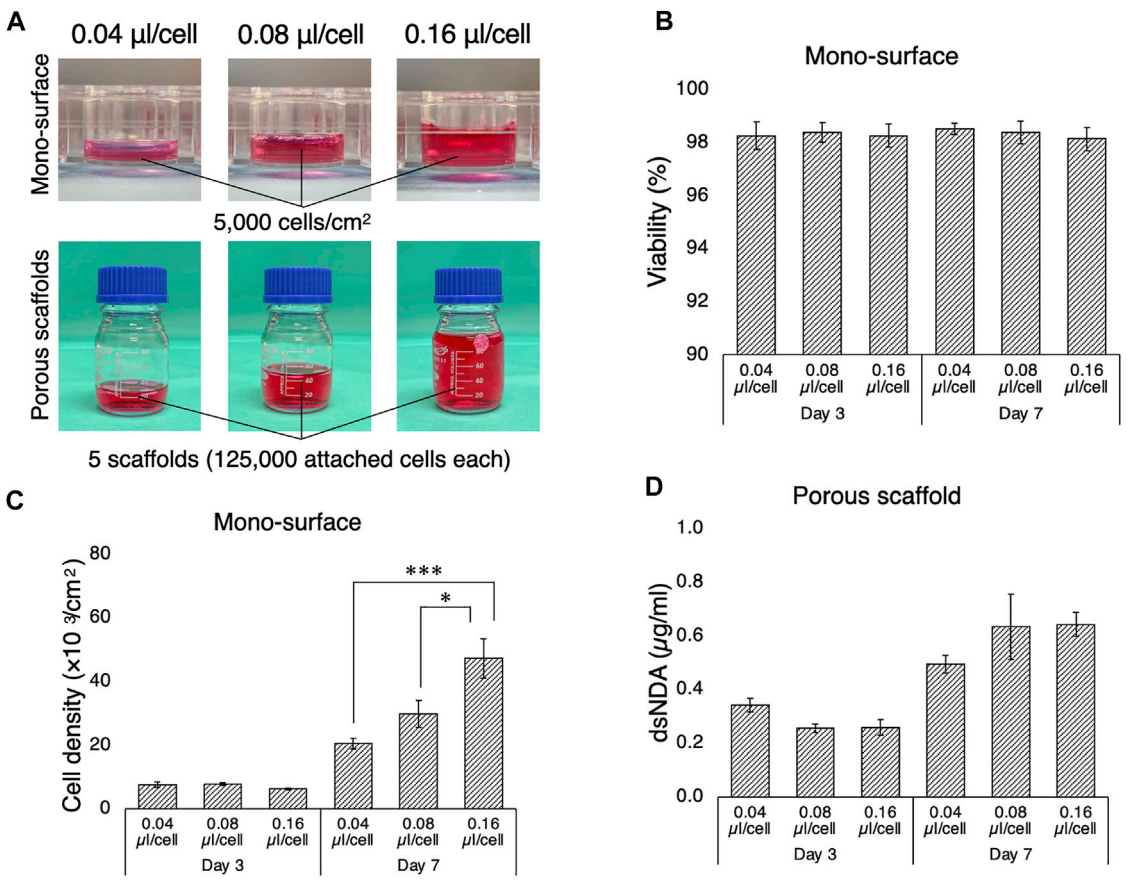

FIGURE 3 | Growth of rBMSC in culture medium at different medium-to-cell ratios. **(A)** Medium-to-cell ratios of 0.04, 0.08, and 0.16 µm/cell at the point of seeding were tested on 2D mono-surface and 3D porous scaffolds. **(B)** Cells seeded on the mono-surface maintained high viability regardless of medium-to-cell ratio. **(C)** On the mono-surface, cell growth was enhanced at a medium-to-cell ratio of 0.04 µl/cell compared to 0.08 and 0.16 µl/cell on day 3, but the tendency was reversed on day 7 when the cell density approached confluence. **(D)** On 3D porous scaffolds, quantification of double-strand DNA (dsDNA) indicated that the medium ratio of 0.04 µl/cell yielded the highest dsDNA on day 3, but medium ratios of 0.08 and 0.16 µl/cell yielded higher dsDNA on day 7. $^{*}p < 0.05$, $^{***}p < 0.001$.

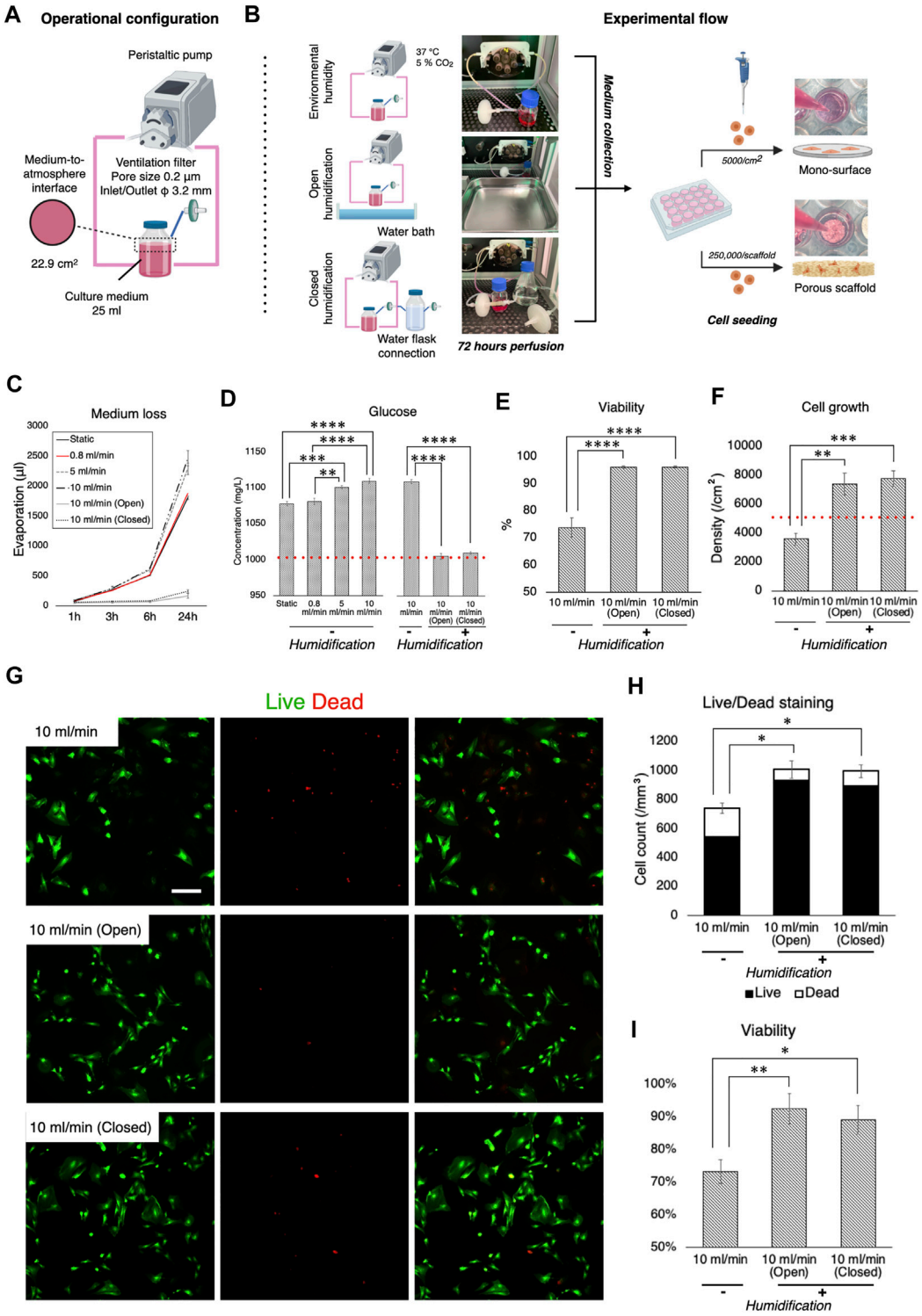

FIGURE 4 | Effect of culture medium loss during perfusion and humidification. **(A)** Operational configuration for the evaluation of medium loss and humidification. **(B)** Illustration of the experimental flow. Culture medium, which was perfused with and without humidification for 72 h, was collected and transferred into cell culture plates where growth of rBMSC on 2D mono-surface and 3D porous scaffolds was observed. **(C)** Evaporation of culture medium occurred in a velocity dependent manner. Humidification with a water bath and a water flask connection effectively prevented evaporation. **(D)** Medium evaporation led to the condensation of medium components (e.g., glucose), disrupting osmotic balance. **(E,F)** On the 2D mono-surface, cell viability and growth of rBMSC incubated in the perfused medium without humidification deteriorated significantly. **(G–I)** Fluorescence images of Live/Dead staining showed that rBMSC incubated in the perfused medium without humidification significantly increased the ratio of dead cells, resulting in low cell density and viability on 3D porous scaffolds. $^{*}p < 0.05$, $^{**}p < 0.01$, $^{***}p < 0.001$, $^{****}p < 0.0001$.

the medium volume increased, and accelerated cell growth was observed in the 0.08 and 0.16 µl/cell groups (0.04 µl/cell vs. 0.16 µl/cell, $p = 0.00002$; 0.08 µl/cell vs. 0.16 µl/cell, $p = 0.012$). A similar tendency, although not statistically significant, was found in the 3D porous scaffolds (**Figure 3D**). The lowest medium volume seemed advantageous for initial cell growth by day 3, but the higher medium-to-cell ratios promoted cell proliferation by day 7, when the cells were nearly confluent on the scaffold.

Minimizing Medium Evaporation During Perfusion Improved Cell Growth and Viability

For optimal cell growth, gas exchange is required. Therefore, although perfusion systems are mostly "closed" by tubing, the medium has contact with the atmosphere through ventilation filters, where evaporation takes place. Ideally, the atmosphere needs to be humidified, but most electronic devices such as pumps and sensors are incompatible with high humidity. Therefore, the impact of non-humidified conditions as well as different humidification methods on cell kinetics was evaluated during dynamic culture. Firstly, loss of medium was measured in the bioreactor system during perfusion at different flow rates, with and without humidification, and then the cellular response to perfused medium under such conditions was evaluated (**Figures 4A**,**B**). It was confirmed that without humidification nearly 10% of the growth medium evaporated within the first 24 h of perfusion and an amount of medium loss was positively associated with flow rate (**Figure 4C**). Humidification significantly suppressed evaporation. Notably, using a water bath as the conventional method (open humidification) and connection of water-containing flasks to the ventilation filter on the medium reservoir (closed humidification) reduced evaporation equivalently. Medium evaporation theoretically led to condensation, resulting in elevated content concentration including a glucose level as represented (static vs. open/closed humidification, $p < 0.0001$) (**Figure 4D**). rBMSC were then incubated under standard culture conditions (i.e., 95% relative humidity, 37°C, 5% CO_2) in the growth medium, which was perfused at 10 ml/min for 72 h (either with or without humidification) on the 2D surface and the 3D porous scaffolds. On the 2D surface, cell viability was significantly affected in the condensed medium, declining by approximately 20% compared to the humidified environment (without vs. with open/closed humidification, $p < 0.0001$) (**Figure 4E**). Similarly, cell growth deteriorated in medium perfused without humidification (without vs. with open humidification, $p = 0.0019$; without vs. with closed humidification, $p = 0.00086$) (**Figure 4F**). On the 3D scaffolds, Live/Dead staining showed that open as well as closed humidification effectively supported cell growth while the condensed medium led to reduced cell growth (without vs. with open humidification, $p = 0.0041$; without vs. with closed humidification, $p = 0.029$) and viability (without vs. with open humidification, $p = 0.025$; without vs. with closed humidification, $p = 0.011$) (**Figures 4G–I**).

Suppression of Air Bubbles During Perfusion is a Determinant of Cell Growth and Osteogenic Properties

The formation of air bubbles is an acknowledged problem in perfusion systems (Lochovsky et al., 2012; Kang et al., 2014), and the system used in this study was no exception. Therefore, according to Henry's law, suppression of air bubble formation was attempted by controlling static pressure (**Figures 5A,A′**). When the medium reservoir was placed at the same level as the culture chamber, air bubbles were generated rapidly within 3 h of perfusion (**Figures 5B,C**). After 24 h of perfusion, airspace dominated in the chamber, with the surfaces of fluid paths mostly dried, although the medium permeated the scaffolds with the help of capillary action (**Figure 5D**). When the reservoir was vertically positioned 30 cm higher than the culture chamber, however, the growth medium filled the chamber space (**Figures 5B′–D′**). This corresponded to a hydrostatic pressure of approximately 20 mmHg. In the environment where air bubbles were formed, the cells appeared to be less elongated and scattered and the expression of a proliferation marker, Ki67, was significantly downregulated (**Figure 5E**). Quantification revealed that approximately 30% of rBMSC were proliferative without air bubbles, while only 12% of the population expressed Ki67 (**Figure 5F**) ($p = 0.041$). The quantification of dsDNA confirmed the adverse effect of air bubble formation on cell growth, significantly suppressing cell proliferation ($p < 0.0001$) (**Figure 5G**).

Optimal Flow Rate Triggers Osteogenic Differentiation of rBMSC

MSC are exquisitely sensitive to mechano-environmental factors. The response varies, depending on the magnitude and duration of fluid stimulation (Maul et al., 2011; Lane et al., 2014). Initially, several flow rates and perfusion time were tested, to determine conditions at which cell growth was optimal: 25 ml of the growth medium was perfused under humidification by a water bath in the bioreactor, wherein 20 mmHg hydrostatic pressure was applied to the culture chamber (**Figure 6A**). Flow rates of 0.8 ml/min, 1.6 ml/min, and 3.2 ml/min were compared, corresponding to shear stress ranging from nearly 0 to 13.1 mPa (mean 0.88 mPa, mode value 0.5–1 mPa) to 26.2 mPa (mean 1.76 mPa, mode value 1.0–1.5 mPa), and to 52.6 mPa (mean 3.51 mPa, mode value 2–3 mPa), respectively, as estimated by the *in silico* modeling (**Figure 6B**). Perfusion for 8 h a day at 0.8 ml/min and 1.6 ml/min supported cell growth while 3.2 ml/min caused fragmentation of cytoskeletal structures (**Figure 6C**). However, perfusion for 24 h was found to suppress cell growth and in particular, perfusion at 1.6 ml/min induced cell damage and apoptotic response. These experiments disclosed that in the present system, perfusion for 8 h at 0.8 ml/min (mean 0.88 mPa, mode value 0.5–1 mPa) provided optimal fluidic stimulus. At the flow magnitude, no noticeable differences in cell distribution were

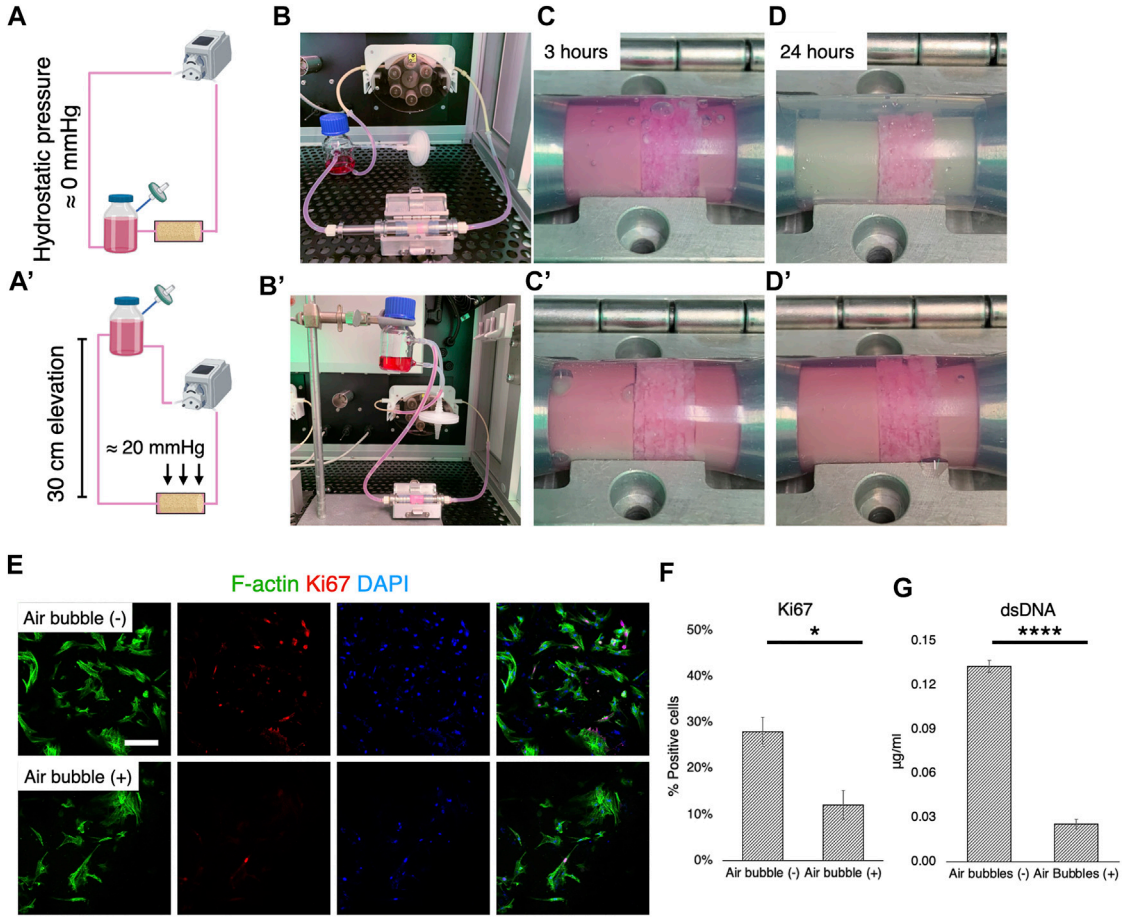

FIGURE 5 | Cell growth deterioration due to air bubbles and suppression. **(A-B, A′-B′)** Schematic illustrations and optical pictures of experimental configuration. The elevation of the medium reservoir by 30 cm corresponded to 20 mmHg hydrostatic pressure. **(C-D, C′-D′)**. With the experimental configuration, air bubbles were vigorously generated, mostly due to hydrophobic porous scaffolds and medium agitation in the scaffold chamber. This was effectively prevented by the application of hydrostatic pressure at 20 mmHg. **(E,F)** Immunofluorescence images and quantification of a proliferation marker, Ki67, showed that cell proliferation was significantly affected under the environment with air bubbles. **(G)** Quantification of double strand DNA confirmed the inhibition of cell growth by air bubbles in the perfusion system. Scale bar: 100 μm. $^{*}p < 0.05$, $^{****}p < 0.00001$.

observed among the first, third, and sixth scaffolds from the inlet, which is consistent with the observation by the computational model (**Figure 7A**). rBMSC subjected to the fluid flow upregulated the key osteogenic transcription factors, RUNX2 and Osterix, on days 7 and 14, while under static conditions the cells gradually lost the osteogenic property (RUNX2, $p = 0.23$; Osterix, $p = 0.032$ on day 7; RUNX2, $p = 0.049$; Osterix, $p = 0.007$ on day 14) (**Figure 7B**). Alizarin Red S staining confirmed that perfusion culture of rBMSC resulted in calcium deposition, (**Figure 7C**), which became more pronounced over time ($p = 0.034$ on day 21) (**Figure D**). This was accompanied by an increase in ALP activity ($p = 0.019$ on day 3; $p = 0.032$ on day 7; $p < 0.0001$ on days 14 and 21) (**Figure 7E**).

DISCUSSION

The application of dynamic cell culture shows promise in bone tissue engineering, in which a 3D porous scaffold is a critical component of successful bone regeneration (Gaspar et al., 2012). This is mainly because medium flow homogenizes gas and nutrient concentrations within the scaffolds while removing waste products, preventing the cells in the core part of the structure from succumbing to deprivation of gases and nutrients (Bergemann et al., 2015). Moreover, previous studies on 2D systems have reported that MSC are mechanosensitive, and appropriate fluidic shear stress may direct them towards the osteogenic lineage (Holtorf et al., 2005; Yourek et al., 2010; Kim et al., 2014; Becquart et al., 2016; Stavenschi et al., 2017; Tsai et al., 2019; Dash et al., 2020). With reference to clinical translation, a number of perfusion bioreactor systems have been developed and tested using 3D porous scaffolds (Livak and Schmittgen, 2001; Yourek et al., 2010; Maul et al., 2011; Kang et al., 2014; Kim et al., 2014; Lane et al., 2014; Bergemann et al., 2015; Becquart et al., 2016; Dash et al., 2020). However, due to the complexity of the 3D culture system, each of the systems has unique features and applies original experimental configurations. The conclusions

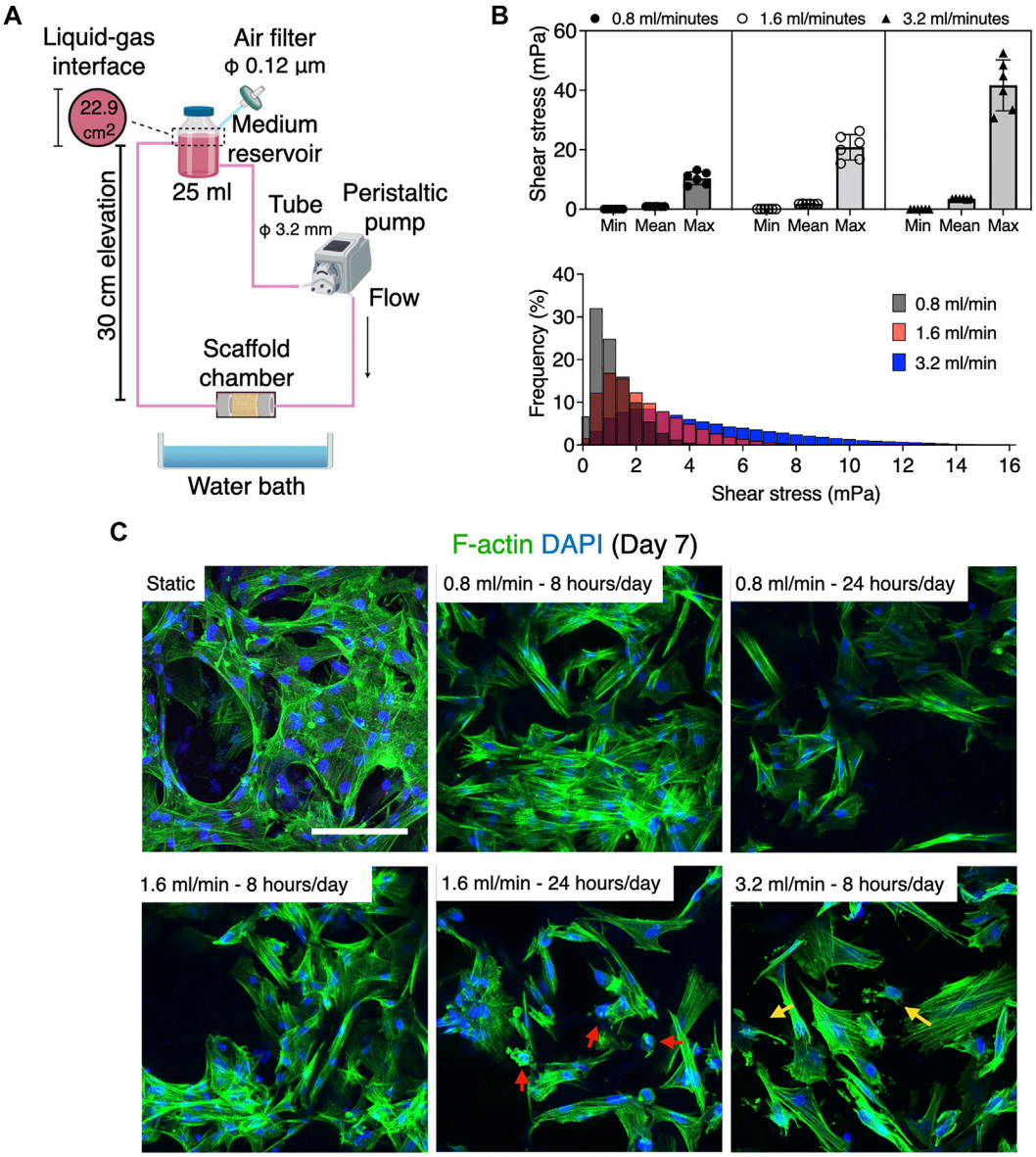

FIGURE 6 | Differential cell response to fluid flow at 0.8, 1.6, and 3.2 ml/min. **(A)** Schematic illustration of experimental configuration. **(B)** Estimation of fluid shear stress by *in silico* modeling using the microCT approach. The medium perfusion at 0.8, 1.6, and 3.2 ml/min in the present system exerted shear stress ranging from nearly 0 to 10 mPa, nearly 0–21 mPa, and nearly 0–41 mPa, respectively. The histogram shows the mode value of shear stress distribution. **(C)** Fluorescence images of rBMSC exposed to fluid flow. While the cells in the static control elongated homogeneously, those under perfusion tended to show more contracted morphology and more filamentous activity. Flow rate at 0.8 and 1.6 ml/min for 8 h supported cell growth, whereas perfusion for 24 h a day inhibited cell proliferation or induced apoptotic response (red arrows). A flow rate of 3.2 ml/min was found to fractionalize the cytoskeleton (yellow arrows). Scale bar: 100 μm.

drawn from various studies are therefore inconsistent and sometimes contradictory. This hinders cross-study comparison of different systems and the development of further optimized systems. Therefore, the aim of the present study was to identify and validate inconsistencies, mainly associated with environmental variables and then to optimize experimental configuration in the perfusion bioreactor system for bone tissue engineering.

Cell response to fluidic stimuli differs according to the magnitude of shear stress exerted by fluid in motion (Yeatts and Fisher, 2011). Despite the wide application of flow rate (e.g., ml/minute) or pump speed (e.g., rpm) as parameters to describe the characteristics of fluid stimuli, neither represents the magnitude of flow to which the cells respond or can be used to compare the results of different bioreactor systems unless the flow rate/pump speed is correlated with the magnitude of fluid force to the cells by mathematical models or computational simulation (Sladkova and de Peppo, 2014). To reduce uncertainty when comparing study results, the accurate estimation of fluid shear stress serves as a common

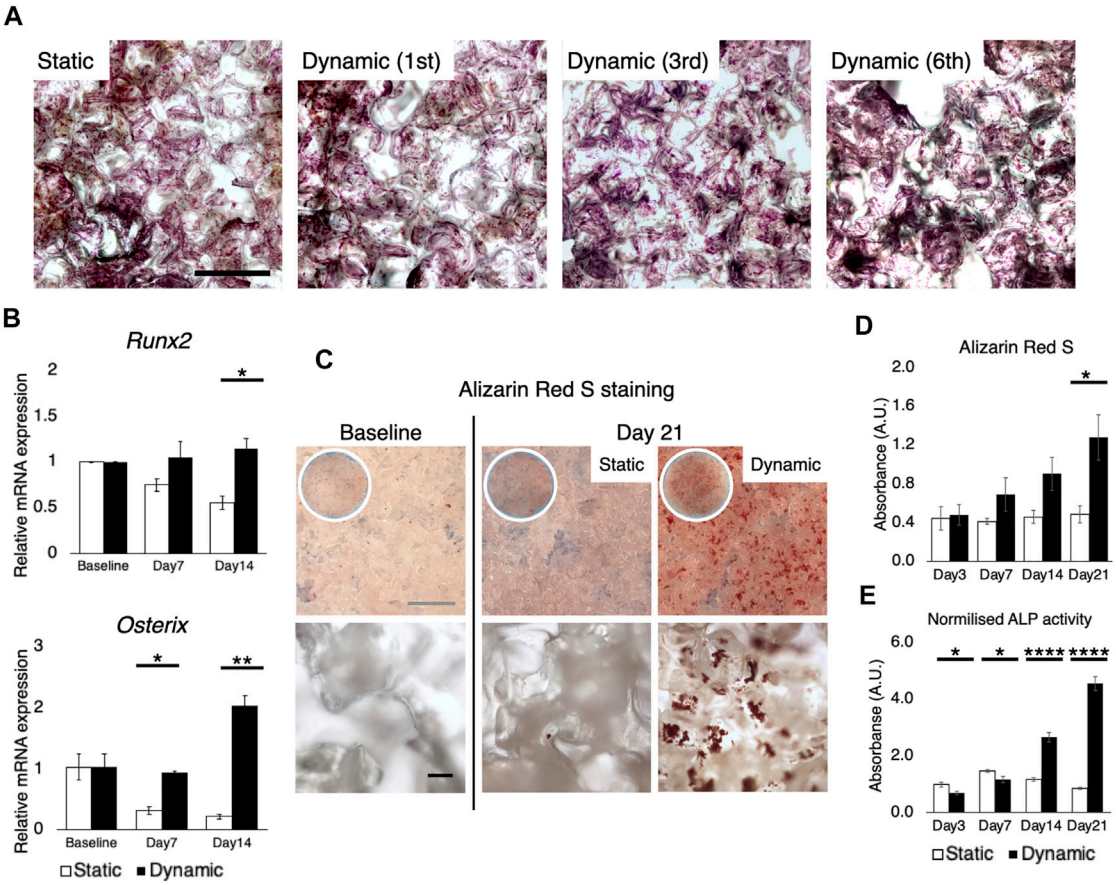

FIGURE 7 | Osteogenic differentiation induced solely by fluid stimuli at 0.8 ml/min. **(A)** Crystal violet staining showed, as expected from the computational simulation, that the cells were uniformly distributed throughout the stack of scaffolds, regardless of the distance from the inlet. Scale bar: 500 μm **(B)** RT-qPCR showed the upregulation of key transcription factors for osteogenesis, RUNX2 and osterix, on days 7 and 14 under perfusion while the cells gradually lost the osteogenic property in the static environment. Baseline stands for 24 h after cell seeding on the scaffold **(C,D)** Alizarin red S staining confirmed the formation of mineralized deposit on the scaffolds subjected to perfusion for 21 days. Scale bar: (grey) 1 mm, (black) 100 μm **(E)** Perfusion culture led to the activation of alkaline phosphatase activity on days 14 and 21. $^{*}p < 0.05$, $^{**}p < 0.01$, $^{***}p < 0.001$, $^{****}p < 0.0001$.

reference point. The magnitude of shear stress is determined by local velocity. In contrast to 2D experimental settings, where fluid motion is limited to the *X-Y* direction, evaluation of fluid shear stress in 3D bioreactor systems presents a major challenge. This is attributable primarily to the geometry of porous scaffolds, in which local velocity varies from one point to another and possibly from moment to moment. Conventionally, the mathematical model applying Kozeny-Carman equation has been used to analyze shear stress within a homogeneous porous domain (Podichetty and Madihally, 2014). For the analysis of spatial shear stress distribution, an *in silico* modeling is a powerful alternative for studying microfluidics in such a complex environment. It allows fluid to be virtually traced within a given geometry and fluid dynamics to be computed. The tool has been applied in some tissue engineering studies, to examine microfluidics in bioreactor systems (Geris et al., 2016). In most cases, *in silico* modeling was performed using a simplified geometry (e.g., a cylinder), idealized by parameterization to reduce the computational burden (Zhao et al., 2019; Ramani-Mohan et al., 2018; Egger et al., 2017; Nokhbatolfoghahaei et al., 2020; Pereira et al., 2021; Melke et al., 2020). Parameterization with porosity and permeability allows the geometry to be considered as a porous domain to which Darcy flow model may be applied. This approach could be used even if a scaffold consists of several domains as long as each domain possesses a homogeneous structure. Alternatively, a CAD geometry in the case of, e.g., 3D printed scaffolds, or a geometry acquired by microCT may be used as more accurate methods where Navier-Stokes equation may be applied by assuming that a liquid property is defined as an incompressible Newtonian fluid (**Figure 8**). The present study indicates that the simplified approach may capture the averaged characteristics of fluid dynamics within the porous domains, but it does not resolve the velocity field in detail because the model does not include the geometrical information of pores. Indeed, the velocity within the porous domains is expressed as the Darcy velocity. This indicates that

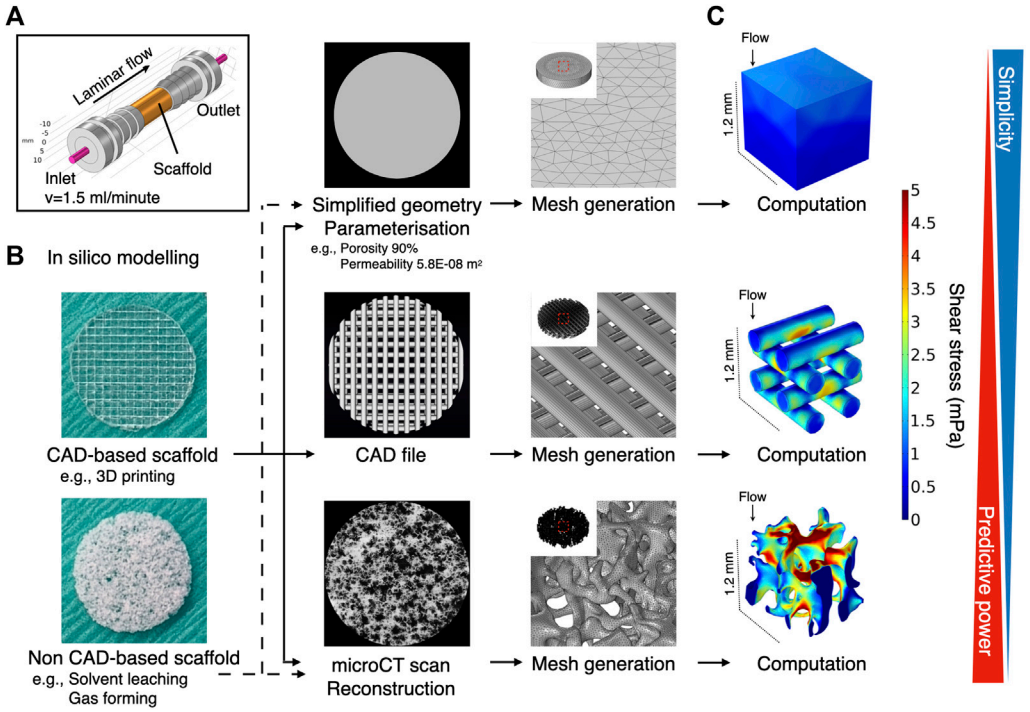

FIGURE 8 | Schematic illustration of common methods for computational fluid dynamic simulation in scaffold-based perfusion cell culture. **(A)** Expedient culture chamber design. Porous scaffolds were placed in the culture chamber and perfused at 1.5 ml/min. **(B)** The computational reproduction of scaffold geometry can be undertaken using different methodologies, depending on the availability of hardware resources and feasibility. At its simplest, expedient geometry (e.g., a cylinder) may be assigned as a porous domain where porous parameters are input. The generated mesh for such a geometry tends to be coarse, being less demanding computationally. Alternatively, CAD data may be used when the scaffold is designed in CAD software (e.g., 3D printed scaffold). The mesh required for computation tends to be finer than the simplified geometry, but regular. The highest predictive power may be expected when microCT data are imported to acquire the actual geometry used in the study. Mesh generation and computation entail high computational time and costs. **(C)** The Darcy (-Brinkman) model may be applied to calculate shear stress for porous domain, whereas laminar flow may be defined by the Navier-Stokes equation by assuming that culture medium is an incompressible Newtonian fluid.

the velocity within the porous domains is expected to be uniform compared to the velocity within the pores in the detailed model, and the gradients associated with the Darcy velocity are likely to be computed smaller than the counterpart. Therefore, the simplified approach can only compute shear stress in an average sense expediently and is not suited for spatial estimation in detail. This highlights the superiority of the microCT approach where actual shear stress within the pores is explicitly resolved. The microCT-based modeling revealed great spatial variations in estimated shear stress. This suggests that cell response within the scaffold constructs is likely to be heterogeneous. In other words, it would be recommendable that biological events in a 3D perfusion system is explained by the range and frequency of shear stress distribution, but not just by the mean. For visualization of local shear stress distribution, microCT geometry is advantageous. This fact also emphasizes that the microCT approach provides possibility to correlate observed cell behavior with a magnitude of shear stress in a single cell resolution, leading to more accurate investigation on dynamic cell culture (Jungreuthmayer et al., 2009). However, the considerably greater computational burden may be a major disadvantage in the case where a complex or large scaffold geometry is to be modeled for computation. In fact, a great amount of time was often required, not only to analyze, but also to repair and reconstruct microCT data to be compatible with CAD and *in silico* modeling software (Acosta Santamaría et al., 2013). It is acknowledged that simulation of fluid dynamics using a full-scale scaffold is not always feasible, depending on available hardware and model complexity (Acosta Santamaría et al., 2013; Zhao et al., 2019). To achieve a balance between predictive visualization and computational cost, segmentation of region of interest (ROI) from the whole scaffold geometry seems a valid procedure for demonstrating representative shear distribution (Lane et al., 2014; Sellgren and Ma, 2015; Daish et al., 2017; Pasini et al., 2019). In short, the simplified method is effective for estimating a range of shear stress with a minimal computational burden when the porous property is properly parameterized, but simulation with microCT geometry is essential to gain insight into local fluctuations of fluid dynamics. Noteworthily, in the study, the simulation was performed using an acellular scaffold, and the values may not necessarily represent later timepoints because of cell

growth and deposited extracellular matrix (Ramani-Mohan et al., 2018; Nokhbatolfoghahaei et al., 2020). Furthermore, it identified the fluid property of culture medium with water at 37°C, and therefore, further investigation is required for culture medium specific dynamics in the perfusion systems.

Next, the volume of culture medium was optimized in the present system. Perfusion bioreactors commonly consist of medium reservoirs, tubes, and culture chambers. These hold unique dimensions specifically adapted to each system and the volume of medium required needs to be modified accordingly. In general, a perfusion bioreactor requires a large volume to establish continuous flow, but the amount needs to be adjusted with reference to the vital cells on the scaffolds. Therefore, cell growth was compared in different medium-to-cell ratios, on 2D mono-surfaces and on 3D porous scaffolds. Regardless of the medium-to-cell ratio, by day 7 cell viability was maintained at nearly 98%. On both 2D and 3D cultures, 0.04 µl per cell at seeding promoted greater cell proliferation than 0.08 and 0.16 µl per cell during the initial phase of culture. This trend was reversed on day 7, when the cells approached confluence. In the present study, 25 ml medium in the bioreactor, corresponding to 0.04 µl per cell initially, was considered to be optimal because cell proliferation was expected to be suppressed by fluid shear stress (Yamada et al., 2021a). It is of interest to note that the volume of culture medium influences not only cell growth but also osteogenic differentiation. Previous studies using osteoblastic cells showed that reduction of mineralization occurred in a medium volume-dependent manner: the more medium used, the less mineralization (Yoshimura et al., 2017). Furthermore, Schreivogel et al. reported that mechanical stimuli in their bioreactor increased the secretion of bone morphogenetic protein 2 by MSC but did not induce activation of downstream signaling in their original experimental configuration. This discrepancy was solved simply by reducing the volume of culture medium and increasing the number of cells, indicating that the excessive use of culture medium dilutes secreted factors and masks phenotypical amelioration (Schreivogel et al., 2019). On 3D polymeric scaffolds, high seeding density supports the osteogenic phenotype of BMSC and enhances bone regeneration after transplantation (Yassin et al., 2015). This may be convenient for perfusion systems where a large volume of medium is required to maintain continuous flow. Together, these results confirm the importance in dynamic cell culture systems, of determining the optimal seeding density and the minimum necessary medium volume, i.e., conditions which do not cause nutrient depletion but allow the cells to condition the medium by paracrine factors.

Humidity control is a key consideration during cell culture because medium condensation disturbs the osmotic balance, and the resulting high tonicity leads to cell dehydration (Triaud et al., 2003; Chi et al., 2020). This study demonstrated that medium perfusion without humidification concentrated medium components taking glucose concentration as an example, and the concentrated medium significantly affected cell viability and growth. The concept of developing tissue engineering bioreactors is mainly classified into systems installed in conventional incubators and stand-alone bioreactor, i.e., which requires an integrated incubation unit for environmental control (Li et al., 2014). However, unlike a standard incubator, maintaining humidity above 90% is not always agreeable in bioreactors because a humidified environment may cause malfunction or possibly irreparable damage to electrical components such as sensors, pumps, electric sockets and conducting wires from a long-term perspective. Admittedly, there seems a lack of consideration with regards to humidification control in previously developed systems. Furthermore, perfusion accelerates the evaporation ratio in a velocity-dependent manner (Handa et al., 1987; Sumino and Akiyama, 1987). The present study also disclosed notable medium loss during perfusion in the non-humidified condition, and this may potentially be detrimental to cell viability and growth. The placement of a water bath, as with a standard incubator, prevented evaporation as expected. However, aqueous droplets and moisture condensation were actually found on the surface of the bioreactor. As an alternative, an additional flask containing water was connected to the filter to humidify the local atmosphere contacting the culture medium. This measure had a comparable suppressive effect on evaporation, without increasing humidity inside the bioreactor. This procedure may be applicable to most bioreactor systems, to improve the culture environment under conditions in which a water bath may not be feasible.

Air bubble formation is a long-standing issue in fluidics (Lochovsky et al., 2012; Kang et al., 2014). It impedes or blocks fluid flow, and more importantly for bone tissue engineering, air bubbles entrapped in microporous scaffolds disrupt cell growth and migration to some extent, depending on cell type and the size/number of bubbles (Podichetty and Madihally, 2014; Bergemann et al., 2015). Bubbles are a determinant of protein denaturation (Faustino et al., 2009): a gas-liquid interface in form irreversibly alters the superorganization of protein molecules by absorbing and forming aggregates, which may result in loss of biological activity. This happens particularly to proteins with high surface activity (Clarkson et al., 1999). It is reported that approximately 10% of proteins in bovine serum albumin were denatured when the proteins were absorbed to and desorbed from air bubbles (Clarkson et al., 1999). The use of perfusion bioreactors for bone tissue engineering exacerbates conditions conducive to bubble formation. Culture medium is normally supplemented with serum/proteins as nutrient sources, acting as surfactants (Faustino et al., 2009). Surfactants lower the surface tension, facilitating the formation of bubbles in the presence of agitation and stabilizing them. Microporous scaffolds of synthetic polymers, which are preferred in bone tissue engineering for their mechanical strength, formability, biocompatibility and biodegradability, exacerbate the problem because of their high porosity and hydrophobicity (Gunatillake and Adhikari, 2003). When fluid flow encounters micropores, stirring may trigger bubble formation, particularly on hydrophobic materials, which absorb gasses and form thin air layers on the surfaces (Hanwright et al., 2005; Lee et al., 2005; Yu et al., 2017b; Yao et al., 2020). It has been shown that using a bubble trap effectively removes large bubbles from the circulation and prevents them from entering the culture chambers, but the trap neither prevents

bubble formation nor removes bubbles trapped in the scaffold micropores (Li et al., 2014; Schuerlein et al., 2017). Alternatively, a complex tubing strategy is needed to control flow paths to isolate bubbles from the main stream (Bhaskar et al., 2018). Therefore, preventive measures of air bubble formation should be prioritized. In the present system, the formation of air bubbles was so extreme that rBMSC were severely affected. For total prevention, a simple yet rigorous step was taken: namely, elevation of the medium reservoir by 30 cm to apply approximately 20 mmHg (equivalent to 2.7 kPa) hydrostatic pressure onto the culture chamber. This was based on Henry's law, which governs gas solubility in liquid: at a given temperature, gas solubility is proportional to static pressure (Kang et al., 2007). It was shown that a slight increase in static pressure decreased gas release in the culture chambers, which created a bubble-free environment. The degree of pressure required may depend on experimental settings, including material selection, scaffold geometry, and flow characteristics. Previous studies have suggested that BMSC undergo osteogenic differentiation under high static pressure ranging from 10 to 100 kPa (Huang et al., 2015; Zhao et al., 2015; Stavenschi et al., 2018). In the present setting, where 2.7 kPa was sufficient to eliminate bubbles completely, its effect on osteogenesis would be negligible although the present study did not evaluate the effect solely. Nevertheless, the strategy of supressing bubbles by applying a static pressure may interact favorably with osteogenic activity given that continuity is commonly observed in biological events.

Finally, the optimization of flow rate for the purpose of bone tissue engineering was explored by testing relatively low-level shear force. The reasons were twofold: not only is cell fate fine-tuned by mechanical stimuli, but also the results should be relevant to clinical translation. In other words, cells which are maintained in a perfusion bioreactor should be also supported during integration at the recipient site in the absence of the robust perfusion provided in bioreactors. In the present study, we tested a subphysiological level of perfusion, which reportedly initiated osteogenic differentiation on 2D surfaces (Coughlin and Niebur, 2012; Gao et al., 2014; Kim et al., 2014). rBMSC were sensitive enough to distinguish 0.8 ml/min (i.e., shear stress: maximum 13.1 mPa, mean 0.88 mPa, mode value 0.5–1 mPa), 1.6 ml/min (i.e., maximum 26.2 mPa, mean 1.76 mPa, mode value 1.0–1.5 mPa), and 3.2 ml/min (i.e., maximum 52.6 mPa, mean 3.51 mPa, mode value 2–3 mPa), and the cells responded differently. Even at the low levels of fluid stimuli, cell proliferation was either delayed or suppressed. Perfusion for 8 h at 0.8 ml/min was found to be compatible with the cell growth and viability, maintaining intact the morphology of the cells and cell-to-cell integration. The finding agrees with a previous report using an osteoblastic cell line, MC3T3-E1, in which shear stress above 1 mPa suppressed cell growth on a 3D scaffold (Cartmell et al., 2003).

In 2D perfusion settings, MSC as well as osteoblasts seem tolerant of high shear stress over 3 Pa and respond to the stimuli by upregulating the expression of osteogenic markers (McAllister et al., 2000; Jiang et al., 2002; Yourek et al., 2010; Mai et al., 2013; Lim et al., 2014; Liu et al., 2015; Yu et al., 2017c). However, the cells are reportedly more vulnerable to shear stress in 3D environment, and a sub-pascal level of shear stress sufficiently stimulates the osteogenicity without deteriorating general cell health (Porter et al., 2005; Gaspar et al., 2012). Previous studies using 3D dynamic culture systems showed that extremely low shear stress ranging from 5 to 10 mPa shear stress for 16 days increased the calcium deposition by rBMSC under the presence of osteogenic supplement (Sikavitsas et al., 2003; Sikavitsas et al., 2005). The promotion of osteogenesis by a low shear stress magnitude was also reported with human BMSC on various scaffold materials (Grayson et al., 2008; Li et al., 2009).

In our experimental setting, shear stress ranging from nearly 0 to up to 15 mPa (mode value 0.5–1.0 mPa) allowed rBMSC to upregulate the key transcription factors for osteogenesis, RUNX2 and Osterix, even in the absence of osteogenic chemical supplements. Osteogenic differentiation was confirmed by enhanced calcium deposition and ALP activity. Therefore, with the scaffold geometry, material selection, and cell type in the present study, it was concluded that this level of shear stress was optimal for balancing the induction of osteogenesis and the growth of rBMSC. Nevertheless, the optimal magnitude of fluid stimuli would differ according to cell types (e.g., species, donor sites, individual variations) and scaffold properties (e.g., micro-, and macro-geometry, surface chemistry, size). Biological responses may therefore differ, even if the same flow rate is applied. This underlines the importance of flow optimization and its challenges when in future clinical translation, scaffolds are custom-designed and loaded with patient-specific cells (Roseti et al., 2017).

CONCLUSION

In bone tissue engineering, bioreactors are intended to support growth and targeted differentiation of stem/progenitor cells. There is a wide range of bioreactor systems in use, each with unique features. Moreover, dynamic cell culture inevitably involves parametric deviations from conventional static culture, which may mask or exaggerate effects of interest. As a previous study confirmed, exact comparative studies can probably be done only by using an identical "standardized" system under the same conditions (Israelowitz et al., 2012). However, some optimized parameters would be transferable to other systems and study designs. The present study explored some of basic but crucial optimization steps, namely the computational estimation of fluid force, the determination of culture medium volume, humidification, the strategy of air bubble suppression, and the identification of optimal fluid shear stress magnitude. The accurate estimation of fluid forces acts as a platform for understanding biological behaviors, while optimizing culture environmental factors contributes to stabilized and reproducible experiments. The thorough validation, optimization, and detailed description facilitate the further development of bioreactor applications in bone tissue engineering.

DATA AVAILABILITY STATEMENT

The raw data supporting the conclusion of this article will be made available by the authors, without undue reservation.

ETHICS STATEMENT

The animal study was reviewed and approved by Norwegian Animal Research Authority (local approval number 20146866).

AUTHOR CONTRIBUTIONS

SY, MY, KM, TS, and JH conceived and planned the experiments. TS and JH developed a bioreactor system. SY and MY carried out the experiments. SY, MY, KM, TS, and JH contributed to the interpretation of the results. SY and JH took the lead in writing the manuscript. All authors provided critical feedback and helped shape the research, analysis and manuscript.

FUNDING

This work was supported by Trond Mohn Foundation, Norway (BFS-2018-TMT10). APC was covered by publication fund by the University of Bergen.

ACKNOWLEDGMENTS

The authors gratefully acknowledge the Trond Mohn Foundation (Grant No. BFS2018TMT10) for financial support of this study.

SUPPLEMENTARY MATERIAL

The Supplementary Material for this article can be found online at: https://www.frontiersin.org/articles/10.3389/fbioe.2022.811942/full#supplementary-material

REFERENCES

Acosta Santamaría, V. A., Malvè, M., Duizabo, A., Mena Tobar, A., Gallego Ferrer, G., García Aznar, J. M., et al. (2013). Computational Methodology to Determine Fluid Related Parameters of Non Regular Three-Dimensional Scaffolds. *Ann. Biomed. Eng.* 41, 2367–2380. doi:10.1007/s10439-013-0849-8

Amini, A. R., Laurencin, C. T., and Nukavarapu, S. P. (2012). Bone Tissue Engineering: Recent Advances and Challenges. *Crit. Rev. Biomed. Eng.* 40, 363–408. doi:10.1615/CritRevBiomedEng.v40.i5.10

Arramon, Y. P., and Nauman, E. A. (2001). "The Intrinsic Permeability of Cancellous Bone," in *Bone Mechanics Handbook*. Second Edition.

Becquart, P., Cruel, M., Cruel, M., Hoc, T., Sudre, L., Pernelle, K., et al. (2016). Human Mesenchymal Stem Cell Responses to Hydrostatic Pressure and Shear Stress. *eCM* 31, 160–173. doi:10.22203/ecm.v031a11

Bergemann, C., Elter, P., Lange, R., Weißmann, V., Hansmann, H., Klinkenberg, E.-D., et al. (2015). Cellular Nutrition in Complex Three-Dimensional Scaffolds: A Comparison between Experiments and Computer Simulations. *Int. J. Biomater.* 2015, 1–12. doi:10.1155/2015/584362

Bhaskar, B., Owen, R., Bahmaee, H., Rao, P. S., and Reilly, G. C. (2018). Design and Assessment of a Dynamic Perfusion Bioreactor for Large Bone Tissue Engineering Scaffolds. *Appl. Biochem. Biotechnol.* 185, 555–563. doi:10.1007/s12010-017-2671-5

Blender (2021). *Blender Online Community Blender - a 3D Modelling and Rendering Package*. Available online: http://www.blender.org.

Campos Marin, A., and Lacroix, D. (2015). The Inter-sample Structural Variability of Regular Tissue-Engineered Scaffolds Significantly Affects the Micromechanical Local Cell Environment. *Interf. Focus.* 5, 20140097. doi:10.1098/rsfs.2014.0097

Cartmell, S. H., Porter, B. D., García, A. J., and Guldberg, R. E. (2003). "Effects of Medium Perfusion Rate on Cell-Seeded Three-Dimensional Bone Constructs *In Vitro*," in *Proceedings of the Tissue Engineering*. 9. doi:10.1089/10763270360728107

Chi, H.-J., Park, J.-S., Yoo, C.-S., Kwak, S.-J., Son, H.-J., Kim, S.-G., et al. (2020). Effect of Evaporation-Induced Osmotic Changes in Culture media in a Dry-type Incubator on Clinical Outcomes in *In Vitro* Fertilization-Embryo Transfer Cycles. *Clin. Exp. Reprod. Med.* 47, 284–292. doi:10.5653/cerm.2020.03552

Cignoni, P., Callieri, M., Corsini, M., Dellepiane, M., Ganovelli, F., and Ranzuglia, G. (2008). "MeshLab: An Open-Source Mesh Processing Tool," in Proceedings of the 6th Eurographics Italian Chapter Conference 2008 - Proceedings.

Clarkson, J. R., Cui, Z. F., and Darton, R. C. (1999). Protein Denaturation in Foam. *J. Colloid Interf. Sci.* 215, 333–338. doi:10.1006/jcis.1999.6256

Coughlin, T. R., and Niebur, G. L. (2012). Fluid Shear Stress in Trabecular Bone Marrow Due to Low-Magnitude High-Frequency Vibration. *J. Biomech.* 45, 2222–2229. doi:10.1016/j.jbiomech.2012.06.020

Daish, C., Blanchard, R., Gulati, K., Losic, D., Findlay, D., Harvie, D. J. E., et al. (2017). Estimation of Anisotropic Permeability in Trabecular Bone Based on microCT Imaging and Pore-Scale Fluid Dynamics Simulations. *Bone Rep.* 6, 129–139. doi:10.1016/j.bonr.2016.12.002

Dash, S. K., Sharma, V., Verma, R. S., and Das, S. K. (2020). Low Intermittent Flow Promotes Rat Mesenchymal Stem Cell Differentiation in Logarithmic Fluid Shear Device. *Biomicrofluidics* 14, 054107. doi:10.1063/5.0024437

Egger, D., Fischer, M., Clementi, A., Ribitsch, V., Hansmann, J., and Kasper, C. (2017). Development and Characterization of a Parallelizable Perfusion Bioreactor for 3D Cell Culture. *Bioengineering* 4, 51. doi:10.3390/bioengineering4020051

Faustino, C. M. C., Calado, A. R. T., and Garcia-Rio, L. (2009). Gemini Surfactant–Protein Interactions: Effect of pH, Temperature, and Surfactant Stereochemistry. *Biomacromolecules* 10, 2508–2514. doi:10.1021/bm9004723

Gao, X., Zhang, X., Xu, H., Zhou, B., Wen, W., and Qin, J. (2014). Regulation of Cell Migration and Osteogenic Differentiation in Mesenchymal Stem Cells under Extremely Low Fluidic Shear Stress. *Biomicrofluidics* 8, 052008. doi:10.1063/1.4896557

Gaspar, D. A., Gomide, V., and Monteiro, F. J. (2012). The Role of Perfusion Bioreactors in Bone Tissue Engineering. *Biomatter* 2, 167–175. doi:10.4161/biom.22170

Geris, L., Guyot, Y., Schrooten, J., and Papantoniou, I. (2016). In Silico regenerative Medicine: How Computational Tools Allow Regulatory and Financial Challenges to Be Addressed in a Volatile Market. *Interf. Focus.* 6, 20150105. doi:10.1098/rsfs.2015.0105

Grayson, W. L., Bhumiratana, S., Cannizzaro, C., Chao, P.-H. G., Lennon, D. P., Caplan, A. I., et al. (2008). Effects of Initial Seeding Density and Fluid Perfusion Rate on Formation of Tissue-Engineered Bone. *Tissue Eng. A* 14, 1809–1820. doi:10.1089/ten.tea.2007.0255

Gunatillake, P., and Adhikari, R. (2003). Biodegradable Synthetic Polymers for Tissue Engineering. *eCM* 5, 1–16. discussion 16. doi:10.22203/ecm.v005a01

Handa, A., Emery, A. N., and Spier, R. E. (1987). On the Evaluation of Gas-Liquid Interfacial Effects on Hybridoma Viability in Bubble Column Bioreactors. *Dev. Biol. Stand.* 66, 241–253.

Hanwright, J., Zhou, J., Evans, G. M., and Galvin, K. P. (2005). Influence of Surfactant on Gas Bubble Stability. *Langmuir* 21, 4912–4920. doi:10.1021/la0502894

Holtorf, H. L., Jansen, J. A., and Mikos, A. G. (2005). Flow Perfusion Culture Induces the Osteoblastic Differentiation of Marrow Stromal Cell-Scaffold

Constructs in the Absence of Dexamethasone. *J. Biomed. Mater. Res.* 72A, 326–334. doi:10.1002/jbm.a.30251

Huang, L., Cai, X., Li, H., Xie, Q., Zhang, M., and Yang, C. (2015). The Effects of Static Pressure on Chondrogenic and Osteogenic Differentiation in Condylar Chondrocytes from Temporomandibular Joint. *Arch. Oral Biol.* 60, 622–630. doi:10.1016/j.archoralbio.2015.01.003

Israelowitz, M., Weyand, B., Rizvi, S., Vogt, P., and von Schroeder, H. (2012). Development of a Laminar Flow Bioreactor by Computational Fluid Dynamics. *J. Healthc. Eng.* 3, 455–476. doi:10.1260/2040-2295.3.3.455

Jiang, G.-L., White, C. R., Stevens, H. Y., and Frangos, J. A. (2002). Temporal Gradients in Shear Stimulate Osteoblastic Proliferation via ERK1/2 and Retinoblastoma Protein. *Am. J. Physiology-Endocrinology Metab.* 283, E383–E389. doi:10.1152/ajpendo.00547.2001

Jungreuthmayer, C., Jaasma, M. J., Al-Munajjed, A. A., Zanghellini, J., Kelly, D. J., and O'Brien, F. J. (2009). Deformation Simulation of Cells Seeded on a Collagen-GAG Scaffold in a Flow Perfusion Bioreactor Using a Sequential 3D CFD-Elastostatics Model. *Med. Eng. Phys.* 31, 420–427. doi:10.1016/j.medengphy.2008.11.003

Kang, J. H., Kim, Y. C., and Park, J.-K. (2007). Analysis of Pressure-Driven Air Bubble Elimination in a Microfluidic Device. *Lab. Chip* 8, 176–178. doi:10.1039/b712672g

Kang, Y. J., Yeom, E., Seo, E., and Lee, S.-J. (2014). Bubble-free and Pulse-free Fluid Delivery into Microfluidic Devices. *Biomicrofluidics* 8, 014102. doi:10.1063/1.4863355

Kim, K. M., Choi, Y. J., Hwang, J.-H., Kim, A. R., Cho, H. J., Hwang, E. S., et al. (2014). Shear Stress Induced by an Interstitial Level of Slow Flow Increases the Osteogenic Differentiation of Mesenchymal Stem Cells through TAZ Activation. *PLoS One* 9, e92427. doi:10.1371/journal.pone.0092427

Klein, S. G., Alsolami, S. M., Steckbauer, A., Arossa, S., Parry, A. J., Ramos Mandujano, G., et al. (2021). A Prevalent Neglect of Environmental Control in Mammalian Cell Culture Calls for Best Practices. *Nat. Biomed. Eng.* 5, 787–792. doi:10.1038/s41551-021-00775-0

Lane, S. W., Williams, D. A., and Watt, F. M. (2014). Modulating the Stem Cell Niche for Tissue Regeneration. *Nat. Biotechnol.* 32, 795–803. doi:10.1038/nbt.2978

Lee, J., Kentish, S., and Ashokkumar, M. (2005). Effect of Surfactants on the Rate of Growth of an Air Bubble by Rectified Diffusion. *J. Phys. Chem. B* 109, 14595–14598. doi:10.1021/jp051758d

Li, D.-Q., Li, M., Liu, P.-L., Zhang, Y.-K., Lu, J.-X., and Li, J.-M. (2014). Improved Repair of Bone Defects with Prevascularized Tissue-Engineered Bones Constructed in a Perfusion Bioreactor. *Orthopedics* 37, 685–690. doi:10.3928/01477447-20140924-06

Li, D., Tang, T., Lu, J., and Dai, K. (2009). Effects of Flow Shear Stress and Mass Transport on the Construction of a Large-Scale Tissue-Engineered Bone in a Perfusion Bioreactor. *Tissue Eng. Part A* 15, 2773–2783. doi:10.1089/ten.tea.2008.0540

Lim, K. T., Hexiu, J., Kim, J., Seonwoo, H., Choung, P.-H., and Chung, J. H. (2014). Synergistic Effects of Orbital Shear Stress onIn VitroGrowth and Osteogenic Differentiation of Human Alveolar Bone-Derived Mesenchymal Stem Cells. *Biomed. Res. Int.* 2014, 1–18. doi:10.1155/2014/316803

Liu, Y.-S., Liu, Y.-A., Huang, C.-J., Yen, M.-H., Tseng, C.-T., Chien, S., et al. (2015). Mechanosensitive TRPM7 Mediates Shear Stress and Modulates Osteogenic Differentiation of Mesenchymal Stromal Cells through Osterix Pathway. *Sci. Rep.* 5, 16522. doi:10.1038/srep16522

Livak, K. J., and Schmittgen, T. D. (2001). Analysis of Relative Gene Expression Data Using Real-Time Quantitative PCR and the 2−ΔΔCT Method. *Methods* 25, 402–408. doi:10.1006/meth.2001.1262

Lochovsky, C., Yasotharan, S., and Günther, A. (2012). Bubbles No More: In-Plane Trapping and Removal of Bubbles in Microfluidic Devices. *Lab. Chip* 12, 595–601. doi:10.1039/C1LC20817A

Mai, Z., Peng, Z., Wu, S., Zhang, J., Chen, L., Liang, H., et al. (2013). Single Bout Short Duration Fluid Shear Stress Induces Osteogenic Differentiation of MC3T3-E1 Cells via Integrin β1 and BMP2 Signaling Cross-Talk. *PLoS One* 8, e61600. doi:10.1371/journal.pone.0061600

Mandenius, C. F. (2016). Editor C.-F. Mandenius (Weinheim, Germany: Wiley-VCH Verlag GmbH & Co. KGaA). 53; ISBN 9783527683369. *Bioreactors: Design, Operation and Novel Applications*.

Marquez-Curtis, L. A., Janowska-Wieczorek, A., McGann, L. E., and Elliott, J. A. W. (2015). Mesenchymal Stromal Cells Derived from Various Tissues: Biological, Clinical and Cryopreservation Aspects. *Cryobiology* 71, 181–197. doi:10.1016/j.cryobiol.2015.07.003

Maul, T. M., Chew, D. W., Nieponice, A., and Vorp, D. A. (2011). Mechanical Stimuli Differentially Control Stem Cell Behavior: Morphology, Proliferation, and Differentiation. *Biomech. Model. Mechanobiol.* 10, 939–953. doi:10.1007/s10237-010-0285-8

McAllister, T. N., Du, T., and Frangos, J. A. (2000). Fluid Shear Stress Stimulates Prostaglandin and Nitric Oxide Release in Bone Marrow-Derived Preosteoclast-like Cells. *Biochem. Biophysical Res. Commun.* 270, 643–648. doi:10.1006/bbrc.2000.2467

Melke, J., Zhao, F., Ito, K., and Hofmann, S. (2020). Orbital Seeding of Mesenchymal Stromal Cells Increases Osteogenic Differentiation and Bone-like Tissue Formation. *J. Orthop. Res.* 38, 1228–1237. doi:10.1002/jor.24583

Nokhbatolfoghahaei, H., Bohlouli, M., Adavi, K., Paknejad, Z., Rezai Rad, M., khani, M. M., et al. (2020). Computational Modeling of media Flow through Perfusion-Based Bioreactors for Bone Tissue Engineering. *Proc. Inst. Mech. Eng. H* 234, 1397–1408. doi:10.1177/0954411920944039

Odelius, K., Plikk, P., and Albertsson, A.-C. (2005). Elastomeric Hydrolyzable Porous Scaffolds: Copolymers of Aliphatic Polyesters and a Polyether−ester. *Biomacromolecules* 6, 2718–2725. doi:10.1021/bm050190b

Pasini, A., Lovecchio, J., Ferretti, G., and Giordano, E. (2019). Medium Perfusion Flow Improves Osteogenic Commitment of Human Stromal Cells. *Stem Cell Int.* 2019, 1–10. doi:10.1155/2019/1304194

Pereira, A. R., Lipphaus, A., Ergin, M., Salehi, S., Gehweiler, D., Rudert, M., et al. (2021). Modeling of the Human Bone Environment: Mechanical Stimuli Guide Mesenchymal Stem Cell-Extracellular Matrix Interactions. *Materials* 14, 4431. doi:10.3390/ma14164431

Piola, M., Soncini, M., Cantini, M., Sadr, N., Ferrario, G., and Fiore, G. B. (2013). Design and Functional Testing of a Multichamber Perfusion Platform for Three-Dimensional Scaffolds. *Scientific World J.* 2013, 1–9. doi:10.1155/2013/123974

Podichetty, J. T., and Madihally, S. V. (2014). Modeling of Porous Scaffold Deformation Induced by Medium Perfusion. *J. Biomed. Mater. Res.* 102, 737–748. doi:10.1002/jbm.b.33054

Porter, B., Zauel, R., Stockman, H., Guldberg, R., and Fyhrie, D. (2005). 3-D Computational Modeling of media Flow through Scaffolds in a Perfusion Bioreactor. *J. Biomech.* 38, 543–549. doi:10.1016/j.jbiomech.2004.04.011

Ramani-Mohan, R. K., Schwedhelm, I., Finne-Wistrand, A., Krug, M., Schwarz, T., Jakob, F., et al. (2018). Deformation Strain Is the Main Physical Driver for Skeletal Precursors to Undergo Osteogenesis in Earlier Stages of Osteogenic Cell Maturation. *J. Tissue Eng. Regen. Med.* 12, e1474–e1479. doi:10.1002/term.2565

Rauh, J., Milan, F., Günther, K.-P., and Stiehler, M. (2011). Bioreactor Systems for Bone Tissue Engineering. *Tissue Eng. B: Rev.* 17, 263–280. doi:10.1089/ten.TEB.2010.0612

Roddy, E., DeBaun, M. R., Daoud-Gray, A., Yang, Y. P., and Gardner, M. J. (2018). Treatment of Critical-Sized Bone Defects: Clinical and Tissue Engineering Perspectives. *Eur. J. Orthop. Surg. Traumatol.* 28, 351–362. doi:10.1007/s00590-017-2063-0

Roseti, L., Parisi, V., Petretta, M., Cavallo, C., Desando, G., Bartolotti, I., et al. (2017). Scaffolds for Bone Tissue Engineering: State of the Art and New Perspectives. *Mater. Sci. Eng. C* 78, 1246–1262. doi:10.1016/j.msec.2017.05.017

Rouwkema, J., Koopman, B. F. J. M., Blitterswijk, C. A. V., Dhert, W. J. A., and Malda, J. (2009). Supply of Nutrients to Cells in Engineered Tissues. *Biotechnol. Genet. Eng. Rev.* 26, 163–178. doi:10.5661/bger-26-163

Schindelin, J., Arganda-Carreras, I., Frise, E., Kaynig, V., Longair, M., Pietzsch, T., et al. (2012). Fiji: an Open-Source Platform for Biological-Image Analysis. *Nat. Methods* 9, 676–682. doi:10.1038/nmeth.2019.Fiji

Schreivogel, S., Kuchibhotla, V., Knaus, P., Duda, G. N., and Petersen, A. (2019). Load-induced Osteogenic Differentiation of Mesenchymal Stromal Cells Is Caused by Mechano-regulated Autocrine Signaling. *J. Tissue Eng. Regen. Med.* 13, 1992–2008. doi:10.1002/term.2948

Schuerlein, S., Schwarz, T., Krziminski, S., Gätzner, S., Hoppensack, A., Schwedhelm, I., et al. (2017). A Versatile Modular Bioreactor Platform for Tissue Engineering. *Biotechnol. J.* 12, 1600326. doi:10.1002/biot.201600326

Sellgren, K. L., and Ma, T. (2015). Effects of Flow Configuration on Bone Tissue Engineering Using Human Mesenchymal Stem Cells in 3D Chitosan Composite Scaffolds. *J. Biomed. Mater. Res.* 103, 2509–2520. doi:10.1002/jbm.a.35386

Sikavitsas, V. I., Bancroft, G. N., Lemoine, J. J., Liebschner, M. A., Dauner, M., and Mikos, A. G. (2005). Flow Perfusion Enhances the Calcified Matrix Deposition of Marrow Stromal Cells in Biodegradable Nonwoven Fiber Mesh Scaffolds. *Ann. Biomed. Eng.* 33, 63–70. doi:10.1007/s10439-005-8963-x

Sikavitsas, V. I., Bancroft, G. N., Holtorf, H. L., Jansen, J. A., and Mikos, A. G. (2003). Mineralized Matrix Deposition by Marrow Stromal Osteoblasts in 3D Perfusion Culture Increases with Increasing Fluid Shear Forces. *Proc. Natl. Acad. Sci.* 100, 14683–14688. doi:10.1073/pnas.2434367100

Sladkova, M., and de Peppo, G. (2014). Bioreactor Systems for Human Bone Tissue Engineering. *Processes* 2, 494–525. doi:10.3390/pr2020494

Sobolewski, P., Kandel, J., and Eckmann, D. M. (2012). Air Bubble Contact with Endothelial Cells Causes a Calcium-independent Loss in Mitochondrial Membrane Potential. *PLoS One* 7, e47254. doi:10.1371/journal.pone.0047254

Stavenschi, E., Corrigan, M. A., Johnson, G. P., Riffault, M., and Hoey, D. A. (2018). Physiological Cyclic Hydrostatic Pressure Induces Osteogenic Lineage Commitment of Human Bone Marrow Stem Cells: a Systematic Study. *Stem Cel Res. Ther.* 9, 276. doi:10.1186/s13287-018-1025-8

Stavenschi, E., Labour, M.-N., and Hoey, D. A. (2017). Oscillatory Fluid Flow Induces the Osteogenic Lineage Commitment of Mesenchymal Stem Cells: The Effect of Shear Stress Magnitude, Frequency, and Duration. *J. Biomech.* 55, 99–106. doi:10.1016/j.jbiomech.2017.02.002

Sumino, Y., and Akiyama, S.-i. (1987). Measurement of the Evaporation Rate of Liquid in a Shaking Flask. *J. Ferment. Technology* 65, 291–294. doi:10.1016/0385-6380(87)90090-2

Sung, J. H., and Shuler, M. L. (2009). Prevention of Air Bubble Formation in a Microfluidic Perfusion Cell Culture System Using a Microscale Bubble Trap. *Biomed. Microdevices* 11, 731–738. doi:10.1007/s10544-009-9286-8

Triaud, F., Clenet, D.-H., Cariou, Y., Le Neel, T., Morin, D., and Truchaud, A. (2003). Evaluation of Automated Cell Culture Incubators. *JALA: J. Assoc. Lab. Automation* 8, 82–86. doi:10.1016/s1535-5535(03)00018-2

Truscello, S., Kerckhofs, G., Van Bael, S., Pyka, G., Schrooten, J., and Van Oosterwyck, H. (2012). Prediction of Permeability of Regular Scaffolds for Skeletal Tissue Engineering: A Combined Computational and Experimental Study. *Acta Biomater.* 8, 1648–1658. doi:10.1016/j.actbio.2011.12.021

Tsai, H.-H., Yang, K.-C., Wu, M.-H., Chen, J.-C., and Tseng, C.-L. (2019). The Effects of Different Dynamic Culture Systems on Cell Proliferation and Osteogenic Differentiation in Human Mesenchymal Stem Cells. *Ijms* 20, 4024. doi:10.3390/ijms20164024

Walls, P. L. L., McRae, O., Natarajan, V., Johnson, C., Antoniou, C., and Bird, J. C. (2017). Quantifying the Potential for Bursting Bubbles to Damage Suspended Cells. *Sci. Rep.* 7, 15102. doi:10.1038/s41598-017-14531-5

Walsh, C., Ovenden, N., Stride, E., and Cheema, U. (2017). Quantification of Cell-Bubble Interactions in a 3D Engineered Tissue Phantom. *Sci. Rep.* 7, 6331. doi:10.1038/s41598-017-06678-y

Yamada, S., Yassin, M. A., Schwarz, T., Hansmann, J., and Mustafa, K. (2021). Induction of Osteogenic Differentiation of Bone Marrow Stromal Cells on 3D Polyester-Based Scaffolds Solely by Subphysiological Fluidic Stimulation in a Laminar Flow Bioreactor. *J. Tissue Eng.* 12, 204173142110193. doi:10.1177/20417314211019375

Yamada, S., Yassin, M. A., Weigel, T., Schmitz, T., Hansmann, J., and Mustafa, K. (2021). Surface Activation with Oxygen Plasma Promotes Osteogenesis with Enhanced Extracellular Matrix Formation in Three-dimensional Microporous Scaffolds. *J. Biomed. Mater. Res.* 109, 1560–1574. doi:10.1002/jbm.a.37151

Yao, M., Tijing, L. D., Naidu, G., Kim, S.-H., Matsuyama, H., Fane, A. G., et al. (2020). A Review of Membrane Wettability for the Treatment of saline Water Deploying Membrane Distillation. *Desalination* 479, 114312. doi:10.1016/j.desal.2020.114312

Yassin, M. A., Leknes, K. N., Pedersen, T. O., Xing, Z., Sun, Y., Lie, S. A., et al. (2015). Cell Seeding Density Is a Critical Determinant for Copolymer Scaffolds-induced Bone Regeneration. *J. Biomed. Mater. Res.* 103, 3649–3658. doi:10.1002/jbm.a.35505

Yeatts, A. B., Choquette, D. T., and Fisher, J. P. (2013). Bioreactors to Influence Stem Cell Fate: Augmentation of Mesenchymal Stem Cell Signaling Pathways via Dynamic Culture Systems. *Biochim. Biophys. Acta (Bba) - Gen. Subjects* 1830, 2470–2480. doi:10.1016/j.bbagen.2012.06.007

Yeatts, A. B., and Fisher, J. P. (2011). Bone Tissue Engineering Bioreactors: Dynamic Culture and the Influence of Shear Stress. *Bone* 48, 171–181. doi:10.1016/j.bone.2010.09.138

Yoshimura, Y., Kikuiri, T., Hasegawa, T., Matsuno, M., Minamikawa, H., Deyama, Y., et al. (2017). How Much Medium Do You Use for Cell Culture? Medium Volume Influences Mineralization and Osteoclastogenesis *In Vitro*. *Mol. Med. Rep.* 16, 429–434. doi:10.3892/mmr.2017.6611

Yourek, G., McCormick, S. M., Mao, J. J., and Reilly, G. C. (2010). Shear Stress Induces Osteogenic Differentiation of Human Mesenchymal Stem Cells. *Regenerative Med.* 5, 713–724. doi:10.2217/rme.10.60

Yu, C., Zhang, P., Wang, J., and Jiang, L. (2017). Superwettability of Gas Bubbles and its Application: From Bioinspiration to Advanced Materials. *Adv. Mater.* 29, 1703053. doi:10.1002/adma.201703053

Yu, F., Deng, R., Hao Tong, W., Huan, L., Chan Way, N., IslamBadhan, A., et al. (2017). A Perfusion Incubator Liver Chip for 3D Cell Culture with Application on Chronic Hepatotoxicity Testing. *Sci. Rep.* 7, 14528. doi:10.1038/s41598-017-13848-5

Yu, L., Ma, X., Sun, J., Tong, J., Shi, L., Sun, L., et al. (2017). Fluid Shear Stress Induces Osteoblast Differentiation and Arrests the Cell Cycle at the G0 Phase via the ERK1/2 Pathway. *Mol. Med. Rep.* 16, 8699–8708. doi:10.3892/mmr.2017.7720

Zhang, K., Fan, Y., Dunne, N., and Li, X. (2018). Effect of Microporosity on Scaffolds for Bone Tissue Engineering. *Regen. Biomater.* 5, 115–124. doi:10.1093/rb/rby001

Zhao, F., Melke, J., Ito, K., van Rietbergen, B., and Hofmann, S. (2019). A Multiscale Computational Fluid Dynamics Approach to Simulate the Micro-fluidic Environment within a Tissue Engineering Scaffold with Highly Irregular Pore Geometry. *Biomech. Model. Mechanobiol.* 18, 1965–1977. doi:10.1007/s10237-019-01188-4

Zhao, Y.-H., Lv, X., Liu, Y.-L., Zhao, Y., Li, Q., Chen, Y.-J., et al. (2015). Hydrostatic Pressure Promotes the Proliferation and Osteogenic/chondrogenic Differentiation of Mesenchymal Stem Cells: The Roles of RhoA and Rac1. *Stem Cel Res.* 14, 283–296. doi:10.1016/j.scr.2015.02.006

Conflict of Interest: The authors declare that the research was conducted in the absence of any commercial or financial relationships that could be construed as a potential conflict of interest.

frontiers | Frontiers in Bioengineering and Biotechnology

ORIGINAL RESEARCH
published: 14 April 2022
doi: 10.3389/fbioe.2022.872897

Investigating the Adipogenic Effects of Different Tissue-Derived Decellularized Matrices

Weiya Tang, Jun Qi, Qian Wang, Yaping Qu, Su Fu†* and *Jie Luan*†*

Breast Plastic and Reconstructive Surgery Center, Plastic Surgery Hospital, Chinese Academy of Medical Sciences and Peking Union Medical College, Beijing, China

OPEN ACCESS

Edited by:
Dimitrios Stamatialis, University of Twente, Netherlands

Reviewed by:
Jangwook P. Jung, Louisiana State University, United States
Umber Cheema, University College London, United Kingdom

***Correspondence:**
Su Fu
doctorsufu@163.com
Jie Luan
luanjieplastic@126.com

†*These authors have contributed equally to this work and share last authorship*

Specialty section:
This article was submitted to Tissue Engineering and Regenerative Medicine, a section of the journal Frontiers in Bioengineering and Biotechnology

Received: *10 February 2022*
Accepted: *29 March 2022*
Published: *14 April 2022*

Citation:
Tang W, Qi J, Wang Q, Qu Y, Fu S and Luan J (2022) Investigating the Adipogenic Effects of Different Tissue-Derived Decellularized Matrices. Front. Bioeng. Biotechnol. 10:872897. doi: 10.3389/fbioe.2022.872897

Objective: Decellularized adipose-derived matrix (DAM) can promote adipogenic differentiation and adipose tissue remodeling, but the biological impact of tissue origin on DAM remains unknown. The present study aimed to investigate the effects of tissue origins on the adipogenic capacity of the decellularized matrix by comparing the cellular and tissue responses of DAM versus acellular dermal matrix (ADM).

Methods: The *in vitro* response of adipose-derived stem/stromal cells (ADSCs) to DAM and ADM was characterized by proliferation and differentiation. The *in vivo* remodeling response was evaluated in the subcutaneous injection model of immunocompromised mice, using histology, protein expression, and transcriptome analysis.

Results: Both DAM and ADM exhibited excellent decellularization effects and cytocompatibility. In the absence of exogenous stimuli, DAM could induce adipogenic differentiation of ADSCs compared with ADM. In the animal model, the levels of PDGF, VEGF, and ACRP30 were higher in the DAM groups than in the ADM group, and more neovascularization and extensive adipose tissue remodeling were observed. The mRNA-seq analysis indicated that the DAM implant regulated tissue remodeling by modulating *Lat1/2* expression along with Hippo Signaling pathway in the early stage.

Conclusion: Tissue origin can influence the biological response of the decellularized matrix. DAM can retain favorable tissue-specific characteristics after the decellularization process and have unique adipogenic effects *in vitro* and *vivo*, which can be fully utilized for soft tissue repair and regeneration.

Keywords: decellularized adipose-derived matrix (DAM), acellular dermal matrix (ADM), decellularized matrix, tissue-specific, adipogenesis, tissue remodeling

Abbreviations: ADM, acellular dermal matrix; ADSCs, adipose mesenchymal stem cells; DAM, decellularized adipose-derived matrix; DEGs, Differentially expression genes; DTB, decellularized trabecular bone; ECM, extracellular matrix; eECM, esophageal ECM; GAG, glycosaminoglycans; KEGG; Kyoto Encyclopedia of Genes and Genomes; qRT-PCR, Quantitative real-time polymerase chain reaction.

INTRODUCTION

Decellularized matrix can better mimic the tissue microenvironment and promote the directed differentiation of implant cells and tissue remodeling, Compared with scaffolds made of artificial materials (Kim et al., 2020). Due to the removal of immunogenic cellular components, the decellularized matrix has good biocompatibility and safety, which can be widely used in autologous, allogeneic, and xenogeneic tissue engineering.

Compared to other tissues, adipose tissue is widely distributed in the human body and can be obtained in large quantities through fat aspiration and abdominoplasty. The extraction of the decellularized matrix from adipose tissue has extensive application prospects. Previous studies found that decellularized adipose-derived matrix (DAM) could induce differentiation of stem cells to adipocytes and promote adipose tissue remodeling without additional stimulus (Flynn, 2010; Lauren et al., 2019). However, the mechanisms underlying the adipogenic ability of DAM remain unknown, and adipogenic effects of the decellularized matrix from other tissue origins have not been investigated.

Theoretically, decellularized matrices of homologous tissue origin are ideal substrates for cell proliferation and differentiation and tissue functional remodeling. Many studies have concluded that decellularized matrix of homologous tissue origin can maintain a tissue-specific cell phenotype and induce tissue-specific differentiation. When adipose mesenchymal stem cells (ADSCs) were seeded on DAM and decellularized trabecular bone (DTB)respectively, DAM could enhance adipogenic differentiation of ADSCs, while osteogenetic differentiation of ADSCs was more pronounced in DTB (Shridhar et al., 2019). A study compared the cellular response to esophageal extracellular matrix (eECM) versus small intestinal submucosa extracellular matrix (SIS-ECM) and urinary bladder matrix (UBM), and found eECM retains tissue-specific characteristics that enhance the migration of esophageal stem cells and supports the formation of 3D organoids (Keane et al., 2015). Even so, the tissue-specific effect of Decellularized matrix was not significant in some applications, such as DAM was applied to nerve repair (Lin et al., 2011), bone (Clough et al., 2015), and cartilage degeneration (Choi et al., 2012). It can be noted that the tissue specificity of the decellularised matrix is affected by exogenous stimulus and application environments.

As a decellularized matrix that has been widely used in plastic surgery, acellular dermal matrix (ADM) has good therapeutic results in wound repair (Marston et al., 2003; Reyzelman et al., 2009), mammoplasty (Ouyang et al., 2019), cleft lip, and palate repair (Aldekhayel et al., 2012). Different tissue origins of decellularized matrices have different functional compositions, leading to tissue-specific cellular responses. The objective of the present study was to investigate the effects of tissue origins on the adipogenic capacity of the decellularized matrix by comparing the responses of DAM versus ADM *in vitro* and *in vivo*. In this study, DAM and ADM were prepared for co-culturing with ADSCs, which may play a role in adipose remodeling, and cell responses including proliferation and directed differentiation were investigated. The decellularized matrices were then injected into dorsal subcutaneous locations of immunocompromised mice to observe tissue responses and remodeling. In addition, mRNA-seq analysis was used to systematically compare gene expressions of DAM and ADM implants to elucidate underlying signaling pathways in the early stage of adipose tissue remodeling. This study explores the mechanisms that DAM promotes adipose tissue formation and provides further insight into tissue specificity of the decellularized matrix, which could help develop applications for different tissue-derived decellularized matrices in tissue repair and regeneration.

MATERIALS AND METHODS

Preparation of Human Decellularized Adipose-Derived Matrix and Acellular Dermal Matrix

Fresh human adipose tissue was obtained from four healthy female patients, ranging from 30 to 45 years old (average age 38), who underwent abdominal and femoral negative pressure liposuction surgery at the Chinese Academy of Medical Sciences & Peking Union Medical College Plastic Surgery Hospital (Beijing, China). All protocols using human samples were approved by the Plastic Surgery Hospital Ethics Committee (NO.ZX201843), and the samples were obtained with written informed consent.

The human lipoaspirate was added to distilled water and layered after 15 min at room temperature. Remove the oil in the upper layer and blood in the bottom and retain the adipose tissue in the middle layer. Repeat the cleaning several times, and subject the tissue to three cycles (2–3 h each) of freezing and thawing (−80°C to 37°C) in distilled water. Homogenize the adipose tissue at 28,000 rpm for 1 min by a homogenizer (IKA A11, Germany) and repeat three times to realize sufficient homogenization. The suspension was centrifuged at 1,000 rpm for 5 min, the oil in the upper layer was discarded, and the white precipitate in the lower layer was collected. All precipitates were soaked in 0.5 M NaCl (37°C, 4 h), 1.0 M NaCl (37°C, 4 h), distilled water (37°C, overnight), 1% Triton-X100 (37°C, 48 h), distilled water (37°C, 30 min, three times), using a thermostatic shaker (Zhicheng Analytical Instrument, Shanghai, China) at 100 rpm. Next, the precipitates were soaked in 99.9% isopropanol for 8 h to remove the lipid content. Then repeatedly rinsed with distilled water and 75% ethanol three times. The obtained DAM was stored in 1% penicillin-streptomycin solution at 4°C for further experiment.

Human acellular dermal matrix (ADM) was purchased from Beijing Jayyalife Biotechnology Co., Ltd. (Z200713). The ADM and DAM were lyophilized with a vacuum freeze-drying instrument (Xinmozhen Technology (Beijing) Co., Ltd.) and then sterilized with ethylene oxide. The lyophilized matrix was ground with a low-temperature grinder (JXFSTPRP-II-02, Shanghai Jingxin Industry) at a frequency of 70 Hz for 1 min.

Characterization of Decelluarized Matrices

The samples of fresh adipose tissue, DAM, and ADM were fixed in 4% paraformaldehyde and embedded in paraffin. 5 μm

sections were cut for hematoxylin and eosin (HE), masson's trichrome staining, and picrosirius red staining. The samples were also frozen and stained with oil red O to observe residual oil. In addition, the sample of ADM and DAM were weighed at the same dry weight. Residual DNA and glycosaminoglycans (GAG) were extracted and quantified using Quant-iTTM PicoGreen® dsDNA Reagent and Kits (Thermofisher, United States) and Blyscan Sulfated Glycosaminoglycan Assay (Biocolor, United Kingdom).

Scanning Electron Microscopy

The inner structure of DAM and ADM was observed using scanning electron microscopy (SEM) (Hitachi SU-8010, Japan). The samples were fixed with 2.5% glutaraldehyde solution at room temperature, followed by gradient ethanol dehydration, isoamyl acetate immersion, vacuum drying, gold spraying, and scanning electron microscopy (SEM) observation.

Indentation Testing

The mechanical properties of the tissue before and after decellularization were measured by indentation testing. As previously described (Omidi et al., 2014; Li et al., 2022), the specimens of adipose tissue, dermal tissue, DAM, and ADM were cut into disks with a 6-mm diameter (n = 5) using a corneal trephine and tested using a 5967 Universal Testing Machine with a 100-N load cell (Instron, Norwood, MA). For unconfined compressive testing, the specimens were compressed at 10 mm/min via the indenters until 100N strain was reached. The yield point was determined, and the yield strength (kPa) was recorded. Young's modulus was calculated by the slope of linear compression phase of the stress-strain curve.

Isolation and Culture of Adipose-Derived Stem/Stromal Cells

Sterile adipose tissue was obtained from the liposuction mentioned above. ADSCs were isolated by conventional enzyme digestion (0.5 mg/ml collagenase I, 50 min, 37°C). The primary ADSCs were cultured with low-glucose Dulbecco's Modified Eagle's Medium (10% fetal bovine serum, 1% penicillin, and 1% streptomycin) at 37°C with 5% CO_2 in a humidity atmosphere. Change the culture medium every 2 days and passage the cells after 70%–80% confluence. The third-forth passage ADSCs were chosen for further experiment. The complete growth medium was replaced with the differentiation medium (including 0.25 mM isobutylmethylxanthine and 1 mg/ml of troglitazone) to induce differentiation.

Cell Seeding

The lyophilized matrix was cut into 10 mg pieces then were rinsed in 75% ethanol and sterile PBS. 60 µl ADSCs suspension (10 (Keane et al., 2015) cells) were seeded in the DAM and ADM and placed into 24-well transwell culture inserts in a 0.4 µm layer. After 24 h in culture, the ADSC-matrix composites were transferred to a new 24-well plate for better exposure to the medium.

Cell viability and adhesion rate were determined using the PrestoBlue™ Cell Viability Reagent (Thermo, United States). An equal number of cells were seeded in blank wells as the control group in the 24-well plate (n = 3 for each group). PrestoBlue solution (400 µl) was added to each well, and the plates were incubated at 37°C for 30 min. After incubation, the fluorescence intensity with excitation wavelength at 560 nm and emission wavelength at 590 nm was measured using a microplate reader (Multiskan, Thermo Fisher Scientific, United States). The LIVE/DEAD® Viability/Cytotoxicity Assay Kit (Thermo Fisher) was used to visualize the attachment and stretching of cells at days 2 and 5 after cell seeding. Confocal microscopy was performed using a Leica TCS SPII microscope (Leica, Allendale, NJ).

Quantitative Real-Time Polymerase Chain Reaction

Gene expression of adipogenic marker (PPARγ) was characterized by qRT-PCR analysis. Total RNA of samples at days 7 and 14 were extracted using TRIzol reagent (Invitrogen, Burlington, VT, Canada) from samples following the manufacturer's protocol. Primer sequences of PPARγ is (5′–3′) F: TGGAATTAGATGACAGCGACTTGG R: CTGGAGCAG CTTGGCAAACA. The RNA template was converted into cDNA using SYBR Green Master Mix (Life Technologies). Quantitative reverse-transcription polymerase chain reaction (qRT-PCR) was conducted on a StepOnePlus Real-Time PCR System. The amplification was performed using the cycling conditions- 3 min at 95°C, followed by 40 cycles of 15 s at 95°C and 20 s at 60°C. All samples were tested for three biological replicates. The gene expression level was determined according to the fluorescence signal and calculated by the $2^{-\Delta\Delta ct}$ method, using GAPDH as an internal reference gene standardization.

Experimental Animal Model

The immunocompromised mice used in the experiment were C57Bl/6 (B6.129S7-Rag1^{tm1Mom}/J) female mice aged 6–10 weeks (Shanghai Model Organisms Center Inc., Shanghai, China). The animal experiment protocol strictly followed the regulations and standards of protection and use of experimental animals set forth by the Chinese Academy of Medical Sciences & Peking Union Medical College.

After grinding, the DAM and ADM powders were weighed, and 0.4 ml of normal saline was added into 5 mg of the powders to mix thoroughly. The injection area on the dorsal skin was shaved and aseptically prepared. 0.4 ml matrix suspension was injected into the back of mice per side using 18-gauge needles. So each mouse could get two separate samples. Mice were euthanized at weeks 1, 3, 5, 8, and 12 after injection, and samples of the implants were then obtained.

Histological and Immunohistochemical Staining

After being fixed in the 4% paraformaldehyde for 24–48 h, samples were paraffin-embedded and sectioned (5 µm

sections). Haematoxylin and eosin (HE) and Masson's trichrome staining were used to examine the morphology of the implants at each study time point. Immunohistochemistry against the adipogenic marker perilipin-1 (Abcam ab3526) was performed. In addition, CD31 (Proteintech 28083-1-AP) was used to localize vascular endothelial cells. In order to compare the observed adipogenesis between DAM and ADM, the adipose area was measured across the entire implant cross-section and expressed as a percentage of the total implant area for all time points. Angiogenesis in implants was assessed by measuring the percentage of CD31-positive areas as also. All analyses were conducted in a blinded fashion in 5–10 randomly selected and non-overlapping fields across the implant using Olympus BX51 microscope (Olympus, Center Valley, PA) and Image Pro Plus 6.0.

The mRNA-Seq Analysis

Total RNA was extracted from tissues of DAM and ADM implants at 1 week using standard protocols. The sample size for conventional mRNA-seq libraries was fixed at three biological replicates. After the qualifications of RNA samples, the common transcriptome libraries were constructed. Qubit 3.0 was used for preliminary quantification, and qPCR was used to quantify the effective concentration of the library accurately. After the library inspection, PE150 mode sequencing was performed using Illumina NovaSeq 6000 sequencing platform. The obtained sequencing datum was qualified, then these high-quality sequences were aligned to the reference genome. Differential expression significance analysis was performed using edgeR, and the actual analysis parameters used in this analysis were: | log2(Fold Change) | > 1, qvalue < 0.05. Enrich-KEGG (Kyoto Encyclopedia of Genes and Genomes) method and Enrich-GO method were utilized to calculate enrichment test for KEGG pathways and Gene Ontology terms.

The sequencing results were verified using the qRT-PCR method described above. The primer sequences are listed in **Supplementary Table S1**.

Cytokine Assessment by ELISA and Luminex Assay

After injection for 1, 3, and 5 weeks, the implants were harvested entirely to detect the level of related factors. Each sample was added 300–500 μl of the lysate (abs9225, Absin, China), then was ground at low temperature. Protein suspensions were obtained by centrifugation at 14,000 rpm, 4°C for 10 min after 2 repetitions. The protein concentration in each sample was measured by the BCA method (Beyotime, China). Assays were performed as per the manufacturer's instructions ($n = 3$).

ELISA kits were used to assess acrp30 (R&D Systems) and TNF-a (absin) levels. Samples and standards were added to each well of the plate. Plates were incubated for 2–3 h at room temperature (R.T.) and rinsed 4 times with wash buffer, then the buffer was removed and 200 μl conjugate was added. Plates were incubated for 1–2 h at R.T., rinsed 4 times, the buffer removed, and 100 ml color substrate added. After incubating 30 min in the dark at R.T., 50–100 μl stop solution was added to each well. Plates were read using a Multiskan microplate reader (Thermo) set at 450 nm absorbance with a correction reading set at 570 nm, and values were calculated back to pg/ml of the original sample volume.

The Luminex assay was used to assess CCL2/JE/MCP-1, CCL3/MIP-1 alpha, FGF basic/FGF2/bFGF, IFN-γ, IL-1 beta/IL-1F2, IL-4, IL-6, IL-10, PDGF-AA, and VEGF levels. Prepare all the required reagents and samples. Add 50 μl of diluted beads and 50 μl of standards or samples to each well, shake for 2 h at R.T., place the plate on a magnetic stand to ensure the beads are held in place, and wash three times with washing solution. 50 μl of antibody complex was added to each well and shook for 1 h, 800 rpm at R.T. The plate is then placed on a magnetic stand to ensure that the beads are held in place and washed three times with washing-up liquid. Add 50 μl of streptavidin-labeled P.E. to each well and shake for 0.5 h at R.T. Place the plate on a magnetic stand to ensure that the beads are held and wash three times with washing solution. The beads were resuspended with 100 μl of washing solution, incubated, and shook for 2 min with the speed of 800 rpm. The plate was tested on the Luminexv (X-200).

Statistical Analysis

All data are expressed as the mean ± standard deviation (SD). Statistical analyses were performed using Prism 9.0 software (Graphpad Software, United States). The statistical significance of data was analyzed using analysis of variance (ANOVA) at the 95% confidence level. $p < 0.05$ was considered statistically significant ($^{*}p < 0.05$, $^{**}p < 0.01$, $^{***}p < 0.001$, $^{****}p < 0.0001$).

RESULTS

Evaluation of Decellularized Adipose-Derived Matrix and Acellular Dermal Matrix

Physical and chemical treatments were used to realize the decellularization of adipose tissue. Macroscopically, DAM showed a white, homogeneous, and loose appearance (**Figure 1A**). H&E staining confirmed the absence of cells and cell debris in DAM at the end of the process (**Figure 1A**). Masson's Trichrome staining showed blue-stained collagenous components without red staining nuclei, which also confirmed the effectiveness of the decellularization process (**Figure 1A**). Oil-red O staining showed no red-stained lipid components, indicating that the lipid components in adipose tissue were effectively removed (**Figure 1A**).

Picrosirius red staining (**Figure 1B**) was used to compare the distribution and organization of collagens in the DAM and ADM. Both decellularized matrices contained tightly arranged yellow or red type I collagen, a small amount of green type III collagen, and yellowish type IV collagen. The DAM was arranged in a relatively loose network consisting of a blend of thick and thin fibers. While in ADM, it was arranged in a dense woven pattern with thicker fibers (**Figure 1B**). SEM micrographs depicted the inner microstructure of DAM and ADM (**Figure 1B**) also confirmed the removal of cells from the tissue. After grinding, the overall

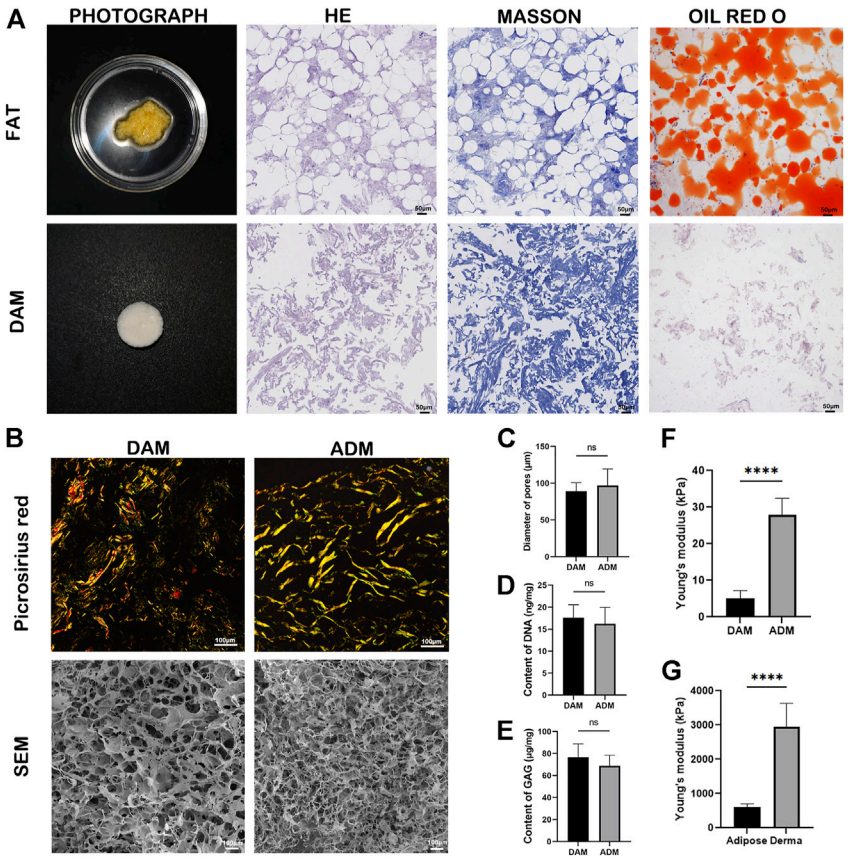

FIGURE 1 | Characterizations of DAM and ADM. **(A)** Photograph, H&E staining, Masson's Trichrome and Oil-red O staining of adipose tissue and DAM. Scale bars = 50 μm. **(B)** Picrosirius red staining and SEM of the DAM and ADM. Scale bars = 100 μm. **(C)** Diameter of DAM and ADM pores in SEM, $n = 5$. **(D)** The content of DNA in DAM and ADM, $n = 5$. **(E)** The content of GAG in DAM and ADM. $n = 5$, ns, no significance. **(F)** The Young's modulus of DAM and ADM. $n = 5$, $^{****}p < 0.0001$. **(G)** The Young's modulus of adipose and derma. $n = 5$, $^{****}p < 0.0001$.

ultrastructure of DAM and ADM were similar with pores and entwined fibers structure. In addition, the pores of DAM were more evenly distributed with the thicker and more orderly fibers. ADM had larger pores (96.80 ± 22.64 μm) than DAM (89.00 ± 11.73 μm) with no significance (**Figure 1C**).

The content of DNA and GAG were detected in prepared DAM, taking commercial ADM as a comparison ($n = 5$). The residue of DNA in the DAM group was 17.60 ± 2.97 ng/mg, and that in the ADM group was 16.20 ± 3.77 ng/mg (**Figure 1D**). The GAG content in the DAM group was 76.6 ± 12.18 μg/mg, and that in the ADM group was 68.80 ± 9.68 ng/mg (**Figure 1E**). There were no significant differences in DNA and GAG content in the two groups. The results showed that the acellular method could effectively remove cellular components and retain active ingredients of the decellularized matrix.

The results of indentation testing showed that Young's modulus measured for each group of samples were: derma (2,952.00 ± 678.80 kPa)> adipose (604.20 ± 96.59 kPa)> ADM (27.94 ± 4.48 kPa)> DAM (5.17 ± 2.11 kPa) (**Figures 1F,G**). Young's modulus of Dermal tissue and ADM were significantly higher than that of adipose tissue and DAM, respectively. Although ADM is closer to adipose tissue in terms of Young's modulus values, it is important to note that fresh tissue is a composite structure containing multiple components compared to decellularized matrix, so it is not suitable to directly compare Young's modulus of both.

The Viability and Differentiation of ADSCs Seeded on Decelluarized Matrices

After ADSCs were seeded in DAM and ADM for 24 h, 77.04 ± 4.46% and 67.94 ± 4.21% of the cells successfully adhered to the DAM and ADM, respectively (**Figure 2A**). The proliferation curve of the ADSCs changed slightly compared with the control group, but the cells remained in a good growth state (**Figure 2B**). Confocal imaging demonstrated that calcein AM–stained ADSCs attached and infiltrated the acellular matrix (**Figure 2C**). From days 2–5, the number of green fluorescence-labeled living cells increased from 75.8 ± 11.08 to 152.2 ± 8.96 in DAM and 49.2 ± 4.38 to 120 ± 11.18 in ADM, with few red fluorescence-labeled dead cells (**Figure 2D**). Also, live ADSCs are more numerous and evenly distributed in the DAM than in the ADM.

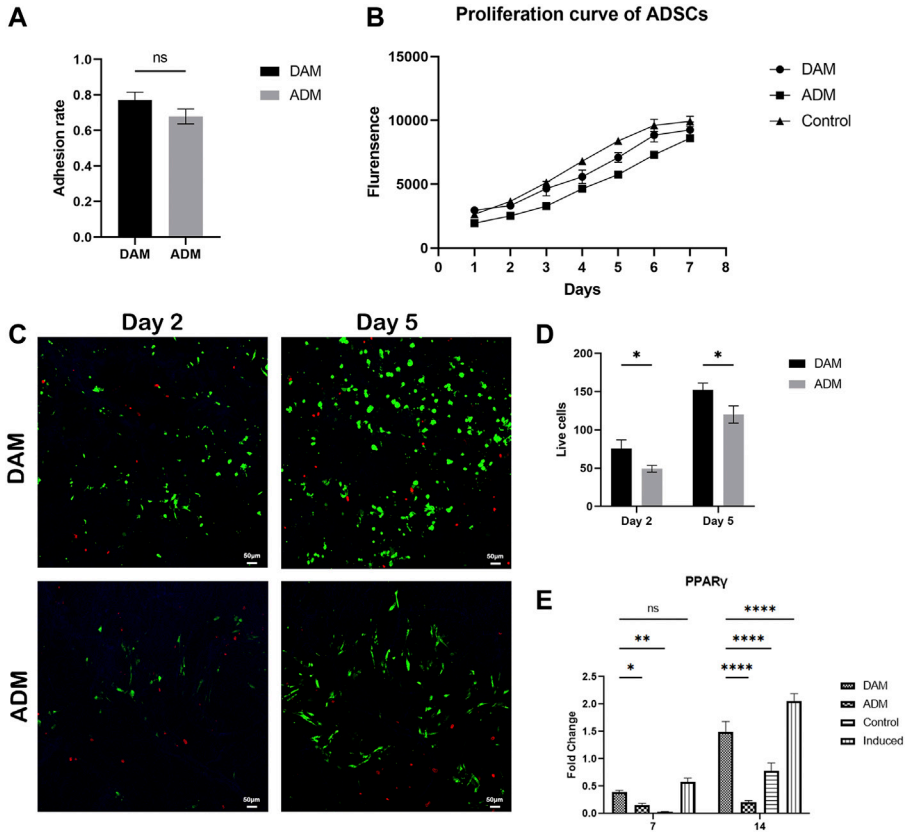

FIGURE 2 | The viability and differentiation of ADSCs seeded on DAM and ADM. **(A)** Adhesion rate of ADSCs to DAM and ADM at 24 h after being seeded, $n = 5$. **(B)** The proliferation and differentiation of ADSCs seeded on DAM and ADM. **(C)** DAM or ADM co-cultured with ADSCs stained by LIVE/DEAD® assay at days 2 and 5. Scale bars = 50 μm. **(D)** The number of green fluorescence-labeled living ADSCs in DAM and ADM, $n = 5$. **(E)** Adipogenic gene *PPARγ* expression of ADSCs in DAM, ADM, control, and induced groups at days 7 and 14. $n = 3$, ns, no significance, $^{*}p < 0.05$, $^{**}p < 0.01$, $^{****}p < 0.0001$.

Quantitative RT-PCR analysis of adipogenic gene revealed that the DAM group and induced group (ADSCs were cultured in differentiation medium) exhibited a higher expression level of *PPARγ* and compared to that on ADM at days 7 and 14. The levels of adipogenic maker were not detectable found in the control group (ADSCs were cultured in growth medium), which were relatively low in the ADM group. The expression of the critical regulator of adipogenesis in the non-induced DAM group suggested the microenvironment was conducive to adipogenesis, while the ADM group was not (**Figure 2E**).

Tissue Response and Implant Remodeling

In order to compare the response of decellularized matrix from different tissue sources implanted *in vivo*, DAM and ADM were injected subcutaneously into the back of immunocompromised mice, and samples were harvested at 1, 3, 5, 8, and 12 weeks after injection. Based on visual observation, the two groups of implants formed a complete capsule on the surface, with clear boundaries with surrounding tissues (**Figure 3A**). The color of implants in the DAM group gradually changed from white to fleshy pink, and the texture was softer, similar to the surrounding subcutaneous adipose tissue. In contrast, the implant in the ADM group always maintained a white appearance with a hard texture. As seen in HE staining, scaffold cellularity was enhanced in the DAM group, particularly at the 3, 5, and 12 weeks (**Figure 3B**; **Supplementary Figure S1**). At 3 weeks, adipocytes aggregated from the edge of the implant to the center in the DAM group, and then, the number of adipocytes increased and gradually occupied the implant at 5–12 weeks. In contrast, infiltrating cells were significantly reduced in the ADM group, and almost no adipocytes were observed. Specifically, most implant regions in the DAM group had been remodeled into mature adipose tissue at 12 weeks.

Masson trichrome staining was used to compare collagen retention and the tissue remodeling between two groups (**Figure 3C**; **Supplementary Figures S2, S3**). The collagen areas were stained as blue and expressed as a percentage of the total implant area at all time points. At 1 week after injection, minimal remodeling was observed in both groups. At 3 weeks, the percentage of collagen was 77.39 ± 4.25% in the DAM group compared to 96.48 ± 4.13% in the ADM group. This difference was enhanced at 5 and 8 weeks, 70.32 ± 8.92% and 51.50 ± 6.95% of the collagen retention were in the DAM group, compared with 93.90 ± 3.54% and 92.48 ± 2.34% in the ADM group separately. Up to week 12, only 22.99 ± 3.21% of the DAM

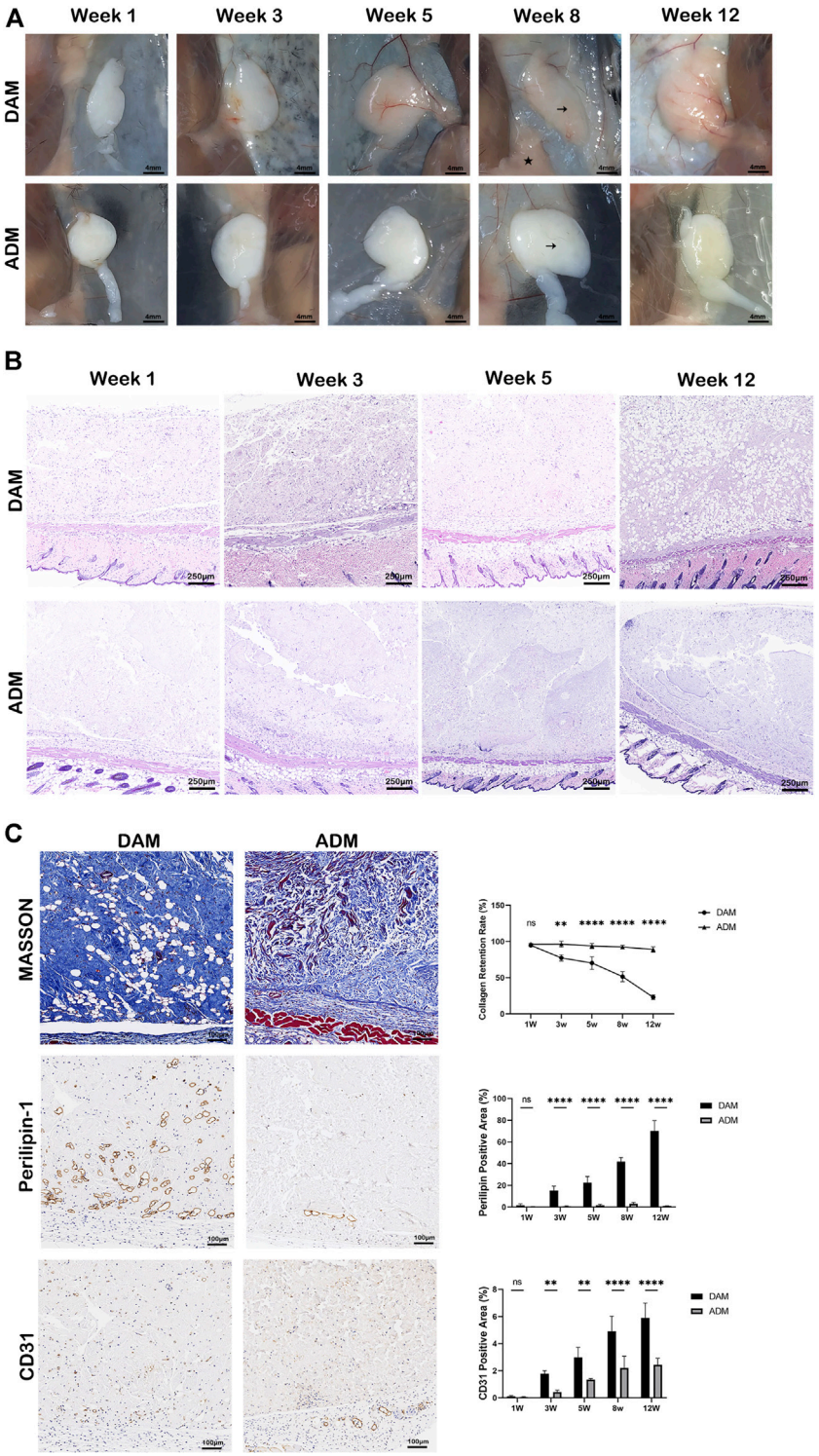

FIGURE 3 | Histology and immunolabeling of DAM and ADM after injection. **(A)** Visual observation of implants at weeks 1, 3, 5, 8, and 12. The DAM and ADM implants (black arrows) were adjacent to mice's subcutaneous adipose tissue (pentacle). Scale bars = 4 mm. **(B)** H&E staining of DAM and ADM implants at weeks 1, 3, 5, and 12. Scale bars = 250 μm. **(C)** Masson trichrome staining and Immunohistochemistry of implants at weeks 5. Collagen retention rate and percentage of perilipin-1 and CD31 positive areas at different time points were displayed. Scale bars = 100 μm, $n = 5$, ns, no significance, $^{*}p < 0.05$, $^{**}p < 0.01$, $^{****}p < 0.0001$.

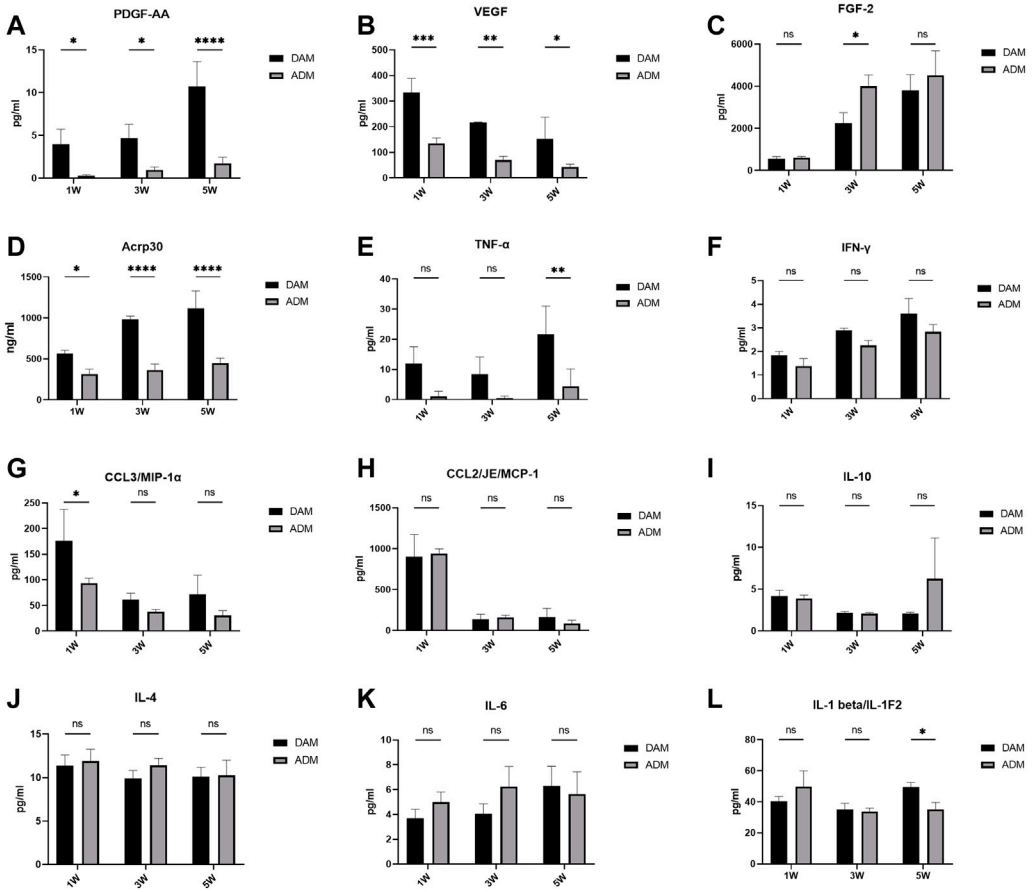

FIGURE 4 | Cytokine and adipokine levels in DAM and ADM implants. $n = 3$. ns, no significance, $^{*}p < 0.05$, $^{**}p < 0.01$, $^{***}p < 0.001$, $^{****}p < 0.0001$.

implant had not been remodeled, while 89.03 ± 3.66% of the ADM implant was still retained.

Immunohistochemistry with antibodies against perilipin-1 revealed positive expression of adipocyte. The percentage of positive perilipin-1 areas was used to compare adipogenesis between two groups at different time points. The trend of the data was opposite to that of collagen retention above. The less collagen left, the more adipose tissue was remodeled. At week 1, no apparent adipocytes were observed in both groups without significant difference. From weeks 3–12, the percentage of adipocytes area ranged from 1.83 ± 1.21% to 70.16 ± 9.50% in the DAM group. While in the ADM group, only a small amount of adipocytes could be observed at weeks 5 (1.76 ± 0.88%) and 8 (3.68 ± 1.85%), which was dropped at weeks 12 (1.08 ± 0.23%). Overall, steady adipogenesis was observed in the DAM group, while rare and unstable in the ADM group (**Figure 3C**; **Supplementary Figures S2, S3**).

Angiogenesis in implants was assessed by the percentage of CD31 positive area of the total implant area. The constant growth of neo-blood vessels could be seen in both groups as time went by. At 3, 5, 8, and 12 weeks, blood vessel densities in the DAM group were higher than the ADM group with significant differences. It was also noted that adipogenesis is inevitably accompanied by angiogenesis in the DAM group (**Figure 3C**; **Supplementary Figures S2, S3**).

Cytokine and Adipokine Levels in Implants

PDGF and VEGF in the implants remained at higher levels in the DAM group than in the ADM group. There was a gradual increase in PDGF levels and a gradual decrease in VEGF levels over time in both groups (**Figures 4A,B**). FGF-2 and Acrp30 were measured at significantly higher levels than other cytokines and constantly increased from 1 to 5 weeks. FGF-2 levels were significantly higher in the ADM group than in the DAM group at week 3 (**Figure 4C**). As an adipose marker mainly secreted by adipocytes, Acrp30 was significantly more in the DAM group than in the ADM group, consistent with the histological observation of adipogenesis (**Figure 4D**).

Related inflammatory cytokines levels were also measured. The level of TNF-α remained consistently low in the ADM group and was significantly lower than in the DAM group at week 5 (**Figure 4E**). DAM groups had higher IFN-γ levels than ADM groups with no significance and an upward trend over time in both (**Figure 4F**). Both MCP-1 and MIP-1α levels remained relatively high in the first week, with MIP-1α levels in the DAM group being significantly higher than in the ADM group, and a substantial number of macrophages were

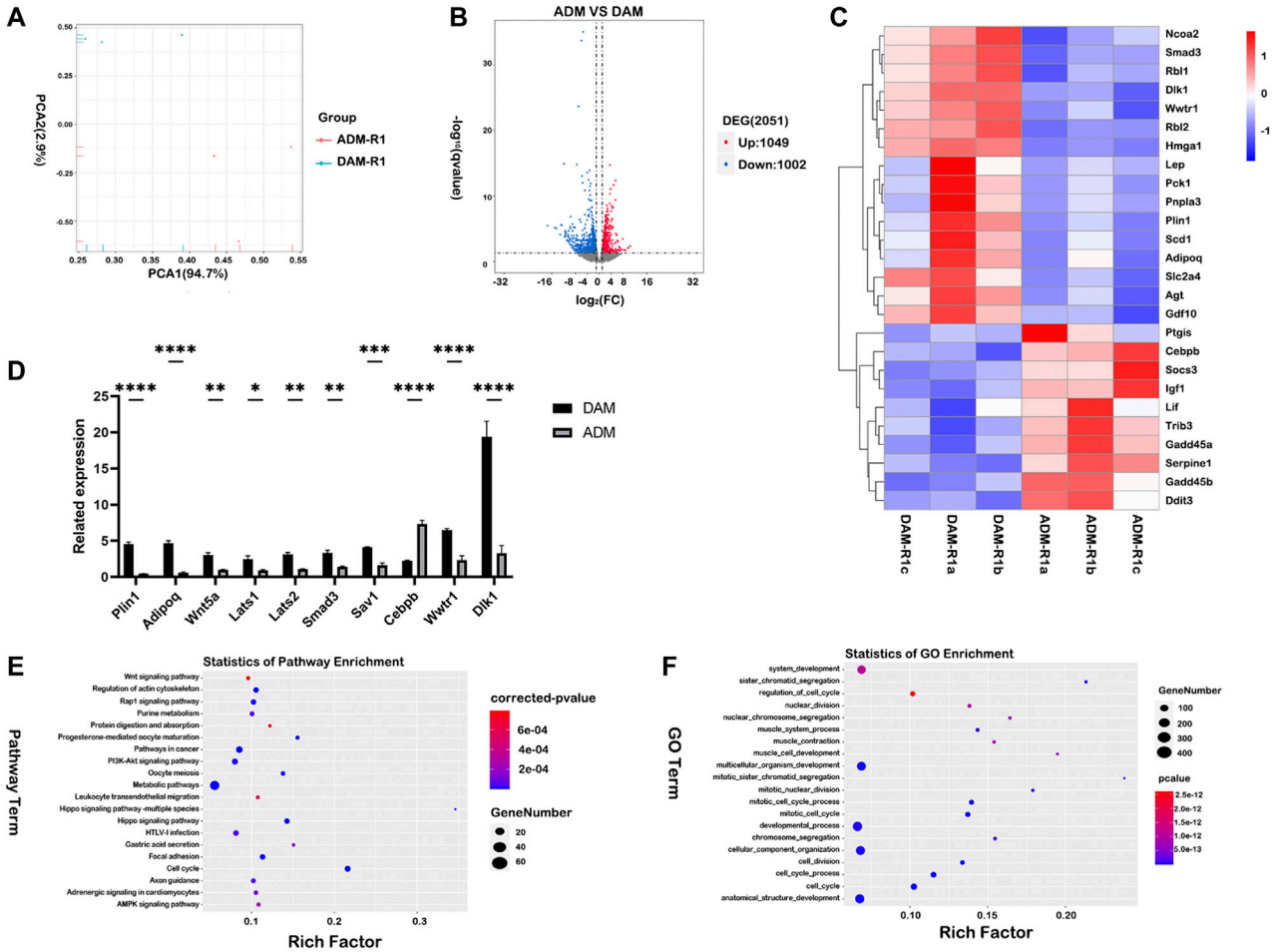

FIGURE 5 | Comparative transcriptome profiling of DAM and ADM implants using functional enrichment analysis. **(A)** Principal component analysis (PCA) was used to show potential similarities between the two groups. **(B)** Differentially expression genes (DEGs) of the two groups showed that a total of 2,051 genes were differentially expressed, of which 1,049 genes were upregulated and 1,002 genes were downregulated. **(C)** Adipogenesis-related genes were selected from DEGs and listed as heatmaps. **(D)** The qRT-PCR analysis verified the results of the microarray analysis. $n = 3$. $^{*}p < 0.05$, $^{**}p < 0.01$, $^{***}p < 0.001$, $^{****}p < 0.0001$. **(E)** The top-20 upregulated KEGG pathways in the DAM group were listed based on DEGs. **(F)** The top-20 upregulated GO terms (Biological Process) in the DAM group were listed based on DEGs.

also observed within the implants in the first week, followed by significant declines in weeks 3 and 5 (**Figures 4G,H**). The levels of IL-10, IL-4, IL-6, and IL-1β fluctuated over time, with no significant differences between the two groups, except at weeks 5, when IL-1β levels in the DAM group were higher than that in the ADM group (**Figures 4I–L**). Although IL-6 levels in the DAM group were lower than in the ADM group at weeks 1 and 3 with no significance, as the number of adipocytes in the DAM increased and could also secrete IL-6, this might lead to higher levels of IL-6 in the DAM than in the ADM at weeks 5 (**Figure 4K**).

Transcriptome Profiling With Functional Enrichment Analysis

Histology indicated DAM and ADM implants generated different tissues remodeling *in vivo*. In order to further investigate the molecular mechanisms for gene regulatory networks in the early stage after injection, mRNA-seq analysis was performed for samples harvested on day 7 ($n = 3$ for each group). Principal component analysis was used to show potential similarities between the two groups (**Figure 5A**). Differentially expression genes (DEGs) of the two groups showed that a total of 2,051 genes were differentially expressed, of which 1,049 genes were upregulated and 1,002 genes were downregulated (**Figure 5B**). The result confirmed that the DAM induced different tissue responses compared with ADM. Adipogenesis-related genes (Dlk1, Rbl2, Hmga1, Plin1, Smad3) were selected from DEGs and listed as heatmaps (**Figure 5C**). Most of the genes were up-regulated in the DAM group at week 1, which might play an essential role in the early stage of adipose tissue remodeling, and the reliability of the transcriptome analysis was verified by qRT-PCR (**Figure 5D**).

Furthermore, gene expression enrichment of several signal pathways using KEGG enrichment analysis was investigated to

understand the specific responses observed in different groups. The top-20 upregulated and downregulated KEGG pathways were listed based on DEGs in the DAM and ADM groups (**Figure 5E**; **Supplementary Figure S4**). Overall, the gene enrichment pathways Hippo signaling pathway, PI3K-Akt signaling pathway, and Rap1 signaling pathway, which were upregulated in DAM, were all associated with lipid metabolism and adipogenesis (**Figure 5E**). In contrast, the listed top-20 upregulated KEGG pathways in the ADM group indicated a large variation between the two decellularized matrices in tissue responses (**Supplementary Figure S4**). Interestingly, metabolic pathways were enriched in both groups with different subpathways.

Analysis of functional enrichment was applied in gene ontology (GO) terms. (**Figure 5F**) At the initial phase of DAM implantation, up-regulated genes involved in cell proliferation (GO:1903047, GO:0022402) and tissue regeneration (GO:0048856, GO:0032502) contained more up-regulated gene expression. Besides, protein targeting (GO: 0006614, GO:0045047) is more concentrated in the ADM group (**Supplementary Figure S5**).

DISCUSSION

In previous studies, multiple types of tissues have been decellularized for various applications (Badylak et al., 2009; Sadtler et al., 2016; Dziki and Badylak, 2018). It remains unclear how different tissue-derived decellularized matrices produce different tissue properties and subsequently cause specific tissue responses. Adipose tissue is more accessible than other tissues (heart, liver, bladder, etc.) and can be an important source of the decellularized matrix. Studies on the tissue specificity of the decellularized matrix will help achieve functional regulation of decellularized matrix and facilitate clinical translation. The present study shows that the decellularized matrix of homologous tissue origin-DAM enhances adipogenic differentiation of ADSCs *in vitro* and promotes adipose tissue remodeling *in vivo*. These results suggest that the tissue-specific properties of adipose tissue are retained after the decellularization process and can be identifiable in the immunocompromised mouse model.

The cell and tissue responses to the decellularized matrix are influenced by many factors, such as the decellularization process, the sterilization method, and the tissue source. Different decellularization methods are chosen because each tissue has different physical properties (Crapo et al., 2011). Therefore, it is also difficult to standardize the method of decellularization for different tissues. Decellularization methods usually include physical, chemical and biological methods, and more than two methods are used together in the processing (Dong et al., 2018). In this study, physical methods combined with chemical methods were used to decellularize the obtained adipose tissue of human origin, taking advantage of adipose tissue's soft and fragile nature. Firstly breaking the adipose tissue by freeze-thawing cycles and grinding can increase the contact area of reagents and improve the decellularization efficiency. Then the cellular components were removed with a milder non-ionic detergent (1% Triton X-100), thus reducing damage to the tissue structure and composition by chemical detergents (Du et al., 2011). Finally, the oil was removed with isopropyl alcohol in a shorter period, which is more conducive to maintaining the natural properties of DAM (Brown et al., 2011). No biological enzymes were used in the experiment, compared with the traditional decellularization method (Flynn, 2010), which can avoid the damage led from enzymes to the matrix structure and reduce the exogenous contamination.

Considering the different textures and compositions of dermal and adipose tissues, clinically available human-derived ADM was purchased directly for the experiment. The properties of the two decellularized matrices obtained are compared in histological staining, microstructure by electron microscopic scanning, and DNA and GAG content. The comparison results demonstrated the validity of the decellularization method employed in the experiments. To facilitate injection and use, many researchers have prepared the decellularized matrix in the form of the hydrogel by enzymatic digestion or polymer material compounding (Wu et al., 2012; Adam Young et al., 2014; Brown et al., 2015). However, we would like to preserve the original state of the decellularized matrix as much as possible and reduce the interference of exogenous factors. Therefore, the two decellularized matrices were ground, and the microstructures of DAM and ADM were similar in scanning electron microscopy, showing a sparse structure with uniform distribution of pores.

Our study demonstrated *in vitro* that DAM provides an inductive microenvironment for adipogenic differentiation of ADSCs. PPARγ is considered the master controller of adipogenic differentiation (Morrison and Farmer, 2000). ADSCs expressed higher levels of PPARγ in the complete medium after seeding in DAM, compared to the ADM group and blank group. There is growing evidence that decellularized matrices can help induce stem cell differentiation *in vitro*. In addition to DAM, DTB can also promote osteogenic differentiation of stem cells without induction factors (Hung et al., 2016; Paduano et al., 2017). Researchers found that DAM showed enhanced adipogenic induction of ADSCs in the adipogenic induction medium, while in the osteogenic induction medium, DTB showed enhanced osteogenic induction (Shridhar et al., 2019). It is important to be noted that ADSCs exhibit differentiation consistent with the induced differentiation medium even in different decellularized matrices. This suggests that the tissue specificity of the decellularized matrix does exist but is also susceptible to exogenous factors. In addition, Young's modulus of DAM was significantly lower than that of ADM, which was also more favorable to the lipogenic differentiation of ADSC in cellular experiments. Previous studies have shown that tissue stiffness is an important factor contributing to the direction of stem cell differentiation (Levy-Mishali et al., 2009; Gilpin and Yang, 2017), and lower stiffness is more favorable for adipogenic differentiation of stem cells compared to osteogenic differentiation (Marinkovic et al., 2016). Currently, Young's modulus and tensile strength are the most common measurements to study the mechanical properties of DAM. However, the relevant data obtained from multiple

studies were not similar and fluctuated over a wide range (Yu et al., 2013a; Omidi et al., 2014), which might be due to the differences in the decellularization method, the physical state, and the measurement method of each study. For these reasons, there is a lack of uniform standards for the mechanical properties of various forms of decellularized matrices.

The environment *in vivo* is more complex than that *in vitro*, and the remodeling reaction of the decellularized matrix *in vivo* is closely associated with tissue regeneration. The DAM implant significantly enhanced adipogenesis in immunocompromised mice in the current study. Adipogenesis is accompanied by collagen degradation and angiogenesis in the decellularized matrix. By Masson staining, it is evident that ADM and DAM have different degradation rates *in vivo*. In fact, until week 12, ADM can maintain more than 80% of collagen residues after subcutaneous injection, which is only about 20% in DAM. The decellularized matrix releases bioactive peptides during degradation and plays a vital role in tissue remodeling. It can initiate and enhance the remodeling process, such as angiogenesis (Li et al., 2004), mitogenesis, and chemotaxis of site-specific cells (Agrawal et al., 2009), and can recruit progenitor cells (Agrawal et al., 2010). The different degradation rates of DAM and ADM may also contribute to the different responses *in vivo*. When ADM combined with tissue expander was used in breast reconstruction surgery, it was found that after several months *in vivo*, ADM occurred with little degradation and local cellular infiltration (Gaster et al., 2013). Although ADM had been ground and injected into the mice, 12 weeks later, it still indicated little degradation, which may be related to the composition of ADM. The decellularized matrix is usually composed mainly of collagen, laminin, elastin, and GAG, including various cytokines (Marçal et al., 2012; Aamodt and Grainger, 2016). The types and amounts of these proteins in decellularized matrices of different tissue origins are not the same, which may affect the cellular responses of the decellularized matrix. However, it is still challenging to determine which protein differences are responsible due to the impacts of different methods for decellularization and protein extraction (He et al., 2019; Jiang et al., 2021).

The development of mature adipose tissue requires the support of an extensive capillary network (Cao, 2007). The neovascularization occurred and grew over time in both decellularized matrices implants, which was more pronounced in the DAM. ADM has been studied and used for a longer period than DAM, and neovascularization has been found in ADM grafts in both clinical trials and animal studies (Gaster et al., 2013; Boháč et al., 2018), of which the mechanism is not clear. It has been shown that implanted extracellular matrix can enhance adipogenesis through local delivery of the pro-angiogenic growth factors VEGF-A, PDGF-BB, and FGF-2 (Ting et al., 2014). PDGF and VEGF in the samples showed significantly higher levels in the DAM group than in the ADM group at different time points, which also indicated that DAM had a better ability to promote angiogenesis *in vivo*. Both groups had similar trends of the growth factors over time, with a gradual increase in PDGF and FGF-2 levels and a gradual decrease in VEGF levels. Some researchers believe DAM stores many growth factors, including VEGF, FGF-2, and PDGF, promoting neovascularization *in vivo* (He et al., 2019; Mohiuddin et al., 2019). It was also attempted to detect the concentrations of growth factors in the decellularized matrices before implantation compared to after implantation, and the proteins in DAM and ADM were extracted using the same method. The detected protein concentrations were too low for the subsequent factor assay, and protein electrophoresis showed almost no significant protein bands (**Supplementary Figure S6**). This result indicates that after the decellularization process, the decellularized matrix comprises insoluble proteins with collagen as the main component. In contrast, soluble proteins, including growth factors, are present in low amounts, so we believe the growth factors secreted by the cells in the organism play the main role in the tissue remodeling process.

In addition to angiogenesis, inflammation plays an essential role in regulating the process of tissue remodeling (Tilg and Moschen, 2006). When the decellularized matrix was implanted in the body, it first caused the aggregation of inflammatory cells and the release of inflammatory factors. High levels of MCP-1 and MIP-1α were detected in samples in the first week in both groups, compared to weeks 3 and 5, indicating recruitment for macrophages and precursor cells early in the implantation period. Then, the levels of the associated cytokines, such as IL-6, IFN-γ, and TNF-α, increased subsequently. The levels of TNF-α and IFN-γ in the DAM group were higher than that in the ADM group, which may be related to the faster degradation rate of DAM. The degradation of the decellularized matrix induces an inflammatory response, and moderate inflammatory stimulation facilitates cell recruitment and tissue regeneration. As a traditional pro-inflammatory factor, TNF-α protein levels significantly increase in adipose tissue of obese animals and humans (Xu et al., 2003; Lumeng et al., 2007), yet many studies have shown that TNF-α plays a negative role in regulating adipogenesis (Tang et al., 2006; Cawthorn et al., 2007). In addition to immune cells, adipocytes can also secrete TNF-α, so the levels of TNF-α in the implant continued to increase at week 5 in the DAM group.

Transcriptomic profiles of implants revealed divergent transcriptomic patterns between DAM and ADM. In the DAM group, 16 adipogenesis-related genes showed high expression, including *adipoq*, which was consistent with the level of protein ACRP30 in the samples. KEGG gene enrichment analysis showed that highly expressed genes in the DAM group were enriched in several signaling pathways. Among them, the Hippo signaling pathway was one of the significant pathways in the enrichment analysis. Previous studies suggested that it had a bidirectional role in regulating adipose cell proliferation, differentiation, and adipogenesis (Hong et al., 2005; An et al., 2013; Yu et al., 2013b; Huang et al., 2013). *MST*, *LATS*, *YAP*, and *TAZ* are essential regulators of adipocyte proliferation and differentiation in the Hippo signaling pathway. The DAM implant activated *LATS1/2*, which induced *TAZ* phosphorylation and its subsequent inhibition, leading to cytoplasmic retention and the inability to activate the transcriptional activity of *TEAD* in the nucleus. Without *TAZ* in the nucleus, the transcriptional activity of *PPARγ* was increased to promote the expressions of pro-adipogenesis

genes (such as *perilipin*, *adipoq*, and *MMP-1*). The expression of MST-related protein *SAV1* was increased in the DAM group, and it was found that *MST1/2* activity promoted direct binding of *SAV1* to *PPARγ*, leading to *PPARγ* protein stabilization and enhanced its lipogenic transcriptional activity (Park and Lee, 2011). In addition, phosphorylated TAZ inhibits the Wnt signaling pathway and exerts lipogenic effects by inhibiting proliferation and promoting differentiation. Both groups showed different degrees of enrichment of the Wnt signaling pathway, induced by the high expression of different Wnt proteins (Wnt5a, Wnt9a, Wnt16), respectively. Wnt signaling is often associated with the control and maintenance of stem cells and can influence the expressions of key transcription factors in adipocyte differentiation. (Han et al., 2019) The primary role of the Wnt/β-catenin signaling pathway is to inhibit mesenchymal stem cell differentiation and increase preadipocytes' population. (Cawthorn et al., 2012; Chen et al., 2018; de Winter and Nusse, 2021) Concurrent enrichment of both pro-adipogenic and anti-adipogenic signaling pathways in the early stages of DAM implantation suggests that adipose tissue regeneration results from sophisticated regulation of multiple factors in the body. Preadipocyte proliferation and adipocyte differentiation are indispensable in remodeling the decellularized matrix to adipose tissue.

The interaction between the extracellular matrix and the cell is reciprocal and is called "dynamic reciprocity"- the extracellular matrix secreted by the cell can activate cell surface receptors and affect cell growth and differentiation (Schultz et al., 2011). The decellularized matrices from tissues in different health states can build up different microenvironments and continuously send signals to regulate cellular behavior (Hussey et al., 2017; Naranjo et al., 2020), so can decellularized matrices derived from different tissues. However, the generation and transmission mechanisms of such regulatory signals are still unknown. Notably, the decellularized matrix is a unique structure composed of multiple structural proteins, basement membrane proteins, etc., and its biological impact cannot be attributed to any single component or combination of components (Hussey et al., 2017). Therefore, the role played by the spatial structure and composition of DAM in tissue remodeling needs to be further explored. Also, many studies have placed DAM in action in different application scenarios (Mohiuddin et al., 2019), and the influence of the local environment on DAM-induced tissue remodeling should be investigated. Researches on the role of decellularized matrix in promoting tissue remodeling are more helpful in revealing the mechanisms of tissue regeneration and facilitating clinical translational applications.

Finally, the present study used a subcutaneous implantation model to verify the difference in response of the two decellularized matrices. Tissue origin can influence the biological response of decellularized matrix, which may also be a key reason for DAM's ability to induce adipogenesis. Therefore, the tissue specificity of DAM can be fully utilized for soft tissue repair and regeneration.

CONCLUSION

As decellularized matrices of different tissue origin-DAM and ADM, DAM retains the specific properties from adipose tissue after decellularization and exhibits different cellular and tissue responses from ADM in the experiment. *In vitro*, DAM induced adipogenic differentiation of ADSCs, and *in vivo*, DAM implantation led to the release of multiple growth factors and inflammatory cytokines to induce adipose tissue remodeling, fully demonstrating tissue specificity's effect on the regenerative capacity of the decellularized matrix. In the early post-implantation period, *Lats1/2* regulated adipocyte proliferation and differentiation in implants via the Hippo Signaling Pathway, in conjunction with the Wnt signaling pathway and PPARγ signaling pathway, which co-regulate the adipose tissue remodeling process. Tissue origin plays a vital role in the biological response of decellularized matrix. Further studies are needed to explore the critical factors of DAM-induced tissue remodeling to establish a rational link between its physical properties, molecular composition, and biological functions. Thus, the modulation of the DAM function can be achieved, facilitating the development of tissue engineering and clinical translation.

DATA AVAILABILITY STATEMENT

The original contributions presented in the study are included in the article/**Supplementary Material**, further inquiries can be directed to the corresponding authors.

ETHICS STATEMENT

The studies involving human participants were reviewed and approved by Plastic Surgery Hospital Ethics Committee. The patients/participants provided their written informed consent to participate in this study. The animal study was reviewed and approved by Plastic Surgery Hospital Ethics Committee.

AUTHOR CONTRIBUTIONS

WT, SF, and JL conceptualized and designed the study. WT performed the experimental studies and analyzed the data in consultation with JQ, YQ, and QW. WT wrote the manuscript, with editorial feedback provided by JQ and QW.

FUNDING

This work was supported by the Key projects of medical school development of Shijingshan district (20078) and CAMS Innovation Fund for Medical Sciences (CIFMS) (2017-I2M-3-006).

ACKNOWLEDGMENTS

Thanks to our colleagues at the Plastic Surgery Hospital for providing fresh and large amounts of adipose tissue aspirates for this study.

SUPPLEMENTARY MATERIAL

The Supplementary Material for this article can be found online at: https://www.frontiersin.org/articles/10.3389/fbioe.2022.872897/full#supplementary-material

REFERENCES

Aamodt, J. M., and Grainger, D. W. (2016). Extracellular Matrix-Based Biomaterial Scaffolds and the Host Response. *Biomaterials* 86, 68–82. doi:10.1016/j.biomaterials.2016.02.003

Adam Young, D., Bajaj, V., and Christman, K. L. (2014). Award winner for Outstanding Research in the PhD Category, 2014 Society for Biomaterials Annual Meeting and Exposition, Denver, Colorado, April 16-19, 2014: Decellularized Adipose Matrix Hydrogels Stimulate *In Vivo* Neovascularization and Adipose Formation. *J. Biomed. Mater. Res.* 102, 1641–1651. doi:10.1002/jbm.a.35109

Agrawal, V., Brown, B. N., Beattie, A. J., Gilbert, T. W., and Badylak, S. F. (2009). Evidence of Innervation Following Extracellular Matrix Scaffold-Mediated Remodelling of Muscular Tissues. *J. Tissue Eng. Regen. Med.* 3, 590–600. doi:10.1002/term.200

Agrawal, V., Johnson, S. A., Reing, J., Zhang, L., Tottey, S., Wang, G., et al. (2010). Epimorphic Regeneration Approach to Tissue Replacement in Adult Mammals. *Proc. Natl. Acad. Sci. U.S.A.* 107, 3351–3355. doi:10.1073/pnas.0905851106

Aldekhayel, S. A., Sinno, H., and Gilardino, M. S. (2012). Acellular Dermal Matrix in Cleft Palate Repair. *Plast. Reconstr. Surg.* 130, 177–182. doi:10.1097/PRS.0b013e318254b2dc

An, Y., Kang, Q., Zhao, Y., Hu, X., and Li, N. (2013). Lats2 Modulates Adipocyte Proliferation and Differentiation via Hippo Signaling. *Plos One* 8, e72042. doi:10.1371/journal.pone.0072042

Badylak, S., Freytes, D., and Gilbert, T. (2009). Extracellular Matrix as a Biological Scaffold Material: Structure and Function. *Acta Biomater.* 5, 1–13. doi:10.1016/j.actbio.2008.09.013

Boháč, M., Danišovič, Ľ., Koller, J., Dragúňová, J., and Varga, I. (2018). What Happens to an Acellular Dermal Matrix after Implantation in the Human Body? A Histological and Electron Microscopic Study. *Eur. J. Histochem.* 62, 1–11. doi:10.4081/ejh.2018.2873

Brown, B. N., Freund, J. M., Han, L., Rubin, J. P., Reing, J. E., Jeffries, E. M., et al. (2011). Comparison of Three Methods for the Derivation of a Biologic Scaffold Composed of Adipose Tissue Extracellular Matrix. *Tissue Eng. C: Methods* 17, 411–421. doi:10.1089/ten.TEC.2010.0342

Brown, C. F. C., Yan, J., Han, T. T. Y., Marecak, D. M., Amsden, B. G., and Flynn, L. E. (2015). Effect of Decellularized Adipose Tissue Particle Size and Cell Density on Adipose-Derived Stem Cell Proliferation and Adipogenic Differentiation in Composite Methacrylated Chondroitin Sulphate Hydrogels. *Biomed. Mater.* 10, 045010. doi:10.1088/1748-6041/10/4/045010

Cao, Y. (2007). Angiogenesis Modulates Adipogenesis and Obesity. *J. Clin. Invest.* 117, 2362–2368. doi:10.1172/JCI32239

Cawthorn, W. P., Bree, A. J., Yao, Y., Du, B., Hemati, N., Martinez-Santibañez, G., et al. (2012). Wnt6, Wnt10a and Wnt10b Inhibit Adipogenesis and Stimulate Osteoblastogenesis through a β-catenin-dependent Mechanism. *Bone* 50, 477–489. doi:10.1016/j.bone.2011.08.010

Cawthorn, W. P., Heyd, F., Hegyi, K., and Sethi, J. K. (2007). Tumour Necrosis Factor-α Inhibits Adipogenesis via a β-catenin/TCF4(TCF7L2)-dependent Pathway. *Cell Death Differ* 14, 1361–1373. doi:10.1038/sj.cdd.4402127

Chen, X., Ayala, I., Shannon, C., Fourcaudot, M., Acharya, N. K., Jenkinson, C. P., et al. (2018). The Diabetes Gene and Wnt Pathway Effector TCF7L2 Regulates Adipocyte Development and Function. *Diabetes* 67, 554–568. doi:10.2337/db17-0318

Choi, Y. C., Choi, J. S., Kim, B. S., Kim, J. D., Yoon, H. I., and Cho, Y. W. (2012). Decellularized Extracellular Matrix Derived from Porcine Adipose Tissue as a Xenogeneic Biomaterial for Tissue Engineering. *Tissue Eng. Part C: Methods* 18, 866–876. doi:10.1089/ten.TEC.2012.0009

Clough, B. H., McCarley, M. R., Krause, U., Zeitouni, S., Froese, J. J., McNeill, E. P., et al. (2015). Bone Regeneration with Osteogenically Enhanced Mesenchymal Stem Cells and Their Extracellular Matrix Proteins. *J. Bone Miner. Res.* 30, 83–94. doi:10.1002/jbmr.2320

Crapo, P. M., Gilbert, T. W., and Badylak, S. F. (2011). An Overview of Tissue and Whole Organ Decellularization Processes. *Biomaterials* 32, 3233–3243. doi:10.1016/j.biomaterials.2011.01.057

de Winter, T. J. J., and Nusse, R. (2021). Running Against the Wnt: How Wnt/β-Catenin Suppresses Adipogenesis. *Front. Cell Dev. Biol.* 9, 627429. doi:10.3389/fcell.2021.627429

Dong, J., Yu, M., Zhang, Y., Yin, Y., and Tian, W. (2018). Recent Developments and Clinical Potential on Decellularized Adipose Tissue. *J. Biomed. Mater. Res.* 106, 2563–2574. doi:10.1002/jbm.a.36435

Du, L., Wu, X., Pang, K., and Yang, Y. (2011). Histological Evaluation and Biomechanical Characterisation of an Acellular Porcine Cornea Scaffold. *Br. J. Ophthalmol.* 95, 410–414. doi:10.1136/bjo.2008.142539

Dziki, J. L., and Badylak, S. F. (2018). Extracellular Matrix for Myocardial Repair. *Adv. Exp. Med. Biol.* 1098, 151–171. doi:10.1007/978-3-319-97421-7_8

Flynn, L. E. (2010). The Use of Decellularized Adipose Tissue to Provide an Inductive Microenvironment for the Adipogenic Differentiation of Human Adipose-Derived Stem Cells. *Biomaterials* 31, 4715–4724. doi:10.1016/j.biomaterials.2010.02.046

Gaster, R. S., Berger, A. J., Monica, S. D., Sweeney, R. T., Endress, R., and Lee, G. K. (2013). Histologic Analysis of Fetal Bovine Derived Acellular Dermal Matrix in Tissue Expander Breast Reconstruction. *Ann. Plast. Surg.* 70, 447–453. doi:10.1097/SAP.0b013e31827e55af

Gilpin, A., and Yang, Y. (2017). Decellularization Strategies for Regenerative Medicine: From Processing Techniques to Applications. *Biomed. Res. Int.* 2017, 1–13. doi:10.1155/2017/9831534

Han, L., Wang, B., Wang, R., Gong, S., Chen, G., and Xu, W. (2019). The Shift in the Balance between Osteoblastogenesis and Adipogenesis of Mesenchymal Stem Cells Mediated by Glucocorticoid Receptor. *Stem Cell Res. Ther.* 10, 377. doi:10.1186/s13287-019-1498-0

He, Y., Xia, J., Chen, H., Wang, L., Deng, C., and Lu, F. (2019). Human Adipose Liquid Extract Induces Angiogenesis and Adipogenesis: a Novel Cell-free Therapeutic Agent. *Stem Cell Res. Ther.* 10, 252.

Hong, J.-H., Hwang, E. S., McManus, M. T., Amsterdam, A., Tian, Y., and Kalmukova, R. (2005). TAZ, a Transcriptional Modulator of Mesenchymal Stem Cell Differentiation. *Science* 309, 1074–1078. doi:10.1126/science.1110955

Huang, H., Wu, W., Zhang, L., and Liu, X.-Y. (2013). Drosophila Ste-20 Family Protein Kinase, Hippo, Modulates Fat Cell Proliferation. *Plos One* 8, e61740. doi:10.1371/journal.pone.0061740

Hung, B. P., Naved, B. A., Nyberg, E. L., Dias, M., Holmes, C. A., Elisseeff, J. H., et al. (2016). Three-Dimensional Printing of Bone Extracellular Matrix for Craniofacial Regeneration. *ACS Biomater. Sci. Eng.* 2, 1806–1816. doi:10.1021/acsbiomaterials.6b00101

Hussey, G. S., Keane, T. J., and Badylak, S. F. (2017). The Extracellular Matrix of the Gastrointestinal Tract: a Regenerative Medicine Platform. *Nat. Rev. Gastroenterol. Hepatol.* 14, 540–552. doi:10.1038/nrgastro.2017.76

Jiang, X., Lai, X.-R., Lu, J.-Q., Tang, L.-Z., Zhang, J.-R., and Liu, H.-W. (2021). Decellularized Adipose Tissue: A Key Factor in Promoting Fat Regeneration by Recruiting and Inducing Mesenchymal Stem Cells. *Biochem. Biophys. Res. Commun.* 541, 63–69. doi:10.1016/j.bbrc.2020.12.108

Keane, T. J., DeWard, A., Londono, R., Saldin, L. T., Castleton, A. A., Carey, L., et al. (2015). Tissue-Specific Effects of Esophageal Extracellular Matrix. *Tissue Eng. A* 21, 2293–2300. doi:10.1089/ten.tea.2015.0322

Kim, B. S., Das, S., Jang, J., and Cho, D.-W. (2020). Decellularized Extracellular Matrix-Based Bioinks for Engineering Tissue- and Organ-specific Microenvironments. *Chem. Rev.* 120, 10608–10661. doi:10.1021/acs.chemrev.9b00808

Lauren, E. K., Benjamin, K. S., Evangelia, C., Yen-Chen, H., Emily, A. I., and Arivarasan, K. (2019). Injectable Allograft Adipose Matrix Supports Adipogenic Tissue Remodeling in the Nude Mouse and Human. *Plast. Reconstr. Surg.* 143 (2), 299e–309e. doi:10.1097/PRS.0000000000005269

Levy-Mishali, M., Zoldan, J., and Levenberg, S. (2009). Effect of Scaffold Stiffness on Myoblast Differentiation. *Tissue Eng. Part A* 15, 935–944. doi:10.1089/ten.tea.2008.0111

Li, F., Li, W., Johnson, S. A., Ingram, D. A., Yoder, M. C., and Badylak, S. F. (2004). Low-molecular-weight Peptides Derived from Extracellular Matrix as Chemoattractants for Primary Endothelial Cells. *Endothelium* 11, 199–206. doi:10.1080/10623320490512390

Li, J., Cao, R., Wang, Q., Shi, H., Wu, Y., Sun, K., et al. (2022). Cadherin-11 Promotes the Mechanical Strength of Engineered Elastic Cartilage by Enhancing Extracellular Matrix Synthesis and Microstructure. *J. Tissue Eng. Regen. Med.* 16, 188–199. doi:10.1002/term.3271

Lin, G., Albersen, M., Harraz, A. M., Fandel, T. M., Garcia, M., and McGrath, M. H. (2011). Cavernous Nerve Repair with Allogenic Adipose Matrix and Autologous Adipose-Derived Stem Cells. *Urology* 77, e1–1509. doi:10.1016/j.urology.2010.12.076

Lumeng, C. N., Bodzin, J. L., and Saltiel, A. R. (2007). Obesity Induces a Phenotypic Switch in Adipose Tissue Macrophage Polarization. *J. Clin. Invest.* 117, 175–184. doi:10.1172/JCI29881

Marinkovic, M., Block, T. J., Rakian, R., Li, Q., Wang, E., Reilly, M. A., et al. (2016). One Size Does Not Fit All: Developing a Cell-specific Niche for *In Vitro* Study of Cell Behavior. *Matrix Biol.* 52-54, 426–441. doi:10.1016/j.matbio.2016.01.004

Marston, W. A., Hanft, J., Norwood, P., and Pollak, R. (2003). The Efficacy and Safety of Dermagraft in Improving the Healing of Chronic Diabetic Foot Ulcers. *Diabetes Care* 26, 1701–1705. doi:10.2337/diacare.26.6.1701

Marçal, H., Ahmed, T., Badylak, S. F., Tottey, S., and Foster, L. J. R. (2012). A Comprehensive Protein Expression Profile of Extracellular Matrix Biomaterial Derived from Porcine Urinary Bladder. *Regen. Med.* 7, 159–166. doi:10.2217/rme.12.6

Mohiuddin, O. A., Campbell, B., Poche, J. N., Thomas-Porch, C., Hayes, D. A., Bunnell, B. A., et al. (2019). Decellularized Adipose Tissue: Biochemical Composition, *In Vivo* Analysis and Potential Clinical Applications. *Adv. Exp. Med. Biol.* 1212, 57–70. doi:10.1007/5584_2019_371

Morrison, R. F., and Farmer, S. R. (2000). Hormonal Signaling and Transcriptional Control of Adipocyte Differentiation. *J. Nutr.* 130, 3116S–3121S. doi:10.1093/jn/130.12.3116S

Naranjo, J. D., Saldin, L. T., Sobieski, E., Quijano, L. M., Hill, R. C., Chan, P. G., et al. (2020). Esophageal Extracellular Matrix Hydrogel Mitigates Metaplastic Change in a Dog Model of Barrett's Esophagus. *Sci. Adv.* 6. doi:10.1126/sciadv.aba4526

Omidi, E., Fuetterer, L., Reza Mousavi, S., Armstrong, R. C., Flynn, L. E., and Samani, A. (2014). Characterization and Assessment of Hyperelastic and Elastic Properties of Decellularized Human Adipose Tissues. *J. Biomech.* 47, 3657–3663. doi:10.1016/j.jbiomech.2014.09.035

Ouyang, Y., Li, C., and Liu, C. (2019). Evaluation of Acellular Dermal Matrix Efficacy in Prosthesis-Based Breast Reconstruction. *Plast. Reconstr. Surg.* 143, 433e–434e. doi:10.1097/PRS.0000000000005226

Paduano, F., Marrelli, M., Alom, N., Amer, M., White, L. J., Shakesheff, K. M., et al. (2017). Decellularized Bone Extracellular Matrix and Human Dental Pulp Stem Cells as a Construct for Bone Regeneration. *J. Biomater. Sci. Polym. Edition* 28, 730–748. doi:10.1080/09205063.2017.1301770

Park, B.-H., and Lee, Y.-H. (2011). Phosphorylation of SAV1 by Mammalian Ste20-like Kinase Promotes Cell Death. *BMB Rep.* 44, 584–589. doi:10.5483/bmbrep.2011.44.9.584

Reyzelman, A., Crews, R. T., Moore, J. C., Moore, L., Mukker, J. S., Offutt, S., et al. (2009). Clinical Effectiveness of an Acellular Dermal Regenerative Tissue Matrix Compared to Standard Wound Management in Healing Diabetic Foot Ulcers: A Prospective, Randomised, Multicentre Study. *Int. Wound J.* 6, 196–208. doi:10.1111/j.1742-481X.2009.00585.x

Sadtler, K., Estrellas, K., Allen, B. W., Wolf, M. T., Fan, H., and Tam, A. J. (2016). Developing a Pro-regenerative Biomaterial Scaffold Microenvironment Requires T Helper 2 Cells. *Science* 352, 366–370. doi:10.1126/science.aad9272

Schultz, G. S., Davidson, J. M., Kirsner, R. S., Bornstein, P., and Herman, I. M. (2011). Dynamic Reciprocity in the Wound Microenvironment. *Wound Repair Regen.* 19, 134–148. doi:10.1111/j.1524-475X.2011.00673.x

Shridhar, A., Amsden, B. G., Gillies, E. R., and Flynn, L. E. (2019). Investigating the Effects of Tissue-specific Extracellular Matrix on the Adipogenic and Osteogenic Differentiation of Human Adipose-Derived Stromal Cells within Composite Hydrogel Scaffolds. *Front. Bioeng. Biotechnol.* 7, 402. doi:10.3389/fbioe.2019.00402

Tang, X., Guilherme, A., Chakladar, A., Powelka, A. M., Konda, S., Virbasius, J. V., et al. (2006). An RNA Interference-Based Screen Identifies MAP4K4/NIK as a Negative Regulator of PPARγ, Adipogenesis, and Insulin-Responsive Hexose Transport. *Proc. Natl. Acad. Sci. U.S.A.* 103, 2087–2092. doi:10.1073/pnas.0507660103

Tilg, H., and Moschen, A. R. (2006). Adipocytokines: Mediators Linking Adipose Tissue, Inflammation and Immunity. *Nat. Rev. Immunol.* 6, 772–783. doi:10.1038/nri1937

Ting, A. C. H., Craft, R. O., Palmer, J. A., Gerrand, Y.-w., Penington, A. J., Morrison, W. A., et al. (2014). The Adipogenic Potential of Various Extracellular Matrices under the Influence of an Angiogenic Growth Factor Combination in a Mouse Tissue Engineering Chamber. *Acta Biomater.* 10, 1907–1918. doi:10.1016/j.actbio.2013.11.019

Wu, I., Nahas, Z., Kimmerling, K. A., Rosson, G. D., and Elisseeff, J. H. (2012). An Injectable Adipose Matrix for Soft-Tissue Reconstruction. *Plast. Reconstr. Surg.* 129, 1247–1257. doi:10.1097/PRS.0b013e31824ec3dc

Xu, H., Barnes, G. T., Yang, Q., Tan, G., Yang, D., Chou, C. J., et al. (2003). Chronic Inflammation in Fat Plays a Crucial Role in the Development of Obesity-Related Insulin Resistance. *J. Clin. Invest.* 112, 1821–1830. doi:10.1172/JCI19451

Yu, C., Bianco, J., Brown, C., Fuetterer, L., Watkins, J. F., Samani, A., et al. (2013). Porous Decellularized Adipose Tissue Foams for Soft Tissue Regeneration. *Biomaterials* 34, 3290–3302. doi:10.1016/j.biomaterials.2013.01.056

Yu, F.-X., Zhang, Y., Park, H. W., Jewell, J. L., Chen, Q., Deng, Y., et al. (2013). Protein Kinase A Activates the Hippo Pathway to Modulate Cell Proliferation and Differentiation. *Genes Dev.* 27, 1223–1232. doi:10.1101/gad.219402.113

Conflict of Interest: The authors declare that the research was conducted in the absence of any commercial or financial relationships that could be construed as a potential conflict of interest.

Publisher's Note: All claims expressed in this article are solely those of the authors and do not necessarily represent those of their affiliated organizations, or those of the publisher, the editors and the reviewers. Any product that may be evaluated in this article, or claim that may be made by its manufacturer, is not guaranteed or endorsed by the publisher.

frontiers | Frontiers in Bioengineering and Biotechnology

BRIEF RESEARCH REPORT
published: 25 April 2022
doi: 10.3389/fbioe.2022.879024

Reversing Epithelial Polarity in Pluripotent Stem Cell-Derived Intestinal Organoids

Panagiota Kakni[1], *Carmen López-Iglesias*[2], *Roman Truckenmüller*[1], *Pamela Habibović*[1] *and Stefan Giselbrecht*[1]*

[1]Department of Instructive Biomaterials Engineering, MERLN Institute for Technology-Inspired Regenerative Medicine, Maastricht University, Maastricht, Netherlands, [2]Microscopy CORE Lab, Maastricht Multimodal Molecular Imaging Institute (M4I), Maastricht University, Maastricht, Netherlands

The inner surface of the intestine is a dynamic system, composed of a single layer of polarized epithelial cells. The development of intestinal organoids was a major breakthrough since they robustly recapitulate intestinal architecture, regional specification and cell composition *in vitro*. However, the cyst-like organization hinders direct access to the apical side of the epithelium, thus limiting their use in functional assays. For the first time, we show an intestinal organoid model from pluripotent stem cells with reversed polarity where the apical side faces the surrounding culture media and the basal side faces the lumen. These inside-out organoids preserve a distinct apico-basolateral orientation for a long period and differentiate into the major intestinal cell types. This novel model lays the foundation for developing new *in vitro* functional assays particularly targeting the apical surface of the epithelium and thus offers a new research tool to study nutrient/drug uptake, metabolism and host-microbiome/pathogen interactions.

Keywords: epithelial organoids, intestinal organoids, apicobasal polarity, reversed polarity, advanced 3D models

OPEN ACCESS

Edited by:
Dimitrios Stamatialis, University of Twente, Netherlands

Reviewed by:
Eva Rath, Technical University of Munich, Germany
Nicole Prior, University of Southampton, United Kingdom

***Correspondence:**
Stefan Giselbrecht
s.giselbrecht@maastrichtuniversity.nl

Specialty section:
This article was submitted to Tissue Engineering and Regenerative Medicine, a section of the journal Frontiers in Bioengineering and Biotechnology

Received: *18 February 2022*
Accepted: *08 April 2022*
Published: *25 April 2022*

Citation:
Kakni P, López-Iglesias C, Truckenmüller R, Habibović P and Giselbrecht S (2022) Reversing Epithelial Polarity in Pluripotent Stem Cell-Derived Intestinal Organoids. Front. Bioeng. Biotechnol. 10:879024. doi: 10.3389/fbioe.2022.879024

INTRODUCTION

The intestinal epithelium is a highly organized, self-renewing tissue mainly serving two roles. First, it forms a physical barrier to avoid the crossing of harmful substances in the intestinal lumen and second, it regulates the nutrient absorption and metabolism. Within this simple columnar epithelial layer, the establishment and maintenance of cell polarity with distinct apical and basolateral surfaces is considered crucial for the proper tissue development and function. Each of these compartments has a different structure, function and macromolecule composition (Klunder et al., 2017). The apical surface faces the lumen and is responsible for the absorption of nutrients while the basolateral surface faces the stroma and mediates nutrient transport. Apart from the apico-basolateral polar organization, the differentiation towards the major intestinal cell types (enterocytes, Paneth cells, goblet cells etc.) is of utmost importance for the proper functioning of the intestine. Various cell lines and animal models have been utilized to model the human intestinal epithelium but the full complexity of it has not yet been accurately recapitulated *in vitro*.

Advances in stem cell research made it possible to create *in vitro* 3D organ-like structures from either adult or pluripotent stem cells that better recapitulate the *in vivo* tissues than traditional 2D cell culture models. The generation of intestinal organoids was a major research breakthrough, yielding a new tool to study the intestinal epithelium (Sato et al., 2009; Sato and Clevers, 2013; Clevers, 2016). The culture of intestinal organoids is a relatively simple process, requiring a tailored cell culture medium and hydrogels (e.g., basement membrane matrix secreted by Engelbreth-Holm-Swarm mouse sarcoma cells) serving as an extracellular matrix (ECM) substitute (Fatehullah et al., 2016).

The resulting 3D multicellular constructs demonstrate an *in vivo*-like architecture with crypt-villus structures surrounding a central lumen and contain both proliferating and differentiated cell types. However, the enclosed position of the lumen hinders access to the apical surface of the epithelium, thus limiting studies related to nutrient uptake and host-microbiome/pathogen interactions. To overcome this, three different approaches have been taken so far. The first is the use of microinjection techniques where microbes or other infectious agents are injected directly to the lumen of organoids (Bartfeld et al., 2015; Hill et al., 2017; Williamson et al., 2018). This is a labor-intensive, time-consuming and often even disruptive process. The second is the formation of 2D cell monolayers by dissociating organoids (VanDussen et al., 2015; Kozuka et al., 2017; Wang et al., 2017; Altay et al., 2019). Although, in this way, access to both the apical and basolateral sides is granted, the 3D tissue-like structure of the organoids is lost thus making the system less physiologically relevant. Finally, the third method is the establishment of organoid models with reversed polarity (Co et al., 2019; Co et al., 2021; Nash et al., 2021; Stroulios et al., 2021). In this case, the apical surface of the epithelium is facing the cell culture media thus allowing direct access to it. This method has been applied to human (Co et al., 2019; Co et al., 2021; Stroulios et al., 2021), porcine (Li et al., 2020) and chicken (Nash et al., 2021) primary cell-derived intestinal organoids.

Here, we report the development of an intestinal organoid model with reversed polarity using pluripotent stem cells (PSCs). Following a stepwise directed differentiation protocol, we generated organoids consisting of a simple columnar epithelium patterned into crypt-like and villus-like structures. They contain the major intestinal differentiated cell types and are surrounded by a mesenchymal compartment. In our novel microwell-based culture protocol, the original embedding of organoids in a solid matrix was replaced by a suspension system, which allowed for a uniform, long-term reversal of the epithelial polarity. These novel pluripotent stem cell-derived apical-out organoids are a powerful new tool for studies relating but not limited to infectious diseases, gut microbiota, nutrient absorption and drug metabolism.

MATERIALS AND METHODS

Maintenance of PSCs

The human embryonic stem cell line WA09 (H9) was obtained from WiCell and the induced pluripotent stem cell line iPSC72_3 was obtained by the Pluripotent Stem Cell Facility at Cincinnati Children's Hospital Medical Center. ES and iPS cell lines were maintained in feeder-free conditions on Matrigel (Corning®) using mTESR®1 (StemCell Technologies). Colonies were passaged every four to 5 days depending on colony density using Gentle Cell Dissociation reagent (StemCell Technologies).

Fabrication and Preparation of Microwell Arrays

Polymer film based microwell arrays were fabricated by microthermorming as described previously (Giselbrecht et al., 2006; Kakni et al., 2020). Every array accommodated 289 U-bottomed microwells and each microwell had a diameter of 500 µm and a depth of approximately 300 µm. Prior to cell culture, microwell arrays were sterilized in a graded series of 2-propanol (VWR) (100%–70%–50%–25%–10%) and then washed twice with Dulbecco's phosphate buffered saline (PBS; Sigma-Aldrich). Subsequently, they were placed at the bottom of non-treated 24-well plates, where they were kept in place by elastomeric O-rings (ERIKS).

Differentiation of PSCs to Definitive Endoderm and Hindgut in Microwells

The protocol for directed differentiation of intestinal organoids was carried out as previously described (Spence et al., 2011) with small modifications. PSCs were dissociated into single cells using TrypLE™ Express Enzyme (Thermofisher) and seeded on microwell arrays at a density of 1,000 cells/microwell in mTesR1 supplemented with Y-27632 (10 µM; Tocris) to create embryoid bodies (EBs). The following 3 days, EBs were treated with Activin A (100 ng/ml; Cell guidance systems) in RPMI 1640 (Thermofisher) medium supplemented with increasing concentrations (0%, 0.2%, 2%) of Hyclone defined fetal bovine serum (dFBS; Fisher scientific). For hindgut specification, the DE spheroids were treated with a combination of FGF4 (500 ng/ml; R&D Systems) and CHIR99021 (3 µM; Stemgent) for four additional days. The medium was exchanged daily. In order to avoid the removal of the spheroids from the microwells, the plate was slightly tilted and the medium was aspirated from the sidewalls.

Differentiation Towards Intestinal Organoids

For the apical-in intestinal organoids, hindgut spheroids were collected, suspended in 50 µl Matrigel and plated as droplets into tissue culture treated 24-well plates. After letting the Matrigel solidify at 37°C and 5% CO_2 for 15 min, the Matrigel drops containing the spheroids, were overlaid with Advanced DMEM/F-12 supplemented with B27, N2, Hepes, penicillin/streptomycin, L-glutamine (all Thermofisher), EGF (50 ng/ml; R&D systems), Noggin (100 ng/ml; R&D systems) and R-Spondin (500 ng/ml; R&D systems). The medium was refreshed every 4 days.

For the apical-out intestinal organoids, on day 8 the hindgut spheroids were placed in suspension culture in non-tissue culture-treated 6-well plates (plates with different sizes can be used as well). To avoid surface-cell adherence, the plates were coated with 1% Pluronic solution in PBS (Sigma-Aldrich) for 2 h at 37°C and then washed two times with PBS. The medium used, had the same composition as the apical-in organoids, but in this case Matrigel was added as a medium supplement at a concentration of 2%.

Immunofluorescence and Confocal Microscopy

EBs, DE spheroids, hindgut spheroids and intestinal organoids were fixed with 4% paraformaldehyde (VWR) in PBS for 30 min.

Following that, permeabilization was performed with 0.5% Triton X-100 (Merck) in PBS for another 30 min at room temperature (RT). Blocking was performed with 5% donkey serum (VWR) in permeabilization solution for 30 min at RT as well. Afterwards, primary antibodies were incubated overnight at 4°C and the next day secondary antibodies were added for 2 h at RT. Finally, samples were counterstained with 4′,6-diamidino-2-phenylindole (DAPI) (Sigma-Aldrich) and mounted with Lab Vision PermaFluor Aqueous Mounting Medium (Thermofisher). A full list of antibodies is provided in the **Supplementary Material**. For the imaging of the immunostained samples, a confocal laser scanning microscopy (Leica TCS SP8) was utilized and the images were processed with ImageJ. Quantification was performed using the open access software QuPath.

RNA Isolation and Quantitative Real-Time PCR (qPCR)

Organoids were collected and the total RNA was extracted using the RNeasy Mini Kit (Qiagen) according to the manufacturer instructions. For the cDNA synthesis, the iScript cDNA Synthesis Kit (Bio-Rad) was utilized. Finally, qPCR was carried out using the iQ SYBR Green Supermix (Bio-Rad), on a CFX96 Real-Time PCR Detection System (Bio-Rad). Gene expression for each sample was normalized using the glyceraldehyde-3-phosphatedehydrogenase (*GAPDH*) or the hypoxanthine phosphoribosyltransferase (*HPRT*) housekeeping genes. *GAPDH* was used for DE and hindgut spheroids, whereas *HPRT* for intestinal organoids. The expression of *GAPDH* could be affected by the different oxygen levels (Caradec et al., 2010) we expect between hydrogel embedded and suspension organoids, thus we chose to use *HPRT* for these samples. Data analysis followed the $2^{-\Delta\Delta Ct}$ method. The results are representative of three independent experiments. The primer sequences are listed in the **Supplementary Material**.

Scanning Electron Microscopy (SEM)

Organoids were chemically fixed for 3 h at room temperature with 1.5% glutaraldehyde in 0.067 M cacodylate buffered to pH 7.4 and 1% sucrose. Then they were washed with 0.1 M cacodylate buffer and postfixed with 1% osmium tetroxide in the same buffer containing 1.5% potassium ferricyanide for 1 h in the dark at 4°C. After rinsing with MQ, organoids were dehydrated at RT in a graded ethanol series (70, 90, up to 100%). Then, organoids were dried using HMDS (Hexamethyldisilazane) (>99.9%, Sigma Aldrich, Germany). After HMDS treatment, the samples were mounted on SEM stubs, coated with a thin layer of gold by a sputter coater SC7620 (Quorum Technologies, United Kingdom) and examined with the electron microscope (Jeol JSM-IT200, Japan).

Transmission Electron Microscopy (TEM)

Organoids were chemically fixed for 3 h at room temperature with 1.5% glutaraldehyde in 0.067 M cacodylate buffered to pH 7.4 and 1% sucrose. Then they were washed with 0.1 M cacodylate buffer and postfixed with 1% osmium tetroxide in the same buffer containing 1.5% potassium ferricyanide for 1 h in the dark at 4°C. After rinsing with MQ, organoids were dehydrated at RT in a graded ethanol series (70, 90, up to 100%), infiltrated with Epon, embedded in the same resin and polymerized for 48 h at 60°C. Ultrathin sections of 60 nm were cut using a diamond knife (Diatome) on a Leica UC7 ultramicrotome, and transferred onto 50 Mesh copper grids covered with a Formvar and carbon film. Sections were stained with 2% uranyl acetate in 50% ethanol and lead citrate. Then, sections were observed in a Tecnai T12 Electron Microscope equipped with an Eagle 4kx4k CCD camera (Thermo Fisher Scientific, Netherlands) or Veleta 2kx2k CCD camera (Olympus Soft Imaging, Germany).

Statistical Analysis

All statistical analysis was performed using GraphPad Prism 9 software. Student's two-tailed *t*-test with Welch's correction (two groups) or one-way ANOVA followed by Tukey's test (> two groups) were used to determine statistical significance. Significant differences were defined as $p < 0.05$. p values of statistical significance are represented as $^{****}p < 0.0001$, $^{***}p < 0.001$, $^{**}p < 0.01$, and $^{*}p < 0.05$. Error bars in figures indicate standard error of the mean (S.E.M.).

RESULTS

Embryoid Body-Based Differentiation Towards Intestinal Tissue

The generation of our PSC-derived intestinal organoids is based on the directed differentiation method developed by Spence et al. (2011). Here, the human embryonic and induced pluripotent stem cells were dissociated into single cells and seeded onto microwell arrays in order to promote the formation of uniform embryoid bodies (EBs). Next, these EBs were differentiated stepwise towards intestinal organoids (definitive endoderm→ hindgut→ intestinal organoids) (**Figure 1A**). The microwell arrays were produced in-house with a custom-made design that fits the needs of our experiments. We identified that around 1,000 cells per EB were adequate for the successful formation of intestinal tissue. These cell aggregates had a diameter of approximately 200 µm (**Figure 1B**). Aggregates of smaller diameter failed to generate intestinal tissue later on. Additionally, to ensure that our cells remain pluripotent after the formation of EBs, we performed immunofluorescence stainings for the widely used pluripotency markers Oct3/4 and Nanog (**Figure 1C**). The results showed co-localization of these markers, thus confirming their applicability for downstream differentiation. Initiation of the differentiation within a 2D culture system demands tightly regulated seeding densities and equal distribution of cells around the cell culture plates for the successful differentiation of PSCs towards intestinal organoids (McCracken et al., 2011). This process is very limiting and often fails. Our system overcomes this obstacle since the use of microwells offers a simple method to create uniform 3D EBs that can be used as the starting material for the differentiation towards intestinal tissue.

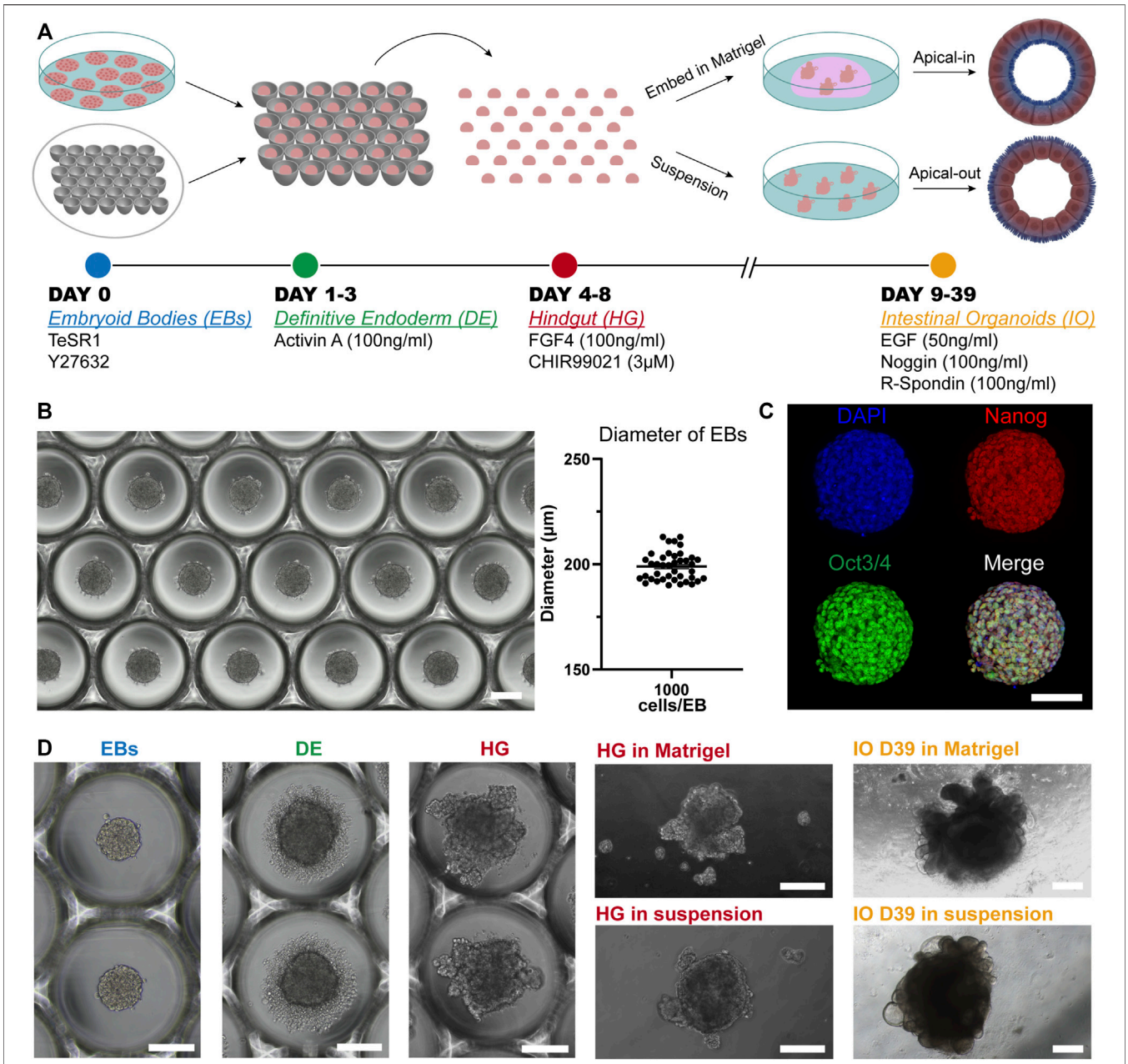

FIGURE 1 | Overview of the *in vitro* culture system established for the directed differentiation of EBs towards intestinal organoids. **(A)** Schematic representation of the protocol. **(B)** Formation of EBs in thermoformed microwell arrays. The graph represents the diameter of EBs 24 h after the cell seeding. Each point displays an individual EB; horizontal line and error bar indicate mean ± S.E.M. ($n = 3$). Scale bar: 200 μm. **(C)** Fluorescence microscopy images of undifferentiated EBs stained for the pluripotency markers Oct3/4 (green) and Nanog (red) and counterstained with DAPI (blue). Scale bar: 100 μm. **(D)** Bright-field images representative of each stage of the differentiation. Scale bars: 200 μm.

Differentiation Towards Definitive Endoderm and Hindgut Specification

The embryonic development of the intestine initiates during gastrulation when the primary germ layers, the endoderm, the mesoderm and the ectoderm, are formed. Specifically, the intestine derives from the definitive endoderm (DE), which following gastrulation transforms into the primitive gut tube that becomes regionally specified into the foregut, midgut and hindgut along the anterior-posterior axis. After this, the mid- and hindgut will give rise to the intestine (Zorn and Wells, 2009). To generate DE, we treated our EBs in the microwells with Activin-A, which is a nodal-related TGF-β molecule (**Figure 1D**). After 3 days of treatment, immunofluorescence stainings showed that 90% of the cells in H9-derived DE spheroids (**Figures 2A,B**) and

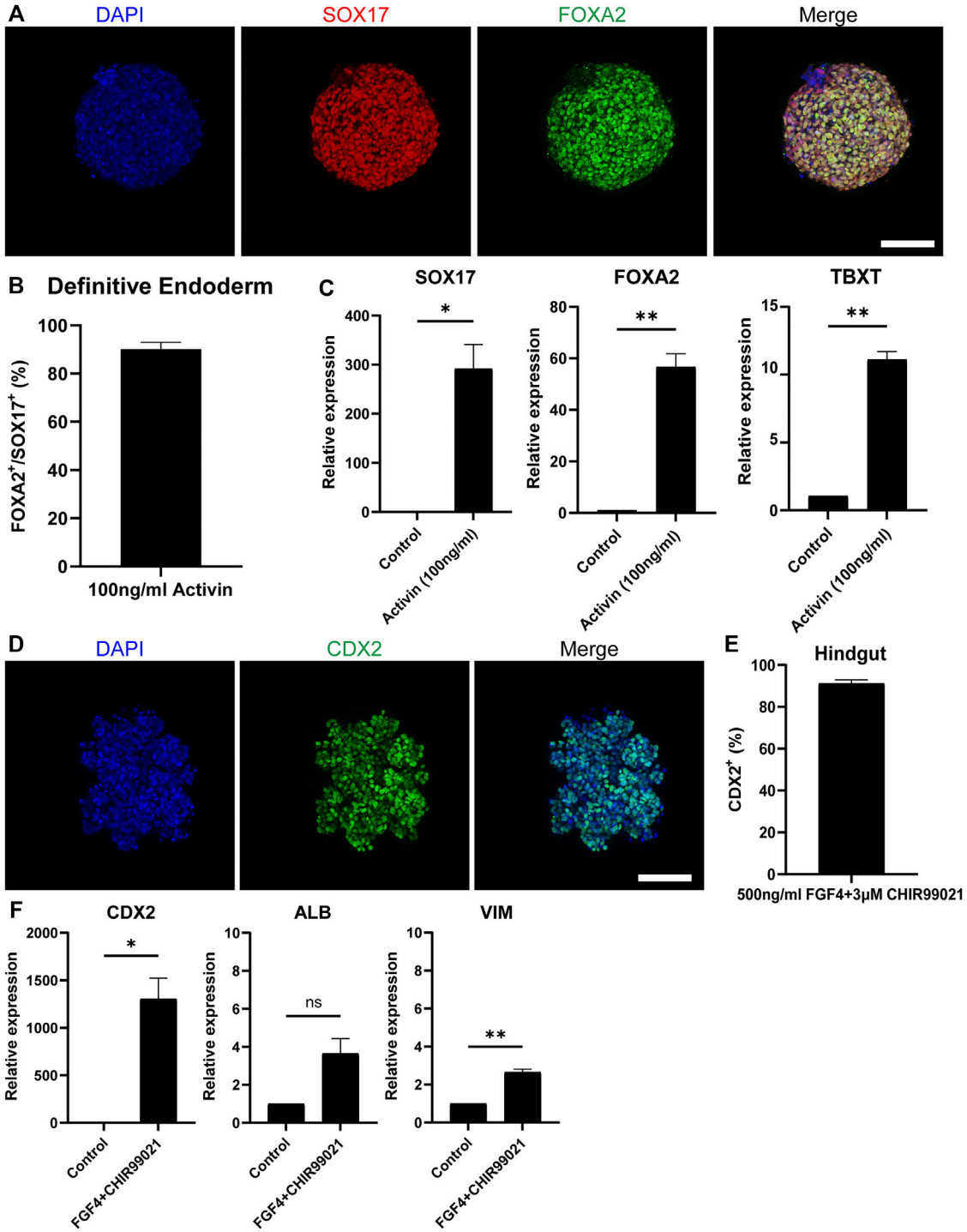

FIGURE 2 | Differentiation towards definitive endoderm followed by hindgut specification. **(A)** H9-derived EBs were treated with 100 ng/ml Activin and the resulting spheroids were stained with the DE markers: SOX17 (red) and FOXA2 (green) and counterstained with DAPI (blue). Scale bar: 100 μm. **(B)** Quantification of the fluorescent images showed that about 92% of the cells in Activin-treated EBs are co-expressing SOX17 and FOXA2. **(C)** qRT-PCR showed significantly increased expression of the DE genes *SOX17* and *FOXA2* and the mesoderm marker *TBXT* but in lower amounts. **(D)** DE spheroids were further treated with FGF4 and CHIR99021 to induce hindgut specification. After 4 days of treatment, the spheroids were stained for the hindgut marker CDX2. Scale bar: 100 μm. **(E)** Quantification of the fluorescent images showed that about 90% of the cells were $CDX2^+$. **(F)** qRT-PCR confirmed the robust expression of *CDX2*, whereas there was no significant expression of the foregut marker *ALB*. Low levels of the mesenchymal marker *VIM* were also detected. Error bars indicate mean ± S.E.M. (n = 3).

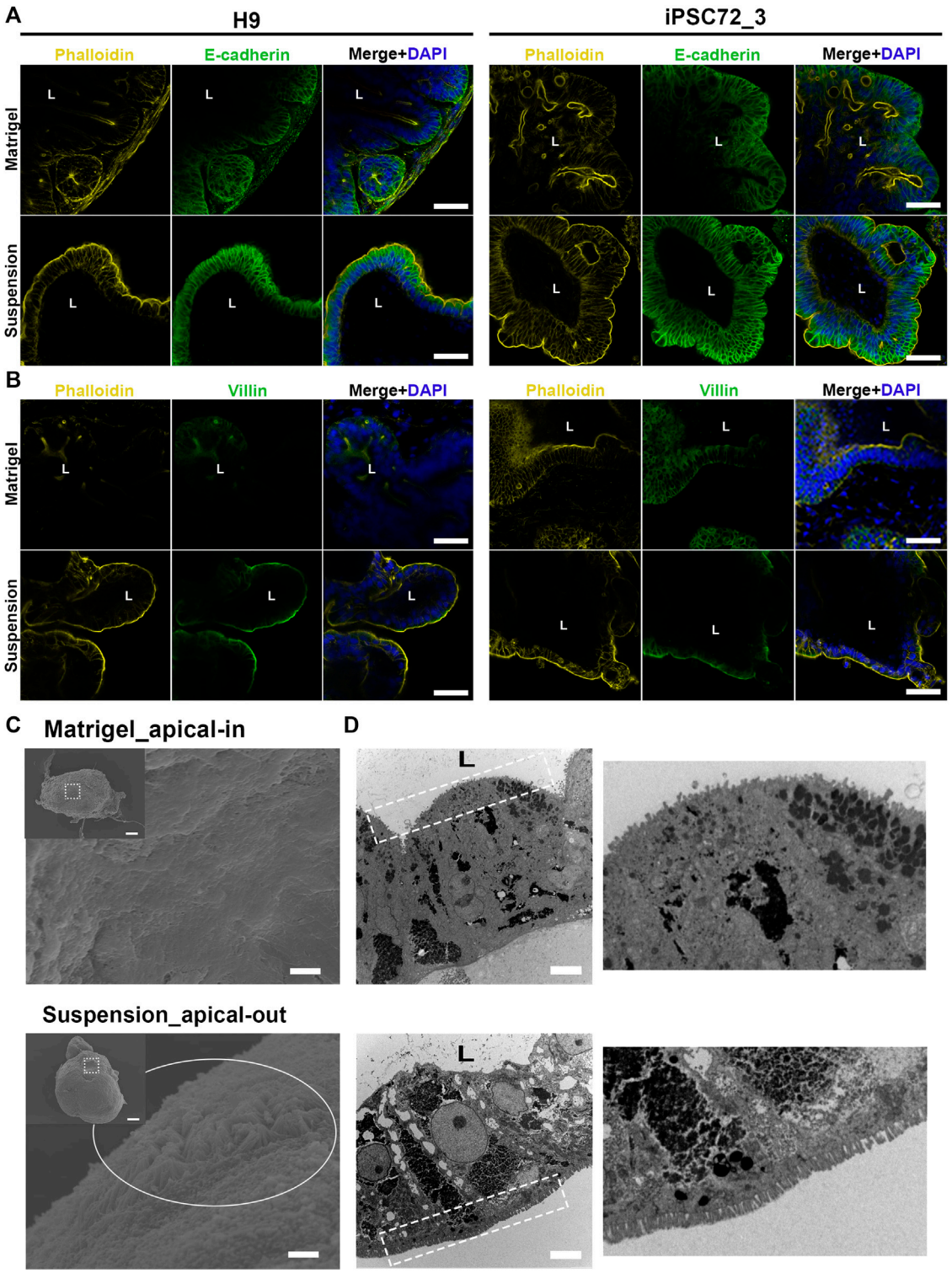

FIGURE 3 | Apico-basolateral organization of human intestinal organoids after 30 days in culture. **(A)** Fluorescent staining of embedded (top) and suspension (bottom) intestinal organoids for the basolateral marker E-cadherin (green) and the apical marker Phalloidin (yellow) shows reversed polarity of the suspension organoids. The left panel demonstrates H9-derived organoids and the right one iPSC72_3-derived organoids. Scale bar: 100 μm. **(B)** These results were confirmed with Villin (green) and Phalloidin (yellow) stainings that were found to co-express in the apical side of the organoids. The left panel demonstrates H9-derived organoids and the right one iPSC-derived organoids. Scale bar: 100 μm. L: lumen. **(C)** SEM was performed in Matrigel embedded (top) and suspension (bottom) organoids showing the presence of microvilli (white circle) in the outer surface of the suspension organoids. Dashed squares represent the area magnified in the corresponding image. Scale bars: 100 μm (inset) and 2 μm. **(D)** TEM indicates that microvilli (white dotted squares) face the lumen in Matrigel embedded (top) organoids, whereas in suspension (bottom) organoids, microvilli face the outer surface. On the right, magnified images demonstrate the microvilli. Scale bars: 5 μm.

92% of the cells in iPSC-derived DE spheroids (**Supplementary Figures S1A,B**) were co-expressing the known DE markers SRY-Box Transcription Factor 17 (SOX17) and Forkhead Box A2 (FOXA2). Gene expression levels confirmed those results demonstrating a significant increase of *SOX17* and *FOXA2* expression, compared to untreated cells, in DE spheroids derived from both cell sources (**Figure 2C**; **Supplementary Figure S1C**). We also detected the expression of T-Box Transcription Factor T (*TBXT*), indicating the presence of mesoderm in our cultures, similar to what was previously reported by Spence et al.

To achieve hindgut specification, an appropriate combination of growth factors targeting the Fibroblast Growth Factor (FGF) and Wingless-related integration site (Wnt) pathways is required to repress the foregut and promote the hindgut development (Dessimoz et al., 2006; McCracken and Wells, 2017). For our experiments, we used a combination of FGF4 (500 ng/ml) and CHIR99021 (3 μM). Four days of treatment were adequate to promote the hindgut endoderm specification in our DE spheroids (**Figure 1D**). The hindgut marker Caudal Type Homeobox 2 (CDX2) was expressed in 91% of the cells in H9-derived hindgut spheroids (**Figures 2D,E**) and in 90% of the cells in iPSC-derived ones (**Supplementary Figures S1D,E**). The high levels of *CDX2* expression were confirmed by qPCR (**Figure 2F**; **Supplementary Figure S1F**). The foregut marker Albumin (*ALB*) had very low expression without statistical significance, when compared to our undifferentiated controls, while Pancreatic and Duodenal Homeobox 1 (*PDX1*) was not detected. Mesenchyme was identified in our hindgut spheroids using qPCR, as indicated by the expression of Vimentin (*VIM*) (**Figure 2F**; **Supplementary Figure S1F**). Overall, our results demonstrate that following a directed differentiation method, EBs can accurately recapitulate both the DE and the hindgut.

Reversal of Epithelial Polarity in Organoids Cultured in Suspension

The intestinal epithelium is a highly organized tissue and the establishment of proper epithelial polarity is instrumental for balancing the communication between the lumen and surrounding body tissues. In the original protocol for PSC-derived intestinal organoids (Spence et al., 2011), hindgut spheroids are embedded in Matrigel thus leading to the formation of a simple columnar polarized epithelium where the apical surface is facing the enclosed lumen and the basal side the surrounding mesenchyme. In a similar manner, when we embedded our hindgut spheroids in Matrigel (**Figure 1D**), the resulting organoids demonstrated the same strong apical-basolateral polarity. Specifically, immunofluorescence stainings showed that Phalloidin, which marks the apical side of the organoids, is expressed at the inner side of the organoids facing the lumen, whereas E-cadherin, which marks the basolateral side, is expressed in the outer part facing the culture medium. The immunostainings were performed at days 7, 15, 30 and 50 after embedding the hindgut spheroids in Matrigel for both H9- and iPSC-derived organoids monitoring their structural organization during the whole culture period (**Figure 3A**; **Supplementary Figures S2, S3**). In addition, stainings for Villin, a marker of the apical side of the enterocytes, and Phalloidin (**Figure 3B**) verified our results.

To facilitate the studies of interactions between the epithelium and luminal contents, we aimed to reverse the polarity of our organoids while maintaining their 3D structure. To achieve that, we developed a suspension culture method that allows for hindgut spheroids to mature into intestinal tissue without being embedded in Matrigel (**Figures 1A,D**). Unlike the original protocol, Matrigel was added at a low concentration to the medium (2%). Already after 7 days, the resulting organoids presented a reversed organization where the apical side was facing the culture medium and the basal side was facing the lumen. Notably, throughout the suspension method, the organoids were grown and matured solely in suspension, whereas in similar protocols the organoids are initially embedded in Matrigel and later on the Matrigel is removed in order to reverse the polarity (Co et al., 2019; Nash et al., 2021). We could show that organoids grown in suspension demonstrate a similar architecture to the Matrigel-embedded ones throughout the culture period, with crypt-villus structures surrounding a central lumen (**Supplementary Figure S4**). Immunofluorescence stainings evidence the F-actin rich brush border (marked by Phalloidin) and the apical side of the enterocytes (marked by Villin) in the outer part of the organoids thus verifying the polarity reversal at all time-points in both H9- and iPSC-derived organoids (**Figures 3A,B**; **Supplementary Figures S2, S3**). Additionally, scanning electron microscopy (SEM) was utilized to verify the two different apico-basolateral organizations. Specifically, the Matrigel-embedded organoids seem to have a "smoother surface," which is anticipated since the basal side of the organoids is visualized, whereas the suspension organoids exhibit a "rougher surface" in which we can clearly identify the presence of microvilli, further proving that a functional apical side of the organoids is facing outwards (**Figure 3C**). Finally, the presence of microvilli in reversed positions is illustrated by transmission electron microscopy (TEM; **Figure 3D**).

To examine the plasticity of these different polarity models, 7 days before reaching full maturation (embedded/suspension day 23), organoids that were initially embedded in Matrigel were placed in suspension culture and organoids that were initially in suspension, were embedded in Matrigel for 1 week. Following this ECM manipulation, the samples were immunofluorescently labelled for E-Cadherin and Phalloidin and the amount of organoids that fully or partially reversed their polarity was quantified (**Supplementary Figure S5**). Interestingly, none of the organoids (H9- or iPSC-derived) that were isolated from Matrigel and placed in suspension changed their polarity during these 7 days. This indicates that the protocols (Co et al., 2019; Nash et al., 2021) previously described for reversing the polarity of established adult stem cell-derived organoids cannot be applied to reverse the polarity of PSC-derived organoids. We hypothesize that a possibly longer time is required to manipulate the apico-basolateral organization of these organoids. In contrast to this, 90% of H9-derived and 85% of iPSC-derived organoids that were initially in suspension and then embedded in Matrigel reversed

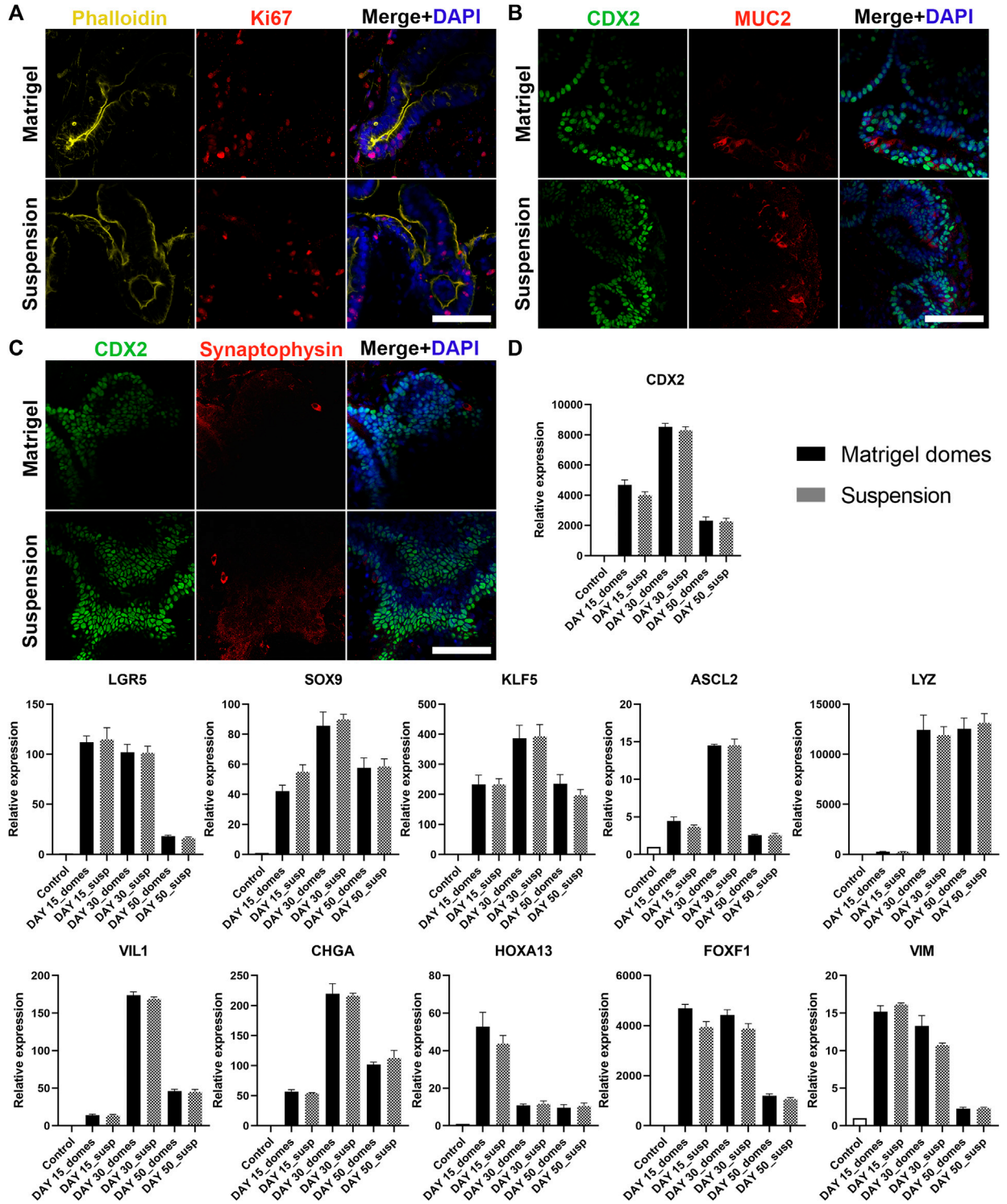

FIGURE 4 | Characterization of H9-derived human intestinal organoids after 30 days in culture. **(A–C)** Immunofluorescence stainings of intestinal markers (Ki67: proliferative cells; CDX2: intestinal transcription factor; MUC2: goblet cells; Synaptophysin: enteroendocrine cells) show similar expression patterns in both embedded and suspension organoids. Scale bars: 100 μm. **(D)** qRT-PCR analysis demonstrates the expression levels of proliferation genes (*LGR5*, *SOX9*, *KLF5*, *ASCL2*), intestinal differentiation genes (*CDX2*, *LYZ*, *VIL1*, *CHGA*, *HOXA13*) and mesenchymal genes (*FOXF1*, *VIM*) after 15, 30 and 50 days in culture. Untreated H9 cells were used as controls. Statistical analysis showed no significant difference between the organoids grown embedded in Matrigel and the organoids grown in suspension at any of the time-points. Error bars indicate mean ± S.E.M. (n = 3).

their polarity (apical side now facing the lumen). The remaining 10% and 15% of the organoids, respectively, demonstrated an intermediate polarity reversal, where the basal side was facing outwards in some regions of the organoids and in some other regions the apical side was facing outwards, suggesting that the apical-out intestinal organoids are more prone to polarity reversal when embedded in Matrigel.

Apical-Out Intestinal Organoids Display Various Intestinal Cell Types

Besides structural organization, the proper function of the intestine is highly dependent on the presence of different intestinal epithelial cell lineages. Indeed, one of the key advantages of organoids as an *in vitro* model is that they can recapitulate to a great extent the cellular diversity of the *in vivo* intestinal epithelium. Therefore, in a next step we verified that our apical-out organoids (derived from H9 or iPSCs) are able to fully mature and differentiate towards the major intestinal cell types. To visualize the intestinal cell differentiation, we used immunofluorescence against the proliferation marker Ki67 and Phalloidin (**Figure 4A**; **Supplementary Figure S6A**), the intestinal differentiation marker CDX2, the goblet cell marker Mucin 2 (MUC2) (**Figure 4B**; **Supplementary Figure S6B**) and the enteroendocrine marker Synaptophysin (**Figure 4C**; **Supplementary Figure S6C**). These stainings were performed at 30 days post Matrigel embedment of hindgut organoids or their transfer to suspension culture. This time-point was selected according to Spence et al. (2011) and Janssen et al. (2020), who demonstrated that intestinal organoids embedded in Matrigel can reach sufficient maturation after approximately 28 days. Organoids from both culture conditions showed similar expression patterns of the mentioned markers. Further characterization of these organoids was performed using relative gene expression quantification. More specifically, the transcriptional expression of multiple intestinal cell lineages was quantified over three developmental stages: days 15, 30 and 50 (**Figure 4D**; **Supplementary Figure S6D**). The expression of the intestinal differentiation marker *CDX2*, gradually increased between days 15 and 30, whereas at day 50 a significant decrease was observed. The proliferation markers sex determining region Y-box 9 (*SOX9*), Krueppel-like factor 5 (*KLF5*) and Achaete scute-like 2 (*ASCL2*) showed a similar trend with their peak expression at day 30, whereas leucine-rich repeat-containing G-protein-coupled receptor 5 (*LGR5*) expression peaked at day 15 and was reduced at later time-points. Lysozyme, which marks the presence of Paneth cells, was expressed at a low level on day 15 but was remarkably increased by day 30. The high expression levels were maintained over 50 days of culture. The expressions of Villin 1 (*VIL1*) (brush border of the enterocytes) and Chromogranin A (*CHGA*) (enteroendrocrine cells) peaked at day 30 and decreased later on as well. Finally, in both apical-in and apical-out organoids we identified the presence of mesenchyme. The distal hindgut mesoderm marker Homeobox A13 (*HOXA13*) peaked at day 15 and gradually decreased over later time-points. In contrast, the expression of the mesenchymal markers Forkhead Box F1 (*FOXF1*) and *VIM* remained unchanged between days 15 and 30, whereas on day 50 it was notably reduced. The expression patterns of the basal-out and apical-out organoids were very similar and no statistical significance was identified at any time-point (both in H9- and iPSC-derived organoids). These results indicate that organoids on day 15 already express intestine-specific markers but are fairly immature, whereas by day 30 the *in vitro* maturation culminates. This is in accordance with findings from Spence et al. (2011) and Janssen et al. (2020). After 50 days in culture, we observed a general decrease in the expression of most markers, although still in detectable levels, showing that organoids' functionality in culture gradually deteriorates from day 30 days. Engraftment of organoids in mice would secure further maturation (Watson et al., 2014), overcoming the short-term culturing periods allowed by *in vitro* methods. However, it is unknown whether the apical-out organoids would be able to maintain their polarity.

DISCUSSION

In recent years, the advent of intestinal organoids has revolutionized the *in vitro* research of the intestinal epithelium. These organoids have been widely used in studies related to gut development, physiology and disease since they recapitulate the properties of the *in vivo* tissue with great fidelity. In the original method, the intestinal organoids demonstrate an organized structure, where the basal side is in contact with the ECM and facing outwards whereas the apical side is enclosed and facing the luminal compartment. Thus, access to the apical surface is restricted and microinjection techniques are required to deliver substances (Bartfeld et al., 2015; Hill et al., 2017; Williamson et al., 2018). Recent advances in the organoid field paved the way for easier access to the lumen by reversing epithelial polarity in adult stem cell-derived organoids (Co et al., 2019; Li et al., 2020; Co et al., 2021; Giobbe et al., 2021; Nash et al., 2021), but whether the same method could be applied in PSC-derived organoids was uncertain. Here, we developed and validated a reversed polarity organoid model using PSCs. In these organoids the apical side is found on the outer surface of the organoids, and, thus, is directly accessible for testing compounds, particles or microbes. Apical-out organoids demonstrate similar functionality to the basal-out organoids as suggested by the retention of self-renewal capacity throughout the whole culture and the expression of all major intestinal cell types. One advantage of the apical-out organoids is that they are grown in a suspension system. In this way, the handling of organoids is uncomplicated since there is no viscous hydrogel surrounding them. This suggests that organoids can be easily selected and (re-) transferred, e.g., into microwells for performing downstream experiments.

The intestinal epithelium acts as a highly selective barrier for the absorption, metabolism and release of nutrients and drugs. Currently, the investigation of these functions is mainly performed with cell monolayers (Transwell systems) and there

are only few examples of organoid applications (Zietek et al., 2020; Youhanna and Lauschke, 2021). This is mainly due to the inaccessibility of the apical surface of the organoids. The formation of cell monolayers, either using cell lines (e.g., Caco-2) (Sun et al., 2008) or dissociated organoids (VanDussen et al., 2015; Kozuka et al., 2017; Wang et al., 2017; Altay et al., 2019) provides access to both the apical and basal sides. However, in this case a large number of cells is required and usually several days of maturation. Also, the 3D organization is disrupted, thus making the system less physiologically relevant. Another limitation is that usually these monolayers are formed in Transwell systems, which restricts *in situ* monitoring, e.g., live cell imaging, during culture. In contrast to this, our apical-out intestinal organoids, both retain their 3D architecture and allow for easy tracking and monitoring throughout the culture period. Hence, apical-out organoids may represent a novel and improved model for nutrient uptake and drug absorption studies.

Although intestinal organoids constitute one of the most physiologically representative *in vitro* models, the integral gut microbiome is missing (Min et al., 2020). In order to incorporate this in organoid models, researchers utilize either microinjections or monolayer cultures. Reversing the polarity of organoids offers an easy access to the apical surface, in which the microbiota is residing *in vivo*. Hence, with this system, host-microbiome interactions can be studied simply by adding microorganisms in the culture medium of organoids. The same method can be applied for the study of host-pathogen interactions where unknown mechanisms of cell invasion can be explored, thus leading to novel, efficient therapies. First successful experiments with apical-out organoids and microorganisms have already been performed by Co et al. (2019), Li et al. (2020), Nash et al. (2021), but so far solely adult stem cell-derived organoids could be used for this. In case of PSC-derived organoids, microbial colonization and pathogen infections can be studied at different stages of development, which is particularly important since the early stages of gut microbiota development remains poorly understood (Senn et al., 2020).

In summary, apical-out intestinal organoids can be successfully generated in microwell arrays, from PSC-derived 3D EBs following a step-wise differentiation method. These organoids reflect the structural and functional characteristics of their *in vivo* counterparts. The long-term reversed polarity grants easy access to the apical compartment thus qualifying these organoids for a wide range of applications.

DATA AVAILABILITY STATEMENT

The original contributions presented in the study are included in the article/**Supplementary Material**, further inquiries can be directed to the corresponding author.

AUTHOR CONTRIBUTIONS

PK conceived the project and designed experiments, performed fabrication of microwells, cell and organoid culture, morphological characterization of the organoids, immunohistochemistry, confocal microscopy, quantitative PCR experiments, SEM microscopy, data analysis, and prepared and edited the manuscript. CL-I contributed in the design, conduct and interpretation of the electron microscopy experiments. RT and PH contributed to scientific discussions and revised the paper. SG conceived the project and designed experiments, oversaw all the experiments, the interpretation of data and the paper preparation.

FUNDING

This study was financially supported by the Dutch Province of Limburg (program "Limburg INvesteert in haar Kenniseconomie/LINK"; SAS-2014-00837 and SAS-2018-02477). The authors gratefully acknowledge the Gravitation Program "Materials Driven Regeneration," funded by the Netherlands Organization for Scientific Research (024.003.013).

ACKNOWLEDGMENTS

The iPSC lines used in this study were generated by the Cincinnati Children's Pluripotent Stem Cell Facility. The authors would like to thank the Microscopy CORE Lab of Maastricht University for the support in the conduction of the SEM experiments.

SUPPLEMENTARY MATERIAL

The Supplementary Material for this article can be found online at: https://www.frontiersin.org/articles/10.3389/fbioe.2022.879024/full#supplementary-material

REFERENCES

Altay, G., Larrañaga, E., Tosi, S., Barriga, F. M., Batlle, E., Fernández-Majada, V., et al. (2019). Self-organized Intestinal Epithelial Monolayers in Crypt and Villus-like Domains Show Effective Barrier Function. *Sci. Rep.* 9 (9), 1–14. doi:10.1038/s41598-019-46497-x

Bartfeld, S., Bayram, T., Van De Wetering, M., Huch, M., Begthel, H., Kujala, P., et al. (2015). *In Vitro* expansion of Human Gastric Epithelial Stem Cells and Their Responses to Bacterial Infection. *Gastroenterology* 148, 126–136. doi:10.1053/j.gastro.2014.09.042

Caradec, J., Sirab, N., Keumeugni, C., Moutereau, S., Chimingqi, M., Matar, C., et al. (2010). 'Desperate House Genes': the Dramatic Example of Hypoxia. *Br. J. Cancer* 102, 1037–1043. doi:10.1038/sj.bjc.6605573

Clevers, H. (2016). Modeling Development and Disease with Organoids. *Cell* 165, 1586–1597. doi:10.1016/J.CELL.2016.05.082

Co, J. Y., Margalef-Català, M., Li, X., Mah, A. T., Kuo, C. J., Monack, D. M., et al. (2019). Controlling Epithelial Polarity: A Human Enteroid Model for Host-Pathogen Interactions. *Cel Rep.* 26, 2509–2520. doi:10.1016/j.celrep.2019.01.108

Co, J. Y., Margalef-Català, M., Monack, D. M., and Amieva, M. R. (2021). Controlling the Polarity of Human Gastrointestinal Organoids to Investigate

Epithelial Biology and Infectious Diseases. *Nat. Protoc.* 16 (16), 5171–5192. doi:10.1038/s41596-021-00607-0

Dessimoz, J., Opoka, R., Kordich, J. J., Grapin-Botton, A., and Wells, J. M. (2006). FGF Signaling Is Necessary for Establishing Gut Tube Domains Alongthe Anterior-Posterior axis *In Vivo*. *Mech. Develop.* 123, 42–55. doi:10.1016/J.MOD.2005.10.001

Fatehullah, A., Tan, S. H., and Barker, N. (2016). Organoids as an *In Vitro* Model of Human Development and Disease. *Nat. Cel Biol.* 18, 246–254. doi:10.1038/ncb3312

Giobbe, G. G., Bonfante, F., Jones, B. C., Gagliano, O., Luni, C., Zambaiti, E., et al. (2021). SARS-CoV-2 Infection and Replication in Human Gastric Organoids. *Nat. Commun.* 12, 1–14. doi:10.1038/s41467-021-26762-2

Giselbrecht, S., Gietzelt, T., Gottwald, E., Trautmann, C., Truckenmüller, R., Weibezahn, K. F., et al. (2006). 3D Tissue Culture Substrates Produced by Microthermoforming of Pre-processed Polymer Films. *Biomed. Microdevices* 8, 191–199. doi:10.1007/s10544-006-8174-8

Hill, D. R., Huang, S., Tsai, Y.-H., Spence, J. R., and Young, V. B. (2017). Real-time Measurement of Epithelial Barrier Permeability in Human Intestinal Organoids. *JoVE* 130, e56960. doi:10.3791/56960

Janssen, A. W. F., Duivenvoorde, L. P. M., Rijkers, D., Nijssen, R., Peijnenburg, A. A. C. M., van der Zande, M., et al. (2020). Cytochrome P450 Expression, Induction and Activity in Human Induced Pluripotent Stem Cell-Derived Intestinal Organoids and Comparison with Primary Human Intestinal Epithelial Cells and Caco-2 Cells. *Arch. Toxicol.* 95, 907–922. doi:10.1007/S00204-020-02953-6

Kakni, P., Hueber, R., Knoops, K., López-Iglesias, C., Truckenmüller, R., Habibovic, P., et al. (2020). Intestinal Organoid Culture in Polymer Film-Based Microwell Arrays. *Adv. Biosys.* 4, 2000126. doi:10.1002/adbi.202000126

Klunder, L. J., Faber, K. N., Dijkstra, G., and van IJzendoorn, S. C. D. (2017). Mechanisms of Cell Polarity-Controlled Epithelial Homeostasis and Immunity in the Intestine. *Cold Spring Harb. Perspect. Biol.* 9, a027888. doi:10.1101/cshperspect.a027888

Kozuka, K., He, Y., Koo-McCoy, S., Kumaraswamy, P., Nie, B., Shaw, K., et al. (2017). Development and Characterization of a Human and Mouse Intestinal Epithelial Cell Monolayer Platform. *Stem Cel Rep.* 9, 1976–1990. doi:10.1016/J.STEMCR.2017.10.013

Li, Y., Yang, N., Chen, J., Huang, X., Zhang, N., Yang, S., et al. (2020). Next-Generation Porcine Intestinal Organoids: an Apical-Out Organoid Model for Swine Enteric Virus Infection and Immune Response Investigations. *J. Virol.* 94, e01006. doi:10.1128/JVI.01006-20

McCracken, K. W., and Wells, J. M. (2017). Mechanisms of Embryonic Stomach Development. *Semin. Cel Develop. Biol.* 66, 36–42. doi:10.1016/j.semcdb.2017.02.004

McCracken, K. W., Howell, J. C., Wells, J. M., and Spence, J. R. (2011). Generating Human Intestinal Tissue from Pluripotent Stem Cells *In Vitro*. *Nat. Protoc.* 6, 1920–1928. doi:10.1038/nprot.2011.410

Min, S., Kim, S., and Cho, S.-W. (2020). Gastrointestinal Tract Modeling Using Organoids Engineered with Cellular and Microbiota Niches. *Exp. Mol. Med.* 52, 227–237. doi:10.1038/s12276-020-0386-0

Nash, T. J., Morris, K. M., Mabbott, N. A., and Vervelde, L. (2021). Inside-out Chicken Enteroids with Leukocyte Component as a Model to Study Host-Pathogen Interactions. *Commun. Biol.* 4, 1–15. doi:10.1038/s42003-021-01901-z

Sato, T., and Clevers, H. (2013). Growing Self-Organizing Mini-Guts from a Single Intestinal Stem Cell: Mechanism and Applications. *Science* 340, 1190–1194. doi:10.1126/science.1234852

Sato, T., Vries, R. G., Snippert, H. J., Van De Wetering, M., Barker, N., Stange, D. E., et al. (2009). Single Lgr5 Stem Cells Build Crypt-Villus Structures *In Vitro* without a Mesenchymal Niche. *Nature* 459, 262–265. doi:10.1038/nature07935

Senn, V., Bassler, D., Choudhury, R., Scholkmann, F., Righini-Grunder, F., Vuille-dit-Bile, R. N., et al. (2020). Microbial Colonization from the Fetus to Early Childhood-A Comprehensive Review. *Front. Cel. Infect. Microbiol.* 10, 573735. doi:10.3389/FCIMB.2020.573735/BIBTEX

Spence, J. R., Mayhew, C. N., Rankin, S. A., Kuhar, M. F., Vallance, J. E., Tolle, K., et al. (2011). Directed Differentiation of Human Pluripotent Stem Cells into Intestinal Tissue *In Vitro*. *Nature* 470, 105–109. doi:10.1038/nature09691

Stroulios, G., Stahl, M., Elstone, F., Chang, W., Louis, S., Eaves, A., et al. (2021). Culture Methods to Study Apical-specific Interactions Using Intestinal Organoid Models. *JoVE* 2021, e62330. doi:10.3791/62330

Sun, H., Chow, E. C. Y., Liu, S., Du, Y., and Pang, K. S. (2008). The Caco-2 Cell Monolayer: Usefulness and Limitations. *Expert Opin. Drug Metab. Toxicol.* 4, 395–411. doi:10.1517/17425255.4.4.395

VanDussen, K. L., Marinshaw, J. M., Shaikh, N., Miyoshi, H., Moon, C., Tarr, P. I., et al. (2015). Development of an Enhanced Human Gastrointestinal Epithelial Culture System to Facilitate Patient-Based Assays. *Gut* 64, 911–920. doi:10.1136/GUTJNL-2013-306651

Wang, Y., DiSalvo, M., Gunasekara, D. B., Dutton, J., Proctor, A., Lebhar, M. S., et al. (2017). Self-renewing Monolayer of Primary Colonic or Rectal Epithelial Cells. *Cell Mol. Gastroenterol. Hepatol.* 4, 165–182. doi:10.1016/J.JCMGH.2017.02.011

Watson, C. L., Mahe, M. M., Múnera, J., Howell, J. C., Sundaram, N., Poling, H. M., et al. (2014). An *In Vivo* Model of Human Small Intestine Using Pluripotent Stem Cells. *Nat. Med.* 20, 1310–1314. doi:10.1038/nm.3737

Williamson, I. A., Arnold, J. W., Samsa, L. A., Gaynor, L., DiSalvo, M., Cocchiaro, J. L., et al. (2018). A High-Throughput Organoid Microinjection Platform to Study Gastrointestinal Microbiota and Luminal Physiology. *Cell Mol. Gastroenterol. Hepatol.* 6, 301–319. doi:10.1016/j.jcmgh.2018.05.004

Youhanna, S., and Lauschke, V. M. (2021). The Past, Present and Future of Intestinal *In Vitro* Cell Systems for Drug Absorption Studies. *J. Pharm. Sci.* 110, 50–65. doi:10.1016/J.XPHS.2020.07.001

Zietek, T., Giesbertz, P., Ewers, M., Reichart, F., Weinmüller, M., Urbauer, E., et al. (2020). Organoids to Study Intestinal Nutrient Transport, Drug Uptake and Metabolism - Update to the Human Model and Expansion of Applications. *Front. Bioeng. Biotechnol.* 8, 1065. doi:10.3389/FBIOE.2020.577656

Zorn, A. M., and Wells, J. M. (2009). Vertebrate Endoderm Development and Organ Formation. *Annu. Rev. Cel Dev. Biol.* 25, 221–251. doi:10.1146/annurev.cellbio.042308.113344

Conflict of Interest: RT and SG are founders and shareholders of 300MICRONS GmbH.

The remaining authors declare that the research was conducted in the absence of any commercial or financial relationships that could be construed as a potential conflict of interest.

Publisher's Note: All claims expressed in this article are solely those of the authors and do not necessarily represent those of their affiliated organizations or those of the publisher, the editors, and the reviewers. Any product that may be evaluated in this article, or claim that may be made by its manufacturer, is not guaranteed or endorsed by the publisher.

frontiers | Frontiers in Bioengineering and Biotechnology

ORIGINAL RESEARCH
published: 13 July 2022
doi: 10.3389/fbioe.2022.910902

Multimodal Magnetic Resonance and Photoacoustic Imaging of Tumor-Specific Enzyme-Responsive Hybrid Nanoparticles for Oxygen Modulation

Maharajan Sivasubramanian[1†], Chia-Hui Chu[1†], Shih-Hsun Cheng[1,2], Nai-Tzu Chen[3], Chin-Tu Chen[2], Yao Chen Chuang[1], Hsia Yu[1], Yu-Lin Chen[1], Lun-De Liao[1] and Leu-Wei Lo[1]**

[1]Institute of Biomedical Engineering and Nanomedicine, National Health Research Institutes, Zhunan, Taiwan, [2]Department of Radiology, The University of Chicago, Chicago, IL, United States, [3]College of Biopharmaceutical and Food Sciences, Institute of New Drug Development, China Medical University, Taichung, Taiwan

OPEN ACCESS

Edited by:
Dimitrios Stamatialis,
University of Twente, Netherlands

Reviewed by:
Sara Pedron,
University of Illinois at Urbana-Champaign, United States
Xianwen Wang,
Anhui Medical University, China

***Correspondence:**
Lun-De Liao
ldliao@nhri.edu.tw
Leu-Wei Lo
lwlo@nhri.edu.tw

[†]These authors have contributed equally to this work and share the first authorship

Specialty section:
This article was submitted to Tissue Engineering and Regenerative Medicine, a section of the journal Frontiers in Bioengineering and Biotechnology

Received: 01 April 2022
Accepted: 01 June 2022
Published: 13 July 2022

Citation:
Sivasubramanian M, Chu C-H, Cheng S-H, Chen N-T, Chen C-T, Chuang YC, Yu H, Chen Y-L, Liao L-D and Lo L-W (2022) Multimodal Magnetic Resonance and Photoacoustic Imaging of Tumor-Specific Enzyme-Responsive Hybrid Nanoparticles for Oxygen Modulation. Front. Bioeng. Biotechnol. 10:910902. doi: 10.3389/fbioe.2022.910902

Multimodal imaging contrast agents for cancer that can not only perform diagnostic functions but also serve as tumor microenvironment–responsive biomaterials are encouraging. In this study, we report the design and fabrication of a novel enzyme-responsive T_1 magnetic resonance imaging (MRI) contrast agent that can modulate oxygen in the tumor microenvironment via the catalytic conversion of H_2O_2 to O_2. The T_1 contrast agent is a core–shell nanoparticle that consists of manganese oxide and hyaluronic acid (HA)–conjugated mesoporous silica nanoparticle (HA-MnO@MSN). The salient features of the nanoparticle developed in this study are as follows: 1) HA serves as a targeting ligand for CD44-expressing cancer cells; 2) HA allows controlled access of water molecules to the MnO core via the digestion of enzyme hyaluronidase; 3) the generation of O_2 bubbles in the tumor by consuming H_2O_2; and 4) the capability to increase the oxygen tension in the tumor. The r_1 relaxivity of HA-MnO@MSN was measured to be 1.29 $mM^{-1}s^{-1}$ at a magnetic field strength of 9.4 T. *In vitro* results demonstrated the ability of continuous oxygen evolution by HA-MnO@MSN. After intratumoral administration of HA-MnO@MSN to an HCT116 xenograft mouse model, T_1 weighted MRI contrast was observed after 5 h postinjection and retained up to 48 h. In addition, *in vivo* photoacoustic imaging of HA-MnO@MSN demonstrated an increase in the tumor oxygen saturation over time after i. t. administration. Thus, the core–shell nanoparticles developed in this study could be helpful in tumor-targeted T_1 MR imaging and oxygen modulation.

Keywords: manganese oxide nanoparticles, tumor-specific T1 contrast agent, hyaluronidase, magnetic resonance imaging, oxygen modulation, photoacoustic imaging

INTRODUCTION

The working principle of magnetic resonance imaging (MRI) is based on protons' absorption and re-emission of radio waves under a magnetic field. In brief, after irradiation with radio waves of a suitable frequency, protons in the presence of a magnetic field flip and relax back to their equilibrium depending on their physiochemical environment, generating an MRI signal. Owing to their high

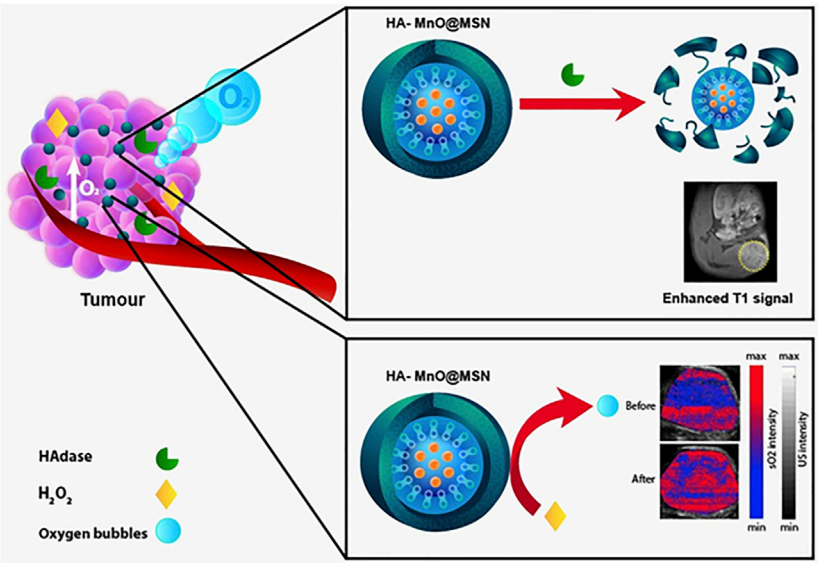

GRAPHICAL ABSTRACT | The hybrid nanoplatform that harnesses the tumor microenvironment factors for dual targeted magnetic resonance imaging and assessment of tumor oxygen status by photoacoustic imaging.

spatial resolution, excellent soft-tissue contrast, and good patient compliance, MRI holds great promise in diagnostic and clinical imaging (Stark and Bradley, 1999; Gibby, 2005; Sosnovik and Weissleder, 2007). Nevertheless, the low sensitivity of MRI is associated with the inability to delineate imaging contrast between normal and abnormal tissues. In consequence, several nanoparticle-based contrast agents were developed to address this issue. For instance, superparamagnetic iron oxide nanoparticles (SPION) are used as T_2 (negative) contrast agents, which reduce T_2 relaxation times by producing dark T_2 weighed contrast images and are already utilized in clinical settings (Saini et al., 1987; Anzai et al., 2003; Neuwelt et al., 2004; Lin et al., 2009). However, SPION induces blooming effects when administered and causes a vague distinction of hypointense pathogenic conditions, such as bleeding and calcification, which severely hampers its application (Bulte and Kraitchman, 2004; Wu et al., 2004).

In contrast, gadolinium (Gd) complexes emerged as T_1 contrast agents that can generate hyperintense regions by increasing the longitudinal relaxation T_1 time, resulting in T_1 weighed positive-contrast images (Anderson et al., 2006; Caravan, 2006; Aime et al., 2007; Caravan et al., 2007; Granot et al., 2007). In addition, a manganese ion (Mn^{2+}) is utilized as a T_1 contrast agent in neuroscience to investigate the structure and functions of the brain (Silva et al., 2004). However, when administered in high doses, Mn^{2+} can deposit in the brain, causing neurotoxicity (Sepulveda et al., 2012). As a different approach, manganese oxide (MnO) nanoparticles have been explored as a T_1 contrast agent for molecular and cellular MR imaging (Gilad et al., 2008). Although they have been shown to offer great promise, weak contrast and the absence of prolonged signal duration remain a critical issue for their use *in vivo* (Yang et al., 2010).

The physical properties of manganese (Mn) ions such as the high spin quantum number, extended longitudinal relaxation times, and fast water exchange rates are comparable to those of gadolinium (Gd) ions, which makes them an efficient T1 MRI contrast agent (Mendonça-Dias et al., 1983). Compared to Gd chelates, MnO synthesized as a nanoformulation allows for further chemical modification (HA-MnO@MSN) and is biogenic. HA coating could be selectively degraded by the enzyme hyaluronidase expressed in tumors to exhibit a targeted MR imaging function. Our MnO nanoparticle (NP) also demonstrated a tumor microenvironment modulation property, through which the tumor resident hydrogen peroxide is converted into oxygen. Such oxygen-enriched tumors are conductive to reactive oxygen species–mediated therapeutic modalities such as photodynamic therapy, radiotherapy, and sonodynamic therapy. Gd-based contrast agents could cause nephrogenic systemic fibrosis, raising severe toxicity concerns. In fact, the FDA issues continued caution, and the American College of Radiology guides patients with acute kidney injury to avoid any Gd-based contrast agents (Perez-Rodriguez et al., 2009; ACR Manual on Contrast Media, 2015). As an alternative, Mn-based materials with MR imaging contrast comparable to Gd-based agents were developed (Anbu et al., 2021). In a recent study by Gale et al. (2018), Mn-PyC3A was developed and demonstrated MRI signal contrast comparable to commercially available Gd-DTPA. The authors evaluated various *in vivo* parameters and implied that Mn-PyC3A could be used for MR angiography in patients with renal complications.

Besides imaging functions, recently, the catalytic functions of nanomaterials have drawn significant attention as tumor microenvironment–responsive oxygen generators (Ding et al., 2020). For instance, manganese ferrite nanomaterials have been shown to alter the tumor microenvironment via the catalytic conversion of H_2O_2 to O_2 (Kim et al., 2017). Such oxygen self-supplying nanomaterials have profound applications in cancer

therapy (Zhang et al., 2020). Photoacoustic (PA) imaging combines light and sound to enable the functional imaging of the tumor microenvironment (Liao et al., 2014; Zackrisson et al., 2014; Liu et al., 2015; Bandla et al., 2018; Leng et al., 2019). In PA imaging, excited endogenous chromophores (e.g., hemoglobin and melanin) under pulsed laser irradiation undergo thermoelastic expansion, generating pressure waves that are detected by ultrasound (US) transducers. Several studies have shown that PAI can exploit differences in optical absorption characteristics between oxygenated hemoglobin and deoxygenated hemoglobin to obtain estimates of tumor oxygen saturation (%sO_2) (Mallidi et al., 2015; Chuang et al., 2020). Taking the advantage of MR and PA imaging techniques, the dual-modality approach will enable us to obtain complementary information on tumor biology. MRI allows us to visualize nanoparticle distribution in the tumor, while PA imaging exhibits the tumor oxygenation saturation status. The strength of this dual-modality approach was explored in this study.

For successful biological applications, nanoparticle-based contrast agents must be highly biocompatible and water-soluble, and their surface should be active for further bioconjugation. This can be achieved by coating with mesoporous silica nanoparticles (MSN), a widely used strategy to functionalize contrast agents for biological applications. MSN is biocompatible and nontoxic, and its surface can be modified for desired applications. Owing to these beneficial properties, the enthusiasm for MSN in biological applications has increased exponentially (Cheng et al., 2009; Tu et al., 2009; Cheng et al., 2011; Li et al., 2015; Liu et al., 2016; Wang et al., 2021a). In addition, nanoparticles with an MSN shell can be accessible by water molecules, which significantly enhance the relaxation of water protons. In this study, we report a core–shell nanoparticle that consists of an MnO core and MSN shell. The MSN shell was further chemically conjugated with hyaluronic acid (HA), a negatively charged, nontoxic, and naturally occurring polysaccharide with extensive biomedical applications, such as tissue engineering, hydrogels, drug delivery, and molecular imaging and therapy (Choi et al., 2009; Choi et al., 2010; Tripodo et al., 2015; Dosio et al., 2016; Yan et al., 2016; Phua et al., 2019; Wang et al., 2021a; Zhou et al., 2021). The nanoplatform design in this study is based on the following considerations: 1) HA provides tumor-targeting; 2) HA facilitates controlled access of water molecules to the MnO core; 3) the generation of O_2 bubbles in the tumor by catalytic decomposition of H_2O_2; and 4) the capability to increase the oxygen saturation in the tumor. The validity of this core–shell nanoparticle as an efficient T_1 contrast agent and its capability as an oxygen generator was further demonstrated both in our *in vitro* and *in vivo* experiments.

MATERIALS AND METHODS

Materials

The chemicals used include tetraethoxysilane (TEOS), cetyltrimethylammonium bromide (CTAB), methanol, sodium hydroxide (NaOH), manganese chloride tetrahydrate, H_2O_2, sodium oleate, n-hexane, chloroform, ethyl acetate, 1-octadecene, HA (M.Wt: 10,000–18,000 Da), (3-aminopropyl) triethoxysilane (APTS), and O-(benzotriazol-1-yl)-N,N,N′,N′-tetramethyluronium hexafluorophosphate (HBTU). All chemicals were purchased from Sigma Chemical Co.

Method Synthesis of Ultrasmall Manganese Oxide Nanoparticles

The synthesis of MnO nanoparticles is described as follows: 1.24 g of the Mn–oleate complex (2 mmol) was dissolved in 10 g of 1-octadecene. The resulting solution was degassed at 70°C for 1 h under vacuum and heated to 300°C with vigorous stirring. The reaction mixture was maintained at this temperature for 1 h to induce sufficient growth. The solution was then cooled to room temperature, and 20 ml of hexane was added to improve the dispersibility of the nanoparticles, followed by adding 80 ml of acetone to precipitate the nanoparticles. The precipitate was obtained by centrifugation. The above purification procedure was repeated two more times to remove the excess surfactant and solvent.

Synthesis of Mesoporous Silica–Encased MnO

MnO@MSN was prepared using the following procedure. The MnO nanoparticles stabilized with oleic amine were dispersed in chloroform at a concentration of 12.8 mg Mn/ml. Next, typical mesoporous silica coating onto MnO nanoparticles was performed using a sol–gel reaction of TEOS in an aqueous solution containing CTAB and MnO nanoparticles stabilized with the oleic amine. First, 1 ml of MnO nanoparticles in chloroform was poured into 5 ml of 0.05-M aqueous CTAB solution, and the resulting solution was stirred for 1 h, forming an oil-in-water microemulsion. The mixture was then heated to 70°C to evaporate chloroform. Next, the resulting transparent solution of MnO/CTAB was added to a mixture of 40 ml of water and 1.4 ml of 2-M NaOH solution, and the mixture was heated to 60°C. Then, 0.25 ml of TEOS and 1.8 ml of ethylacetate were added to the reaction solution in sequence, and the reaction was continued for 2 h. The washing steps for MnO@MSN nanoparticles with ethanol were performed to remove unreacted species, and then, the nanoparticles were redispersed in 5 ml of ethanol.

Synthesis of Hyaluronic Acid–Coated MnO@MSN

For HA coating, we modified the outer surface of MnO@MSN with primary amine groups (MnO@MSN-NH_2) using APTS. Then, 20 mg of HA and 30 mg of HBTU were added to 1 mg of MnO@MSN-NH_2 in the phosphate buffered saline solution. The mixture was stirred at room temperature for 4 h, and then, the resulting HA-MnO@MSN was collected and washed with ethanol and water using a centrifuge (12,000 rpm × 3).

Characterization

The morphology of the samples was characterized using a transmission electron microscope (TEM) (Hitachi, H-7650), operating at an accelerated voltage of 80 kV. Fourier transform

infrared spectroscopy (FTIR) was recorded on a Nicolet 550 spectrometer using KBr pellets (approximately 1 mg of the sample was pressed with 300 mg KBr). ZetaSizer Nano was used to measure the hydrodynamic size of the nanoparticles. MRI acquisitions were performed on a 9.4 T magnet (Bruker-Biospin, Billerica, MA, United States) using a 35-mm volume quad-coil (Bruker-Biospin, Billerica, MA, United States). Mn concentrations were based on the molar concentration of manganese atoms measured using ICP-MS (Perkin Elmer Elan 6100).

Magnetic Resonance Imaging Parameters for *in vitro* Relaxivity Measurements

T_1 relaxation times were calculated using a RAREVTR inversion recovery sequence. Ten experiments were performed with inversion times (TR) ranging from 150 to 10,000 ms, TE = 9.8 ms, matrix = 128 × 128, FOV = 0.30 mm, slice thickness = 0.30 mm, and NEX = 2. The specific relaxivity (r_1) of the MnO nanoparticles was measured as follows. Each sample was prepared in five different concentrations, and T_1 values were measured for each concentration, which was then used for r_1 calculations. Relaxivity was determined from the slope of concentration-dependent T_1 changes.

In vitro US Imaging

In vitro US imaging of MnO@MSN and HA-MnO@MSN was performed in 200-μM H_2O_2 solution. An agarose gel (3%, w/v) phantom was prepared using a 500 μl Eppendorf tube, and the tube was removed after the phantom gel had cooled. Nanoparticles in 200-μM H_2O_2 solutions (1 mg/ml) were prepared and placed in the agarose phantom, and the change in US intensity for each sample was measured up to 30 min using a homemade 128-channel high-frequency US platform (Vantage 128, Verasonics Inc., Washington, DC, United States). The entire US system was controlled using a custom-developed graphical user interface (GUI) based on MATLAB® (R2007a, MathWorks Inc., Natick, MA, United States). The US signals were acquired using a high-frequency 18.5-MHz US transducer (L22-14v, Verasonics Inc., Washington, DC, United States).

Oxygen Evolution and Quenching of H_2O_2

To investigate the ability of oxygen-evolving property, 1 mg of MnO@MSN and HA-MnO@MSN were incubated with 200 μM of H_2O_2, and then, the O_2 concentration was measured using a dissolved oxygen meter (OX10, Unisense Instruments, Denmark). For the quenching experiments, HA-MnO@MSN (1 mg/ml) was added with H_2O_2 (10 mM) to initiate the reaction. The residual concentration of H_2O_2 was determined over time by measuring the absorbance of H_2O_2 at 210 nm. The continuous catalytic effect was verified by repetitive addition of 10 mM of H_2O_2 to HA-MnO@MSN (1 mg/ml) solution, followed by determining the concentration by measuring the absorbance.

In vivo Tumor Oxygen Saturation Measurements by PA Imaging

In vivo tumor oxygenation saturation (sO_2) measurements were performed using a PA imaging system. For this purpose, three HCT116 tumor–bearing mice (size ranging from 600 to 750 mm^3) from the National Laboratory Animal Center, Taiwan, were deeply anesthetized with isoflurane (1–4%) using an inhalation device and placed on a heating pad. Note that these three mice were used for proof-of-concept experiments in this study. Then, 500 μg of HA-MnO@MSN was injected intratumorally into the subcutaneous HCT116 tumor–bearing mice. The baseline image was acquired preinjection and following measurements at various time points postinjection. A 128-channel Verasonics high-frequency US platform (Vantage 128, Verasonics Inc., Washington, DC, United States) was employed for dual-modality imaging (both PA imaging and US imaging). The entire PA system was controlled using a custom-developed GUI based on MATLAB® (R2007a, MathWorks Inc., Natick, MA, United States). In order to operate the system in the PA mode, laser excitation and data acquisition were synchronized using triggering. The excitation laser was a compact Nd:YAG-laser system with an integrated tunable optical parametric oscillator (OPO, SpitLight 600 OPO, InnoLas Laser GmbH, Krailling, Germany). The OPO generates approximately 7-ns duration pulses at a 20-Hz repetition rate with tunable wavelengths from 680 to 2,400 nm. The PA signals were acquired using a high-frequency 18.5-MHz US transducer (L22-14v, Verasonics Inc., Washington, DC, United States). This transducer has a −6-dB fractional bandwidth of 67% and 128 active elements. The acoustic waves were received, reconstructed, and displayed on a computer screen at a frame rate of 20 frames per second. The American National Standards Institute safety limit is 20 mJ/cm^2, and the incident energy density on the sample surface during PA imaging was estimated to be approximately 12 mJ/cm^2, which is within the safety limit. The sO_2 around the tumor was measured via the differential optical absorption of oxygenated and deoxygenated hemoglobin at different wavelengths of 850 and 750 nm, respectively. To facilitate the comparison of sO_2 patterns in different groups, the regions of interest in the tumor were employed in the proximity of the HA-MnO@MSN injection site and identified using US imaging. PA B-scans of mice generating averagely oxygenated and deoxygenated hemoglobin signals were analyzed using custom-developed software based on MATLAB® (R2007a, The MathWorks, United States), and sO_2 is defined as $sO_2 = [HbO_2]/[HbO_2] + [Hb]$. A customized, precision 3D translation stage with motorized x-, y-, and *z*-axes was used to control the transducer to obtain A-scan, B-scan (i.e., two-dimensional; one axis is the lateral scanning distance, and the other axis is the imaging depth), and C-scan (i.e., three-dimensional) images. For *in vivo* imaging, the PA probe was immersed in an acrylic water tank with a rectangular cutout at the bottom serving as an imaging window. The cutout was sealed with a thin polyethylene film of 15-μm thickness. US gel (POC Medical, Inc., Zhongli City, Taiwan) or an agarose pad was then used to provide a coupling interface between the imaging window and the animal.

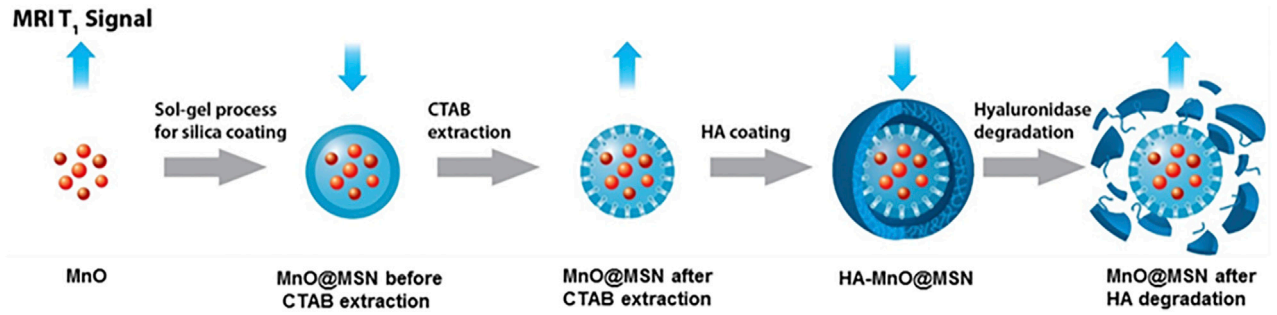

FIGURE 1 | Schematic illustration of the enzyme-responsive and tumor-specific HA MnO@MSN-based T_1 contrast agent.

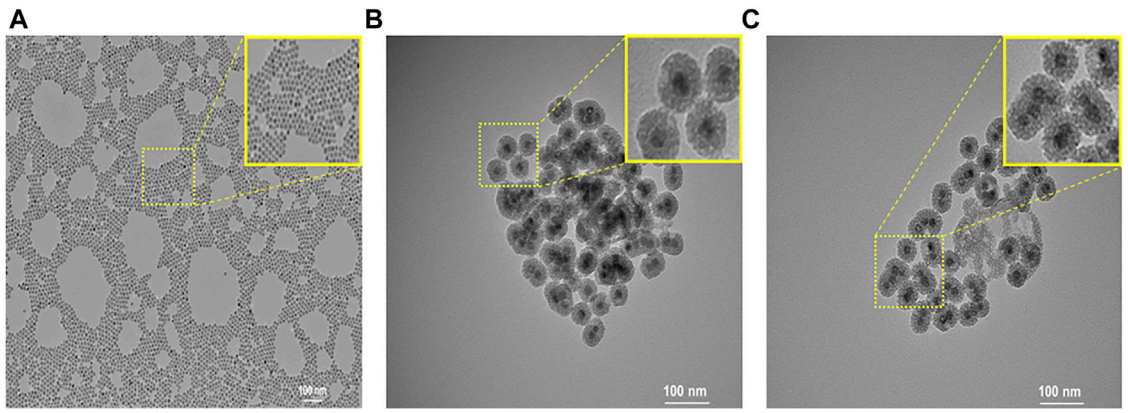

FIGURE 2 | TEM images of **(A)** MnO, **(B)** MnO@MSN, and **(C)** HA-MnO@MSN. Inset shows the magnified image.

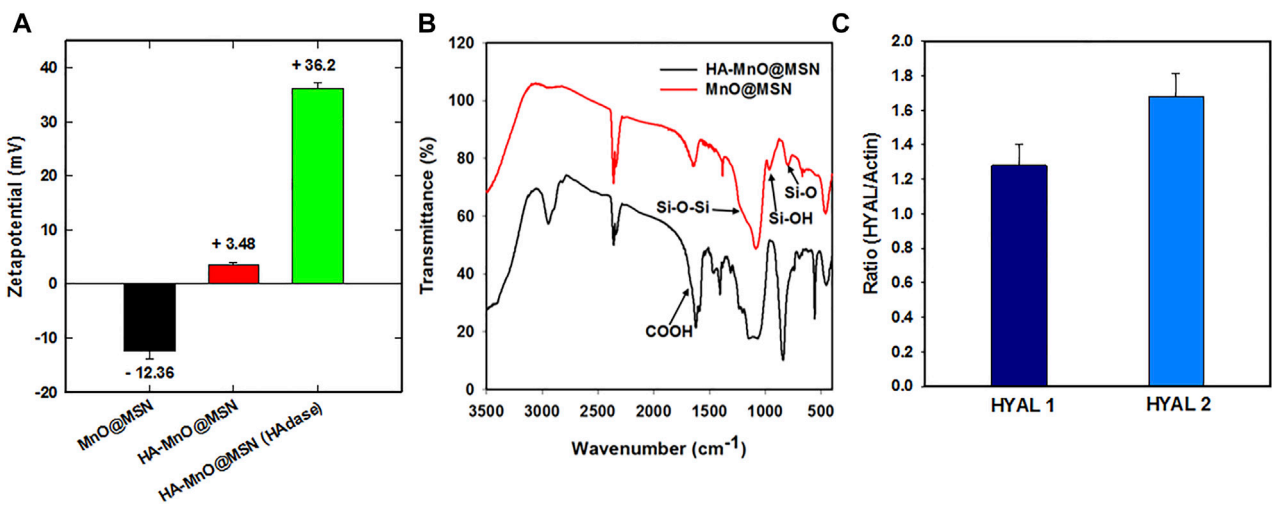

FIGURE 3 | (A) Zeta potential, **(B)** FTIR spectra of HA-MnO@MSN and MnO@MSN, and **(C)** distribution of HYAL1 and HYAL2 in HCT116 using western blot analysis (the *p*-value < 0.005).

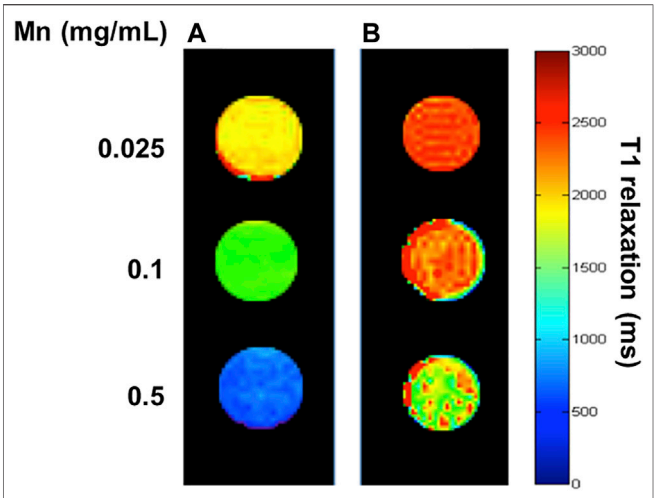

FIGURE 4 | T_1 map of CTAB-extracted MnO@MSN **(A)** and **(B)** non-CTAB–extracted MnO@MSN at various concentrations suspended in water at 9.4 T.

In vivo Magnetic Resonance Imaging of HA-MnO@MSN in an HCT116 Tumor Model

For *in vivo* MR imaging studies, cultured HCT116 cancer cells (2×10^6 cells) were injected into the right thigh regions of mice ($n = 3$) to establish the tumors. Note that these three mice were used for proof-of-concept experiments in this study. After the tumors developed up to a size of approximately 200 mm^3, mice were deeply anesthetized with isoflurane (1–4%) using an inhalation device and placed on a heating pad. Then, 500 μg of HA-MnO@MSN was injected intratumorally. MRI acquisitions were performed on a 9.4 T magnet (Bruker-Biospin, Billerica, MA, United States) using a 35-mm volume quad-coil (Bruker-Biospin, Billerica, MA, United States). T1 relaxation times were calculated using a RAREVTR inversion recovery sequence. The baseline image was acquired preinjection and following measurements at various time points postinjection. The MR parameters were set up as TR = 600 ms, TE = 10.5 ms, FOV = 4 × 4 cm, slice thickness = 1 mm, 20 slices, NEX = 8, and matrix size = 256 × 128 recovered to 256 × 256.

RESULTS

In an attempt to develop a hyaluronidase enzyme (HAdase)–sensitive T_1 contrast agent, HA-conjugated core–shell nanoparticles were prepared. Core–shell nanoparticles consist of an MnO core and HA-MSN as a shell, in which HA was chemically conjugated to the MSN outer surface. A schematic of the concept is presented in **Figure 1**. Because HA is specifically degraded by HAdase, which is abundant in cancer cells, such nanoparticles may offer potential as carriers for selective cancer imaging and drug delivery.

Synthesis

Oleic acid–stabilized MnO nanoparticles with an average diameter of 15 nm were synthesized via the thermal decomposition of the manganese–oleate complex (Na et al., 2007). To prepare the MSN shell, a hydrophobic oleic acid–capped MnO nanoparticle was transferred into an aqueous solution using CTAB. Then, a sol–gel-type condensation reaction with TEOS resulted in the formation of an MSN shell. Next, in order to prepare enzyme-responsive nanoparticles, we modified the outer surface of MSN with primary amine using APTS. This is because the repeating unit of HA contains carboxylic acid, which was chemically conjugated to primary amine-functionalized MSN in the presence of HBTU via amide bond formation. At last, CTAB was removed by extraction with acidic ethanol to generate a mesoporous silica shell. **Figure 2** shows the TEM images of nanoparticles. MnO nanoparticles were highly monodisperse and spherical in shape, with an average diameter of 15 nm (**Figure 2A**). The TEM image (**Figure 2B**) of MnO@MSN shows the MSN coating of MnO with a distinct core–shell morphology, and HA-MnO@MSN particles exhibited a spherical or quasispherical shape with an average diameter of 50 nm (**Figure 2C**).

The surface coverage of HA on MnO@MSN was supported by the zeta potential results (**Figure 3A**), which increased from −18 (MnO@MSN) to 5 mV. When treated with the enzyme HAdase, the zeta potential of HA-MnO@MSN increased further to 37 mV. This might be due to the digestion of HA by HAdase revealing primary amine groups on the MSN outer surface. **Figure 3B** shows the FTIR spectra of MnO@MSN and HA-MnO@MSN. From the MnO@MSN spectrum, we can observe the characteristic peak of the silica structure at 760 cm^{-1} (Si–O stretching), 960 cm^{-1} (Si–OH stretching), and 1,200 cm^{-1} (Si–O–Si stretching). After conjugation with HA, the resulting HA-MnO@MSN exhibited similar peaks of silica and a notable sharp peak at 1,620 cm^{-1}, which corresponds to the COOH asymmetric stretching of HA, which confirms successful chemical conjugation. Western blot analysis was utilized to study the expression of the HAdase enzyme in HCT116 cancer cells. The analysis showed that HCT116 cells expressed both hyaluronoglucosaminidase 1 (HYAL1) and hyaluronoglucosaminidase 2 (HYAL2) (**Figure 3C**). HYALl and HYAL2 were present in cell lysate, which indicates that HCT116 cells express and secrete both HAdases.

Relaxivity Measurements

The primary strategy to increase the r_1 relaxivity of MnO NP is to increase the availability of water molecules in closer proximity to the magnetic core. Because the major relaxation mechanism constitutes the dipole-dipole coupling between water protons and the manganese ions (Hsu et al., 2016). In the case of the core-shell-structured HA-MnO@MSN in this study, we achieved the r1 relaxivity increase via the structural modifications of the coating to enhance its water permeability. To test the use of MnO@MSN as a T_1 contrast agent, its longitudinal relaxivity was characterized using a 9.4 T MRI scanner in aqueous suspension. **Figures 4A,B** show a significant decrease in relaxation time for the incremental MnO concentrations. The molar relaxivity of CTAB-extracted MnO@MSN was determined to be 1.29 $mM^{-1}s^{-1}$, which was calculated by measuring the

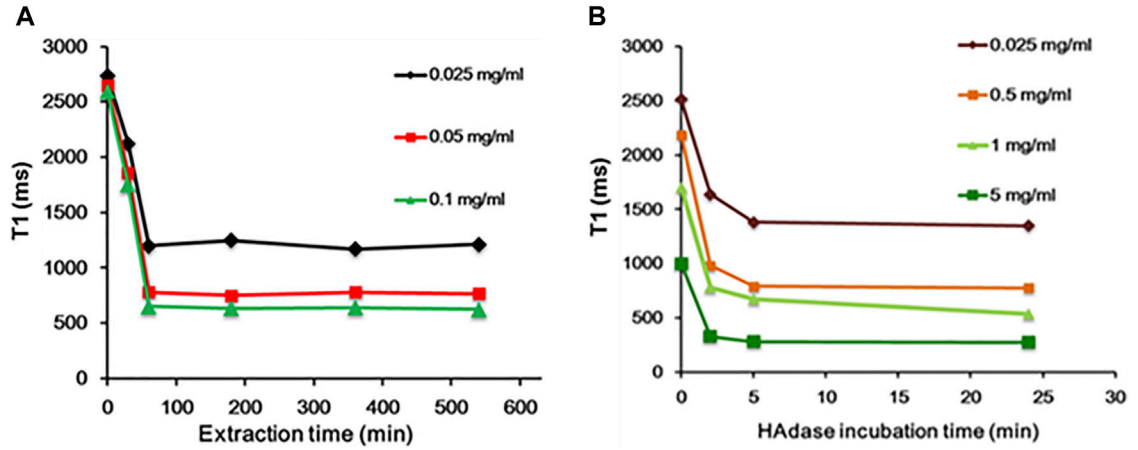

FIGURE 5 | Time-dependent analysis. **(A)** Decrease in T_1 of MnO@MSN during CTAB extraction and **(B)** decrease in T_1 of HA-MnO@MSN during incubation with the HAdase enzyme.

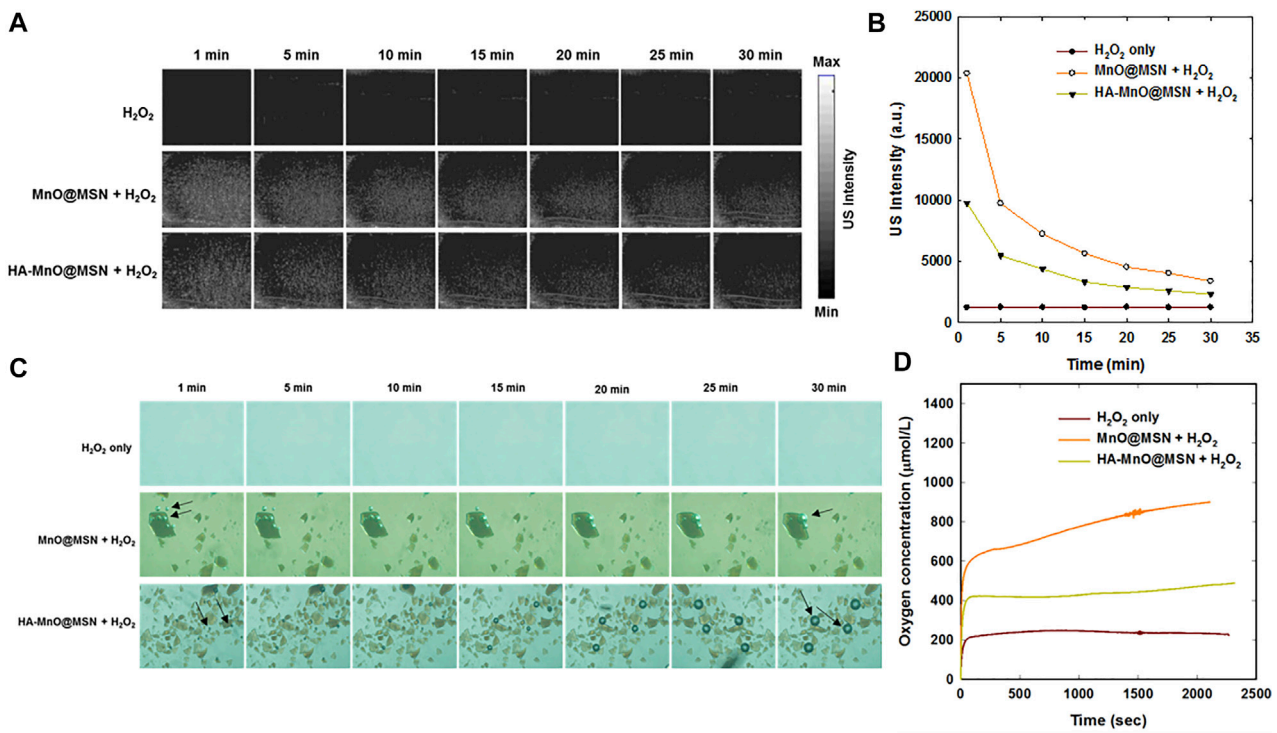

FIGURE 6 | (A) Time-dependent *in vitro* US images, **(B)** quantitative analysis of time-dependent US images, **(C)** optical images of oxygen bubble profiles at various time points (arrow indicates oxygen bubbles), and **(D)** evaluation of the oxygen evolution profile measured using an oxygen electrode.

relaxation rate with increasing MnO concentrations. Relaxivity is defined as the change in the relaxation rate of water protons in the presence of contrast agents. The r_1 value of CTAB-extracted MnO@MSN was significantly greater than the values of bare MnO (~0.28 mM^{-1} s^{-1}) and non-CTAB–removed MnO@MSN (~0.108 mM^{-1} s^{-1}). It should be noted that the increase in r_1 value is mainly due to the MSN shell, which is consistent with previous reports (Kim et al., 2007; Kim et al., 2011). MSN allowed optimal access of water molecules through its nanochannels to the MnO core, thus effectively relaxing the nearby water protons. For non-CTAB–removed MnO@MSN with similar MnO concentrations, the presence of CTAB in the MSN nanochannel significantly affected the interaction between the MnO core and water, thus indicating poor T_1 relaxation.

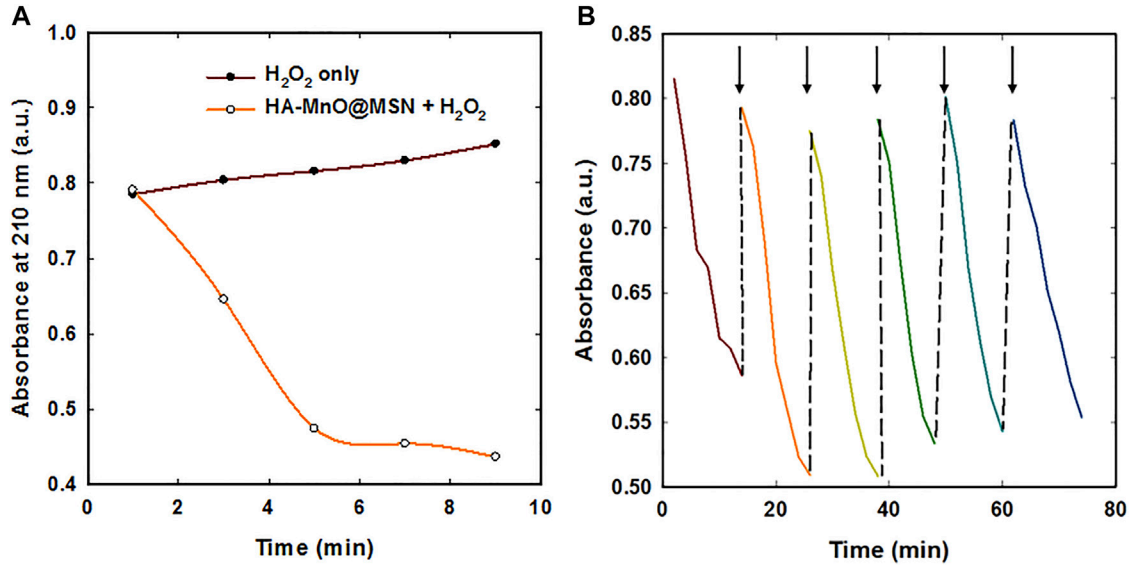

FIGURE 7 | (A) H_2O_2 quenching over time by HA-MnO@MSN and **(B)** continuous catalytic activity of HA-MnO@MSN by repeated addition of H_2O_2 measured by UV–Vis absorption spectra (arrow indicates H_2O_2 addition).

Effect of CTAB and HAdase on Relaxivity

In general, CTAB used as a structural directing agent in the synthesis of MSN must be completely removed from nanochannels for successful loading of guest molecules, such as anticancer drugs (Wu et al., 2013). In this study, CTAB was removed by acidic extraction with ethanol for 3 h. The presence of CTAB in MSN nanochannels could act as a barrier to the diffusion of water molecules to the MnO core, which will significantly affect MRI properties. In addition, CTAB is known to induce dose-dependent cytotoxicity (Wang et al., 2008; He et al., 2011; Schachter, 2013), and thus, removal of CTAB is essential for clinical applications. Hence, we evaluated relaxivity at various time intervals during CTAB extraction. As shown in **Figure 5A**, during CTAB extraction from 0 to 60 min, a steady decrease in the relaxivity of MnO@MSN was observed, followed by little or no significant decrease in the relaxivity up to 9 h. This indicates that CTAB was partially removed in 30 min, followed by the complete removal at 60 min. This result suggests that CTAB removal is crucial for the molar relaxivity of MnO@MSN.

Likewise, the molar relaxivity of HA-MnO@MSN was also investigated in the presence of HAdase (**Figure 5B**), an enzyme degrading the backbone of HA. Upon incubation with HAdase, the relaxivity of HA-MnO@MSN decreased remarkably, which might be due to the degradation of the HA backbone. This result indicates that HA-MnO@MSN can be used as an enzyme-responsive contrast agent for MR imaging. It is well known that HAdase is abundant in the cytosol of cancer cells. Hence, this unique behavior of HA-MnO@MSN may allow the development of site-specific drug delivery systems for cancer therapy.

Owing to their tunable structures and unique physiochemical properties, manganese oxide nanomaterials (MON) have drawn attention in various biomedical applications such as bioimaging, biosensing, and drug/gene delivery (Ding et al., 2020). Of late, the catalytic activity of these nanomaterials found significant applications as tumor microenvironment–responsive biomaterials. It is well known that the tumor microenvironment is characterized by hypoxia, mild acidity, and elevated production of H_2O_2 (Brown and Wilson, 2004). MON has the potential to alter the tumor microenvironment by catalyzing H_2O_2 to O_2, which can be utilized for bioimaging and anticancer therapies.

We investigated the generation of oxygen bubbles by HA-MnO@MSN using US imaging. Gas bubbles are excellent contrast agents for US imaging. However, gas- or air-filled bubbles suffer from poor stability *in vivo*, and their inability to target disease constitutes major challenges. In addition, tumor vasculature permeation is difficult because of their size (3–10 μm) (Paefgen et al., 2015). The formation of oxygen bubbles through the catalytic conversion of H_2O_2 to O_2 by HA-MnO@MSN could serve as an excellent US contrast agent due to the ability of gas bubbles to reflect US by generating strong signals. **Figure 6A** shows the US imaging of H_2O_2 alone and NP treated with H_2O_2. In the H_2O_2-only group, there was no US signal throughout the study because H_2O_2 alone could not generate bubbles. Although both HA-MnO@MSN and MnO@MSN showed strong US signal intensities, this was due to the catalytic conversion of H_2O_2 to O_2. The formation of oxygen as nanobubbles or microbubbles was able to strongly reflect US by generating strong signals. Quantitative analysis showed that the US signal generated from HA-MnO@MSN was slightly weaker than that from MnO@MSN, and this might be due to the presence of HA coating delaying the access of H_2O_2 to reach the MnO core to start the catalytic reaction (**Figure 6B**). We observed the direct formation of oxygen bubbles through optical imaging under the same conditions to support US imaging. The formation and growth of oxygen bubbles can be clearly seen in both MnO@MSN and HA-MnO@MSN treated with H_2O_2 (**Figure 6C**).

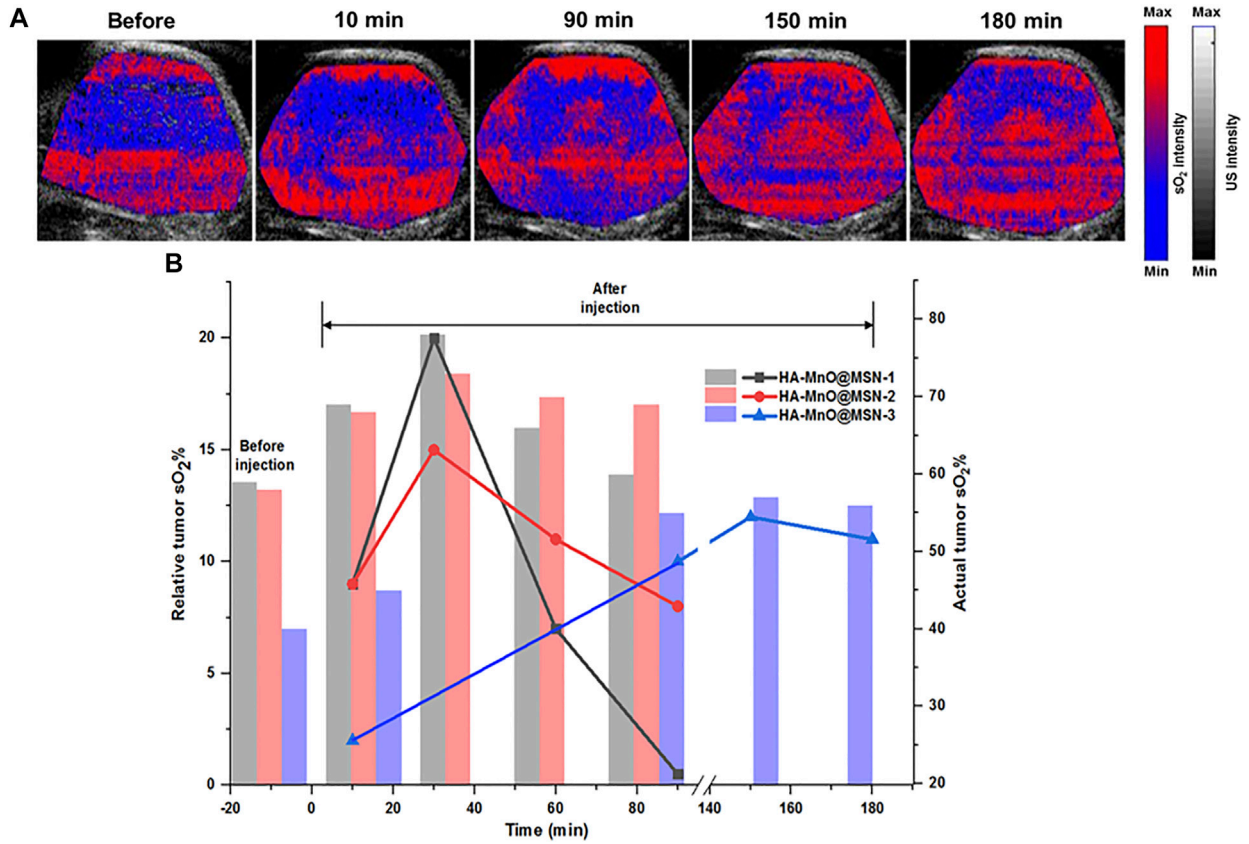

FIGURE 8 | (A) Time-dependent PA tumor sO_2 images of HCT116 tumor–bearing mouse at various time points after i. t. administration of HA-MnO@MSN-3 and **(B)** quantitative PA tumor sO_2 values at various time points. The bar represents actual tumor sO_2, and the line represents relative tumor sO_2 (n = 3).

We further tested whether our NP can generate a sufficient amount of oxygen at a low H_2O_2 concentration using an oxygen electrode. As anticipated, a significant amount of oxygen was generated by both MnO@MSN and HA-MnO@MSN (**Figure 6D**). Then, we evaluated the catalytic effect of HA-MnO@MSN by measuring residual H_2O_2 after the addition of HA-MnO@MSN, and we found that H_2O_2 was quenched by HA-MnO@MSN (**Figure 7A**). One of the important features of HA-MnO@MSN is its capability to continuously generate O_2. The continuous catalytic activity of the nanoparticles was maintained, even after the repetitive addition of H_2O_2 (**Figure 7B**).

In vivo Tumor Oxygen Modulation by HA-MnO@MSN

Therapeutic approaches such as radiotherapy, photodynamic therapy, and sonodynamic therapy exert their therapeutic effects via copious ROS generation to kill cancer cells (Yang et al., 2019; Wang et al., 2021a). One of the important pitfalls of these therapeutic approaches is the presence of low oxygen tension in the tumor that results in low or partial therapeutic effects, which encourages the residual tumor mass to migrate to various organs, resulting in metastasis. As a consequence, supplemental tumor oxygenation is imperative for better therapeutic outcomes. The rationale for supplemental tumor oxygenation is that the resulting increase in arterial pO_2 will enhance the diffusion of soluble oxygen into tissues. For instance, carbogen breathing has been shown to improve the oxygenation of both experimental and human tumors. Carbogen is a normobaric high-oxygen-content gas mixture (95% O_2 with 5% CO_2 or 98% O_2 with 2% CO_2) that increases intravascular oxygen availability, resulting in greater oxygen uptake by tumors (Alonzi et al., 2009). Moreover, various nanomaterials have been recently used to supply oxygen to tumors. These nanomaterials catalytically generate oxygen by consuming hydrogen peroxide in the tumor microenvironment (Zhang et al., 2019; Liu et al., 2020).

Herein, synthesized MnO@MSN will serve as an oxygen generator by catalase-like activity. From the *in vitro* results, which demonstrated the ability of HA-MnO@MSN to decompose H_2O_2, as a consequence, continuous oxygen generation was proved. These results encouraged us to test the capability of our nanoplatform to modulate oxygen saturation in blood inside tumors by PA imaging based on the differential absorption characteristics of oxygenated and deoxygenated hemoglobin. **Figure 8A** shows the representative sO_2 map of HCT116 tumors before and after i. t. injection of HA-MnO@MSN 3. The sO_2 map of the tumor before NP treatment shows the presence of a hypoxia core. After NP injection, the hypoxia level

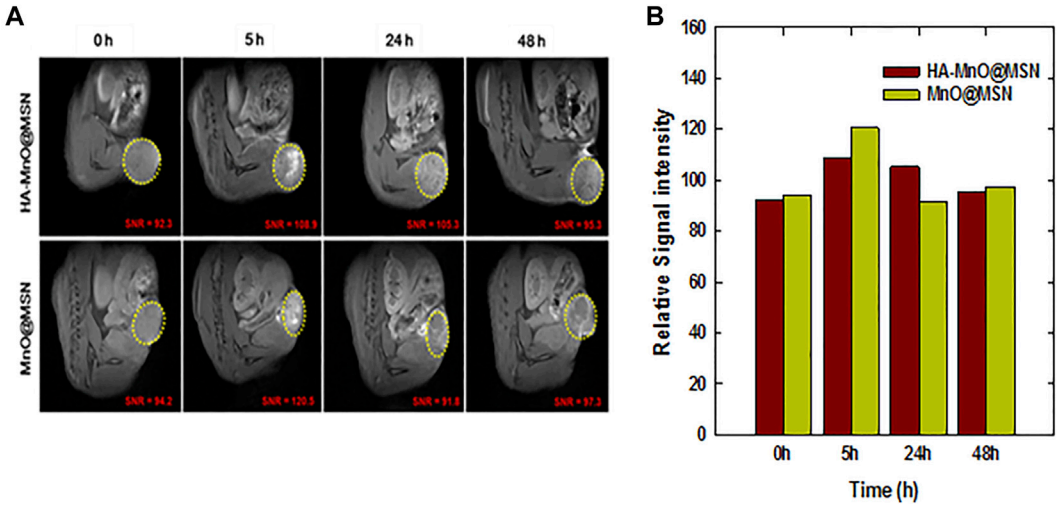

FIGURE 9 | *In vivo* MR imaging of HA-MnO@MSN and MnO@MSN in tumor-bearing mice. **(A)** Time-dependent T_1 images of nude mice bearing HCT116 tumors after i. t. injection of HA-MnO@MSN and MnO@MSN and **(B)** quantification of HA-MnO@MSN and MnO@MSN in tumor tissue (n = 3).

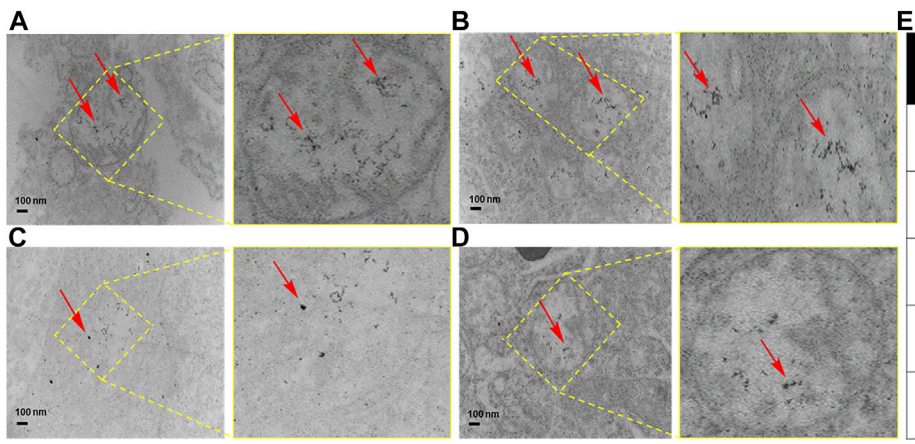

Groups	Mn (μg/g)	Si (mg/g)
0 min	0.707	0.486
10 min	80.61	2.097
2 h	40.17	0.847
5 h	57.39	1.113
24 h	50.67	0.892

FIGURE 10 | TEM images of tumor tissues obtained from treatment with HA-MnO@MSN at various time intervals with magnified images at **(A)** 10 min, **(B)** 2 h, **(C)** 5 h, **(D)** 24 h, and **(E)** the corresponding ICP-MS of HA-MnO@MSN. The arrows indicate HA-MnO@MSN accumulation in tumor tissues.

in the tumor core was reduced gradually with an increase in sO_2 over time due to the catalytic activity of HA-MnO@MSN-3 by converting H_2O_2 to O_2. The observed pattern might be due to the continuous catalytic conversion of H_2O_2 by HA-MnO@MSN-3 to generate O_2 up to 150 min and decreased because of the insufficient levels of H_2O_2 for O_2 generation.

Figure 8B shows the quantitative analysis of relative tumor sO_2 values from three different experiments after NP injection. HA-MnO@MSN 1 and 2 showed similar tumor sO_2 trends. For both HA-MnO@MSN 1 and 2, sO_2 steadily increased from 9% at 10 min to reach a maximum of 20% (actual sO_2, 69%) (HA-MnO@MSN 1) and 15% (actual sO_2, 68%) (HA-MnO@MSN 2) at 30 min and then decreased to 0.5 and 8% at 90 min. Next, HA-MnO@MSN 3 demonstrated a unique trend in sO_2. After i. t. injection, sO_2 increased to 2% (actual sO_2, 42%) at 10 min, which is significantly less compared to the sO_2 values of HA-MnO@MSN 1 and 2, and slowly reached a maximum of 15% (actual sO_2, 57%) at 150 min, followed by a slight decrease. This relative sO_2 pattern is inconsistent with actual sO_2. As previously explained, the presence of a hypoxic core influences the sO_2 pattern, and tumor hypoxia is characterized by abnormal vasculature, which hinders the supply of nutrients (Brown and Wilson, 2004). Here, HA-MnO@MSN 3 after injection was not able to diffuse in all regions of the tumor because of defective vasculature. Hence, only a few NP had a chance to interact and be digested by HAdase, followed by H_2O_2 diffusion to the NP core to generate O_2 slowly.

In vivo Magnetic Resonance Imaging

The relaxivity of traditional MnO-based core–shell structures depends on the interaction of MnO with water molecules based on the porosity

of the coating material. Herein, HA as a coating material in HA-MnO@MSN would be digested by tumor-specific hyaluronidase to allow the optimal accessibility of the water molecules to the MnO core through nanochannels of MSN. Our *in vitro* results encouraged us to test the potential of HA-MnO@MSN for MR imaging of a tumor, and we administered an intratumoral injection of HA-MnO@MSN and MnO@MSN dispersion to HCT116 human colon tumor-xenograft-bearing nude mice and monitored MR images as a function of time (**Figures 9A,B**). For HA-MnO@MSN, immediately after injection, we did not observe any contrast enhancement at the tumor site. However, enhancement in T_1 weighted images was observed at 5 h postinjection. In addition, this contrast enhancement lasted up to 48 h. The T_1 contrast enhancement was consistently supported by *in vitro* data (**Figure 5B**), which is due to the time-dependent enzymatic digestion of the HA backbone by HAdase. For MnO@MSN, T_1 contrast enhancement was observed at 2 h postinjection (data not shown) and slowly decreased after 5 h. This might be a result of the rapid interactions between water molecules and the MnO core due to the lack of HA coating. Thus, MnO@MSN exhibited a rapid but transient T_1 signal.

To further confirm that HA-MnO@MSN indeed accumulated in the tumor, we used TEM to examine tissue samples obtained from animal models after imaging at various time intervals. As shown in **Figures 10A–D**, many HA-MnO@MSN (black dots) were clearly seen in tumor samples from 10 min followed by up to 2 h. Then, the slow clearance of nanoparticles from tumor was observed at 24 h. This trend is consistent with ICP-MS data (**Figure 10E**).

DISCUSSION

For biomedical applications, we designed HA-coated MnO@MSN NP, which demonstrated various functions such as tumor-specific T1 contrast agent and oxygen modulation. The application of HA as a coating agent offers potential advantages, such as specific binding to cancer cells that overexpress CD44 and digestion by HAdase, found in various metastatic cancers. Hence, HA-based therapeutics have found an integral role in anticancer applications (Huang et al., 2016; Liu et al., 2016; Yan et al., 2016). The controlled degradation of HA by HAdase elicited time-dependent MR imaging functions as a T1 contrast agent as proved here. In particular, we showed here for the first time that MnO is an oxygen generator, which has the potential to modulate oxygen tension in the tumor. In contrast to enzyme catalase, MnO@MSN could be taken up by cells and could have a prolonged *in vivo* half-life. It is well documented that tumor cells express high levels of H_2O_2 compared to normal cells. Our nanoplatform's ability to harness H_2O_2 in tumors and oxygenate could instigate the development of smart cancer treatments. *In vivo* PA imaging showed the detailed quantitative assessment of tumor oxygenation in a time-dependent manner after i. t. administration of HA-MnO@MSN. Such NP when combined with ROS-based therapies like PDT will not only improve therapeutic efficacy by enhanced ROS generation but also serve as a marker for treatment efficacy prediction. Furthermore, the use of the MSN shell in this study can be further extended as a host to accommodate guest molecules, such as anticancer drugs or photosensitizers, in its nanochannels with high loading contents. Overall, the unique hyaluronidase-responsive HA-MnO@MSN nanoparticles developed in this study could be used as a tumor-specific theranostic system.

CONCLUSION

In summary, we developed HA-MnO@MSN nanoparticles as an MR T_1 contrast agent, which exhibited higher r_1 relaxivity over bare MnO nanoparticles. HA-MSN coating provides tumor-targeting and allows controlled access of water molecules to the MnO core, resulting in enhanced T_1 contrast. Our results also demonstrated the continuous oxygen generation ability of HA-MnO@MSN by catalytic reaction both *in vitro* and *in vivo*. These findings demonstrate that the HA-MnO@MSN prepared in this study could be useful for oxygen modulation and targeted MRI.

DATA AVAILABILITY STATEMENT

The original contributions presented in the study are included in the article/supplementary material. Further inquiries can be directed to the corresponding authors.

ETHICS STATEMENT

The animal study was reviewed and approved by the Institutional Animal Care and Use Committee of the National Health Research Institutes (Taiwan).

AUTHOR CONTRIBUTIONS

L-WL and C-TC conceptualized the research and L-DL designed the photoacoustic experiments. C-HC, S-HC, and N-TC performed both *in vitro* and *in vivo* magnetic resonance imaging experiments and analyzed the data. MS, Y-LC, YC, and HY performed *in vitro*, photoacoustic experiments and analyzed the data. MS, C-HC, S-HC, and N-TC wrote the paper. All authors contributed to the article and approved the submitted version.

FUNDING

This study was supported by the grants BN-110-PP-04 and NHRI-EX110-10829EI from National Health Research Institutes of Taiwan, and MOST 105-2113-M-400-007-MY3 and MOST 110-2112-M-400-001 from the Ministry of Science and Technology of Taiwan and MR-110-GP-13 from Central Government S & T grant, Taiwan and 110-EC-17-A-22-1650 from Ministry of Economic Affairs of Taiwan.

ACKNOWLEDGMENTS

We thank Dr. Guo-Chung Dong for his assistance to carry out the synthesis of manganese oxide nanoparticles in his laboratory.

REFERENCES

ACR Manual on Contrast Media (2015). *ACR Manual on Contrast Media V 10.1*. USA: American College of Radiology.

Aime, S., Castelli, D. D., Lawson, D., and Terreno, E. (2007). Gd-Loaded Liposomes as T1, Susceptibility, and CEST Agents, All in One. *J. Am. Chem. Soc.* 129, 2430–2431. doi:10.1021/ja0677867

Alonzi, R., Padhani, A. R., Maxwell, R. J., Taylor, N. J., Stirling, J. J., Wilson, J. I., et al. (2009). Carbogen Breathing Increases Prostate Cancer Oxygenation: a Translational MRI Study in Murine Xenografts and Humans. *Br. J. Cancer* 100, 644–648. doi:10.1038/sj.bjc.6604903

Anbu, S., Hoffmann, S. H. L., Carniato, F., Kenning, L., Price, T. W., Prior, T. J., et al. (2021). A Single-Pot Template Reaction towards a Manganese-Based T1 Contrast Agent. *Angew. Chem. Int.* 60, 70136–10744. doi:10.1002/anie.202100885

Anderson, S. A., Lee, K. K., and Frank, J. A. (2006). Gadolinium-Fullerenol as a Paramagnetic Contrast Agent for Cellular Imaging. *Investig. Radiol.* 41, 332–338. doi:10.1097/01.rli.0000192420.94038.9e

Anzai, Y., Piccoli, C. W., Outwater, E. K., Stanford, W., Bluemke, D. A., Nurenberg, P., et al. (2003). Evaluation of Neck and Body Metastases to Nodes with Ferumoxtran 10-enhanced MR Imaging: Phase III Safety and Efficacy Study. *Radiology* 228, 777–788. doi:10.1148/radiol.2283020872

Bandla, A., Liao, L.-D., Chan, S. J., Ling, J. M., Liu, Y.-H., Shih, Y.-Y. I., et al. (2018). Simultaneous Functional Photoacoustic Microscopy and Electrocorticography Reveal the Impact of rtPA on Dynamic Neurovascular Functions after Cerebral Ischemia. *J. Cereb. Blood Flow. Metab.* 38 (6), 980–995. doi:10.1177/0271678X17712399

Brown, J. M., and Wilson, W. R. (2004). Exploiting Tumour Hypoxia in Cancer Treatment. *Nat. Rev. Cancer* 4, 437–447. doi:10.1038/nrc1367

Bulte, J. W. M., and Kraitchman, D. L. (2004). Iron Oxide MR Contrast Agents for Molecular and Cellular Imaging. *NMR Biomed.* 17, 484–499. doi:10.1002/nbm.924

Caravan, P., Das, B., Dumas, S., Epstein, F. H., Helm, P. A., Jacques, V., et al. (2007). Collagen-Targeted MRI Contrast Agent for Molecular Imaging of Fibrosis. *Angew. Chem. Int. Ed.* 46, 8171–8173. doi:10.1002/anie.200700700

Caravan, P. (2006). Strategies for Increasing the Sensitivity of Gadolinium Based MRI Contrast Agents. *Chem. Soc. Rev.* 35, 512–523. doi:10.1039/b510982p

Cheng, S.-H., Hsieh, C.-C., Chen, N.-T., Chu, C.-H., Huang, C.-M., Chou, P.-T., et al. (2011). Well-defined Mesoporous Nanostructure Modulates Three-Dimensional Interface Energy Transfer for Two-Photon Activated Photodynamic Therapy. *Nano Today* 6, 552–563. doi:10.1016/j.nantod.2011.10.003

Cheng, S.-H., Lee, C.-H., Yang, C.-S., Tseng, F.-G., Mou, C.-Y., and Lo, L.-W. (2009). Mesoporous Silica Nanoparticles Functionalized with an Oxygen-Sensing Probe for Cell Photodynamic Therapy: Potential Cancer Theranostics. *J. Mat. Chem.* 19, 1252–1257. doi:10.1039/b816636f

Choi, K. Y., Chung, H., Min, K. H., Yoon, H. Y., Kim, K., Park, J. H., et al. (2010). Self-assembled Hyaluronic Acid Nanoparticles for Active Tumor Targeting. *Biomaterials* 31, 106–114. doi:10.1016/j.biomaterials.2009.09.030

Choi, K. Y., Min, K. H., Na, J. H., Choi, K., Kim, K., Park, J. H., et al. (2009). Self-assembled Hyaluronic Acid Nanoparticles as a Potential Drug Carrier for Cancer Therapy: Synthesis, Characterization, and *In Vivo* Biodistribution. *J. Mat. Chem.* 19, 4102–4107. doi:10.1039/b900456d

Chuang, Y.-C., Chu, C.-H., Cheng, S.-H., Liao, L.-D., Chu, T.-S., Chen, N.-T., et al. (2020). Annealing-modulated Nanoscintillators for Nonconventional X-Ray Activation of Comprehensive Photodynamic Effects in Deep Cancer Theranostics. *Theranostics* 10, 6758–6773. doi:10.7150/thno.41752

Ding, B., Zheng, P., Ma, P., and Lin, J. (2020). Manganese Oxide Nanomaterials: Synthesis, Properties, and Theranostic Applications. *Adv. Mat.* 32, e1905823–35. doi:10.1002/adma.201905823

Dosio, F., Arpicco, S., Stella, B., and Fattal, E. (2016). Hyaluronic Acid for Anticancer Drug and Nucleic Acid Delivery. *Adv. Drug Deliv. Rev.* 97, 204–236. doi:10.1016/j.addr.2015.11.011

Gale, E. M., Wey, H.-Y., Ramsay, I., Yen, Y.-F., Sosnovik, D. E., and Caravan, P. (2018). A Manganese-Based Alternative to Gadolinium: Contrast-Enhanced MR Angiography, Excretion, Pharmacokinetics, and Metabolism. *Radiology* 286, 865–872. doi:10.1148/radiol.2017170977

Gibby, W. A. (2005). Basic Principles of Magnetic Resonance Imaging. *Neurosurg. Clin. N. Am.* 16, 1–64. doi:10.1016/j.nec.2004.08.017

Gilad, A. A., Walczak, P., McMahon, M. T., Na, H. B., Lee, J. H., An, K., et al. (2008). MR Tracking of Transplanted Cells with "Positive Contrast" Using Manganese Oxide Nanoparticles. *Magn. Reson. Med.* 60, 1–7. doi:10.1002/mrm.21622

Granot, D., Addadi, Y., Kalchenko, V., Harmelin, A., Kunz-Schughart, L. A., and Neeman, M. (2007). *In Vivo* Imaging of the Systemic Recruitment of Fibroblasts to the Angiogenic Rim of Ovarian Carcinoma Tumors. *Cancer Res.* 67, 9180–9189. doi:10.1158/0008-5472.CAN-07-0684

He, Q., Zhang, Y., Zhang, L., Zhang, Z., Gao, F., Ji, X., et al. (2011). A pH-Responsive Mesoporous Silica Nanoparticles-Based Multi-Drug Delivery System for Overcoming Multi-Drug Resistance. *Biomaterials* 32, 7711–7720. doi:10.1016/j.biomaterials.2011.06.066

Hsu, B. Y. W., Kirby, G., Tan, A., Seifalian, A. M., Li, X., and Wang, J. (2016). Relaxivity and Toxicological Properties of Manganese Oxide Nanoparticles for MRI Applications. *RSC Adv.* 6, 45462–45474. doi:10.1039/c6ra04421b

Huang, W.-Y., Lin, J.-N., Hsieh, J.-T., Chou, S.-C., Lai, C.-H., Yun, E.-J., et al. (2016). Nanoparticle Targeting CD44-Positive Cancer Cells for Site-specific Drug Delivery in Prostate Cancer Therapy. *ACS Appl. Mat. Interfaces* 8, 30722–30734. doi:10.1021/acsami.6b10029

Jellinger, K. A., and Bradley, W. J. (2001). Magnetic Resonance Imaging, 3rd Edition. David D. Stark and William G. Bradley, Jr (Eds). Volumes I-III. Mosby, St. Louis, MO, USA, 1999. 1936 + =100 Pp. ISBN 0-8151-8518-9; 28607. *Eur. J. Neurol.* 8, 96–97. doi:10.1046/j.1468-1331.2001.00174.x

Jiao, Y., Pang, X., and Zhai, G. (2016). Advances in Hyaluronic Acid-Based Drug Delivery Systems. *Cdt* 17, 720–730. doi:10.2174/1389450116666150531155200

Kim, J., Cho, H. R., Jeon, H., Kim, D., Song, C., Lee, N., et al. (2017). Continuous O2-Evolving MnFe2O4 Nanoparticle-Anchored Mesoporous Silica Nanoparticles for Efficient Photodynamic Therapy in Hypoxic Cancer. *J. Am. Chem. Soc.* 139, 10992–10995. doi:10.1021/jacs.7b05559

Kim, J. S., Rieter, W. J., Taylor, K. M. L., An, H., Lin, W., and Lin, W. (2007). Self-Assembled Hybrid Nanoparticles for Cancer-specific Multimodal Imaging. *J. Am. Chem. Soc.* 129, 8962–8963. doi:10.1021/ja073062z

Kim, T., Momin, E., Choi, J., Yuan, K., Zaidi, H., Kim, J., et al. (2011). Mesoporous Silica-Coated Hollow Manganese Oxide Nanoparticles as Positive T1 Contrast Agents for Labeling and MRI Tracking of Adipose-Derived Mesenchymal Stem Cells. *J. Am. Chem. Soc.* 133, 2955–2961. doi:10.1021/ja1084095

Leng, H., Wang, Y., Jhang, D.-F., Chu, T.-S., Tsao, C.-H., Tsai, C.-H., et al. (2019). Characterization of a Fiber Bundle-Based Real-Time Ultrasound/Photoacoustic Imaging System and its *In Vivo* Functional Imaging Applications. *Micromachines* 10 (1012), 820. doi:10.3390/mi10120820

Li, Z., Clemens, D. L., Lee, B.-Y., Dillon, B. J., Horwitz, M. A., and Zink, J. I. (2015). Mesoporous Silica Nanoparticles with pH-Sensitive Nanovalves for Delivery of Moxifloxacin Provide Improved Treatment of Lethal Pneumonic Tularemia. *ACS Nano* 9, 10778–10789. doi:10.1021/acsnano.5b04306

Liao, L.-D., Bandla, A., Ling, J. M., Liu, Y.-H., Kuo, L.-W., Chen, Y.-Y., et al. (2014). Improving Neurovascular Outcomes with Bilateral Forepaw Stimulation in a Rat Photothrombotic Ischemic Stroke Model. *Neurophoton* 1 (1), 011007. doi:10.1117/1.NPh.1.1.011007

Lin, W., Hyeon, T., Lanza, G. M., Zhang, M., and Meade, T. J. (2009). Magnetic Nanoparticles for Early Detection of Cancer by Magnetic Resonance Imaging. *MRS Bull.* 34, 441–448. doi:10.1557/mrs2009.120

Liu, H., Jiang, W., Wang, Q., Xia, J., Yu, W., Wang, Y., et al. (2020). Microenvironment-activated Nanoparticles for Oxygen Self-Supplemented Photodynamic Cancer Therapy. *Biomater. Sci.* 8, 370–378. doi:10.1039/c9bm01537j

Liu, X., Situ, A., Kang, Y., Villabroza, K. R., Liao, Y., Chang, C. H., et al. (2016). Irinotecan Delivery by Lipid-Coated Mesoporous Silica Nanoparticles Shows Improved Efficacy and Safety over Liposomes for Pancreatic Cancer. *ACS Nano* 10, 2702–2715. doi:10.1021/acsnano.5b07781

Liu, Y.-H., Liao, L.-D., Tan, S. S. H., Kwon, K. Y., Ling, J. M., Bandla, A., et al. (2015). Assessment of Neurovascular Dynamics during Transient Ischemic Attack by the Novel Integration of Micro-electrocorticography Electrode Array with Functional Photoacoustic Microscopy. *Neurobiol. Dis.* 82, 455–465. doi:10.1016/j.nbd.2015.06.019

Mallidi, S., Watanabe, K., Timerman, D., Schoenfeld, D., and Hasan, T. (2015). Prediction of Tumor Recurrence and Therapy Monitoring Using Ultrasound-Guided Photoacoustic Imaging. *Theranostics* 5, 289–301. doi:10.7150/thno.10155

Mendonça-Dias, M. H., Gaggelli, E., and Lauterbur, P. C. (1983). Paramagnetic Contrast Agents in Nuclear Magnetic Resonance Medical Imaging. *Seminars Nucl. Med.* 13 (4), 364–376. doi:10.1016/s0001-2998(83)80048-8

Na, H. B., Lee, J. H., An, K., Park, Y. I., Park, M., Lee, I. S., et al. (2007). Development of aT1 Contrast Agent for Magnetic Resonance Imaging Using MnO Nanoparticles. *Angew. Chem. Int. Ed.* 46, 5397–5401. doi:10.1002/anie.200604775

Neuwelt, E. A., Várallyay, P., Bagó, A. G., Muldoon, L. L., Nesbit, G., and Nixon, R. (2004). Imaging of Iron Oxide Nanoparticles by MR and Light Microscopy in Patients with Malignant Brain Tumours. *Neuropathol. Appl. Neurobiol.* 30, 456–471. doi:10.1111/j.1365-2990.2004.00557.x

Paefgen, V., Doleschel, D., and Kiessling, F. (2015). Evolution of Contrast Agents for Ultrasound Imaging and Ultrasound-Mediated Drug Delivery. *Front. Pharmacol.* 6, 1–16. doi:10.3389/fphar.2015.00197

Perez-Rodriguez, J., Lai, S., Ehst, B. D., Fine, D. M., and Bluemke, D. A. (2009). Nephrogenic Systemic Fibrosis: Incidence, Associations, and Effect of Risk Factor Assessment-Report of 33 Cases. *Radiology* 250, 371–377. doi:10.1148/radiol.2502080498

Phua, S. Z. F., Yang, G., Lim, W. Q., Verma, A., Chen, H., Thanabalu, T., et al. (2019). Catalase-Integrated Hyaluronic Acid as Nanocarriers for Enhanced Photodynamic Therapy in Solid Tumor. *ACS Nano* 13, 4742–4751. doi:10.1021/acsnano.9b01087

Saini, S., Stark, D. D., Hahn, P. F., Wittenberg, T. J., and Ferrucci, J. T. (1987). Ferrite Particles: a Superparamagnetic MR Contrast Agent for the Reticuloendothelial System. *Radiology* 162, 211–216. doi:10.1148/radiology.162.1.3786765

Schachter, D. (2013). *The Source of Toxicity in CTAB and CTAB-Stabilized Gold Nanorods, Master's Thesis*. New Jersey: University of Medicine and Dentistry of. doi:10.7282/T3X63KMS

Sepúlveda, M. R., Wuytack, F., and Mata, A. M. (2012). High Levels of Mn2+inhibit Secretory Pathway Ca2+/Mn2+-ATPase (SPCA) Activity and Cause Golgi Fragmentation in Neurons and Glia. *J. Neurochem.* 123, 824–836. doi:10.1111/j.1471-4159.2012.07888.x

Silva, A. C., Lee, J. H., Aoki, I., and Koretsky, A. P. (2004). Manganese-enhanced Magnetic Resonance Imaging (MEMRI): Methodological and Practical Considerations. *NMR Biomed.* 17, 532–543. doi:10.1002/nbm.945

Sosnovik, D. E., and Weissleder, R. (2007). Emerging Concepts in Molecular MRI. *Curr. Opin. Biotechnol.* 18, 4–10. doi:10.1016/j.copbio.2006.11.001

Tripodo, G., Trapani, A., Torre, M. L., Giammona, G., Trapani, G., and Mandracchia, D. (2015). Hyaluronic Acid and its Derivatives in Drug Delivery and Imaging: Recent Advances and Challenges. *Eur. J. Pharm. Biopharm.* 97, 400–416. doi:10.1016/j.ejpb.2015.03.032

Tu, H.-L., Lin, Y.-S., Lin, H.-Y., Hung, Y., Lo, L.-W., Chen, Y.-F., et al. (2009). *In Vitro* Studies of Functionalized Mesoporous Silica Nanoparticles for Photodynamic Therapy. *Adv. Mat.* 21, 172–177. doi:10.1002/adma.200800548

Wang R, R., Yang, H., Khan, A. R., Yang, X., Xu, J., Ji, J., et al. (2021). Redox-responsive Hyaluronic Acid-Based Nanoparticles for Targeted Photodynamic Therapy/chemotherapy against Breast Cancer. *J. Colloid Interface Sci.* 598, 213–228. doi:10.1016/j.jcis.2021.04.056

Wang, S., Lu, W., Tovmachenko, O., Rai, U. S., Yu, H., and Ray, P. C. (2008). Challenge in Understanding Size and Shape Dependent Toxicity of Gold Nanomaterials in Human Skin Keratinocytes. *Chem. Phys. Lett.* 463, 145–149. doi:10.1016/j.cplett.2008.08.039

Wang, X., Wang, X., Yue, Q., Xu, H., Zhong, X., Sun, L., et al. (2021b). Liquid Exfoliation of TiN Nanodots as Novel Sonosensitizers for Photothermal-Enhanced Sonodynamic Therapy against Cancer. *Nano Today* 39, 101170. doi:10.1016/j.nantod.2021.101170

Wang, X., Zhong, X., Li, J., Liu, Z., and Cheng, L. (2021a). Inorganic Nanomaterials with Rapid Clearance for Biomedical Applications. *Chem. Soc. Rev.* 50 (15), 8669–8742. doi:10.1039/d0cs00461h

Wu, E. X., Tang, H., and Jensen, J. H. (2004). Applications of Ultrasmall Superparamagnetic Iron Oxide Contrast Agents in the MR Study of Animal Models. *NMR Biomed.* 17, 478–483. doi:10.1002/nbm.923

Wu, S.-H., Mou, C.-Y., and Lin, H.-P. (2013). Synthesis of Mesoporous Silica Nanoparticles. *Chem. Soc. Rev.* 42, 3862–3875. doi:10.1039/c3cs35405a

Yang, B., Chen, Y., and Shi, J. (2019). Reactive Oxygen Species (ROS)-Based Nanomedicine. *Chem. Rev.* 119, 4881–4985. doi:10.1021/acs.chemrev.8b00626

Yang, H., Zhuang, Y., Hu, H., Du, X., Zhang, C., Shi, X., et al. (2010). Silica-Coated Manganese Oxide Nanoparticles as a Platform for Targeted Magnetic Resonance and Fluorescence Imaging of Cancer Cells. *Adv. Funct. Mat.* 20, 1733–1741. doi:10.1002/adfm.200902445

Zackrisson, S., van de Ven, S. M. W. Y., and Gambhir, S. S. (2014). Light in and Sound Out: Emerging Translational Strategies for Photoacoustic Imaging. *Cancer Res.* 74, 979–1004. doi:10.1158/0008-5472.CAN-13-2387

Zhang, C., Yan, L., Gu, Z., and Zhao, Y. (2019). Strategies Based on Metal-Based Nanoparticles for Hypoxic-Tumor Radiotherapy. *Chem. Sci.* 10, 6932–6943. doi:10.1039/c9sc02107h

Zhang, C., Qinc, W. J., Bai, X. F., and Zhang, X. Z. (2020). Nanomaterials to Relieve Tumor Hypoxia for Enhanced Photodynamic Therapy. *Nanotoday* 35, 1–17. doi:10.1016/j.nantod.2020.100960

Zhou, X., He, C., Liu, M., Chen, Q., Zhang, L., Xu, X., et al. (2021). Self-assembly of Hyaluronic Acid-Mediated Tumor-Targeting Theranostic Nanoparticles. *Biomater. Sci.* 9, 2221–2229. doi:10.1039/d0bm01855d

Conflict of Interest: The authors declare that the research was conducted in the absence of any commercial or financial relationships that could be construed as a potential conflict of interest.

Publisher's Note: All claims expressed in this article are solely those of the authors and do not necessarily represent those of their affiliated organizations or those of the publisher, the editors, and the reviewers. Any product that may be evaluated in this article or claim that may be made by its manufacturer is not guaranteed or endorsed by the publisher.

frontiers | Frontiers in Bioengineering and Biotechnology

ORIGINAL RESEARCH
published: 24 June 2022
doi: 10.3389/fbioe.2022.868857

Human Cholangiocytes Form a Polarized and Functional Bile Duct on Hollow Fiber Membranes

Zhenguo Wang[1,2], João Faria[1], Luc J. W. van der Laan[3], Louis C. Penning[2], Rosalinde Masereeuw[1] and Bart Spee[2]**

[1]Division of Pharmacology, Department of Pharmaceutical Sciences, Faculty of Sciences, Utrecht Institute for Pharmaceutical Sciences, Utrecht University, Utrecht, Netherlands, [2]Department of Clinical Sciences, Faculty of Veterinary Medicine, Utrecht University, Utrecht, Netherlands, [3]Department of Surgery, Erasmus MC-University Medical Center, Rotterdam, Netherlands

Liver diseases affect hundreds of millions of people worldwide; most often the hepatocytes or cholangiocytes are damaged. Diseases of the biliary tract cause severe patient burden, and cholangiocytes, the cells lining the biliary tract, are sensitive to numerous drugs. Therefore, investigations into proper cholangiocyte functions are of utmost importance, which is restricted, *in vitro*, by the lack of primary human cholangiocytes allowing such screening. To investigate biliary function, including transepithelial transport, cholangiocytes must be cultured as three-dimensional (3D) ductular structures. We previously established murine intrahepatic cholangiocyte organoid-derived cholangiocyte-like cells (CLCs) and cultured them onto polyethersulfone hollow fiber membranes (HFMs) to generate 3D duct structures that resemble native bile ducts at the structural and functional level. Here, we established an efficient, stepwise method for directed differentiation of human intrahepatic cholangiocyte organoids (ICOs) into CLCs. Human ICO-derived CLCs showed key characteristics of cholangiocytes, such as the expression of structural and functional markers, formation of primary cilia, and P-glycoprotein-mediated transport in a polarized fashion. The organoid cultures exhibit farnesoid X receptor (FXR)-dependent functions that are vital to liver bile acid homeostasis *in vivo*. Furthermore, human ICO-derived CLCs cultured on HFMs in a differentiation medium form tubular architecture with some tight, confluent, and polarized monolayers that better mimic native bile duct characteristics than differentiated cultures in standard 2D or Matrigel-based 3D culture plates. Together, our optimized differentiation protocol to obtain CLC organoids, when applied on HFMs to form bioengineered bile ducts, will facilitate studying cholangiopathies and allow developing therapeutic strategies.

Keywords: intrahepatic cholangiocyte organoids, cholangiocytes, bioengineered bile duct, hollow fiber membrane, monolayer, polarity, perfusable

OPEN ACCESS

Edited by:
Feng-Huei Lin,
National Taiwan University, Taiwan

Reviewed by:
Elizabeth Stahl,
University of California, Berkeley, United States
Zaozao Chen,
Southeast University, China

****Correspondence:***
Rosalinde Masereeuw
R.Masereeuw@uu.nl
Bart Spee
B.Spee@uu.nl

Specialty section:
This article was submitted to Tissue Engineering and Regenerative Medicine, a section of the journal Frontiers in Bioengineering and Biotechnology

Received: *03 February 2022*
Accepted: *12 May 2022*
Published: *24 June 2022*

Citation:
Wang Z, Faria J, van der Laan LJW, Penning LC, Masereeuw R and Spee B (2022) Human Cholangiocytes Form a Polarized and Functional Bile Duct on Hollow Fiber Membranes. Front. Bioeng. Biotechnol. 10:868857. doi: 10.3389/fbioe.2022.868857

INTRODUCTION

Cholangiocytes are epithelial cells that line both intra- and extra-hepatic bile ducts. They comprise only 3–5% of the total liver mass; however, their physiological function is important for regulating bile acids synthesis by the liver and their transport (Banales et al., 2019). Functional impairment of cholangiocytes plays an essential role in the development of various types of biliary disorders, collectively termed cholangiopathies. The physiology and pathophysiology of cholangiocytes and

cholangiopathies are not fully elucidated as of yet (Lazaridis and Larusso, 2015) despite the large global burden and post-liver transplantation complications associated with cholangiopathies (Spada et al., 2009). This is mainly because research on the pathophysiology and the development of new treatment methods have been limited by the lack of robust platforms for disease modeling and drug screening studies, especially in men. Thus, novel *in vitro* models are needed to bring further progress in the field and mimic (intrahepatic) bile ducts in detail.

To create *in vitro* models that mimic cholangiocyte activity, several cell sources are available. Primary cholangiocytes can be freshly isolated from the human liver and cultured for a few weeks (Joplin, 1994). However, they tend to dedifferentiate due to the lack of a native environment. Another cell source frequently used is the cholangiocytes derived from human induced pluripotent stem cells (iPSCs). Advantages of iPSCs are the ability to undergo self-renewal and differentiation into cholangiocytes *in vitro*, but the efficiency for generating iPSC-derived cholangiocytes is low (Sampaziotis et al., 2017a). Moreover, this procedure is time-consuming, and their restricted differentiation and high cellular heterogeneity hamper their application. Hence, there is an obvious need for novel 3D *in vitro* models that more closely mimic the *in vivo* biliary trees in order to gain further insight into the physiology and pathophysiology of cholangiocytes.

Organoids offer ideal possibilities as a cell source in tissue engineering or regenerative medicine (Yin et al., 2016; Kim et al., 2020). Originally, liver organoids were generated from adult tissue progenitor/stem cells located in the intrahepatic bile ducts (Huch et al., 2015). *In vitro* culture of these progenitor/stem cells under Wnt/β-catenin-inducing conditions reveals organoids with an upregulation of the leucine-rich repeat-containing G protein-coupled receptor 5 (LGR5) stem cell marker (Planas-Paz et al., 2019). According to the new consensus on the nomenclature of the liver organoids originating from intrahepatic bile ducts, these are now termed intrahepatic cholangiocyte organoids (ICOs) (Marsee et al., 2021). The ICOs are highly proliferative and can be genetically stable and expanded for over several months *in vitro* (Huch et al., 2015). Furthermore, upon culturing with specific medium compositions, the ICOs have the capacity to differentiate into either hepatocyte (Schneeberger et al., 2020; Ye et al., 2020) or cholangiocyte (Chen et al., 2018) lineages. In addition, a novel method for the isolation and propagation of human cholangiocytes expanded from extrahepatic cholangiocyte organoids (ECOs) has been established. It should be noted that these ECOs were not cultured under Wnt/β-catenin-inducing conditions but under non-canonical Wnt-stimulated conditions. When implanted in mice, these human ECOs can reconstruct the common bile duct and replace its function in extrahepatic biliary injury (Sampaziotis et al., 2017b). Therefore, organoids can be an important cell source for regenerative medicine, but having a 3D platform that can replicate cholangiocyte (patho)physiology, including cholestasis, and allow drug screening is still not available.

Here, we reported a bioengineered 3D platform based on human ICOs differentiation toward CLCs. Furthermore, to acquire anatomical tubular architecture and an environment that mimics an intrahepatic bile duct, we cultured ICOs onto the polyethersulfone hollow fiber membrane (HFM). Genomic and functional analyses of CLCs demonstrated that this organoid culture manifested essential morphological and functional features of mature cholangiocytes, such as a polarized monolayer and tight barrier. Together, this bioengineered human bile duct more closely replicates the biological structure and function of native bile ducts and may be suitable for studying cholangiopathies and therapeutic interventions for these disorders.

MATERIALS AND METHODS

ICO Establishment and Expansion

Healthy tissue samples of the human liver from two males and two females were obtained during liver transplantation at the Erasmus Medical Center in Rotterdam under the approval of the Medical Ethical Council (MEC-2014-060). The human liver-derived ICOs were isolated and cultured, as described previously (Broutier et al., 2016). Briefly, the liver biopsies were washed in cold phosphate-buffered saline (PBS) and minced into small pieces. Minced tissues were washed in cold DMEM GlutaMAX medium (Gibco, Thermo Fisher Scientific, Waltham, MA, United States) supplemented with 1% (v/v) fetal calf serum (FCS; Gibco) and 1% (v/v) penicillin/streptomycin (P/S; Gibco). This was followed by digestion with 0.125 mg/ml type II collagenase (Gibco) and 0.125 mg/ml dispase (Gibco) in the DMEM GlutaMAX medium supplemented with 0.1 mg/ml DNase I (Roche, Basel, Switzerland), 1% (v/v) FCS, and 1% (v/v) P/S at 37°C in a shaking water bath. Every 10–15 min, the supernatant was collected, and the fresh digestion-supplemented medium was added and allowed for digestion three times. Single cells were obtained by passing through a 70-μm filter, and the filtrate was washed in cold DMEM GlutaMAX medium (supplemented with 1% (v/v) FCS and 1% (v/v) P/S) and centrifuged (400 g for 5 min at 4°C). The cells were diluted in cold Matrigel (Corning, New York, NY, United States) and seeded in 50 μL droplets in 24-well plates (Corning). After gelatinization of the Matrigel, a culture medium was added, and cells were incubated at 37°C, 5% CO_2 (v/v). The culture medium (expansion medium, EM) was based on the Advanced DMEM/F12 medium (Gibco) consisting of 1% (v/v) P/S, 1% (v/v) HEPES (10 mM; Gibco), and 1% (v/v) GlutaMax (Gibco). The EM was supplemented with 10% (v/v) R-Spondin-1–conditioned medium (the Rspon1-Fc-expressing cell line was a kind gift from Calvin J. Kuo), 2% (v/v) B27 supplement without vitamin A (Invitrogen, Carlsbad, CA, United States), 1% (v/v) N2 supplement (Invitrogen), 10 mM nicotinamide (Sigma-Aldrich, St. Louis, MO, United States), 1.25 mM N-acetylcysteine (NAC; Sigma-Aldrich), 100 ng/ml fibroblast growth factor 10 (FGF10; Peprotech, Rocky Hill, NJ, United States), 10 nM recombinant human (Leu15)-gastrin I (GAS; Tocris Bioscience, Bristol, United Kingdom), 10 μM forskolin (Tocris Bioscience), 50 ng/ml epidermal growth factor (EGF; Peprotech), 25 ng/ml hepatocyte growth factor (HGF; Peprotech), and 5 μM A8301 (transforming growth factor ß inhibitor; Tocris Bioscience). Organoids were mechanically split weekly at 1:3–1:4 ratio, and the medium was changed every 2–3 days.

Differentiation of Human ICOs to CLCs

ICOs were removed from Matrigel using cold Advanced DMEM/F12, mechanically dissociated into cell clusters using a pipette tip, and transferred to fresh Matrigel mixed with 1.2 mg/ml rat-tail type I collagen (Merck Millipore, Darmstadt, Germany) at a ratio of 2:3. Cultures were subsequently incubated at 37°C for 2 hours in a culture incubator for the hydrogel to polymerize after which the EM medium was added. After 1 day, the medium was changed to defined medium (cholangiocyte differentiation medium, CDM) consisting of Advanced DMEM/F12 medium supplemented with 1% (v/v) P/S, 1% (v/v) HEPES, 1% (v/v) GlutaMax, 2% (v/v) B27 supplement without vitamin A, 1% (v/v) ITS Premix (contains insulin, human transferrin, and selenous acid; Corning), 1.25 mM NAC, 100 ng/ml FGF10, 10 nM GAS, 50 ng/ml EGF, 25 ng/ml HGF, and 5 μM A8301. Under differentiating conditions, cells were cultured for 1 week, and the medium (CDM) was refreshed every other day.

RNA Isolation and RT-qPCR

The RNeasy Micro kit (QIAGEN, Hilden, Germany) was used to isolate RNA from liver organoids, M/C (Matrigel/collagen)- and HFM-cultured CLCs, following the manufacturer's instructions. RNA concentration and purity were measured with the ND-1000 spectrophotometer (NanoDrop, Thermo Fisher Scientific). cDNA was prepared with the iScript cDNA synthesis kit, according to the manufacturer's instructions (Bio-Rad, Hercules, California, United States). qPCR was performed to measure the relative gene expression using the SYBR Green method (Bio-Rad). Hypoxanthine phosphoribosyltransferase 1 (*HPRT1*) and ribosomal protein L19 (*RPL19*) were selected as stably expressed reference genes, and their average expression was used for normalization (Bustin et al., 2010). Details of all primers are described in **Supplementary Table S1**. Primary cells might lose some characteristics upon *in vitro* culturing. Therefore, we used the human gallbladder that contains mature cholangiocytes to compare the gene expression of markers in CLCs. Hence, we normalized the CLC gene expression to gallbladder samples for data analysis.

Cholangiocyte Functional Studies

A rhodamine 123 (Sigma-Aldrich) transport assay was performed on day 4. Organoids were pretreated with DMSO or 10 μM verapamil [an inhibitor of the efflux pump P-glycoprotein also known as multidrug resistance protein 1 (MDR1); Sigma-Aldrich] and incubated at 37°C for 30 min. Subsequently, organoids were gently removed from Matrigel/collagen and resuspended in CDM containing 100 μM of rhodamine 123 and incubated at 37°C for 10 min. Then, organoids were centrifuged (400 g for 5 min at room temperature), and the supernatant was removed. Organoids were washed with warm Advanced DMEM/F12 and centrifuged again. Fluorescence (excitation wavelength: 470 nm; emission wavelength: 535 nm) was measured using the BZ-9000 microscope (Keyence, Osaka, Japan).

For the farnesoid X receptor (FXR) activity assay, CLCs were incubated in CDM consisting of 10 μM GW4064 (an agonist of FXR; Sigma-Aldrich) or DMSO (control) for 24 h. RNA was isolated and used to evaluate the gene expression of downstream signaling of FXR target genes (solute carrier family 51 subunit alpha and solute carrier family 51 subunit beta, *SLC51A* and *SLC51B*) in the CLCs.

Culture of CLCs on the HFM

The polyethersulfone HFM (SENUO Filtration Technology, Tianjin, China) was double-coated to provide the cells with an extracellular matrix, as described previously (Chen et al., 2018). Briefly, HFM were cut into 3-cm pieces and sterilized in 70% (v/v) ethanol for 30 min. Next, the HFM was washed in PBS and precoated with filter-sterilized L-DOPA solution (2 mg/ml of 3,4-Dihydroxy-L-phenylalanine in 10 mM Tris buffer, pH 8.5) for 4 h at 37°C in an incubator, during which the fibers were turned 90° every hour. Subsequently, fibers were washed with PBS and put in rat-tail type I collagen solution (25 μg/ml in PBS) for another 2 h at 37°C in an incubator, during which the fibers were turned 90° every 30 min. The collagen solution was removed, and the fibers were washed with PBS prior to cell seeding. Single cells were prepared from liver organoids by in-gel trypsinization into single cells using TrypLE™ Express (Gibco) in a culture plate for 30–45 min at 37°C in an incubator. The single cells were collected and washed with Advanced DMEM/F12. Next, the double-coated HFMs were incubated with the cell suspension (5×10^5 cells/3-cm fiber in 1.5-ml Eppendorf tubes) in 1 ml EM for 4–5 h at 37°C to allow cell adherence to the membrane. The tubes were turned 90° every hour. Finally, the cells covered HFM were transferred to 6-well plates and cultured in EM for 1–2 weeks for expansion and subsequently in CDM for 1 week for differentiation to create the bile duct tubules.

Immunofluorescence Analysis

ICO-derived CLCs were removed from M/C using ice-cold cell recovery solution (Corning) and incubated on a horizontal shaker at 4°C (60 rpm) for 30–60 min until the 3D drops were dissolved. M/C- and HFM-cultured CLCs were washed with PBS and fixed with 4% (v/v) paraformaldehyde solution for 30 min at 4°C and permeabilized with 0.3% (v/v) Triton X-100 in PBS for 30 min at 4°C. To avoid non-specific antibody binding, the samples were incubated with block solution [2% (v/v) goat serum (Sigma-Aldrich), 2% (w/v) bovine serum albumin (Sigma-Aldrich), and 0.1% (v/v) Tween-20 in PBS (0.1% PBST)] for 1 h. Primary antibodies were diluted in block solution, and samples were incubated overnight at 4°C with shaking (60 rpm on a horizontal shaker). After being washed with 0.1% PBST three times for 20 min while shaking at 4°C (60 rpm on a horizontal shaker), the samples were incubated with secondary antibodies (5 μM Alexa Fluor 488 or 568; Life Technologies, Thermo Fisher Scientific) and with DAPI to stain nuclei (1:1,000; Sigma-Aldrich) overnight at 4°C while shaking (60 rpm on a horizontal shaker). Finally, tissues were washed three times for 20 min while shaking at 4°C (60 rpm on a horizontal shaker) and mounted on slides with ProLong Diamond Antifade mounting medium (Invitrogen). Images were acquired using a Leica TCS SP8 X imaging system. Antibody details for experiments are shown in **Supplementary Table S2**.

Trans-Epithelial Barrier Function

To measure the permeability of the bioengineered bile duct, an inulin-fluorescein isothiocyanate (2–5 kDa; inulin-FITC, Sigma-Aldrich) leakage assay was performed. The bile duct fiber was connected to inlet and outlet blunt needles (18 g; 0.5-inch length; OctoInkjet, Hoyland, United Kingdom) assembled in a custom-made 3D-printed biocompatible polylactide chamber

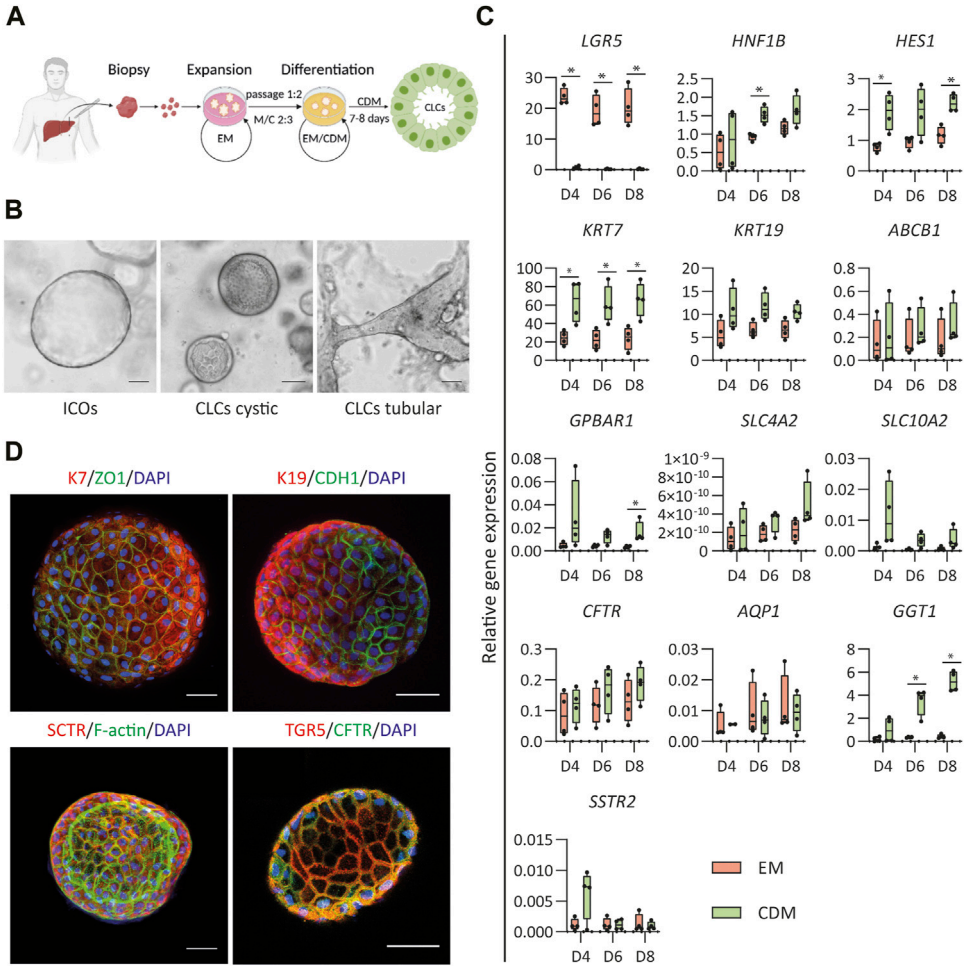

FIGURE 1 | Differentiation of human intrahepatic cholangiocyte organoids (ICOs) toward cholangiocyte-like cells (CLCs). **(A)** Schematic overview of the protocol for differentiation of human ICOs to CLCs. EM, expansion medium; CDM, cholangiocyte differentiation medium; M/C, Matrigel/collagen type I mixture. **(B)** ICOs in EM condition and cystic/tubular structures of CLCs formed in CDM. Left, ICOs; Middle, CLCs cystic; Right, CLCs tubular structure. Scale bar = 100 μm. **(C)** Gene expression analysis for ICOs under EM and CDM conditions. N = 4 independent donors for EM and CDM conditions at three time points (days 4, 6, and 8). Results are shown as fold change relative to the human gallbladder for cholangiocyte markers and the liver tissue for adult stem cell markers. Data are shown as box and whisker plots. Center line, median; box, interquartile; whiskers: minimum to maximum, show all points. Statistical differences between groups (EM and CDM) were determined by the two-tailed Mann–Whitney U test (see also **Supplementary Table S3**). *$p < 0.05$. **(D)** Immunofluorescence analysis of the CLCs expression of key cholangiocyte markers. Typically, in a well of a 96-well plate, about 50 organoids are cultured: keratin (K) 7 and K19, transport markers [secretin receptor (SCTR), G protein-coupled bile acid receptor 1 (GPBAR1, also known as TGR5), cystic fibrosis transmembrane conductance regulator (CFTR)], epithelial markers [cadherin 1 (CDH1), and tight junction protein 1 (ZO1)]. In addition, the F-actin is performed on the organoids' apical surface facing the central lumen. Scale bar = 50 μm.

(**Supplementary Figure S1**). Bile ducts were perfused (2 ml/h) with 0.1 mg/ml inulin-FITC in HBSS buffer supplemented with 10 mM HEPES for 10 min at room temperature. Samples were taken from the outer compartment of the bile duct, and fluorescence was measured at an excitation wavelength of 475 nm and an emission wavelength of 500–550 nm by using a fluorometer (Promega; Madison, Wisconsin, United States).

Statistical Analysis

Statistical graphs were determined by GraphPad Prism 9 (GraphPad Software). RT-qPCR results' data were presented as data points in box and whiskers (Min to Max; **Figures 1C**, **2**) and the mean ± standard deviation (mean with SD; **Figures 3C**,D, **4C**). The statistical test used was the two-tailed Mann–Whitney *U* test, and *p*-value details are described in the figure legends.

RESULTS

In Vitro Generation of CLCs From ICOs

The generation of CLCs from human ICOs was based on our previous strategy for murine liver organoids (Chen et al., 2018) with some modifications to enhance further differentiation (**Figure 1A**). Compared to the study by Chen et al., we modified the medium and used a serum-free culture system to drive the human ICOs to CLCs. Details of expansion and

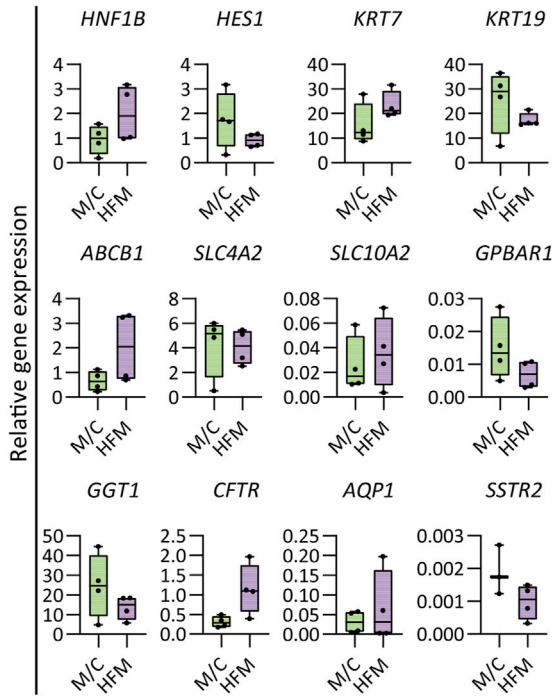

FIGURE 2 | Gene expression in mature bile ducts. Gene expression analysis demonstrating the HFM culture maintained cholangiocyte characteristics and expressed some more mature cholangiocyte characteristics compared to M/C-cultured CLCs. Results are shown as fold change relative to the human gallbladder for cholangiocyte markers. $N = 4$ independent donors for M/C- and HFM-cultured CLCs in CDM conditions on day 7. Data are shown as box and whisker plots. Center line, median; box, interquartile; whiskers: minimum to maximum and show all points. Statistical differences between groups were analyzed using the two-tailed Mann–Whitney U test (see also **Supplementary Table S4**).

differentiation medium are described in **Supplementary Table S5**. ICOs were expanded from the liver tissue biopsy, as previously described (Broutier et al., 2016), and seeded in a matrix that consisted of Matrigel and type I collagen. After 8 days of cholangiocyte differentiation, organoids formed cystic and tubular structures whereas the organoids growing in expanding conditions remained cystic (**Figure 1B**). The cholangiocyte organoids showed an increase in wall thickness, and the central lumen became more visible. In addition, the CLCs demonstrated more clearly visible membrane junctions than the organoids cultured under expansion conditions.

Next, the efficiency of the differentiation was evaluated through gene expression analysis performed at three different time points (day 4, 6, and 8) in expanding (EM) and differentiating (CDM) conditions. EM analysis served as a control to assure differentiation was performed toward more mature cholangiocytes. The first indicator of differentiation was the decreased expression of the stem/progenitor cell marker *LGR5* in the CDM condition compared to EM (**Figure 1C**), which was decreased at all time points. The enhanced mRNA expression of the biliary markers hepatocyte nuclear factor-1β (*HNF1β*) and hairy and enhancer of split-1 (*HES1*) demonstrated a more efficient cholangiocytic phenotype. Under the CDM condition, *HNF1β* was increased on day 6, and *HES1* was increased on days 4 and 8. This differentiation was further corroborated by the increased mRNA expression of keratin 7 (*KRT7*) at all time points (days 4, 6, and 8). G protein-coupled bile acid receptor 1 (*GPBAR1*) on day 8 and gamma-glutamyl transferase 1 (*GGT1*) on days 6 and 8 were increased under differentiation conditions. No significant difference in *HNF1β* (days 4 and 8), *HES1* (day 6), keratin 19 (*KRT19*; days 4, 6, and 8), ATP binding cassette subfamily B member 1 (*ABCB1*; days 4, 6, and 8), *GPBAR1* (days 4 and 6), solute carrier family 4 membrane 2 (*SLC4A2*; days 4, 6, and 8), solute carrier family 10 membrane 2 (*SLC10A2*; days 4, 6, and 8), cystic fibrosis transmembrane conductance regulator (*CFTR*; days 4, 6, and 8), *GGT1* (day 4), and somatostatin receptor 2 (*SSTR2*; day 4) were found, although the mRNA expressions under CDM conditions were higher than EM. Only for the biliary markers, aquaporin 1 (*AQP1*; days 4, 6, and 8) and *SSTR2* (days 6 and 8), the mRNA expression was slightly lower under CDM conditions than EM. More details on the statistical analyses are presented in **Supplementary Table S3**.

To further verify the organoid differentiation to CLCs, immunofluorescence staining was performed (**Figure 1D**). Epithelial markers, tight junction protein 1 (TJP1, also known as ZO1), and E-cadherin 1 (CDH1), as well as cholangiocyte markers K7 and K19, were present in CLCs. More importantly, the CLCs expressed cholangiocyte-specific transporters, secretin receptor (SCTR), and TGR5 (also known as GPBAR1, encoded by *GPBAR1*) that play an important role in sensing and signaling and appear in mature cholangiocytes (Guo et al., 2016; Sato et al., 2018; Wang et al., 2021). In addition, the CLCs showed F-actin indicated by the staining for phalloidin, as a marker for the apical domains which demonstrates the CLCs developed apicobasal epithelial polarity, with the apical surface facing the lumen.

Functional Characterization of CLCs

In the liver, cholangiocyte functions including the reabsorption and secretion of bile acids, water, and small molecules are performed by a series of transmembrane channel proteins. Cholangiocytes harbor a variety of transport channels, for instance, P-glycoprotein (also known as MDR1, encoded by *ABCB1*), a mediator of multidrug resistance expressed at the apical surface. To determine the functionality of *in vitro*-generated CLCs, the function of P-glycoprotein was investigated by incubating CLC organoids with the fluorescent dye rhodamine 123. Functional P-glycoprotein activity, located at the apical membrane, was confirmed by the accumulation of rhodamine 123 inside the lumen of CLC organoids. Moreover, blocking the transport activity with verapamil resulted in the accumulation of the fluorescent dye in the cytoplasm of organoid cells, verifying specific P-glycoprotein-mediated transport activity (**Figures 3A–C**).

Activation of the nuclear bile acid receptor farnesoid X receptor (FXR) leads to bile excretion whereas its inhibition causes bile accumulation or cholestasis (Shin and Wang, 2019). Bile acid excretion is performed by two transporters: one of ASBT located at the apical membrane of the cholangiocyte and the organic solute transporter α/β (OST α/β) (encoded by *SLC51A* and *SLC51B*, respectively) at the basolateral membrane. ASBT is responsible for the uptake of

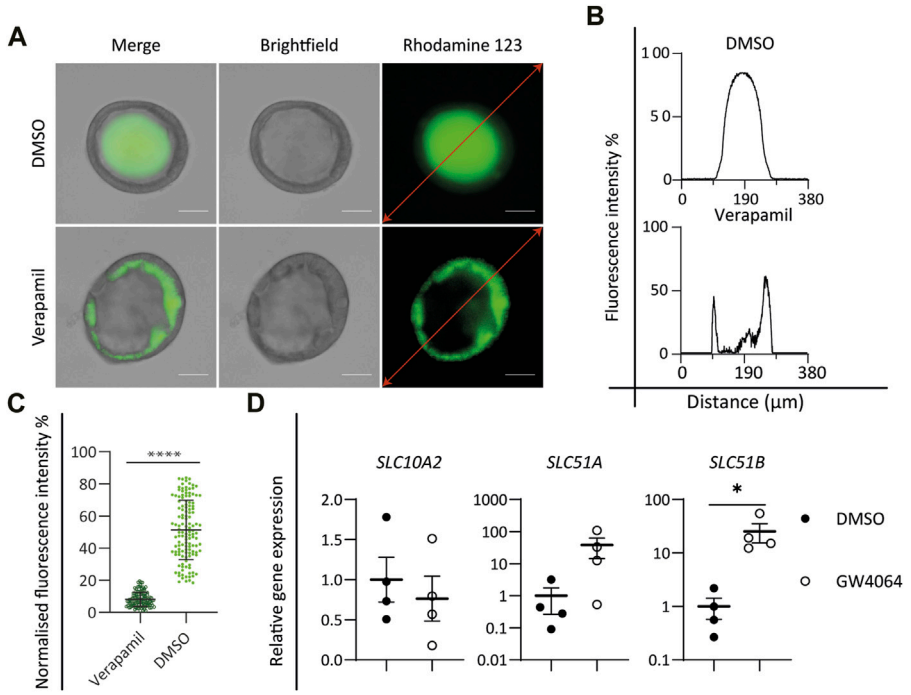

FIGURE 3 | Functional characterization of cholangiocyte-like cells (CLCs). **(A–C)** Rhodamine 123 transport assay. **(A)** Brightfield and fluorescent images showing the P-glycoprotein transport function by active transport of rhodamine 123, DMSO as control, and verapamil as an inhibitor of P-glycoprotein function. Scale bar = 50 μm. Graphs depicting the fluorescence intensity along the red lines in the images in **(A)**. **(C)** Mean intraluminal fluorescence intensity normalized to background levels for cystic cholangiocyte. Data are shown as mean ± SD for each group. Statistical differences between groups were analyzed using the two-tailed Mann–Whitney U test; verapamil, $N = 127$; DMSO, N = 132; $^{****}p < 0.0001$. **(D)** FXR assay. Gene expression analysis showing the activation of FXR signaling downstream target genes, *SLC10A2, SLC51A*, and *SLC51B* in DMSO versus the FXR agonist (GW4064)-treated group. $N = 4$ independent donors for each group. Data are shown as mean ± SEM of four independent experiments for each group. Statistical differences between groups were determined using the paired *t*-test; DMSO, $N = 4$; GW4064, $N = 4$; $^{*}p < 0.05$.

bile acids and can be downregulated by FXR activation. On the other hand, OST α/β are upregulated by FXR and support bile acid excretion. Incubation of the CLC organoids with the well-known FXR agonist GW4064 resulted in the downregulation of *SLC10A2* and in the upregulation of *SLC51A* and *SLC51B* (**Figure 3D**), indicating that the ICO-derived CLCs express functional FXR-mediated bile homeostasis.

CLCs Form Tight and Mature Bile Ducts When Cultured on the HFM

The observed polarization and functionality of the organoids prompted us to create a HFM system amendable for transport studies. For this, single cells were acquired from trypsinized organoids and seeded on the HFM scaffold (**Figure 4A**). The cell-seeded constructs were cultured for 10–14 days under expanding conditions (EM) until a confluent monolayer was formed and subsequently switched to differentiating conditions (CDM) for seven more days. CLCs formed an epithelial barrier on the HFM, as confirmed by immunofluorescence staining of the tight junction proteins ZO1 and CDH1 (**Figure 4B**). Furthermore, the restricted inulin-FITC diffusion represented the bile duct barrier function (**Figure 4C**). The bile ducts show an inside-out polarization as staining for the tight junction protein and phalloidin demonstrated extraluminally expressed TJP1/ZO1 and F-actin, whereas the basolateral E-cadherin/CDH1 and SCTR appeared at the luminal side. In addition, staining for K7, K19, TGR5/GPBAR1, and CFTR confirmed that HFM-cultured CLCs also maintained cholangiocyte-specific markers while being cultured on HFM (**Figure 4B**).

The bioengineered bile ducts were characterized further by comparing gene expression profiles to organoids cultured in CDM on a culture plate (M/C). The results revealed that CLCs cultured on HFMs maintained a stable expression of key cholangiocyte markers (*HES1*, *KRT19*, *SLC4A2*, *GPBAR1*, *GGT1*, and *SSTR2*). Interestingly, the cholangiocyte markers *HNF1β*, *KRT7*, *ABCB1*, *SLC10A2*, *CFTR*, and *AQP1* showed a trend toward upregulation in CLCs cultured on HFMs as compared to plates cultured under differentiating conditions, suggesting that some cholangiocyte markers show a more mature phenotype in these tubular structures (**Figure 2**). The details of the statistical analyses are presented in **Supplementary Table S4**.

DISCUSSION

The current study and application show that ICOs can be differentiated into more mature and functional cholangiocytes. In addition to the well-described differentiation toward

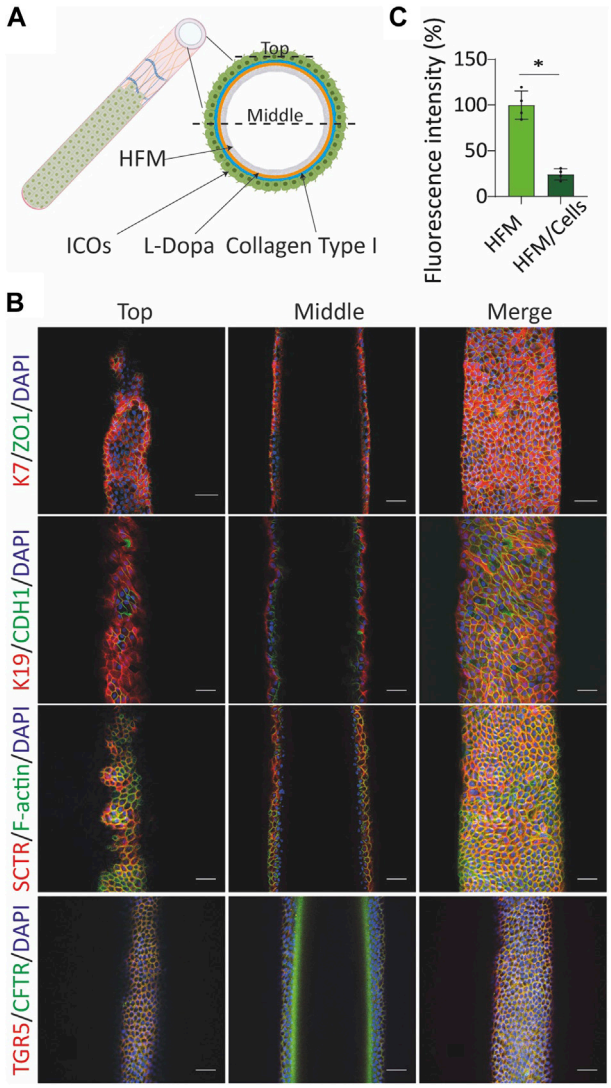

FIGURE 4 | Culture of cholangiocyte-like cells (CLCs) on the extracellular matrix (ECM)-coated hollow fiber membrane (HFM) form tight and mature bile duct. **(A)** Illustrative image of HFM-cultured CLCs. **(B)** Bioengineered bile duct immunostaining. Immunofluorescence analysis of the bioengineered bile duct expression of key cholangiocyte markers [keratin (K) 7 and 19], transport markers [(secretin receptor (SCTR), G protein-coupled bile acid receptor 1 (GPBAR1, also known as TGR5), cystic fibrosis transmembrane conductance regulator (CFTR)], F-actin, epithelial markers [cadherin 1 (CDH1), and tight junction protein 1 (ZO1)]. Scale bar = 50 μm. **(C)** Trans-epithelial barrier function. The inulin-FITC leakage was assessed in the presence or absence of CLCs; data are shown as mean ± SD of four independent experiments for each group. Statistical differences between groups were analyzed using the two-tailed Mann–Whitney U test; HFM, $N = 4$; HFM/Cells, $N = 4$; $^{*}p < 0.05$.

hepatocyte-like cells, these data clearly confirm the bipotentiality of the human ICOs (Kruitwagen et al., 2020; Schneeberger et al., 2020; Ye et al., 2020; Bouwmeester et al., 2021). Moreover, this study provides a robust protocol to reproduce functional cholangiocytes from human ICOs and form a polarized and functional bioengineered human bile duct on the polyethersulfone HFM, making this bioengineered system compliable for transport studies, disease modeling, and drug development.

To develop an efficient cholangiocyte differentiation method, Chen et al. (2018) demonstrated that gastrin, N-acetylcysteine, and FGF10 maturated murine ICOs toward cholangiocyte-like cells, and EGF played an important role in directing cholangiocyte differentiation of liver progenitor cells (Kitade et al., 2013). In addition, Tanimizu et al. (2007) reported that a combination of EGF and HGF induced cyst formation for liver progenitor cells more than either EGF or HGF alone. Matrigel matrix is effective for the liver organoid culturing and differentiation (Nuciforo and Heim, 2021), but the combined Matrigel/collagen (M/C) better supports cyst formation of progenitor cells and cholangiocyte function (Tanimizu et al., 2007). Here, we showed that a combination of these compounds and hydrogel mixture, in combination with serum-free conditions, is sufficient to promote ICO differentiation into cholangiocyte-like cells with high efficiency. Importantly, our data show the CLCs expressed mature cholangiocyte markers and obtained several vital functions of cholangiocytes, including P-glycoprotein-mediated transport and FXR-dependent regulation. Most *in vitro* studies of cholangiopathies that have been reported relied on 3D organoid modeling (Artegiani et al., 2019; Ye et al., 2020; Zhao et al., 2020). Primary cell or stem-cell derived cholangiocytes in 3D organoid cultures better mimic the *in vivo* environment and differentiate well and can be used for barrier functions and transport measurements. However, 3D organoids are highly heterogeneous in shape and size, and their location is difficult to control in hydrogels. As the apical surface is located at the inside of the organoids, studying transepithelial transport is also extremely difficult. The device presented here represents a bile duct-on-chip platform that can build an actual tissue structure with cholangiocyte function and reduced variability and offers a novel tool to model and study cholangiopathies (Chen et al., 2018; Du et al., 2020).

Recently, synthetic and natural materials have been used to construct bioengineered bile ducts for transplantation purposes (Wang et al., 2021). Sampaziotis et al. (2017b) described collagen scaffolds populated by human extrahepatic organoids (ECOs) that formed a bioengineered bile duct, which were able to replace the native mouse extrahepatic bile duct. These results provided potential clinical applications for bioengineered bile duct transplantation. However, natural materials as scaffolds can easily collapse and degrade when transplanted. In addition, the ECOs used to create these bioengineered bile ducts are quite distinct to ICOs and show region-specific differentiation potential (Verstegen et al., 2020). Synthetic materials have also been used which have the main benefit of being durable and better chemically defined (Du et al., 2020). Du et al. (2022) reported polydimethylsiloxane (PDMS) support with a collagen scaffold to construct murine bile ducts, which are polarized and can be used to mimic barrier function (Du et al., 2020). However, these microfluidic devices were difficult to apply for transepithelial transport studies as the basal surface of the bioengineered bile

duct attached to the collagen gel will hamper the diffusion speed, and/or compounds can get trapped in the collagen. In addition, even if the bioengineered bile duct consists of PDMS scaffolds, the inner channel formed with collagen and degradability of collagen (Meyer, 2019) could influence the bioengineered bile duct stability (Du et al., 2020). Therefore, alternative scaffold materials should be investigated and applied in *in vitro* studies or for clinical application. The polyethersulfone HFM used in the current study possesses biocompatibility and hemocompatibility, as well as excellent mechanical properties and ease of application in different types of organ biofabrication (Jansen et al., 2015; Jochems et al., 2019). In addition, we previously reported the use of HFM to model (murine) the liver (Chen et al., 2018). Due to the low cell adhesion capability of HFM scaffolds, the modified membrane using a double coating of L-3,4-dihydroxydiphenylalanine (L-DOPA) and collagen IV (Oo et al., 2011), the extracellular matrix coatings that promote formation and maintenance of epithelial monolayers (Zhang et al., 2009; Ni et al., 2011). To develop the murine bioengineered bile duct, Chen et al. (2018) described HFM coated with L-DOPA and collagen I. This coating contributed to liver organoid-derived CLC monolayer formation and allowed polarized bile acid transport activity (Chen et al., 2018). Even though Chen et al. (2018) and Du et al. (2020) established the murine bioengineered bile ducts to study bile acid transport and disease modeling, respectively, the human bioengineered bile ducts are yet to be established for translational research.

In this study, we showed the combination of a scaffold of a double-coated biofunctionalized HFM together with CLCs organized into a human bioengineered bile duct. The generated human bioengineered bile duct recapitulated characteristics of bile ducts *in vivo*, including the 3D architecture. Furthermore, we demonstrated that ICO-derived CLCs polarized on the HFM and produced a confluent and tight monolayer with a barrier function. Even though the apical-basolateral polarity is opposite to the native bile duct and therefore not suitable for transplantation, it can still be applied in studying transepithelial transport or in drug screening. The opposite polarity of bioreactor devices has been applied earlier in drug screening and transport studies using a murine bile duct (Chen et al., 2018), as well as a bioengineered kidney (Jansen et al., 2015) and intestinal tubules (Jochems et al., 2019). In native bile ducts, the cholangiocytes lining the intrahepatic biliary tree display phenotypical heterogeneity (Banales et al., 2019). The large, but not small cholangiocytes, expressed the secretin and somatostatin receptors (Han et al., 2013). Importantly, our bioengineered bile ducts showed expressions of SCTR and *SSTR2*, which indicates that they have large bile duct characteristics. Cholangiocytes also expressed ASBT, which mediates bile acid uptake (Claro Da Silva et al., 2013), and TGR5, which plays an important role in bile acid signaling (Keitel and Haussinger, 2013; Masyuk et al., 2013). The cholangiocyte's primary cilia are also different between small and large cholangiocytes (Huang et al., 2006). Primary cilia provide mechanosensory, chemosensory, and osmosensory functions and can detect changes in bile flow (Masyuk et al., 2006; Mansini et al., 2018). To identify the primary cilia presence, we selected *a*-tubulin as an indicator for immunostaining. We could confirm primary cilia presence; however, the organelles were small compared to a kidney cell line that demonstrated to have long primary cilia on each cell (**Supplementary Figure S2A**) and more infrequently. Recently, Ogawa et al. (2021) reported that human pluripotent stem cells induced the CFTR-positive cholangiocyte population that could generate functional ciliated cholangiocytes. Some of the described culture conditions in this article could benefit by helping with a more homogenous cilia formation in CLCs derived from ICOs. Overall, CLCs cultured on the HFM appear very similar to cholangiocytes *in vivo*, and their polarization allows cross-epithelial transport studies.

In conclusion, this study shows a robust methodology to differentiate ICOs toward the cholangiocytic lineage and provides a novel method to generate human bioengineered bile ducts. This methodology provides a novel *in vitro* model for studying bile duct function and will aid in drug development for cholangiopathies.

DATA AVAILABILITY STATEMENT

The original contributions presented in the study are included in the article/**Supplementary Material**; further inquiries can be directed to the corresponding authors.

AUTHOR CONTRIBUTIONS

ZW, RM, and BS conceived the project and designed the experiment. ZW performed the experimental work, data analysis, and the original draft preparation. JF provided the experimental help, and LP critically revised the draft. RM and BS guided the project and critically revised the manuscript. LL provided the liver samples. All authors read and approved the final submitted manuscript.

FUNDING

This work was supported by the China Scholarship Council (No. 201808620130), and the European Union's Horizon 2020 research and innovation programme under the Marie Skłodowska-Curie Grant agreement no. 813839 (JF). Furthermore, this work was co-funded by the PPP Allowance made available by Health ~ Holland, Top Sector Life Sciences & Health, Netherlands (No. LSHM20045-HSGF), to stimulate public–private partnerships.

SUPPLEMENTARY MATERIAL

The Supplementary Material for this article can be found online at: https://www.frontiersin.org/articles/10.3389/fbioe.2022.868857/full#supplementary-material

REFERENCES

Artegiani, B., Van Voorthuijsen, L., Lindeboom, R. G. H., Seinstra, D., Heo, I., Tapia, P., et al. (2019). Probing the Tumor Suppressor Function of BAP1 in CRISPR-Engineered Human Liver Organoids. *Cell Stem Cell* 24 (6), 927–943. e926. doi:10.1016/j.stem.2019.04.017

Banales, J. M., Huebert, R. C., Karlsen, T., Strazzabosco, M., Larusso, N. F., and Gores, G. J. (2019). Cholangiocyte Pathobiology. *Nat. Rev. Gastroenterol. Hepatol.* 16 (5), 269–281. doi:10.1038/s41575-019-0125-y

Bouwmeester, M. C., Bernal, P. N., Oosterhoff, L. A., Van Wolferen, M. E., Lehmann, V., Vermaas, M., et al. (2021). Bioprinting of Human Liver-Derived Epithelial Organoids for Toxicity Studies. *Macromol. Biosci.* 21 (12), e2100327. doi:10.1002/mabi.202100327

Broutier, L., Andersson-Rolf, A., Hindley, C. J., Boj, S. F., Clevers, H., Koo, B.-K., et al. (2016). Culture and Establishment of Self-Renewing Human and Mouse Adult Liver and Pancreas 3D Organoids and Their Genetic Manipulation. *Nat. Protoc.* 11 (9), 1724–1743. doi:10.1038/nprot.2016.097

Bustin, S. A., Beaulieu, J.-F., Huggett, J., Jaggi, R., Kibenge, F. S., Olsvik, P. A., et al. (2010). MIQE Précis: Practical Implementation of Minimum Standard Guidelines for Fluorescence-Based Quantitative Real-Time PCR Experiments. *BMC Mol. Biol.* 11, 74. doi:10.1186/1471-2199-11-74

Chen, C., Jochems, P. G. M., Salz, L., Schneeberger, K., Penning, L. C., Van De Graaf, S. F. J., et al. (2018). Bioengineered Bile Ducts Recapitulate Key Cholangiocyte Functions. *Biofabrication* 10 (3), 034103. doi:10.1088/1758-5090/aac8fd

Claro Da Silva, T., Polli, J. E., and Swaan, P. W. (2013). The Solute Carrier Family 10 (SLC10): beyond Bile Acid Transport. *Mol. Asp. Med.* 34 (2-3), 252–269. doi:10.1016/j.mam.2012.07.004

Du, Y., Khandekar, G., Llewellyn, J., Polacheck, W., Chen, C. S., and Wells, R. G. (2020). A Bile Duct-on-a-Chip with Organ-Level Functions. *Hepatology* 71 (4), 1350–1363. doi:10.1002/hep.30918

Guo, C., Chen, W. D., and Wang, Y. D. (2016). TGR5, Not Only a Metabolic Regulator. *Front. Physiol.* 7, 646. doi:10.3389/fphys.2016.00646

Han, Y., Glaser, S., Meng, F., Francis, H., Marzioni, M., Mcdaniel, K., et al. (2013). Recent Advances in the Morphological and Functional Heterogeneity of the Biliary Epithelium. *Exp. Biol. Med. (Maywood)* 238 (5), 549–565. doi:10.1177/1535370213489926

Huang, B. Q., Masyuk, T. V., Muff, M. A., Tietz, P. S., Masyuk, A. I., and Larusso, N. F. (2006). Isolation and Characterization of Cholangiocyte Primary Cilia. *Am. J. Physiology-Gastrointestinal Liver Physiology* 291 (3), G500–G509. doi:10.1152/ajpgi.00064.2006

Huch, M., Gehart, H., Van Boxtel, R., Hamer, K., Blokzijl, F., Verstegen, M. M., et al. (2015). Long-term Culture of Genome-Stable Bipotent Stem Cells from Adult Human Liver. *Cell* 160 (1-2), 299–312. doi:10.1016/j.cell.2014.11.050

Jansen, J., De Napoli, I. E., Fedecostante, M., Schophuizen, C. M. S., Chevtchik, N. V., Wilmer, M. J., et al. (2015). Human Proximal Tubule Epithelial Cells Cultured on Hollow Fibers: Living Membranes that Actively Transport Organic Cations. *Sci. Rep.* 5, 16702. doi:10.1038/srep16702

Jochems, P. G. M., Van Bergenhenegouwen, J., Van Genderen, A. M., Eis, S. T., Wilod Versprille, L. J. F., Wichers, H. J., et al. (2019). Development and Validation of Bioengineered Intestinal Tubules for Translational Research Aimed at Safety and Efficacy Testing of Drugs and Nutrients. *Toxicol. Vitro* 60, 1–11. doi:10.1016/j.tiv.2019.04.019

Joplin, R. (1994). Isolation and Culture of Biliary Epithelial Cells. *Gut* 35 (7), 875–878. doi:10.1136/gut.35.7.875

Keitel, V., and Häussinger, D. (2013). TGR5 in Cholangiocytes. *Curr. Opin. Gastroenterology* 29 (3), 299–304. doi:10.1097/mog.0b013e32835f3f14

Kim, J., Koo, B.-K., and Knoblich, J. A. (2020). Human Organoids: Model Systems for Human Biology and Medicine. *Nat. Rev. Mol. Cell Biol.* 21 (10), 571–584. doi:10.1038/s41580-020-0259-3

Kitade, M., Factor, V. M., Andersen, J. B., Tomokuni, A., Kaji, K., Akita, H., et al. (2013). Specific Fate Decisions in Adult Hepatic Progenitor Cells Driven by MET and EGFR Signaling. *Genes Dev.* 27 (15), 1706–1717. doi:10.1101/gad.214601.113

Kruitwagen, H. S., Oosterhoff, L. A., Van Wolferen, M. E., Chen, C., Nantasanti Assawarachan, S., Schneeberger, K., et al. (2020). Long-Term Survival of Transplanted Autologous Canine Liver Organoids in a COMMD1-Deficient Dog Model of Metabolic Liver Disease. *Cells* 9 (2). doi:10.3390/cells9020410

Lazaridis, K. N., and Larusso, N. F. (2015). The Cholangiopathies. *Mayo Clin. Proc.* 90 (6), 791–800. doi:10.1016/j.mayocp.2015.03.017

Mansini, A. P., Peixoto, E., Thelen, K. M., Gaspari, C., Jin, S., and Gradilone, S. A. (2018). The Cholangiocyte Primary Cilium in Health and Disease. *Biochim. Biophys. Acta Mol. Basis Dis.* 1864 (4 Pt B), 1245–1253. doi:10.1016/j.bbadis.2017.06.006

Marsee, A., Roos, F. J. M., Verstegen, M. M. A., Gehart, H., de Koning, E., Lemaigre, F., et al. (2021). Building Consensus on Definition and Nomenclature of Hepatic, Pancreatic, and Biliary Organoids. *Cell Stem Cell* 28 (5), 816–832. doi:10.1016/j.stem.2021.04.005

Masyuk, A. I., Huang, B. Q., Radtke, B. N., Gajdos, G. B., Splinter, P. L., Masyuk, T. V., et al. (2013). Ciliary Subcellular Localization of TGR5 Determines the Cholangiocyte Functional Response to Bile Acid Signaling. *Am. J. Physiology-Gastrointestinal Liver Physiology* 304 (11), G1013–G1024. doi:10.1152/ajpgi.00383.2012

Masyuk, A. I., Masyuk, T. V., Splinter, P. L., Huang, B. Q., Stroope, A. J., and Larusso, N. F. (2006). Cholangiocyte Cilia Detect Changes in Luminal Fluid Flow and Transmit Them into Intracellular Ca2+ and cAMP Signaling. *Gastroenterology* 131 (3), 911–920. doi:10.1053/j.gastro.2006.07.003

Meyer, M. (2019). Processing of Collagen Based Biomaterials and the Resulting Materials Properties. *Biomed. Eng. Online* 18 (1), 24. doi:10.1186/s12938-019-0647-0

Ni, M., Teo, J. C. M., Ibrahim, M. S. b., Zhang, K., Tasnim, F., Chow, P.-Y., et al. (2011). Characterization of Membrane Materials and Membrane Coatings for Bioreactor Units of Bioartificial Kidneys. *Biomaterials* 32 (6), 1465–1476. doi:10.1016/j.biomaterials.2010.10.061

Nuciforo, S., and Heim, M. H. (2021). Organoids to Model Liver Disease. *JHEP Rep.* 3 (1), 100198. doi:10.1016/j.jhepr.2020.100198

Ogawa, M., Jiang, J.-X., Xia, S., Yang, D., Ding, A., Laselva, O., et al. (2021). Generation of Functional Ciliated Cholangiocytes from Human Pluripotent Stem Cells. *Nat. Commun.* 12 (1), 6504. doi:10.1038/s41467-021-26764-0

Oo, Z. Y., Deng, R., Hu, M., Ni, M., Kandasamy, K., Bin Ibrahim, M. S., et al. (2011). The Performance of Primary Human Renal Cells in Hollow Fiber Bioreactors for Bioartificial Kidneys. *Biomaterials* 32 (34), 8806–8815. doi:10.1016/j.biomaterials.2011.08.030

Planas-Paz, L., Sun, T., Pikiolek, M., Cochran, N. R., Bergling, S., Orsini, V., et al. (2019). YAP, but Not RSPO-Lgr4/5, Signaling in Biliary Epithelial Cells Promotes a Ductular Reaction in Response to Liver Injury. *Cell Stem Cell* 25 (1), 39–53. doi:10.1016/j.stem.2019.04.005

Sampaziotis, F., De Brito, M. C., Geti, I., Bertero, A., Hannan, N. R., and Vallier, L. (2017a). Directed Differentiation of Human Induced Pluripotent Stem Cells into Functional Cholangiocyte-like Cells. *Nat. Protoc.* 12 (4), 814–827. doi:10.1038/nprot.2017.011

Sampaziotis, F., Justin, A. W., Tysoe, O. C., Sawiak, S., Godfrey, E. M., Upponi, S. S., et al. (2017b). Reconstruction of the Mouse Extrahepatic Biliary Tree Using Primary Human Extrahepatic Cholangiocyte Organoids. *Nat. Med.* 23 (8), 954–963. doi:10.1038/nm.4360

Sato, K., Meng, F., Venter, J., Giang, T., Glaser, S., and Alpini, G. (2018). Author Correction: The Role of the Secretin/secretin Receptor axis in Inflammatory Cholangiocyte Communication via Extracellular Vesicles. *Sci. Rep.* 8 (1), 11238. doi:10.1038/s41598-018-29609-x

Schneeberger, K., Sánchez-Romero, N., Ye, S., Steenbeek, F. G., Oosterhoff, L. A., Pla Palacin, I., et al. (2020). Large-Scale Production of LGR5-Positive Bipotential Human Liver Stem Cells. *Hepatology* 72 (1), 257–270. doi:10.1002/hep.31037

Shin, D.-J., and Wang, L. (2019). Bile Acid-Activated Receptors: A Review on FXR and Other Nuclear Receptors. *Handb. Exp. Pharmacol.* 256, 51–72. doi:10.1007/164_2019_236

Spada, M., Riva, S., Maggiore, G., Cintorino, D., and Gridelli, B. (2009). Pediatric Liver Transplantation. *Wjg* 15 (6), 648–674. doi:10.3748/wjg.15.648

Tanimizu, N., Miyajima, A., and Mostov, K. E. (2007). Liver Progenitor Cells Develop Cholangiocyte-type Epithelial Polarity in Three-Dimensional Culture. *MBoC* 18 (4), 1472–1479. doi:10.1091/mbc.e06-09-0848

Verstegen, M. M. A., Roos, F. J. M., Burka, K., Gehart, H., Jager, M., De Wolf, M., et al. (2020). Human Extrahepatic and Intrahepatic Cholangiocyte Organoids Show Region-specific Differentiation Potential and Model Cystic Fibrosis-

Related Bile Duct Disease. *Sci. Rep.* 10 (1), 21900. doi:10.1038/s41598-020-79082-8

Wang, Z., Faria, J., Penning, L. C., Masereeuw, R., and Spee, B. (2021). Tissue-Engineered Bile Ducts for Disease Modeling and Therapy. *Tissue Eng. Part C. Methods* 27 (2), 59–76. doi:10.1089/ten.tec.2020.0283

Ye, S. C., Boeter, J. W. B., Mihajlovic, M., Van Steenbeek, F. G., Van Wolferen, M. E., Oosterhoff, L. A., et al. (2020). A Chemically Defined Hydrogel for Human Liver Organoid Culture. *Adv. Funct. Mater.* 30 (48). doi:10.1002/adfm.202000893

Yin, X., Mead, B. E., Safaee, H., Langer, R., Karp, J. M., and Levy, O. (2016). Engineering Stem Cell Organoids. *Cell Stem Cell* 18 (1), 25–38. doi:10.1016/j.stem.2015.12.005

Zhang, H., Tasnim, F., Ying, J. Y., and Zink, D. (2009). The Impact of Extracellular Matrix Coatings on the Performance of Human Renal Cells Applied in Bioartificial Kidneys. *Biomaterials* 30 (15), 2899–2911. doi:10.1016/j.biomaterials.2009.01.046

Zhao, B., Ni, C., Gao, R., Wang, Y., Yang, L., Wei, J., et al. (2020). Recapitulation of SARS-CoV-2 Infection and Cholangiocyte Damage with Human Liver Ductal Organoids. *Protein Cell* 11 (10), 771–775. doi:10.1007/s13238-020-00718-6

Conflict of Interest: The authors declare that the research was conducted in the absence of any commercial or financial relationships that could be construed as a potential conflict of interest.

frontiers | Frontiers in Bioengineering and Biotechnology

TYPE Original Research
PUBLISHED 22 July 2022
DOI 10.3389/fbioe.2022.920929

OPEN ACCESS

EDITED BY
Loredana De Bartolo,
National Research Council (CNR), Italy

REVIEWED BY
Menekse Ermis Sen,
Terasaki Institute for Biomedical Innovation, United States
Dana Akilbekova,
Nazarbayev University, Kazakhstan

*CORRESPONDENCE
Franck Halary,
franck.halary@univ-nantes.fr

†These authors have contributed equally to this work

SPECIALTY SECTION
This article was submitted to Tissue Engineering and Regenerative Medicine, a section of the journal Frontiers in Bioengineering and Biotechnology

RECEIVED 15 April 2022
ACCEPTED 29 June 2022
PUBLISHED 22 July 2022

CITATION
Boucard E, Vidal L, Coulon F, Mota C, Hascoët J-Y and Halary F (2022), The degradation of gelatin/alginate/fibrin hydrogels is cell type dependent and can be modulated by targeting fibrinolysis.
Front. Bioeng. Biotechnol. 10:920929.
doi: 10.3389/fbioe.2022.920929

The degradation of gelatin/alginate/fibrin hydrogels is cell type dependent and can be modulated by targeting fibrinolysis

Elea Boucard[1†], Luciano Vidal[2†], Flora Coulon[1], Carlos Mota[3], Jean-Yves Hascoët[2] and Franck Halary[1*]

[1]Nantes Université, INSERM, Center for Research in Transplantation and Translational Immunology, UMR 1064, Nantes, France, [2]Rapid Manufacturing Platform, Institut de Recherche en Génie Civil et Mécanique (GeM), UMR 7 CNRS 6183 Ecole Centrale de Nantes, Nantes, France, [3]Department of Complex Tissue Regeneration, MERLN Institute for Technology-inspired Regenerative Medicine, Maastricht University, Maastricht, Netherlands

In tissue engineering, cell origin is important to ensure outcome quality. However, the impact of the cell type chosen for seeding in a biocompatible matrix has been less investigated. Here, we investigated the capacity of primary and immortalized fibroblasts of distinct origins to degrade a gelatin/alginate/fibrin (GAF)-based biomaterial. We further established that fibrin was targeted by degradative fibroblasts through the secretion of fibrinolytic matrix-metalloproteinases (MMPs) and urokinase, two types of serine protease. Finally, we demonstrated that besides aprotinin, specific targeting of fibrinolytic MMPs and urokinase led to cell-laden GAF stability for at least forty-eight hours. These results support the use of specific strategies to tune fibrin-based biomaterials degradation over time. It emphasizes the need to choose the right cell type and further bring targeted solutions to avoid the degradation of fibrin-containing hydrogels or bioinks.

KEYWORDS

gelatin, sodium alginate, fibrinolysis, fibroblasts, aprotinin, matrix metalloproteinases, connective tissue, tissue engineering

Introduction

The oral cavity is lined with mucosal tissues which protect from physical, chemical, thermal and microbial threats (Presland and Dale, 2000). Like skin, oral mucosae are defined as composite tissues with a typical two-layer architecture: a connective tissue (CT) or *lamina propria* which consists in an extracellular matrix (ECM) containing stromal cells, e.g., fibroblasts or endothelial cells, supporting a squamous pluristratified epithelium mainly composed of specialized keratinocytes (Presland and Dale, 2000; Stecco et al., 2015). Both layers are separated by a basement membrane (Kinikoglu et al., 2015). In general, the CT ECM is a complex network surrounding cells, mostly composed of

proteins, e.g., collagens and elastin, glycoproteins proteoglycans and glycosaminoglycans (Frantz et al., 2010; Skardal et al., 2015; Naba et al., 2016). It undergoes a constant cell-mediated remodeling most notably via matrix metalloproteinases or MMPs (Frantz et al., 2010; Bonnans et al., 2014).

Tissue engineering (TE) has allowed recapitulating part of the complexity of human skin and mucosal tissues through the development of 3D models *in vitro* as well as, more recently, *in vivo* (Albouy et al., 2022). The current advantages of *in vitro* 3D models are: they mimic the structure and functions of their native counterparts, they support the use of genetically-modified cell lines, they can be fully humanized, and they comply with the reduction in animal testing. To date, manual-, e.g., with cell culture inserts (Reijnders et al., 2015; Buskermolen et al., 2016), and automated engineering, e.g., bioplotting (Pourchet et al., 2017), of humanized CT equivalents (CTE) have already been described. Biomaterials frequently used for CTE biofabrication are natural-based (e.g., collagen, gelatin, fibrinogen, hyaluronic acid, and alginate) or synthetic polymers (e.g., PEG, PLGA) (Urciuolo et al., 2019) of various stiffness (Skardal et al., 2015; Pepelanova et al., 2018; Vidal et al., 2020) as single component or blended hydrogels (Skardal et al., 2012; Skardal et al., 2015). Furthermore, to select appropriate hydrogels needs to consider other parameters such as the cytocompatibility and remodeling, mainly driven by a fine balance in ECM degradation versus neosynthesis (Caliari and Burdick, 2016). A 3D bioprinted dermis equivalent, made of gelatin (GL), sodium alginate (SA) and fibrin (FB), was recently described by Pourchet et al. (2017). A thermosensitive mixture of degraded ECM, GL, was used to maintain shape fidelity upon printing. GL was mixed with SA, which improves the scaffold stability after cross-linking, and fibrinogen (FBG), a secreted blood glycoprotein responsible for blood clots formation, leading to FB fibers formation after cleavage by thrombin. Both GL and FB harbor RGD motifs to promote cell attachment in the 3D network formed by the three distinct compounds after cross-linking. Likewise, similar blended hydrogels were shown to support the biofabrication of 3D models of metabolic syndrome (Xu et al., 2010), cervical and brain cancers (Zhao et al., 2014; Dai et al., 2016), cartilage implants (Henrionnet et al., 2020) and oral mucosa regeneration (Yi et al., 2022). Fibroblasts are the most abundant cells in CT under physiological conditions although their proportion may vary according to the tissue location. They are key players in the CT homeostasis, displaying extensive heterogeneity, plasticity and exhibiting various functions like remodeling ECM, providing signals essential to epithelial cell survival, proliferation and differentiation (Merne and Syrjänen, 2003; Okazaki et al., 2003; Lebleu and Neilson, 2020; Tsukui et al., 2020; Buechler et al., 2021; Reynolds et al., 2021) or promoting angiogenesis, immune control and tissue regeneration (Lebleu and Neilson, 2020). Human primary and hTERT-immortalized fibroblasts have already been used successfully in CTE reconstruction based on GL/SA/FB hydrogels, termed GAF in this study (Pourchet et al., 2017; Henrionnet et al., 2020). However, their ability to remodel GAF blends has not been clearly addressed to date.

Our study aimed at assessing the capacity of primary and immortalized human fibroblasts of distinct origins to degrade GAF hydrogels. We confirmed the efficacy of the well-known aprotinin, a serine protease inhibitor, in controlling fibrinolysis (Lorentz et al., 2010; Lesman et al., 2011; Thomson et al., 2014). However, we showed that human, plasminogen-depleted fibrinogen, mixed with GL and SA, leads to less GAF degradation compared to human or even bovine fibrinogens. Both can be used alone or simultaneously to tune fibrinolysis thus achieving stable, bioengineered CTEs.

Materials and methods

Reagents

Collagenase IV from *Clostridium histolyticum*, porcine gelatin (GL), fibrinogen (FBG) from bovine or human origin, dehydrated calcium chloride (C7902), thrombin from bovine plasma, Marimastat ((2S, 3R)-N-[(1S)-2,2-dimethyl-1-(methylcarbamoyl)propyl]-N′,2-dihydroxy-3-(2-methylpropyl) butanediamide) were purchased from Sigma-Aldrich (Saint-Louis, MI). Sodium alginate (SA) was obtained from Alfa Aesar (Haverhill, MA). Human plasminogen-depleted fibrinogen was utilized for hydrogel preparation when stated (Merck, Darmstadt, Germany). Aprotinin was purchased from R&D Systems (Minneapolis, MI). All reagents for cell culture were purchased from Gibco (ThermoFisher Scientific, Waltham, MA).

Isolation of human primary fibroblasts

Primary human gingival (HGF) or foreskin (FSF) fibroblasts were isolated from adult tissues. Samples were obtained from healthy donors undergoing surgery under informed consent. Surgical discards were stored in Hanks' Balanced Salt Solution supplemented with 200 U/ml of penicillin, 200 µg/ml of streptomycin and 2.5 µg/ml amphotericin B, later referred to as antibiotics (ABX), and processed within 24 h post-sampling. Biopsies were washed three times in ABX-containing dPBS 1X and incubated overnight at 4°C in trypsin 0.05% to detach epithelium from the CT enzymatically. Subsequently, epithelial sheets were gently separated from CT with fine forceps. Epithelium-free CTs were digested in a mixture of DMEM and 2 mg/ml collagenase IV at 37°C for 1 h and vortexed vigorously every 15 min. HGF primary cultures were also kindly gifted by Dr Philippe Lesclous (Université de Nantes, CHU Hôtel Dieu, INSERM U1229, RMeS). FSF were isolated from fresh biopsies. Briefly, after mechanical removal of the

hypodermis and deep dermis, samples were cut into pieces of 4 mm^2 and incubated 2 h at 37°C in dispase 1X (Invitrogen, Cergy Pontoise France). Epidermis and dermis were dissociated with forceps. Dermal pieces were incubated in RPMI supplemented with 10% FBS in 24-well plates under standard cell culture conditions with ABX. Culture medium was replaced every 2–3 days until FSF migrated out and started to proliferate, usually between day 10 and 14. At confluency, FSF were harvested and cultivated in culture flasks or frozen until use.

Cell culture

HGF, FSF and embryonic lung fibroblasts MRC-5 (RD-Biotech, Besançon, France) were expanded in DMEM supplemented with, 10% FBS, 2 mM L-glutamine and ABX. Cells were cultured in a humidified incubator at 37°C in 5% CO_2. Medium was changed every 2–3 days and cell passages were carried out using a TrypLE Express solution (Gibco). Human TERT-immortalized gingival fibroblasts (hTERT-HGF, CRL-4061, ATCC, London, United Kingdom) were cultivated according to the manufacturer's instructions.

In-gel 3D cell culture

GAF was formulated as previously described by Pourchet et al. (2017). Briefly, GL, SA and FBG were dissolved in 0.9% NaCl at 37°C. Alternatively, GL/SA- or FBG-based hydrogels were obtained by mixing the respective compounds with MRC-5 cells. In all hydrogel formulations, cells were seeded at 1×10^6 cells/mL as described elsewhere (Almela et al., 2016; Pourchet et al., 2017). Equivalent cell quantities were seeded onto cell culture treated 6-well plates as 2D culture controls. All hydrogel formulations were poured into 12-well, 3 µm pore-sized PET membrane culture inserts (Falcon, Corning, NY). Crosslinking of GAF and GL/SA gels was performed by incubating the conditions for 30 min at 25°C in 100 mM $CaCl_2$ (GL/SA gels) and an additional 20 U/mL of thrombin (GAF). FBG gels were produced by mixing thrombin solution to the FBG and immediately poured into the inserts. All gels were washed in 0.9% NaCl and subsequently placed under standard cell culture conditions.

Gel degradation assessment

Gel degradation was assessed by measuring white light diffusion through manually-deposited GAF cast in culture inserts (3 mm thick). The experimental setup was made of a LED light source (4000 K) and a digital microscope (Dino-Lite, Taiwan) as an image collector. Mean grey values of five separate regions of interest (ROIs) of each gel were normalized over DMEM alone (set as 100% degradation) or GAF without cells (set as no degradation). The results are displayed as the percentage of degradation. Proteasomal inhibition was performed on MRC-5-laden gels using aprotinin (20 or 40 µg/ml) or Marimastat (100 µM). MRC-5 cells were resuspended in NaCl 0.9% containing tested drugs and seeded in GAF at 1×10^6 cells/mL. Culture medium was supplemented with tested drugs as well for the duration of the assay. Degradation was assessed after 48 h of culture at 37°C, 5% CO_2 unless otherwise stated.

Gene expression analysis

2D-cultured cells were detached using TrypLE Express and pelleted by centrifugation. Total RNA extraction was performed on cell pellets with TRIzol Reagent (Invitrogen) according to the manufacturer's guidelines. RNA precipitation was performed overnight at −20°C, with absolute ethanol. Quality of total RNAs was determined by absorbance ratios at 260 nm/280 nm using a NanoDrop 2000 spectrophotometer (ThermoFisher). Single-stranded cDNA synthesis was performed from 1 µg of RNA with M-MLV reverse transcriptase (ThermoFisher Scientific). Reverse transcription (RT) was performed using the following thermocycling conditions: 72°C for 10 min, 37°C for 1 h and −20°C for storage until use. Quantitative PCR amplifications were performed on a Viia7 thermal cycler (ThermoFisher Scientific) in 10 µl reaction mix containing 5 µl of Taqman Buffer 2X, 0.5 µl of probes, 2.5 µl of sterile water and 2 µl sample diluted 1:5 in sterile water. Expression level of genes coding for Epidermal growth factor receptor (*EGFR*), Vimentin (*VIM*), S100 calcium binding protein A4 (*S100A4*), Fibroblast Activation Protein Alpha (*FAP*), Short stature homeobox 2 (*SHOX-2*), Thy-1 cell surface antigen (*THY-1*), amine oxidase, copper containing 3 (*AOC-3*), α-smooth muscle actin (*ACTA2*), platelet-derived growth factor receptor A (*PDGFRA*) and type I collagen (COL1A1) (Thermo Fisher, Waltham, Massachusetts) was investigated. Probe references, amplicon sizes and target genes are listed in Supplementary Table S1. The housekeeping gene *GAPDH* (Glyceraldehyde 3-phosphate dehydrogenase) was used as a reference gene. All runs were performed in duplicates.

Secreted protease analysis

After 48 h, supernatants from MRC-5 and hTERT-HGF 2D and 3D cultures were harvested, pooled and filtered through a 100 µm filter (3D condition). Supernatants were centrifuged at 2500 rpm for 5 min to remove insoluble material and stored at −80°C until use. Gels without cells or containing hTERT-HGF were incubated with supernatants from 3D MRC-5 cultures (condition medium, MRC-5 CM) when required. Soluble protease expression profile of MRC-5 and hTERT-HGF 2D and 3D conditions were performed using a Human Protease

Array kit according to the manufacturer's guidelines (R&D Systems, Minneapolis, MI). Images were acquired on a LAS-4000 Fujifilm imager and analyzed after subtraction of background using "Protein Array Analyzer" plugin in (Carpentier and Henault, 2010) ImageJ software. The mean pixel density of analyte spots was normalized on reference spots (100%) and negative controls (0%) mean pixel density for each membrane. Results are expressed as Mean Pixel Density (MPD) ± SD. The threshold for significance was inferred from background values and set up at 15%.

Confocal imaging of GL/SA and fibrinogen hydrogels

GL/SA and FBG gels were stained using calcein AM (04511, Supelco, Bellefonte, Pennsylvania, United States) according to manufacturer's instructions. Each sample was placed on a coverslip and subsequently imaged using a Nikon A1-Rsi confocal microscope equipped with Nikon Plan Fluor 10×0.30 NA objective. Image stacks were acquired and treated using NIS-Elements AR software. All acquisitions were performed using the same parameters. Poisson shot noise was removed using the deep learning *Denoise* algorithm. Images are represented as a volume view using Depth Coded Alpha Blending (color gradient perpendicular to the Z-stacks).

Statistical analysis

Statistical analyses were performed by GraphPad Prism 8. *p*-values below 0.05 were considered as statistically significant. Results are expressed as mean ± SD. For degradation assays and proteome profile analysis, two-way ANOVA tests were used. Comparison of cell types using RT-qPCR was conducted by the Kruskal–Wallis test.

Results

Fibroblasts display different abilities to degrade the gelatin/alginate/fibrin hydrogel

In order to fabricate a stable model of CTE to support further viral infection studies we first sought to characterize appropriate primary fibroblasts or immortalized fibroblastic cell lines of various origins, namely HGF and hTERT-HGF (oral mucosa), FSF (foreskin) and MRC-5 cells (embryonic lung). To that purpose, each cell type was seeded in a GAF hydrogel and immersed in culture medium for 48 h. Gel stability was then monitored by quantifying transmitted white light through hydrogels by image analysis thanks to a home-made image collection system (Figure 1). We observed that GAF alone, or containing hTERT-HGF and FSF showed no degradation for at least 48 h in culture. Conversely, MRC-5 cells and HGF demonstrated a rapid degradation compared to the cell-free control (Figure 2A). We wondered whether these differences in GAF degradation abilities between cell types could be linked to different gene expression known to segregate between resting and activated fibroblasts or even myofibroblastic cells like cancer-associated fibroblasts (CAFs), all being known to have quite distinct ECM-degradation abilities. The expression of *EGFR, VIM, FAP, THY-1, S100A4, SHOX-2, AOC-3, ACTA2, PDGFRA*, and *COL1A1* in HGF, FSF, hTERT-HGF and MCR-5 was assessed (Figure 2B; Supplementary Figure S1). The four cell types express moderate to high levels of *COL1A1, VIM, THY-1* and *PDGFRA*. Conversely, they all express low amounts of *AOC-3* and *FAP* RNAs, typical of myofibroblasts or CAFs. Both observations confirmed a well-established resting or weakly activated fibroblast signature. Significant differences were noted between HGF and MRC-5 for *ACTA-2* or in *EGFR* differential expression between primary and hTERT-immortalized HGF but without obvious correlation with their GAF-degradation status. Interestingly, *SHOX-2* was shown to be expressed at higher levels in cells unable to degrade hydrogels, the FSF and hTERT-HGF (Figure 2B; Supplementary Figure S1). Altogether, these results demonstrated that the four tested cell types harbor a resting fibroblast signature but no clear RNA expression profile compatible with an ECM degradation program.

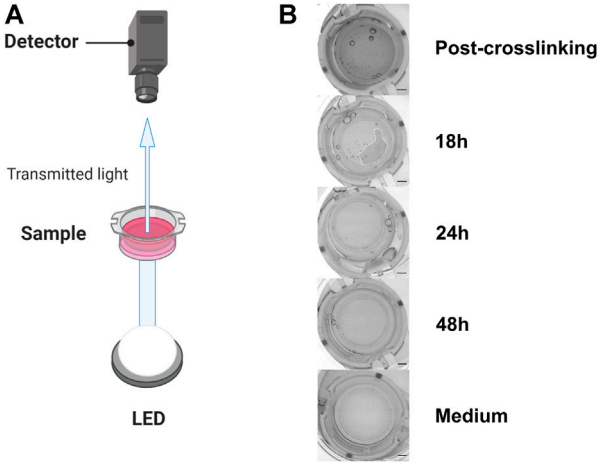

FIGURE 1
Experimental setup to evaluate GAF degradation **(A)**. **(B)** From top to bottom, typical images of culture inserts containing GAF with MRC-5 cells right after crosslinking (Post-crosslinking), 18 (partial GAF degradation, degradation foci are visible), 24 and 48 h post-crosslinking showing the rapid GAF degradation kinetics and without hydrogel (Medium). Scale bar, 2 mm. Created with BioRender.com.

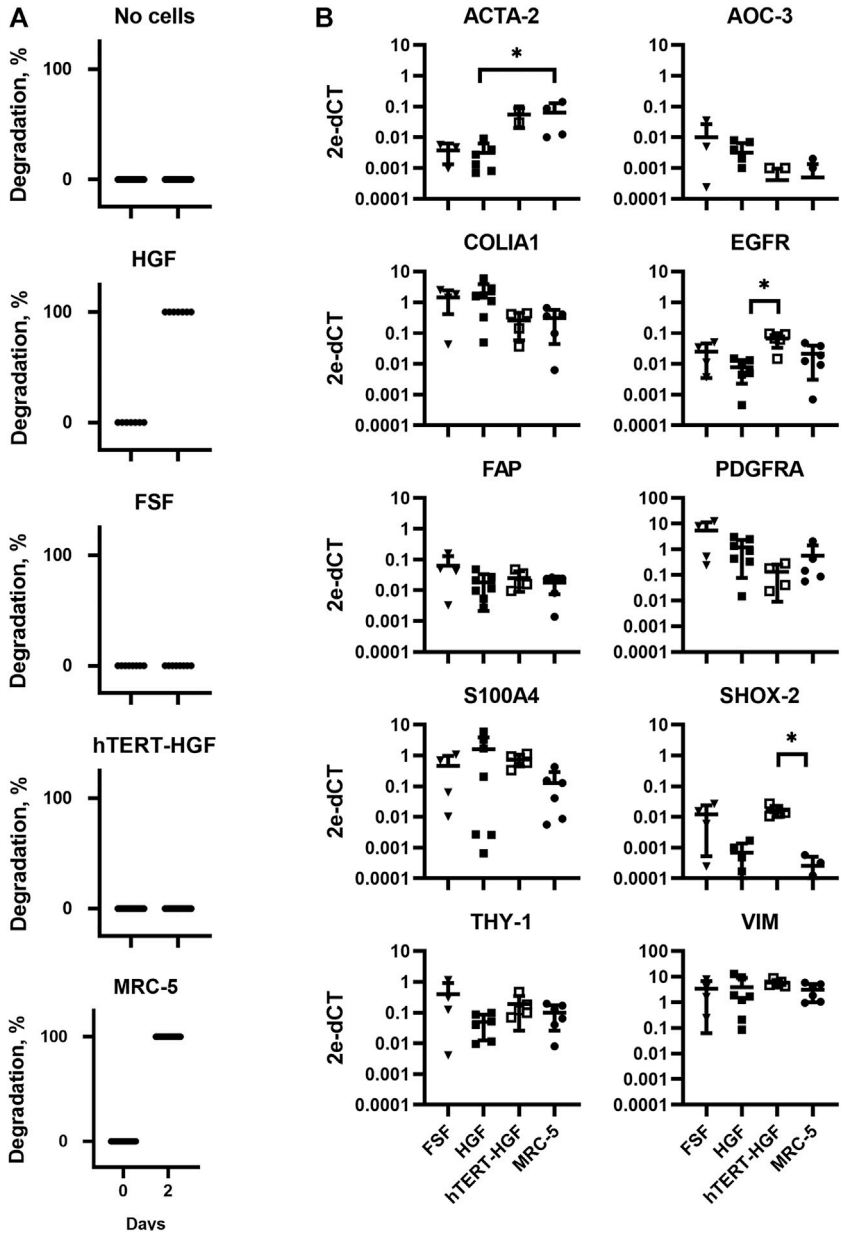

FIGURE 2
Assessment of GAF degradation by HGF, FSF, immortalized HGF (hTERT-HGF) and MRC-5 cells two days post-crosslinking. **(A)** Degradation at day zero, i.e., right after GAF crosslinking, is the non-degradation control for each cell type. Individual values are plotted ($n \leq 16$). **(B)** Gene expression analysis in FSF, HGF, hTERT-HGF and MRC-5 cells for ACTA-2, AOC-3, FAP, EGFR, COLIA1, THY-1, PDGFRA, SHOX-2 and S100A4 genes in standard 2D in vitro cultures by RT-qPCR. HGF and FSF were isolated from three independent donors; mean values are displayed for all samples. Values were normalized on RFPL0. Statistically significant results were marked by one or several asterisks according to the level of significance: *$p < 0.05$; Kruskal-Wallis tests.

MRC-5 cells degrade fibrin-based hydrogels

To figure out why MCR-5 cells were actively degrading GAF hydrogels, we first investigated which component of the GAF was targeted during degradation. GL provides stability during the formulation of the hydrogel but has been shown to progressively leak out of the hydrogel at least for low-molecular weight GL fractions whereas SA and FBG provide a dual structural network. As some fibroblasts are known to exhibit gelatinase or fibrinolytic activities, MRC-5 were seeded in either GL/SA (10:0.5%) or 2% FBG 3D scaffolds. Confocal 3D reconstructions showed that both

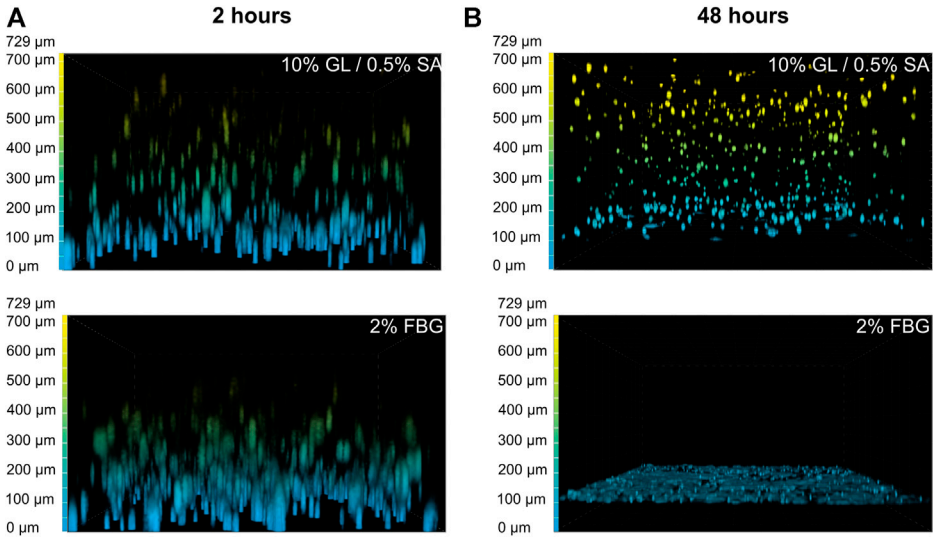

FIGURE 3
GAF degradation by MRC-5 cells results from fibrin network disruption. MRC-5 cell-seeded GL/SA or FBG crosslinked matrices in culture inserts were analyzed by confocal microscopy (×10 objective) after 2 h **(A)** or 24 h **(B)**. Cells were labeled with calcein AM prior to image acquisition. Images are represented as false-colored by Depth Coded Alpha Blending on NIS-Elements AR, i.e., blue-colored cells are close or adherent to the membrane of culture inserts while yellow-colored cells are the most distant.

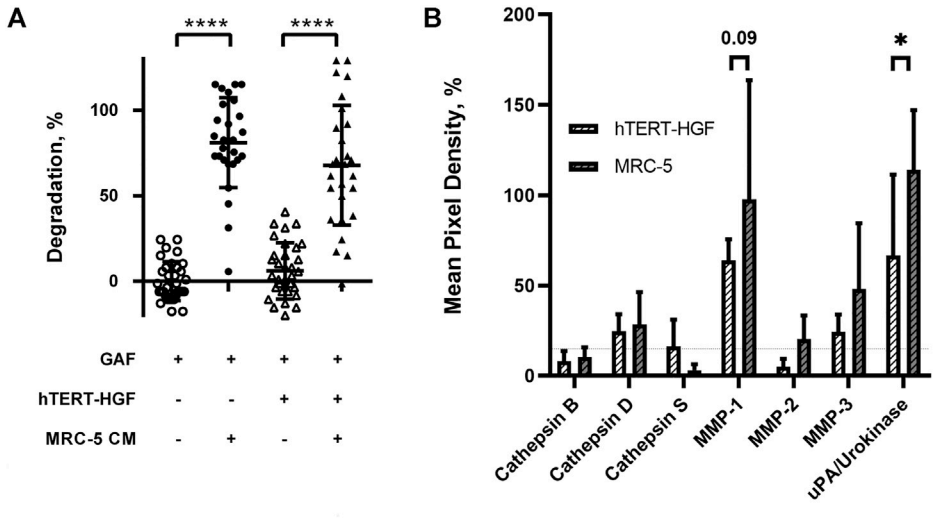

FIGURE 4
Fibrinolytic proteases are released in MRC-5 and hTERT-HGF culture supernatants. **(A)** MRC-5 conditioned medium or MCR-5 CM promotes GAF degradation with (triangle) or w/o hTERT-HGF (circle). Degradation was assessed at 72 h by image analysis of light transmission as described in Figure 1 and Materials and Methods. **(B)** Secreted serine proteases analyses in culture medium of 3D-cultured hTERT-HGF (dashed white) and MRC-5 cells (dashed gray). Values are represented as percentages of Mean Pixel Density ± SD in positive controls. Threshold was set at 15% (horizontal thin dashed line). Statistically significant results were marked by one or several asterisks according to the level of significance: *$p < 0.05$, ***$p < 0.001$ and ****$p < 0.0001$; two-way ANOVA tests.

GL/SA and FBG hydrogels contained fluorescent-labeled cells homogeneously spreading throughout the gel volume, i.e., from the membrane up to approximately 700 µm in-gel towards the hydrogel surface in the insert, at 2 hours post-seeding, suggesting both were properly cross-linked (Figure 3A). After 48 h in culture, GL/SA embedded cells display similar pattern whereas

in fibrin gels, cells were all confined to the insert membrane surface (Figure 3B). These data demonstrated that MRC-5 cells degrade only fibrin hydrogels within two days leading to cell sedimentation. We assumed this was also the case in GAF although we did not prove it directly in this work.

MRC-5 cells secrete fibrinolytic serine proteases to degrade gelatin/alginate/fibrin hydrogels

We then investigated whether the degradation was caused by soluble factors or cell interaction with the surrounding environment. Forty-eight-hour 3D MRC-5 culture supernatant, namely MRC-5 conditioned medium (CM) was collected and added to cell-free or hTERT-HGF-containing GAF scaffolds, both harboring no significant difference. After a 72 h incubation with CM, GAF and hTERT-HGF-containing gels underwent degradation (80.96 ± 26.27% and 67.79 ± 34.96%) demonstrating that CM contained fibrinolytic secreted factors (Figure 4A). No difference were seen between with or w/o hTER-HGF conditions suggesting that CM was the only cause for degradation. The individual value distributions reflect the heterogeneity in the ability to degrade GAF. To characterize the soluble factors involved, 2D and 3D culture supernatants from MRC-5 and hTERT-HGF were analyzed using specific antibody coated nitrocellulose membranes allowing for the detection of various secreted proteases. Mean Pixel Intensities (MPDs) were obtained from the analysis of digitalized images of several membranes. Data were normalized on negative and positive controls to infer the amount of secreted proteases through MPD values displayed in Figure 4B (and Supplementary Table S2). MPDs for all considered proteases in 3D-culture of MRC-5 cells in-gel tended to be or were superior to those of hTERT-HGF 3D supernatants, except for cathepsin S (3.1 ± 3.3% and 16.3 ± 14.7%, respectively), the most expressed being MMP-1, MMP-3 and urokinase for hTERT-HGF and MRC-5 cells (63.9 ± 11.6 vs. 97.7 ± 65.8, 24.4 ± 9.6 vs. 48.1 ± 36.4 and 66.7 ± 44.8 vs. 114 ± 33.1, respectively), all three of which are known to be directly or indirectly involved in fibrinolysis (Kluft, 2003; Lijnen, 2006). Urokinase expression was statistically higher in MRC-5 3D supernatant then hTERT-HGF 3D supernatant and MMP-1 tended to be higher (p-value 0.09). To compensate the non-significant observed differences, we investigated the dynamic changes in protease secretion that may occur when converting 2D cultures into a 3D environment. To that purpose we compared protease secretion in 2D vs. 3D culture supernatants. Interestingly, hTERT-HGF displayed a decreased ability to secrete all considered proteases with significant decrease in levels for MMP-1 (122.3 ± 59.2% to 63.9 ± 11.6%) and MMP-2 (70.5 ± 13.4% to 5.1 ± 4.4%) except for urokinase (2.9 ± 2.6% to 66.7 ± 44.8%) when moved to in-gel cultures (Supplementary Figure S2). Similarly, MRC-5 cells tended to secrete more of them in 3D conditions (Supplementary Figure S2) with significant decrease of gelatinase MMP-2 levels (73.2 ± 27.8% and 20.4 ± 13.0%) but no consequence on GAF degradation documented in that setting. Altogether, these results suggested that 2D cultures secreted large amounts of proteases with fibrinolytic activities like urokinase and possibly MMP-1- while 3D-cultured MCR-5 cells promoted in turn the fibrin degradation of GAF hydrogels.

Simultaneous targeting of plasmin and matrix-metalloproteinases activities prevent fibrin degradation

Based on the secreted protease profiling of MRC-5-containing degraded scaffolds we next evaluated whether we could slow down GAF degradation. Urokinase acts on plasmin activation by cleaving its precursor, plasminogen, and a well-known contaminant of FBG extracted from bovine and human plasmas (Markus and Ambrus, 1960; Yaron et al., 2021) (Figure 5). We compared the stability of MRC-5 cell-containing GAFs prepared with bovine, human and plasminogen-depleted human FBGs. None of them remained stable after a 48-h incubation (85.5% ± 11.4%, 94.7 ± 42.11% and 64.8% ± 35.9% degradation, respectively). Noticeably, both human FBGs displayed heterogeneous degradation compared to bovine FBG with no clear explanation, all three exhibiting similar activities ranging between 90% and 95% clottable protein contents (Figure 6). Moreover, plasminogen depletion significantly decreased degradation (up to 29.8% ± 4.5% reduction). Then, we tested the aprotinin, a broad serine protease inhibitor, to counteract the degradation process. At 20 μg/ml, inhibition of degradation was observed only when used with human FBG (38.8% ± 5.0% reduction) and more potent with plasminogen-depleted human FBG (42.8 ± 5.0% reduction). As expected, at a higher dose (40 μg/ml), aprotinin inhibited GAF degradation (39.5% ± 7.6% for bovine FBG, 16% ± 14.8% for human FBG and 8.0% ± 11.5% plasminogen-depleted human FBG), demonstrating a dose-effect of aprotinin on fibrin degradation. To further increase evidence that plasmin and fibrinolytic MMPs were involved in GAF degradation, we next assessed the addition of Marimastat to plasminogen-depleted FBG-based GAF for 48 h. Results showed that the use of Marimastat did not significantly improve the stability of hydrogel using plasminogen-depleted human FBG (Figure 6). These data demonstrated significant and consistent inhibition of GAF degradation by aprotinin. Moreover, the use of plasminogen-

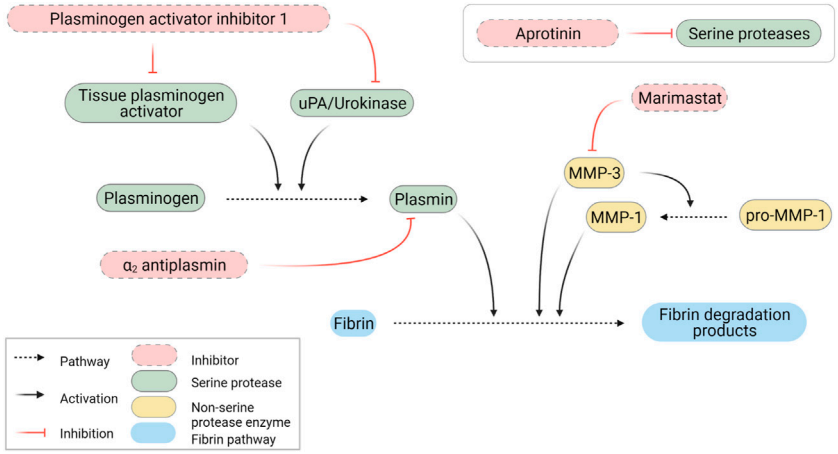

FIGURE 5
Schematic representation of fibrinolytic pathways. Created with BioRender.com.

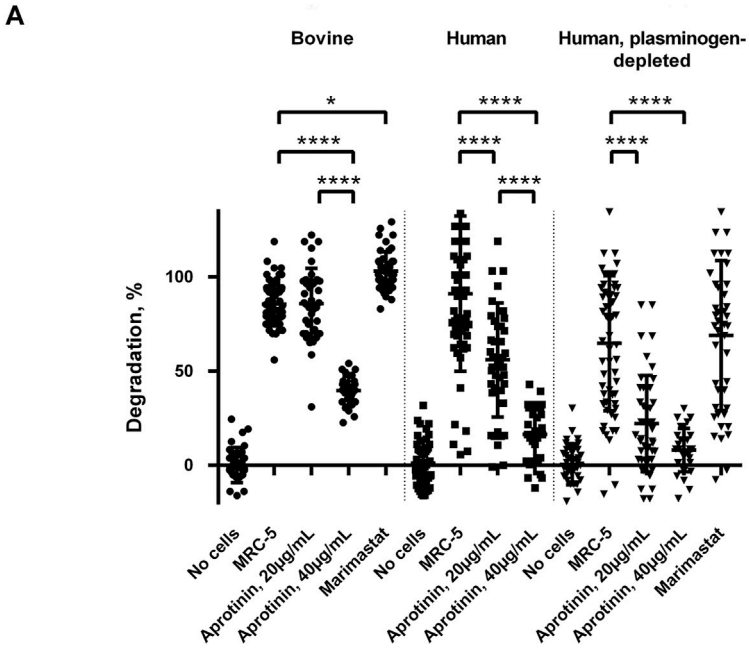

B

	Bovine *vs* Human	Bovine *vs* Plasminogen-depleted human	Human *vs* Plasminogen-depleted human
MRC-5	ns	***	****
Aprotinin, 20µg/mL	****	****	****
Aprotinin, 40µg/mL	*	****	ns
Marimastat	N.A.	****	N.A.

FIGURE 6
GAF degradation inhibition by MMPs and/or plasmin inhibitors or using plasminogen-depleted FBG. **(A)** MRC-5 cell-containing GAF prepared with either bovine (circle), human (square) or human plasminogen-depleted FBG (triangle) were treated with aprotinin (20 µg/mL or 40 µg/mL) or Marimastat (100 µM). GAF degradation was assessed as described in Materials and Methods section. Individual values are plotted, $n \geq 30$. Statistically significant results were marked by one or several asterisks according to the level of significance: *$p < 0.05$, **$p < 0.01$, ***$p < 0.001$ and ****$p < 0.0001$; Tukey's multiple comparisons tests. **(B)** Statistical significance of the comparisons between various experimental conditions shown in **Panel A**.

depleted human FBG has shown some reduction in GAF degradation compared to human FBG suggesting it could be used without aprotinin to control the degradation of gels embedding cells with low or no fibrinolytic activities.

Discussion

In tissue engineering, choosing appropriate cell types is of paramount importance as suggested by Langer and Vacanti several decades ago (Langer and Vacanti, 1993). This was also highlighted more recently by Manita et al. (2021) by focusing on the impact of cells on engineered skin stability and composition changes over time. Achieving assembly of tissues containing multiple cell types could be even more challenging due to intercellular cross-talk or interference between 3D matrix components and cells. In this study, we identified cellular determinants of fibrin network degradation in a blended biomaterial made of gelatin, sodium alginate and fibrin or GAF by transcriptionally distinct human fibroblastic cell types exhibiting a functional heterogeneity towards fibrin degradation. Previous work has described the use of GAF to support normal skin fibroblast (Reijnders et al., 2015; Pourchet et al., 2017) 3D cultures without degradation, highlighting the necessity to select non-degradative cells as a first option.

Fibrin degradation has long been described as a critical player in engineered tissue remodeling (Neuss et al., 2010). On the other hand, fibrinolysis impairs 3D matrix stability, thus limiting the use of fibrin with cells that actively remodel or secrete factors that promote degradation, like primary gingival or dermal fibroblasts Lorimier et al. (1996). Here, we demonstrated that degradation was due to an enhanced secretion of fibrinolytic MMPs and urokinase by GAF-embedded MRC-5 cells in line with previous studies. Interestingly, Ahmed et al. (2007) reported a direct upregulation of MMPs when 2D cell cultures were shifted to 3D. Here, we showed that the MRC-5 degradative potential towards GAF was mediated by soluble factors secreted in the culture medium and active on cell-free as well as on hTERT-HGF-laden GAF within the first 24 h. These results confirmed a previous observation showing that MRC-5 CM can increase invasion and migration capacities of the MHCC-LM3 cell line, a hepatocellular carcinoma, through a non-classical epithelial-to-mesenchymal transition pathway (Ding et al., 2015). Here, we showed a possible link between the fibrinolytic activity of various fibroblastic cell lines and the *SHOX-2* gene expression levels, i.e., low expression being observed in highly degradative cells, namely MRC-5 and primary HGF. Interestingly, Hsia and colleagues demonstrated that *SHOX-2* expression is high to moderate in skin fibroblasts or activated fibroblasts respectively, but almost absent from myofibroblasts in cancer and normal tissues (Hsia et al., 2016). Although a high *SHOX-2* expression was correlated to enhanced migration and invasion capacities for breast cancer cells through a SHOX-2/STAT3/WASF3 axis, no relation has been established between the *SHOX-2* expression and fibrinolysis (Teng et al., 2021). In this work, we did not compare the *SHOX-2* expression of the tested cell lines to myofibroblasts. However, we noticed a lower *SHOX-2* expression in fibrinolytic cells. Further studies are required to establish whether *SHOX-2* plays a role in fibrinolysis.

In this study, MRC-5 cells and primary HGF were shown to degrade GAF through fibrinolysis induction. Fibrinolysis is mediated through serine proteases, mainly MMP-3 and plasmin generated from urokinase- or tissue plasminogen activator (tPA)-activated plasminogen. Several studies have investigated the possibility to extend the stability of adipose-stromal cell (Xu et al., 2009) or HeLa cell-laden (Zhao et al., 2014) fibrin-containing matrices using aprotinin, a non-specific protease inhibitor targeting plasmin, tPA, urokinase and MMPs among other proteases. Aprotinin was previously used alone or in combination with galardin, a wide spectrum MMPs inhibitor (Ahmed et al., 2007). Ye et al. demonstrated that cardiac myofibroblasts would degrade fibrin matrices in two days (Ye et al., 2000) while no degradation was observed for a month using aprotinin at 15–20 µg/ml (Lesman et al., 2011). Similar results were also reported by Thompson et al. (2013) on a cardiac tissue model. Studies focusing on Duchenne muscular dystrophy (Gerard et al., 2012), metabolic syndrome (Xu et al., 2010) or 3D-bioprinted tissues with matrix-remodeling cells (Kang et al., 2016) reported addition of aprotinin to preserve hydrogel or bioink integrity in the course of long-lasting experiments without investigating potential phenotypic or functional changes for cells. Aprotinin also showed efficacy in blocking the degradation of electrospun fibrin fibers (McManus et al., 2006) as well as cell-laden blended hydrogels to obtain various tissues like cartilage (Lee et al., 2005), cornea (Foroushani et al., 2021), retina (Gandhi et al., 2018) and CNS stroma (Seyedhassantehrani et al., 2016). Finally, molar excess of aprotinin has proven efficacy in slowing down fibrinolysis of commercial homologous fibrin surgical sealants made of human plasma-purified FBG and activated factor XIII cross-linked with thrombin and calcium ions (Buchta et al., 2005). Ahmann and colleagues previously proposed defined concentrations of ε-aminocaproic acid (ACA) to achieve similar results (Ahmann et al., 2010). ACA inhibits urokinase (Bakker et al., 1995) and plasmin (Anonick et al., 1992) and has been widely used also in tissue engineering to slow down fibrin degradation (Ramaswamy et al., 2019). With regards to the broad usage of aprotinin or ACA to stabilize engineered fibrin-based matrices, very few adverse effects were reported to date when inhibitor concentrations are optimized. One example was brought by Kim et al. (2015) by showing that aprotinin concentrations above 0.05 TIU/ml allowed HS-5 cells, a human bone marrow

stromal cell line, to grow and remodel their fibrin-based matrix further leading to T-cells invasion and establishment of heterotypic cell-to-cell interactions. One exception concerns an observation made by Mühleder et al. (2018) who demonstrated that aprotinin supplementation could impair vessel formation without affecting branching or ECM deposition in an engineered vascular network model. Although few alterations of cellular functions have been documented to date when using aprotinin, we believe that comprehensive studies on the impact of protease inhibitor treatments on various cell types would be necessary to fully estimate their optimal concentrations to limit fibrinolysis without impairing cellular functions.

In addition to aprotinin supplementation to strongly delay GAF degradation, we demonstrated that hTERT-HGF or FSF did not display intrinsic fibrinolytic activity making them suitable for fibroblast embedding in fibrin-based matrices. In association with immortalized gingival keratinocytes, hTERT-HGF were shown to reconstitute a stable full-thickness gingiva (Buskermolen et al., 2016). A similar approach with immortalized cells from skin origin led to the generation of a full-thickness skin equivalent (Reijnders et al., 2015). However, fibroblasts were embedded in collagen-based hydrogels devoid of fibrin in both studies. In this study, we proved that using plasminogen-depleted FBG of human origin allowed for the fabrication of more stable MRC-5-containing hydrogels for at least two days, supporting the idea that plasmin and/or Marimastat-insensitive MMP inhibition leads to slow down fibrinolysis. We have tested broad inhibitor for MMP and serine proteases, however, we did not evaluate the activity of proteases in the supernatant, nor the effect of addition to FCS to the medium in terms on addition of proteases or their possible excess compared to inhibitors quantities. Similar results were obtained by Jarrell et al. (2021) who demonstrated that increasing sodium chloride concentrations up to 250 mM, i.e., hyperosmotic, instead of 150mM, i.e., a physiological concentration, led to transparent fibrin gel formation degrading two to three times slower than controls. However, two limitations were foreseen in the study by Jarrell et al. (2021) when considering to apply this protocol to cell-laden hydrogels. First, hyperosmolar culture media or buffers can cause an osmotic shock leading to a rapid cell shrinkage and associated cell death. Then, surviving cells could undergo substantial transcriptomic changes, as shown for gingival fibroblasts, most notably altering genes whose products are involved in extracellular matrix remodeling potentially leading to undesirable effects (Schroder et al., 2019).

In summary, this study provides new insights to understand mechanisms behind GAF degradation by some human fibroblast sub-types. We confirmed that blocking proteases and plasmin is an efficient way to prevent fibrinolysis which drives GAF degradation. We also proposed to use a combination of plasminogen-depleted FBG and aprotinin to enhance the degradation slow down when utilizing fibrinolytic cells like MRC-5. In conclusion, we believe that our results will contribute to extend possibilities to engineer fibroblast-embedded CTs by emphasizing primarily on the choice for cells with no or low fibrin remodeling properties, and either as primary cultures or immortalized cell lines. HTERT-immortalized cell lines usually present the advantage of supporting long-lasting cultures with rather stable phenotypes. Therefore, they can support genetic modifications, e.g., genome editing, to establish experimental models for basic science and precision medicine.

Data availability statement

The raw data supporting the conclusions of this manuscript will be made available by the authors, without undue reservation.

Author Contributions

All authors listed have made a substantial, direct, and intellectual contribution to the work and approved it for publication. Conceptualization: J-YH, LV and FH; Data curation: EB, LV, J-YH and FH; Formal analysis: EB, FC, LV, J-YH, CM, and FH; Funding acquisition: FH; Investigation: EB, FC, and LV; Methodology: EB, FC, LV, J-YH, CM, and FH; Project administration: J-YH and FH; Supervision: J-YH and FH; Validation: LV, J-YH, and FH; Writing—original draft: EB and FH; Writing—review and editing: LV, J-YH, CM and FH.

Funding

This work received a financial support from the University of Nantes (2018 Transdisciplinary UN call, Eléa Boucard's salary) and the SATT Ouest Valorisation under the MUQUOPRINT designation (no grant number available). The funders had no role in study design, data collection and analysis, decision to publish, or preparation of the manuscript.

Acknowledgments

We thank Philippe Lesclous, Alexandra Cloitre and Boris Halgand for their help in HGF isolation and cells. We acknowledge the MicroPICell facility, Centre Excellence Nikon Nantes, SFR-Santé, INSERM, CNRS, UNIV Nantes, CHU Nantes, Nantes, France, member of the national infrastructure France-Bio Imaging supported by the French National Research Agency (ANR-10-INBS-04).

Conflict of interest

The authors declare that the research was conducted in the absence of any commercial or financial relationships that could be construed as a potential conflict of interest.

Publisher's note

All claims expressed in this article are solely those of the authors and do not necessarily represent those of their affiliated organizations, or those of the publisher, the editors and the reviewers. Any product that may be evaluated in this article, or claim that may be made by its manufacturer, is not guaranteed or endorsed by the publisher.

Supplementary material

The Supplementary Material for this article can be found online at: https://www.frontiersin.org/articles/10.3389/fbioe.2022.920929/full#supplementary-material

References

Ahmann, K. A., Weinbaum, J. S., Johnson, S. L., and Tranquillo, R. T. (2010). Fibrin degradation enhances vascular smooth muscle cell proliferation and matrix deposition in fibrin-based tissue constructs fabricated *in vitro*. *Tissue Eng. Part A* 16, 3261–3270. doi:10.1089/ten.tea.2009.0708

Ahmed, T. A., Griffith, M., and Hincke, M. (2007). Characterization and inhibition of fibrin hydrogel-degrading enzymes during development of tissue engineering scaffolds. *Tissue Eng.* 13, 1469–1477. doi:10.1089/ten.2006.0354

Albouy, M., Desanlis, A., Brosset, S., Auxenfans, C., Courtial, E. J., Eli, K., et al. (2022). A preliminary study for an intraoperative 3D bioprinting treatment of severe burn injuries. *Plastic Reconstr. Surg. - Glob. Open* 10, e4056. doi:10.1097/gox.0000000000004056

Almela, T., Brook, I. M., and Moharamzadeh, K. (2016). Development of three-dimensional tissue engineered bone-oral mucosal composite models. *J. Mat. Sci. Mat. Med.* 27, 65. doi:10.1007/s10856-016-5676-7

Anonick, P. K., Vasudevan, J., and Gonias, S. L. (1992). Antifibrinolytic activities of alpha-N-acetyl-L-lysine methyl ester, epsilon-aminocaproic acid, and tranexamic acid. Importance of kringle interactions and active site inhibition. *Arterioscler. Thromb.* 12, 708–716. doi:10.1161/01.atv.12.6.708

Bakker, A. H., Weening-Verhoeff, E. J., and Verheijen, J. H. (1995). The role of the lysyl binding site of tissue-type plasminogen activator in the interaction with a forming fibrin clot. *J. Biol. Chem.* 270, 12355–12360. doi:10.1074/jbc.270.21.12355

Bonnans, C., Chou, J., and Werb, Z. (2014). Remodelling the extracellular matrix in development and disease. *Nat. Rev. Mol. Cell Biol.* 15, 786–801. doi:10.1038/nrm3904

Buchta, C., Hedrich, H. C., Macher, M., Hocker, P., and Redl, H. (2005). Biochemical characterization of autologous fibrin sealants produced by CryoSeal and Vivostat in comparison to the homologous fibrin sealant product Tissucol/Tisseel. *Biomaterials* 26, 6233–6241. doi:10.1016/j.biomaterials.2005.04.014

Buechler, M. B., Pradhan, R. N., Krishnamurty, A. T., Cox, C., Calviello, A. K., Wang, A. W., et al. (2021). Cross-tissue organization of the fibroblast lineage. *Nature* 593, 575–579. doi:10.1038/s41586-021-03549-5

Buskermolen, J. K., Reijnders, C. M., Spiekstra, S. W., Steinberg, T., Kleverlaan, C. J., Feilzer, A. J., et al. (2016). Development of a full-thickness human gingiva equivalent constructed from immortalized keratinocytes and fibroblasts. *Tissue Eng. Part C. Methods* 22, 781–791. doi:10.1089/ten.tec.2016.0066

Caliari, S. R., and Burdick, J. A. (2016). A practical guide to hydrogels for cell culture. *Nat. Methods* 13, 405–414. doi:10.1038/nmeth.3839

Carpentier, G., and Henault, E. (2010). "Protein array analyzer for ImageJ," in Proceedings of the imageJ user and developer conference, Centre de recherche public henri tudor, 238–240.

Dai, X., Ma, C., Lan, Q., and Xu, T. (2016). 3D bioprinted glioma stem cells for brain tumor model and applications of drug susceptibility. *Biofabrication* 8, 045005. doi:10.1088/1758-5090/8/4/045005

Ding, S., Chen, G., Zhang, W., Xing, C., Xu, X., Xie, H., et al. (2015). MRC-5 fibroblast-conditioned medium influences multiple pathways regulating invasion, migration, proliferation, and apoptosis in hepatocellular carcinoma. *J. Transl. Med.* 13, 237. doi:10.1186/s12967-015-0588-8

Foroushani, Z. H., Mahdavi, S. S., Abdekhodaie, M. J., Baradaran-Rafii, A., Tabatabei, M. R., Mehrvar, M., et al. (2021). A hybrid scaffold of gelatin glycosaminoglycan matrix and fibrin as a carrier of human corneal fibroblast cells. *Mater. Sci. Eng. C* 118, 111430. doi:10.1016/j.msec.2020.111430

Frantz, C., Stewart, K. M., and Weaver, V. M. (2010). The extracellular matrix at a glance. *J. Cell Sci.* 123, 4195–4200. doi:10.1242/jcs.023820

Gandhi, J. K., Manzar, Z., Bachman, L. A., Andrews-Pfannkoch, C., Knudsen, T., Hill, M., et al. (2018). Fibrin hydrogels as a xenofree and rapidly degradable support for transplantation of retinal pigment epithelium monolayers. *Acta Biomater.* 67, 134–146. doi:10.1016/j.actbio.2017.11.058

Gerard, C., Forest, M. A., Beauregard, G., Skuk, D., and Tremblay, J. P. (2012). Fibrin gel improves the survival of transplanted myoblasts. *Cell Transpl.* 21, 127–138. doi:10.3727/096368911x576018

Henrionnet, C., Pourchet, L., Neybecker, P., Messaoudi, O., Gillet, P., Loeuille, D., et al. (2020). Combining innovative bioink and low cell density for the production of 3D-bioprinted cartilage substitutes: A pilot study. *Stem Cells Int.* 2020, 1–16. doi:10.1155/2020/2487072

Hsia, L. T., Ashley, N., Ouaret, D., Wang, L. M., Wilding, J., Bodmer, W. F., et al. (2016). Myofibroblasts are distinguished from activated skin fibroblasts by the expression of AOC3 and other associated markers. *Proc. Natl. Acad. Sci. U. S. A.* 113, E2162–E2171. doi:10.1073/pnas.1603534113

Jarrell, D. K., Vanderslice, E. J., Lennon, M. L., Lyons, A. C., Vedepo, M. C., Jacot, J. G., et al. (2021). Increasing salinity of fibrinogen solvent generates stable fibrin hydrogels for cell delivery or tissue engineering. *PLoS One* 16, e0239242. doi:10.1371/journal.pone.0239242

Kang, H. W., Lee, S. J., Ko, I. K., Kengla, C., Yoo, J. J., Atala, A., et al. (2016). A 3D bioprinting system to produce human-scale tissue constructs with structural integrity. *Nat. Biotechnol.* 34, 312–319. doi:10.1038/nbt.3413

Kim, J., Wu, B., Niedzielski, S. M., Hill, M. T., Coleman, R. M., Ono, A., et al. (2015). Characterizing natural hydrogel for reconstruction of three-dimensional lymphoid stromal network to model T-cell interactions. *J. Biomed. Mat. Res. A* 103, 2701–2710. doi:10.1002/jbm.a.35409

Kinikoglu, B., Damour, O., and Hasirci, V. (2015). Tissue engineering of oral mucosa: A shared concept with skin. *J. Artif. Organs* 18, 8–19. doi:10.1007/s10047-014-0798-5

Kluft, C. (2003). The fibrinolytic system and thrombotic tendency. *Pathophysiol. Haemost. Thromb.* 33, 425–429. doi:10.1159/000083840

Langer, R., and Vacanti, J. P. (1993). Tissue engineering. *Science* 260, 920–926. doi:10.1126/science.8493529

Lebleu, V. S., and Neilson, E. G. 2020. Origin and functional heterogeneity of fibroblasts. *Faseb J.* 34(3):3519–3536. doi:10.1096/fj.201903188R

Lee, C. R., Grad, S., Gorna, K., Gogolewski, S., Goessl, A., Alini, M., et al. (2005). Fibrin-polyurethane composites for articular cartilage tissue engineering: A preliminary analysis. *Tissue Eng.* 11, 1562–1573. doi:10.1089/ten.2005.11.1562

Lesman, A., Koffler, J., Atlas, R., Blinder, Y. J., Kam, Z., Levenberg, S., et al. (2011). Engineering vessel-like networks within multicellular fibrin-based constructs. *Biomaterials* 32, 7856–7869. doi:10.1016/j.biomaterials.2011.07.003

Lijnen, H. R. (2006). Elements of the fibrinolytic system. *FIBRINOGEN XVIth Int. FIBRINOGEN WORKSHOP* 936 (1), 226–236. doi:10.1111/j.1749-6632.2001.tb03511.x

Lorentz, K. M., Kontos, S., Frey, P., and Hubbell, J. A. (2010). Engineered aprotinin for improved stability of fibrin biomaterials. *Biomaterials* 32 (2), 430–438. doi:10.1016/j.biomaterials.2010.08.109

Lorimier, S., Gillery, P., Hornebeck, W., Chastang, F., Laurent-Maquin, D., Bouthors, S., et al. (1996). Tissue origin and extracellular matrix control neutral proteinase activity in human fibroblast three-dimensional cultures. *J. Cell. Physiol.* 168, 188–198. doi:10.1002/(sici)1097-4652(199607)168:1<188:aid-jcp23>3.0.co;2-2

Manita, P. G., Garcia-Orue, I., Santos-Vizcaino, E., Hernandez, R. M., and Igartua, M. (2021). 3D bioprinting of functional skin substitutes: From current achievements to future goals. *Pharm. (Basel)* 14, 362. doi:10.3390/ph14040362

Markus, G., and Ambrus, C. M. (1960). Selective inactivation of the plasminogen contaminant in thrombin. *Nature* 188, 582–583. doi:10.1038/188582a0

Mcmanus, M. C., Boland, E. D., Koo, H. P., Barnes, C. P., Pawlowski, K. J., Wnek, G. E., et al. (2006). Mechanical properties of electrospun fibrinogen structures. *Acta Biomater.* 2, 19–28. doi:10.1016/j.actbio.2005.09.008

Merne, M., and Syrjänen, S. (2003). The mesenchymal substrate influences the epithelial phenotype in a three-dimensional cell culture. *Archives Dermatological Res.* 295, 190–198. doi:10.1007/s00403-003-0419-2

Mühleder, S., Pill, K., Schaupper, M., Labuda, K., Priglinger, E., Hofbauer, P., et al. (2018). The role of fibrinolysis inhibition in engineered vascular networks derived from endothelial cells and adipose-derived stem cells. *Stem Cell Res. Ther.* 9, 35. doi:10.1186/s13287-017-0764-2

Naba, A., Clauser, K. R., Ding, H., Whittaker, C. A., Carr, S. A., Hynes, R. O., et al. (2016). The extracellular matrix: Tools and insights for the "omics" era. *Matrix Biol.* 49, 10–24. doi:10.1016/j.matbio.2015.06.003

Neuss, S., Schneider, R. K., Tietze, L., Knuchel, R., and Jahnen-Dechent, W. (2010). Secretion of fibrinolytic enzymes facilitates human mesenchymal stem cell invasion into fibrin clots. *Cells Tissues Organs* 191, 36–46. doi:10.1159/000215579

Okazaki, M., Yoshimura, K., Suzuki, Y., and Harii, K. (2003). Effects of subepithelial fibroblasts on epithelial differentiation in human skin and oral mucosa: Heterotypically recombined organotypic culture model. *Plastic Reconstr. Surg.* 112, 784–792. doi:10.1097/01.prs.0000069710.48139.4e

Pepelanova, I., Kruppa, K., Scheper, T., and Lavrentieva, A. (2018). Gelatin-methacryloyl (GelMA) hydrogels with defined degree of functionalization as a versatile toolkit for 3D cell culture and extrusion bioprinting. *Bioeng. (Basel)* 5, 55. doi:10.3390/bioengineering5030055

Pourchet, L. J., Thepot, A., Albouy, M., Courtial, E. J., Boher, A., Blum, L. J., et al. (2017). Human skin 3D bioprinting using scaffold-free approach. *Adv. Healthc. Mat.* 6, 1–8. doi:10.1002/adhm.201601101

Presland, R. B., and Dale, B. A. (2000). Epithelial structural proteins of the skin and oral cavity: Function in health and disease. *Crit. Rev. Oral Biol. Med.* 11, 383–408. doi:10.1177/10454411000110040101

Ramaswamy, A. K., Sides, R. E., Cunnane, E. M., Lorentz, K. L., Reines, L. M., Vorp, D. A., et al. (2019). Adipose-derived stromal cell secreted factors induce the elastogenesis cascade within 3D aortic smooth muscle cell constructs. *Matrix Biol. Plus* 4, 100014. doi:10.1016/j.mbplus.2019.100014

Reijnders, C. M., van Lier, A., Roffel, S., Kramer, D., Scheper, R. J., Gibbs, S., et al. (2015). Development of a full-thickness human skin equivalent *in vitro* model derived from TERT-immortalized keratinocytes and fibroblasts. *Tissue Eng. Part A* 21, 2448–2459. doi:10.1089/ten.tea.2015.0139

Reynolds, G., Vegh, P., Fletcher, J., Poyner, E. F. M., Stephenson, E., Goh, I., et al. (2021). Developmental cell programs are co-opted in inflammatory skin disease. *Science* 371, eaba6500. doi:10.1126/science.aba6500

Schroder, A., Nazet, U., Neubert, P., Jantsch, J., Spanier, G., Proff, P., et al. (2019). Sodium-chloride-induced effects on the expression profile of human periodontal ligament fibroblasts with focus on simulated orthodontic tooth movement. *Eur. J. Oral Sci.* 127, 386–395. doi:10.1111/eos.12643

Seyedhassantehrani, N., Li, Y., and Yao, L. (2016). Dynamic behaviors of astrocytes in chemically modified fibrin and collagen hydrogels. *Integr. Biol.* 8, 624–634. doi:10.1039/c6ib00003g

Skardal, A., Devarasetty, M., Kang, H. W., Mead, I., Bishop, C., Shupe, T., et al. (2015). A hydrogel bioink toolkit for mimicking native tissue biochemical and mechanical properties in bioprinted tissue constructs. *Acta Biomater.* 25, 24–34. doi:10.1016/j.actbio.2015.07.030

Skardal, A., Smith, L., Bharadwaj, S., Atala, A., Soker, S., Zhang, Y., et al. (2012). Tissue specific synthetic ECM hydrogels for 3-D *in vitro* maintenance of hepatocyte function. *Biomaterials* 33, 4565–4575. doi:10.1016/j.biomaterials.2012.03.034

Stecco, C., Hammer, W., Vleeming, A., and de Caro, R. (2015). *Connective tissues*. Elsevier. Amsterdam, Netherlands.

Teng, Y., Loveless, R., Benson, E. M., Sun, L., Shull, A. Y., Shay, C., et al. (2021). SHOX2 cooperates with STAT3 to promote breast cancer metastasis through the transcriptional activation of WASF3. *J. Exp. Clin. Cancer Res.* 40, 274. doi:10.1186/s13046-021-02083-6

Thomson, K. S., Dupras, S. K., Murry, C. E., Scatena, M., and Regnier, M. (2014). Proangiogenic microtemplated fibrin scaffolds containing aprotinin promote improved wound healing responses. *Angiogenesis* 17, 195–205. doi:10.1007/s10456-013-9388-z

Thomson, K. S., Korte, F. S., Giachelli, C. M., Ratner, B. D., Regnier, M., Scatena, M., et al. (2013). Prevascularized microtemplated fibrin scaffolds for cardiac tissue engineering applications. *Tissue Eng. Part A* 19, 967–977. doi:10.1089/ten.tea.2012.0286

Tsukui, T., Sun, K. H., Wetter, J. B., Wilson-Kanamori, J. R., Hazelwood, L. A., Henderson, N. C., et al. (2020). Collagen-producing lung cell atlas identifies multiple subsets with distinct localization and relevance to fibrosis. *Nat. Commun.* 11, 1920. doi:10.1038/s41467-020-15647-5

Urciuolo, F., Casale, C., Imparato, G., and Netti, P. A. (2019). Bioengineered skin substitutes: The role of extracellular matrix and vascularization in the healing of deep wounds. *J. Clin. Med.* 8, 2083. doi:10.3390/jcm8122083

Vidal, L., Kampleitner, C., Krissian, S., Brennan, M. A., Hoffmann, O., Raymond, Y., et al. (2020). Regeneration of segmental defects in metatarsus of sheep with vascularized and customized 3D-printed calcium phosphate scaffolds. *Sci. Rep.* 10, 7068. doi:10.1038/s41598-020-63742-w

Xu, M., Wang, X., Yan, Y., Yao, R., and Ge, Y. (2010). An cell-assembly derived physiological 3D model of the metabolic syndrome, based on adipose-derived stromal cells and a gelatin/alginate/fibrinogen matrix. *Biomaterials* 31, 3868–3877. doi:10.1016/j.biomaterials.2010.01.111

Xu, M., Yan, Y., Liu, H., Yao, R., and Wang, X. (2009). Controlled adipose-derived stromal cells differentiation into adipose and endothelial cells in a 3D structure established by cell-assembly technique. *J. Bioact. Compatible Polym.* 24, 31–47. doi:10.1177/0883911509102794

Yaron, J. R., Zhang, L., Guo, Q., Haydel, S. E., and Lucas, A. R. (2021). Fibrinolytic serine proteases, therapeutic serpins and inflammation: Fire dancers and firestorms. *Front. Cardiovasc. Med.* 8, 648947. doi:10.3389/fcvm.2021.648947

Ye, Q., Zünd, G., Benedikt, P., Jockenhoevel, S., Hoerstrup, S. P., Sakyama, S., et al. (2014). Fibrin gel as a three dimensional matrix in cardiovascular tissue engineering. *Eur. J. Cardiothorac. Surg.* 17 (5), 587–591. doi:10.1016/s1010-7940(00)00373-0

Yi, K., Li, Q., Lian, X., Wang, Y., and Tang, Z. (2022). Utilizing 3D bioprinted platelet-rich fibrin-based materials to promote the regeneration of oral soft tissue. *Regen. Biomater.* 9, rbac021. doi:10.1093/rb/rbac021

Zhao, Y., Yao, R., Ouyang, L., Ding, H., Zhang, T., Zhang, K., et al. (2014). Three-dimensional printing of Hela cells for cervical tumor model *in vitro*. *Biofabrication* 6, 035001. doi:10.1088/1758-5082/6/3/035001

frontiers | Frontiers in Bioengineering and Biotechnology

TYPE Original Research
PUBLISHED 25 July 2022
DOI 10.3389/fbioe.2022.945149

OPEN ACCESS

EDITED BY
Dimitrios Stamatialis,
University of Twente, Netherlands

REVIEWED BY
Massimo Mastrangeli,
Delft University of Technology, Netherlands
Franck Halary,
Université de Nantes, France

*CORRESPONDENCE
Silvia Scaglione,
silvia.scaglione@cnr.it

SPECIALTY SECTION
This article was submitted to Tissue Engineering and Regenerative Medicine, a section of the journal Frontiers in Bioengineering and Biotechnology

RECEIVED 16 May 2022
ACCEPTED 29 June 2022
PUBLISHED 25 July 2022

CITATION
Marzagalli M, Pelizzoni G, Fedi A, Vitale C, Fontana F, Bruno S, Poggi A, Dondero A, Aiello M, Castriconi R, Bottino C and Scaglione S (2022), A multi-organ-on-chip to recapitulate the infiltration and the cytotoxic activity of circulating NK cells in 3D matrix-based tumor model.
Front. Bioeng. Biotechnol. 10:945149.
doi: 10.3389/fbioe.2022.945149

A multi-organ-on-chip to recapitulate the infiltration and the cytotoxic activity of circulating NK cells in 3D matrix-based tumor model

Monica Marzagalli [1], Giorgia Pelizzoni[2], Arianna Fedi [3], Chiara Vitale [3,4], Fabrizio Fontana [5], Silvia Bruno [4], Alessandro Poggi [6], Alessandra Dondero [4,7], Maurizio Aiello [3], Roberta Castriconi [4,7], Cristina Bottino [4,7] and Silvia Scaglione [3]*

[1]React4life S.r.l, Genoa, Italy, [2]Department of Biotechnology and Bioscience, University of Milano-Bicocca, Piazza Della Scienza, Milan, Italy, [3]National Research Council, CNR-IEIIT, Genoa, Italy, [4]Department of Experimental Medicine (DIMES), University of Genoa, Genoa, Italy, [5]Department of Pharmacological and Biomolecular Sciences (DiSFeB), University of Milan, Milan, Italy, [6]Molecular Oncology and Angiogenesis Unit, IRCCS Ospedale Policlinico San Martino, Genoa, Italy, [7]IRCCS Istituto Giannina Gaslini, Genoa, Italy

The success of immunotherapeutic approaches strictly depends on the immune cells interaction with cancer cells. While conventional *in vitro* cell cultures under-represent the complexity and dynamic crosstalk of the tumor microenvironment, animal models do not allow deciphering the anti-tumor activity of the human immune system. Therefore, the development of reliable and predictive preclinical models has become crucial for the screening of immune-therapeutic approaches. We here present an organ-on-chip organ on chips (OOC)-based approach for recapitulating the immune cell Natural Killer (NK) migration under physiological fluid flow, infiltration within a 3D tumor matrix, and activation against neuroblastoma cancer cells in a humanized, fluid-dynamic environment. Circulating NK cells actively initiate a spontaneous "extravasation" process toward the physically separated tumor niche, retaining their ability to interact with matrix-embedded tumor cells, and to display a cytotoxic effect (tumor cell apoptosis). Since NK cells infiltration and phenotype is correlated with prognosis and response to immunotherapy, their phenotype is also investigated: most importantly, a clear decrease in CD16-positive NK cells within the migrated and infiltrated population is observed. The proposed immune-tumor OOC-based model represents a promising approach for faithfully recapitulating the human pathology and efficiently employing the immunotherapies testing, eventually in a personalized perspective. An immune-organ on chip to recapitulate the tumor-mediated infiltration of circulating immune cells within 3D tumor model.

KEYWORDS

immune-organ-on-chip, 3D human tumor model, natural killer cells, neuroblastoma, cells migration, cells infiltration

Introduction

Immunotherapies represent one of the current most promising challenges in cancer treatment. These are based on the concept of boosting the host's immune system toward the elimination of cancer and include several strategies such as the use of monoclonal antibodies (mAb) targeting tumor-associated molecules or blocking immune checkpoints, anti-cancer vaccines and cell-based therapies (Ringquist et al., 2021; Shelton et al., 2021). The success of immunotherapeutic approaches aimed to unleash the activity of cytotoxic cells such as $CD8^+$ T lymphocytes or Natural Killer (NK) cells strictly depends on their interaction with cancer cells and other immune cells. Such interaction might be profoundly affected by the highly complex niche of the tumor microenvironment (TME), which is populated by different type of cells (i.e., stromal cells, tumor cells, immune cells), interconnected within a complex three-dimensional vascularized matrix. Given these premises, the development of reliable preclinical human models has become crucial for the assessment of the best immune therapeutic approaches (Boucherit et al., 2020; Ando et al., 2021; Ringquist et al., 2021).

To date, preclinical safety and efficacy assessment of immunotherapies are carried out through 1) extensive *in vitro* cultures, addressing the cellular and molecular basis of immune responses, cancer initiation and development, and its interactions with immune cells 2) *in vivo* xenografts and genetically engineered animal models, for a necessary systemic contextualization. However, both approaches show limitations. Conventional *in vitro* models use 2D cultures that under-represent the complexity of the TME (three-dimensionality, shear stresses due to fluidic exposure, irroration affecting molecule distribution) (Rodrigues et al., 2021). On the other side, the animal models classically used in oncology often rely on immunodeficient mice xenografted with human cell lines or patient-derived tumor cells (PDX). These models, although useful for testing anti-tumor drugs, do not allow to obtain information regarding the anti-tumor activity of the human immune system. Other *in vivo* approaches are based on syngeneic mice with a fully competent immune system with results that not always recapitulate the human setting (Franklin et al., 2022). The more sophisticated and informative animal models to date are the so called "humanized mice" having a human HSC-derived immune system which can be engrafted with human tumors. However, some limitations are related to the often incomplete reconstitution of the human immune system, in terms of cell lineage development, wrong proportion of the various immune cell subtypes and degree of their activity and maturation. These defects are due to the presence of a mouse-specific microenvironment lacking human stroma and growth factors (Cogels et al., 2021). Moreover, such models are very expensive, time-consuming, and hardly usable in personalized medicine.

Therefore, 3D, human *in vitro* tumor models, including spheroids and organoids, as well as microfluidics approaches integrating the human immune components, are increasingly being developed and adopted (Rodrigues et al., 2021; Vitale et al., 2022). 3D tumor models have advantages over conventional 2D cultures, such as an increased cellular and architectural cancer complexity, like the presence of a biomimetic TME with the proper chemical and biomechanical features (Cavo et al., 2016), beside to the possibility of coculturing stromal, endothelial and cancer cells where cells can migrate and infiltrate in a 3D space. Moreover, from a technical point of view, the adoption of 3D cancer models allows to scale up cell yields, with a sample size compatible with a wide variety of standard downstream analysis, such as molecular and cytofluorimetric analysis, beside immunohistochemistry maintaining a possible anisotropic cells behavior (Ballester-Beltran et al., 2015).

The arising microfluidic platforms display the potential to recapitulate the physiological blood flows affecting the survival of circulating tumor cells (Marrella et al., 2021a), the intra/extravasation of circulating cells (tumor cells or activated immune cells), besides a reliable drug distribution (Marrella et al., 2021b). However, some microfluidic models used to co-culture immune and tumor cells in physically separated compartments are currently adopted in static conditions (Lee et al., 2018). Moreover, the over-miniaturization of some organ on chips (OOC) allow to host only few cells and very small amount of tumor samples, thus limiting the downstream analytical approaches.

From a manufacturing point of view, the conventional OOC models and microfluidic models under development are typically fabricated using the polydimethylsiloxane (PDMS) elastomer, in which UV lithography is utilized to create an overall chip architecture with microscale fluid channels across the compartments where few microliters of media circulate without any sampling/injection port (Amin et al., 2016; Lee et al., 2018). Besides suffering the difficulty of mimicking the complex structures of the microenvironment *in vivo* (Amin et al., 2016), these PDMS-based devices lead to the adsorption of small hydrophobic compounds on the chip, causing the reduction of their bioavailability, finally resulting in issues in terms of cellular responses and/or *bias* in biochemical analysis.

In this paper, we present a unique and promising approach aimed at recapitulating the immune cell infiltration and activation against cancer cells in a humanized, fluid-dynamic and 3D environment. An organ-on-chip technology (MIVO®) has been recently adopted by authors for recapitulating the systemic administration of anticancer drugs and for carrying out efficacy assays in comparison with the standard xenograft model, demonstrating the high predictability of this *in vitro* 3R approach (Marrella et al., 2021b). Similarly, the same technological platform has been adopted for culturing aggressive breast cancer models and recapitulating the cancer cells migration and infiltration in the fluid flow circuit, which

represents the first physio-pathological step towards the metastatic onset (Cavo et al., 2018). Here, the generation of a humanized and immunocompetent *in vitro* cancer model (Marrella et al., 2019), where tumor cells are cultured in a compartment physically separated through a porous permeable membrane from the fluid flow compartment, relies on the capability to emulate the microcirculation as well as the circulatory behavior of immune cells within the TME. The possible access to both the tumor and the circulating compartments allows to monitor and quantify the changes that occur in the TME (soluble molecules, cell death, tumor cell invasion), in circulating immune cells, and potentially in additional compartments physically connected each other through the circulating fluid flows (i.e., evaluation of the metastatic site). The flexibility of this approach carries the important potential of better recapitulating a clinical scenario, opening the way for a more reliable platform for 1) a personalized investigation of the specific migratory and infiltrative capacity of immune cells, 2) the analysis of the anti-tumor activity of both drug-based and cell-based therapies, 3) the investigation of the effects of tumor-immune cell cross-talk often leading to the onset of resistant tumor variants (Bottino et al., 2021).

Results

Assessment of natural killer cell viability in standard 2D culture vs. 3D alginate embedding

High-risk neuroblastoma (NB) is an aggressive, metastatic pediatric cancer difficult to treat and still characterized by poor overall survival. We have recently developed an alginate-based 3D NB culture as *in vitro* model characterized by a more physio-pathological setting showing only a partial overlap with the standard 2D culture in terms of expression of immune-related molecules (Marrella et al., 2019). We also demonstrated that the NB cell viability and proliferation are preserved after embedding NB cells within the 3D alginate matrix.

The aim of the present work is the implementation of such three-dimensional culture with features mimicking 1) the dynamic microcirculation within the tumor microenvironment and 2) the circulatory behavior of immune cells. Then, a reliable dynamic culture, consisting in the 3D NB model cultured with circulating NK cells, has been generated as a suitable tool for analyzing immune cell migration and infiltration, as well as tumor cell killing.

Given the hypothesis that circulating NK cells could be able to specifically infiltrate the alginate-based NB culture, we wanted to verify whether the alginate matrix per se could be detrimental for the NK cell viability. NK cells were cultured in standard conditions (suspended culture within a 96-well plate) or embedded in the alginate-based 3D matrix; the cells were then collected from the standard culture by pipetting or recovered from the 3D culture through alginate dissolution, stained with a Viability Dye, and analyzed by flow cytometry.

In the NK 3D culture, a clear population of unstained (thus viable) cells is shown beside to a clear stained population of dead cells (Figure 1A, lower histogram); conversely, in the 2D culture the presence of a mid-stained population might be indicative of early cell death/structural degradation of the cell, enriching the population of non-viable cells (Figure 1A, upper histogram). According to the clearly viable population, a significant difference was observed in cell viability between the standard suspended NK culture and the 3D embedding (Figures 1B,C).

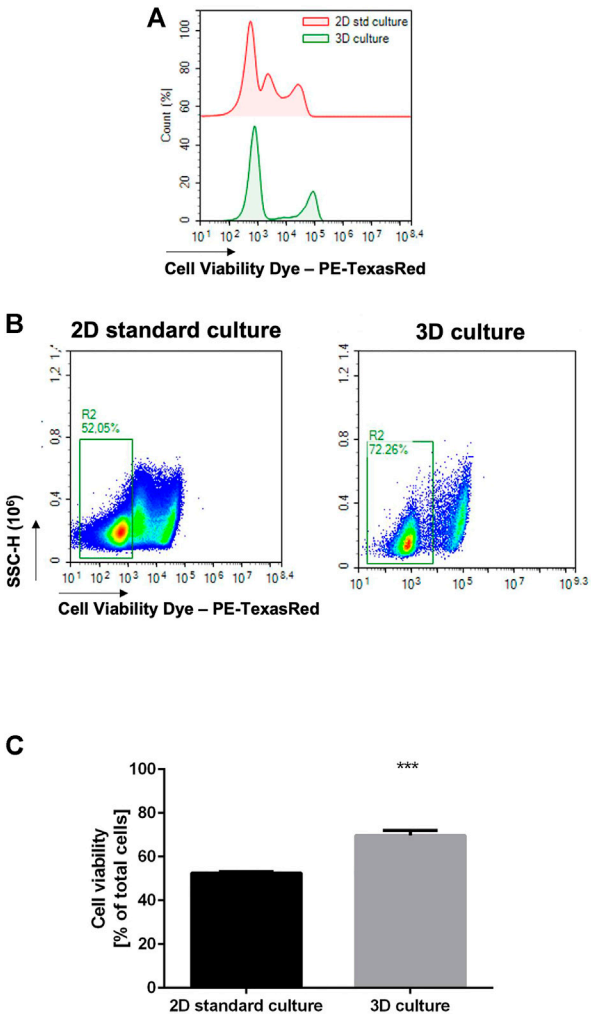

FIGURE 1
3D alginate embedding does not negatively affect cell viability. NK cells were cultured in the standard setting (n = 6) or in 3D alginate hydrogel (n = 6) for 24 h. The cells were then recovered and stained with a Fixable Cell Viability Dye (PE-TexasRed). **(A)** Flow cytometry analysis on NK cells, histograms: three distinct populations are observed in the 2D standard culture. **(B)** Flow cytometry analysis on NK cells showing % of low-staining population. **(C)** Statistical analysis of **(B)**.

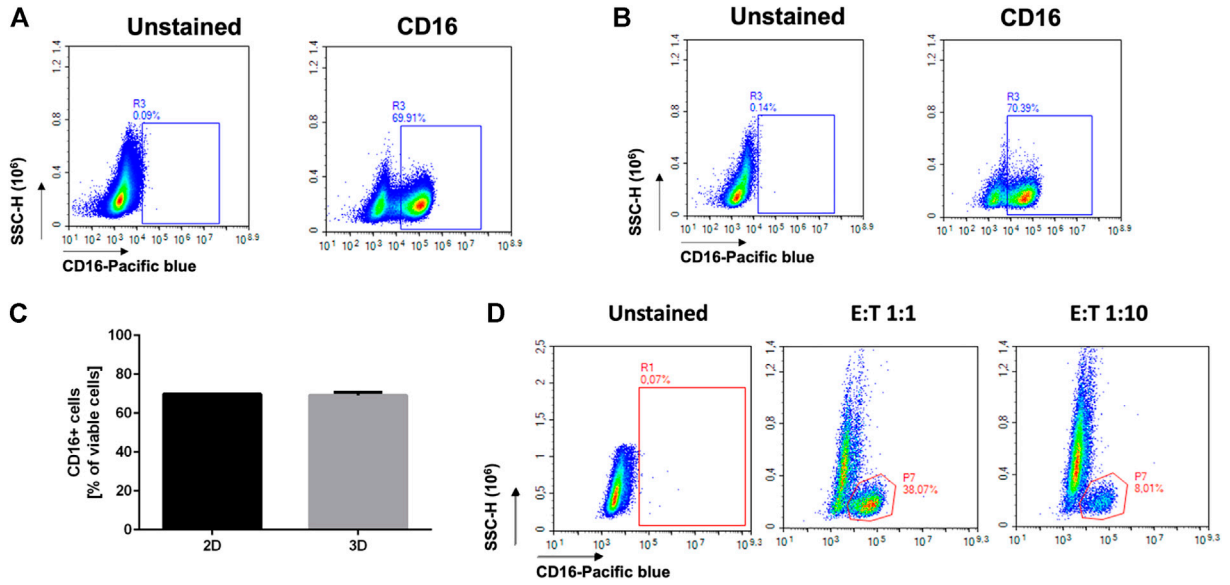

FIGURE 2
Reliability of flow cytometry analysis after cell recovery. NK cells were cultured in the standard 2D setting **(A)**, in 3D alginate embedding **(B)**, or co-cultured with tumor cells in the 3D alginate matrix **(C)**. The cells were then recovered and analyzed for the expression of the NK marker CD16. **(A)** CD16 expression on NK cells cultured in standard conditions (96-well plate, n = =6). **(B)** CD16 expression on NK cells cultured in a 3D alginate scaffold (n = =6). **(C)** No significant difference in CD16 expression is highlighted by flow cytometry in standard vs. 3D culture. **(D)** CD16 expression on NK cells recovered from a 3D alginate-based co-culture with HTLA-230 cells, at different E:T ratios (n = =12).

Reliability of flow cytometry analysis after cell recovery

Flow cytometry is one of the most widely adopted approaches for quantitative and qualitative assessment of the composition of TME. With the aim to generate a reliable *in vitro* model, to support some preclinical studies in a 3Rs perspective, we wanted to check if flow cytometry could be successfully employed to analyze heterogeneous cell populations recovered from the alginate scaffold, as a model of a complex 3D tumor. We started by analyzing simple NK monocultures. NK cells were cultured in standard 2D conditions or in 3D embedding over/night, and the cells directly collecting from the cell suspension or dissociating the alginate, respectively. We assessed the expression of the NK-associated marker CD16, being aware that such marker is highly expressed in polyclonal NK cells (Figure 2). Indeed, as expected, we found high percentage (70%) of $CD16^+$ positive cells (Figures 2A,B). No significant differences were observed between the 2D and 3D culture setting in terms of percentage (Figure 2C) of positive cells (69.91% vs. 70.39%).

We then prepared cocultures with NK and the HTLA-230 NB cell line, to assess the reliability of the staining of hetero-cultures. In particular, we performed cocultures with two different effector/target (E: T) ratio (1:1 and 1:10). The lowest NK: NB ratio was specifically chosen with the aim to get closer to *in vivo* scenario where few NK cells generally infiltrate the most aggressive solid tumors including NB (Balsamo et al., 2012; Castriconi et al., 2018; Melaiu et al., 2020).

We then verified by flow cytometry the percentage of CD16-positive cells, gated on total cells. Considering that, in the NK monocultures, approximately 70% of the cells show CD16 positivity (Figures 2A–C), as expected, we detected around 38% $CD16^+$ cells in the 1:1 coculture and around 8% $CD16^+$ cells in the 1:10 coculture.

Assessment of the natural killer-tumor cell interaction within the 3D model

To verify if NK cells could infiltrate the alginate matrix and interact with tumor cells, we co-cultured NK cells and NB at different E:T ratios (1:1 and 1:10).

When embedded in the alginate matrix, NK cells and tumor cells are homogeneously dispersed in a single-cell suspension. To assess the ability of NK cells to move within the matrix for reaching the tumor cells, we performed a confocal microscopy analysis. NK cells were labelled with the cell tracker CFSE (green) and then co-embedded with the unlabeled tumor cells. Then, the 3D co-culture was fixed in paraformaldehyde and stained with a mAb specific for the NB-specific marker GD2 (red). We observed several NK cells start to interact with NB cells (Figure 3).

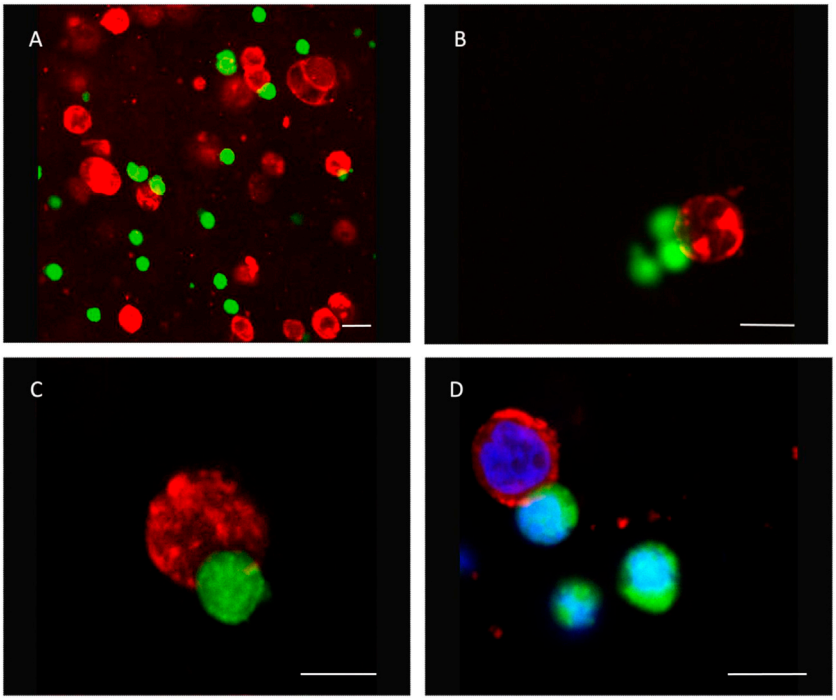

FIGURE 3
NK cells and NB cells coembedded in a 3D alginate scaffold. Confocal Microscopy Acquisition and Analysis of CFSE-labeled NK cells (green) and GD2-positive NB cells (red) co-embedded in 3D alginate scaffold and cultured for 24 h. In panel D, nuclei have been stained with DAPI. **(A)** ×20 magnification (representative square field of ×173173 micron); **(B–D)** ×40 magnification. Scale bar: 10 micron.

This leads to a significant tumor cell death paralleled by a high NK cell viability (Figure 4): cells co-culture analysis showed that tumor cell death significantly increased when NB cells were co-cultured with NK cells in 3D models, indicating that NK cells are able to interact and effectively kill tumor cells grown in 3D cultures. As expected, the percentage of dead tumor cells in the presence of NK cells was also significantly increased in 2D culture, whereas at T = 0 was negligible. Moreover, NK cells recovered from hydrogels showed a high viability, demonstrating that 3D alginate spheres are suitable models for testing NK cell-mediated immunotherapy.

Dynamic culture and assessment of natural killer cell "extravasation"

Once we have analyzed the feasibility of 3D cultures in static conditions, we carried out the dynamic co-culture by using MIVO®. The dynamic culture has been specifically planned to allow the circulation of NK cells below hydrogel-embedded tumor cells (E:T ratio 10:1), which are accommodated in a standard 24-well plate transwell insert, fitting the MIVO® chamber (Figure 5).

The device has been connected to a pumping system, which enable the imposition of a fluid flow, driving NK cells throughout the circulation, thus mimicking the circulatory system within the tumor microenvironment. The MIVO material is PDMS free, to avoid any molecule binding issues, and no immune cells adhesion at the walls was observed (data not shown). As evidence of that, Computational Fluid Dynamics (CFD) simulations have been performed. Results show that velocity values within MIVO® range from 0 to 1.2 cm/s, which are characteristic of capillary blood flow, when the imposed inlet flow rate is 0.3 ml/min (Figure 6A).

We then verified the ability of NK cells to migrate upward (thus against the gravity force), following an active, chemoattractant-driven "extravasation", with no driving forces dependent on the fluid flow per se. To this purpose, additional experimental groups included 1) a positive control of cell migration ("empty" 3D alginate scaffolds, without tumor cells, in culture medium enriched with 40% FBS as a chemoattractant), and 2) a negative control (without alginate scaffolds, with culture medium without any chemoattracting supplement). The tumor samples were represented by 3D alginate cultures of HTLA-230 cells, kept in standard conditions (cell culture medium with 10% FBS). After co-culturing the cells for 4 h in a dynamic microenvironment, the supernatants into the transwell inserts

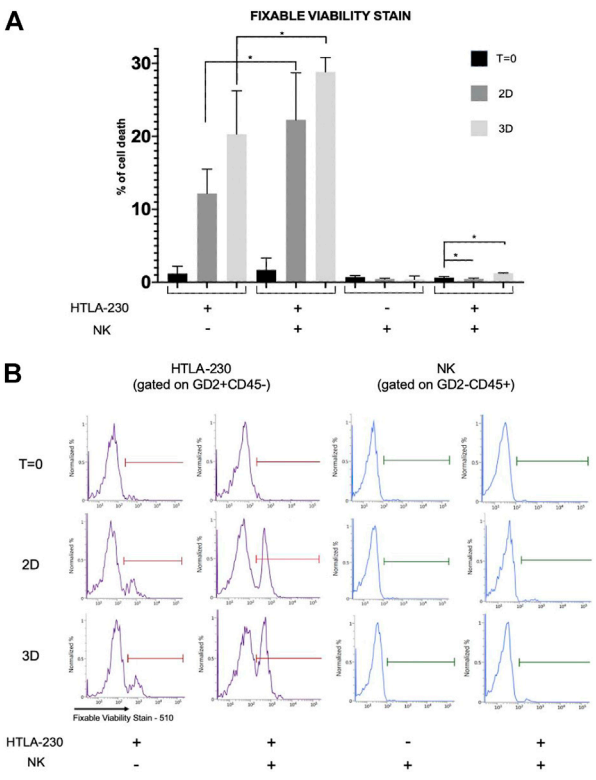

FIGURE 4
Viability assessment of NB and NK cells in 2D and 3D cultures. **(A)** Percentage of dead NB or NK cells (i.e., Fixable Viability Stain 510 positive cells) recovered from 2D cultures or 3D alginate spheres, both in monoculture and coculture, gated on GD2+CD45− and CD45+GD2−, respectively. Mean fluorescence intensity with 95% CI is reported ($n = 4$, $*p < 0.05$). **(B)** Representative experiment.

were collected, and the migrated cells were counted by means of a hemocytometer. As shown in Figure 6B, we did observe a significant increase of cell migration in the tumor group as well as in the positive control, whereas little or no NK cell migration was observed in the negative control group, demonstrating an active, tumor-specific, NK cell "extravasation". The biochemical-driven specificity of the "extravasation" process is further corroborated by the CFD simulation aimed at investigating fluid flow-driven NK cells trajectories: the simulation does not report cells "extravasation" events from the bottom chamber towards the tumor, because of the fluid motion alone, as shown in Figure 6C.

Natural killer cell infiltration

To understand if the migrated NK cells were capable to infiltrate the 3D tumor despite the presence of the alginate matrix, and eventually to interact with tumor cells, we performed the same dynamic culture described above. After co-culturing the cells for 4 h under microcirculation, the 3D alginate cultures were recovered, fixed with 4% PFA, NK cells stained for the DNAM-1 marker (Castriconi et al., 2004), and observed under a fluorescence microscopy. As shown in Figure 6D, DNAM-1+ cells were mostly located along the border of the gels. This is indicative of the ability of NK cells not only to specifically migrate toward the tumor culture, but also to infiltrate the alginate matrix.

The same experiment was performed by labelling NK cells with the cell tracker CFSE before the establishment of the coculture, and then following their journey toward the NB culture (Figures 7A,B). This served also as a proof of concept that all the cells found within the transwell inserts during the dynamic culture were CFSE-positive, thus NK only. No tumor cells migrated outside the alginate gels, excluding a bias in the quantification of the "extravasation" of immune cells (data not shown). After 4 h dynamic co-culture, the 3D alginate gels were recovered, fixed and stained for the tumor marker GD2, and observed under confocal microscopy, with the aim to highlight possible effector-to-tumor cell interactions. As shown in Figures 7C,D, CSFE-positive NK cells were found among the GD2-positive tumor ones within the alginate cultures.

Assessment of the natural killer cell phenotype in circulating, extravasating, and infiltrating populations

The NK cell phenotype is critical for their anti-tumor effect, with CD16-positive NK cells being related to a high cytotoxic activity. However, because of the tumor microenvironment, the CD16-negative infiltrating NK cells may prevail, which are characterized by low-cytotoxicity.

Given these premises, we sought to verify if our dynamic culture could recapitulate the selection of a specific NK cell phenotype in the extravasated and infiltrated NK cell fraction. We then performed a dynamic culture, incubating HTLA-230 3D hydrogels with circulating, CFSE labelled NK cells over/night (10:1 E:T ratio). Then, we collected 1) the 3D tumor hydrogels, 2) the migrated NK cells, found into the transwell inserts, and 3) the circulating NK cells, which were analyzed for CD45 and CD16 expression through flow cytometry. The hydrogels were dissociated as described above, and the single cell suspension was analyzed identifying the CSFE-labelled NK cells infiltrating the tumor model. As shown in Figure 7A a clear, although small, CSFE-labeled cell population was present within the hydrogel, corroborating the findings (Figures 7C,D) on the ability of the "extravasated" NK cells to infiltrate the 3D tumor culture. As a further demonstration, CD45 staining confirmed that all and only the CFSE-positive cells were belonging to the immunity lineage (Figure 7B).

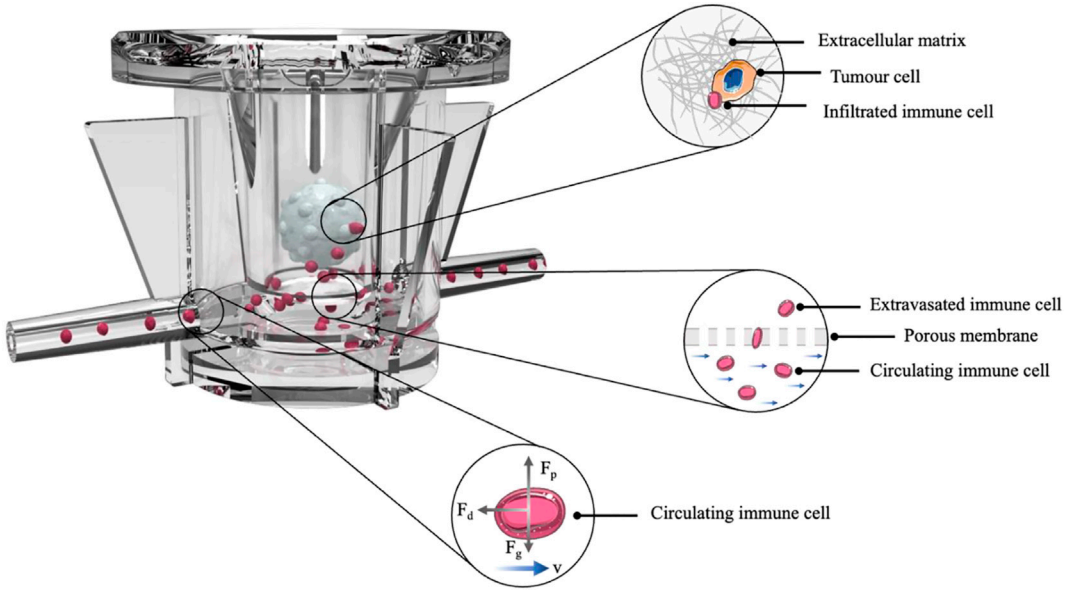

FIGURE 5
Organ on chip platform for immune-tumor cells cross-talk. Representative scheme of the experiment: HTLA-230 cells were embedded in a 3D alginate scaffold and cultured above a microcirculation of NK cells, for 4 h.

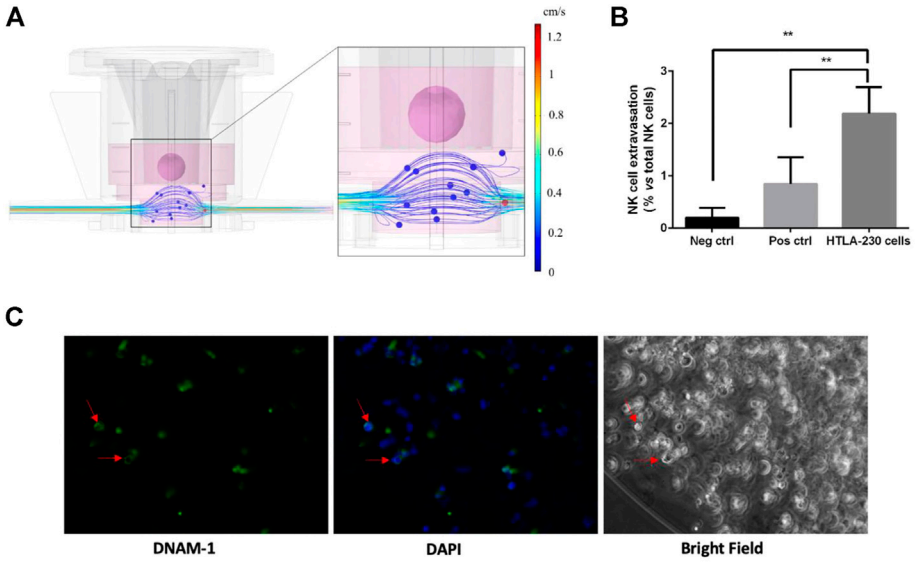

FIGURE 6
Dynamic culture with circulating NK cells (4 h coculture). **(A)** CFD simulation of the fluid velocity profiles within the organ on chip and the fluid flow-driven immune cells trajectories. **(B)** Tumor-specific NK cell extravasation (neg ctrl: DMEM w/o supplements; pos ctrl: alginate gels w/o HTLA-230 cells, plus 30% FBS; HTLA-230 gels with standard 10% FBS) (n = 6). **(C)** NK cell infiltration within the gel, as indicated by DNAM-1-positive cells highlighted by red arrows.

Moreover, Figure 8 shows the proportion of CD45 and CD16 co-expressing NK cells, gated out on the total CFSE-positivity. We compared the standard NK culture (positive control), the circulating NK cells recovered from the MIVO® devices, the migrated NK cells recovered from the transwell inserts, and the infiltrated NK cells recovered from the

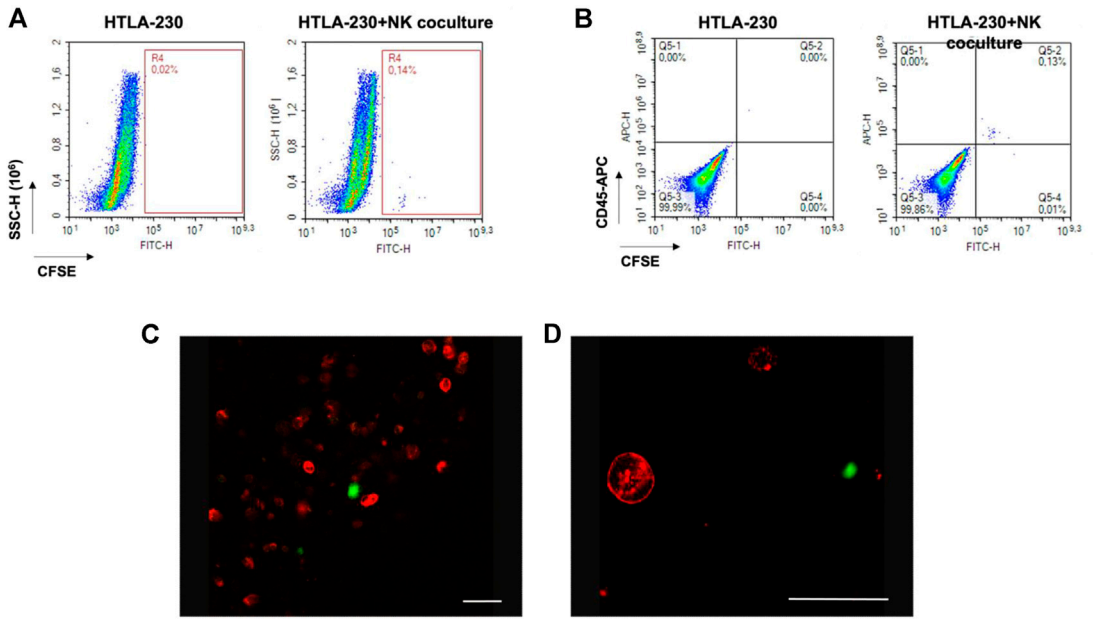

FIGURE 7
Over/night dynamic co-culture of alginate-embedded neuroblastoma cells with circulating NK cells. **(A)** Representative experiment showing a flow cytometry analysis of the cells recovered from the gels. A clear population of CFSE-labelled cells (corresponding to NK cells) is visible in the co-cultured sample (n = 6). **(B)** Perfect concordance between CFSE-labelling and CD45 expression (n = 6). **(C and D)** Confocal Analysis of different 3D alginate scaffold isolated from 3D dynamic cultures (4 h). Representative confocal microscopy xy fields (370 × 370 micron) acquired in 3D alginate scaffolds containing GD2-positive NB cells (red) that were previously embedded in the gel, and subjected to 4 h of dynamic flow of CFSE-labeled NK cells (green). Merged fluorescence images show that NK cells were able to infiltrate the gel. Scale bar is 50 micron.

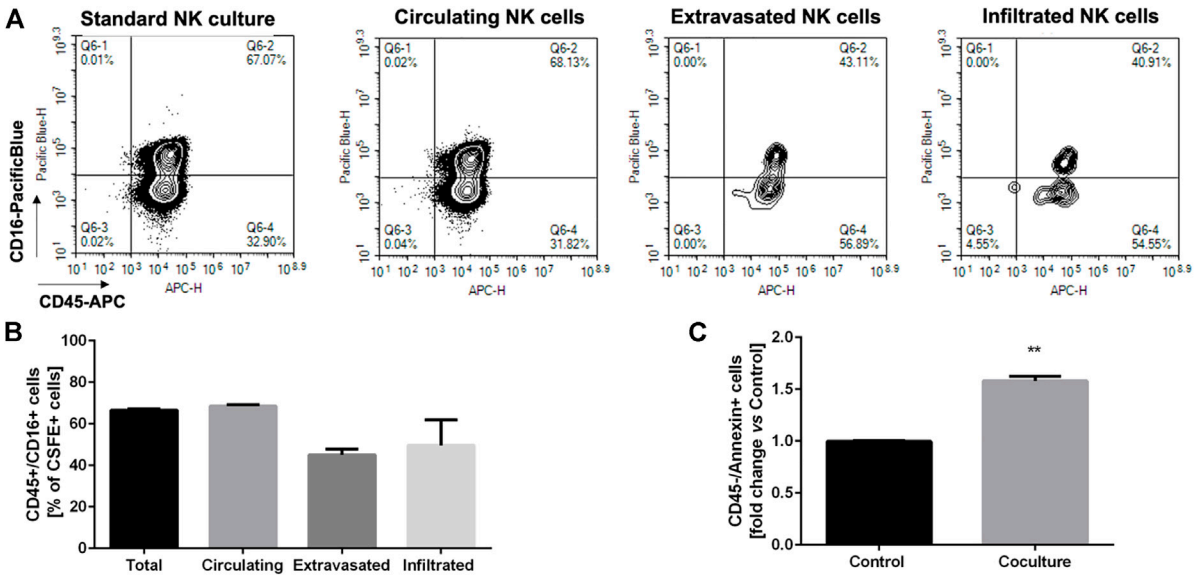

FIGURE 8
Phenotypic characterization of the different fractions of NK cells **(A)** Representative plotes showing the phenotypic characterization of the different fractions of NK cells recovered from the dynamic culture (infiltrated, extravasated, circulating vs. the standard NK culture) based on CD45/CD16 expression, gated on the CFSE-positive population (n = 6). **(B)** Statistical analysis of CD16 expression in the different fractions of NK cells, recovered from the dynamic culture (n = 6). **(C)** Induction of apoptosis in tumor cells, assessed through flow cytometry as annexin-V staining on CD45-negative cells (n = 6). Control: HTLA-230 3D monoculture.

hydrogels. As highlighted in the representative plots in Figure 8A, as well as in Figure 8B, the proportion of NK cells expressing CD16 is markedly reduced in the "extravasated" and infiltrated groups, if compared with the circulating group, which conversely is similar to the standard NK culture. This might reflect a preferential recruitment of CD16-negative NK cell population, recapitulating data observed in different solid tumors (Balsamo et al., 2012; Castriconi et al., 2018; Melaiu et al., 2020).

Finally, we aimed at analyzing the induction of apoptosis in tumor cells, after overnight coculturing with circulating NK cells. Figure 8C shows a significant increase in the exposure of annexin-V on tumor cells membrane, indicating that the migrated infiltrating NK cells are able to specifically induce tumor cell death, thus retaining, at least in part, their cytotoxic potential.

Discussion

The improvement of preclinical cancer models represents the basis for the acceleration of the development of more effective and personalized therapeutic strategies, and the reduction of clinical failure rate of oncology drugs, mainly due to the lack of both 1) complex clinically relevant *in vitro* models that better recapitulate the physio-pathological features occurring in patients (Jardim et al., 2017; Wong et al., 2019; Honkala et al., 2021), and 2) fully humanized animal models (Mak et al., 2014; Maulana et al., 2021; Bjornson-Hooper et al., 2022). For instance, and importantly, immune-oncology therapies would need a fully integrated human microenvironment to be tested, given the intricate interplay between the different immune cell subsets, tumor cells, and other cells within the TME. Moreover, the vascularization state, the accessibility of the tumor bulk and the presence of immunosuppressive signals within the human TME must be considered for both drug-based and cell-based immunotherapies.

Starting from a two-dimensional "flat biology", across the development of three-dimensional cultures and co-cultures, the current rise of microfluidic technologies enables the implementation of a "fourth dimension", with the introduction of fluid flows mimicking the tissue dynamic environment. In this context, the organ-on-chip technology represents a new generation of *in vitro* models, which consists in the realization of hyper organized cell cultures building tissue-level structures, the corresponding physiological functions (Bhatia and Ingber, 2014; Sontheimer-Phelps et al., 2019) and different cellular compartments which can cross-communicate through channels interconnection, and/or porous membranes (Maulana et al., 2021).

For instance, the cultivation of cancer cells and immune cells in two separated compartments, connected through microchannels within the same planar chip, allows the establishment of a biochemical gradient for immune cell recruitment from the first chamber toward the side chamber, hosting tumor cells. However, most of these tumor-on-chip are used either in static conditions (Hsu et al., 2012; Businaro et al., 2013; Parlato et al., 2017; Pavesi et al., 2017; Lee et al., 2018; Guo et al., 2019; Um et al., 2019; Yu et al., 2019; Ren et al., 2020; Ayuso et al., 2021), or through simple gravity-driven flow (Song et al., 2021), or perfusion with very low fluid flow rates, being far from physiological conditions. For instance, in a tumor-on-chip model, Aung et al. perfused T cells applying a fluid flow rate of 50 ul/hr (corresponding to 0,8 ul/min) (Aung et al., 2020); similarly, in an immune system-on-chip recently developed by Goyal et al., immune cells were cultured through a flow rate of 60 ul/hr (corresponding to 1 ul/min) (Goyal et al., 2022).

Instead, these devices could be further implemented with microfluidic motion, generating more reliable cell culture models with shear stresses and stimuli associated with fluid flows mimicking the dynamics of real tissues (e.g., interstitial flows, blood flows) as well as the biological and biochemical processes that physiologically rely upon dynamic flows (e.g., circulation of immune cells, drug kinetics). Here, we provide a fluid-dynamic technology for performing dynamic experiments with a 300 ul/min flow rate, corresponding to a physiological capillary blood flow velocity (Marrella et al., 2020; Marrella et al., 2021b), for mimicking the microcirculation of the TME. Specifically, NK cells were driven by the fluid flow motion below the tumor model, which was in turn cultured in a 3D matrix. NK cells and the tumor model were physically separated in two different compartments through a porous permeable membrane supporting the adoption of different culture media (e.g. serum percentage, selective growth factors), while NK cells were free to sense the chemo-attractive gradient exerted by tumor cells and to actively initiate a spontaneous "extravasation" process toward the tumor cells themselves.

Importantly, NK cells were able to migrate upward, against the gravity and viscous forces exerted by the fluid flow, demonstrating that their migration is specifically mediated by soluble factors released by tumor cells, as little or no migration has been observed in the negative control group (w/o chemo attractants, w/o tumor cells). In particular, the gradient of chemoattractant molecules activates the inner filament network of the cells, leading to a cell chemotactic response (Yang et al., 2015). This force that drives the cells to move towards the chemoattractant source is also named protrusion force. In our experiments, the protrusion force generated by the presence of tumor cells led to a migration of immune cells that was significantly higher than that obtained with increased serum percentage in the medium, demonstrating for the first time a tumor-mediated migration of immune cells in a biologically relevant organ-on-chip platform.

Interestingly, NK cells and tumor cells were co-cultured in the dynamic setting in a standard 10:1 E:T ratio (Ayuso et al., 2019; Sargenti et al., 2020; Gopal et al., 2021; Morimoto et al., 2021). However, we observed that only around 2% of circulating

NK cells were able to specifically extravasate in the upper compartment, in line with the low number of NK cells generally observed in tumor tissues (Balsamo et al., 2012; Castriconi et al., 2018; Melaiu et al., 2020); then, only this cellular subset had the potential to really interact with tumor cells, highlighting the limitations of the current static co-culture modalities, where often high E/T ratios are used simply adding NK cells into the well/circuit, leading to a possible overestimation of their efficacy in tumor control. This technical issue of the current approaches might lead to a deep impact in the preclinical evaluation of immunotherapies, in which the activation and recruitment of specific subsets of immune cells (for drug-based therapies) as well as of infused, often engineered cells (for cell-based therapies) represent the crucial first step for their efficacy. Furthermore, this may explain at least in part the high success rate of immunotherapies at the preclinical level, which is not mirrored by the same success once translated into the clinic.

The second step for activated immune cells to be effective against the tumor is their capability to infiltrate the tumor bulk, keeping an activation state without being affected by the adverse/immunosuppressive signals from the TME. This is, for instance, the main challenge of CAR-T (and -NK) cell therapy for solid tumors: indeed, despite being successful for hematological malignancies, such cell-based therapy has not found a successful application for solid tumors yet (Guerra et al., 2021; Kumari et al., 2021). In this context, our experiments show that, beside the importance of determining the extravasation rate as indicative of immune cell recruitment, it is mandatory to assess the immune cell infiltration within real three-dimensional matrix-based tumor cultures, where the chemo-physics and biomechanics (i.e. stiffness) of the matrix itself better resemble the immune-tumor cross talk occurring *in vivo*. Importantly, the over-miniaturization of the "classical" microfluidic devices, beside failing in recapitulating the biological and clinical features of TME, possibly leads to the underrepresentation of the tumor heterogeneity occurring into the clinic. Moreover, this also carries some technical limitations related to downstream biochemical assays and to small volumes/bubbles handling (Ayuso et al., 2021; Song et al., 2021): indeed, the use of very small cell numbers (e.g., 1,000 cells/spheroid (Ayuso et al., 2019), 2,500 cells/well (Gopal et al., 2021)) and/or very small volumes (e.g., 10–20 ul containing 10^5-2×10^5 cells (Ren et al., 2020)) are not always suitable for standard analytical methods such as immunofluorescence and flow cytometry analysis. Consequently, the user adaptation to a different cell culture technology, with a less comfortable handling with respect to the standard cultures and a narrowed range of analytical methods (i.e., often confined to cell imaging) make these microfluidic devices not easy to adopt in conventional laboratory practices. On the contrary, following the approach here described, 3D cultures were obtained with more cells (min. 3×10^4 cells/matrix) co-cultured with 10-fold higher NK circulating cells. Furthermore, given the increased sample size (up to 5 mm), our experiments represent the proof-of-concept for the use of this platform with more complex 3D cultures (i.e., based on bioprinted scaffolds and/or seeded with different cell types) to better mimic the TME, as well as with patient biopsies. The latter could have a profound impact on personalized screening, for tailoring patients based on the better response or for assessing the efficacy of cell-based therapies.

We already demonstrated the reliability of alginate-based cultures for different tumors (Cavo et al., 2018; Marrella et al., 2019; Marrella et al., 2021b), and in particular for NB cultures, where the susceptibility to therapies and the tumor cells immune-phenotype were properly predicted and recapitulated (Marrella et al., 2019). Here, we demonstrated that the alginate matrix is suitable also for culturing NK cells, without affecting their viability or their phenotype. Moreover, when NK cells and NB cells were co-embedded in alginate matrix, we observed that NK cells retained their ability to interact with tumor cells and to kill them, providing evidence of their migratory/infiltrating behavior within the hydrogel. After co-culturing NK cells and the 3D tumor in dynamic conditions, we also assessed the cytotoxic effect of infiltrated NK cells: since we observed a significant increase of annexin-V exposure on tumor cells, we demonstrated that NK cells also retained their killing capacity within the alginate matrix.

Importantly, we analyzed NK cell phenotype in terms of CD16 expression, within the circulating environment (administered NK cells), the migrated and infiltrated fractions, after 24 h of dynamic co-culture: we observed a clear decrease in CD16-positive NK cells within the recruited populations (both migrated and infiltrated). $CD16^+$ cells represent a subpopulation of NK cells displaying cytotoxic activity higher than that exerted by the $CD16^-$population (Orange, 2008; Myers and Miller, 2021). Since the infiltration and phenotype of NK cells have been correlated with prognosis and response to immunotherapy in NB tumors (Melaiu et al., 2020; Szanto et al., 2021), it is crucial to dispose of a preclinical model that faithfully recapitulates the human pathology.

In this context, our NB/NK model represents a paradigm for the establishment of advanced *in vitro* models that can be efficiently employed for testing immunotherapies also in different tumors, eventually in a personalized perspective. Here, by using HTLA-230, a human cell line highly recapitulating the most aggressive NB disease (Castriconi et al., 2007a), we provided a humanized and immunocompetent platform bridging the gap between standard *in vitro* methods, advanced miniaturized organ-on-chips and animal models. With its further optimization by the addition of cells and molecules characterizing the TME, this model could be more successfully utilized for deciphering or consolidating the mechanisms supposed to drive the quality and the amount of human NK cell infiltration in tumors (Castriconi et al., 2013; Regis et al.,

2017). In the present model this infiltration could depend on the activity of factors such as TGF-β, MIF, or VEGF shown to be highly secreted by HTLA-230 cells line (Castriconi et al., 2013). Finally, these mechanisms could be finely tuned in combined personalized strategies to potentiate the efficacy of immunotherapies.

Materials and methods

Cell cultures

The MYC-N amplified neuroblastoma (NB) cell line HTLA-230 was provided by Dr. E. Bogenmann (Children's Hospital Los Angeles, CA) (Corrias et al., 1996) and cultured in RPMI-1640 medium supplemented with 10% heat-inactivated FCS (Biochrom, Berlin, Germany), 50 mg/ml streptomycin, 50 mg/ml penicillin (Sigma-Aldrich), and 2 mm glutamine (Euroclone). The cells were cultured in a humidified environment (95% air/5% CO_2) at 37°C and were used to generate 3D tumor models.

Peripheral blood mononuclear cells (PBMCs) were obtained from blood of volunteer healthy donors by Ficoll-Hypaque gradients (Sigma Aldrich). NK cells were purified by using the NK-cell isolation kit II (Miltenyi Biotec) and were cultured on irradiated PBMCs in RPMI-1640 supplemented with 10% heat-inactivated FCS, 50 mg/ml streptomycin, 50 mg/ml penicillin (Sigma-Aldrich), 2 mm glutamine (Euroclone), 600 IU/ml rhIL-2 (Proleukin; Chiron, Emeryville, CA) and 0.5% v/v phytohemagglutinin (Gibco, Paisley, United Kingdom). After 10 passages, NK cells were checked for purity (>95%) analyzing classical NK cell markers (Castriconi et al., 2007b).

Computational fluid-dynamic simulations

Fluid dynamics within Single-Flow MIVO® device was investigated to predict 1) the fluid velocity profiles within the device and 2) the fluid flow-driven NK cells trajectories.

First, the analysis was performed by using the Single-Phase Laminar Fluid Flow model of Comsol Multiphysics 5.6 assuming 1) a laminar flow regime, 2) an incompressible Newtonian fluid (Vitale et al., 2020; Pulsoni et al., 2022). The equations to be solved are the Navier-Stokes ones for the conservation of momentum Eq. 1 and the continuity law for conservation of mass Eq. 1:

$$\begin{cases} \rho\left[\frac{\partial \boldsymbol{u}_f}{\partial t} + \boldsymbol{u}_f \cdot \left(\nabla \boldsymbol{u}_f\right)\right] = -\nabla p + \mu\left(\nabla^2 \boldsymbol{u}_f\right) \\ \left(\nabla \cdot \boldsymbol{u}_f\right) = 0 \end{cases} \quad (1)$$

where u_f is the fluid velocity and p the pressure across the circuit. The values of the density ρ (1,000 kg/m^3) and the viscosity μ (10^{-3} Pa·s) was selected as water at room temperature (25°C). A flow rate of 0.3 ml/min was set as input according to the value impose experimentally to generate the fluid motion, whereas as output the atmospheric pressure was set as null, avoiding a backflow. A no-slip boundary condition was set. Finally, an iterative geometric multigrid (GMRES) algorithm was used to solve the equations.

Subsequently, the particle tracing module for fluid flow was added to the model to identify the position and velocity of the NK cells dispersed in the moving fluid as a function of time. The Newtonian model was used to estimate the behaviour of the particles in the fluid flow. Such model is based on the conservation of total momentum:

$$\frac{d\left(m_p \boldsymbol{v}_p\right)}{dt} = \boldsymbol{F}_d + \boldsymbol{F}_g \quad (2)$$

where m_p is the mass of the particle, v_p its velocity, F_d and F_g the drag force and the gravity force, respectively. The drag force was calculated through the Stokes drag law:

$$\boldsymbol{F}_d = 6\pi\mu r_p\left(\boldsymbol{u}_f - \boldsymbol{v}_p\right) \quad (3)$$

where μ is viscosity defined above, r_p is the particle radius (assuming NK cells as spheres) equal to 0.006 mm (Dickinson et al., 2015) The gravity force was calculated as:

$$\boldsymbol{F}_g = m_p \boldsymbol{g} \frac{\left(\boldsymbol{\rho}_p - \rho\right)}{\boldsymbol{\rho}_p} \quad (4)$$

where g is the gravity acceleration, ρ_p the particle density equal to 1,080 kg/m^3 (Zhao et al., 2015) and ρ the fluid density defined above. A rebound condition on the walls was set, meaning that the momentum of the particles that encounter the wall is preserved.

3D cultures

Three-dimensional NB models were generated as previously described (Marrella et al., 2019). Briefly, HTLA-230 cells were resuspended in DMEM (Euroclone) supplemented with 10% heat-inactivated FBS, 1% penicillin/streptomycin and 1% glutamine and mixed with a 1% alginate solution (1:1 V/V), to obtain a final 0.5% alginate concentration (w/V). This cell suspension was dropped into a 0.5 M $CaCl_2$ gelling bath gel spheroids formation. The hydrogels were then washed with sterile distilled water and transferred in a 96-well plate, cultured in DMEM supplemented with 10% FBS, 1% penicillin/streptomycin and 1% glutamine, and 5 mm $CaCl_2$, ensuring gel maintenance.

For the establishment of NK cell 3D cultures, after thawing NK cells were recovered for 72 h, and then cultured for additional 24 h in

the standard 2D setting (96-well plate) or embedded within the alginate matrix. Specifically, the 3D culture was obtained resuspending NK cells in DMEM supplemented with 10% FBS, 1% penicillin/streptomycin, 1% glutamine and 600 UI/ml IL2, and mixed with a 1% alginate solution (1:1 V/V). The 3D hydrogels were obtained following the procedure described above. The cells were then analyzed by flow cytometry in terms of cell viability through staining with a Cell Viability Dye.

For NB/NK cell 3D co-cultures, HTLA-230 cells or NK cells were resuspended in DMEM supplemented with 10% FBS, 1% penicillin/streptomycin and 1% glutamine or DMEM supplemented with 10% FBS, 1% pen/strep, 1% glutamine and 600 UI/ml IL2, respectively, and then mixed at different E:T ratios (1:1; 1:10). The 3D hydrogels were obtained following the procedure described above and kept in culture over/night before analyzing the expression of the NK marker CD16 through flow cytometry.

Dynamic culture

The dynamic co-cultures were performed by using the Single-Flow MIVO® device, with the aim to recapitulate the complexity of a 3D, dynamic TME. NK cells were counted, eventually stained with CFSE Cell Proliferation Kit (ThermoFisher Scientific), resuspended in RPMI-1640 medium (Euroclone) supplemented with 10% FBS, 1% penicillin/streptomycin, 1% glutamine and 600 UI/ml IL2, and loaded within the MIVO® chamber (1.5 ml/chamber), to get an effector: target (E: T) ratio of 10:1 with tumor cells. The circulation of NK cells was allowed by a pumping system, through the imposition of a fluid flow rate of 0.3 ml/min, simulating capillary flows, while 3D NB hydrogels were cultured with the maintenance medium physically separated through a permeable porous membrane.

For extravasation experiments, after 4 h dynamic co-culture, both circulating (within the capillary circuit) and extravasating (within the tumor niche) NK cells were harvested and counted by means of a hemocytometer. NK cells were also cultured when the MIVO chamber contained either DMEM w/o supplement (negative control) or an alginate gel w/o NB cells supplemented with 40% FBS as a chemoattractant factor (positive control).

Immunofluorescence analysis of 3D cultures

For 3D dynamic or static NK/NB co-cultures, NK cells were used unlabeled or labeled with carboxyfluorescein succinimidyl ester (CFSE) (CellTrace CFSE Cell proliferation kit, Molecular Probes). Briefly, NK cells were washed three times with RPMI-1640 and resuspended at 1×10^7/ml in the same medium. CFSE was added at the final concentration of 100uM and incubated for 10 min at 37°C in water bath. The reaction was stopped by adding complete culture medium and cells were washed twice before performing the experiments.

For NK cell or NB staining, 3D cultures, either from dynamic or static conditions, were washed with a 0.9% sodium chloride solution supplemented with 5 mm $CaCl_2$ and fixed in 4% paraformaldehyde supplemented with 1 mm $CaCl_2$. For experiments performed with unlabeled NK cells, after incubation with blocking solution (2% BSA, 5 mm $CaCl_2$ in 0.9% sodium chloride solution), the hydrogels were stained for the NK-associated marker DNAM-1 (Castriconi et al., 2004) (F5, mouse anti-human, IgM) primary antibody for 2 h, followed by a goat anti-mouse IgM FITC-conjugated secondary antibody (Southern Biotech, Birmingham, AL). Cell nuclei were counterstained with DAPI. The hydrogels were mounted on a microscope slide, squeezed with a glass coverslip, and then observed under a fluorescence microscope (Nikon ECLIPSE Ts2-FL).

For experiments performed with CFSE-labelled NK cells, after incubation with blocking solution (2% BSA, 5 mm $CaCl_2$ in 0.9% sodium chloride solution), the hydrogels were stained for the NB-specific marker GD2, by using a direct Alexa Fluor 647 mouse anti-human Disialoganglioside GD2 (IgG2a, BD Biosciences) antibody. Cell nuclei were counterstained with DAPI. The 3D hydrogels were layered on a 0.17 mm-thick microscope coverslip (optically clear borosilicate glass) and examined on the laser scanning confocal microscope SP2-AOBS (Leica Microsystems, Mannheim, Germany), using either a 20x/0.70 (Plan Apochromat) objective or a HCX PL APO ×40/0.75–1.25 oil immersion objective, on a DM IRE2 inverted microscope. Fluorescent dye excitation was performed using a 488 nm laser for CFSE excitation (emission detection range 500–560 nm), a 633 nm laser for Alexa 647 excitation (emission detection range 655–760 nm), a 405 nm diode laser for DAPI excitation (emission detection range 410–480). Image merging was performed with Leica proprietary software or ImageJ.

To provide a formal proof of the NK cell-mediated tumor killing in 3D cultures, NB and NK cells were cultured alone or in co-cultures overnight (E:T 1:1). After cell recovering, cells were stained with direct Alexa Fluor 647 mouse anti-human GD2 (IgG2a, BD Pharmigen) and direct APC-H7 mouse anti-human CD45 (IgG1, BD Pharmigen) antibodies to discriminate NB cells ($GD2^+CD45^-$) from NK cells ($GD2^-CD45^+$). Then, cells were stained with Fixable Viability Stain 510 (BD Horizon) following manufacturer's procedures and analyzed by flow cytometry (FACSVerse flow cytometer-BD).

Flow cytometry analysis

To assess NK cell viability, cells were recovered from the 2D standard (96-well plate) culture or from the 3D culture.

The latter was achieved by hydrogel dissolution, through incubation in an alginate solubilizing solution (0.15 M NaCl, 100 mm trisodium citrate dihydrate), for 10 min in a 37°C water bath. Cells were then washed with PBS w/o Ca^{2+} and Mg^{2+} and stained with a PE-TexasRed Fixable Cell Viability dye (ThermoFisher Scientific), following manufacturer's protocol.

To assess NK cell infiltration within the 3D tumor culture, as well as their phenotype, the cells were recovered from the alginate scaffold as described above. Cells were also recovered from the medium surrounding the hydrogels within the transwell inserts (to analyze extravasated NK cells) and from the circulating compartment (to analyze circulating NK cells). The cells were then washed with PBS w/o Ca^{2+} and Mg^{2+} and incubated with the staining solutions, for 30 min: the cells were stained with an anti-human CD45-APC and an anti-human CD16-PacificBlue antibody (ThermoFisher Scientific). For the analysis of tumor cell death after dynamic co-culture, the cells were recovered from the alginate scaffold and subsequently stained with an anti-human CD45-APC antibody and an Annexin V-FITC Apoptosis Detection Kit (eBioscience).

After incubation with the staining solution, the cells were washed and run through a NovoCyte3000 Flow Cytometer System. Data were analyzed with the NovoExpress software (Agilent Technologies).

Statistical analysis

Statistical analysis was performed with the GraphPad Software GraphPad Prism5. Differences between groups were assessed by *t* test, where applicable, or by one-way analysis of variance (ANOVA. A p value < 0.05 was considered statistically significant), or by Mann-Whitney test (p value < 0.05 was considered statistically significant). At least three independent experiments have been performed with a minimum of three technical replicates.

Data availability statement

The original contributions presented in the study are included in the article/Supplementary Material, further inquiries can be directed to the corresponding author.

Ethics statement

The studies involving human participants were reviewed and approved by the DIMES, University of Genoa. The patients/participants provided their written informed consent to participate in this study.

Author contributions

MM, designed the 3D experiments with the help of SS, RC, and CB; MM and GP with the support of all, performed the 3D experiments and analyzed the data; FF and AD performed cytofluorimetric analysis and analyzed the data; CV, SB, and AP performed confocal analysis and analyzed the data; AF and MA performed computational fluid dynamic simulation and theoretical modeling; MM wrote the manuscript that was revised by all the co-Authors.

Funding

This work was supported by the funding awarded by the Italian Ministry of Health ("Ricerca Corrente 2021" and "5 per mille" project 5M-2018-23680422, to CB). FF was supported by an AIRC Fellowship for Italy. This research was funded by the European Union's Horizon 2020 Research and Innovation Programme under Grant no. 801159.

Conflict of interest

MA, SS, and MM are employed by the company React4life S.r.l.

The remaining authors declare that the research was conducted in the absence of any commercial or financial relationships that could be construed as a potential conflict of interest.

Publisher's note

References

Amin, R., Knowlton, S., Hart, A., Yenilmez, B., Ghaderinezhad, F., Katebifar, S., et al. (2016). 3D-printed microfluidic devices. *Biofabrication* 8, 022001. doi:10.1088/1758-5090/8/2/022001

Ando, Y., Mariano, C., and Shen, K. (2021). Engineered *in vitro* tumor models for cell-based immunotherapy. *Acta Biomater.* 132, 345–359. doi:10.1016/j.actbio.2021.03.076

Aung, A., Kumar, V., Theprungsirikul, J., Davey, S. K., and Varghese, S. (2020). An engineered tumor-on-a-chip device with breast cancer–immune cell interactions for assessing T-cell recruitment. *Cancer Res.* 80, 263–275. doi:10.1158/0008-5472.can-19-0342

Ayuso, J. M., Rehman, S., Virumbrales-Munoz, M., McMinn, P. H., Geiger, P., Fitzgerald, C., et al. (2021). Microfluidic tumor-on-a-chip model to evaluate the role of tumor environmental stress on NK cell exhaustion. *Sci. Adv.* 7, eabc2331. doi:10.1126/sciadv.abc2331

Ayuso, J. M., Truttschel, R., Gong, M. M., Humayun, M., Virumbrales-Munoz, M., Vitek, R., et al. (2019). Evaluating natural killer cell cytotoxicity against solid tumors using a microfluidic model. *Oncoimmunology* 8, 1553477. doi:10.1080/2162402x.2018.1553477

Ballester-Beltran, J., Biggs, M. J. P., Dalby, M. J., Salmeron-Sanchez, M., and Leal-Egana, A. (2015). Sensing the difference: The influence of anisotropic cues on cell behav. *Front. Mat.* 2, 39. doi:10.3389/fmats.2015.00039

Balsamo, M., Vermi, W., Parodi, M., Pietra, G., Manzini, C., Queirolo, P., et al. (2012). Melanoma cells become resistant to NK-cell-mediated killing when exposed to NK-cell numbers compatible with NK-cell infiltration in the tumor. *Eur. J. Immunol.* 42, 1833–1842. doi:10.1002/eji.201142179

Bhatia, S. N., and Ingber, D. E. (2014). Microfluidic organs-on-chips. *Nat. Biotechnol.* 32, 760–772. doi:10.1038/nbt.2989

Bjornson-Hooper, Z. B., Fragiadakis, G. K., Spitzer, M. H., Chen, H., Madhireddy, D., Hu, K., et al. (2022). A comprehensive atlas of immunological differences between humans, mice, and non-human primates. *Front. Immunol.* 13, 867015. doi:10.3389/fimmu.2022.867015

Bottino, C., Dondero, A., and Castriconi, R. (2021). Inhibitory axes impacting on the activity and fate of Innate Lymphoid Cells. *Mol. Asp. Med.* 80, 100985. doi:10.1016/j.mam.2021.100985

Boucherit, N., Gorvel, L., and Olive, D. (2020). 3D tumor models and their use for the testing of immunotherapies. *Front. Immunol.* 11, 603640. doi:10.3389/fimmu.2020.603640

Businaro, L., De Ninno, A., Schiavoni, G., Lucarini, V., Ciasca, G., Gerardino, A., et al. (2013). Cross talk between cancer and immune cells: Exploring complex dynamics in a microfluidic environment. *Lab. Chip* 13, 229–239. doi:10.1039/c2lc40887b

Castriconi, R., Carrega, P., Dondero, A., Bellora, F., Casu, B., Regis, S., et al. (2018). Molecular mechanisms directing migration and retention of natural killer cells in human tissues. *Front. Immunol.* 9, 2324. doi:10.3389/fimmu.2018.02324

Castriconi, R., Dondero, A., Bellora, F., Moretta, L., Castellano, A., Locatelli, F., et al. (2013). Neuroblastoma-derived TGF-β1 modulates the chemokine receptor repertoire of human resting NK cells. *J. I.* 190, 5321–5328. doi:10.4049/jimmunol.1202693

Castriconi, R., Dondero, A., Cantoni, C., Della Chiesa, M., Prato, C., Nanni, M., et al. (2007). Functional characterization of natural killer cells in type I leukocyte adhesion deficiency. *Blood* 109, 4873–4881. doi:10.1182/blood-2006-08-038760

Castriconi, R., Dondero, A., Cilli, M., Ognio, E., Pezzolo, A., De Giovanni, B., et al. (2007). Human NK cell infusions prolong survival of metastatic human neuroblastoma-bearing NOD/scid mice. *Cancer Immunol. Immunother.* 56, 1733–1742. doi:10.1007/s00262-007-0317-0

Castriconi, R., Dondero, A., Corrias, M. V., Lanino, E., Pende, D., Moretta, L., et al. (2004). Natural killer cell-mediated killing of freshly isolated neuroblastoma cells. *Cancer Res.* 64, 9180–9184. doi:10.1158/0008-5472.can-04-2682

Cavo, M., Caria, M., Pulsoni, I., Beltrame, F., Fato, M., Scaglione, S., et al. (2018). A new cell-laden 3D Alginate-Matrigel hydrogel resembles human breast cancer cell malignant morphology, spread and invasion capability observed "*in vivo*". *Sci. Rep.* 8, 5333. doi:10.1038/s41598-018-23250-4

Cavo, M., Fato, M., Peñuela, L., Beltrame, F., Raiteri, R., Scaglione, S., et al. (2016). Microenvironment complexity and matrix stiffness regulate breast cancer cell activity in a 3D *in vitro* model. *Sci. Rep.* 6, 35367. doi:10.1038/srep35367

Cogels, M. M., Rouas, R., Ghanem, G. E., Martinive, P., Awada, A., Van Gestel, D., et al. (2021). Humanized mice as a valuable pre-clinical model for cancer immunotherapy research. *Front. Oncol.* 11, 784947. doi:10.3389/fonc.2021.784947

Corrias, M. V., Scaruffi, P., Occhino, M., De Bernardi, B., Tonini, G. P., and Pistoia, V. (1996). Expression of MAGE-1, MAGE-3 and MART-1 genes in neuroblastoma. *Int. J. Cancer* 69, 403. doi:10.1002/(SICI)1097-0215(19961021)69:5<403::AID-IJC9>3.0.CO;2-9

Dickinson, A. J., Meyer, M., Pawlak, E. A., Gomez, S., Jaspers, I., Allbritton, N. L., et al. (2015). Analysis of sphingosine kinase activity in single natural killer cells from peripheral blood. *Integr. Biol.* 7, 392–401. doi:10.1039/c5ib00007f

Franklin, M. R., Platero, S., Saini, K. S., Curigliano, G., and Anderson, S. (2022). Immuno-oncology trends: Preclinical models, biomarkers, and clinical development. *J. Immunother. Cancer* 10, e003231. doi:10.1136/jitc-2021-003231

Gopal, S., Kwon, S.-J., Ku, B., Lee, D. W., Kim, J., Dordick, J. S., et al. (2021). 3D tumor spheroid microarray for high-throughput, high-content natural killer cell-mediated cytotoxicity. *Commun. Biol.* 4, 893. doi:10.1038/s42003-021-02417-2

Goyal, G., Prabhala, P., Mahajan, G., Bausk, B., Gilboa, T., Xie, L., et al. (2022). Ectopic lymphoid follicle formation and human seasonal influenza vaccination responses recapitulated in an organ-on-a-chip. *Adv. Sci.* 2022, 2103241. doi:10.1002/advs.202103241

Guerra, E., Di Pietro, R., Basile, M., Trerotola, M., and Alberti, S. (2021). Cancer-homing CAR-T cells and endogenous immune population dynamics. *Int. J. Mol. Sci.* 23, 405. doi:10.3390/ijms23010405

Guo, Z., Song, J., Hao, J., Zhao, H., Du, X., Li, E., et al. (2019). M2 macrophages promote NSCLC metastasis by upregulating CRYAB. *Cell. Death Dis.* 10, 377. doi:10.1038/s41419-019-1618-x

Honkala, A., V Malhotra, S., Kummar, S., and Junttila, M. R. (2021). Harnessing the predictive power of preclinical models for oncology drug development. *Nat. Rev. Drug Discov.* 21, 99–114. doi:10.1038/s41573-021-00301

Hsu, T.-H., Kao, Y.-L., Lin, W.-L., Xiao, J.-L., Kuo, P.-L., Wu, C.-W., et al. (2012). The migration speed of cancer cells influenced by macrophages and myofibroblasts co-cultured in a microfluidic chip. *Integr. Biol.* 4, 177–182. doi:10.1039/c2ib00112h

Jardim, D. L., Groves, E. S., Breitfeld, P. P., and Kurzrock, R. (2017). Factors associated with failure of oncology drugs in late-stage clinical development: A systematic review. *Cancer Treat. Rev.* 52, 12–21. doi:10.1016/j.ctrv.2016.10.009

Kumari, R., Ouyang, X., Wang, J., Xu, X., Zheng, M., An, X., et al. (2021). Preclinical pharmacology modeling of chimeric antigen receptor T therapies. *Curr. Opin. Pharmacol.* 61, 49. doi:10.1016/j.coph.2021.08.008

Lee, S. W. L., Adriani, G., Ceccarello, E., Pavesi, A., Tan, A. T., Bertoletti, A., et al. (2018). Characterizing the role of monocytes in T cell cancer immunotherapy using a 3D microfluidic model. *Front. Immunol.* 9, 416. doi:10.3389/fimmu.2018.00416

Mak, I. W. Y., Evaniew, N., and Ghert, M. (2014). Lost in translation: Animal models and clinical trials in cancer treatment. *Am. J. Transl. Res.* 6, 114.

Marrella, A., Buratti, P., Markus, J., Firpo, G., Pesenti, M., Landry, T., et al. (2020). *In vitro* demonstration of intestinal absorption mechanisms of different sugars using 3D organotypic tissues in a fluidic device. *ALTEX* 37, 255–264. doi:10.14573/altex.1908311

Marrella, A., Dondero, A., Aiello, M., Casu, B., Olive, D., Regis, S., et al. (2019). Cell-Laden hydrogel as a clinical-relevant 3D model for analyzing neuroblastoma growth, immunophenotype, and susceptibility to therapies. *Front. Immunol.* 10, 1876. doi:10.3389/fimmu.2019.01876

Marrella, A., Fedi, A., Varani, G., Vaccari, I., Fato, M., Firpo, G., et al. (2021). High blood flow shear stress values are associated with circulating tumor cells cluster disaggregation in a multi-channel microfluidic device. *PLoS One* 16, e0245536. doi:10.1371/journal.pone.0245536

Marrella, A., Varani, G., Aiello, M., Vaccari, I., Vitale, C., Mojzisek, M., et al. (2021). 3D fluid-dynamic ovarian cancer model resembling systemic drug administration for efficacy assay. *ALTEX-Alternatives Anim. Exp.* 38, 82–94. doi:10.14573/altex.2003131

Maulana, T. I., Kromidas, E., Wallstabe, L., Cipriano, M., Alb, M., Zaupa, C., et al. (2021). Immunocompetent cancer-on-chip models to assess immuno-oncology therapy. *Adv. Drug Deliv. Rev.* 173, 281–305. doi:10.1016/j.addr.2021.03.015

Melaiu, O., Chierici, M., Lucarini, V., Jurman, G., Conti, L. A., De Vito, R., et al. (2020). Cellular and gene signatures of tumor-infiltrating dendritic cells and natural-killer cells predict prognosis of neuroblastoma. *Nat. Commun.* 11, 5992. doi:10.1038/s41467-020-19781-y

Morimoto, T., Nakazawa, T., Matsuda, R., Nishimura, F., Nakamura, M., Yamada, S., et al. (2021). Evaluation of comprehensive gene expression and NK cell-mediated killing in glioblastoma cell line-derived spheroids. *Cancers (Basel)* 13, 4896. doi:10.3390/cancers13194896

Myers, J. A., and Miller, J. S. (2021). Exploring the NK cell platform for cancer immunotherapy. *Nat. Rev. Clin. Oncol.* 18, 85–100. doi:10.1038/s41571-020-0426-7

Orange, J. S. (2008). Formation and function of the lytic NK-cell immunological synapse. *Nat. Rev. Immunol.* 8, 713–725. doi:10.1038/nri2381

Parlato, S., De Ninno, A., Molfetta, R., Toschi, E., Salerno, D., Mencattini, A., et al. (2017). 3D Microfluidic model for evaluating immunotherapy efficacy by tracking dendritic cell behaviour toward tumor cells. *Sci. Rep.* 7, 1093. doi:10.1038/s41598-017-01013-x

Pavesi, A., Tan, A. T., Koh, S., Chia, A., Colombo, M., Antonecchia, E., et al. (2017). A 3D microfluidic model for preclinical evaluation of TCR-engineered T cells against solid tumors. *JCI Insight* 2, 89762. doi:10.1172/jci.insight.89762

Pulsoni, I., Lubda, M., Aiello, M., Fedi, A., Marzagalli, M., von Hagen, J., et al. (2022). Comparison between franz diffusion cell and a novel micro-physiological system for *in vitro* penetration assay using different skin models. *SLAS Technol.* 27 (3), 161–171. doi:10.1016/j.slast.2021.12.006

Regis, S., Caliendo, F., Dondero, A., Casu, B., Romano, F., Loiacono, F., et al. (2017). TGF-β1 downregulates the expression of CX3CR1 by inducing miR-27a-5p in primary human NK cells. *Front. Immunol.* 8, 868. doi:10.3389/fimmu.2017.00868

Ren, X., Alamri, A., Hipolito, J., Lin, F., and Kung, S. K. P. (2020). *Methods in enzymol*. Amsterdam, Netherlands: Elsevier, 357.

Ringquist, R., Ghoshal, D., Jain, R., and Roy, K. (2021). Understanding and improving cellular immunotherapies against cancer: From cell-manufacturing to tumor-immune models. *Adv. Drug Deliv. Rev.* 179, 114003. doi:10.1016/j.addr.2021.114003

Rodrigues, J., Heinrich, M. A., Teixeira, L. M., and Prakash, J. (2021). 3D *in vitro* model (R)evolution: Unveiling tumor–stroma interactions. *Trends Cancer* 7, 249–264. doi:10.1016/j.trecan.2020.10.009

Sargenti, A., Musmeci, F., Bacchi, F., Delprete, C., Cristaldi, D. A., Cannas, F., et al. (2020). Physical characterization of colorectal cancer spheroids and evaluation of NK cell infiltration through a flow-based analysis. *Front. Immunol.* 11, 564887. doi:10.3389/fimmu.2020.564887

Shelton, S. E., Nguyen, H. T., Barbie, D. A., and Kamm, R. D. (2021). Engineering approaches for studying immune-tumor cell interactions and immunotherapy. *IScience* 24, 101985. doi:10.1016/j.isci.2020.101985

Song, J., Choi, H., Koh, S. K., Park, D., Yu, J., Kang, H., et al. (2021). High-throughput 3D *in vitro* tumor vasculature model for real-time monitoring of immune cell infiltration and cytotoxicity. *Front. Immunol.* 12, 733317. doi:10.3389/fimmu.2021.733317

Sontheimer-Phelps, A., Hassell, B. A., and Ingber, D. E. (2019). Modelling cancer in microfluidic human organs-on-chips. *Nat. Rev. Cancer* 19, 65. doi:10.1038/s41568-018-0104-6

Szanto, C. L., Cornel, A. M., Tamminga, S. M., Delemarre, E. M., de Koning, C. C. H., van den Beemt, D. A. M. H., et al. (2021). Immune monitoring during therapy reveals activitory and regulatory immune responses in high-risk neuroblastoma. *Cancers (Basel)* 13, 2096. doi:10.3390/cancers13092096

Um, E., Oh, J. M., Park, J., Song, T., Kim, T.-E., Choi, Y., et al. (2019). Immature dendritic cells navigate microscopic mazes to find tumor cells. *Lab. Chip* 19, 1665–1675. doi:10.1039/c9lc00150f

Vitale, C., Fedi, A., Marrella, A., Varani, G., Fato, M., Scaglione, S., et al. (2020). 3D perfusable hydrogel recapitulating the cancer dynamic environment to *in vitro* investigate metastatic colonization. *Polym. (Basel)* 12, 2467. doi:10.3390/polym12112467

Vitale, C., Marzagalli, M., Scaglione, S., Dondero, A., Bottino, C., Castriconi, R., et al. (2022). Tumor microenvironment and hydrogel-based 3D cancer models for *in vitro* testing immunotherapies. *Cancers (Basel)* 14, 1013. doi:10.3390/cancers14041013

Wong, C. H., Siah, K. W., and Lo, A. W. (2019). Estimation of clinical trial success rates and related parameters. *Biostatistics* 20, 273–286. doi:10.1093/biostatistics/kxx069

Yang, H., Gou, X., Wang, Y., Fahmy, T. M., Leung, A. Y.-H., Lu, J., et al. (2015). A dynamic model of chemoattractant-induced cell migration. *Biophys. J.* 108, 1645–1651. doi:10.1016/j.bpj.2014.12.060

Yu, J., Berthier, E., Craig, A., de Groot, T. E., Sparks, S., Ingram, P. N., et al. (2019). Reconfigurable open microfluidics for studying the spatiotemporal dynamics of paracrine signalling. *Nat. Biomed. Eng.* 3, 830–841. doi:10.1038/s41551-019-0421-4

Zhao, Q., Shirinzadeh, B., Cui, M., Sun, M., and Zhao, X. (2015). A simple weighing method for spherical cells. *SLAS Technol.* 20, 471–480. doi:10.1177/2211068215583629

frontiers | Frontiers in Bioengineering and Biotechnology

TYPE Original Research
PUBLISHED 09 September 2022
DOI 10.3389/fbioe.2022.965200

OPEN ACCESS

EDITED BY
Antonella Piscioneri,
Institute for Membrane Technology, Department of Chemical Sciences and Materials Technologies, National Research Council (CNR), Italy

REVIEWED BY
Klaus Eyer,
ETH Zürich, Switzerland
Antonietta Messina,
INSERM U1193 Physiopathogénèse et Traitement des Maladies du Foie, France

*CORRESPONDENCE
Jannik B. Larsen,
jannla@dtu.dk
Thomas L. Andresen,
tlan@dtu.dk

SPECIALTY SECTION
This article was submitted to Tissue Engineering and Regenerative Medicine, a section of the journal Frontiers in Bioengineering and Biotechnology

RECEIVED 09 June 2022
ACCEPTED 18 July 2022
PUBLISHED 09 September 2022

CITATION
Weller A, Hansen MB, Marie R, Hundahl AC, Hempel C, Kempen PJ, Frandsen HL, Parhamifar L, Larsen JB and Andresen TL (2022), Quantifying the transport of biologics across intestinal barrier models in real-time by fluorescent imaging.
Front. Bioeng. Biotechnol. 10:965200.
doi: 10.3389/fbioe.2022.965200

Quantifying the transport of biologics across intestinal barrier models in real-time by fluorescent imaging

Arjen Weller[1,2], Morten B. Hansen[1,2], Rodolphe Marie[1,2], Adam C. Hundahl[1,2], Casper Hempel[1,2], Paul J. Kempen[2,3], Henrik L. Frandsen[4], Ladan Parhamifar[1,2], Jannik B. Larsen[1,2]* and Thomas L. Andresen[1,2]*

[1]Center for Intestinal Absorption and Transport of Biopharmaceuticals, Technical University of Denmark, Lyngby, Denmark, [2]Department of Health Technology, Technical University of Denmark, Lyngby, Denmark, [3]The National Centre for Nano Fabrication and Characterization, DTU Nanolab, Technical University of Denmark, Lyngby, Denmark, [4]National Food Institute, Technical University of Denmark, Lyngby, Denmark

Unsuccessful clinical translation of orally delivered biological drugs remains a challenge in pharmaceutical development and has been linked to insufficient mechanistic understanding of intestinal drug transport. Live cell imaging could provide such mechanistic insights by directly tracking drug transport across intestinal barriers at subcellular resolution, however traditional intestinal *in vitro* models are not compatible with the necessary live cell imaging modalities. Here, we employed a novel microfluidic platform to develop an *in vitro* intestinal epithelial barrier compatible with advanced widefield- and confocal microscopy. We established a quantitative, multiplexed and high-temporal resolution imaging assay for investigating the cellular uptake and cross-barrier transport of biologics while simultaneously monitoring barrier integrity. As a proof-of-principle, we use the generic model to monitor the transport of co-administrated cell penetrating peptide (TAT) and insulin. We show that while TAT displayed a concentration dependent difference in its transport mechanism and efficiency, insulin displayed cellular internalization, but was restricted from transport across the barrier. This illustrates how such a sophisticated imaging based barrier model can facilitate mechanistic studies of drug transport across intestinal barriers and aid *in vivo* and clinical translation in drug development.

KEYWORDS

organ-on-a-chip, drug transport, fluorescence live cell imaging, drug development, high through put screening platform

1 Introduction

Drug formulation development to allow for oral drug administration has been pursued for decades due to high patient compliance (Balimane et al., 2000; Masaoka et al., 2006). However, especially for biologics, such as peptides and proteins, the success has been limited and only five orally administered peptide formulations have reached the clinic (Drucker, 2020; Maher et al., 2021). These issues reflect the translational struggles seen broadly within the field of drug delivery, spurring the push for a deeper mechanistic understanding of drug transport, allowing for better rational design of drug formulations (Mechanism matters, 2010; Time to deliver, 2014).

To identify and understand the mode of action employed by drug formulations for crossing the intestinal barrier, assays compatible with live cell imaging techniques for monitoring the drug-cell barrier penetration in real-time would be ideal (Gumbleton, 2005; Watson, 2005; Larsen et al., 2021). The most popular and established *in vitro* platform for studying drug transport has been the Transwell system (TW), where cells are cultivated on a rigid membrane that separates two medium-containing chambers under static conditions (Hidalgo et al., 1989; Hubatsch et al., 2007). However, the structural build of TW limits its compatibility with live cell-imaging modalities (Zaderer et al., 2019), impeding high-resolution kinetic measurements and image-based readouts, and therefore provides only limited direct information on the underlying transport mechanisms. In addition, the TW system is incapable of incorporating three-dimensional cell cultures, extracellular matrix support and perfusion flow, all aspects shown to be highly important for cell proliferation and differentiation (Basson et al., 1996; Simon-Assmann et al., 2007; Huh et al., 2011; Youhanna and Lauschke, 2021). In recent years advanced microfluidic platforms were developed in order to recapitulate the three-dimensional physiology of the intestinal epithelial and the gastrointestinal environment *in vitro* (Bein et al., 2018). Among these, the OrganoPlate represents a user-friendly platform facilitating real-time fluorescent readouts. However until now, the OrganoPlate have primarily been used for toxicity assessment (Trietsch et al., 2017; Beaurivage et al., 2019), or disease modeling (Beaurivage et al., 2019). Only recently, did Hagiwara et al. apply the platform in the context of drug delivery as they investigated how the cross barrier transport of two well-known small molecule drugs was affected by simulated intestinal fluids. However, taking full advantage of the compatibility of the OrganoPlate with live cell imaging for studying the cross barrier transport mechanism of biologics is yet to be achieved. Furthermore, a prerequisite for this is a systematic validation of the OrganoPlate as a reliable *in vitro* model with a high *in vivo* drug absorption predictability by a direct correlation to standard drugs with known human absorption values. Expanding and validating models for use in transport studies is non-trivial, as highlighted by recent accounts showing that it is paramount to perform a comprehensive validation as they often are limited by poor abilities to predict the *in vivo* level of drug transport (Dahlgren et al., 2015). Together this highlights how there are still room for new methodologies facilitating the study of *in vitro* drug transport in validated, easy-to-use and reproducible platforms (Gleeson and McCartney, 2019), especially compatible with real-time fluorescent imaging (Wong et al., 2020; Halamoda-Kenzaoui et al., 2021; Larsen et al., 2021; Yilmaz et al., 2022).

Here, we employed the OrganoPlate microfluidic chip as a platform for developing an *in vitro* intestinal barrier model allowing us to study drug transport and uptake mechanisms using advanced fluorescent imaging modalities. An image-based in-chip validation of epithelial differentiation and polarization markers in generated monolayer cell tubules revealed a leak-tight, fully differentiated epithelial cell barrier, encompassing important features of the *in vivo* barrier, including a complex mucus layer and a functional metabolic machinery known to influence drug transport efficiency. We validate, for the first time, the microfluidic platform as a suitable model for intestinal drug transport studies by correlating the transport of small molecule drugs to the corresponding human absorption data. Furthermore, we use the model as a multiplexed live-cell imaging-based assay to obtain mechanistic in-depth knowledge about the mobility of biologics across fully differentiated and polarized cell barrier tubules. This epitomizes how the developed epithelial barrier system can facilitate sensitive real-time image-based quantitative studies on the transport and intracellular fate of biologics.

2 Materials and methods

2.1 Cell culture

The human colon adenocarcinoma cell line Caco-2 (European Collection of Authenticated Cell Cultures (0,9,042,001, ECACC) were maintained in Eagle's Minimum Essential Medium (EMEM) (30–2003, ATCC) supplemented with 10% fetal bovine serum (FBS) (S1810-500, Biowest), 1% MEM non-essential amino acids (NEAA) (M7145, Sigma) and 1% penicillin/streptomycin (P/S) (P0781, Sigma). The clone HT29-MTX-E12 generated from the parental human colon adenocarcinoma cells (12,040,401, ECACC), HT29, were cultured in Dulbecco's Modified Eagle's Medium (DMEM) (D5796, Sigma) supplemented with 10% FBS, 1% NEAA and 1% P/S. Both cell lines were maintained at 37°C, 5% CO_2 in a humidified incubator. Caco-2 cells with passage numbers between 47–61 and HT29-MTX-E12 cells between passage numbers 50–70 were used for all experiments. Cells were seeded for experiments after reaching 80–90% confluency in

parental flasks. For coculture experiments, both cell lines were cultured in Caco-2 cell growth media.

2.2 OrganoPlate culture

For all experiments the three-lane OrganoPlate (4,004–400-B, Mimetas BV) with 40 individual chips was used, where each chip consists of a seeding channel, an ECM-channel and a perfusion channel (220 µm height x 300 µm width). Cell seeding into the OrganoPlate was performed as previously described (Trietsch et al., 2017). In brief, a 4 mg ml^{-1} Collagen 1 (3,447–020–01, R&D Systems) ECM-gel supplemented with 100 mM HEPES (H0887, Sigma) and 3.7 mg ml^{-1} $NaHCO_3$ was prepared. The ECM-mixture was dispensed into the ECM-channel (2 µL) and placed in the incubator for 30 min to polymerize. After polymerization 30 µL Hanks' Balanced Salt solution (HBSS) was added to the ECM-channel to avoid gel drying. Next, cells were detached with 0.25% trypsin EDTA and diluted to a final concentration of 1×10^7 cells mL^{-1}. For coculture of Caco-2 and HT29-MTX E12 cells, a ratio of 6:1 was used. The upper channel of the chip was filled with 2 µL cell suspension (a total of 20×10^3 cells/channel) and the OrganoPlate was placed vertically inside the incubator for 3 h to allow cell attachment. Thereafter, 50 µL medium was added to the seeding channel (inlet and outlet) and the perfusion channel (inlet and outlet). The OrganoPlate was incubated horizontally for 4 days on an interval rocker (± 7° angle, 8 min rocking interval) at 37°C, 5% CO_2 resulting in a formation of a tubule inside the chip. The medium was replaced every 2–3 days.

2.3 Transwell culture

Caco-2 cells were seeded at a final cell density of 5×10^4 cells cm^{-2} in a 24-well format Transwell system with a surface area of 0.33 cm^2 (CLS3413, Corning). The cells were grown in EMEM with 10% FBS and 1% P/S over 19–21 days and the medium was replaced every 2–3 days.

2.4 Transepithelial resistance measurements

The barrier integrity of cells seeded in the Transwell system was monitored routinely using an EVOM2 system equipped with an EndOhm-6G cup for measurements TEER (World Precision Instruments, Sarasota, FL). Raw resistance data were translated into TEER using the equation:

$$TEER[\Omega \times cm^2] = TEER\_RAW[\Omega] \times surface\ area[cm^2] \quad (1)$$

Caco-2 monolayers with a TEER above 1,500 Ω*cm^2 were selected for further drug absorption studies.

2.5 Imaging modalities

Spinning disc (SD) confocal microscopy was performed on a Nikon Ti2 inverted microscope equipped with a Yokogawa CSU-W1 module and a Photometrics Prime 95B sCMOS camera was used for all experiments (excl. Image-based TAT transport). The set-up includes four excitation lasers 405/488/561/638 nm with 442/42, 520/28 BrightLine HC filters and 600/50 ET, 700/75 ET bandpass filters. For this work, a set of CFI Plan Apochromat Lambda objectives were used: ×4/0.2, 20x/0.75, 60x/1.4 and 100x/1.45. For image-based transport experiments, epi-fluorescence microscopy was performed using a Nikon Eclipse Ti2 microscope equipped with an LED source (CoolLED), a dual-band filter cube (AHF, Excitation 455–489 nm, 557–588 nm; Emission 506–542 nm, 605–660 nm) and a Photometrics Evolve 512 electron-multiplying charge-coupled device camera was used (10x N.A. 0.30).

2.6 Barrier integrity assay

The BI of the mono- and coculture systems was analyzed on day 1, 2 and 4. The Medium in the seeding channel was replaced with EMEM containing 0.5 mg ml^{-1} 4.4 kDa TD (T1037, Sigma) and placed on an interval rocker for 15 min in the incubator. After incubation, the plate was imaged using a SD confocal microscope at ×4 magnification. Inhomogeneous cell coverage in the seeding channel over during the cultivation leads to an inhomogeneous fluorescence intensity profile. To ensure an accurate comparison of BI values the whole channel (Seeding and ECM channel) was selected for measuring the intensity.

2.7 Immunostaining

Cells seeded in the OrganoPlate were fixed with 4% paraformaldehyde in phosphate-buffered saline (PBS) (D8537, Sigma) for 15 min, washed with PBS and permeabilized for 10 min in 0.3% Triton-X (T8787, Sigma). Subsequently, cells were washed with 4% FBS/PBS and incubated for 30 min in blocking solution 3% Bovine Serum Albumin (BSA)/PBS followed by incubation with primary antibody for 60 min at room temperature. Cells were then washed with 4% FBS/PBS and incubated for 30 min with the secondary antibody. Primary antibodies against Rabbit-a-Zonula occludens-1 (ZO-1) (61–7,300, Thermo Fischer, 1:200), Rabbit-a-Mucin 2 (Muc2) (PA5-21329, Thermo Fischer, 1:200), Mouse-a-Ezrin (610,602, BD Transduction, 1:100), Mouse-a-Multidrug Resistance Protein 2 (MRP2) (SC-59608, Santa Cruz, 100 µg ml-1), Mouse-a-Breast *Cancer* Resistance Protein (BCRP) (ab3380, Abcam, 1:50) were used. For the secondary antibody staining, Goat Anti-Rabbit IgG (H + L) Alexa Fluor 488 (ab150077, Abcam, 1:200) and Goat anti-Mouse IgG (H + L) Alexa Fluor 647 (A-21236, Thermo Fisher, 1:200) were used. Following antibody staining cells were washed three times with 4% FBS/PBS and nuclei

were stained with 4′,6-diamidino-2-phenylindole (DAPI) (D1306, Thermo Fisher, 1:1,000) for 5 min. Cells were kept in PBS at 4°C and imaged using the previously described SD confocal microscope. All protein stainings were repeated at least three times in mono-and coculture tubules. Images in Figure 2 display representative immunostained cell-tubules.

2.8 Microvilli visualization using transmission electron microscopy

The coculture tubules were fixed by filling all three channels of the chip system with a solution of 2% glutaraldehyde, 4% paraformaldehyde in 0.1 M Na cacodylate buffer at pH 7.4. After fixation for 30 min at room temperature, the plate was stored at 4°C to await further processing. Each channel was washed three times with 0.1 M Na cacodylate buffer and stained with 1% osmium tetroxide in a 0.1 M Na-cacodylate buffer for 2 h at room temperature. After staining with osmium tetroxide, the channels were washed three times in milliQ water and stained with a 1% uranyl acetate solution overnight. The following day, the channels were washed twice in milliQ water followed by dehydration in increasing concentrations of ethanol, 50, 70, 95% and twice 100% with 20 min between solvent exchanges, to ensure complete dehydration. The channels were further dehydrated three times in acetonitrile for 10 min each before the start of resin infiltration. The channels were infiltrated with a 1:1 solution of TAAB 812 medium hardness embedding resin and acetonitrile. After 1 h, the channels were re-infiltrated with the same 1:1 solution to ensure complete infiltration. After one more hour, the channels were infiltrated with a 2:1 resin: acetonitrile solution overnight. The next morning the channels were re-infiltrated with the 2:1 solution for 6 h. The channels were then infiltrated with pure resin overnight. The following morning the channels were again re-infiltrated with pure resin to ensure complete infiltration. After 6 hours the plate was cured at 60°C for 72 h.

After the resin was completely cured, individual channel setups were cut from the larger plate for further processing. The samples were placed in a concentrated hydrofluoric acid solution, 48 wt%, to dissolve the glass substrate. After 45 min, the sample was removed from the hydrofluoric acid and rinsed with a saturated calcium chloride solution, 45 wt%. The sample was then rinsed with milliQ water. The now exposed channel was cut from the remaining device and re-embedded in TAAB resin which was cured overnight at 60°C. The resin block was trimmed with a razor blade, exposing a surface perpendicular to the channel. Thin sections, 120 nm thick, were cut using a Leica EM UC7 ultramicrotome and placed on a nickel slot grid coated with carbon-stabilized formvar. TEM was performed utilizing a FEI Tecnai T20 G2 TEM located at the Center for Electron Nanoscopy at the Technical University of Denmark, and images were acquired using TVIPS XF416 CCD camera.

2.9 Microvilli visualization using transmission electron microscopy

The coculture tubules were fixed by filling all three channels of the chip system with a solution of 2% glutaraldehyde, 4% paraformaldehyde in 0.1 M Na cacodylate buffer at pH 7.4. After fixation for 30 min at room temperature, the plate was stored at 4°C to await further processing. Each channel was washed three times with 0.1 M Na cacodylate buffer and stained with 1% osmium tetroxide in a 0.1 M Na cacodylate buffer for 2 h at room temperature. After staining with osmium tetroxide, the channels were washed three times in milliQ water and stained with a 1% uranyl acetate solution overnight. The following day, the channels were washed twice in milliQ water followed by dehydration in increasing concentrations of ethanol, 50, 70, 95% and twice 100% with 20 min between solvent exchanges, to ensure complete dehydration. The channels were further dehydrated three times in acetonitrile for 10 min each before the start of resin infiltration. The channels were infiltrated with a 1:1 solution of TAAB 812 medium hardness embedding resin and acetonitrile. After 1 h, the channels were re-infiltrated with the same 1:1 solution to ensure complete infiltration. After one more hour, the channels were infiltrated with a 2:1 resin: acetonitrile solution overnight. The next morning the channels were re-infiltrated with the 2:1 solution for 6 h. The channels were then infiltrated with pure resin overnight. The following morning the channels were again re-infiltrated with pure resin to ensure complete infiltration. After 6 hours the plate was cured at 60°C for 72 h.

After the resin was completely cured, individual channel setups were cut from the larger plate for further processing. The samples were placed in a concentrated hydrofluoric acid solution, 48 wt%, to dissolve the glass substrate. After 45 min, the sample was removed from the hydrofluoric acid and rinsed with a saturated calcium chloride solution, 45 wt%. The sample was then rinsed with milliQ water. The now exposed channel was cut from the remaining device and re-embedded in TAAB resin which was cured overnight at 60°C. The resin block was trimmed with a razor blade, exposing a surface perpendicular to the channel. Thin sections, 120 nm thick, were cut using a Leica EM UC7 ultramicrotome and placed on a nickel slot grid coated with carbon-stabilized formvar. TEM was performed utilizing a FEI Tecnai T20 G2 TEM located at the Center for Electron Nanoscopy at the Technical University of Denmark, and images were acquired using TVIPS XF416 CCD camera.

2.10 Mucus determination with alcian blue staining

Leak tight tubules in the OrganoPlate were fixed with 4% PFA for 15 min and washed afterwards three times with PBS. The cell tubules were acidified with 3% acidic acid and stained

with Alcian blue (B8438, Sigma) for 30 min at room temperature. Next, cells were washed three times with PBS for 5 min and bright-field images were acquired with a light microscope.

2.11 P-glycoprotein mediated calcein efflux

Calcein-AM is a substrate of the P-gp efflux transporter. After internalization, it fluoresces until it is pumped out the cells (see Supplementary Figure S3). All channels in the OrganoPlate were washed with Opti-buffer containing Phenolred-free medium (DMEM) and HBSS (H6648, Sigma, Ratio of 1 DMEM: 3 HBSS). For detection of Calcein-AM efflux, the Opti-buffer in the seeding channel was replaced with Calcein-AM (C3099, 10 µM in 0.1% DMSO). Inhibition of the P-gp transporter was achieved by pre-incubation with Verapamil (V4629, Sigma, 50 µM in 0.5% Methanol) in the cell-seeding channel. The OrganoPlate was incubated for 60 min on an interval rocker at 37°C with 10 µM Calcein-AM or 50 µM Verapamil +10 µM Calcein-AM. To ensure that the presence of neither 0.5% methanol nor 0.1% DMSO affected the cross membrane partitioning of calcein-AM, both ± verapamil experiments contained the same amount of these compounds. Following incubation, all solutions in all inlets/outlets were replaced with ice cold stopping solution (20 µM Verapamil and nuclei stain Hoechst (H1399, Thermo Fischer, 10 µg ml^{-1}). After 15 min of incubation the cells were imaged immediately by SD confocal microscopy using 405 nm (442/42 BrightLine HC emission filter) and 488 nm (520/28 BrightLine HC emission filter) excitation lasers using a ×20 air objective. Analyzing tubule intensity was performed in Fiji, and the whole tubule was selected as the region of interest (ROI) and the fluorescence intensities for both, calcein and nuclei were extracted. The ratio of calcein and nuclei fluorescence intensity was calculated, representing the intracellular fluorescence of the cell.

2.12 Aminopeptidase-N activity determination

Aminopeptidase-N activity of cells was determined using 1.5 µM L-Alanine 4-nitroanilide hydrochloride (A4N) (A9325, Sigma) as a substrate. Serum-free medium was used for the bottom flow channel and the medium in the seeding channel was replaced with A4N. The OrganoPlate was incubated on the interval rocker for 2 h at 37°C, 5% CO_2. After incubation, the solution in the inlet and outlets of the seeding channels were collected and transferred to a 96-well plate. The absorbance of the cleaved product 4-nitroanaline was measured at 405 nm in a plate reader (Tecan, Switzerland).

2.13 *In vitro* drug absorption study

All drugs were purchased from Sigma Aldrich. Cells seeded in Transwells and OrganoPlate were washed with transport buffer (TB; 10 mM HANKS/HBSS). For the apical side, the pH of TB was adjusted to 6.5 (TB-apical) and for the basolateral side the pH was set to 7.4 (TB-basal). All drugs were diluted to a final concentration of 10 µM in 0.1% DMSO. The cultured monolayers were exposed to the drug for 2 h at 37°C, 5% CO_2. Control cells were exposed to TB without drugs but supplemented with a final concentration of 0.1% DMSO on the apical side. The OrganoPlate was placed for the total 2 h of drug incubation under constant flow, whereas the Transwells were incubated for 2 h under static conditions according to standard protocols (Artursson and Karlsson, 1991; Pontier et al., 2001; Béduneau et al., 2014; Twarog et al., 2020). For the permeability quantification of each drug, samples were analyzed using LC-MS and correlated to a standard curve. As a control for barrier integrity, 100 µM Lucifer Yellow (LY) were added to all samples (Ayehunie et al., 2018).

2.14 Quantification of absorbed drugs with liquid chromatography mass spectrometry

Samples and standards were analyzed with a Shimadzu Nexera X2/Prominence HPLC (Shimadzu Europe, Duisburg, Germany) and ESI micrOTOF-Q III (Bruker Daltonics, Bremen, Germany) LC-MS setup. The LC was performed by injection of the analyte (5 µL) on a Poroshell 120 SB-C8 column, 2.7 µm, 2.1 × 50 mm (Agilent, Santa Clara, CA, United States) followed by elution with a linear gradient of MeCN and 2.5 mM NH_4OH in water with 0.1% formic acid (from 0 to 100% over 9 min) at a flow rate of 0.4 ml min^{-1} (a detailed description of the HPLC setup and gradient is reported in Supplementary Table S1). The chromatographic front (1.75 min) was diverted to waste while the remaining run was injected into the ion source. A calibration solution consisting of 2.5 mM NaOH, 2.25 mM formic acid in 90% *i*-PrOH/water was injected into the ion source between 1.75 and 1.85 min at a flowrate of 30 µL h^{-1} for internal calibration of the spectra. MS analysis was performed in positive mode in the range 50–2,000 m z^{-1} at a rate of 2 Hz. The MS settings used for analysis of the various drugs are listed in the Supplementary Table S2. The concentration determination of each individual drug was used to calculate the apparent permeability of a compound (apical to basolateral) according to the equation (Lennernäs et al., 1997):

$$P_{app} = \frac{dQ}{dt} * 1/AC_0 \quad (2)$$

Where dQ/dt is the flux of drug across the cell monolayer per time [μM sec^{-1}], A is the surface area of the monolayer exposed to the drug (cm^2) and C_0 is the initial concentration of the drug.

A two-tailed non-parametric Spearman's correlation function was applied to determine the Spearman correlation coefficient R (von Erlach et al., 2020). The R-value defines the correlation between the quantified P_{app} of the drugs in the used model with the known human absorption values, a value closer to one represents a stronger correlation. Furthermore, a four-parametric logistic model curve fit was applied (Sjöberg et al., 2013) to better visualize the correlation between the quantified P_{app} values and the known human absorption.

2.15 Image-based localization and quantification of TAT and TAT/INS transport across epithelial monolayer tubules

Coculture tubules were used on day 4 after seeding and after confirming their leak-tight BI. Varying concentrations of TAT (24 μM; 2 μM) were applied to the coculture-tubules for capturing the internalization. Here, the cells were counterstained with Hoechst (H1399, Thermo Fischer, 10 μg ml^{-1}) and incubated for 1 h at 37°C, 5% CO_2, washed with PBS and images were acquired using SD confocal microscopy with 488 nm laser and 520/28 BrightLine HC filters for detecting FITC-labelled TAT and the 405 nm laser and 442/42 BrightLine HC filter for acquiring Hoechst. The cell tubules exposed to TAT/INS (24 μM/50 μM, IS1-AF647-1, Nanocs) were stained with above mentioned cellular dyes and CellMask-green (C37608, Thermo Fisher, 1:500) for 30 min on ice after 3 h of incubation. The transport of TAT was tracked over 2 h, acquiring time lapse images every 30 s using epi-fluorescence microscopy (see Imaging modalities). Two different concentrations of TAT (24 μM; 2 μM) or TAT/INS were applied to the coculture chips and imaged. To simultaneously monitor the barrier integrity TD (0.5 mg ml^{-1}) was co-applied to the chips and measured in parallel to TAT. For the quantification of both TAT, INS and TD transport across the cell barrier, calibration curves were established. The rate of transport was extracted by a linear fit of each individual curve (Supplementary Figures S7, S8). In-house developed MATLAB based macro was used for analysis.

2.16 Image based analysis of salcaprozate sodium (SNAC) induced semaglutide transport

Coculture tubules were exposed to SNAC (20 mM or 40 mM) in combination with semaglutide-Cy3 (5 μM) and FITC-dextran (46,944, Sigma Aldrich, 0.5 mg ml^{-1}) and imaged over approx. 4 h as described above.

3 Results

3.1 Development and verification of leak-tight small intestinal chip model

To develop an imaging compatible intestinal *in vitro* model we utilized the OrganoPlate, constituting a 348-Microwell set up with 40 individual chips and a 150 μm thick glass bottom (Trietsch et al., 2017; Gijzen et al., 2020). The chips are constructed with a seeding channel, an extracellular matrix (ECM) channel and a (fluidic) perfusion channel (Figures 1A,B). To enable the use of the chip as a model for studying intestinal transport, we first ensured that an intact and tight cellular barrier was formed. We seeded either pure Caco-2 cells (Monoculture) or a 6:1 ratio of Caco-2:HT29-MTX E12 cells (Coculture), the latter in an attempt to increase the biological relevance through the presence of mucus-producing goblet cells. For both systems, we facilitated the formation of a differentiated epithelial monolayer by inducing constant shear stress of 0.13 Pa and a mean flow rate of 2.02 μL min^{-1} using a pump free perfusion system for the total culturing period of only 4 days (Schutgens et al., 2019). To evaluate the barrier integrity (BI) we then applied a 0.5 mg ml^{-1} solution of 4.4 kDa Tetramethylrhodamine isothiocyanate (TRITC)-dextran (TD) in the seeding channel and used confocal microscopy to image the TD distribution in the chip. If no cells were added to the chip the TD intensity spread through the whole chip, a distribution also seen for both mono- and coculture systems after 1 day of barrier formation (Figure 1C). After 2 days we recorded a partial decrease in the TD intensity in the ECM and medium channels, while after 4 days both mono- and coculture chips displayed complete restriction of TD intensity to the seeding channel, demonstrating that a tight barrier had formed (Figure 1C, Day 4). In comparison, culturing of HT29-MTX E12 cells as a monoculture did not result in the formation of a tubules structure capable of restricting TD diffusion (Supplementary Figure S1). To quantitatively verify the presence of a tight barrier after 4 days of incubation, we determined the BI value by extracting the integrated intensity inside a region of interest in the ECM- and seeding channels (Figure 1C). We calculated the BI value for each chip as F_{ECM}/F_{cell}. This allowed us to ascertain cell barrier tightness, with values ranging from 1 (leaky) - 0 (tight), noting that BI values below 0.4 have previously been defined to represent a tight barrier (Trietsch et al., 2017) (Figure 1D). On day one post cell seeding we quantified $BI_{Mono} = 0.95 \pm 0.07$ and $BI_{Co} = 0.96 \pm 0.05$, constituting leaky cell barriers. After 2 days in culture $BI_{Mono} = 0.32 \pm 0.08$ and $BI_{Co} = 0.43 \pm 0.05$ values were calculated, representing a semi-tight cell barrier (Figure 1D, Day 2). On day four post seeding, the low TD intensity in the receiving channels lead to $BI_{Mono} = 0.05 \pm 0.01$ and $BI_{Co} = 0.07 \pm 0.01$ values, verifying that for both systems a tight barrier was established (Figure 1D, Day 4).

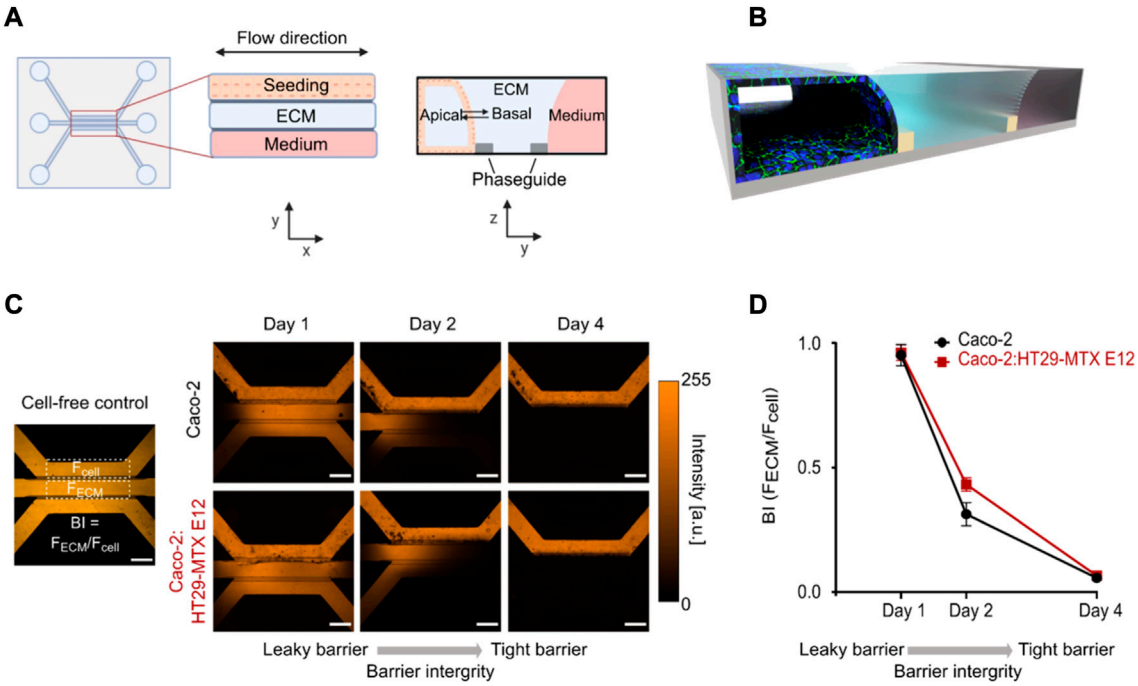

FIGURE 1
Mono- and coculture systems produce leak-tight epithelial monolayer tubules after 4 days. **(A)** Design of the 3-lane OrganoPlate system with a top view (left) and side view (right) illustrated in 2d. **(B)** 3D-schematic of the one chip after the formation of an epithelial monolayer tubule stained for tight junctions (green) and cell nuclei (blue) in the seeding channel. **(C)** Micrographs displaying TD distribution in cell free control (left) and in perfused mono-and coculture chips at days 1, 2, 4 post seeding (right). **(D)** Quantifying the BI of mono- and coculture tubules by depicting the BI determined as the ratio between the TD intensity in the ECM channel (F_{ECM}) and seeding channel (F_{cell}) (see C) as a function of days post cell seeding. Error bars represent the standard deviation (n = 3). Scale bar in all micrographs is 500 µm.

3.2 The epithelial tubule represents a fully polarized and differentiated cell monolayer

To confirm the polarization and differentiation of the cell-tubules into an epithelial monolayer we relied on conventional staining strategies for characteristic phenotypical epithelial cell markers (Anderson et al., 1989; Sambuy et al., 2005; Englund et al., 2006). The unique ability of the microfluidic platform of immunostaining and imaging directly in the system bypasses the need for cell monolayer extraction necessary in traditional *in vitro* TW models. Both culture systems revealed a homogenous expression of the tight junction protein Zonula occludens-1 (ZO-1) along the whole tubule, demonstrating its differentiation into a compact epithelial cellular network (Figure 2A). We next determined the apicobasal membrane orientation of the cell-tubules by immunostaining the known apically expressed brush border protein ezrin (Cao et al., 2014). Performing z-stack imaging allowed us to investigate ezrin staining in vertical cross-section of the cell tubule (Figure 2B, top). For all individual cells, ezrin staining was completely restricted to the cellular membrane facing the tubule lumen, as determined by a distinct fluorescence signal of ezrin above the cell nucleus (Figure 2B). This demonstrates that the cellular tubules are differentiated into monolayers of correctly polarized epithelial cells. Next, we identified two major intestinal efflux transporters of the ABC-family, the Breast *Cancer* Resistance Protein (BCRP) and the Multi Drug Resistant Protein (MRP2), which are key regulators of drug localization and thus essential for the *in vitro* platform accurately predicting intestinal transport (Giacomini et al., 2010; Billat et al., 2017). By staining for BCRP and MRP2 we observed the expected expression profile along the whole monolayer tubules, strengthening the conclusion that the cells are fully differentiated (Figures 2C,D). All apicobasal membrane orientation assessments described above were performed at least three times in both mono- and coculture tubules finding equivalent expression and localization of ZO-1, ezrin, MRP2 or BCRP for both systems (Supplementary Figure S2). Overall, the in-chip immunostaining revealed the formation of a fully differentiated and polarized epithelial tubule.

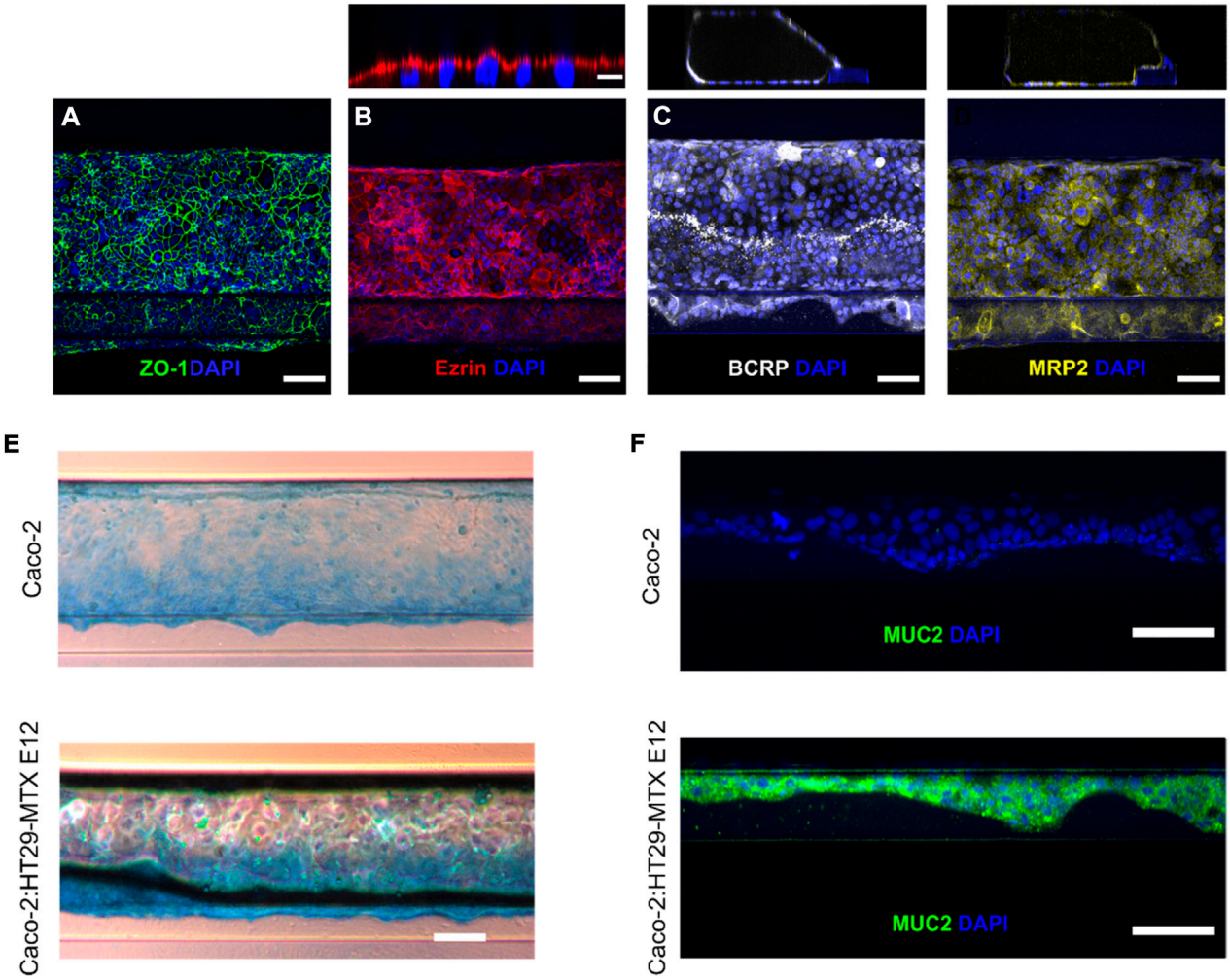

FIGURE 2
Verification of a differentiated and polarized epithelial monolayer using direct in-chip immunostaining. **(A)** Tight junction formation depicted by maximum intensity projection (MIP) from confocal z-stack of ZO-1 (green) and DAPI (blue) (scale bar is 100 µm). **(B)** Bottom, brush borders are visualized as MIP from confocal z-stack of ezrin (red) and DAPI (blue) (scale bar is 100 µm). Top, the apical orientation of ezrin expression is depicted as a vertical cross-section of the cell-tubule (Scale bar is 10 µm). **(C)** Bottom, BCRP efflux transporter (white) and DAPI (blue) are visualized as MIP from confocal z-stack (scale bar is 100 µm). Top, A vertical cross section of the BCRP stained cell-tubule. **(D)** Bottom, MIP of cell-tubule stained for the efflux transporter MRP2 (yellow) (scale bar is 100 µm). Top, vertical cross section of the MRP2 stained cell-tubule. **(E)** Brightfield microscopy images showing Alcian Blue staining of acidic mucins in mono- (top) and coculture (bottom) tubules (scale bar is 200 µm). **(F)** Micrograph of single z-slice of the cell layer along the ECM interface for mono- and coculture depicting Muc2 (green) and DAPI (blue) (scale bar is 100 µm).

3.3 Homogenous Muc2-expression in coculture-tubules along the extracellular matrix-cell interface

To evaluate if introducing the goblet cells in the coculture induced the expected mucus production we performed various imaging-based assays to evaluate the mucus expression in both the mono- and coculture system. First, we studied the presence and expression profile of unspecific mucins by staining the cultured cell-tubules with Alcian blue, which binds to all acidic mucins (Figure 2E, Supplementary Figure S2) (Béduneau et al., 2014). The coculture tubules showed a notable higher mucus expression compared to the monoculture tubule (Gijzen et al., 2020). This was especially observed along the ECM-interface, highlighting the need for an ECM support to promote adequate cell differentiation. To verify the presence of Muc2, which is the small intestinal specific mucus type produced by goblet cells (Schneider et al., 2018), we visualized Muc2 by confocal imaging of immunostained cell-tubules. The staining for Muc2 proteins showed a strong and homogenous expression in coculture tubules but was completely absent in monoculture tubules (Figure 2F). Again, it was

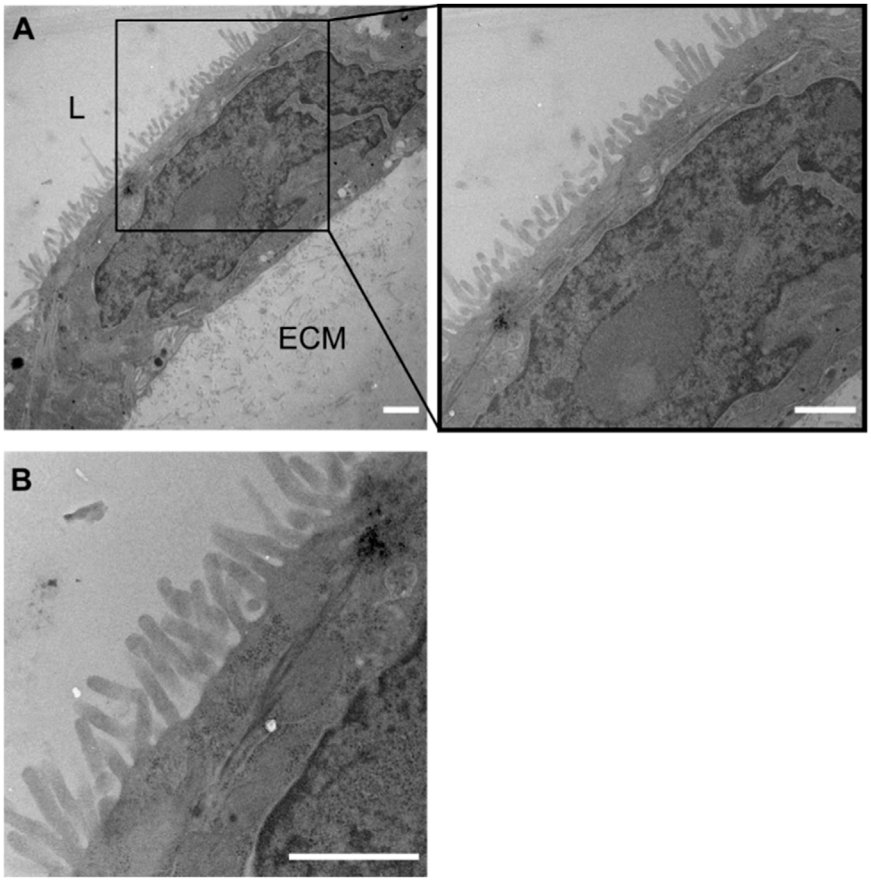

FIGURE 3
Formation of microvilli in coculture tubules identified by TEM. **(A)** Micrograph of a monolayer cell tubule with the lumen top left (marked by L) and the ECM located towards the bottom right (marked by ECM). Clear microvilli formation towards the luminal side of the coculture tubule, but a complete lack of microvilli on the side facing the ECM demonstrating the correct apicobasal morphological differentiation after 4 days of culture. **(B)** Zoom **(A)** represents the organization of dense microvilli. Scale bar is 1 μm in all images.

primarily the cells supported by the ECM that displayed high expression of Muc2 in coculture tubules. Thus, the introduction of the goblet-like cells in coculture systems leads to strong and homogeneous mucus production in contrast to Caco-2 cells in monoculture. This addition increases the biological relevance of the epithelial monolayer system (Karlsson et al., 1993; Hilgendorf et al., 2000; Doherty and Charman, 2002) and permits its use for studying how the mucus layer affects drug transport across the intestinal cell barrier, by comparing the mono and coculture tubules.

3.4 Microvilli formation in coculture tubules corroborates an *in vivo* mimicking cellular morphology

To further corroborate the correct polarization of the cell monolayer we visualized cell morphology in detail by extracting the coculture tubule samples and imaging them using transmission electron microscopy (TEM) (Figure 3). Cell tubules were fixed, stained, embedded and sectioned into 120 nm thick slices after 4 days of culture before the tubule sections of the cell-ECM interface were imaged. The micrographs of the tubule sections displayed a distinct and homogenous formation of microvilli along the whole tubule, restricted only on the side facing the lumen opposite to the ECM, clearly illustrating the development of a well-defined apical side (Figure 3A). The basal side of the cells, which is attached to the ECM did not show any morphological changes. Additionally, each individual cell expressed a dense network of microvilli and thus a membrane surface area expansion typically seen for differentiated intestinal epithelial (Figure 3B). Having this characteristic cellular morphology in an *in vitro* assay is pivotal for its *in vivo* absorption predictability as the cell membrane surface area is a strong regulator of the total drug absorption. Thus, the generated cell tubules fully differentiated

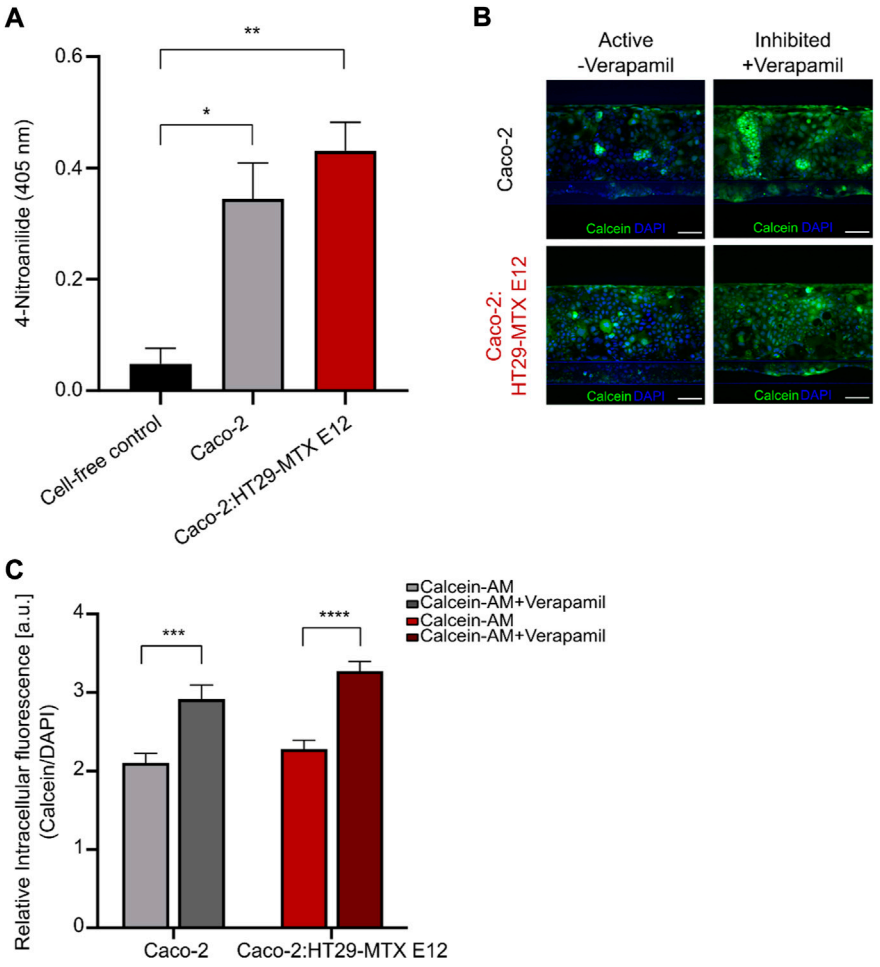

FIGURE 4
Identification of active intestinal metabolic enzyme and P-gp transporter in mono-and coculture tubules. **(A)** Brush border enzyme aminopeptidase N quantification in cell free (black), monoculture (grey) or coculture (red) systems measured as the absorbance of the cleavage product 4-Nitroanailide. Error bars represent the standard error of the mean (SEM) of at least three biological replicates per condition (*$p < 0.05$, **$p < 0.005$). **(B)** Left, micrographs depicting the non-inhibited calcein (green) and DAPI (blue) fluorescence intensities after 1 h incubation for monoculture (top) and coculture (bottom). Right, micrographs depicting the Verapamil-inhibited calcein (green) and DAPI (blue) fluorescence intensity after 1 h incubation for monoculture (top) and coculture (bottom). Scale bar is 100 µm. **(C)** Quantification of the relative intracellular fluorescence ($I_{relative}$) in non-inhibited monoculture (light grey), Verapamil-inhibited monoculture (dark grey), non-inhibited coculture (light red) and Verapamil-inhibited coculture (dark red). Error bars represent the SEM of at least three biological replicates per condition. (*$p = 0.047$, **$p = 0.0019$, ***$p = 0.0004$, ****$p < 0.0001$).

into epithelial cells evidenced by their apicobasal characteristic membrane morphologies.

3.5 Intestinal metabolic markers are expressed in mono- and coculture tubules

To establish a physiological relevant small intestinal *in vitro* platform for drug transport studies the presence and activity of proteolytic enzymes and drug transporters are crucial (Gan and Thakker, 1997; Langguth et al., 1997; Estudante et al., 2013). A highly relevant group of intestinal metabolic enzymes are the aminopeptidases, therefore we evaluated the presence of the brush border aminopeptidase N by employing a standard absorbance based assay, measuring the enzymatic cleavage product 4-Nitroanilide (Figure 4A) (Kim et al., 2012). Both mono- and coculture tubules showed a significant increase in measured 4-Nitroanilide compared to the cell-free control, confirming the presence of functional aminopeptidase N in both mono- and coculture tubules after 4 days of culture.

After having verified the presence of intestinal efflux transporters (Figures 2C,D) we wanted to ensure that these also constituted a functional efflux transport machinery, therefore we examined the function of the intestinal

P-glycoprotein (P-gp) efflux transporter by following the change in intracellular calcein upon inhibition with Verapamil (Figures 4B,C, Supplementary Figure S3). We added 10 μM of calcein to the tubular lumen and incubated for 60 min before imaging the whole tubule (Figure 4B, active). The relative intracellular fluorescence ($I_{relative}$) was then determined as the ratio of the calcein and DAPI intracellular fluorescence intensities for the whole tubule. For both the mono- and coculture systems we found similar low $I_{relative}$ values for mono- and coculture tubules, due to the continuous efflux of calcein mediated by the active P-gp transporter (Figure 4C, light grey (mono) and light red (coculture)). Next, we repeated the experiment while adding the P-gp inhibitor Verapamil leading to a significant increase in $I_{relative}$ values for both the mono- and coculture systems (Figure 4B, Inhibited; Figure 4C, dark grey (mono) and dark red (coculture)). This demonstrated the presence of functional P-gp transporters, representing a key component of the dynamic efflux machinery known to affect drug transport and thus vital for creating an *in vitro* model with high *in vivo* transport predictability.

3.6 Mono and coculture tubules display strong *in vivo* drug transport predictability

To validate the chip platform for drug transport studies, we correlated the absorption of twelve small model drugs in both the mono- and coculture tubules to their known human absorption values. To ensure a complete evaluation across the whole range of known human absorption values, as recommended by the Food and Drug Administration (FDA), we selected model drugs from all Biopharmaceutical Classification System (BCS) classes with quantifiable transport (Supplementary Table S4) (Amidon et al., 1995; Niazi, 2019). For comparison, we performed the same correlative analysis for a classical TW system (Lipka and Amidon, 1999), which was set up following standard protocols (see experimental section). To quantify the transport, we added the drugs to either chips or TW and extracted both the apical and basolateral fractions after 2 h (Supplementary Figure S4, Supplementary Tables S3, S4). The concentration in all samples was determined using liquid chromatography mass spectrometry (LC-MS) and internal standards (see experimental section, Supplementary Tables S1, S2). The apparent permeability (P_{app}) of each drug was calculated as described in the method section and summarized in Supplementary Table S4. Comparing the TW and the monoculture tubules systems we quantified ranges of P_{app} values from 1.20×10^{-6} cm s^{-1} for Erythromycin to 243.41×10^{-6} cm s^{-1} for Warfarin in TW and 1.33×10^{-6} cm s^{-1} for Erythromycin to 213.99×10^{-6} cm s^{-1} for Carbamazepine in the chip monoculture. We correlated the obtained permeability data of each system to the known human absorption values (Cheng et al., 2007; Skolnik et al., 2010; Takenaka et al., 2016; Youhanna and Lauschke, 2021) by plotting the P_{app} values against the fraction absorbed in humans (FA) and extracted the Spearman correlation coefficient (SCC-R) (von Erlach et al., 2020). This statistic represents a measure of how well an *in vitro* model recapitulates the *in vivo* transport and thus allows for comparison between models (Figures 5A,B) (Li et al., 2007; Skolnik et al., 2010; Takenaka et al., 2016). We determined a SCC-R of 0.77 for the TW system, indicating a strong correlation to *in vivo transport*. In addition, the transport in monoculture tubules showed a similar SCC-R to TW with 0.88. This demonstrates that the monoculture is a qualified platform for drug transport studies, with an ability to predict *in vivo* intestinal transport at least on the level of the widely employed TW system, additionally having the unique ability to be directly compatible with advanced imaging modalities.

It has previously been shown that the utilization of Caco-2 monocultures for drug transport studies suffers from 1) underestimation of transport through the paracellular route due to a high density of tight junctions and 2) an overestimation of passively absorbed drugs due to the lack of mucus (Hilgendorf et al., 2000; Pontier et al., 2001; Béduneau et al., 2014). This underscores the importance of developing more biological complex *in vitro* models like the coculture tubules described in this work. Like for the TW and monoculture tubules, we next measured the transport of the twelve drugs in the coculture platform using LC-MS and quantified the P_{app} (Supplementary Table S4). The detected ranges of P_{app} values for the coculture system were from 0.99×10^{-6} cm s^{-1} for Erythromycin to 300.39×10^{-6} cm s^{-1} for Warfarin. Plotting the FA against the P_{app} for the coculture revealed a SCC-R of 0.89, which is overall similar to the values found for the monoculture tubules and TW (Figure 5C). Thus, while the coculture system did not directly improve the *in vivo* predictability as compared to the TW system it is encouraging that this more physiologically relevant model can be established in a platform compatible with advanced imaging. Also, to further compare the mono- and coculture tubule system and delineate the effect of introducing the goblet cells we performed a direct comparison of P_{app} (monoculture) versus P_{app} (coculture) for each individual drug (Figure 5D). No systematic trend towards elevated or diminished transport for one system in particular, was evident (Figure 5D), however, knowing the transport route employed by the individual drugs allowed us to selectively plot the relative difference in average P_{app}, using a Bland-Altman comparison analysis (Altman and Bland, 1983). For all four paracellular transported drugs we saw increased relative transport for the coculture (red) versus the monoculture (black), up to 27% seen for Terbutaline (Figure 5E, top). This corroborates the believed increase in the monolayer permeability introduced when adding another cell line into the Caco-2 monolayer, directly increasing paracellular drug transport (Hilgendorf et al., 2000). Plotting the

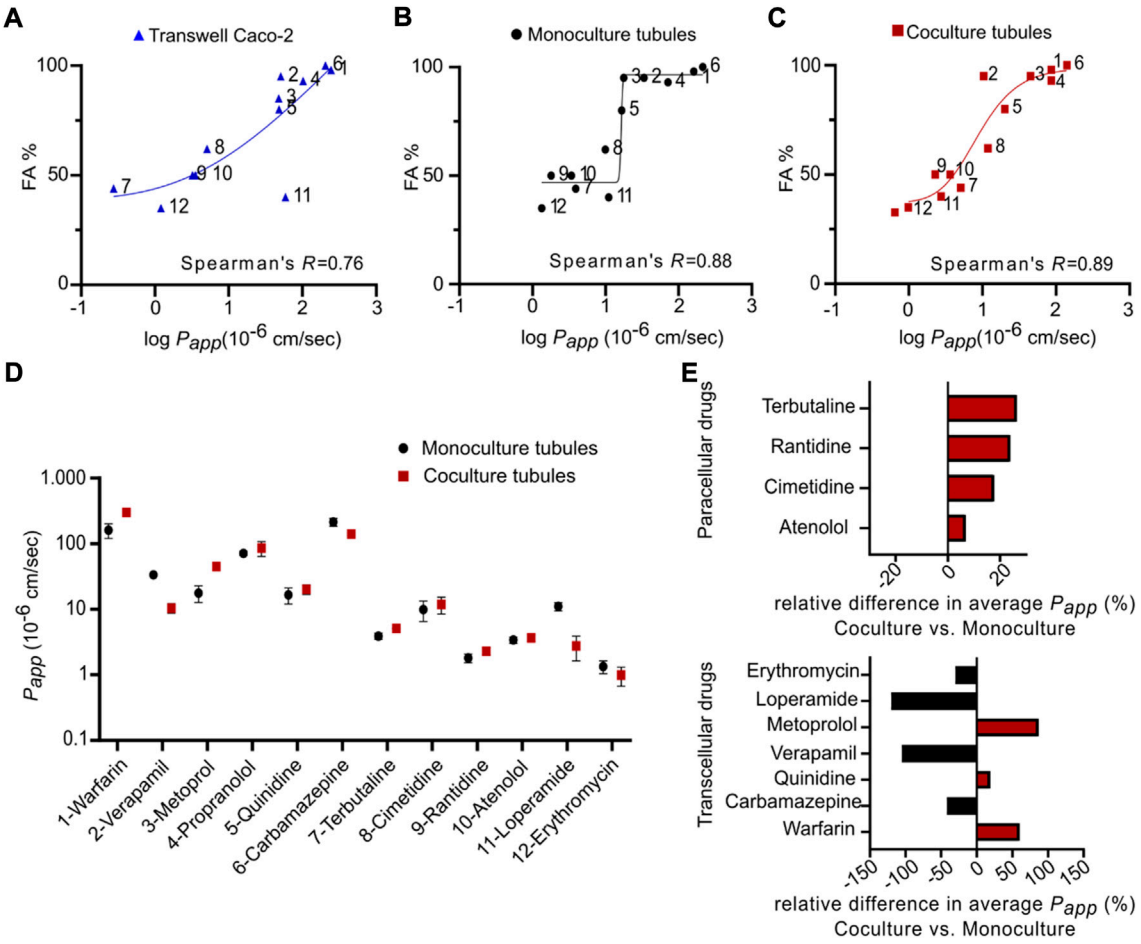

FIGURE 5
Correlation between fractions absorbed in human and apparent permeability coefficient of twelve model drugs in mono- and coculture tubules as well as standard Transwells. **(A–C)** The FA for each drug plotted against the average log *Papp* obtained from **(A)** Transwell (blue) **(B)** monoculture tubules (black) and **(C)** coculture tubules (red). All fits represent non-linear regression analysis using a two-tailed non-parametric Spearman's correlation function, generating Spearman's coefficients (*R*). Compounds 1–12 are listed in Supplementary Table S4. **(D)** The average P_{app} found for either the monoculture (black) or the coculture (red) tubules plotted for each individual drug tested. **(E)** The relative difference of the average P_{app} for paracellular transported drugs (top) and transcellular transported drugs (bottom). Error bars represent the SEM for each drug transport measured for at least three biological replicates (n = 3).

same relative difference in average P_{app} for the transcellular drugs, we did not see any systematic change towards elevated or diminished transport for either the mono- (black) or the coculture (red) tubules (Figure 5E, bottom, Supplementary Table S5). This suggests that the presence of a mucus layer only had a minute effect on the transcellular transport. However, we caution on underestimating the importance of the mucus layer based on experiments with only small molecule drugs. We imagine that for larger peptide and protein drugs, the presence of a mucus layer might strongly affect the transport rate and thus give a more biological accurate measure of their transport across an intestinal cell layer. Based on this, we choose to continue with the coculture tubule for subsequent transport studies of biologics.

3.7 Multiplexed live cell imaging technique on coculture tubules allows for simulations assessment of cellular uptake, transport and barrier integrity

We next used the developed and verified coculture tubules to use imaging-based live cell assays to untangle the uptake and transport mechanism of biologics. To validate the platform for quantitative image based intestinal transport studies, we first employed the FITC-labeled transcriptional activator peptide in HIV (TAT), an arginine-rich cell-penetrating peptide (CPP) extensively used to deliver therapeutic proteins or peptides across cellular barriers (Morris et al., 2001; Kristensen and Nielsen, 2016; Guo et al., 2019). While the ability of TAT to

10.3389/fbioe.2022.965200

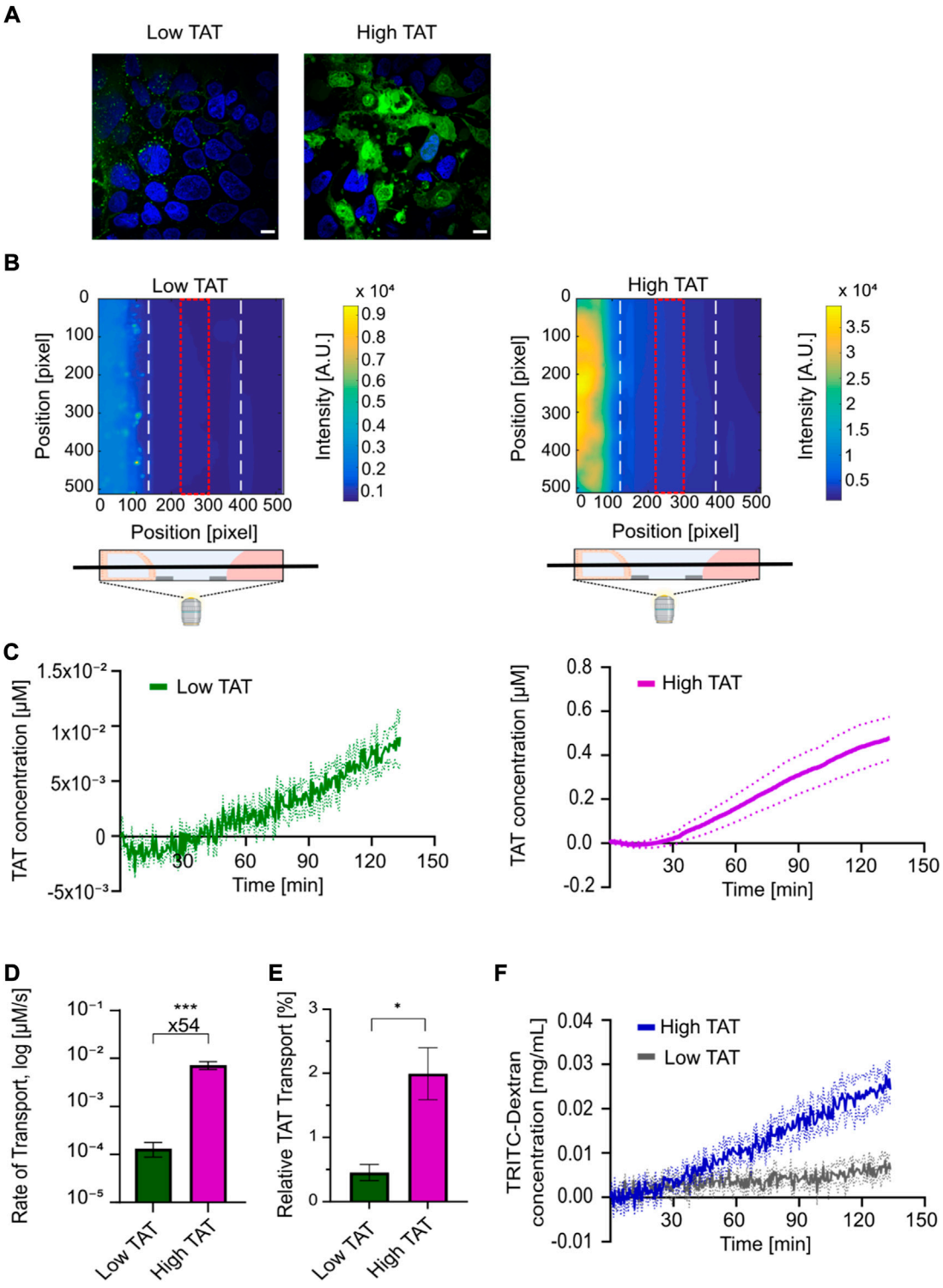

FIGURE 6
Live cell imaging-based uptake and transport quantification of TAT for determining high-temporal resolution kinetic transport profiles reveals a strong concentration dependent TAT transport in coculture tubules. **(A)** Live cell micrographs depicting TAT (green) and Hoechst (blue) intensities in coculture tubules treated with (left) low concentration of TAT (2 µM) or (right) high concentrations of TAT (24 µM). Scale bar is 10 µm. **(B)** Representative fluorescence surface intensity plot after 130 min incubation with the low TAT (left) and high TAT (right) concentrations. The surface intensity plots are taken from time series acquired using high-temporal resolution live cell imaging of TAT transport. The field of view was set as a z-plane in the middle of each chip-system, including all three connected channels as depicted. The fluorescence intensity summed along the

(*Continued*)

FIGURE 6 (Continued)
red dotted line at the center of the ECM-channel was selected for quantification of transport. **(C)** Image-based quantification of kinetic transport profile plotted as the average TAT concentration within the red square in **(B)** as a function of time for both the low (green) and high concentration (purple) of TAT (n = 4). Dashed lines represent the SEM of each condition. **(D)** Comparison of the average rate of TAT transport for low and high TAT concentration systems. (n = 7) (***p = 0.0002). **(E)** Comparison of the relative TAT transport after 130 min of incubation (n = 4) (*p = 0.01). **(F)** Determination of BI kinetic quantified using the TD concentration for the low (grey) and high (blue) TAT concentration systems (n = 4). Dashed lines in the figure represent the SEM. All error bars in the figure represent the SEM of each condition.

cross cellular-membranes and barriers are uniformly reported, the transport mechanism of TAT remains debated, potentially due to previously studies being restricted to fixed cell samples or undifferentiated single cell experiments (Frankel and Pabo, 1988; Brock, 2014). Here, the unique imaging capabilities of the cell-tubule platform allowed us to quantify, for the first time, TAT transport across a differentiated cellular barrier using high-temporal live cell imaging. We first investigated how the TAT concentration affected its transport mechanism by applying either a low (2 μM) or a high (24 μM) concentration of TAT to the cell-tubules and imaged the coculture chips after 1 h of incubation. We detected a clear concentration dependent difference in the intracellular localization of TAT, with the low TAT concentration system displaying a punctate distribution of TAT inside the cells, suggesting endosomal uptake (Figure 6A). In contrast, the high TAT concentration (24 μM) system displayed a diffuse TAT intensity in the cytoplasm, indicating uptake predominantly via transduction (cell membrane accumulation and destabilization) into the cells (Figure 6A). These results corroborate previous studies on undifferentiated single cell models, showing a concentration dependence of the cellular internalization mechanisms of TAT (Tünnemann et al., 2006, 2008; Duchardt et al., 2007; Brock, 2014). Here, we expand this to a fully differentiated coculture system demonstrating that concentrations differences down to a factor of 12 can lead to distinctly different uptake mechanisms of TAT.

Next we used the platform to study the barrier transport kinetics of TAT. We performed whole-chip real-time live cell imaging, to quantify the concentration of TAT transported across the coculture cell layer and reaching the receiving channel (Figure 6B). Here, we took advantage of the high temporal resolution and strong detection sensitivity offered by the imaging-compatible chip system. The same two concentrations of TAT (2 μM, 24 μM) were added to coculture tubules along with a 0.5 mg ml^{-1} concentration of TD, allowing us to simultaneously track barrier integrity over time. Both the FITC and TRITC channels were recorded for each tubular system every 30 s for a total of 2.5 h. The well-plate format of the microfluidic platform allowed us to mark the position of numerous coculture tubules and use automated multi-spot imaging to perform several experiments in parallel. A calibration experiment where known concentrations of TAT or TD were added to a chip without cells allowed us to convert the measured intensities to actual concentration in μM and mg mL^{-1} respectively (Supplementary Figure S5). A TAT surface intensity plot of the seeding, ECM and perfusion channels after 130 min of incubation showed a clear intensity gradient in the ECM-channel for both concentrations, demonstrating that TAT is capable of crossing the tubular cell layer and migrate through the ECM (Figure 6B). To quantify the transport of TAT we integrated the intensity within the ECM facing the receiving channel in the region displayed in Figure 6B (red square). We then used the calibration control to convert this intensity to concentration, which we plotted as a function of time for both the low- and high TAT concentration systems (Figure 6C). For both systems, we record a lag time of approx. 30 min showing a high noise to signal ratio, indicating the detection limit of the individual molecules before a significant signal above the background was detected. Subsequently, both systems reach a linear regime displaying a steady increase in transported peptide. Thus, to decouple the transport efficiency from the initial difference in concentration we quantified the transport rate for the linear regime for both the low and high TAT systems (Supplementary Figures S6, S7). Calculating the average transport rate for all experiments revealed a 54-fold higher rate for the high versus the low TAT system (Figure 6D). To elucidate how this affected the overall amount of transported TAT we again normalized for the initial difference in concentration by converting the quantified TAT concentration after 2.5 h to a percentage of the initially added concentration of TAT. Doing this, we quantified average relative transport percentages of 0.5 ± 0.1% for low TAT and 2.0 ± 0.4% for high TAT, demonstrating a 4.4 fold higher relative amount of TAT transported in the high versus low TAT concentration system (Figure 6E). Finally, the influence of TAT on the barrier integrity was displayed using the acquired TD time series, showing an intact barrier indicated by an overall transport of TD below 5%. However, the sensitivity of the assay allows to detect a TAT concentration dependent difference in the TD transport profile. In the high TAT system a steady increase of TD was observed, but only a minimal transport of TD was detected in the low TAT system (Figure 6F). This TAT concentration dependent differences in the barrier interaction, further support that TAT can use two very different transport pathways, governed by the initial TAT concentration. Additionally, our data demonstrate that the transduction pathway employed by TAT at higher concentrations is vastly more efficient than the endocytic pathway employed at lower concentrations.

3.8 Intracellular entrapment of insulin restricts its transport across the epithelial cell barrier

Insulin is considered to be at the forefront of oral drug delivery, but despite immense efforts, no insulin-based oral formulation has reached the market, primarily due to extremely low bioavailability, originating both from low stability of free insulin in the harsh gastro-intestinal environment and an extremely low intrinsically cross barrier transport efficiency (Goldberg and Gomez-Orellana, 2003). Next, we took advantage of the subcellular resolution of the platform to study 1) the transport of AlexaFluor647-labeled insulin (INS) alone or 2) the transport of INS when using TAT as a vehicle for the attempted delivery across the cell barrier. In the latter case, we relied on the well-established strategy of electrostatic CPP and peptide complexation (Chen et al., 2017; Guo et al., 2019) and thus simultaneously added both TAT and INS to the tubule system. Additionally we added TD allowing us to track, in real-time, the transport of both the drug delivery vehicle (TAT) and the cargo (INS), while also monitoring how these affected the barrier integrity (TD). We detected no INS transport across the cell barrier independent of whether or not TAT was present, whereas a clear transport of TAT was again detected (Figure 7A). Also here, the barrier integrity was not compromised significantly in chips with and without TAT (Supplementary Figure S8). To ascertain the lack of INS transport we investigated its fate along the transport pathway after 3 h. We described the distribution of internalized INS by live cell imaging of the tubules showing that INS was indeed internalized into the enterocyte cell layer even without TAT (Figure 7B). Additionally, to investigate the intracellular we changed the magnification from ×20 to 100x for live cell imaging, allowing us to elucidate that for both INS and INS/TAT, the INS was localized inside the cytosol in punctual patterns, indicating endosomal uptake (Figure 7C). This suggests that the main limiting factor for the INS delivery across the cellular barrier in our setup was an inability to escape endosomes and/or be moved across the basolateral membrane.

Additionally, we attempted to use the model to study other pharmacological relevant transport mixtures including the permeation enhancer SNAC and the glucagon-like peptide 1 analog semaglutide (SG) used in the recently FDA approved treatment for type II diabetes (Buckley et al., 2018). However, from tracking the transport of SG-Cy3 and the BI by TD, in combination with a direct visual inspection of the cell layer in the bright field channel, we concluded that before any significant semaglutide-Cy3 transport across the barrier could be detected, SNAC had caused irreversible damage to the cell layer (Supplementary Figure S9). This illustrate the substantial impact on barrier morphology and integrity imposed by SNAC and suggests that its *in vivo* feasibility strongly relies on the regenerative nature of the epithelium cell layer. Overall, these findings illustrate the immense potential of employing imaging modality compatible *in vitro* intestinal barrier models, offering the ability to simultaneously perform detailed studies on uptake mechanisms and high-quality quantitative kinetic transport measurements and with that obtaining valuable mechanistic insights.

4 Discussion

Drug screening platforms compatible with live-cell imaging could offer the possibility to directly track how biologics cross the intestinal epithelial barrier and hereby offer mechanistic insights facilitating the rational design of new and improved oral administrated drugs (Gumbleton, 2005; Watson, 2005; Mechanism matters, 2010; Time to deliver, 2014; Sahay et al., 2010; Larsen et al., 2021). Here we developed a fully polarized and differentiated *in vitro* model from mono- and coculture epithelial tubules in the microfluidic OrganoPlate system. Both systems exhibited the correct expression patterns of standard epithelial cell markers such as brush border enzymes and efflux-transporters after 4 days of culture. In comparison, Caco-2 cells grown in Transwells require 17–21 days of culture for the differentiation into epithelial cells, proposed to be due to their static culture condition, as the importance of shear stress on Caco-2 cells for distinct and fast differentiation into an epithelial monolayer was reported in previous studies (Shemesh et al., 2015; Langerak et al., 2020). In our model, we applied bidirectional flow during the whole cultivation time and the resulting shear stress on the cell tubules induced the fast differentiation kinetics, greatly reducing the period from initial cell seeding to having a functional model for experiments.

In coculture tubules, we visualized and quantified the real-time transport of peptide transport using fluorescent microscopy. We employed TAT, a well-known vehicle for cellular drug delivery (Kristensen and Nielsen, 2016; Zhu et al., 2016), due to its proven ability to translocate across cell membranes, resulting in a push for identifying its underlying mechanism (Wadia et al., 2004; Brooks et al., 2005). Initially, it was proposed that TAT was mainly transported to the nuclei, but this was later disputed as concerns about potential artefacts from sample fixation were raised (Richard et al., 2003). Therefore, to avoid fixation investigators turned to live imaging of single cells, however, such systems do not accurately represent a biological cell barrier and are neither differentiated nor polarized cells. Therefore, we here investigated the uptake of TAT in the fully differentiated and polarized cell layer with mucus and microvilli, revealing a concentration dependent mode of uptake, corroborating earlier findings (Brock, 2014). Then we expanded this by showing that the difference in uptake mechanism also led to a significant concentration dependent difference in transport efficiency, quantifying a 54-fold increase in transport efficiency for a 12-fold difference in initial TAT concentration. This illustrates how our system can circumvent

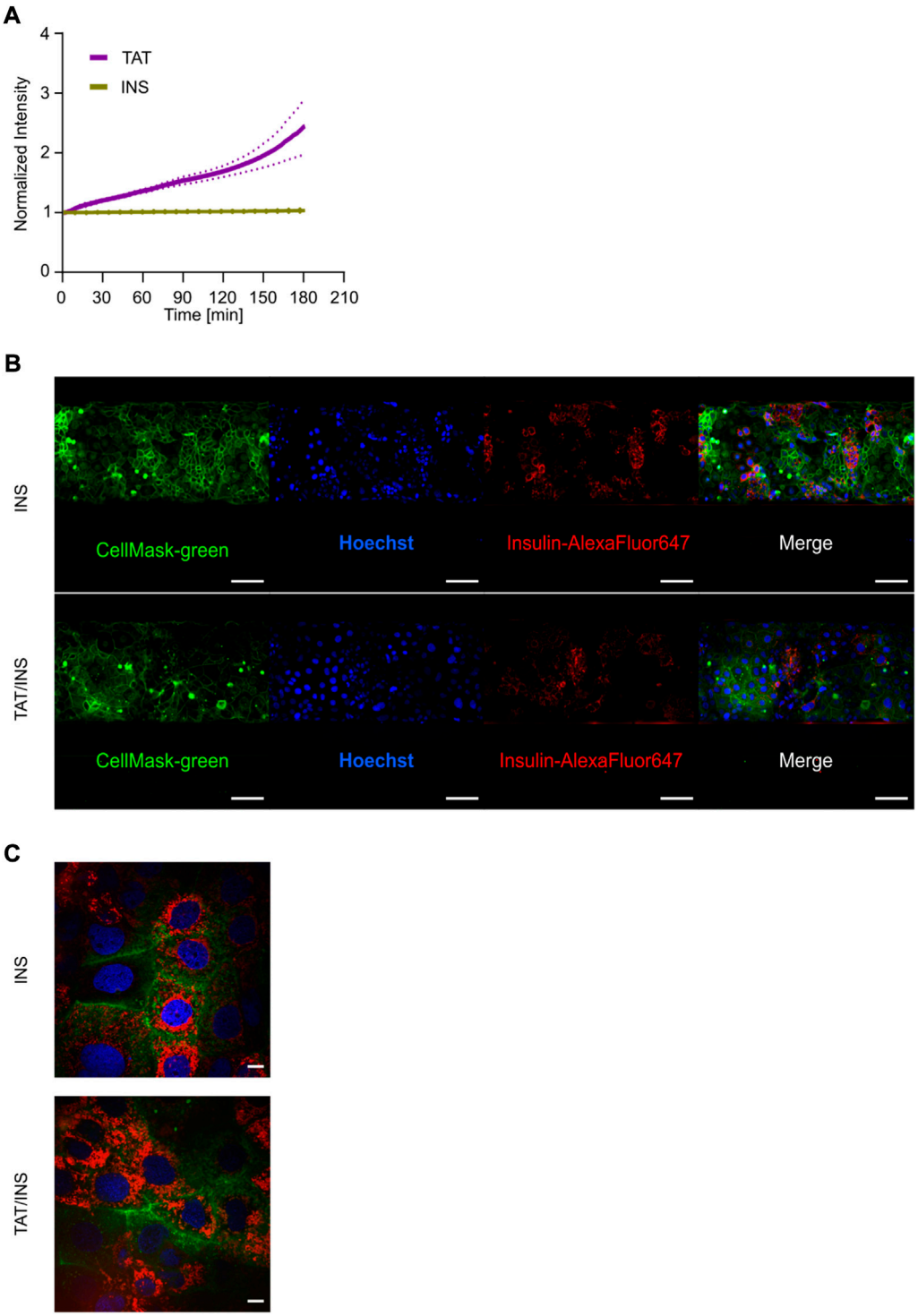

FIGURE 7
Multiplexed live cell imaging for assessing the intracellular localization and quantitative transport of Insulin. **(A)** Normalized intensities of INS (yellow) and TAT (purple) transport over 3 h. Data reflect the average of three independent biological replicates depicted with the SEM in dashed lines (n = 3). **(B)** Live cell micrographs showing the intracellular distribution of INS (red) with (bottom) and without (top) co-incubation of TAT for 3 h in coculture tubules. Tubules were stained with CellMask-green (green) for representation of the plasma membrane and Hoechst (blue) as nuclei staining. Scale bar is 500 µm. **(C)** The uptake and intracellular localization of INS with (left) and without the addition of TAT after 3 h of incubation. Scale bar is 10 µm.

many of the shortcomings of previous *in vitro* models and provide detailed imaging based insights on the cellular uptake and barrier transport of peptides.

The finding that co-delivery of TAT/insulin does not lead to strong transport of insulin is in line with previous studies (Kamei et al., 2008), whereas the features of the platform enabled to disclose the intracellular accumulation and entrapment of insulin in endosomal compartments, despite TATs ability of performing endosomal escape mechanisms and hence being transported across the epithelium (Lönn et al., 2016). This demonstrates the versatility of the advanced model allowing for simultaneous mechanistic studies on uptake and intracellular transport as well as sensitive kinetic measurements of barrier translocation.

While the microscopy-based readout offers great advantages for tracking the transport of biologics, it also poses a limitation to the current setup, as the selected drug needs to be modified with a fluorescent reporter. It is known that the modification could potentially alter the transport behavior of biologics, especially for smaller peptides (Szeto et al., 2005; Hedegaard et al., 2018). Consequently, it is paramount to select fluorescent dyes that to a minimal extent interfere with the physicochemical property of the biologics and e.g. select one of the number of fluorophores that has been shown to display minimal propensity for interaction with lipid membranes (Hughes et al., 2014). Additionally, while the applied Caco-2 cell line is a workhorse within the *in vitro* intestinal barrier community, it is still not capable of fully replicating the complex cellular environment seen *in vivo* epithelium (Englund et al., 2006; Maubon et al., 2007; Harwood et al., 2016; Vaessen et al., 2017). Thus, the biological complexity of the model could potentially be increased by replacing the commonly used Caco-2 and HT29 cell lines with a more biological relevant cell pool, e.g. from intestinal organoids (Bein et al., 2018; Beaurivage et al., 2020; Naumovska et al., 2020; Pimenta et al., 2022)."

Due to the intrinsic low bioavailability of most biologics, the transport of orally delivered formulations across the intestinal cell layer typically requires some extent of barrier disruption (Brayden et al., 2020). Therefore, most oral biologics formulations include excipients that can increase the transport across the cellular barrier (Brown et al., 2020). To facilitate safe transport using this strategy for oral drug delivery it is crucial that the barrier disruption is only transient and can be fully reversed to avoid inducing long term degradation of the intestinal tissue (Maher et al., 2021). Therefore, monitoring barrier integrity is a cornerstone of traditional Transwell assay, however high-temporal measurements of the transient cell barrier disruption are difficult in Transwell setups. Consequently, specialized transepithelial resistance (TEER) instruments with the ability to record the barrier integrity with a temporal resolution down to seconds have to be employed (Srinivasan et al., 2015; Gerasimenko et al., 2020). However, these setups have major drawbacks including being expensive and have limited experimental throughput as simultaneous monitoring of transport and TEER are unfeasible. The real-time read-out feature of the tubule platform presented here allowed for continuous evaluation of the barrier integrity by tracking the TD intensity with high temporal resolution. Additionally, we demonstrated that such BI measurements can run simultaneously with drug transport studies without the measurements affecting each other, as long as the chosen fluorophores do not display significant spectral overlap. This possibility of multiplexing within the same experiment greatly increases the throughput and flexibility of the assay.

In summary, the developed cell tubule setup represents a novel *in vitro* model system of the small intestine epithelium with a very high *in vivo* predictability and is thus directly applicable for drug transport studies. The unique compatibility of the platform with common microscopy modalities for live cell imaging allowed for studying the uptake mechanism and real-time transport of TAT and insulin across a fully differentiated epithelial barrier with high sensitivity and temporal kinetics. The generic ability of the model to perform detailed mechanistic studies for all fluorescently labeled biologics underscores how its widespread implementation could greatly benefit early-stage oral drug development.

Data availability statement

The original contributions presented in the study are included in the article/Supplementary Material, further inquiries can be directed to the corresponding authors.

Author contributions

AW designed and performed experiments as well as analyzed the data, with help from JL and LP. AW and JL wrote the manuscript. RM, AH and MH contributed with data acquisition and data interpretation. CH provided input for the statistical analysis. PK contributed with generating TEM images. HF assisted setting up the Q-TOF. TA, JL and LP designed the project and were responsible for overall project management.

Funding

This work has been supported by the Novo Nordisk foundation Grant No. NNF16OC0022166.

Acknowledgments

Schemes were created by BioRender.com. We thank S. Vasudevan for the graphical design in this study and the Novo Nordisk compound sharing program for providing us with Semaglutide-Cy3.

Conflict of interest

The authors declare that the research was conducted in the absence of any commercial or financial relationships that could be construed as a potential conflict of interest.

Publisher's note

All claims expressed in this article are solely those of the authors and do not necessarily represent those of their affiliated organizations, or those of the publisher, the editors and the reviewers. Any product that may be evaluated in this article, or claim that may be made by its manufacturer, is not guaranteed or endorsed by the publisher.

Supplementary material

The Supplementary Material for this article can be found online at: https://www.frontiersin.org/articles/10.3389/fbioe.2022.965200/full#supplementary-material

References

Altman, D. G., and Bland, J. M. (1983). Measurement in medicine: The analysis of method comparison studies. *Statistician* 32, 307. doi:10.2307/2987937

Amidon, G. L., Lennernäs, H., Shah, V. P., and Crison, J. R. (1995). A theoretical basis for a biopharmaceutic drug classification: The correlation of *in vitro* drug product dissolution and *in vivo* bioavailability. *Pharm. Res.* 12, 413–420. doi:10.1023/a:1016212804288

Anderson, J. M., Van Itallie, C. M., Peterson, M. D., Stevenson, B. R., Carew, E. A., and Mooseker, M. S. (1989). ZO-1 mRNA and protein expression during tight junction assembly in Caco-2 cells. *J. Cell Biol.* 109, 1047–1056. doi:10.1083/jcb.109.3.1047

Artursson, P., and Karlsson, J. (1991). Correlation between oral drug absorption in humans and apparent drug permeability coefficients in human intestinal epithelial (Caco-2) cells. *Biochem. Biophysical Res. Commun.* 175, 880–885. doi:10.1016/0006-291X(91)91647-U

Ayehunie, S., Landry, T., Stevens, Z., Armento, A., Hayden, P., and Klausner, M. (2018). Human primary cell-based organotypic microtissues for modeling small intestinal drug absorption. *Pharm. Res.* 35, 72. doi:10.1007/s11095-018-2362-0

Balimane, P. V., Chong, S., and Morrison, R. A. (2000). Current methodologies used for evaluation of intestinal permeability and absorption. *J. Pharmacol. Toxicol. Methods* 44, 301–312. doi:10.1016/S1056-8719(00)00113-1

Basson, M. D., Turowski, G., and Emenaker, N. J. (1996). Regulation of human (Caco-2) intestinal epithelial cell differentiation by extracellular matrix proteins. *Exp. Cell Res.* 225, 301–305. doi:10.1006/excr.1996.0180

Beaurivage, C., Kanapeckaite, A., Loomans, C., Erdmann, K. S., Stallen, J., and Janssen, R. A. J. (2020). Development of a human primary gut-on-a-chip to model inflammatory processes. *Sci. Rep.* 10, 21475. doi:10.1038/s41598-020-78359-2

Beaurivage, C., Naumovska, E., Chang, Y. X., Elstak, E. D., Nicolas, A., Wouters, H., et al. (2019). Development of a gut-on-a-chip model for high throughput disease modeling and drug discovery. *Int. J. Mol. Sci.* 20, 5661. doi:10.3390/IJMS20225661

Béduneau, A., Tempesta, C., Fimbel, S., Pellequer, Y., Jannin, V., Demarne, F., et al. (2014). A tunable Caco-2/HT29-MTX co-culture model mimicking variable permeabilities of the human intestine obtained by an original seeding procedure. *Eur. J. Pharm. Biopharm.* 87, 290–298. doi:10.1016/j.ejpb.2014.03.017

Bein, A., Shin, W., Jalili-Firoozinezhad, S., Park, M. H., Sontheimer-Phelps, A., Tovaglieri, A., et al. (2018). Microfluidic organ-on-a-chip models of human intestine. *Cell. Mol. Gastroenterology Hepatology* 5, 659–668. doi:10.1016/j.jcmgh.2017.12.010

Billat, P.-A., Roger, E., Faure, S., and Lagarce, F. (2017). Models for drug absorption from the small intestine: Where are we and where are we going? *Drug Discov. Today* 22, 761–775. doi:10.1016/j.drudis.2017.01.007

Brayden, D. J., Hill, T. A., Fairlie, D. P., Maher, S., and Mrsny, R. J. (2020). Systemic delivery of peptides by the oral route: Formulation and medicinal chemistry approaches. *Adv. Drug Deliv. Rev.* 157, 2–36. doi:10.1016/j.addr.2020.05.007

Brock, R. (2014). The uptake of arginine-rich cell-penetrating peptides: Putting the puzzle together. *Bioconjug. Chem.* 25, 863–868. doi:10.1021/bc500017t

Brooks, H., Lebleu, B., and Vives, E. (2005). Tat peptide-mediated cellular delivery: Back to basics. *Adv. Drug Deliv. Rev.* 57, 559–577. doi:10.1016/j.addr.2004.12.001

Brown, T. D., Whitehead, K. A., and Mitragotri, S. (2020). Materials for oral delivery of proteins and peptides. *Nat. Rev. Mat.* 5, 127–148. doi:10.1038/s41578-019-0156-6

Buckley, S. T., Bækdal, T. A., Vegge, A., Maarbjerg, S. J., Pyke, C., Ahnfelt-Rønne, J., et al. (2018). Transcellular stomach absorption of a derivatized glucagon-like peptide-1 receptor agonist. *Sci. Transl. Med.* 10, eaar7047. doi:10.1126/scitranslmed.aar7047

Cao, L., McCaig, C. D., Scott, R. H., Zhao, S., Milne, G., Clevers, H., et al. (2014). Polarizing intestinal epithelial cells electrically through Ror2. *J. Cell Sci.* 127, 3233–3239. doi:10.1242/jcs.146357

Chen, S., Guo, F., Deng, T., Zhu, S., Liu, W., Zhong, H., et al. (2017). Eudragit S100-coated chitosan nanoparticles Co-loading tat for enhanced oral colon absorption of insulin. *AAPS PharmSciTech* 18, 1277–1287. doi:10.1208/s12249-016-0594-z

Cheng, L., Liu, T., Cui, X., Uss, A. S., and Cheng, K.-C. (2007). Development of *in vitro* pharmacokinetic screens using caco-2, human hepatocyte, and caco-2/human hepatocyte hybrid systems for the prediction of oral bioavailability in humans. *SLAS Discov.* 12, 1084–1091. doi:10.1177/1087057107308892

Dahlgren, D., Roos, C., Sjögren, E., and Lennernäs, H. (2015). Direct *in vivo* human intestinal permeability (peff) determined with different clinical perfusion and intubation methods. *J. Pharm. Sci.* 104, 2702–2726. doi:10.1002/jps.24258

Doherty, M. M., and Charman, W. N. (2002). The mucosa of the small intestine. *Clin. Pharmacokinet.* 41, 235–253. doi:10.2165/00003088-200241040-00001

Drucker, D. J. (2020). Advances in oral peptide therapeutics. *Nat. Rev. Drug Discov.* 19, 277–289. doi:10.1038/s41573-019-0053-0

Duchardt, F., Fotin-Mleczek, M., Schwarz, H., Fischer, R., and Brock, R. (2007). A comprehensive model for the cellular uptake of cationic cell-penetrating peptides. *Traffic* 8, 848–866. doi:10.1111/j.1600-0854.2007.00572.x

Englund, G., Rorsman, F., Rönnblom, A., Karlbom, U., Lazorova, L., Gråsjö, J., et al. (2006). Regional levels of drug transporters along the human intestinal tract: Co-expression of ABC and SLC transporters and comparison with caco-2 cells. *Eur. J. Pharm. Sci.* 29, 269–277. doi:10.1016/j.ejps.2006.04.010

Estudante, M., Morais, J. G., Soveral, G., and Benet, L. Z. (2013). Intestinal drug transporters: An overview. *Adv. Drug Deliv. Rev.* 65, 1340–1356. doi:10.1016/j.addr.2012.09.042

Frankel, A. D., and Pabo, C. O. (1988). Cellular uptake of the tat protein from human immunodeficiency virus. *Cell* 55, 1189–1193. doi:10.1016/0092-8674(88)90263-2

Gan, L.-S. L., and Thakker, D. R. (1997). Applications of the caco-2 model in the design and development of orally active drugs: elucidation of biochemical and physical barriers posed by the intestinal epithelium. *Adv. Drug Deliv. Rev.* 23, 77–98. doi:10.1016/S0169-409X(96)00427-9

Gerasimenko, T., Nikulin, S., Zakharova, G., Poloznikov, A., Petrov, V., Baranova, A., et al. (2020). Impedance spectroscopy as a tool for monitoring performance in 3D models of epithelial tissues. *Front. Bioeng. Biotechnol.* 7, 474. doi:10.3389/fbioe.2019.00474

Giacomini, K. M., Huang, S. M., Tweedie, D. J., Benet, L. Z., Brouwer, K. L. R., Chu, X., et al. (2010). Membrane transporters in drug development. *Nat. Rev. Drug Discov.* 9, 215–236. doi:10.1038/nrd3028

Gijzen, L., Marescotti, D., Raineri, E., Nicolas, A., Lanz, H. L., Guerrera, D., et al. (2020). An intestine-on-a-chip model of plug-and-play modularity to study inflammatory processes. *SLAS Technol.* 25, 585–597. doi:10.1177/2472630320924999

Gleeson, J. P., and McCartney, F. (2019). Striving towards the perfect *in vitro* oral drug absorption model. *Trends Pharmacol. Sci.* 40, 720–724. doi:10.1016/j.tips.2019.07.010

Goldberg, M., and Gomez-Orellana, I. (2003). Challenges for the oral delivery of macromolecules. *Nat. Rev. Drug Discov.* 2, 289–295. doi:10.1038/nrd1067

Gumbleton, M. (2005). Coming out of the dark: The evolving role of fluorescence imaging in drug delivery research. *Adv. Drug Deliv. Rev.* 57, 5–15. doi:10.1016/j.addr.2004.08.002

Guo, F., Ouyang, T., Peng, T., Zhang, X., Xie, B., Yang, X., et al. (2019). Enhanced oral absorption of insulin using colon-specific nanoparticles co-modified with amphiphilic chitosan derivatives and cell-penetrating peptides. *Biomater. Sci.* 7, 1493–1506. doi:10.1039/c8bm01485j

Halamoda-Kenzaoui, B., Vandebriel, R. J., Howarth, A., Siccardi, M., David, C. A. W., Liptrott, N. J., et al. (2021). Methodological needs in the quality and safety characterisation of nanotechnology-based health products: Priorities for method development and standardisation. *J. Control. Release* 336, 192–206. doi:10.1016/J.JCONREL.2021.06.016

Harwood, M. D., Achour, B., Neuhoff, S., Russell, M. R., Carlson, G., and Warhurst, G. (2016). *In vitro*-in vivo extrapolation scaling factors for intestinal P-glycoprotein and Breast cancer resistance protein: Part I: A cross-laboratory comparison of transporter-protein abundances and relative expression factors in human intestine and caco-2 cells. *Drug Metabolism Dispos.* 44, 297–307. doi:10.1124/dmd.115.067371

Hedegaard, S. F., Derbas, M. S., Lind, T. K., Kasimova, M. R., Christensen, M. V., Michaelsen, M. H., et al. (2018). Fluorophore labeling of a cell-penetrating peptide significantly alters the mode and degree of biomembrane interaction. *Sci. Rep.* 8, 6327. doi:10.1038/s41598-018-24154-z

Hidalgo, I. J., Raub, T. J., and Borchardt, R. T. (1989). Characterization of the human colon carcinoma cell line (Caco-2) as a model system for intestinal epithelial permeability. *Gastroenterology* 96, 736–749. doi:10.1016/S0016-5085(89)80072-1

Hilgendorf, C., Spahn-Langguth, H., Regårdh, C. G., Lipka, E., Amidon, G. L., and Langguth, P. (2000). Caco-2 versus caco-2/HT29-MTX Co-cultured cell lines: Permeabilities via diffusion, inside- and outside-directed carrier-mediated transport. *J. Pharm. Sci.* 89, 63–75. doi:10.1002/(SICI)1520-6017(200001)89:1<63:AID-JPS7>3.0.CO;2-6

Hubatsch, I., Ragnarsson, E. G. E., and Artursson, P. (2007). Determination of drug permeability and prediction of drug absorption in Caco-2 monolayers. *Nat. Protoc.* 2, 2111–2119. doi:10.1038/nprot.2007.303

Hughes, L. D., Rawle, R. J., and Boxer, S. G. (2014). Choose your label wisely: Water-soluble fluorophores often interact with lipid bilayers. *PLOS ONE* 9, e87649. doi:10.1371/JOURNAL.PONE.0087649

Huh, D., Hamilton, G. A., and Ingber, D. E. (2011). From 3D cell culture to organs-on-chips. *Trends Cell Biol.* 21, 745–754. doi:10.1016/j.tcb.2011.09.005

Kamei, N., Morishita, M., Eda, Y., Ida, N., Nishio, R., and Takayama, K. (2008). Usefulness of cell-penetrating peptides to improve intestinal insulin absorption. *J. Control. Release* 132, 21–25. doi:10.1016/j.jconrel.2008.08.001

Karlsson, J., Wikman, A., and Artursson, P. (1993). The mucus layer as a barrier to drug absorption in monolayers of human intestinal epithelial HT29-H goblet cells. *Int. J. Pharm.* 99, 209–218. doi:10.1016/0378-5173(93)90363-K

Kim, H. J., Huh, D., Hamilton, G., and Ingber, D. E. (2012). Human gut-on-a-chip inhabited by microbial flora that experiences intestinal peristalsis-like motions and flow. *Lab. Chip* 12, 2165. doi:10.1039/c2lc40074j

Kristensen, M., and Nielsen, H. M. (2016). Cell-penetrating peptides as carriers for oral delivery of biopharmaceuticals. *Basic Clin. Pharmacol. Toxicol.* 118, 99–106. doi:10.1111/bcpt.12515

Langerak, N., Ahmed, H. M. M., Li, Y., Middel, I. R., Eslami Amirabadi, H., Malda, J., et al. (2020). A theoretical and experimental study to optimize cell differentiation in a novel intestinal chip. *Front. Bioeng. Biotechnol.* 8, 763. doi:10.3389/fbioe.2020.00763

Langguth, P., Bohner, V., Heizmann, J., Merkle, H. P., Wolffram, S., Amidon, G. L., et al. (1997). The challenge of proteolytic enzymes in intestinal peptide delivery. *J. Control. Release* 46, 39–57. doi:10.1016/S0168-3659(96)01586-6

Larsen, J. B., Taebnia, N., Dolatshahi-Pirouz, A., Eriksen, A. Z., Hjørringgaard, C., Kristensen, K., et al. (2021). Imaging therapeutic peptide transport across intestinal barriers. *RSC Chem. Biol.* 2, 1115–1143. doi:10.1039/D1CB00024A

Lennernäs, H., Nylander, S., and Ungell, A. L. (1997). Jejunal permeability: a comparison between the ussing chamber technique and the single-pass perfusion in humans. *Pharm. Res.* 14, 667–671. doi:10.1023/a:1012121632357

Li, C., Liu, T., Cui, X., Uss, A. S., and Cheng, K.-C. (2007). Development of *in vitro* pharmacokinetic screens using caco-2, human hepatocyte, and caco-2/human hepatocyte hybrid systems for the prediction of oral bioavailability in humans. *SLAS Discov.* 12, 1084–1091. doi:10.1177/1087057107308892

Lipka, E., and Amidon, G. L. (1999). Setting bioequivalence requirements for drug development based on preclinical data: optimizing oral drug delivery systems. *J. Control. Release* 62, 41–49. doi:10.1016/S0168-3659(99)00022-X

Lönn, P., Kacsinta, A. D., Cui, X.-S., Hamil, A. S., Kaulich, M., Gogoi, K., et al. (2016). Enhancing endosomal escape for intracellular delivery of macromolecular biologic therapeutics. *Sci. Rep.* 6, 32301. doi:10.1038/srep32301

Maher, S., Geoghegan, C., and Brayden, D. J. (2021). Intestinal permeation enhancers to improve oral bioavailability of macromolecules: reasons for low efficacy in humans. *Expert Opin. Drug Deliv.* 18, 273–300. doi:10.1080/17425247.2021.1825375

Masaoka, Y., Tanaka, Y., Kataoka, M., Sakuma, S., and Yamashita, S. (2006). Site of drug absorption after oral administration: Assessment of membrane permeability and luminal concentration of drugs in each segment of gastrointestinal tract. *Eur. J. Pharm. Sci.* 29, 240–250. doi:10.1016/j.ejps.2006.06.004

Maubon, N., Le Vee, M., Fossati, L., Audry, M., Le Ferrec, E., Bolze, S., et al. (2007). Analysis of drug transporter expression in human intestinal Caco-2 cells by real-time PCR. *Fundam. Clin. Pharmacol.* 21, 659–663. doi:10.1111/j.1472-8206.2007.00550.x

Mechanism matters (2010). Mechanism matters. *Nat. Med.* 16, 347. doi:10.1038/nm0410-347

Morris, M. C., Depollier, J., Mery, J., Heitz, F., and Divita, G. (2001). A peptide carrier for the delivery of biologically active proteins into mammalian cells. *Nat. Biotechnol.* 19, 1173–1176. doi:10.1038/nbt1201-1173

Naumovska, E., Aalderink, G., Wong Valencia, C., Kosim, K., Nicolas, A., Brown, S., et al. (2020). Direct on-chip differentiation of intestinal tubules from induced pluripotent stem cells. *Int. J. Mol. Sci.* 21, 4964. doi:10.3390/ijms21144964

Niazi, S. K. (2019). "Waiver of *in vivo* bioavailability and bioequivalence studies for immediate-release solid oral dosage forms based on a biopharmaceutics classification system," in *Handbook of pharmaceutical manufacturing formulations*. Third Edition. Boca Raton, FL: CRC Press, 27–35. doi:10.1201/9781315103389-2

Pimenta, J., Ribeiro, R., Almeida, R., Costa, P. F., da Silva, M. A., and Pereira, B. (2022). Organ-on-Chip approaches for intestinal 3D *in vitro* modeling. *Cell. Mol. Gastroenterol. Hepatol.* 13, 351–367. doi:10.1016/J.JCMGH.2021.08.015

Pontier, C., Pachot, J., Botham, R., Lenfant, B., and Arnaud, P. (2001). HT29-MTX and Caco-2/TC7 monolayers as predictive models for human intestinal absorption: Role of the mucus layer. *J. Pharm. Sci.* 90, 1608–1619. doi:10.1002/jps.1111

Richard, J. P., Melikov, K., Vives, E., Ramos, C., Verbeure, B., Gait, M. J., et al. (2003). Cell-penetrating peptides: A reevaluation of the mechanism of cellular uptake. *J. Biol. Chem.* 278, 585–590. doi:10.1074/jbc.M209548200

Sahay, G., Alakhova, D. Y., and Kabanov, A. V. (2010). Endocytosis of nanomedicines. *J. Control. Release* 145, 182–195. doi:10.1016/J.JCONREL.2010.01.036

Sambuy, Y., De Angelis, I., Ranaldi, G., Scarino, M. L., Stammati, A., and Zucco, F. (2005). The caco-2 cell line as a model of the intestinal barrier: Influence of cell and culture-related factors on caco-2 cell functional characteristics. *Cell Biol. Toxicol.* 21, 1–26. doi:10.1007/s10565-005-0085-6

Schneider, H., Pelaseyed, T., Svensson, F., and Johansson, M. E. V. (2018). Study of mucin turnover in the small intestine by *in vivo* labeling. *Sci. Rep.* 8, 5760. doi:10.1038/s41598-018-24148-x

Schutgens, F., Rookmaaker, M. B., Margaritis, T., Rios, A., Ammerlaan, C., Jansen, J., et al. (2019). Tubuloids derived from human adult kidney and urine for personalized disease modeling. *Nat. Biotechnol.* 37, 303–313. doi:10.1038/s41587-019-0048-8

Shemesh, J., Jalilian, I., Shi, A., Heng Yeoh, G., Knothe Tate, M. L., and Ebrahimi Warkiani, M. (2015). Flow-induced stress on adherent cells in microfluidic devices. *Lab. Chip* 15, 4114–4127. doi:10.1039/C5LC00633C

Shin, M. K., Kim, S. K., and Jung, H. (2011). Integration of intra- and extravasation in one cell-based microfluidic chip for the study of cancer metastasis. *Lab. Chip* 11, 3880. doi:10.1039/c1lc20671k

Simon-Assmann, P., Turck, N., Sidhoum-Jenny, M., Gradwohl, G., and Kedinger, M. (2007). *In vitro* models of intestinal epithelial cell differentiation. *Cell Biol. Toxicol.* 23, 241–256. doi:10.1007/s10565-006-0175-0

Sjöberg, Å., Lutz, M., Tannergren, C., Wingolf, C., Borde, A., and Ungell, A. L. (2013). Comprehensive study on regional human intestinal permeability and prediction of fraction absorbed of drugs using the Ussing chamber technique. *Eur. J. Pharm. Sci.* 48, 166–180. doi:10.1016/j.ejps.2012.10.007

Skolnik, S., Lin, X., Wang, J., Chen, X.-H., He, T., and Zhang, B. (2010). Towards prediction of *in vivo* intestinal absorption using a 96-well caco-2 assay. *J. Pharm. Sci.* 99, 3246–3265. doi:10.1002/jps.22080

Srinivasan, B., Kolli, A. R., Esch, M. B., Abaci, H. E., Shuler, M. L., and Hickman, J. J. (2015). TEER measurement techniques for *in vitro* barrier model systems. *SLAS Technol.* 20, 107–126. doi:10.1177/2211068214561025

Szeto, H. H., Schiller, P. W., Zhao, K., and Luo, G. (2005). Fluorescent dyes alter intracellular targeting and function of cell-penetrating tetrapeptides. *FASEB J.* 19, 118–120. doi:10.1096/fj.04-1982fje

Takenaka, T., Harada, N., Kuze, J., Chiba, M., Iwao, T., and Matsunaga, T. (2016). Application of a human intestinal epithelial cell monolayer to the prediction of oral drug absorption in humans as a superior alternative to the caco-2 cell monolayer. *J. Pharm. Sci.* 105, 915–924. doi:10.1016/j.xphs.2015.11.035

Time to deliver (2014). Time to deliver. *Nat. Biotechnol.* 32, 961. doi:10.1038/nbt.3045

Trietsch, S. J., Naumovska, E., Kurek, D., Setyawati, M. C., Vormann, M. K., Wilschut, K. J., et al. (2017). Membrane-free culture and real-time barrier integrity assessment of perfused intestinal epithelium tubes. *Nat. Commun.* 8, 262. doi:10.1038/s41467-017-00259-3

Tünnemann, G., Martin, R. M., Haupt, S., Patsch, C., Edenhofer, F., and Cardoso, M. C. (2006). Cargo-dependent mode of uptake and bioavailability of TAT-containing proteins and peptides in living cells. *FASEB J.* 20, 1775–1784. doi:10.1096/fj.05-5523com

Tünnemann, G., Ter-Avetisyan, G., Martin, R. M., Stöckl, M., Herrmann, A., and Cardoso, M. C. (2008). Live-cell analysis of cell penetration ability and toxicity of oligo-arginines. *J. Pept. Sci.* 14, 469–476. doi:10.1002/psc.968

Twarog, C., Liu, K., O'Brien, P. J., Dawson, K. A., Fattal, E., Illel, B., et al. (2020). A head-to-head caco-2 assay comparison of the mechanisms of action of the intestinal permeation enhancers: SNAC and sodium caprate (C10). *Eur. J. Pharm. Biopharm.* 152, 95–107. doi:10.1016/j.ejpb.2020.04.023

Vaessen, S. F. C., van Lipzig, M. M. H., Pieters, R. H. H., Krul, C. A. M., Wortelboer, H. M., and van de Steeg, E. (2017). Regional expression levels of drug transporters and metabolizing enzymes along the pig and human intestinal tract and comparison with caco-2 cells. *Drug Metab. Dispos.* 45, 353–360. doi:10.1124/dmd.116.072231

von Erlach, T., Saxton, S., Shi, Y., Minahan, D., Reker, D., Javid, F., et al. (2020). Robotically handled whole-tissue culture system for the screening of oral drug formulations. *Nat. Biomed. Eng.* 4, 544–559. doi:10.1038/s41551-020-0545-6

Wadia, J. S., Stan, R. V., and Dowdy, S. F. (2004). Transducible TAT-HA fusogenic peptide enhances escape of TAT-fusion proteins after lipid raft macropinocytosis. *Nat. Med.* 10, 310–315. doi:10.1038/nm996

Watson, P. (2005). Intracellular trafficking pathways and drug delivery: Fluorescence imaging of living and fixed cells. *Adv. Drug Deliv. Rev.* 57, 43–61. doi:10.1016/j.addr.2004.05.003

Wong, C. Y., Al-Salami, H., and Dass, C. R. (2020). Cellular assays and applied technologies for characterisation of orally administered protein nanoparticles: a systematic review. *J. Drug Target.* 28, 585–599. doi:10.1080/1061186x.2020.1726356

Yilmaz, D., Sharp, P. S., Main, M. J., and Simpson, P. B. (2022). Advanced molecular imaging for the characterisation of complex medicines. *Drug Discov. Today* 27, 1716–1723. doi:10.1016/J.DRUDIS.2022.03.001

Youhanna, S., and Lauschke, V. M. (2021). The past, present and future of intestinal *in vitro* cell systems for drug absorption studies. *J. Pharm. Sci.* 110, 50–65. doi:10.1016/j.xphs.2020.07.001

Zaderer, V., Hermann, M., Lass-Flörl, C., Posch, W., and Wilflingseder, D. (2019). Turning the world upside-down in cellulose for improved culturing and imaging of respiratory challenges within a human 3D model. *Cells* 8, 1292. doi:10.3390/cells8101292

Zhu, S., Chen, S., Gao, Y., Guo, F., Li, F., Xie, B., et al. (2016). Enhanced oral bioavailability of insulin using PLGA nanoparticles co-modified with cell-penetrating peptides and Engrailed secretion peptide (Sec). *Drug Deliv.* 23, 1980–1991. doi:10.3109/10717544.2015.1043472

Frontiers in
Bioengineering and Biotechnology

Accelerates the development of therapies, devices, and technologies to improve our lives

A multidisciplinary journal that accelerates the development of biological therapies, devices, processes and technologies to improve our lives by bridging the gap between discoveries and their application.

Discover the latest Research Topics

See more →

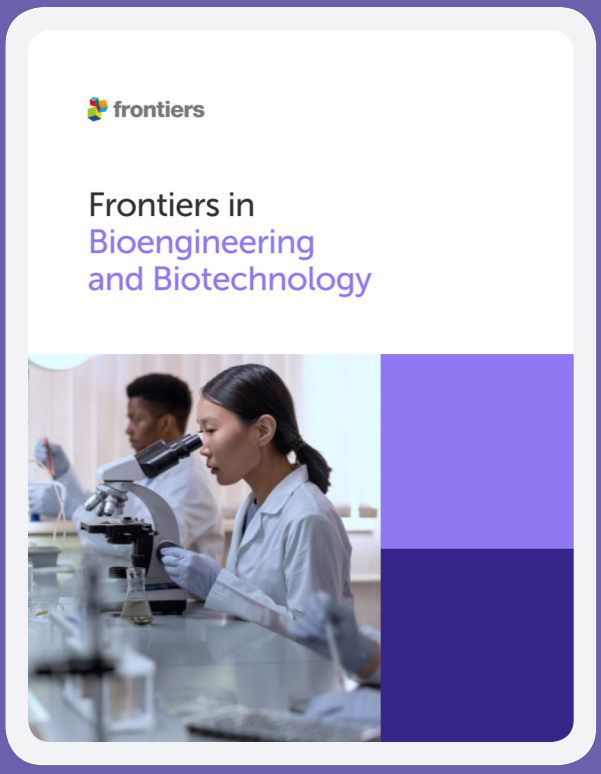

Frontiers

Avenue du Tribunal-Fédéral 34
1005 Lausanne, Switzerland
frontiersin.org

Contact us

+41 (0)21 510 17 00
frontiersin.org/about/contact